

# Integrative computational modeling of calcium handling and cardiac arrhythmias

Citation for published version (APA):

Sutanto, H. (2021). *Integrative computational modeling of calcium handling and cardiac arrhythmias*. [Doctoral Thesis, Maastricht University]. Maastricht University. <https://doi.org/10.26481/dis.20210115hs>

## Document status and date:

Published: 01/01/2021

## DOI:

[10.26481/dis.20210115hs](https://doi.org/10.26481/dis.20210115hs)

## Document Version:

Publisher's PDF, also known as Version of record

## Please check the document version of this publication:

- A submitted manuscript is the version of the article upon submission and before peer-review. There can be important differences between the submitted version and the official published version of record. People interested in the research are advised to contact the author for the final version of the publication, or visit the DOI to the publisher's website.
- The final author version and the galley proof are versions of the publication after peer review.
- The final published version features the final layout of the paper including the volume, issue and page numbers.

[Link to publication](#)

## General rights

Copyright and moral rights for the publications made accessible in the public portal are retained by the authors and/or other copyright owners and it is a condition of accessing publications that users recognise and abide by the legal requirements associated with these rights.

- Users may download and print one copy of any publication from the public portal for the purpose of private study or research.
- You may not further distribute the material or use it for any profit-making activity or commercial gain
- You may freely distribute the URL identifying the publication in the public portal.

If the publication is distributed under the terms of Article 25fa of the Dutch Copyright Act, indicated by the "Taverne" license above, please follow below link for the End User Agreement:

[www.umlib.nl/taverne-license](http://www.umlib.nl/taverne-license)

## Take down policy

If you believe that this document breaches copyright please contact us at:

[repository@maastrichtuniversity.nl](mailto:repository@maastrichtuniversity.nl)

providing details and we will investigate your claim.

# **Integrative Computational Modeling of Calcium Handling and Cardiac Arrhythmias**

**Henry Sutanto  
2021**

*“No greater opportunity, responsibility, or obligation can fall to the lot of a human being than to become a physician. In the care of the suffering he needs technical skill, scientific knowledge, and human understanding. He who uses these with courage, with humility, and with wisdom will provide a unique service for his fellow man, and will build an enduring edifice of character within himself. The physician should ask of his destiny no more than this; he should be content with no less.”*

**Tinsley Randolph Harrison**  
(1900-1978)

# **Integrative Computational Modeling of Calcium Handling and Cardiac Arrhythmias**

**DISSERTATION**

To obtain the degree of Doctor  
at Maastricht University,  
on the authority of the Rector Magnificus,  
Prof. dr. Rianne M. Letschert,  
in accordance with the decision of the Board of Deans,  
to be defended in public  
on Friday, January 15<sup>th</sup>, 2021, at 16.00

by  
**Henry Sutanto**

**Promotor:**

Assoc. Prof. Jordi Heijman  
Prof. Harry J.G.M. Crijns  
Prof. Paul G.A. Volders

**Assessment Committee:**

Prof. Frits W. Prinzen (Maastricht – NL) - Chair  
Prof. Ralf L.M. Peeters (Maastricht – NL)  
Dr. Dominik Linz (Maastricht – NL)  
Prof. Antonio Zaza (Milan – IT)  
Prof. Stefano Severi (Bologna – IT)

The research in this thesis was supported by the Netherlands Organization for Scientific Research / Nederlandse Organisatie voor Wetenschappelijk Onderzoek (NWO) Veni grant to Jordi Heijman (No. 91616057). Financial support for the printing of this thesis by Stichting CinC 2018 is gratefully acknowledged.

© Henry Sutanto, 2021  
ISBN 978-94-6423-105-2

Cover art and design © Henry Sutanto, 2021



# Table of Contents

---

---

List of abbreviations	7
<b>CHAPTERS</b>	
<b>1 General Introduction</b>	<b>11</b>
<i>Front Young Minds.</i> 7:65. doi: 10.3389/frym.2019.00065	
<b>2 Cardiomyocyte calcium handling in health and disease: insights from <i>in vitro</i> and <i>in silico</i> studies</b>	<b>19</b>
<i>Prog Biophys Mol Biol.</i> doi: 10.1016/j.pbiomolbio.2020.02.008	
<b>3 The subcellular distribution of ryanodine receptors and L-type calcium channels modulates calcium transient properties and spontaneous calcium release events in atrial cardiomyocytes</b>	<b>53</b>
<i>Front Physiol.</i> 9:1108. doi: 10.3389/fphys.2018.01108	
<b>4 Computational modeling of subcellular calcium-handling identified calcium-handling abnormalities in patients with post-operative atrial fibrillation</b>	<b>91</b>
<i>Circ Res.</i> 127:1036-1055. doi: 10.1161/CIRCRESAHA.120.316710	
<b>5 Calcium-dependent regulation of cardiac ionic currents modulates atrial electrophysiology and arrhythmogenesis: insights from computational modeling</b>	<b>105</b>
<i>In Preparation</i>	
<b>6 Acute effects of alcohol on cardiac electrophysiology and arrhythmogenesis: insights from multiscale <i>in silico</i> analyses</b>	<b>135</b>
<i>J Mol Cell Cardiol.</i> 146:69-83. doi: 10.1016/j.yjmcc.2020.07.007	
<b>7 Maastricht antiarrhythmic drug evaluator (MANTA): A computational tool for better understanding of antiarrhythmic drugs</b>	<b>167</b>
<i>Pharmacol Res.</i> 148:104444. doi: 10.1016/j.phrs.2019.104444	
<b>8 Beta-adrenergic receptor stimulation modulates the cellular proarrhythmic effects of chloroquine and azithromycin</b>	<b>229</b>
<i>Front Physiol.</i> 11:587709. doi: 10.3389/fphys.2020.587709	
<b>9 Discussion</b>	<b>253</b>
<b>Summary</b>	<b>269</b>

<b>Impact</b>	<b>275</b>
<b>Acknowledgements</b>	<b>283</b>
<b>Curriculum vitae, publications and awards</b>	<b>289</b>
<b>Appendices</b>	<b>297</b>
<b>References</b>	<b>307</b>

---

---

## **List of abbreviations**

---

---

### **A**

AAD	Antiarrhythmic drug
ACE2	Angiotensin converting enzyme type 2
AF	Atrial fibrillation
AP	Action potential
APD	Action potential duration
AZM	Azithromycin

### **C**

Ca <sup>2+</sup>	Calcium
[Ca <sup>2+</sup> ] <sub>o</sub>	Extracellular calcium concentration
cAF	Long-standing persistent ('chronic') AF
CaM	Calmodulin
CaMKII	Calcium/calmodulin-dependent protein kinase-II
cAMP	Cyclic adenosine monophosphate
CASQ2	Calsequestrin
CaT	Calcium transient
CHO	Chinese hamster ovary
CICR	Calcium-induced calcium release
CoV	Coronavirus
COVID-19	Coronavirus disease 2019
CPVT	Catecholaminergic polymorphic ventricular tachycardia
CQ	Chloroquine
CRP	C-reactive protein
CRU	Calcium-release unit
CV	Conduction velocity

### **D**

DAD	Delayed afterdepolarization
DAG	Diacylglycerol
DREAM	Downstream regulatory element agonist modulator

### **E**

E-C	Excitation-contraction
EAD	Early afterdepolarization
Endo	Endocardium
Epac	Exchange-protein activated by cAMP
Epi	Epicardium
ERP	Effective refractory period

### **F**

FDA	the U.S. Food and Drug Administration
-----	---------------------------------------

## *List of abbreviations*

FKBP                    FK506-binding protein

### **H**

HDAC                    Histone deacetylase complex

HEK                      Human embryonic kidney

HF                        Heart failure

### **I**

IC<sub>50</sub>                    Half-maximal inhibitory concentration

I<sub>Ca,L</sub>                    L-type calcium current

I<sub>K1</sub>                        Inward-rectifier potassium current

I<sub>K,ACh</sub>                    Acetylcholine-activated inward-rectifier potassium current

I<sub>Kr</sub>                        Rapid delayed-rectifier potassium current

I<sub>Ks</sub>                        Slow delayed-rectifier potassium current

I<sub>Kur</sub>                      Ultra-rapid delayed-rectifier potassium current

IL                         Interleukin

I<sub>Na</sub>                        Fast sodium current

I<sub>NCX</sub>                    Sodium/calcium-exchange current

IP<sub>3</sub>                      Inositol triphosphate

ISO                        Isoproterenol

I<sub>to</sub>                        Transient-outward potassium current

IQR                        Interquartile range

### **K**

K<sup>+</sup>                        Potassium

[K<sup>+</sup>]<sub>o</sub>                    Extracellular potassium concentration

### **L**

LA                        Left atrium

LTCC                    L-type calcium channel

LV                        Left ventricle

### **M**

MANTA                    Maastricht ANTiarrhythmic drug evAluator

MI                        Myocardial infarction

Mid                        Mid-myocardium

MRI                        Magnetic resonance imaging

MyBP-C                    Myosin binding protein-C

### **N**

Na<sup>+</sup>                        Sodium

[Na<sup>+</sup>]<sub>o</sub>                    Extracellular sodium concentration

NCX1                    Sodium-calcium exchanger type-1

NFAT                      Nuclear factor of activated T-cells

NLRP3                    NACHT, LRR, and PYD domains containing protein-3

**P**

pAF	Paroxysmal atrial fibrillation
PDE	Phosphodiesterase
PKA	Protein kinase-A
PKC	Protein kinase-C
PKP2	Plakophilin-2
PLM	Phospholemman
PLN	Phospholamban
PMCA	Plasmalemmal calcium-ATPase
POAF	Post-operative atrial fibrillation
PP1	Protein phosphatase 1

**R**

RA	Right atrium
RF	Repolarization failure
RMP	Resting membrane potential
ROS	Reactive oxygen species
RyR2	Ryanodine Receptor type-2

**S**

SAC	Stretch-activated ion channel
SARS	Severe acute respiratory syndrome
SCaE	Spontaneous calcium release event
SERCA2a	Sarco/endoplasmic reticulum calcium-ATPase 2a
SLN	Sarcolipin
SK channel	Small-conductance calcium-activated potassium channel
SOICR	Store overload-induced calcium release
SR	Sarcoplasmic reticulum

**T**

TA	Triggered activity
TNF- $\alpha$	Tumor necrosis factor- $\alpha$
TRPC channel	Transient receptor potential canonical channel

$$\frac{dV_m}{dt} = -\frac{1}{C_m} * I$$

$$y_{Ca,L} = \frac{1 - I_{V,\infty}}{I_{V,\tau}}$$

### The function of the heart

*"The heart is the household divinity which, discharging its function, nourishes, cherishes, quickens the whole body, and is indeed the foundation of life, the source of all action."*

**Sir William Harvey**

(1578 - 1657)



### The organ by number

*"Numero pondere et mensura Deus omnia condidit"*  
(God created everything by number, weight and measure)

**Sir Isaac Newton**

(1642 - 1727)



### Cell: the core of life science

*"The cell concept is the axis around which the whole of modern science of life revolves"*

**Paul Ehrlich**

(1854 - 1915)



### The art of scientific programming

*"Programming is a skill best acquired by practice and example rather than from books. Codes are a puzzle. A game, just like any other game."*

**Sir Alan Mathison Turing**

(1912 - 1954)

$$ACT_{\tau} = 0.59$$

# Chapter 1

## General Introduction

Adapted from: *The role of calcium in the human heart: with great power comes great responsibility*

H. Sutanto and J. Heijman  
*Front Young Minds*, 7:65.



$$\frac{dV}{dt} = \frac{I_{stim} - (I_K + I_{Na} + I_{leak})}{C_m}$$



## 1.1 Background

### 1.1.1 Why is calcium so important for the heart?

Calcium is present in most foods, notably dairy products, such as milk and cheese, and is often found in small fish and some vegetables. It has been known for a long time that calcium is beneficial for the strength of our bones. In addition, scientists have discovered that calcium also plays an important role in the heart (**Figure 1.1**). The heart beats more than 2 billion times during an average person's lifetime to circulate the blood, which is needed to provide energy to every part of the body. The heart consists, among many other things, of 3 billion heart muscle cells that squeeze together (“contract”) during each heartbeat and together are responsible for the pumping function of the heart. To make sure that each cell contracts at the right moment, the heart uses an electrical signal that moves from cell to cell, much like a wave in a stadium, where the activity of one person activates their neighbor. Research during the last decades has revealed that calcium particles are responsible for the link between electrical activation and mechanical contraction (**Figure 1.1**). Calcium particles, which have an electrical charge, enter the heart muscle cells during each beat and contribute to the electrical signal. In addition, these calcium particles initiate contraction by binding to specialized machinery within the cell. When the calcium binds, the machinery starts to move and makes the cell squeeze together. On the other hand, when the calcium particles are removed from the heart cells, this triggers relaxation, allowing the heart to be refilled with blood before the start of the next heartbeat. Thus, without calcium, our hearts would stop beating immediately, which was already shown experimentally by Dr. Sydney Ringer in the early 1880s.

### 1.1.2 The heart muscle cell: a house with multiple doors and chambers

A heart muscle cell is like a big house with multiple doors and chambers (**Figure 1.2**). Calcium particles can flow in and out of the cell through gate-like structures named ion channels (1). These ion channels help the cell to control the amount of calcium inside of it. In addition to the supply of calcium from outside the cell, there is a big chamber inside the cell, named the sarcoplasmic reticulum, that stores most of the calcium required for heart contraction. The sarcoplasmic reticulum chamber also has entrance and exit doors for calcium. The entrance doors to the sarcoplasmic reticulum are named SERCA and the exit doors are named ryanodine receptors. The calcium that enters the heart cell through the calcium ion channel activates the ryanodine receptor to release enough calcium from the sarcoplasmic reticulum to initiate heart muscle contraction. This is done by binding to another structure, named troponin, inside the heart muscle cell. During relaxation, calcium has to be detached from troponin and expelled out of the cell or stored back inside the sarcoplasmic reticulum.

In addition to the calcium doors, heart muscle cells are also equipped with other doors responsible for the movements of other particles in and out of the cell, such as sodium, potassium, and chloride. Recently, scientists have found that calcium can regulate the activity of these other doors, making them easier or harder to open, highlighting the large responsibility of calcium in heart muscle cells (2).

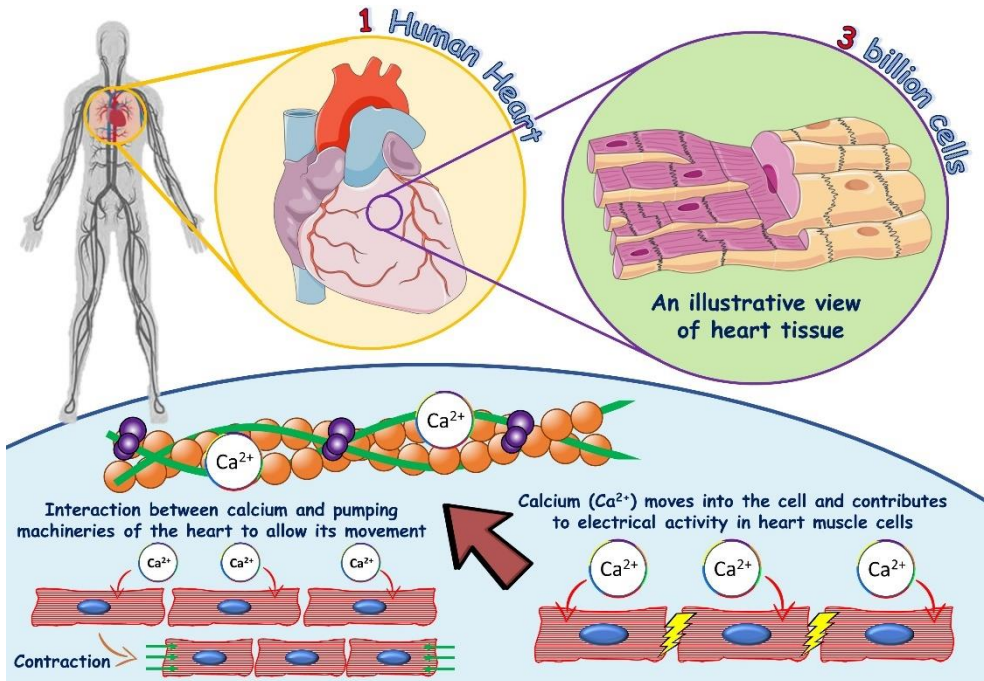


**Figure 1.1:** The role of calcium in heart muscle cells. One human heart consists of more than three billion heart muscle cells and each cell contains its own machinery to provide contraction and relaxation of the heart muscle. The blue shaded area shows the important role of calcium in heart muscle cells. Calcium binds to the troponin complex in the cells (indicated by the large red arrow), which makes the cells squeeze together, a process called excitation-contraction coupling (shown by green arrows on the left-hand side of the blue shaded area). In addition, calcium contributes to the electrical signal which moves from cell to cell to produce a uniform contraction (shown on the right-hand side of the blue shaded area).

### 1.1.3 What happens if calcium gets out of control?

In some cases, the doors controlling the movement of calcium malfunction, causing too much or too little calcium to enter the cell. Sometimes, this malfunction is caused by advancing age or other diseases. Alternatively, changes/variations in our genes (called genetic mutations) can change the shape of the ion channel which, in extreme cases, may prevent the channel from opening or closing properly. This can lead to abnormal electrical signals, which may cause a group of heart diseases called heart rhythm disorders.

Heart rhythm disorders happen when the electrical communication between cells becomes uncoordinated or when groups of cells spontaneously produce additional electrical signals. As we previously mentioned, electrical communication in the heart is similar to the wave in a soccer stadium, which also relies on clear communication. If the lights are off and the spectators cannot see each other, communication will not happen and it will not be possible to create a nice wave. The wave also only works properly if people move only when the wave reaches their seat. Uncoordinated, chaotic electrical

activity of the heart is called fibrillation. Fibrillation causes the heart to pump blood ineffectively, leading to a lower energy supply to a person's organs.

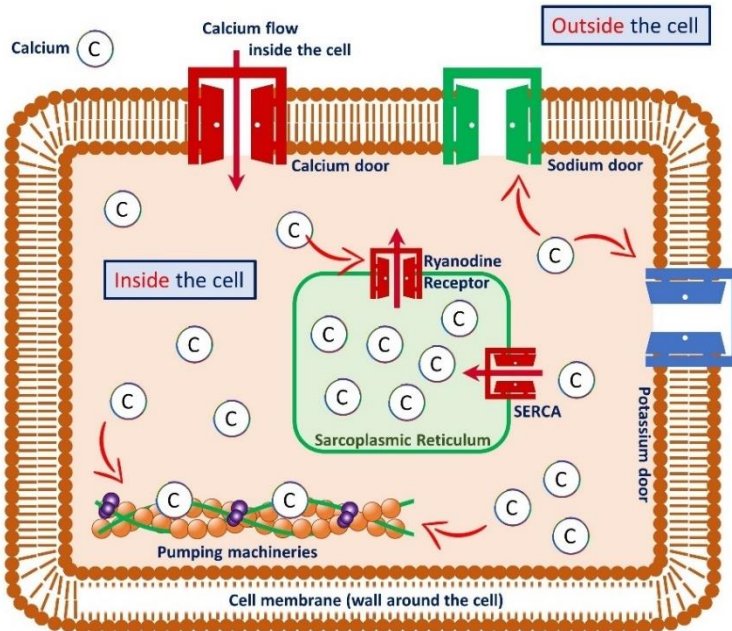


**Figure 1.2: A heart muscle cell and its components.** Calcium enters the cell through “doors” called ion channels and interacts with various components of the cell. For example, calcium regulates the opening and closing of sodium and potassium doors and ryanodine receptors, and it binds to the troponin complex to make the heart cell squeeze together (“contract”), which produces the pumping function of the heart. In heart muscle cells, most of the calcium is stored inside a chamber named the sarcoplasmic reticulum. The calcium in the sarcoplasmic reticulum is released during heart muscle contraction and transported back inside the sarcoplasmic reticulum during relaxation. Red arrows indicate the movement/flow of calcium from one place to another.

In addition, abnormal calcium movement may directly impair contraction or relaxation of the heart, hindering the normal pump function. Under these conditions, the heart cells can eventually become “tired” and fail. Heart failure can cause a wide range of problems, from mild (coughing and tiredness) to severe (shortness of breath and organ swelling). This, of course, will reduce a person's productivity. Recently, scientists found that calcium is strongly associated with the progression of heart failure. Heart failure also makes the occurrence of potentially deadly heart rhythm disorders more likely (3).

#### **1.1.4 What has been done by scientists so far to better understand calcium in the human heart?**

Given the impact of heart disease, we may wonder what scientists can do to stop those diseases from occurring. For several decades, scientists have been studying the role of calcium in heart muscle cells. They now know that in some heart diseases, such as fibrillation and heart failure, abnormalities in calcium regulation play a major role (2).

Nowadays, scientists can study calcium movement by taking single heart muscle cells from animals or patients and investigating these single cells using a sophisticated method called patch clamp, which makes it possible to measure the electrical signals that pass through specific ion channels. This is done by attaching a very small glass needle (more than 20 times smaller than a single hair) to the surface of the cell. Scientists can also measure the number and location of channels inside the heart cell by attaching light-emitting indicators to the channels, which can be visualized under a microscope. More recently, scientists have started to use computer models to put all these data together, to help them predict the effect that changes in calcium regulation will have within heart cells (4).

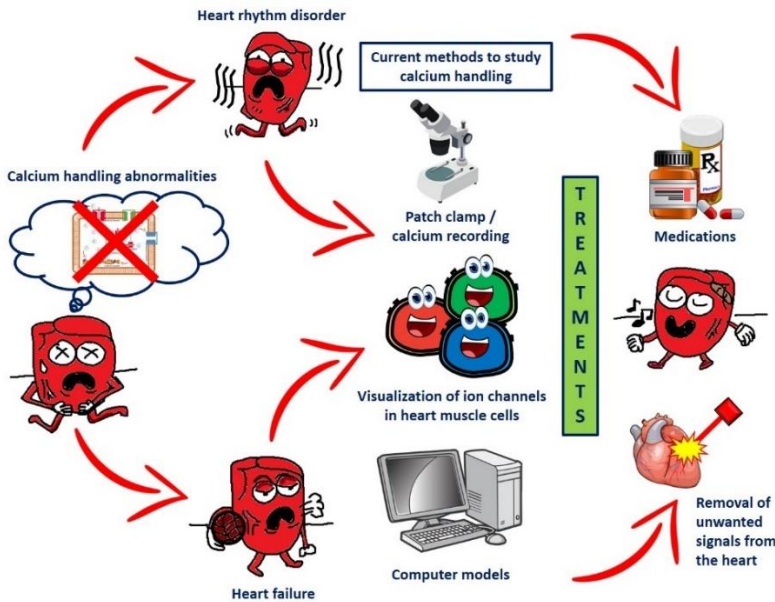


**Figure 1.3:** The effects of calcium-handling abnormalities in the heart and currently available methods to detect and treat these problems. Problems with calcium handling in heart muscle cells (shown on the left) may result in heart rhythm disorders and/or heart failure (first set of red arrows). Several methods are currently available to study the role of calcium in these diseases, including calcium recording, protein staining/coloring, and analysis with computer models (shown in the third column). Using these methods, new treatments for these heart conditions are being developed, including medications to block the ion channels and techniques to remove the cells of the heart that produce unwanted electrical signals (shown on the right).

The improved understanding of heart rhythm disorders has helped to predict which patients have a high risk of these problems and has also resulted in better therapies (5). For example, drugs can be used to block the ion channels so that the doors stay closed and the amount of calcium inside the cell is controlled. Alternatively, specialized doctors can put a small device into the heart, through the blood vessels, to take out the heart cells that produce unwanted signals so that they no longer cause fibrillation (**Figure 1.3**). Despite the impressive advancements in (bio)medical technologies, numerous important questions about the mechanisms and treatment of

calcium-related problems inside heart muscle cells remain. Several research groups across the world are working hard to answer these questions.

## 1.2 Thesis overview

In addition to the brief general overview of cardiomyocyte calcium handling in this introductory chapter, this thesis consists of other 8 chapters as follows:

**Chapter 2** summarizes the role of cardiomyocyte calcium handling in health and disease, focusing on the significance of calcium handling and calcium handling abnormalities in arrhythmogenesis and how *in silico* studies may support current and future *in vitro* experiments.

**Chapter 3** discusses the significance of subcellular distribution of calcium-handling proteins: ryanodine receptors (RyR2s) and L-type calcium channels (LTCCs) on the propensity of diastolic spontaneous calcium release events (SCaEs), a substrate for ectopic activities in the heart.

**Chapter 4** illustrates an application of the spatially-detailed model of atrial cardiomyocyte developed in the previous chapter to address some experimental questions in the setting of post-operative atrial fibrillation (POAF).

**Chapter 5** studies the consequences of calcium-dependent regulation of atrial ionic currents on cardiac electrophysiology, investigating the impact of such regulation on the action potential (AP) properties, delayed afterdepolarization (DAD) and the behavior of cardiac reentry using computer simulations.

**Chapter 6** demonstrated the role of multi-scale computational modeling to elucidate the acute effects of ethanol on cardiac electrophysiology and arrhythmogenesis at the cellular and tissue levels.

**Chapter 7** presents the Maastricht ANTIarrhythmic drug eAluator (MANTA), a computational tool developed in Maastricht to better understand the cellular effects of antiarrhythmic drugs (AADs). In this chapter, some applications of MANTA are also discussed.

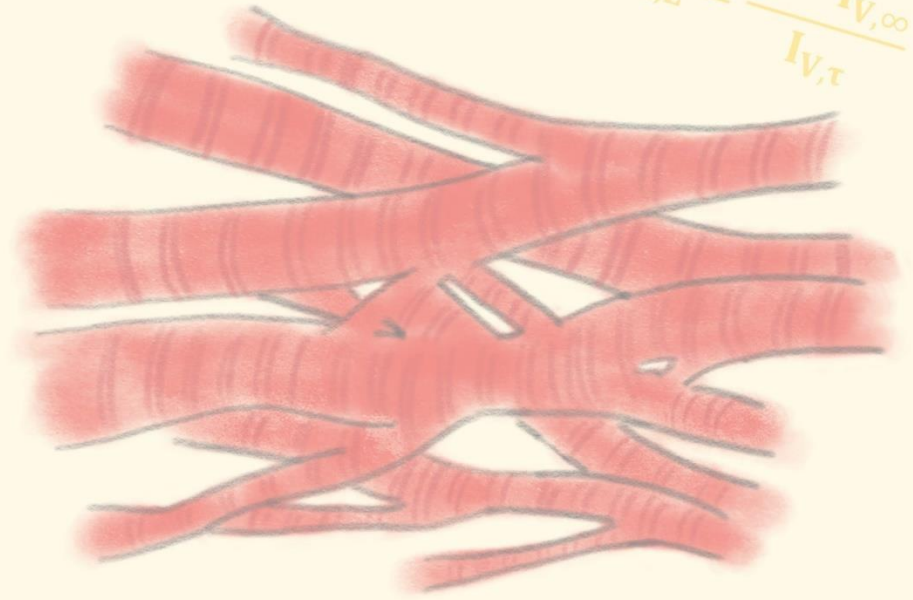
**Chapter 8** exemplifies the application of computational modeling to investigate the effect of  $\beta$ -adrenergic receptor stimulation on ventricular AP in the presence of repolarization reserve-lowering medications (e.g., chloroquine and azithromycin).

**Chapter 9** contains the general discussion of the thesis, elaborating the previous chapters and underlining the role of integrative computational modeling of cardiac calcium handling to better understand the basic mechanisms of cardiac arrhythmias. Current challenges, future recommendations and the potential benefits of multiscale modeling are also discussed.



$$\frac{dV_m}{dt} = -\frac{1}{C_m} * I$$

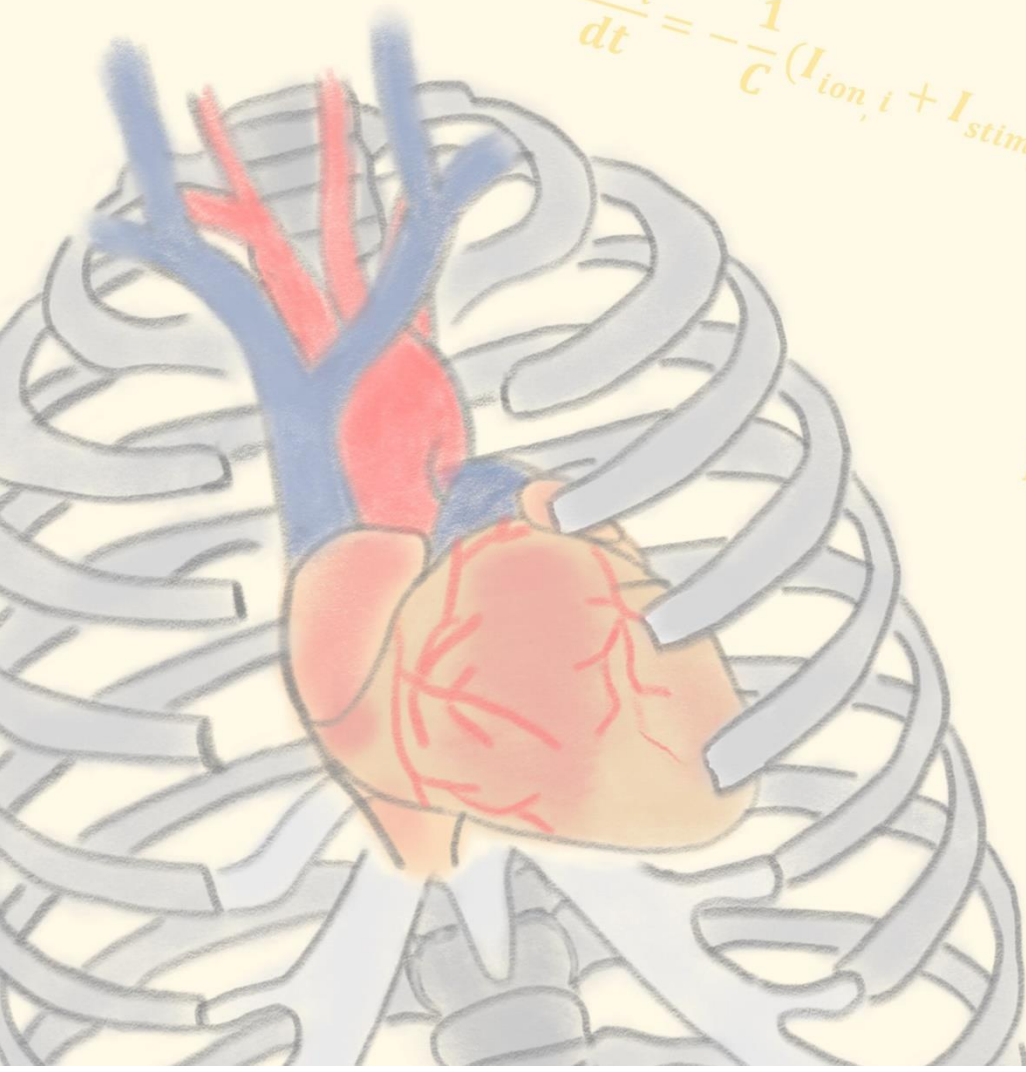
$$y_{Ca,L} = \frac{1 - I_{V,\infty}}{I_{V,\tau}}$$



$$x_{Ca,L} = \frac{I_{V,\infty}}{I_{V,\tau}}$$

$$\delta I_{Ca,L}^{s,m} =$$

$$\frac{dV_i}{dt} = -\frac{1}{C} (I_{ion,i} + I_{stim,i} + I_{diff,i})$$



$$\bar{I}_{Ca,L}^{s,m} = P_{Ca,L} \cdot (z$$

$$ACT_{\tau} = 0.59$$

# Chapter 2

## Cardiomyocyte calcium handling in health and disease: insights from *in vitro* and *in silico* studies

H. Sutanto, A. Lyon, J. Lumens, U. Schotten, D. Dobrev and J. Heijman  
*Prog Biophys Mol Biol.* 157:54-75.



$$\frac{dV}{dt} = \frac{I_{stim} - (I_K + I_{Na} + I_{leak})}{C_m}$$

## ABSTRACT

Calcium plays a central role in cardiomyocyte excitation-contraction coupling. To ensure an optimal electrical impulse propagation and cardiac contraction, calcium levels are regulated by a variety of calcium-handling proteins. In turn, calcium modulates numerous electrophysiological processes. Accordingly, calcium-handling abnormalities can promote cardiac arrhythmias via various mechanisms, including the promotion of afterdepolarizations, ion-channel modulation and structural remodeling. In the last 30 years, significant improvements have been made in the computational modeling of cardiomyocyte calcium handling under physiological and pathological conditions. However, numerous questions involving the calcium-dependent regulation of different macromolecular complexes, cross-talk between calcium-dependent regulatory pathways operating over a wide range of time scales, and bidirectional interactions between electrophysiology and mechanics remain to be addressed by *in vitro* and *in silico* studies. A better understanding of disease-specific calcium-dependent proarrhythmic mechanisms may facilitate the development of improved therapeutic strategies. In this review, we describe the fundamental mechanisms of cardiomyocyte calcium handling in health and disease, and provide an overview of currently available computational models for cardiomyocyte calcium handling. Finally, we discuss important uncertainties and open questions about cardiomyocyte calcium handling and highlight how synergy between *in vitro* and *in silico* studies may help to answer several of these issues.

## 2.1 Introduction

Tightly-controlled calcium handling in each cardiomyocyte is essential for optimal electrical and mechanical functioning of the heart. Calcium-handling abnormalities have been implicated in inherited cardiovascular diseases, including Timothy syndrome, catecholaminergic polymorphic ventricular tachycardia (CPVT) and arrhythmogenic cardiomyopathy, as well as acquired cardiovascular diseases such as heart failure (HF) and atrial fibrillation (AF) (6, 7). However, the precise mechanistic role of calcium in the initiation and progression of those diseases remains incompletely understood due to the complex interaction of calcium with many electrophysiological targets and signaling cascades, operating across a wide range of spatial and temporal scales (6). Despite significant advances in experimental techniques, many open questions remain due to the limitations and uncertainties associated with current experimental procedures (8, 9). In recent years, computational models have been increasingly employed to investigate numerous physiological and pathological phenomena, support clinical decision making, and improve the sensitivity, specificity and accuracy of biomedical devices and treatments (10-12). Here, we review the state-of-the-art in our understanding of cardiomyocyte calcium handling in health and disease, with a focus on synergistic interactions between computational modeling and experimental advances.

## 2.2 Calcium handling and excitation-contraction coupling in the healthy heart

### 2.2.1 Cardiomyocyte calcium handling

During systole, calcium enters the cardiomyocyte through voltage-gated L-type calcium channels (LTCCs) and triggers calcium-induced calcium release (CICR) through the calcium-dependent opening of ryanodine receptor type-2 (RyR2) channels organized together in local nanodomains (dyads). The interaction between multiple LTCC and RyR2 in calcium-release units (CRUs) strongly depends on subcellular structure. For example, in ventricular cardiomyocytes an extensive T-tubular network of membrane invaginations brings LTCC in close proximity of RyR2 located deep inside the cardiomyocyte. RyR2 opening leads to a much larger calcium release from the sarcoplasmic reticulum (SR) to the cytosolic space. The resultant calcium transient affects multiple targets inside a cardiomyocyte, including several transmembrane ion channels (including the LTCC itself, which undergoes calcium-dependent inactivation), contractile proteins, and calcium-dependent signaling pathways (13, 14), thereby controlling the electromechanical function of the heart (**Figure 2.1**). Store-operated calcium entry, the primary mechanism of calcium entry in non-excitable cells, may also contribute to cardiomyocyte calcium influx, specifically at the intercalated disk, and has recently been implicated in proarrhythmic cardiomyocyte calcium signaling (15). During diastole, calcium is returned to the SR by the sarco/endoplasmic reticulum calcium-ATPase 2a (SERCA2a), which hydrolyzes 1 ATP to pump 2 calcium ions back to the SR. Calcium is also extruded from the cell via the sodium-calcium exchanger (NCX), which exchanges 1 calcium for 3 sodium ions, and to a lesser extent via the plasmalemmal calcium-ATPase (PMCA), an active pump that contributes to approximately 5–10% of the calcium efflux in large mammals (9, 13). The activity of all

these calcium-handling proteins is regulated through large macromolecular complexes in which numerous interacting proteins and enzymes controlling post-translational modifications integrate a wide range of feedback and feedforward signals. Key examples will be discussed in **Section 2.5.1**.

### **2.2.2 Excitation-contraction coupling**

Excitation-contraction (E-C) coupling is the process by which the electrical activation of cardiomyocytes leads to contraction. It occurs following SR calcium release when the high calcium levels promote calcium binding to troponin-C, a molecule of the thin filament of the sarcomere. At rest, tropomyosin wraps around actin, blocking its myosin binding site and preventing contraction. The binding of calcium to troponin-C shifts the tropomyosin strand away from the actin binding sites, enabling the formation of cross-bridges and the generation of force (13). The amount of calcium released during CICR largely controls E-C coupling and cardiomyocyte contraction, and depends on structural coupling (e.g., configurations of the dyadic space where T-tubule and SR interact), and functional coupling (characteristics of calcium fluxes) (9). Relaxation occurs with the unbinding of calcium from troponin-C, changing the filament conformation back to a blocked, non-force-generating state. In addition, contractility is regulated by myofilament calcium sensitivity. The higher this sensitivity, the larger the force generation, but the faster the relaxation for a given concentration of free calcium (16). Myofilament calcium sensitivity may be altered in pathology (e.g., hypertrophic cardiomyopathy), leading to abnormalities in contraction or relaxation. Various sarcomeric proteins such as Tn-I, myosin binding protein-C (MyBP-C) or titin also exhibit degrees of calcium sensitivity, therefore modulating cross-bridge formation and contraction. Finally, cardiac mechanics can also affect the regulation of intracellular calcium, with mechanical alterations potentially modifying stretch-activated ion channels (SACs) or calcium-buffering properties through changes in myofilament calcium sensitivity (17, 18).

## **2.3 General overview of calcium-dependent arrhythmogenesis**

Conceptually, two major mechanisms control the generation and maintenance of cardiac arrhythmias: ectopic (triggered) activity and reentry (5, 19), both of which are modulated by calcium-handling abnormalities (**Figure 2.2**). Focal ectopic activity is the generation of uncoordinated electrical activity outside the physiological activation sequence driven by the sinoatrial node. It can be triggered through early or delayed afterdepolarizations (EADs or DADs, respectively), or result from abnormal automaticity (19). EADs are additional depolarizations occurring before full repolarization of the action potential (AP) and are commonly due to excessive prolongation of the repolarization phase of the AP, providing time for recovery from inactivation of LTCC. DADs are secondary depolarizations occurring after the full repolarization of the AP, typically due to spontaneous diastolic SR calcium-release events (SCaEs) (20). Reentry is considered the major arrhythmia-maintaining mechanism and can be initiated in the setting of unidirectional block when an activation wavefront propagates around anatomical or functional obstacles and re-excites the site

of origin. In the normal heart, reentrant activation wavefronts fail to perpetuate as they encounter refractory, non-excitable tissue. However, in pathological conditions alterations in the balance between effective refractory period (ERP) and conduction velocity (CV), or promotion of conduction block, may create a vulnerable substrate in which reentry can be maintained (5, 19). Calcium-dependent ion-channel modulation can alter ERP and CV via direct and indirect pathways (e.g., transcriptional regulation or phosphorylation by calcium-dependent kinases), thereby promoting reentry. Finally, calcium-handling abnormalities can promote reentry by supporting the evolution of structural remodeling, leading to slow heterogeneous conduction and conduction block (2, 21). The autonomic nervous system plays a central role in cardiac arrhythmogenesis, with autonomic dysbalance promoting both ectopic activity and reentry through calcium-dependent and non-calcium-dependent mechanisms.

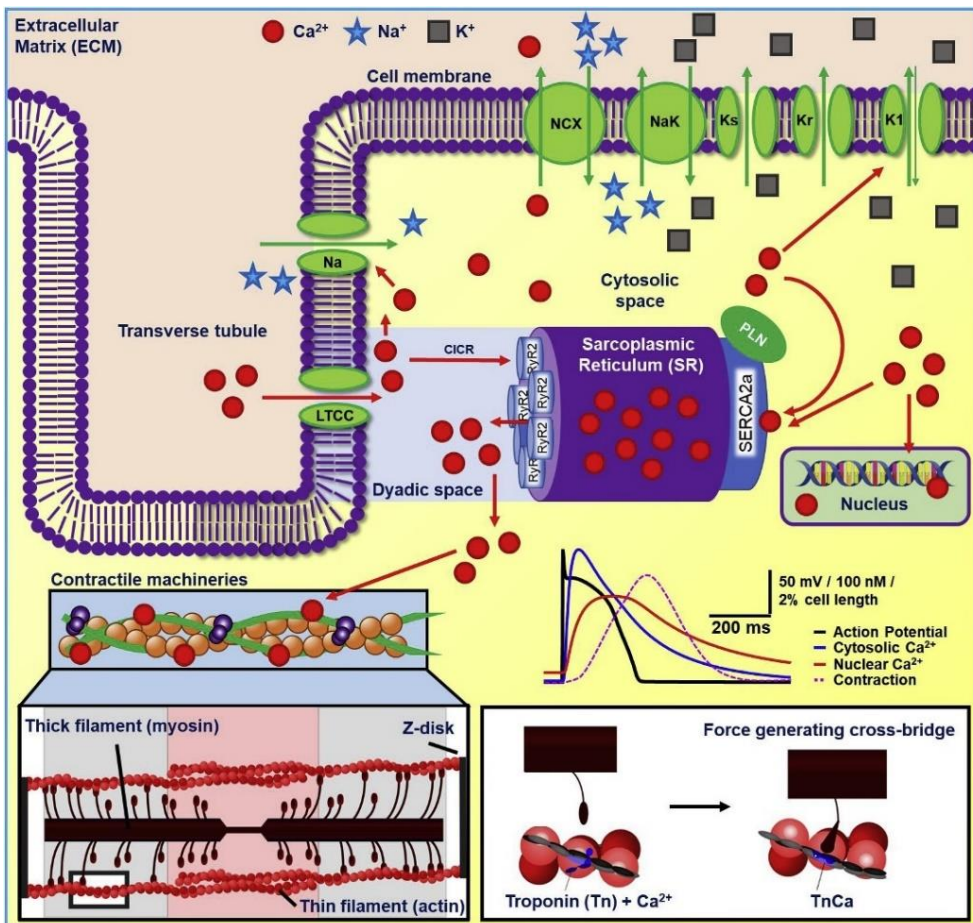


**Figure 2.1:** Schematic illustration of (ventricular) cardiomyocyte calcium handling. Membrane depolarization leads to the opening of L-type calcium channels (LTCCs) which trigger the release of calcium ions from the sarcoplasmic reticulum to the dyadic and cytosolic space. Subsequently, calcium interacts with many molecular targets within the cardiomyocyte, including transmembrane ion channels (e.g., the voltage

dependent sodium channel, rapid and slow delayed-rectifier potassium (Kr and Ks) channels, and inward-rectifier potassium (K1) channel), contractile machineries and calcium-dependent signaling molecules. Additionally, intracellular calcium also plays an important role in transcriptional regulation of ion channels in the heart. A schematic representation of the cytosolic and nuclear calcium transients (in relation to the action potential of human ventricular cardiomyocyte) is also depicted in the figure.

**2.3.1 Calcium-handling abnormalities as determinants of triggered activity**

Under pathophysiological conditions, cardiomyocytes can exhibit spontaneous (i.e., not triggered by CICR due to LTCC-mediated calcium influx) calcium releases from the SR, occurring primarily during diastole, termed SCaEs (22). SCaEs that are restricted to a small local nanodomain are termed calcium sparks (23), whereas SCaEs that propagate over larger areas are termed calcium waves. These triggered activity-promoting SCaEs can result from RyR2 dysfunction or SR calcium overload. The proarrhythmic consequences of RyR2 dysfunction are exemplified by CPVT, an inherited arrhythmogenic syndrome primarily caused by mutations in RyR2 or the SR calcium-binding protein calsequestrin (CASQ2). CASQ2 functions as a cooperative, high capacity and low affinity SR-calcium buffer, which can interact with RyR2 either directly or via triadin and junctin (24). Most CPVT-associated mutations increase RyR2 open probability, leading to inappropriate diastolic SR calcium release and triggered activity. This phenomenon is exacerbated in the presence of RyR2 hyperphosphorylation during sympathetic stimulation, further increasing the risk for atrial and ventricular arrhythmias, and sudden cardiac death (25, 26). RyR2-dysfunction-induced SCaEs have recently also been implicated in arrhythmogenic cardiomyopathy due to plakophilin-2 (PKP2) deficiency and resulted from excessive connexin-43 hemichannel-mediated calcium influx and remodeling of calcium handling (27, 28). Pharmacological stabilization of RyR2 prevents calcium-handling abnormalities and has antiarrhythmic effects in CPVT (25). RyR2 stabilization also improves survival in pressure overload and myocardial infarction animal models, although HF progression and contractile dysfunction remain, underlining the significance of RyR2-mediated calcium-handling abnormalities in cardiac arrhythmias (29).

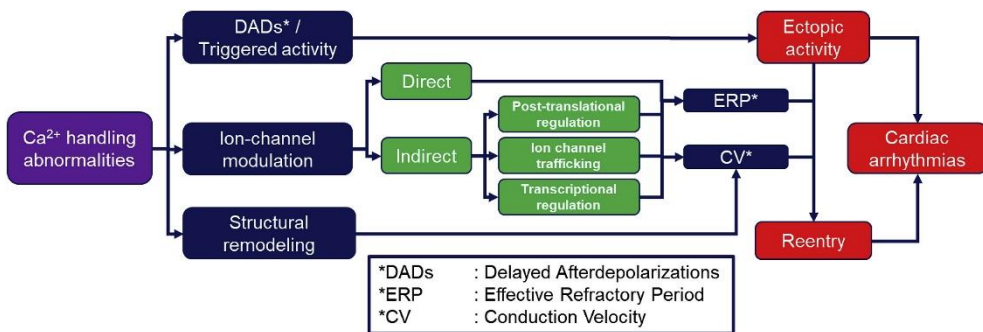


**Figure 2.2: Cardiomyocyte calcium handling and cardiac arrhythmias.** Cardiomyocyte calcium-handling abnormalities may trigger cardiac arrhythmias through several mechanisms: the initiation of afterdepolarizations and triggered activities, direct and indirect ion-channel modulation, and structural remodeling. Those processes promote ectopic activity and alter the effective refractory period (ERP) and conduction velocity (CV), contributing to a vulnerable substrate for cardiac arrhythmias.

Besides RyR2 dysfunction, store overload-induced calcium release (SOICR) can also cause DADs (26). SOICR can result from excessive calcium influx (e.g., due to impaired LTCC inactivation in the setting of Timothy syndrome (30)), from inhibition of calcium extrusion by NCX (e.g., due to elevation of intracellular sodium by cardiac glycosides), or from increased SERCA activity. Phospholamban (PLN) is a small protein that inhibits SERCA function by reducing its calcium affinity. Phosphorylation of PLN at Ser16 by protein kinase-A (PKA) or at Thr17 by calcium/calmodulin-dependent protein kinase-II (CaMKII) reduces the inhibitory effect, permitting a faster reuptake of calcium in the SR, reducing the cytoplasmic calcium concentration during diastole (31). Under physiological conditions, PKA-mediated PLN phosphorylation occurs during  $\beta$ -adrenoceptor stimulation, contributing to faster relaxation (31), but may also promote SR calcium overload. For example, PKA-dependent phosphorylation of PLN and SERCA activity are increased in paroxysmal AF, promoting SR calcium overload and SCAEs (32). On the other hand, SERCA stimulation may also reduce the likelihood of SCAEs and triggered activity by impairing the communication between RyR2 clusters, elevating the intra-SR threshold for the generation of calcium waves and slowing calcium-wave propagation (33). Antiarrhythmic effects of SERCA stimulation have been observed in HF rats (34) and a porcine model of ischemia reperfusion (35). The notion of SERCA-induced stabilization of calcium handling might also explain the arrhythmogenic risk of PLN-R14del, a Dutch founder mutation associated with arrhythmogenic cardiomyopathy (36), which produces 'super-inhibition' of SERCA (7). In addition, activation of CaMKII signaling due to PLN-induced elevation of diastolic calcium levels may contribute to the R14del-associated arrhythmogenesis (37). Of note, both SCAE mechanisms may interact, with RyR2 dysfunction lowering the threshold for SOICR (26), highlighting the complexity of the mechanisms underlying calcium-handling abnormalities.

### **2.3.2 Direct calcium-dependent regulation of ion channels and arrhythmogenesis**

Numerous macromolecular complexes of cardiac ion channel include the calcium sensor calmodulin (CaM), enabling direct calcium-dependent regulation of ion-channel function. For example, calcium influx through LTCC and SR calcium release during CICR promote calcium/CaM-dependent LTCC inactivation, thereby tightly controlling calcium influx into cardiomyocytes. Experimental and computational studies in the setting of Timothy syndrome-associated mutations in LTCC have demonstrated that calcium-dependent inactivation of LTCC represents a vital feedback mechanism required for proper calcium signaling in cardiomyocytes and its disruption leads to APD prolongation and EADs (38). In agreement, several CaM mutants suppress calcium/CaM-dependent inactivation of LTCCs, promoting APD prolongation and arrhythmogenesis (39).

LTCC-mediated calcium-influx and SR calcium release also directly activate small-conductance calcium-activated potassium (SK) channels, shortening action potential duration (APD). Since a longer baseline APD promotes calcium influx, subsequent activation of SK channels may represent a feedback mechanism to prevent excessive APD prolongation (40). Indeed, SK2-knockout mice exhibit prolongation of

atrial APD, EADs and an increased propensity for AF (41). On the other hand, excessive SK-channel activation may shorten ERP and promote reentry. In agreement, SK3 overexpression was found to induce atrial arrhythmias (42) and SK-channel inhibition has significant antiarrhythmic effects in AF animal models resulting from atrial tachypacing (43, 44) or  $\beta$ -adrenoceptor and muscarinic-receptor stimulation (45). Moreover, SK-channel inhibition may also slightly depolarize resting membrane potential (RMP), which may affect sodium-channel availability and destabilize reentrant activity (45). However, there have been inconsistent reports on SK-channel remodeling in AF patients, with both increased and decreased SK current reported (46, 47). There have also been conflicting findings on the proarrhythmic (48-50) vs. antiarrhythmic (51, 52) effects of ventricular SK-channel inhibition, highlighting the need for more comprehensive experimental and computational studies (53).

Accumulating evidence suggests that other ion channels are also regulated by intracellular calcium handling (54-56). For example, intracellular calcium enhances the slow delayed-rectifier potassium current ( $I_{Ks}$ ) in rabbit ventricular cardiomyocytes by negatively shifting the voltage dependence of activation and slowing channel deactivation, resulting in APD shortening during increased calcium loading and  $\beta$ -adrenoceptor stimulation. These data suggest that calcium-dependent regulation of  $I_{Ks}$  creates a repolarization reserve when depolarizing LTCC current is increased. Direct calcium-dependent regulation of the inward-rectifier potassium current ( $I_{K1}$ ) and sodium current has also been implicated in arrhythmogenesis (56-58). The binding of CaM to the C-terminus of human cardiac sodium channels modulates (recovery from) inactivation and may promote life-threatening ventricular arrhythmias (58, 59). In addition, recent cryo-electron microscopy structures of RyR2 revealed that calcium/CaM is one of the many competing regulators of RyR2 gating (60). Accordingly, computational modeling of direct calcium/CaM-mediated regulation of  $I_{SK}$ ,  $I_{Ks}$  and  $I_{K1}$  suggests that the effects on APD and reentry are modest under basal conditions, but may be augmented during calcium-handling abnormalities, such as in AF and HF (61). Nonetheless, the relative contributions of calcium-dependent regulation of different ion channels to arrhythmogenesis remain incompletely understood due to the limited control over calcium dynamics in *in vitro* studies and the confounding effects of indirect calcium-mediated ion-channel modulations (e.g., CaMKII-mediated phosphorylation) (62). Therefore, the perfect control and observability provided by computer models may enable a more systematic approach to investigate the complex interplay between direct and indirect calcium-dependent regulation of ion-channel function.

### **2.3.3 Calcium-dependent proarrhythmic structural remodeling**

Calcium-handling abnormalities and structural remodeling are closely related and influence each other's progression. Mice overexpressing  $\beta$ 1-adrenoceptors had a marked calcium-transient prolongation and altered intracellular calcium handling, which are responsible for early contractile dysfunction and interstitial fibrosis. Furthermore, the expression of the RyR2-interacting protein junctin was significantly decreased, and such reduction was closely associated with the progression of hypertrophic remodeling (63). RyR2-mediated SR calcium leak also drives the

progressive development of an AF-promoting substrate in a transgenic mouse model via the nuclear factor of activated T-cells (NFAT) pathway (21). Moreover, profibrotic mediators modulate endoplasmic reticulum calcium release and calcium influx into fibroblasts, resulting in an increased cytosolic calcium concentration and initiating fibrosis-promoting proliferation/differentiation of fibroblasts (64). Canonical transient receptor potential (TRPC) channels, voltage-independent calcium channels activated by cell stretch and other stimuli, contribute to this calcium-dependent fibrosis formation (65). In turn, fibroblasts can couple electrically to atrial cardiomyocytes, influencing the AP properties and promoting arrhythmogenesis (66, 67). Finally, changes in extracellular calcium can regulate desmosomes, thereby destabilizing anchoring cell junctions that preserve myocardium tissue integrity and promoting cardiac remodeling, for example in arrhythmogenic cardiomyopathy (68).

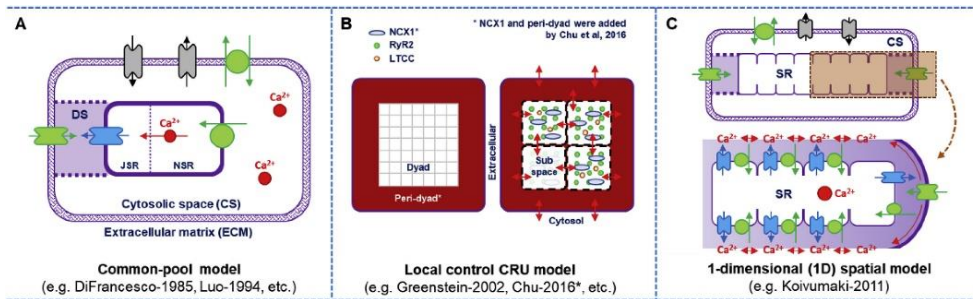
## 2.4 Progress in the computational modeling of cardiomyocyte calcium handling

Since the 1950s, significant progress has been made in the computational modeling of cellular electrophysiology to address unanswered experimental questions. The laboratory experiments by Hodgkin and Huxley in squid giant axon led to the first model of the AP (69, 70), which provided the basis for the >100 computational models of cardiac cellular electrophysiology from different species that have been developed to date. One of the earliest cardiac cellular models was the mammalian ventricular cardiomyocyte model by Beeler and Reuter, incorporating only 4 individual ionic currents: the excitatory  $I_{Na}$ , the slow inward current ( $I_s$ ), the time-independent outward potassium current ( $I_{K1}$ ), and the voltage-/time-dependent outward current ( $I_{Kr}$ ) (71). This model did not yet include calcium-handling components. Since then, the complexity of computational models of cardiomyocyte calcium handling has grown substantially, reflecting advances in experimental research. For example, DiFrancesco and Noble developed an integrated model with temporal details of calcium fluxes, which became the basic framework for other studies (72, 73). In 1994, the Luo-Rudy model of the guinea pig ventricular cardiomyocyte was already used to study the mechanisms of DADs (74).

CICR exhibits both graded response (the SR calcium release is proportional to the trigger influx of calcium across the cell membrane via LTCC) and high gain (a small triggering calcium influx across the cell membrane results in a much larger SR calcium release). Both properties cannot coexist in typical common-pool models (in which the total influx across the cell membrane and total SR calcium release occur in the same compartment, either the cytosol or a dyadic subspace), without a non-physiologically tight control over model parameters. As such, most common-pool models produce a full release of calcium from the SR when the trigger influx of calcium reaches the threshold for CICR (all-or-none response) (75). To address this limitation, multi-compartmental calcium-handling models have been developed, implementing a phenomenological approach to simulate the graded response of CICR (**Figure 2.3A**). These models remain commonly used (e.g., for multicellular simulations) due to their low computational

complexity and have started to incorporate direct calcium-dependent ion-channel regulation (10, 61, 76) and signaling pathways related to calcium handling (77-81). However, these models do not simulate local control of calcium handling (82) and assume that all parts of the cell have identical calcium-handling behavior, precluding mechanistic studies into calcium sparks, SCaEs, or the subcellular distribution of calcium-handling proteins. Therefore, computational models with detailed spatial calcium-handling properties have been emerging. Initially, local-control models of a single CRU (**Figure 2.3B**) were developed to reproduce the graded response of calcium sparks in the T-tubule/SR junction (83, 84). These CRU models were divided into 4 (2x2) dyadic subspaces, each containing 1 LTCC and 5 RyRs communicating via a single local junctional SR volume. Each subspace was treated as a single compartment with uniform calcium concentration and calcium could diffuse passively to neighboring subspaces within the same CRU (83). Over the past 15 years, these local-control models have become the foundation for more complex 3-dimensional ventricular cardiomyocyte models (**Figure 2.3H-M**) (85-90).

Important differences in the subcellular structure between atrial and ventricular cardiomyocytes exist. In contrast to adult ventricular cardiomyocytes, atrial myocytes do not generally express an extensive T-tubular network and therefore largely rely on LTCCs around their periphery for the initiation of CICR, which then propagate towards the center of the cell in a centripetal manner to interact with contractile machineries (91, 92). These experimental findings motivated the development of atrial-specific configurations of spatial calcium-handling models with distinct transverse (93) or transverse and longitudinal (32) compartments, allowing simulation of centripetal calcium waves (4, 94) (**Figure 2.3C and D**). The 2-dimensional atrial cardiomyocyte models (4) also allow simulation of axial tubules, which have been identified recently as a common feature of atrial cardiomyocytes and promote a more homogeneous CICR (95). An overview of cardiac computational models with detailed (sub)cellular calcium-handling properties is provided in **Table 2.1**.



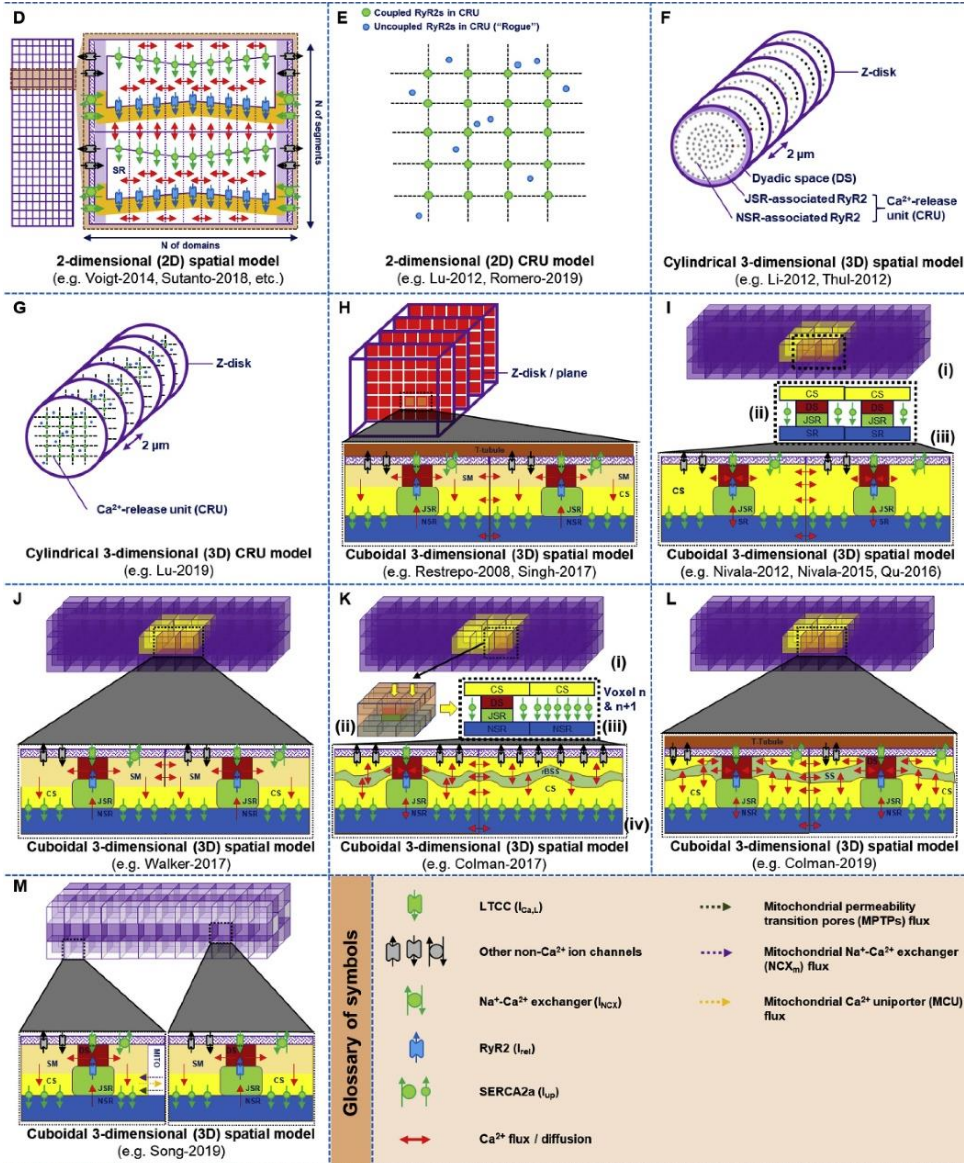


**Figure 2.3:** Representative examples of the subcellular structure of previously published computational models of cardiomyocyte calcium handling. A) Common-pool model with subcellular compartments but without explicit spatial structure. B) Local control calcium-release unit (CRU) model in which the dyadic space is divided into 4 subspaces, which allow diffusion of calcium from one to another and to cytosolic space. In Chu et al. (85), a peri-dyadic space and NCX1 were added to the model to simulate the effect of NCX distribution on CICR. C) The 1D spatial atrial model (93) included the centripetal wave propagation (the characteristic of atrial wave propagation due to lack of T-tubules). D) Such 2D spatial models of human atrial cardiomyocyte allow the investigation of the distribution of subcellular structures as observed experimentally. E) 2D CRU model with coupled and uncoupled (“rogue”) RyR2s. LTCC distribution is not shown. F-G) Cylindrical 3D spatial models with various arrangements of CRUs. H-M) Cuboidal 3D spatial models with various arrangement of subcellular compartments. Several models also incorporate the

experimental T-tubular structures from electron microscopy, confocal microscopy and STED. For further details, see **Table 2.1**. (CS = cytosolic space; DS = dyadic space; JSR = junctional SR; MITO = mitochondria; NSR = network SR; rBSS = restricted buffering subspace; SM = submembrane space; SS = sub-space).

No.	Region [Species]	Structure	Subcellular compartments	Current use	Reference
1	Ventricular [rat]	Cylindrical 3D CRU model (G)	Electron tomography-based calcium-release unit (CRU)	to evaluate the performance of a recently proposed method (the “CaCLEAN” method) for detecting the functional response of calcium release sites in live cells.	(96)
2	Ventricular [generic]	Cuboidal 3D spatial model (M)	Cytosol, NSR, JSR, dyadic space (DS), submembrane space (SM), mitochondria	to investigate the effects of mitochondria on intracellular calcium cycling and action potential dynamics in ventricular myocytes.	(88)
3	Ventricular [generic]	Cuboidal 3D spatial model (L)	Cytosol, NSR, JSR, DS, subspace (SS), T-tubule (TT)	to study bi-directional coupling between calcium-dependent sub-cellular and tissue-scale arrhythmia phenomena.	(97)
4	Ventricle [generic]	Cylindrical 3D CRU model (G)	Calcium-release unit (CRU)	to investigate the relationship between LTCC-RyR structure and cardiac electro-mechanical function.	(98)
5	Generic [generic]	2D CRU model (E)	Calcium-release unit (CRU)	to explore how nonlinearity and stochasticity determine the spatial distribution of calcium-release events within a cardiac cell.	(99)
6	Atrial [generic]	2D CRU model (E)	Calcium-release unit (CRU)	to study the effect of CRU spatial structure and distribution	(100)
7	Atrial [human]	2D spatial model (D)	100× longitudinal, 18× transverse (banded pattern); cytosol, SR, subsarcolemmal space, SR release space, axial tubules	to determine the impact of variations in subcellular RyR2 and L-type calcium-channel distributions on calcium-transient properties and SCAEs.	(4)
8	Generic [generic]	2D CRU model (E)	20,000 calcium-release units (CRUs) containing NSR,	to investigate SR countercurrent and the role of SR TRIC potassium channels by	(101)

			JSR, endoplasmic reticulum, subspace, cytosol.	modeling possible countercurrent sources during cardiac SR calcium release and subsequent reuptake.	
9	Generic [generic]	2D CRU model (E)	20,000 calcium-release units (CRUs) containing NSR, JSR, endoplasmic reticulum, subspace, cytosol.	to understand the heart rate dependence of SR ion homeostasis.	(102)
10	Ventricular [sheep]	Cuboidal 3D spatial model (K)	Cytosol, NSR, JSR, dyadic space (DS), restricted buffer subspace (rBSS), EM reconstructed T-tubule (TT)	to develop an approach to overcome the challenges of modelling spatio-temporal calcium dynamics using experimentally reconstructed 3-dimensional structures for the TT and SR at the whole-cell scale.	(103)
11	Ventricular [rat]	Cuboidal 3D spatial model (H)	Dyadic junction, submembrane space, bulk myoplasm, JSR, NSR, confocal image reconstructed T-tubule	to model the spatiotemporal distribution of calcium in ventricular myocytes and explore the relationship between T-tubule organization and calcium cycling.	(104)
12	Ventricular [canine]	Cuboidal 3D spatial model (J)	Dyadic subspace, submembrane space, cytosolic space, NSR, JSR	to study the roles of stochastic RyR2 gating and calcium wave dynamics on the statistical distribution of DADs under pathophysiological conditions.	(90)
13	Ventricular [generic]	Local control CRU model (B)	Dyad (4 dyadic subspaces), NSR, JSR, peridyad (PD), cytosol	to examine the ways in which differential placement of NCX1 into cytosolic, PD, and dyadic compartments influences properties of CICR and the cardiac AP.	(85)
14	Ventricular [generic]	Cuboidal 3D spatial model (I)	SR, JSR, DS, Cytosol	to provide novel predictions and insights into the mechanisms of calcium alternans in ventricular myocytes.	(105)

15	Generic [generic]	Cuboidal 3D spatial model (H)	Dyadic junction, submembrane space, bulk myoplasm, JSR, NSR	to simulate the calcium sparks and waves in VMs with PLN inhibition	(106)
16	Ventricular [generic]	Cuboidal 3D spatial model (I)	SR, JSR, DS, Cytosol	to investigate the effects of TT disruption and other HF remodeling factors on calcium alternans in ventricular myocytes using computer modeling.	(107)
17	Atrial [generic]	Cylindrical 3D CRU model (F)	Calcium-release unit (CRU)	to follow the triggering and evolution of calcium signals within a realistic 3D cellular volume of an atrial myocyte, but with low computational costs.	(108)
18	Generic [generic]	2D CRU model (E)	Calcium-release unit (CRU)	to develop a 3D, biophysically-detailed model of cardiac calcium- release events (3D spark model)	(109)
19	Generic [generic]	2D CRU model (E)	Calcium-release unit (CRU)	To study the roles of RyR2 gating properties, spark fidelity, and CRU anatomy on CICR	(110)
20	Atrial [human]	2D spatial model (D)	50× longitudinal, 18× transverse; cytosol, SR, subsarcolemmal space, SR release space	To study occurrence and mechanisms of sarcoplasmic reticulum calcium-release events in paroxysmal AF (pAF)	(32)
21	Atrial [generic]	Cylindrical 3D CRU model (F)	subsarcolemmal space and 13× transverse cytosol/SR	To investigate the mechanisms underlying the propagation of cytoplasmic calcium waves and the genesis of systolic calcium alternans in cardiac myocytes lacking T- tubules.	(111)
22	Ventricle [generic]	2D CRU model (E)	Calcium-release unit (CRU)	to study the effects of rogue RyRs on calcium cycling and membrane potential in failing heart.	(112)
23	Ventricular [generic]	Cuboidal 3D spatial model (I)	SR, JSR, DS, Cytosol	to simulate calcium cycling dynamics, such as calcium sparks, calcium waves, and calcium alternans.	(113)

24	Atrial [generic]	Cylindrical 3D CRU model (F)	Calcium-release unit (CRU)	to produce a geometrically realistic model of an atrial myocyte to explore calcium-release sites interaction and involvement in calcium wave initiation and propagation.	(114)
25	Atrial [human]	1D spatial model (C)	dyadic subspace and 8× transverse cytosol/SR	to develop a mathematical model of the human atrial myocyte that, in addition to the sarcolemmal (SL) ion currents, accounts for the heterogeneity of intracellular calcium dynamics emerging from a structurally detailed sarcoplasmic reticulum (SR).	(93)
26	Generic [generic]	2D CRU model (E)	NSR, JSR, subspace, Myoplasm	to study how the molecular-level characteristics of individual RyR2s influence the emergent property of cellular SR calcium leak	(115)
27	Generic [generic]	Quasi-2D spatial model (H)	NSR, JSR, DS, Myoplasm / Cytosol	to study how randomly occurring calcium sparks interact collectively to result in whole-cell calcium alternans.	(116)
28	Generic [generic]	Cuboidal 3D spatial model (H)	Dyadic junction, submembrane space, bulk myoplasm, JSR, NSR	to identify a new mechanism to explain experimental observations using a physiologically more realistic model where both luminal gating of SR calcium release and the spatially distributed nature of unitary calcium release events are treated explicitly.	(87)
29	Generic [generic]	Cylindrical 3D CRU model (F)	Calcium-release unit (CRU)	to examine the factors that influence calcium wave initiation	(117)
30	Ventricular [canine]	Local control CRU model	Dyad (4 dyadic subspaces), NSR, JSR, cytosol	to develop a comprehensive model of the ventricular myocyte based on the theory of	(83)

		(B)		local control of SR calcium release.	
--	--	-----	--	--------------------------------------	--

**Table 2.1:** Cardiac (sub)cellular models with detailed spatial cardiomyocyte calcium-handling properties. Letters between parentheses under "Structure" refer to panels in **Figure 2.3**.

## 2.5 Opportunities for synergy between *in vitro* and *in silico* studies to improve insights in cardiomyocyte calcium handling

### 2.5.1 Elucidating the regulation of calcium-handling proteins by interacting molecules

#### 2.5.1.1 The SERCA2a macromolecular complex

Sarcolipin (SLN) is a short helical peptide that is primarily expressed in the atria (118). Like PLN, SLN binds to SERCA2a, inhibiting its function and modulating cardiomyocyte calcium handling. Homozygous SLN deletion increases atrial SERCA activity, leading to abnormal cardiomyocyte calcium handling, SCaEs, DADs, and atrial structural remodeling (119). On the other hand, heterozygous SLN deletion results in a normal cardiac phenotype at baseline without increased AF susceptibility and a protective effect against chronic  $\beta$ -adrenoceptor stimulation-induced cardiac impairment. Because the activity of SERCA and other calcium-handling proteins (CASQ2, NCX1, RyR2, PLN) were unchanged in heterozygous knockout mice, such protective effects might reflect interaction of SLN with other proteins within the cardiomyocyte (120). Expression of SLN (but not PLN) is reduced in atrial samples of HF patients with reduced ejection fraction with or without long-standing persistent AF, likely contributing to increased SR calcium load (121, 122). A significantly reduced SLN expression but unchanged PLN has also been observed in post-operative AF (123). However, determining the functional consequences of alterations in the SERCA2a macromolecular complex is experimentally challenging. In contrast to ion-channel function, SERCA activity in an intact cardiomyocyte can only be estimated indirectly by subtracting the rate of decay of the systolic and caffeine-induced calcium transients (124). Therefore, having an *in silico* model of the SERCA complex able to predict the functional consequences of altered subunit expression or phosphorylation would be highly relevant. However, most cardiomyocyte models available to date simulate SERCA function with a Hill equation, whereby the affinity for cytosolic calcium is sometimes reduced to reflect PLN phosphorylation (125). A preliminary model simulating effects of PLN/SLN pentamerization and phosphorylation on human atrial calcium handling has been proposed and may provide insights in the role of these proteins (126). Similarly, detailed SERCA models based on Markov-chain models of various states of SERCA phosphorylation (127) and thermodynamics (128) are available, but none of those models simulates the combined PLN and SLN-mediated SERCA2a regulation.

#### 2.5.1.2 Phospholemman (PLM)

Phospholemman (PLM) is a member of the family of FXYD proteins that inhibits the sodium-potassium ATPase. Similar to the effect of PLN on SERCA, phosphorylated PLM relieves its inhibition of the sodium-potassium ATPase, increasing pump activity (129). PLM phosphorylation at Ser63 and Ser68 is reduced in rabbits with rapid atrial pacing-

induced remodeling (130). Such PLM hypophosphorylation may be a compensatory mechanism against the reduction of intracellular sodium resulting from the reduced SR calcium release, increased calcium buffering, shortened APs, and reduced  $I_{Ca,L}$  after rapid atrial pacing-induced remodeling (130). A rabbit ventricular cardiomyocyte model simulating  $\beta$ -adrenoceptor stimulation confirmed that enhanced sodium-potassium ATPase activity due to an increased affinity for intracellular sodium reduced calcium loading and calcium-transient amplitude (131). Recent work has shown that HF blunts local  $\beta_2$ -adrenoceptor control and alters the phosphodiesterase (PDE) 2/PDE3 balance in the sodium-potassium ATPase-PLM microdomain, making it insensitive to cyclic adenosine monophosphate (cAMP) signaling (132). These data highlight the importance of local regulation of cardiac electrophysiology. Unfortunately, it is currently not possible to simulate the functional consequences of altered local signaling, as this level of detail is not yet incorporated in most models. Of note, PLM also regulates NCX1 and LTCC activity in cardiomyocytes. Unlike the sodium-potassium ATPase, PKA- and protein kinase-C (PKC)-mediated phosphorylation of PLM at Ser68 increases NCX1 inhibition, contributing to intracellular calcium overload (133). Finally, PLM limits calcium influx in cardiac myocytes by reducing maximal  $I_{Ca,L}$  and accelerating voltage-dependent inactivation (134). These functional roles of PLM have also not yet been incorporated in computational models.

### 2.5.1.3 Other macromolecular complexes

There are many other macromolecular complexes involved in cardiomyocyte calcium handling. For example, the LTCC and RyR2 macromolecular complexes include calmodulin, as well as multiple phosphodiesterases, phosphatases and kinases anchored via A-kinase anchoring proteins. In addition, LTCCs also interact with Ahnak1, Nedd4-1, USP2-45, RGK and caveolin-3. The RyR2 macromolecular complex includes, among other things, junctin, triadin, calsequestrin-2, and FKBP12.6. Finally, sorcin and junctophilin-2 link the LTCC and RyR2 macromolecular complexes, thereby controlling their close interaction in dyads (6, 135, 136). At present, computational models only incorporate phenomenological representations of these macromolecular complexes. While this is likely sufficient for many studies, it makes it impossible to directly extrapolate the functional consequences of alterations in specific component(s), e.g., as obtained with Western blot studies in specific animal models or patient populations.

### 2.5.2 Understanding the subcellular mechanisms and proarrhythmic consequences of SCaEs

Despite extensive research, the mechanisms and proarrhythmic consequences of SCaEs remain incompletely understood. For example, several experimental studies have identified alterations in major calcium-handling proteins and increased SCaE incidence in atrial cardiomyocytes from AF patients (32, 121, 124, 137-139), whereas other studies have observed reduced SCaE incidence and calcium-signaling silencing (130, 140-142). Methodological considerations as well as pronounced differences in the molecular mechanisms underlying different forms of AF may contribute to these findings (143). In patients with long-standing persistent ('chronic') AF (cAF), RyR2

dysfunction due to CaMKII-dependent hyperphosphorylation at Ser2814 appears to underlie SCAEs (124, 139). Despite increased RyR2 open probability, reduced SERCA activity, increased NCX function and reduced  $I_{Ca,L}$ , all of which would be expected to reduce SR calcium levels, there is only a mild, non-significant decrease in SR calcium load in cAF patients (121, 124). Computational modeling has suggested that maintenance of SR calcium load is critical for the development of propagating SCAEs, as RyR2 dysfunction in the absence of maintained SR calcium load led to small, non-propagating calcium releases (32, 144). The studies which observed reduced SCAE proclivity in response to catecholamine stimulation in atrial cardiomyocytes from cAF patients compared to sinus rhythm patients also support the importance of SR calcium load for SCAE development. In particular, the lower incidence of SCAEs in cAF was attributed to impaired CaMKII-mediated regulation of LTCC and PLN (140), which would be expected to reduce SR calcium load (143).

In addition, SR calcium load can be modulated by experimental conditions such as the extracellular calcium concentration and the sodium concentration in the patch pipette, which regulate NCX activity (9, 145). For example, elevation of extracellular calcium elicited transient-inward NCX currents and promoted early and delayed afterdepolarizations in zebrafish ventricular cardiomyocytes (146). Also, an increased frequency of relatively small calcium releases may not be able to generate aftercontractions, especially in the presence of additional remodeling of the contractile machinery, as occurs in cAF (147, 148). This limited sensitivity to detect SCAEs may in part explain why some experiments employing contractility as read-out observed fewer SCAEs in cAF samples (140, 149). In agreement, the (late) sodium current blocker ranolazine reduced aftercontractions in trabeculae from AF patients through an NCX-mediated reduction of SR calcium load and inhibition of RyR2 open probability, highlighting the central role of sodium in cardiomyocyte calcium handling (149). On the other hand, it is unclear whether SCAEs that are too small to produce aftercontractions can have direct proarrhythmic consequences, although they may promote long-term calcium-dependent remodeling (discussed in [Section 2.5.4](#)). Multiscale electromechanical simulations may help to elucidate the number of cells, SCAE size and synchronicity required to produce triggered activity and aftercontractions (in the absence or presence of contractile remodeling), as discussed below, although not all models are able to accurately reproduce alterations in electrophysiology and calcium-handling in response to changes in extracellular concentrations (150). Fluorescent measurements are also indirect and require careful calibration (151). Moreover, fluorescent indicators can act as calcium buffers and may affect calcium-transient properties. Different fluorescent indicators penetrate differently across the cell membrane and exhibit distinct subcellular compartmentalization, which can cause variations in the observed calcium transients and fractional shortening (152, 153). However, the frequency of spontaneous transient-inward currents measured in the absence of calcium indicators was also increased in AF patients (121), suggesting that the calcium-buffering effect of fluorescent calcium indicators may be limited.

The perfect control and observability offered by computer models may help to assess the relative role of SR calcium load and RyR2 dysfunction in promoting SCAEs, as well as the impact of different experimental conditions. However, since arrhythmias are inherently multiscale phenomena, multicellular simulations are necessary to study the role of SCAEs in arrhythmogenesis. For example, the role of triggered activity in the maintenance of atrial and ventricular arrhythmias remains largely unknown, and the therapeutic value of RyR2-targeting compounds has not yet been clinically validated (143). Unfortunately, the computational complexity of local-control cardiomyocyte models with detailed subcellular structure and stochastic RyR2 gating required to simulate SCAEs precludes such multicellular simulations. However, recently a novel computational approach with simplified cardiomyocyte models suitable for tissue simulations, which can produce realistic SCAEs, has been proposed (97). This approach has, for example, highlighted how calcium loading during reentry can promote ectopic activity and arrhythmia reinduction after reentry termination (97).

SCAEs and RyR2 dysfunction are also present in patients with paroxysmal AF and in atria of HF patients, but are not due to increased total RyR2 phosphorylation levels (32, 121). Instead, altered expression of RyR2-interacting proteins, including a relative paucity of junctophilin-2 and overabundance of junctin have been implicated in paroxysmal AF and HF patients, respectively (32, 121, 137). In addition, altered distribution of calcium-handling proteins may play an important role (154-156). Advanced imaging techniques, including electron microscopy and (super-resolution) confocal microscopy, as well as combinations of the two (correlative light and electron microscopy), supported by advances in immunostaining approaches have enabled detailed studies of cardiomyocyte subcellular structure (157). For example, an increased number of RyR2 clusters per CRU and a shortening of the distance between clusters has been observed in sheep with persistent AF and increase the likelihood of propagating diastolic calcium releases (158). Fluorescent labeling of FKBP/RyR2 to simultaneously measure the RyR2 distribution and calcium-spark properties at the same site in adult cardiomyocytes also highlighted the dependence of calcium-spark frequencies on RyR2 cluster size. By contrast, calcium-spark amplitudes and CICR were independent of RyR2 cluster size (159). Advanced imaging also suggested an important role for axial tubules in synchronizing SR calcium release and promoting spontaneous SCAEs due to local RyR2 hyperphosphorylation around axial tubules, which may not be detected using Western blot techniques in atrial tissue homogenates (160). Whether an altered RyR2 distribution contributes to SCAEs in AF patients is at present unknown.

In general, characterizing the functional consequences of altered protein distribution is experimentally challenging due to the different experimental setups involved (cell fixation for staining vs. live-cell calcium imaging), although this limitation can be partly resolved using fluorescent labeling of RyR2-interacting proteins (159), and the limited options to deliberately perturb the localization of proteins. Computer models make it possible to selectively redistribute calcium-handling proteins and a recent computational study of the human atrial cardiomyocyte showed that a heterogeneous RyR2 distribution increases the propensity for SCAEs, with SCAEs

originating from regions with high local RyR2 expression. SCAEs were also promoted by local RyR2 hyperphosphorylation around virtual axial tubules (4), in line with experimental observations (95, 160). Together, these data strongly suggest that in isolation, Western blot experiments using whole-tissue lysates, although often useful, are not always sufficient to characterize RyR2-dependent proarrhythmia. Recent work has shown that T-tubules have a complex 3-dimensional structure and are not only a docking site for LTCC, but also NCX, suggesting a central role in intracellular calcium cycling (161). Indeed, RyR2 calcium release may also be triggered by the NCX (86), but this requires close localization of the two proteins, which has been difficult to ascertain in studies employing diffraction-limited microscopy (162). Three-dimensional super-resolution microscopy has been used to visualize the nanoscale organization of RyR2 in ventricular cardiomyocytes and enabled discernment of clusters overlapping in the z-axis, which was not possible with conventional imaging techniques (163, 164). Furthermore, cardiovascular diseases such as HF lead to remodeling of the T-tubular network, resulting in a loss of synchronous calcium release (165). The SR itself also has a unique network structure spanning the entire cardiomyocyte, including connections with the nuclear envelope. Intra-SR calcium diffusion can regulate RyR2 function, thereby modulating calcium-wave propagation within cardiomyocytes (166). Faster calcium diffusion limits spatial SR calcium gradients and leads to more uniform release throughout the cell, while slower diffusion rate allows spatial inhomogeneities before or during SR calcium release (166). Several combined experimental and computational studies have attempted to characterize intra-SR calcium diffusion and its impact on proarrhythmic calcium-handling abnormalities in cardiomyocytes and both fast (167) and slow (168) diffusion have been reported. Further investigations, including detailed spatial calcium-handling models, are needed to better characterize intra-SR calcium diffusion (166-168). Several 3-dimensional computational cardiomyocyte models have recently been developed based on these experimental data and have provided insight into the role of subcellular structure in cardiomyocyte calcium handling and the consequences of HF-related T-tubular remodeling, highlighting the synergy between both approaches (97, 103, 169-172).

### **2.5.3 Calcium-mediated signaling cascades in cardiomyocytes**

In addition to its role in E-C coupling, calcium is a major signaling molecule. Several calcium-dependent signaling pathways are activated under pathological conditions and contribute to the initiation and progression of cardiac arrhythmias, including calpain, PKC, CaMKII and the calcineurin/NFAT signaling pathway (**Figure 2.4**). The latter primarily controls cardiomyocyte hypertrophy and long-term transcriptional regulation (6, 173), which are discussed in **Section 2.5.4**.

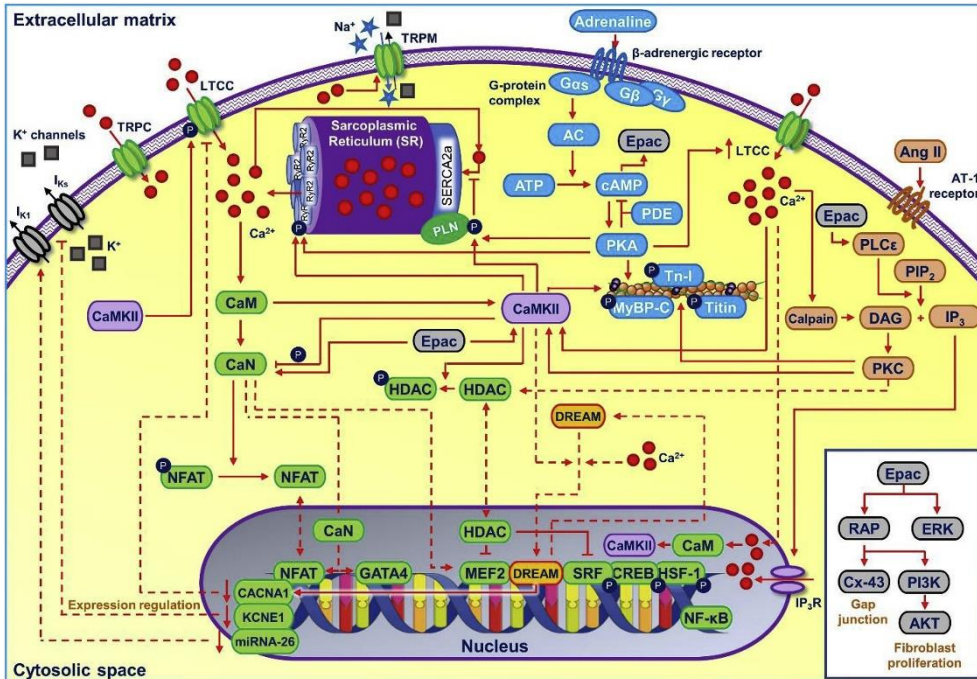


**Figure 2.4:** Key calcium-dependent signaling cascades within a cardiomyocyte. The signaling cascades can be activated through several ways: via direct calcium-dependent regulation of signaling proteins (e.g., CaM, CaMKII and calpain) and via the activation of G-protein coupled receptors (e.g.,  $\beta$ -adrenergic receptor and AT-1 receptor). Activation of these signaling cascades promotes the nuclear translocation of signaling proteins and transcription factors, including NFAT, CaN, HDAC and DREAM, to regulate the expression of cardiac ion channels and the adaptive response to stress/injury (structural and electrical remodeling of cardiomyocytes). Moreover, these signaling cascades can alter the contractile machineries of the heart, e.g., through phosphorylation of Tn-I. (AC = adenylyl cyclase; Ang II = angiotensin II; ATP = adenosine triphosphate; CaM = calmodulin; CaMKII = calmodulin-dependent protein kinase II; cAMP = cyclic adenosine monophosphate; CaN = calcineurin; DAG = diacyl glycerol; DREAM = downstream regulatory element agonist modulator; HDAC = histone deacetylase; IP<sub>3</sub> = inositol triphosphate; NFAT = nuclear factor of activated T-cells; PDE = phosphodiesterase; PIP<sub>2</sub> = phosphatidylinositol biphosphate; PKA = protein kinase A; PKC = protein kinase C; PLC = phospholipase C; Tn-I = troponin-I; TRPC = transient receptor potential canonical channel; TRPM = transient receptor potential melastatin channel).

### 2.5.3.1 Calpain

Calpain is a calcium-activated protease involved in the calcium-dependent regulation of many cellular processes, including signal transduction, cell proliferation, differentiation, cell cycle progression, and apoptosis (174, 175). Hence, calpain dysregulation due to calcium-handling abnormalities during cardiac pathologies such as AF, HF, or hypertrophy may have a significant impact on cellular homeostasis. The PKC signaling pathway (discussed below) is a major target of calpain (Figure 2.4). In addition, calpain directly regulates LTCC (176) by cleaving the distal C-terminus, which plays a role in autoinhibition (i.e., calcium-dependent inactivation), leaving a truncated form that produces a significantly greater current than the full-length LTCC (177). Calpain-mediated cleavage and subsequent degradation / downregulation of other

calcium-handling proteins, including NCX1, SERCA and RyR2, and myofilament components (e.g., MyBP-C), have also been identified in ischemia reperfusion injury and HF (178-182). Finally, calpain also increases late sodium current ( $I_{NaL}$ ) in the setting of HF and simulations suggest that calpain inhibition may reduce intracellular diastolic calcium accumulation by decreasing  $I_{NaL}$  and shortening APD (175).

### 2.5.3.2 PKC

The PKC family of phospholipid-dependent serine-threonine protein kinases can be subdivided into three groups: the conventional, novel and atypical PKCs. These groups differ in their activation by calcium, diacylglycerol (DAG) and phosphatidylserine. Of those, only conventional PKC depends on calcium for activation (183). PKCs have been implicated in cardiac arrhythmias due to their role in cardiac electrical remodeling (184). Other publications have also linked PKC activation with AF (185-188). For example, tachycardia-induced calcium loading and calpain activation have been demonstrated to downregulate PKC $\alpha$  (a conventional PKC isoform), contributing to an altered conventional/novel PKC-isoform balance. This imbalance could contribute to the increased constitutive activity of the acetylcholine-activated inward-rectifier potassium current, which shortens the APD and hyperpolarizes the RMP, which support reentry and AF promotion (186, 189). Moreover, an increased PKC-mediated phosphorylation of troponin-I and -T were observed in failing hearts, which alters the myofilament calcium sensitivity (190, 191). Computational models of several protein kinase signaling cascades (including PKA and CaMKII) have been developed and have provided insight in their potential proarrhythmic consequences (80, 192, 193). Although several papers have discussed the potential importance of including PKC-dependent regulation in cardiac electrophysiology models (193, 194), to the best of our knowledge, no computational model available to date includes this calcium-dependent signaling cascade.

### 2.5.3.3 CaMKII

CaMKII consists of 4 different isoforms with the  $\delta$  and  $\gamma$  isoforms expressed in the heart. CaMKII $\delta$  is considered the main cardiac CaMKII isoform (195). In the resting state at low intracellular calcium levels, the CaMKII regulatory domain autoinhibits its catalytic domain. Once the intracellular calcium concentration rises, 4 calcium ions interact with CaM, separating the catalytic domain from its regulatory domain and activating CaMKII. Subsequent autophosphorylation at Thr287 can promote persistent, calcium-independent activation. During cellular stress several mechanisms promote CaMKII hyperactivation. For example, sympathetic stimulation increases CaMKII activation via increased heart rate, elevated intracellular calcium concentrations, I-1-mediated regulation of protein phosphatase 1 (PP1, involved in dephosphorylation of CaMKII-Thr287) and regulation of exchange-protein activated by cAMP (Epac) (78, 196, 197). In addition, CaMKII can be activated by oxidative stress through oxidation of Met281/Met282 and in the presence of hyperglycemia by glycosylation of Ser280 (198). Active CaMKII regulates several major components of cardiomyocyte calcium handling, such as LTCC, RyR2, SERCA2a, SLN and PLN (**Table 2.2**), and plays an important role in

cardiac contraction (through the phosphorylation of MyBP-C and titin), gene transcription, intracellular trafficking, cellular energetics, hypertrophy, inflammation and cell death in a tightly controlled spatiotemporal manner (198-200). CaMKII-mediated regulation involves direct phosphorylation of targets, as well as indirect regulation of reactive oxygen species, nitric oxide signaling, phosphatases and phosphodiesterases, intracellular trafficking and gene expression (185, 199, 201). CaMKII-dependent phosphorylation of RyR2 is increased in transverse aortic constriction-induced HF and contributes to pathological SR calcium leak and HF progression (202, 203). The proarrhythmic consequences of CaMKII hyperactivity have been demonstrated in various experimental models (204). For example, CaMKII-mediated phosphorylation of RyR2 at Ser2814 is required for the CPVT phenotype of engineered heart tissue derived from human pluripotent stem cell-derived cardiomyocytes harboring the RyR2-R4651I or RyR2-D358N mutations (205). Furthermore, CaMKII inhibition suppresses CPVT in mouse models and human pluripotent stem cells (206, 207), although the potential antiarrhythmic efficacy in AF patients remains a topic of debate (130, 140, 143, 185, 208-210). Additionally, CaMKII-mediated phosphorylation of Nav1.5 increases  $I_{NaL}$ , and prolongs APD, leading to calcium-handling abnormalities, and promotes DADs and AF susceptibility (211). Subsequently, calcium-handling abnormalities may further activate CaMKII and  $I_{NaL}$ , creating a vicious cycle.

Several computational models incorporating  $\beta$ -adrenoceptor and CaMKII signaling and their downstream effects have been developed to provide a better understanding of the complex electrophysiological effects of these pathways (78, 81, 131, 196, 212-215). For example, a computational model of the rabbit ventricular cardiomyocyte has shown that CaMKII-dependent upregulation of  $I_{NaL}$  in HF leads to increased arrhythmia propensity, and is further exacerbated by  $\beta$ -adrenoceptor stimulation (212). Similarly, CaMKII-dependent phosphorylation of Nav1.5 increases  $I_{NaL}$  in a human atrial cardiomyocyte model, promoting intracellular calcium overload through reduced NCX, increased RyR2 open probability and proarrhythmic afterdepolarizations and repolarization alternans under  $\beta$ -adrenoceptor stimulation (214). These computational studies have helped characterize one of several positive feedback loops promoting CaMKII hyperactivity under disease conditions and suggest that pharmacological inhibition of intracellular sodium loading can contribute to normalizing calcium and stabilization of membrane potential dynamics (213). Nonetheless, these computational models only integrated some components of the complex CaMKII signaling cascade and did not consider differences in subcellular distribution of CaMKII. More comprehensive computational studies are needed to assess the antiarrhythmic potential of CaMKII modulation.

No.	Ion channel / calcium-handling protein	Effect
1	L-type calcium channel / LTCC (Cav1.2)	$\uparrow I_{Ca,L}$ , $\downarrow$ inactivation, $\uparrow$ open probability (mode 2 gating), $\uparrow$ recovery from inactivation (acute)

		↓ Cav1.2 expression (chronic)
2	T-type calcium channel (Cav3.1-3)	↑ open probability, (-) SSA shift (acute)
3	Voltage-gated sodium channel (Nav1.5)	↓ I <sub>Na,T</sub> inactivation, ↑ intermediate inactivation, ↓ recovery from inactivation, (-) SSI shift (acute & chronic)
		↓ SSA
		↑ I <sub>NaL</sub>
4	Sodium-calcium exchanger (NCX)	↑ I <sub>NCX</sub> (inward)
5	Transient-outward potassium channel (Kv1.4, 4.2, 4.3)	↓ inactivation, ↑ recovery from inactivation, (+) SSI shift (acute)
		↓ I <sub>to</sub> , ↓ Kv4.2/4.3 expression (chronic)
6	Slow delayed-rectifier potassium (Ks) channel (Kv7.1)	Phosphorylation of SAP97, ↑ I <sub>to</sub>
		↑ I <sub>Ks</sub> (acute) ↓ I <sub>Ks</sub> , (+) SSA shift, ↓ KCNE1 expression (chronic)
7	Inward-rectifier potassium (K1) channel (Kir2.1-3)	↑ I <sub>K1</sub> (acute)
		↓ I <sub>K1</sub> , ↓ Kir2.1 expression (chronic)
8	Ultra-rapid delayed rectifier potassium (Kur) channel	↑ I <sub>Kur</sub>
9	ATP-dependent potassium current (Kir6.1-2)	↑ open probability (acute)
		↓ Kir6.2 expression (chronic)
10	Small-conductance calcium-activated potassium (SK) channel (Kca2.1-3)	↑ I <sub>SK</sub> (acute)
11	Transient receptor potential (TRP) channels	↑ TRPC6 current (acute)
12	Calcium-activated chloride channel	↑ I <sub>Cl,Ca</sub> (acute)
		↓ I <sub>Cl,Ca</sub> (chronic)
13	Ryanodine receptor type 2 (RyR2)	Phosphorylation at Ser2808/Ser2811/Ser2814, ↑ open probability, ↑ SR calcium release
14	IP <sub>3</sub> type 2 receptor	Phosphorylation at Ser150, ↓ open probability
15	Phospholamban (PLN)	Phosphorylation at Thr17, ↓ PLN-mediated tonic inhibition to SERCA
16	Sarcolipin (SLN)	↓ SLN-mediated inhibition to SERCA, ↑ SR calcium uptake (phosphorylation at Thr5)
17	Myosin binding protein C (MyBP-C)	Phosphorylation at Ser302 & Ser282 (at non-physiological calcium concentration)
18	Titin (TTN)	Phosphorylation of the N2B element

**Table 2.2:** CaMKII-dependent regulation of cardiac ion channels and calcium-handling proteins. (SSA = steady-state of activation; SSI = steady-state of inactivation). Details can be found in (62, 185, 199, 216-218).

## 2.5.4 Long-term calcium-dependent transcriptional regulation

### 2.5.4.1 Nuclear calcium handling

Calcium can enter the nucleus via passive membrane diffusion or calcium-release from inositol triphosphate (IP<sub>3</sub>)-receptors on the nuclear membrane (**Figure 2.4**). The nuclear calcium transient exhibits a slower and delayed upstroke, a lower peak amplitude, and a prolonged decay compared to its cytosolic counterpart (**Figure 2.1**). Calcium diffuses out of the nucleus via nuclear pore complexes and is taken up by SERCA on the outer nuclear membrane, by nearby mitochondria, or is extruded by NCX on T-tubules in close proximity to the nuclear envelope (14). Nuclear calcium plays

significant roles in long-term cardiac remodeling (219), including the activation of nuclear CaMKII, and calcineurin/NFAT pathways (discussed below). In addition, recent work has suggested that nuclear calcium regulates gene expression through several other transcription factors, such as CREB, HSF-1 and SRF (14).

In line with the experimental efforts, computational modeling has also been employed to investigate the role of nuclear calcium signaling in health and disease (220). However, until recently, there was no quantitative model coupling cardiomyocyte electrophysiology with calcium and IP<sub>3</sub> signaling in the cytosol and nucleus. In 2014, a model describing nuclear calcium dynamics and its dependence on intracellular calcium, nuclear calcium buffering and calcium transport via nuclear pore complexes and nuclear envelope was introduced (220). This model may be a stepping stone to study the consequences of CaM, calcineurin, and CaMKII in the nucleus, and can potentially be coupled to the previously described models of CaM/CaMKII/calcineurin signaling (221) to study the mechanisms underlying long-term calcium-dependent transcriptional regulation (220).

#### 2.5.4.2 Calcineurin-dependent transcriptional regulation

Calcineurin is a serine/threonine-specific phosphatase activated by intracellular calcium. Activated calcineurin dephosphorylates cytosolic NFAT, leading to its translocation to the nucleus where it regulates gene expression. Among other targets, NFAT inhibits the expression of the cardiac LTCC through reduced expression of CACNA1, providing a negative feedback loop (222, 223). Experimentally, calcium-induced activation of calcineurin/NFAT signaling was observed in canine atrial cardiomyocytes during tachypacing, leading to the transcriptional downregulation of LTCC (223). Although this mechanism protects cardiomyocytes from potential cytotoxic calcium overload, the consequent reduction in APD may have proarrhythmic consequences. Calcium-dependent signaling may also contribute to the increased RyR2 expression in pAF (through a reduction in the miR 106b-25 cluster; (188, 224)) and is involved in the transcriptional regulation of several potassium channels. For example, activation of calcium/calcineurin/NFAT signaling increases I<sub>K1</sub> through NFAT-mediated downregulation of the inhibitory microRNA-26 (173, 225). I<sub>K1</sub> was also increased in stretched neonatal rat atrial cardiomyocytes, which was also associated with augmented calcineurin activity and increased levels of nuclear NFAT3, as well as increased mRNA and protein expression of Kir2.1 (226). On the other hand, long-term β-adrenoceptor stimulation reduced I<sub>Ks</sub> with a corresponding decrease in mRNA and protein expression of its β-subunit KCNE1. BAPTA-AM (calcium chelator), cyclosporine (calcineurin inhibitor) and INCA6 (NFAT blocker) prevented the β-adrenoceptor-induced KCNE1 downregulation, indicating that prolonged β<sub>1</sub>-adrenoceptor stimulation suppressed I<sub>Ks</sub> via Epac-mediated calcium/calcineurin/NFAT signaling (227). Interestingly, APD prolongation due to changes in potassium channel expression can itself increase intracellular calcium and activate calcineurin-mediated excitation-transcription coupling. For example, knockdown of KCNE2 increased intracellular calcium transient, calcineurin activity and nuclear NFAT levels, and pretreatment with

inhibitors of LTCC or calcineurin attenuated the activation of calcineurin/NFAT and cardiomyocyte hypertrophy (228).

These data highlight the complex positive and negative feedback loops involved in proarrhythmic calcium-dependent, calcineurin-mediated transcriptional regulation. Moreover, the activation of NFAT in cardiomyocytes is isoform- and tissue-specific, and tightly controlled by nuclear export. For example, under physiological conditions, NFATc1 is expressed predominantly in the nucleus of both atria and ventricle, while NFATc3 is localized in the cytoplasm and can be translocated to the nucleus by angiotensin II and endothelin-1 only in the atria (229). Ventricular cardiomyocytes from HF rabbits showed an increased basal nuclear localization of endogenous NFATc3 and a reduced responsiveness of NFAT translocation to phenylephrine stimulation (229). In ranolazine-treated HF mice, calcineurin expression and NFATc3 nuclear localization were diminished (230). Finally, recent data suggest that nuclear translocation of calcineurin might be required for full transcriptional activity of NFAT. Such nuclear calcineurin can act as an intranuclear calcium sensor in cardiac hypertrophy, detecting local calcium release via IP<sub>3</sub>R (231).

Several computational models have been developed for different components of the calcium/calcineurin/NFAT pathway. A model of the rabbit ventricular cardiomyocyte with dynamic interaction of calcium with CaM, CaMKII and calcineurin predicted that the different affinities of CaM for CaMKII and calcineurin determines their sensitivity to dynamic changes in local calcium in cardiomyocytes (221). Furthermore, a model of calcineurin-dependent nuclear NFAT translocation has been used to study the role of calcineurin in cardiac hypertrophy (232, 233). Finally, a recent computational study has evaluated the activation of calcium/CaM/calcineurin/NFAT pathway during  $\beta$ -adrenoceptor stimulation (234). The model showed that  $\beta$ -adrenoceptor stimulation increases intracellular calcium concentrations, which activate calcineurin and promote NFAT translocation, similar to experimental observations (234). However, none of the available models have closed the loop and integrated calcineurin/NFAT signaling with transcriptional regulation of cardiomyocyte calcium-handling proteins or ion channels to study the role of this pathway in long-term proarrhythmic cardiac remodeling.

### **2.5.4.3 CaMKII-dependent transcriptional regulation**

Calcium-dependent transcriptional regulation is also mediated by CaMKII via the histone deacetylase (HDAC) and MEF2 signaling cascades, as well as the downstream regulatory element agonist modulator (DREAM) transcription factor (14, 235). CaMKII regulates HDAC4 via binding to a unique docking site and phosphorylation of Ser467 and Ser632 (236, 237). In the nucleus, HDAC4 inhibits several transcription factors, including MEF2, a mediator of cardiac structural remodeling. Phosphorylation of HDAC4 by cytosolic CaMKII prevents its nuclear import (**Figure 2.4**), thus releasing the inhibition of MEF2 (237, 238). CaMKII $\delta$  knockout mice are protected from structural remodeling in response to pressure overload due to reduced HDAC4 phosphorylation, confirming the role of CaMKII and HDAC4 phosphorylation in pathological cardiac

remodeling (239). Similarly, CaMKII promotes the nuclear translocation of the transcriptional repressor DREAM, resulting in inhibition of various target genes. CaMKII-dependent DREAM translocation is part of a negative feedback mechanism involved in LTCC downregulation to control calcium influx within cardiomyocytes (235, 240). Computational modeling has been employed to investigate CaMKII-mediated LTCC regulation via DREAM (240). In this model, simulation of dynamic DREAM-dependent modulation of  $I_{Ca,L}$  showed that in the presence of high intracellular calcium, CaMKII activation gradually decreased  $I_{Ca,L}$ , thereby reducing the intracellular calcium and CaMKII activity as a feedback mechanism (240). These studies illustrate how computational modeling may be used to link intracellular calcium handling and arrhythmia-maintaining electrical remodeling.

### **2.5.5 Deciphering bidirectional electromechanical interactions**

Bidirectional electromechanical interactions (E-C coupling and mechanoelectrical feedback) are strongly present in the heart. When altered, these interactions play a key role in arrhythmogenesis (241) and mechanical pump failure (18). Dysregulation of intracellular calcium may affect the contractile properties of the heart and lead to mechanical dysfunction, including impaired contraction and pump failure, but also diastolic dysfunction and impaired relaxation. For example, down-regulation of SERCA, together with reduction of calcium influx through LTCC and NCX upregulation, reduces SR calcium content, decreases calcium-transient amplitude and contributes to slower time-to-peak and calcium-transient decay in the ventricle during HF (165). Alterations in the myofilament calcium sensitivity also affect calcium-buffering properties and normal E-C coupling, contributing to cardiac arrhythmias and impaired mechanical function (242). For example, mutations in sarcomeric proteins such as MyBP-C (MYBPC3) can increase myofilament calcium sensitivity and promote diastolic dysfunction and cardiac hypertrophy because of the inability of the myofilament to release calcium and relax from contraction (243). In addition, these abnormalities in cardiomyocyte contraction may lead to mitochondrial calcium-handling abnormalities, leading to an increased mitochondrial ROS production. This may impair cellular electrical function by ROS-mediated signaling and oxidative damage, potentially leading to proarrhythmic events (244).

The importance of the interplay between calcium handling and contraction for arrhythmogenesis is highlighted by studies reporting the effect of pharmacological electromechanical uncouplers, used for example during optical mapping experiments, on the inducibility of ventricular arrhythmias. Arrhythmia inducibility was greatly impaired by electromechanical uncouplers (245). Mechanical abnormalities may impact calcium handling through mechano-sensitive mechanisms including length-dependent activation, slow force response (or Anrep effect), SACs, or myofilament sensitization. These may lead to potentially proarrhythmic calcium waves or modulate repolarization, promoting arrhythmia initiation and maintenance (3). Length-dependent activation is the property of the cardiac muscle by which an increase in sarcomere length leads to a decrease in the amount of calcium required for contraction (246). This process is due to an increase in buffered calcium with stretch because of an

increased troponin-C calcium affinity and forms the basis of the Frank-Starling law of the heart at the organ and circulation level. The Anrep effect is another mechanism by which mechanics may impact calcium handling. It corresponds to the response of the heart to increased afterload by an increase in contractility to maintain cardiac output by an increase in sarcolemmal sodium upon sustained stretch, reducing NCX activity and leading to an accumulation of calcium in the sarcolemma and SR by SERCA uptake. SACs produce a current in response to mechanical stimuli and can contribute to ectopic activity, as well as proarrhythmic changes in APD, CV, and dispersion of repolarization (247). Stretch may also initiate calcium sparks, which remain localized in the normal heart, but may evolve into arrhythmogenic calcium waves in the situation of high mechanical load. Indeed, changes in cardiac mechanical load such as stretch or sudden release of stretched myocardium can generate calcium release from cross-bridge detachment in the non-uniform cardiac muscle, which may trigger calcium waves (248, 249). The main multiscale mechanisms through which mechanics may alter intracellular calcium and promote arrhythmias are summarized in **Figure 2.5**.

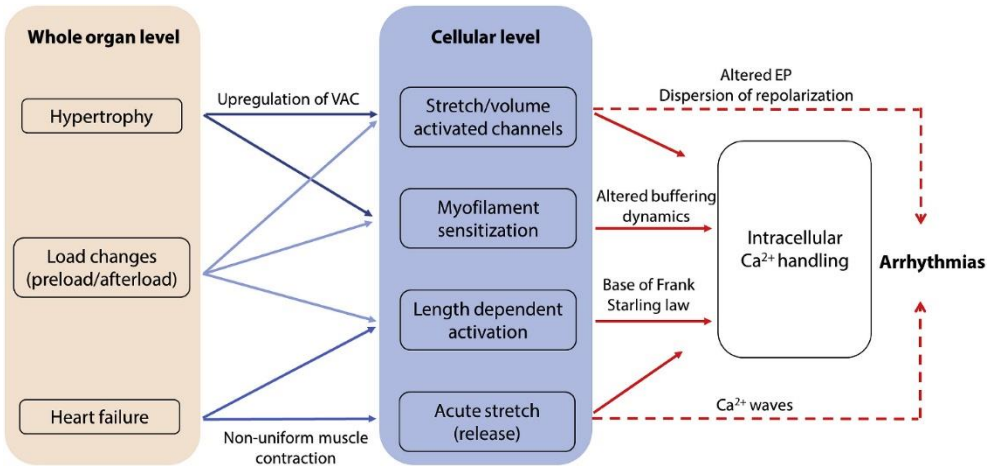


**Figure 2.5:** Effects of mechanical changes on intracellular calcium properties. At the whole organ level, mechanical changes observed for example in hypertrophy or heart failure affect cellular and molecular properties through myofilament sensitization, stretch or volume activated channels (SACs and VACs, respectively), length dependent sarcomere activation or acute stretch. These factors directly affect calcium properties and may have proarrhythmic effects through altered electrophysiology or the generation of calcium waves.

Advances in experimental techniques have, to a certain extent, enabled investigation of the interplay between calcium regulation and mechanical function of the heart. Early on, calcium imaging and patch-clamp experiments in stretched cardiomyocytes (250-252) have revealed the direct impact of stretch on calcium-handling properties. More recently, mechanisms such as ROS production activated by the microtubule network (253) have been reported to be involved in calcium-handling abnormalities and altered contractile function. Novel techniques such as the cell-in-gel system (254) also allowed the application of stress during cardiomyocyte contraction and the measurement of calcium and stress properties. Other experiments altering

mechanical load and electrical stimuli, such as quick-release protocols (255) or force frequency (256) experiments, have also highlighted the bidirectionality of electromechanical interactions. Imaging techniques such as confocal microscopy (257), optical mapping (258), and more recently 3-dimensional super-resolution imaging (164) have made it possible to visualize the structures involved. However, most imaging modalities, except for recent work using high-resolution 4-dimensional ultrasound-based strain imaging (259), require electromechanical uncoupling. For example, optical mapping often uses blebbistatin, a myosin-II inhibitor, to reduce motion artifacts during measurements (260). Newer techniques such as hydrogels or 3-dimensional cell-in-gel setups (261) also allow to study the effects of mechanical load on action potential and ion channels. However, most of these experiments are performed in small animals such as rodents or rabbits. New techniques aiming at replicating human cardiac properties have emerged, such as 3-dimensional engineered heart tissue, but they remain relatively immature (262). Assessing calcium and contractile properties in human cardiomyocytes in the presence of controlled electromechanical feedback therefore remains a challenge. In addition, at the organ level, dynamic situations such as exercise have both electrical and mechanical effects. As such, understanding their individual contribution to arrhythmic risk under specific pathological conditions is challenging for current experimental techniques.

Computational models are a powerful tool to better understand electromechanical coupling and the individual contributions of cardiac electrics and mechanics in cardiac dysfunction. Most models developed so far have focused on simulating electrophysiology, but some have been developed to investigate electromechanical interactions. Among these, most have combined an existing electrophysiological model (263, 264) with a model of sarcomere contraction (265-267) (Table 2.3). Such models, developed for species ranging from rodents (268) to human (269), have been applied to a range of multiscale applications such as understanding the effect of stretch on the slow force response (268), highlighting the impact of strain and fibrosis on cellular electrophysiology through SAC (270), simulating the effect of phasic  $\beta$ -adrenoceptor stimulation on APD, or investigating the relations between force, calcium and AP alternans in heart failure (269) (Table 2.3). However, validation of these models remains challenging because of the sparsity and heterogeneity of the experimental data available, as shown in Table 2.3. Moreover, current electromechanical computational models have several limitations. For example, in all models, SACs have been implemented phenomenologically, using linear current-voltage relationships (268, 271). Furthermore, the most widely used contraction model for EM model development (267) is based on a non-physiological calcium-handling model. Finally, prospectively designed *in vitro* human data for model development and validation is urgently needed. These computational models therefore hold great promise to better understand electromechanical interactions and especially the strong interplay between mechanics and calcium regulation, but future developments, in close synergy with experiments, are needed to ensure better insight in electromechanical coupling.

Electro-mechanical model	Electro-physiological model	Contraction model	Application	Validation	Species
<b>Timmermann</b> (270)	Winslow et al., Grandi et al., O'Hara et al.	Rice et al. and Land et al.	Effect of strain and fibrosis on cellular electrophysiology (through SAC).	Qualitative comparison of force, calcium and length to experimental data	Canine / Human
<b>Pueyo</b> (272)	O'Hara et al. and ten Tusscher et al.	Niederer et al.	Phasic $\beta$ -adrenergic stimulation effect on phasic changes in APD	No model validation in paper	Human, rabbit and rat
<b>Zile</b> (269)	Ten Tusscher et al.	Rice et al.	Generation of force and AP alternans in heart failure	No model validation in paper	Human
<b>Campbell</b> (273)	Flaim et al.	Rice et al.	Sources of heterogeneous electromechanical behavior in cardiac transmural cells	Qualitative comparison of calcium, AP, shortening and transmural APD trends for one beat with experimental data	Canine
<b>Rice</b> (267)	Shannon et al. (Chicago model)	Rice et al.	Simulation of electromechanical coupling and its feedback effect	Comparison of AP, calcium, and contraction to experimental data	Rabbit
<b>Niederer</b> (268)	Pandit et al., Hinch et al.	Niederer et al.	Effect of stretch on the slow force response	Based on previous validation of model components. Qualitative comparison of maximum tension and APD as function of frequency	Rat
<b>Iribe</b> (274)	Noble et al.	Rice et al.	CaMKII involvement in calcium handling, interval-force relation and alternans	Interval dependence of twitch duration, restitution, potentiation and staircase phenomenon	Rat
<b>Ekaterinburg</b> (275, 276)	Noble et al.	Ekaterinburg	Effect of mechanical heterogeneity on APD and dispersion of repolarization	No model validation in paper	Rat
<b>Matsuoka</b> (277)	Shirokov et al.	Negroni and Lascano	Simulation of electromechanical coupling	Qualitative comparison of sarcomere length with experiments	Guinea pig
<b>Sachse</b> (278)	Priebe-Beuckelmann and Luo-Rudy	Sachse et al.	Effect of regional electrophysiological	Comparison to the EP model but no validation of	Human

			heterogeneities on force development	the coupled model	
--	--	--	--------------------------------------	-------------------	--

**Table 2.3:** Previously published electromechanical cardiomyocyte models.

## 2.6 Conclusion

Cardiomyocyte calcium handling is a major determinant of E-C coupling and alterations of one or more calcium-handling proteins may induce arrhythmias through the formation of ectopic activity, direct and indirect ion channel modulations, and structural remodeling. Computational modeling of cardiac cellular electrophysiology has made significant progress in the last decades and is now employed together with *in vitro* experiments to provide new insights on cardiomyocyte calcium-handling and its abnormalities. However, many issues remain unresolved, including the complex molecular interactions mediating calcium-dependent ion-channel regulation, the molecular mechanisms and proarrhythmic consequences of SCAEs, and the complex post translational calcium signaling pathways and mechanisms of long-term transcriptional regulation of calcium handling. Therefore, combined *in vitro* and *in silico* studies to address such issues will be required. Detailed experimental studies are needed for model development and validation. At the same time, well-validated models can be employed to confirm cause-effect relationships suggested by experimental findings, address experimental limitations (e.g., the inability to control subcellular structure) and to extrapolate experimental findings to a higher scale (e.g., tissue or organ level). Key highlights and challenges for *in vitro* and *in silico* studies of cardiomyocyte calcium handling are summarized in **Table 2.4**.

Highlights	
1.	Calcium affects multiple targets inside a cardiomyocyte, including transmembrane ion channels, contractile proteins, and calcium-dependent signaling pathways to ensure an optimal electromechanical function of the heart.
2.	Calcium-handling abnormalities trigger cardiac arrhythmias through several pathogenic processes: initiation of ectopic activity, ion channel modulation (direct and indirect), and structural remodeling.
3.	The many interacting calcium-dependent arrhythmia mechanisms, with feed-back and feed-forward loops operating over a wide range of spatial and temporal scales make a detailed experimental characterization challenging, highlighting the potential benefits of combining <i>in vitro</i> studies with <i>in silico</i> studies.
4.	Computational modeling has undergone major improvements in the past 80 years and is now being used to support <i>in vitro</i> studies and assist clinical decision-making.
5.	Atrial and ventricular calcium-handling models with different level of complexities have been developed based on experimental data and are increasingly reflecting the complex subcellular structure responsible for cardiomyocyte calcium handling and alterations in the spatiotemporal distribution of calcium-handling proteins in disease.
6.	Some cellular models have started to incorporate the electrophysiological effects of calcium-dependent signaling pathways (e.g., CaMKII- and calcineurin-NFAT signaling cascades), although long-term regulation (e.g., through calcium-dependent transcriptional regulation) is missing in almost all models.
7.	Computational modeling has also been employed to investigate the impact of electromechanical coupling and mechanoelectrical feedback on cardiac arrhythmogenesis and contractile dysfunction.

<p>8. Computer models rely on high-quality experimental data. At the same time, they offer perfect observability and perfect control, making it possible to evaluate cause-and-effect relations that at present cannot be addressed experimentally. Studies exploiting the synergistic potential between both approaches will help to further our understanding of cardiac arrhythmias.</p>
<p><b>Challenges</b></p>
<ol style="list-style-type: none"> <li>1. Comparison of existing <i>in vitro</i> data is challenging, partly due to differences in experimental models and methodologies, resulting in apparent inconsistent findings, which complicate the investigation of the role of calcium-handling abnormalities in cardiac arrhythmias.</li> <li>2. There is increasing evidence that many ion channels undergo direct and indirect calcium-dependent regulation, but their role in arrhythmogenesis is incompletely understood and not incorporated in most computational models.</li> <li>3. Many calcium-handling properties can only be measured indirectly in living cardiomyocytes (e.g., SERCA function), or require correlation between experiments under different conditions (e.g., immunocytochemistry in fixated cells and live-cell calcium imaging to study structure-function relationships)</li> <li>4. The bidirectional interactions between mechanical load and calcium-handling mechanisms remain incompletely understood.</li> <li>5. Most of the computational models of calcium handling focus on a single element and/or condition, due to the limited availability of <i>in vitro</i> data, ignoring potential relevant interactions between different calcium-dependent signaling cascades.</li> </ol>

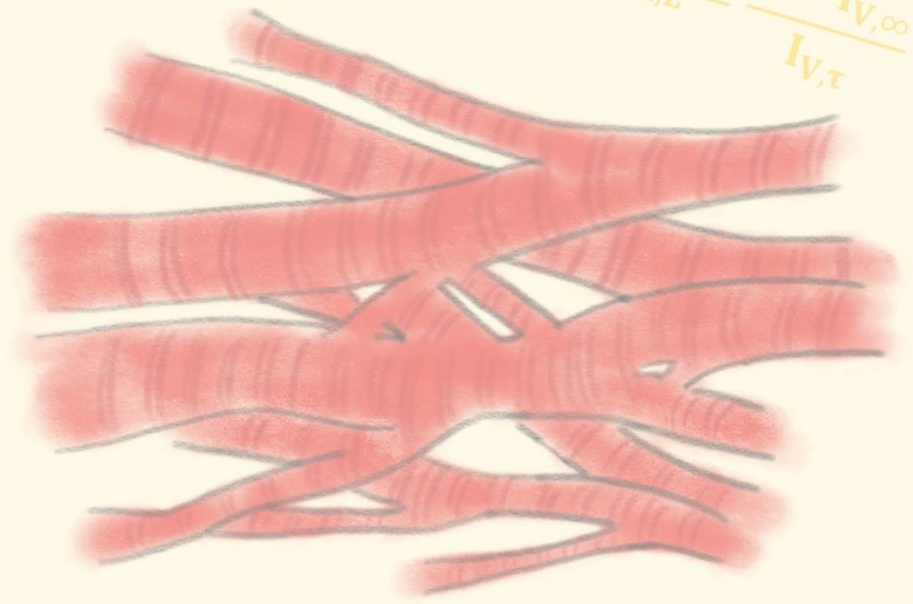
**Table 2.4:** Summary of highlights and challenges for *in vitro* and *in silico* studies of cardiomyocyte calcium handling.





$$\frac{dV_m}{dt} = -\frac{1}{C_m} * I$$

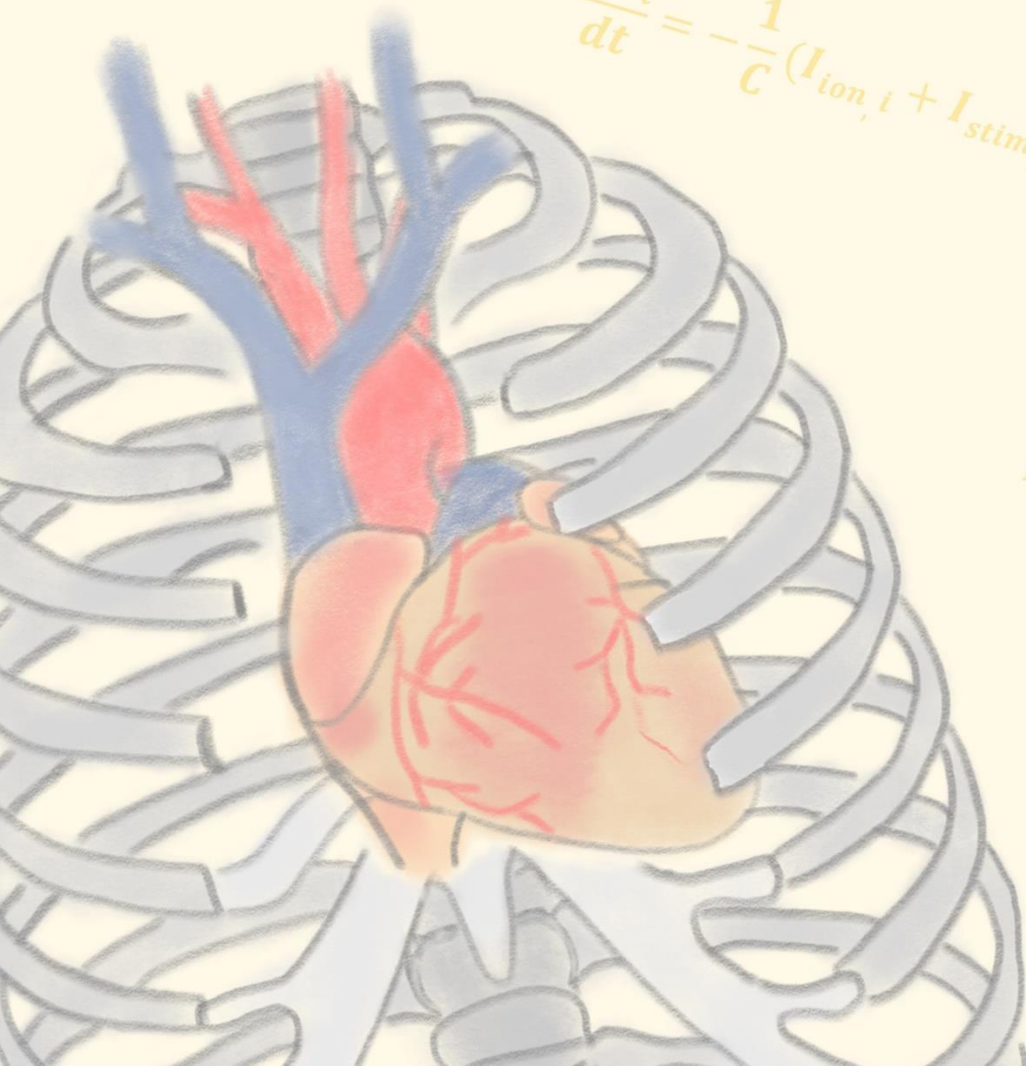
$$y_{Ca,L} = \frac{1 - I_{V,\infty}}{I_{V,\tau}}$$



$$x_{Ca,L} = \frac{I_{V,\infty}}{I_{V,\tau}}$$

$$\delta I_{Ca,L}^{s,m} =$$

$$\frac{dV_i}{dt} = -\frac{1}{C} (I_{ion,i} + I_{stim,i} + I_{diff,i})$$



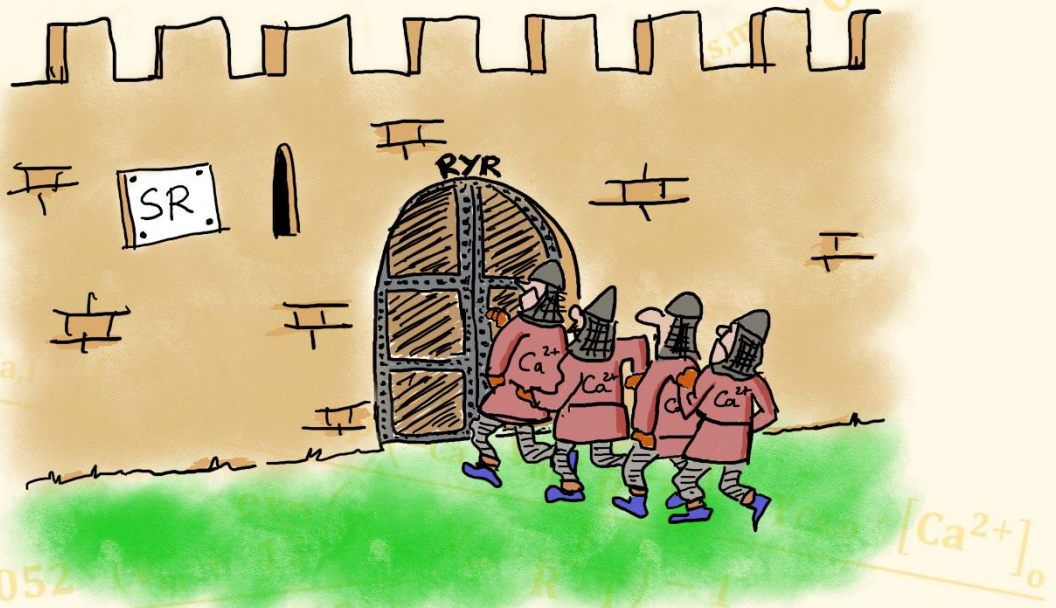
$$\bar{I}_{Ca,L}^{s,m} = P_{Ca,L} \cdot (z$$

$$ACT_{\tau} = 0.59$$

# Chapter 3

**The subcellular distribution of ryanodine receptors and L-type calcium channels modulates calcium transient properties and spontaneous calcium release events in atrial cardiomyocytes**

H. Sutanto\*, B. van Sloun\*, P. Schönleitner, M. van Zandvoort, G. Antoons and J. Heijman  
(\* ) equally contributed  
*Front Physiol.* 9:1108.



$$\frac{dV}{dt} = \frac{I_{stim} - (I_K + I_{Na} + I_{leak})}{C_m}$$

## ABSTRACT

SCaEs from the sarcoplasmic reticulum play crucial roles in the initiation of cardiac arrhythmias by promoting triggered activity. However, the subcellular determinants of these SCaEs remain incompletely understood. Structural differences between atrial and ventricular cardiomyocytes, e.g., regarding the density of T-tubular membrane invaginations, may influence cardiomyocyte calcium handling and the distribution of cardiac RyR2 has recently been shown to undergo remodeling in AF. These data suggest that the subcellular distribution of calcium handling proteins influences proarrhythmic calcium handling abnormalities. Here, we employ computational modeling to provide an in-depth analysis of the impact of variations in subcellular RyR2 and LTCC distributions on calcium transient (CaT) properties and SCaEs in a human atrial cardiomyocyte model. We incorporate experimentally observed RyR2 expression patterns and various configurations of axial tubules in a previously published model of the human atrial cardiomyocyte. We identify an increased SCaE incidence for larger heterogeneity in RyR2 expression, in which SCaEs preferentially arise from regions of high local RyR2 expression. Furthermore, we show that the propagation of calcium waves is modulated by the distance between RyR2 bands, as well as the presence of experimentally observed RyR2 clusters between bands near the lateral membranes. We also show that incorporation of axial tubules in various amounts and locations reduces CaT time to peak. Furthermore, selective hyperphosphorylation of RyR2 around axial tubules increases the number of spontaneous waves. Finally, we present a novel model of the human atrial cardiomyocyte with physiological RyR2 and LTCC distributions that reproduces experimentally observed calcium handling properties. Taken together, these results significantly enhance our understanding of the structure-function relationship in cardiomyocytes, identifying that RyR2 and LTCC distributions have a major impact on systolic CaTs and SCaEs.

### 3.1 Introduction

Despite the significant advances in the treatment of cardiovascular diseases during the past 50 years, the frequency of cardiac arrhythmias, particularly AF, is projected to increase, placing a significant burden on modern healthcare systems (279-281). Calcium handling abnormalities play a key role in ectopic activity and reentry, the two major arrhythmogenic mechanisms underlying AF (2, 6, 64). Dysfunctional RyR2s, and/or sarcoplasmic reticulum (SR) calcium overload can promote the occurrence of SCaEs (2), which transiently increase the cytosolic calcium concentration, activating the sodium-calcium exchanger type-1 (NCX1), resulting in a depolarizing transient-inward current and promoting DADs and triggered activity. Although potential proarrhythmic effects of changes in RyR2 expression and phosphorylation have been extensively discussed (204, 282), these studies have generally employed tissue homogenates, ignoring the subcellular structure of calcium handling proteins. However, there is increasing evidence that differences in subcellular structure critically influence cardiomyocyte calcium handling. For example, there are important structural differences between atrial and ventricular cardiomyocytes that affect calcium handling, including a relative paucity of transverse T-tubular structures in atrial cardiomyocytes, resulting in a centripetal calcium wave propagating from RyR2 opposing LTCC at the sarcolemma to RyR2 in the cell center (283). On the other hand, there is increasing evidence for a role of axial tubules in atrial cardiomyocyte calcium handling (284-287). Axial tubules promote a faster calcium release from the SR in the center of the cell, which is partly mediated by coupling of LTCC to hyperphosphorylated RyR2 surrounding axial tubules (160). Moreover, this axial tubular system undergoes extensive remodeling during cardiovascular disease, e.g., proliferating in the presence of atrial hypertrophy (160) or disappearing in mice with atrial-specific knock-out of NCX1 (287). AF-related remodeling of the RyR2 distribution has also been reported, with RyR2 cluster fragmentation and redistribution in sheep with AF, which was associated with increased calcium spark frequency (158). However, the exact impact of the subcellular distribution of RyR2 and LTCC on cardiomyocyte calcium handling remains largely unknown. It is currently experimentally challenging to study both (sub)cellular structure and functional calcium handling in human atrial cardiomyocytes, as the former usually requires fixation of the cardiomyocyte for antibody staining. The perfect control and observability provided by computational modeling may help to overcome this challenge (94).

A number of ventricular cardiomyocyte models have been developed that are able to simulate local calcium handling and SCaEs (90, 103). Models of atrial subcellular calcium handling, on the other hand, are relatively scarce (94). We recently developed a human atrial cardiomyocyte model with stochastic gating of RyR2 channels and both transverse and longitudinal compartmentation of calcium handling. Our model has a simple cell-type specific subcellular structure with LTCC only present on the lateral membranes, reflecting the relative paucity of T-tubules in isolated atrial cardiomyocytes (32). However, all currently available atrial and ventricular cardiomyocyte models assume a homogeneous distribution of calcium handling

proteins. Here, we hypothesized that changes in the subcellular distribution of RyR2 and LTCC may promote proarrhythmic SCAEs. We employed both confocal microscopy and computational modeling to study for the first time the impact of the subcellular distribution of RyR2 and LTCC on calcium handling in atrial cardiomyocytes.

## 3.2 Materials and methods

### 3.2.1 Animal model, cardiomyocyte isolation, and confocal imaging

This investigation conformed with the Guide for the Care and Use of Laboratory Animals Published by the US National Institutes of Health (NIH Publications No. 85-23, revised 1996). All animal handling conformed with directive 2010/63/EU and experimental protocols were approved by the local ethical committee (DEC2014-112). New Zealand white rabbits (2.5–3.5 kg) were anesthetized and hearts were rapidly removed, excised, washed, perfused and cut into smaller pieces, as previously described (130). Atrial cardiomyocytes were seeded on laminin coated coverslips. RyR2s were labeled with primary (mouse monoclonal (C3-33), IgG1, Sigma-Aldrich®, MO, 1:50) and secondary (Alexa® 488, goat anti-mouse, Abcam, UK, 1:100) antibodies (288, 289). The RyR2-stained atrial cardiomyocytes were imaged with a Leica TCS SP8 confocal microscope using a 63x objective (NA 1.40, oil immersion). The RyR2-Alexa® 488 antibody complex was detected at 420–520 nm under 488 nm laser illumination. Z-stacks were taken with a step size of 0.26  $\mu\text{m}$  and an xy-resolution of 0.07  $\mu\text{m}$ .

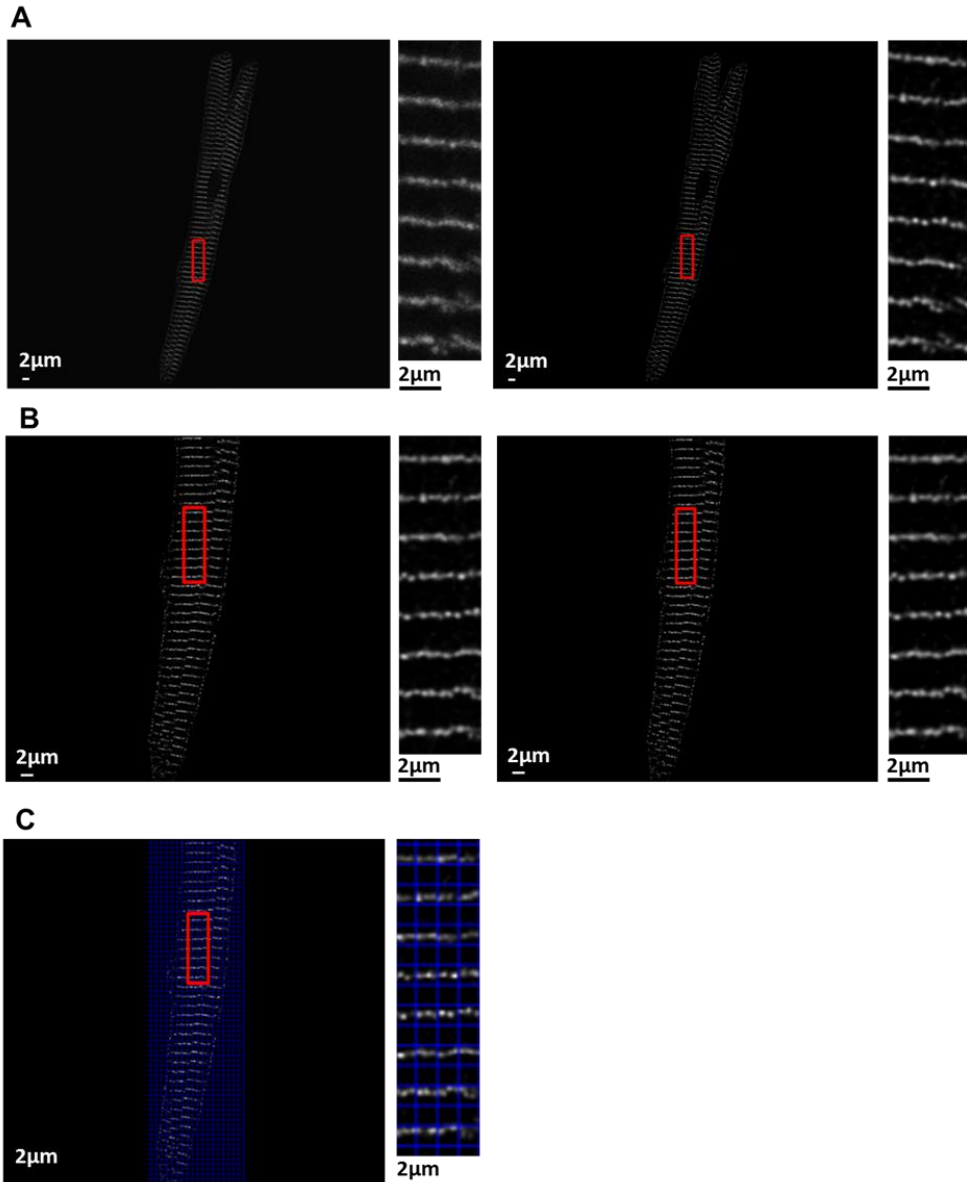
### 3.2.2 Image processing

Image processing was employed to enable simulation with the experimental data (Figure 3.1). The raw z-stacks were deconvolved using Huygens Professional (SVI, Netherlands). A single slice from the z-stack was selected and rotated to obtain a horizontal alignment of the RyR2. The image was thresholded and overlaid with a grid of  $\sim 1 \mu\text{m}^2$  units, in which the mean pixel intensity was calculated for every square of the grid as an indirect readout of local RyR2 density. The edges of the RyR2 expression matrix were detected and stretched to accommodate the rectangular dimensions of the virtual cardiomyocyte (100x18  $\mu\text{m}$ ). The resulting RyR2 distribution matrix was implemented in the computational model and employed for simulation.

### 3.2.3 Computational modeling

Simulations were based on a previously published model of the human atrial cardiomyocyte in which local calcium handling was simulated by dividing the virtual cardiomyocyte into 50 segments, each containing 18 subcellular calcium domains located between two membrane domains (32, 94). The RyR2 expression in the published model was identical in every unit. We further optimized the 50-segment model with uniform RyR2 distribution based on experimental values (32, 124, 130, 285, 290–292) of calcium handling properties and SCAE properties reported in previous publications (Figures 3.2, 3.3). In the present work, the model was extended to enable simulations with heterogeneous RyR2 distributions. Heterogeneity in RyR2 distribution across all 50x18 units was incorporated by drawing a random number

from a Gaussian distribution with mean 1.0 and standard deviation  $\sigma$  for each unit and subsequently scaling these numbers to achieve the desired total RyR2 density.



**Figure 3.1: Image processing workflow.** A) Single slice of the RyR2 z-stack in a rabbit atrial cardiomyocyte stained with Alexa® 488 antibodies, before (left) and after deconvolution (right). B) Rotated region of interest before (left) and after thresholding (right). C) Alignment with a regular grid of  $\sim 1 \mu\text{m}^2$  units, which was subsequently employed to determine the average RyR2 expression level. Smaller panels show region indicated in the red box at a higher magnification.

We also developed a model with a higher longitudinal resolution (100 segments), enabling simulation of the experimentally observed banded expression of RyR2. Axial tubules were simulated in the 100-segment model by including LTCC in axial-tubule-associated calcium domains. Parameters of the 100-segment model with uniform RyR2 expression were adjusted to achieve similar calcium handling properties as the 50-segment model (Figures 3.2, 3.3) and heterogeneous RyR2 expression patterns were generated analogous to the 50-segment model. The values of the optimized parameters for both model versions are given in Table 3.1. For the LTCC, the 8-state Markov model was used as previously described (32, 94). Parameters of this Markov model are shown in Appendix A. All results in the 100-segment model are provided following pacing for 250 beats at 0.5 Hz to achieve a quasi-steady state (Figure 3.4).

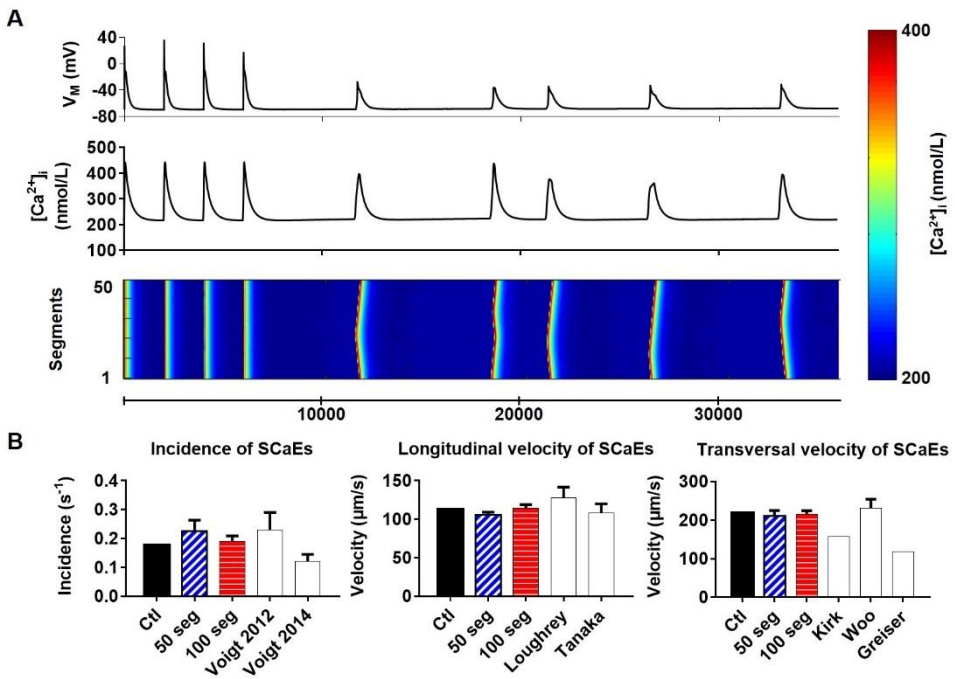


**Figure 3.2:** Validation of SCAEs in the published (Ctl), adapted 50-segment (50 seg) and 100-segment (100 seg) models. A) Membrane potential ( $V_M$ ), CaT and longitudinal line scan of three triggered CaTs and 5 SCAEs during follow-up in the 50 seg model. B) Validation of SCAE incidence, as well as velocity of calcium waves in longitudinal and transversal directions for the three model versions (based on  $n=6$  simulations each) compared to experimental data (32, 124, 130, 285, 290-292).

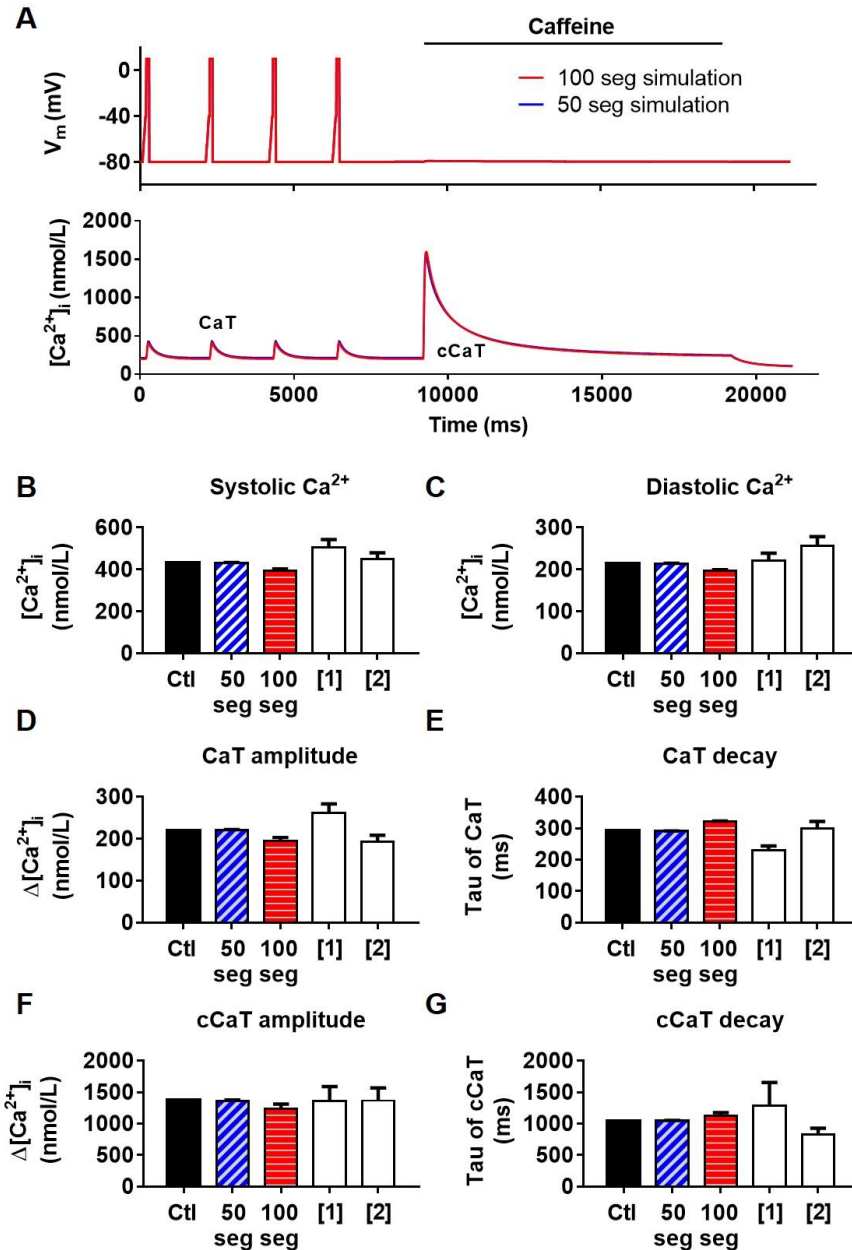


**Figure 3.3:** Validation of calcium handling properties of the models. A) Membrane potential ( $V_M$ ) and intracellular calcium showing protocol used during simulation: Four triggered waves were applied prior to the simulated administration of caffeine to induce calcium release from the sarcoplasmic reticulum. B-G) Comparison of the calcium handling properties of control, 50-segment and 100-segment models to experimental data; [1] = (124), [2] = (32).

Parameter	Published model (32)	50-segment model	100-segment model	Exp. RyR2 + axial tubules + hyperphos. RyR
$\tau_{diff,SRS} \leftrightarrow cyt$ (ms)	12	12	10	10
$\tau_{diff,seg,SRS}$ (ms)	0.3	0.3	0.22	0.10
$\tau_{diff,dom,SRS}$ (ms)	0.125	0.125	0.16	0.10
$\tau_{diff,seg,cyt}$ (ms)	0.6	0.6	0.6	0.6
$\tau_{diff,dom,cyt}$ (ms)	0.6	0.6	0.6	0.6
$\tau_{diff,seg,SR}$ (ms)	15	15	5	5
$\tau_{diff,dom,SR}$ (ms)	15	15	5	5
$N_{RyRs}$	594,000	514,800	2,772,000	79,200,000
SERCA2a (K <sub>mr</sub> )	1.00	1.00	1.25	1.25
<b>I<sub>CaL</sub> parameters</b>		<b>As in (94):</b>	<b>As in (94):</b>	<b>As in (32) with adjusted P<sub>1</sub>:</b>
	P <sub>1</sub> = 9.45	P <sub>1</sub> = 9.45	P <sub>1</sub> = 9.45	P <sub>1</sub> = 8.50
	P <sub>2</sub> = 49.1	P <sub>2</sub> = 65.0	P <sub>2</sub> = 65.0	P <sub>2</sub> = 49.1
	P <sub>3</sub> = 10.349	P <sub>3</sub> = 6.000	P <sub>3</sub> = 6.00	P <sub>3</sub> = 10.349
	P <sub>4</sub> = 26.553	P <sub>4</sub> = 12.00	P <sub>4</sub> = 12.00	P <sub>4</sub> = 26.553
	P <sub>5</sub> = 17.5	P <sub>5</sub> = 27.5	P <sub>5</sub> = 27.5	P <sub>5</sub> = 17.5
	P <sub>6</sub> = 3.0	P <sub>6</sub> = 5.0	P <sub>6</sub> = 5.0	P <sub>6</sub> = 3.0
	P <sub>7</sub> = 13.825	P <sub>7</sub> = 43.825	P <sub>7</sub> = 43.825	P <sub>7</sub> = 13.825
	P <sub>8</sub> = 6.3836	P <sub>8</sub> = 45.00	P <sub>8</sub> = 45.00	P <sub>8</sub> = 6.3836
	P <sub>9</sub> = 14.9186	P <sub>9</sub> = 5.000	P <sub>9</sub> = 5.000	P <sub>9</sub> = 14.9186
	P <sub>10</sub> = 1.100	P <sub>10</sub> = 5.000	P <sub>10</sub> = 5.000	P <sub>10</sub> = 1.100

**Table 3.1:** Parameters changes applied to the published model (32) with 50 segments to fit the previously published experimental data. Subsequently, slight modifications of the parameters, including the number of RyR (NRyRs), K<sub>mr</sub> of SERCA and time constant ( $\tau$ ) SRS, were made to the 100-segment models to obtain similar physiological calcium handling properties.

### 3.2.4 Data Analysis and Statistics

Due to the stochastic nature of the simulations, each condition was simulated at least 6 times and data were expressed as mean  $\pm$  standard deviation. Statistical differences between conditions were evaluated using one- or two-way ANOVA with Tukey post-hoc test for multiple comparisons, or independent t-test, depending on the number of groups and the type of the data. Statistical analyses were performed using GraphPad Prism 7 (GraphPad Software Inc., La Jolla, CA).

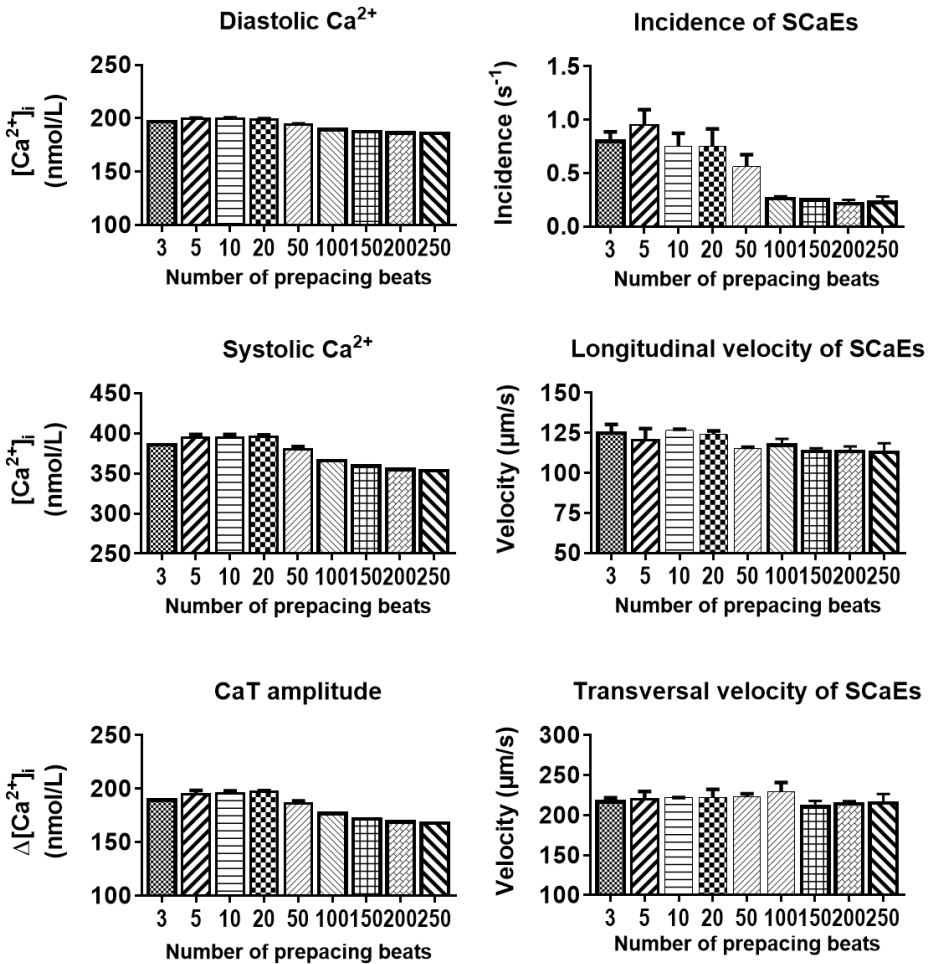


**Figure 3.4:** Analysis of calcium handling properties for different prepacing durations in the 100-segment model. Simulations were run for various numbers of prepacing beats to find a value that represents a quasi-steady state condition. Calcium handling parameters of triggered CaTs (diastolic levels, systolic levels and CaT amplitude; left panels) and SCAEs (incidence, longitudinal and transversal velocity; right panels) were documented. After prepacing for 200-250 beats, calcium handling parameters reach an acceptable steady state. Accordingly, results in the main manuscript for the 100-segment model are shown after 250 beats prepacing.

### 3.3 Results

#### 3.3.1 Effects of heterogeneity in RyR2 distribution on SCAEs

The model with uniform RyR2 distribution ( $\sigma = 0.0$ ) produced a few large calcium waves and corresponding DADs during follow-up after pacing at 0.5 Hz, in line with experimental data (Figure 3.2). Increasing the heterogeneity of RyR2 distribution from  $\sigma = 0.0$  to  $\sigma = 0.4$  while keeping the total number of RyR2 constant substantially increased the incidence of SCAEs, but decreased their size (Figures 3.5A–C). For

example, with  $\sigma = 0.4$ , the incidence of SCAEs was 14x larger ( $3.31 \pm 0.51 \text{ s}^{-1}$  vs.  $0.23 \pm 0.04 \text{ s}^{-1}$ ,  $n = 6$ ,  $p < 0.05$ ) and the average size of a calcium wave as fraction of cardiomyocyte volume was 5x smaller than with  $\sigma = 0.0$  ( $0.18 \pm 0.02$  vs.  $0.91 \pm 0.11$ ,  $n = 6$ ,  $p < 0.05$ ). Increasing RyR2 heterogeneity also reduced the longitudinal ( $100.94 \pm 3.66 \text{ }\mu\text{m/s}$  vs.  $211.24 \pm 7.24 \text{ }\mu\text{m/s}$ ,  $n = 6$ ,  $p < 0.05$ ) and transversal ( $102.81 \pm 3.94 \text{ }\mu\text{m/s}$  vs.  $210.79 \pm 14 \text{ }\mu\text{m/s}$ ,  $n = 6$ ,  $p < 0.05$ ) velocity of calcium waves. We compared the magnitude of the effect of altered RyR2 distribution to a 25% change in total RyR2 expression. In line with previous results (32), increasing calcium flux led to an increased number of SCAEs and smaller SCAE size (**Figures 3.5B, C**). Likewise, a 25% decrease in total RyR2 led to lower SCAE incidence and bigger SCAE size. Increasing RyR2 heterogeneity and total expression had synergistic effects on SCAE incidence.

Next, we investigated the origins of SCAEs in simulations with heterogeneous RyR2 distributions (crosses in **Figure 3.6A**). SCAEs preferentially arose from units with high local RyR2 expression. In agreement, comparison of the histograms of relative RyR2 expression of all  $50 \times 18$  units with those of SCAE-inducing units revealed that SCAE-inducing units had significantly higher local RyR2 expression (**Figure 3.6B**). The difference in mean RyR2 expression between SCAE-inducing units and all units was most pronounced in simulations with large heterogeneity in RyR2 distribution (**Figure 3.6C**), establishing units with high local RyR2 expression as foci for SCAEs.

### **3.3.2 Simulation of experimentally characterized RyR2 distributions**

RyR2 distributions were studied in rabbit atrial cardiomyocytes. In line with previous results, we observed a banded RyR2 pattern with  $\sim 2 \text{ }\mu\text{m}$  inter-band distance (**Figures 3.7A, B**). We analyzed the average RyR2 intensity after image-processing of the confocal images based on a square grid with  $1 \text{ }\mu\text{m}^2$  units and identified a significant variation in RyR2 distribution along the bands (**Figure 3.7C**). The histogram of relative RyR2 expression showed a large peak at near-zero levels, reflecting the units between RyR2 bands and a normal distribution with standard deviation  $\sigma = 0.253$  for the RyR2 intensity within the bands (**Figure 3.7D**). In order to simulate this physiological RyR2 distribution, we increased the resolution of our model, simulating 100 segments of  $1 \text{ }\mu\text{m}$  with alternating pattern of RyR2 expression (**Figure 3.8**) and validated its calcium handling properties based on experimental data (**Figures 3.2, 3.3**). We also incorporated the option to simulate the regional expression of LTCC localized in axial tubules and the experimentally observed hyperphosphorylation of axial-tubule-associated RyR2 (discussed below). A schematic representation of the subcellular structure of the model is shown in **Figure 3.9**.

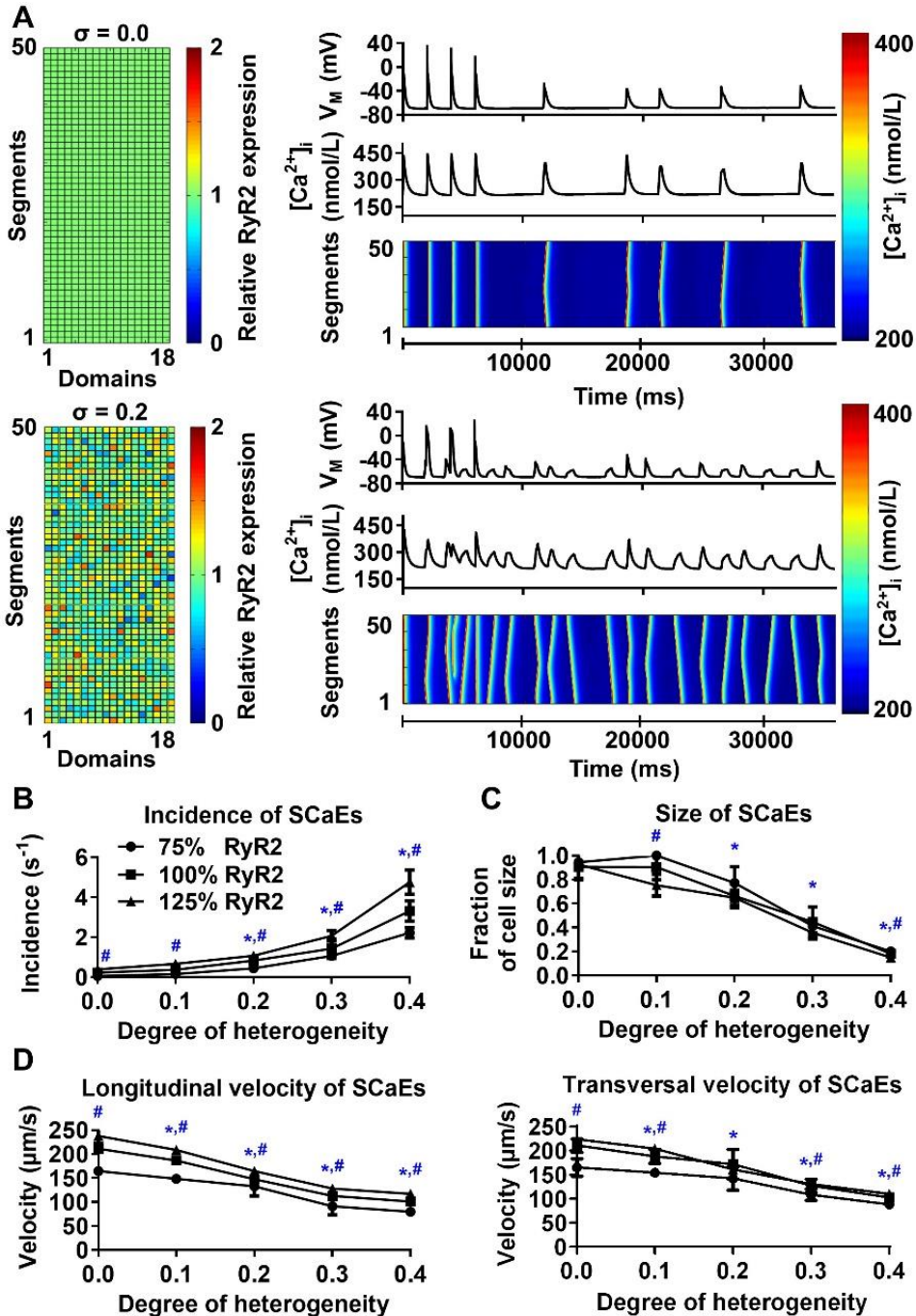


**Figure 3.5:** Effects of RyR2 distribution heterogeneity on SCAEs in the 50-segment model. (A) Representative examples comparing heterogeneity ( $\sigma$ ) of 0.0 (uniform expression, top) and 0.2 (bottom). The 50x18 matrices (left) show the relative RyR2 distribution. The membrane potential ( $V_M$ ), whole-cell calcium concentration, and longitudinal line scan on the right show marked differences in number of SCAEs and corresponding

*Subcellular structures modulate spontaneous releases in atrial cardiomyocyte*

delayed afterdepolarizations between both groups. (B–D) SCAE incidence (B) and size (C), as well as longitudinal and transversal velocity of calcium waves (D) as a function of RyR2 heterogeneity  $\sigma$  for different levels of total RyR2 expression (75% of control: circles; 100% of control: squares; 125% of control: triangles). SCAE incidence increases, while size decreases with increasing RyR2 heterogeneity. \* indicates  $P < 0.05$  vs. the group with heterogeneity 0.0 and # indicates statistically significant differences among three levels of RyR2 expression;  $n = 6$  per condition.

Chapter 3

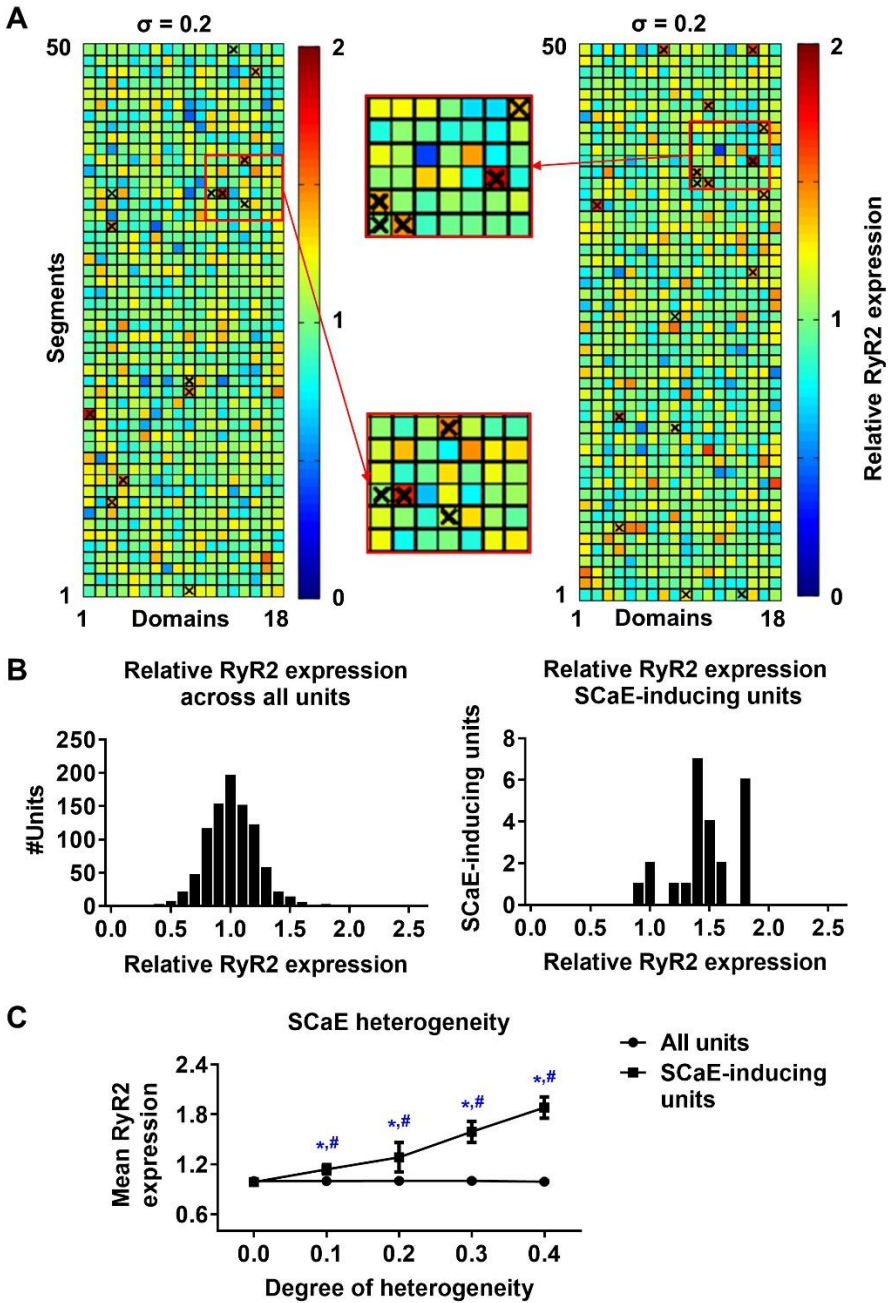


**Figure 3.6: Origins of SCaEs.** (A) Two representative examples of 50x18 matrices with heterogeneous RyR2 distribution ( $\sigma = 0.2$ ). Red colors indicate high local RyR2 expression and blue colors low local RyR2 expression. The origins of individual calcium waves are marked with crosses. Insets depict enlarged portions of the RyR2 distribution, showing that crosses mainly coincide with regions of high local RyR2 expression. (B) Histograms of relative RyR2 expression in all units (left) and units which were the origin of a SCaE (SCaE-inducing units). SCaEs arise mainly from units with high local RyR2 expression. (C) Mean relative RyR2 expression in SCaE-inducing units (squares) and all units (circles, 1.0 on average by definition) for different degrees of RyR2 heterogeneities. \* indicates  $P < 0.05$  vs. the group with heterogeneity 0.0 and # indicates  $P < 0.05$  between mean relative RyR2 expression in SCaE-inducing units and all units;  $n = 6$  per condition.

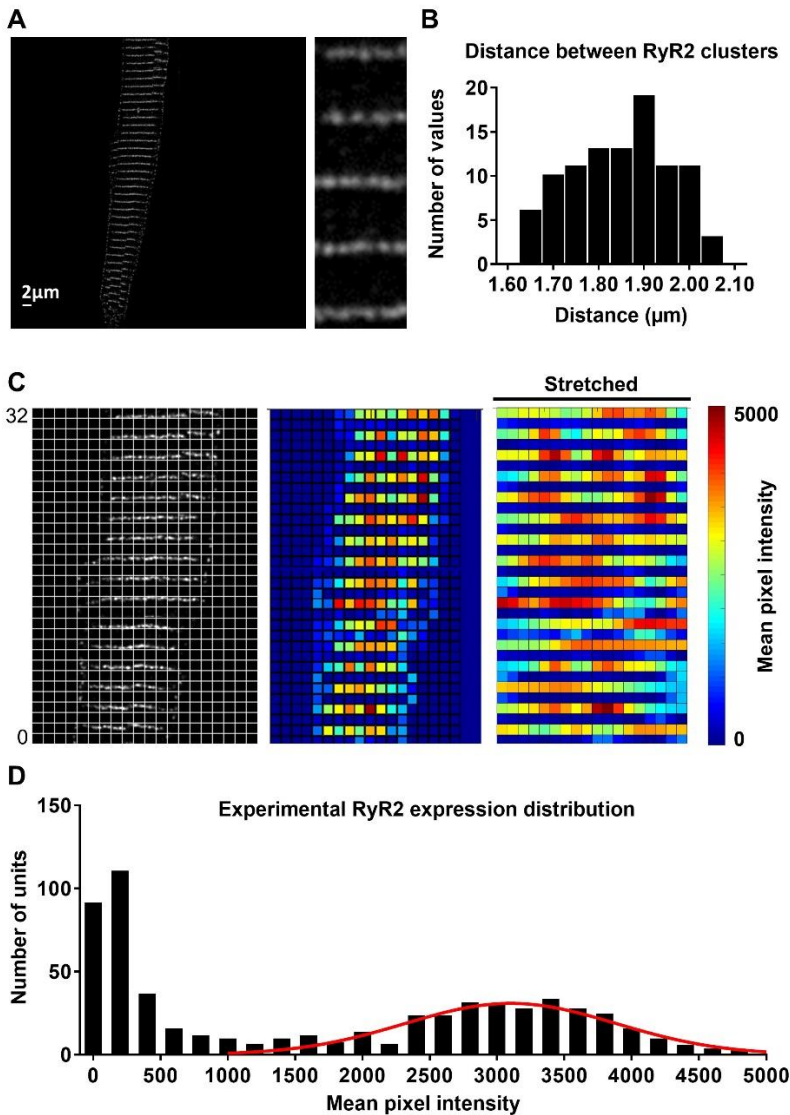


**Figure 3.7: Experimental distribution of RyR2 expression in atrial cardiomyocytes.** (A) Confocal image of RyR2 staining in a rabbit atrial cardiomyocyte. Inset shows region of interest at higher magnification, revealing that RyR2 clusters assemble in a regular banded pattern along the Z-band. (B) Distribution of

distances between RyR2 bands, showing that majority of these gaps were around 1.8–1.9  $\mu\text{m}$ . (C) Image processing of confocal images and alignment with a regular grid of  $\sim 1 \mu\text{m}^2$  units (left) enabled quantification of local RyR2 expression (right panel, red indicates high local RyR2 expression and blue low local RyR2 expression). (D) Histogram of experimental RyR2 expression distribution across all units with a large peak around 0, representing units between bands of RyR2 expression and a normal distribution of RyR2 expression within bands (line shows normal distribution with standard deviation of 0.253).

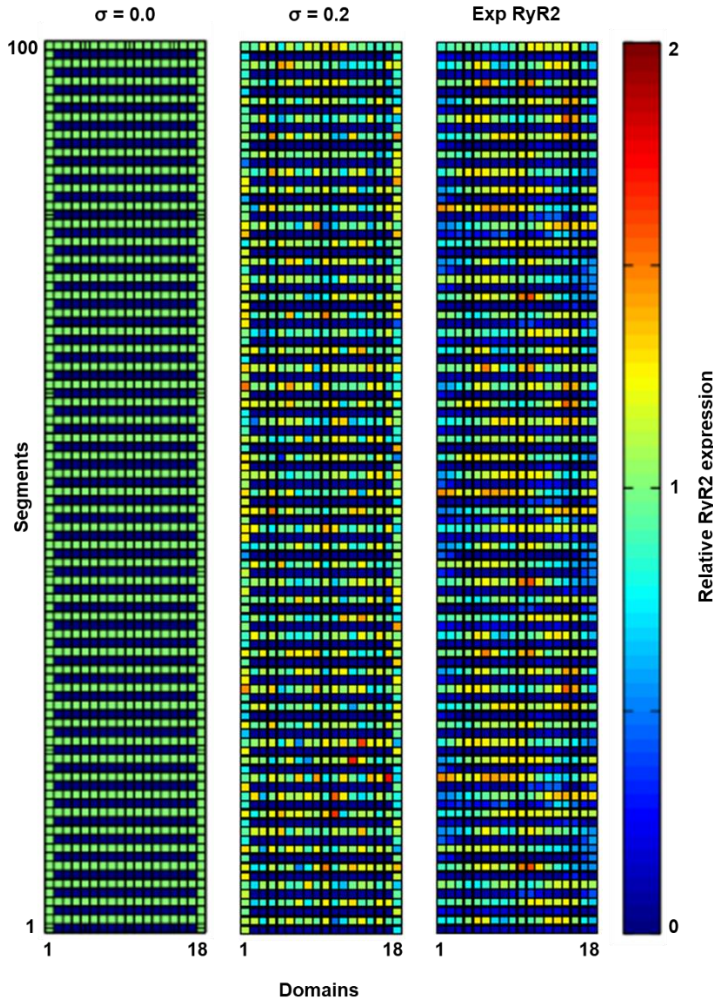


**Figure 3.8:** Comparison of RyR2 distribution in 100-segment simulations with  $\sigma = 0.0$ ,  $\sigma = 0.2$  and with experimental RyR2 distribution. Simulation of experimental RyR2 distribution displayed banded patterns with several areas with local high RyR2 expressions.

Similar to the 50-segment model, increasing heterogeneity of RyR2 expression in the 100-segment model led to an increase in SCAE incidence and reduction in SCAE size, longitudinal and transversal velocity (**Figure 3.10**), with SCAEs originating from units with high local RyR2 expression (**Figure 3.11**). However, despite similar SCAE-incidence with a uniform RyR2 distribution, the increase in SCAEs with increasing RyR2

heterogeneity was more pronounced in the 100-segment model (115-fold vs. 14-fold increase from  $\sigma = 0.0$  to  $\sigma = 0.4$  in the 100-segment and 50-segment models, respectively; **Figure 3.12**, **Figure 3.5**). Implementation of the experimentally observed RyR2 distribution pattern in the 100-segment model resulted in the occurrence of many small SCaEs, similar to our 100-segment simulations with heterogeneity ( $\sigma$ ) 0.3 and 0.4 (with SCaE incidence of  $12.96 \pm 0.28 \text{ s}^{-1}$  in the experimentally observed RyR2 distribution vs.  $9.88 \pm 1.16 \text{ s}^{-1}$  in  $\sigma = 0.3$  and  $21.83 \pm 2.62 \text{ s}^{-1}$  in  $\sigma = 0.4$ , **Figure 3.10B** and **Figure 3.12**). Longitudinal and transversal velocity of SCaEs in the experimentally observed RyR2 distribution model were similar to 100-segment simulations with  $\sigma = 0.2$  (**Figure 3.10D**). Heterogeneities in RyR2 expression did not affect properties of the LTCC-triggered CaT in the absence of preceding SCaEs (**Figure 3.13**).

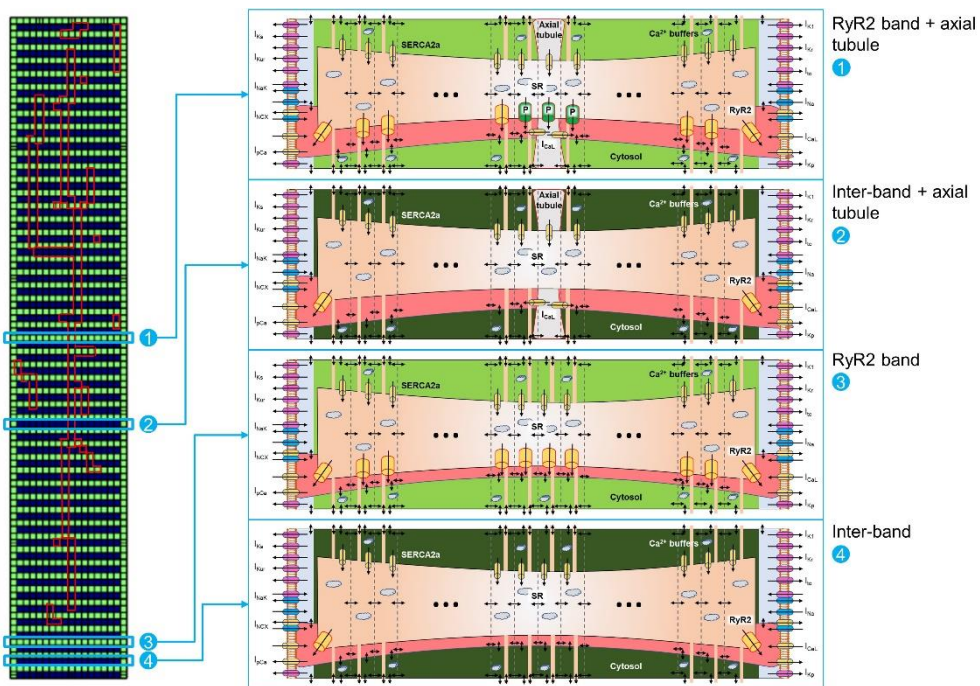


**Figure 3.9:** Schematic representation of 100-segment model. The model is represented by four different locations in the virtual cardiomyocyte. [1] represents an RyR2 band with axial tubule and hyperphosphorylated RyR2 (indicated with “P” in the scheme) adjacent to the axial tubule, as reported by [160]. [2] represents an inter-band gap with axial tubule. [3] represents an RyR2 band without axial tubule. [4] represents an inter-band gap without axial tubule. Each segment is divided into 18 domains, as depicted in the matrix on the left, but only a subset of domains is shown for clarity. Please note the expression of RyR2 in the first and last domains in the segments located between RyR2 bands (i.e., [2] and [4]).

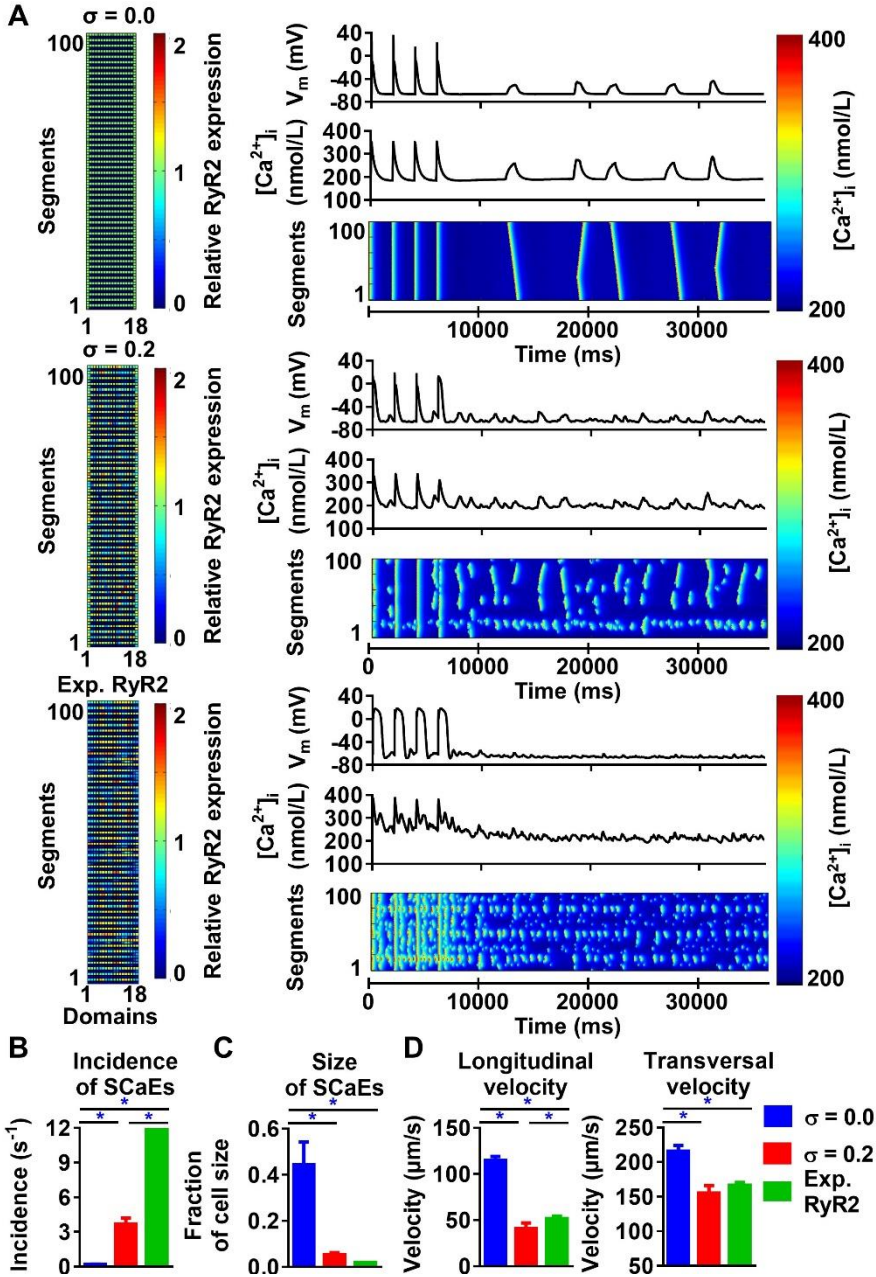


**Figure 3.10:** Effects of RyR2 distribution heterogeneity on SCAEs in the 100-segment model. (A) Representative examples comparing heterogeneity ( $\sigma$ ) of 0.0 (uniform expression, top), 0.2 (middle), and experimentally observed RyR2 expression patterns (bottom) on membrane potential ( $V_m$ ), whole-cell CaT, and longitudinal line scan (right panels). The 100x18 matrices (left) of relative RyR2 expression incorporate the experimentally observed 2  $\mu m$  inter-band distance. (B–D) SCAE incidence (B), size (C), as well as longitudinal and transversal velocity of calcium waves (D) in 100-segment simulations with  $\sigma = 0.0$ ,  $\sigma = 0.2$ , and experimentally observed RyR2 expression. Incorporation of the experimentally observed RyR2

expression in the original 100-segment model results in a large (non-physiological) number of small SCAEs. \* indicates  $P < 0.05$  between indicated groups;  $n = 6$  per condition.

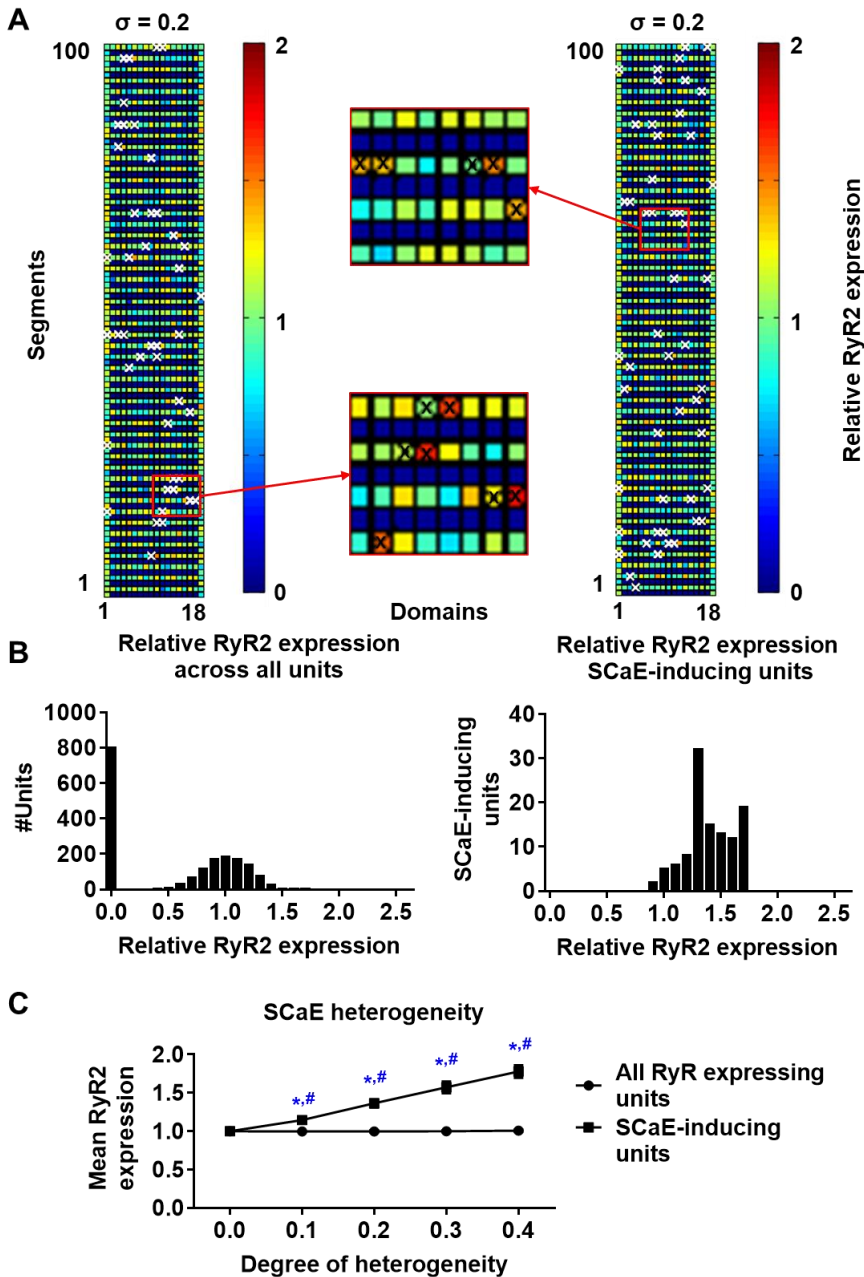


**Figure 3.11: Origins of SCAEs.** A) Two representative examples of 100x18 matrices with heterogeneous RyR2 distribution ( $\sigma = 0.2$ ). Red colors indicate high local RyR2 expression and blue colors low local RyR2 expression. The origins of individual calcium waves are marked with crosses. Insets depict enlarged portions of the RyR2 distribution. B) Histograms of relative RyR2 expression in all units (left) and units which were

the origin of a SCaE (SCaE-inducing units). C) Mean relative RyR2 expression in SCaE-inducing units (squares) and all units (circles, 1.0 by definition) for different degrees of RyR2 heterogeneities. Consistent with the 50-segments simulations (Figure 3.6), the spontaneous waves originated from units with local high RyR2 expression. \* indicates  $P < 0.05$  vs. heterogeneity 0.0; # indicates  $P < 0.05$  between mean relative RyR2 expression in SCaE-inducing units and all units;  $n = 6$  per condition.

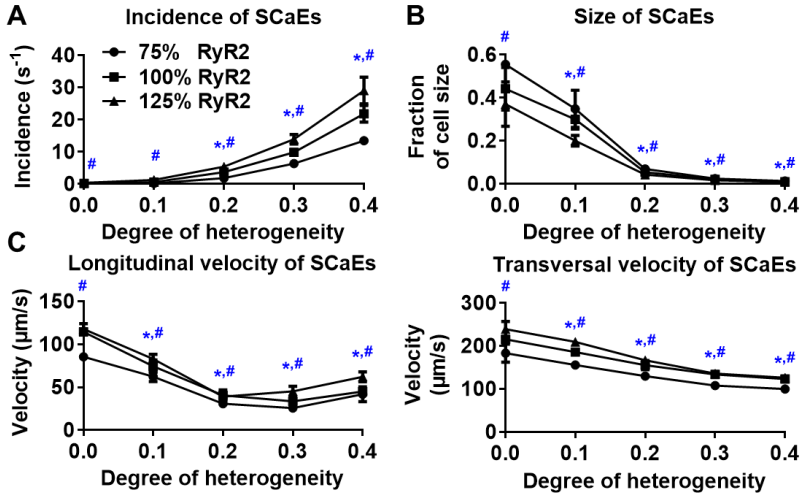


**Figure 3.12:** Comparison of SCaE properties for various degrees of RyR2 heterogeneity and total expression in the 100-segment model. A-C) SCaE incidence (A) and size (B), as well as longitudinal and transversal velocity of calcium waves (C) as a function of RyR2 heterogeneity  $\sigma$  for different levels of total RyR2 expression (75% of control: circles; 100% of control: squares; 125% of control: triangles). In line with the 50-segment simulations, increasing the total RyR2 expression also increased the incidence and lowered the size of the wave. \* indicates  $P < 0.05$  vs. the group with heterogeneity 0.0; # indicates significant difference among the three levels of RyR2 expression;  $n = 6$  per condition.

### 3.3.3 Modulation of SCaE propagation by the distance between RyR2s and RyR2 clusters at the lateral membrane

Previous studies have reported a closer spacing between RyR2s around the lateral membrane in rat atrial and ventricular cardiomyocytes (159, 293), rabbit atrial (294), ventricular (294, 295) and SA nodal cells (294), and human atrial cardiomyocytes (160). We similarly observed a higher density of RyR2 clusters at the lateral membrane in rabbit atrial cardiomyocytes (Figure 3.14A) and accordingly incorporated RyR2 expression in the first and last calcium unit of every segment of the virtual cardiomyocyte for the simulations of Figure 3.10. Next, we employed the model to assess the impact of these lateral RyR2s by comparing simulations with and without RyR2 in the outer calcium units for segments located between RyR2 bands. The absence of RyR2s in the lateral region of the cardiomyocyte prevented the propagation of SCaEs, resulting in a reduced longitudinal velocity and numerous small SR calcium releases (Figure 3.15A). This behavior could be fully restored by reducing the time constant of calcium diffusion between segments and normalizing the total RyR expression (SCaE incidence of  $0.24 \pm 0.04 \text{ s}^{-1}$  in the group with normalized RyR2 expression and corrected

longitudinal velocity vs.  $0.19 \pm 0.02 \text{ s}^{-1}$  in the control group,  $n = 6$ ,  $p > 0.05$ ; **Figure 3.15B**).

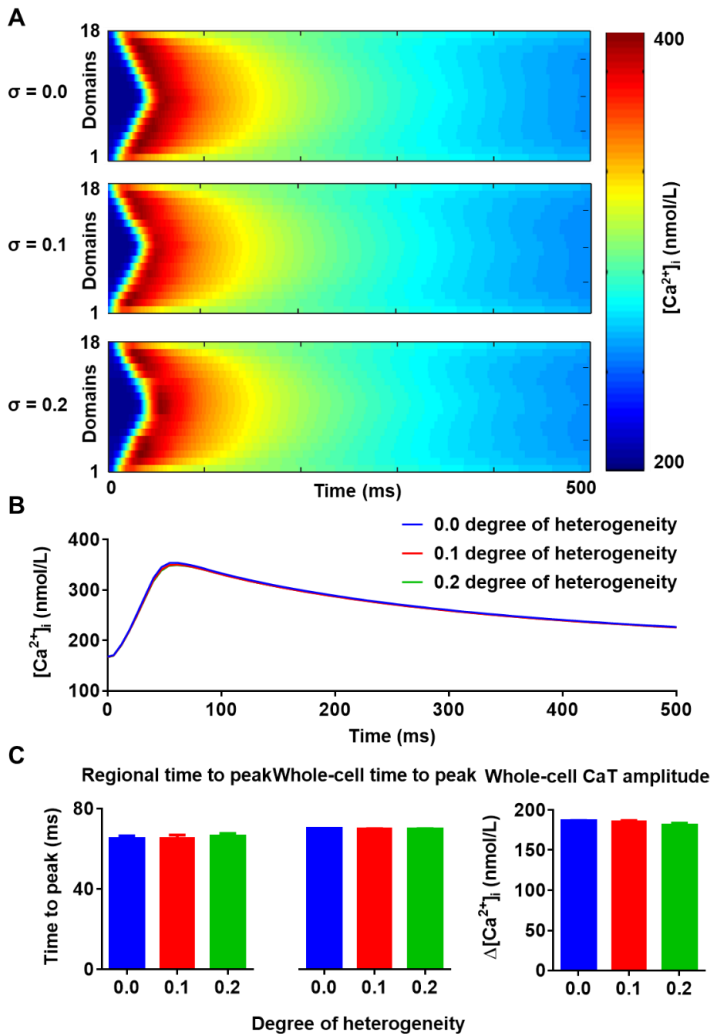


**Figure 3.13:** Effect of RyR2 heterogeneity on systolic calcium wave propagation in the absence of SCaEs. Comparison of the transversal calcium waves (A) and whole-cell CaT (B) during 0.5 Hz pacing for three different degrees of heterogeneity. As expected, the “V” shape pattern of atrial calcium wave propagation can be observed, reflecting the lack of transversal tubules. C) Quantification of time to peak and CaT amplitude (right) for the indicated line scan (“local”) or for the whole-cell CaT (“global”) for three levels of RyR2 heterogeneity. RyR2 heterogeneity did not affect the characteristics of systolic calcium wave propagation.

Next, we investigated the effect of alterations in the distance between RyR2 bands by simulating two or three segments without RyR2 expression between bands (instead of one). Although an increased RyR2 inter-band distance indeed slowed down the longitudinal velocity of SCaEs, it surprisingly did not impair propagation of SCaEs

and resulted in an increased SCAE incidence (Figure 3.14B, left column; Figures 3.14C-E). Subsequent analyses showed that the RyR2 expressed at the lateral membrane in segments without RyR2 bands are critical for the propagation of SCAEs. In particular, a similar increase in RyR2 inter-band distance in the model without lateral RyR2 between bands (but with corrected longitudinal velocity of SCAEs at baseline) resulted in failure of calcium wave propagation and many fragmented SCAEs (Figure 3.14B, right column). These data strongly suggest that the closer spacing of RyR2 at the lateral membrane that we observed experimentally may provide a safety factor for synchronous SR calcium release but may also facilitate propagation of large proarrhythmic calcium waves.

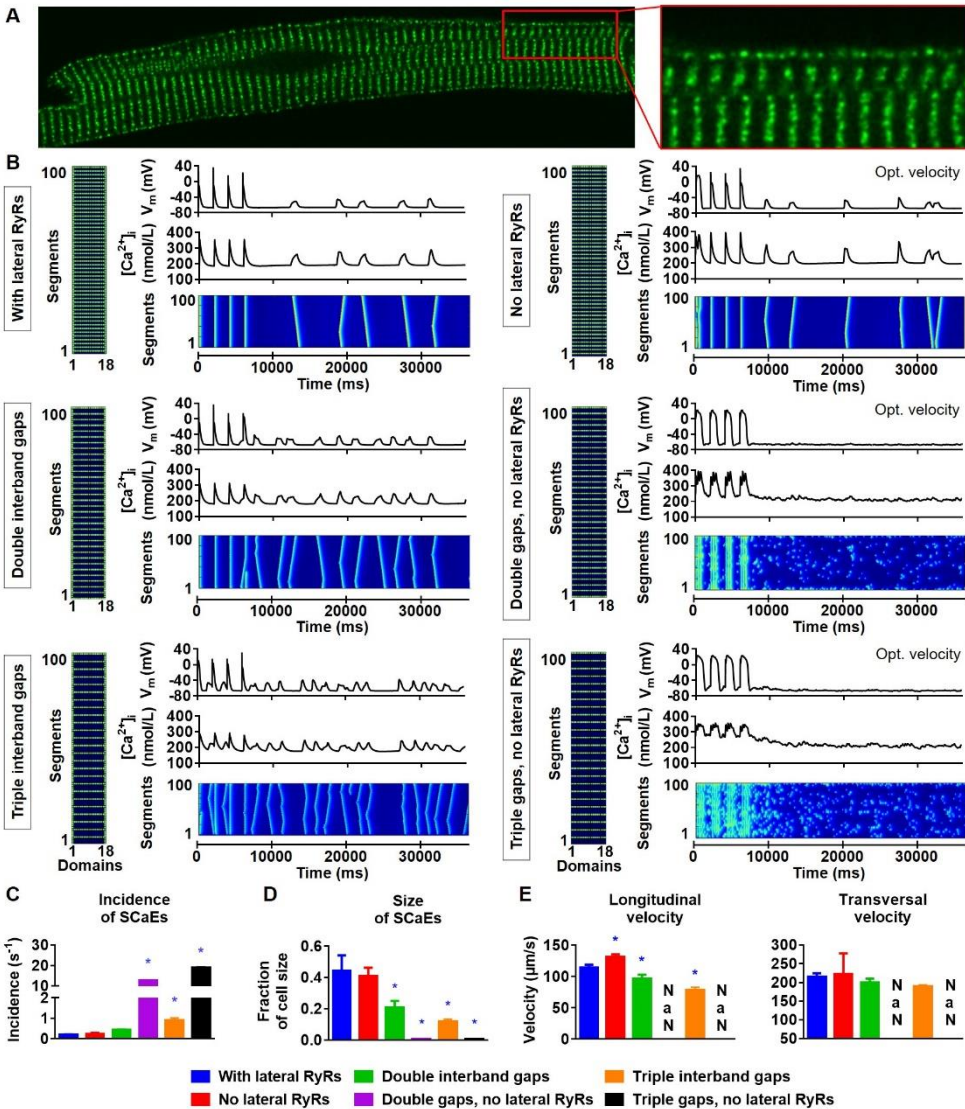


**Figure 3.14: Lateral RyR2s, inter-band distance and the propagation of SCAEs.** (A) Confocal image showing an increased density of RyR2 close to the lateral membrane in a rabbit atrial cardiomyocyte. (B) Representative examples of membrane potential ( $V_m$ ), whole-cell  $Ca^{2+}$ , and longitudinal line scan for the 100-segment model with single ( $\sim 2 \mu\text{m}$ ; top row), double (middle row) or triple (bottom row) inter-band distance, with (left column) or without (right column) expression of lateral RyR2s between bands. In all panels, the total number of RyR2 was adjusted to achieve a density of 2,772 RyR2 per unit. The time constant of longitudinal calcium diffusion between SR release spaces was adjusted from 0.22 to 0.07 ms in the model without lateral RyR2 expression to obtain similar SCAE properties for physiological inter-band distances. (C-E) SCAE incidence (C), size (D), as well as longitudinal and transversal velocity of calcium waves (E) for the six model versions. An increased inter-band distance increased the incidence of SCAEs, reduced their size and altered the longitudinal velocity without affecting the transversal velocity. \* indicates  $P < 0.05$  vs. the control model (100-segment model of single inter-band distance with lateral RyR2s; blue bars),  $n = 6$  per condition.

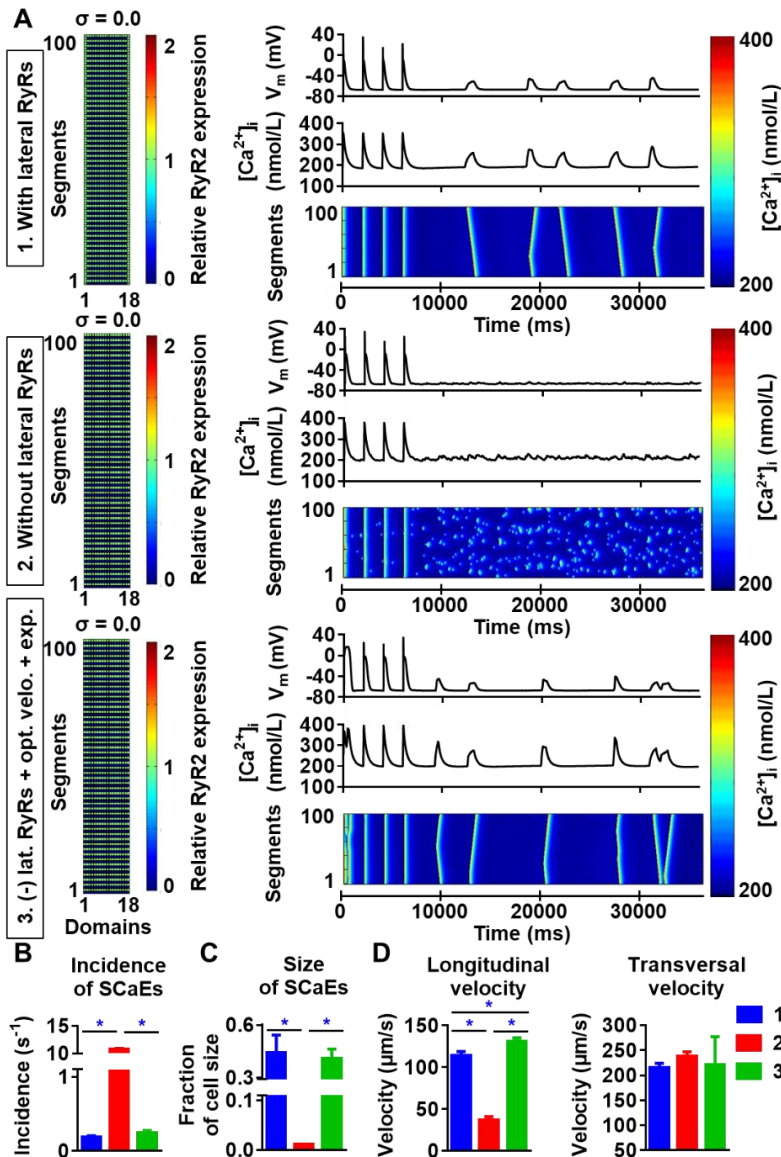


**Figure 3.15:** The importance of lateral RyR2s in the propagation of SCaEs. A) Membrane potential ( $V_M$ ), intracellular calcium and longitudinal line scan (top to bottom) for the baseline model with lateral RyR2 (A.1), the model without lateral RyR2s (A.2), and the model without lateral RyR2 after the adjustment of total RyR2 expression and correction of longitudinal velocity (A.3). B-D) incidence (B), size (C), as well as longitudinal and transversal velocity (D) of SCaEs for the three model conditions. Absence of lateral RyR2 resulted in more and smaller waves compared to baseline, presumably due to relocation and redistribution of RyR2. After correction of total RyR2 expression and longitudinal velocity, the incidence and size of SCaEs recovered. \* indicates  $P < 0.05$  between groups;  $n = 6$  per condition.

### **3.3.4 Inter-band RyR2 expression and SCaEs**

Similar to the results described by (158), our confocal images also showed occasional RyR2 expression between individual bands. We employed the 100-segment model to better understand the functional effects of these inter-band RyR2 clusters. For any degree of heterogeneity, the presence of inter-band RyR2 clusters resulted in fewer, slightly larger SCaEs compared to simulations without inter-band clusters (**Figures 3.16A–C**, compare blue and red bars), without affecting longitudinal and transversal velocity of SCaEs (**Figure 3.16D**). We hypothesized that the reduction in SCaEs was due to a reduction in maximal local RyR2 expression resulting from the redistribution of RyR2 from the bands to the inter-band clusters. RyR2 expression per unit was indeed lower in the homogeneous simulations with inter-band clusters (2,543 vs. 2,772 RyR2 per unit) and increasing the total RyR2 expression of the 100-segment model with inter-band clusters to 2,772 in all units containing RyR2 normalized SCaE incidence for low levels of RyR2 heterogeneity ( $0.185 \pm 0.015 \text{ s}^{-1}$  in the normalized RyR2 expression group vs.  $0.191 \pm 0.018 \text{ s}^{-1}$  in the group without inter-band clusters ( $\sigma = 0.0$ ),  $p > 0.05$  and  $0.470 \pm 0.138 \text{ s}^{-1}$  for normalized RyR2 expression vs.  $0.565 \pm 0.105 \text{ s}^{-1}$  without inter-band clusters ( $\sigma = 0.1$ ),  $p > 0.05$ ; **Figure 3.16B**). For high RyR2 heterogeneities, SCaE incidence remained lower in the presence of inter-band RyR2 cluster, even after adjusting the total RyR2 expression. Under these conditions, SCaEs are frequent, suggesting that annihilation or merging of small SCaEs arising around inter-band clusters contributes to a lower incidence of observed SCaEs, even after adjusting RyR2 expression.

### **3.3.5 The impact of axial tubules on atrial calcium handling**

Axial tubules are unique to atrial cardiomyocytes, but their role in calcium handling is not fully understood. Axial tubules contain LTCCs, modulating CICR and centripetal calcium wave propagation. We incorporated various configurations of axial tubules in the 100-segment model and investigated their impact on depolarization-induced, LTCC-triggered CaTs and SCaEs. Addition of an axial tubule to the model reduced time-to-peak of the regional LTCC-triggered CaT (based on a virtual transversal line scan through the region with the axial tubule) and slightly increased the CaT amplitude (**Figure 3.17**). Moreover, time to peak of the transversal-line-scan-based CaT is influenced by both the number of parallel axial tubules and their location. The reduction in time to peak was largest with an axial tubule located in the center of the virtual cardiomyocyte, and addition of two or more parallel axial tubules further reduced the time to peak (**Figure 3.17**). The impact of axial tubules on whole-cell CaT properties depended on axial-tubule length and was limited for short axial tubules (compare

regional and whole-cell time to peak in **Figure 3.17B**). However, a longer axial tubule network, such as that observed experimentally (160), also significantly shortened time to peak of the whole-cell CaT (**Figure 3.17B**, rightmost columns).

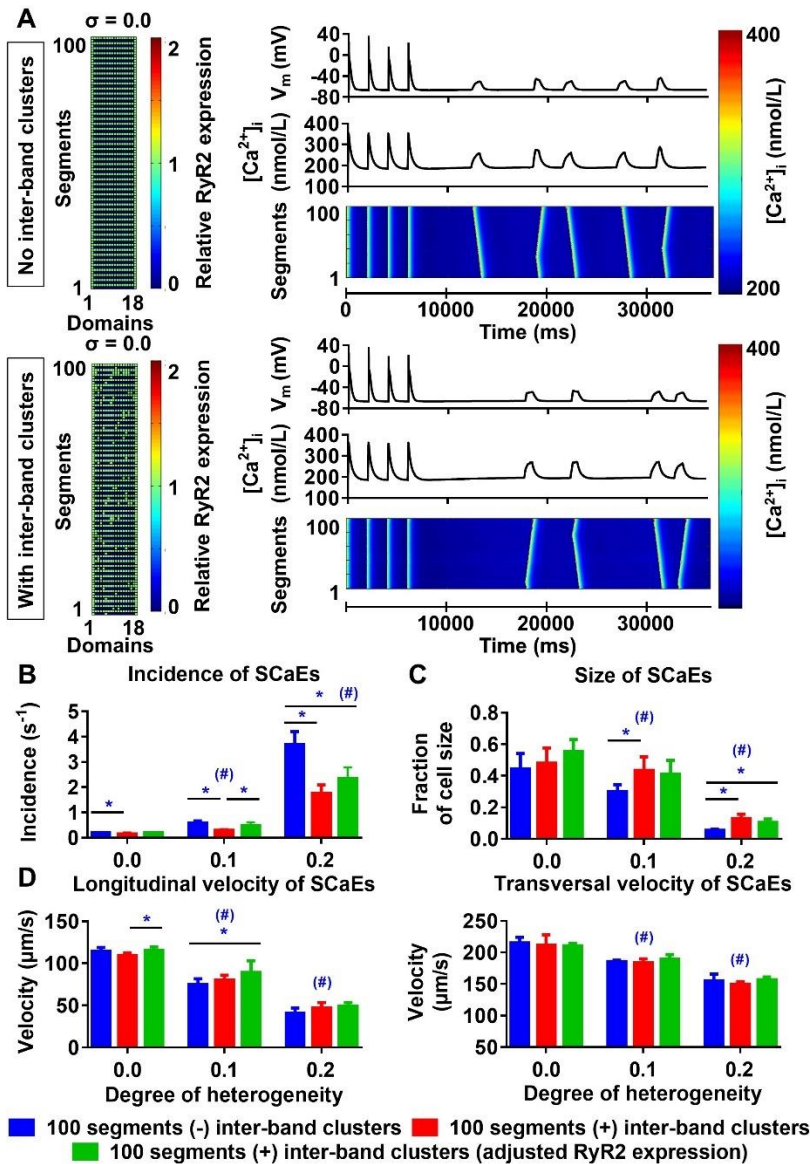


**Figure 3.16:** Effects of inter-band RyR2 clusters on SCAEs. (A) Comparison of RyR2 expression matrix (left), membrane potential ( $V_m$ ), whole-cell CaT, and longitudinal line scan (right, top to bottom) in the model without inter-band RyR2 clusters (top) and with inter-band clusters (bottom) with uniform RyR2 expression ( $\sigma = 0.0$ ). (B–D) SCAE incidence (B) and size (C), as well as longitudinal and transversal velocity of calcium waves (D) as a function of RyR2 heterogeneity  $\sigma$  (0.0–0.2) in the absence of inter-band RyR2 clusters (blue), in the presence of 10% inter-band RyR2 clusters (red), or in the presence of 10% inter-band RyR2 clusters with increased global RyR2 expression to ensure similar RyR2 density within the bands (green). \* indicates

## Subcellular structures modulate spontaneous releases in atrial cardiomyocyte

$P < 0.05$  between groups and # indicates  $P < 0.05$  between a given level of heterogeneity and the group with heterogeneity 0.0;  $n = 6$  per condition.

There were no differences in the longitudinal calcium wave velocity between simulations with and without axial tubules. Similarly, the presence of axial tubules with LTCC did not affect the number of SCaEs (Figures 3.18A, B; compare red and blue bars), consistent with the idea that SCaEs result from stochastic RyR2 openings that are independent of LTCCs. However, a recent study (160) noted that although RyR2 expression adjacent to the axial tubule was not different from other parts of the cardiomyocyte, these RyR2 near axial tubules were hyperphosphorylated. We simulated RyR2 hyperphosphorylation in our model by increasing RyR2 open probability for all RyR2 located in units surrounding axial tubules. In the presence of hyperphosphorylated RyR2 surrounding axial tubules, the number of SCaEs was increased, with a corresponding reduction in their size (Figures 3.18B, C). Of note, SCaEs indeed primarily originated around the axial tubule (Figure 3.18D, Figure 3.19), although in the presence of a heterogeneous RyR2 distribution, regions with high local RyR2 expression may also act as foci (Figure 3.19).

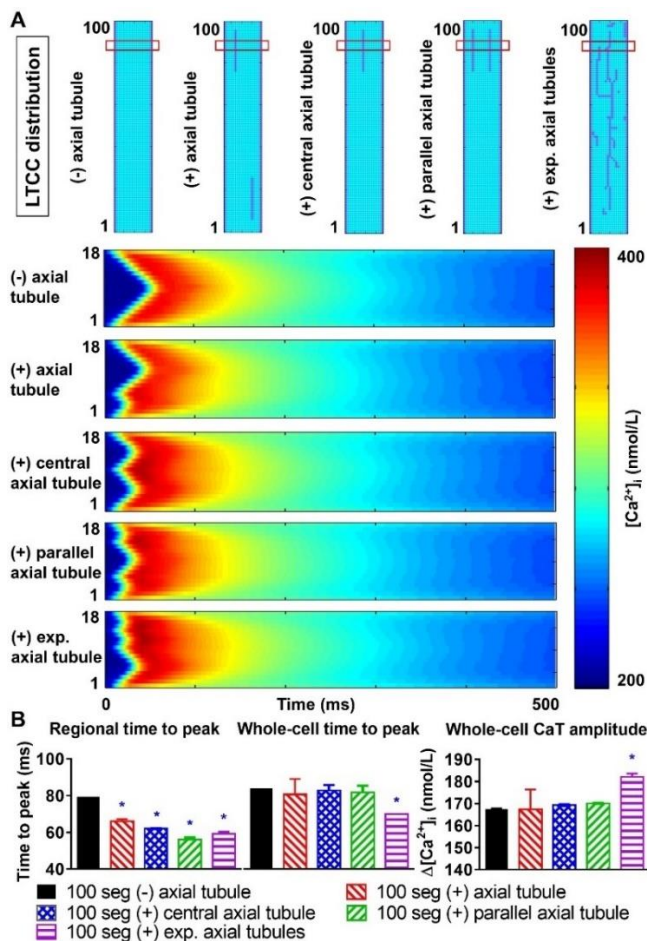


**Figure 3.17:** Effects of axial tubule(s) on centripetal calcium wave propagation. (A) Schematic representations of model structure: no axial tubule (LTCC only at lateral membranes), single axial tubule at 33% of cell width, single central axial tubule at 50% of cell width, two parallel axial tubules at 33 and 66% of cell width, or experimentally observed axial tubules based on [160] (top) and corresponding transversal line scans of CICR during an AP, showing centripetal calcium wave propagation (bottom). (B) Quantification of time to peak (left) and CaT amplitude (right) for the indicated line scan in the four groups ("regional") or for the whole-cell CaT. Increasing numbers of axial tubules and more centrally located axial tubules decrease the time-to-peak and slightly increase the CaT amplitude. The magnitude of the increase depends on the number of axial tubules. \* indicates  $P < 0.05$  vs. the 100-segment group without axial tubules (black bars);  $n = 6$  per condition.

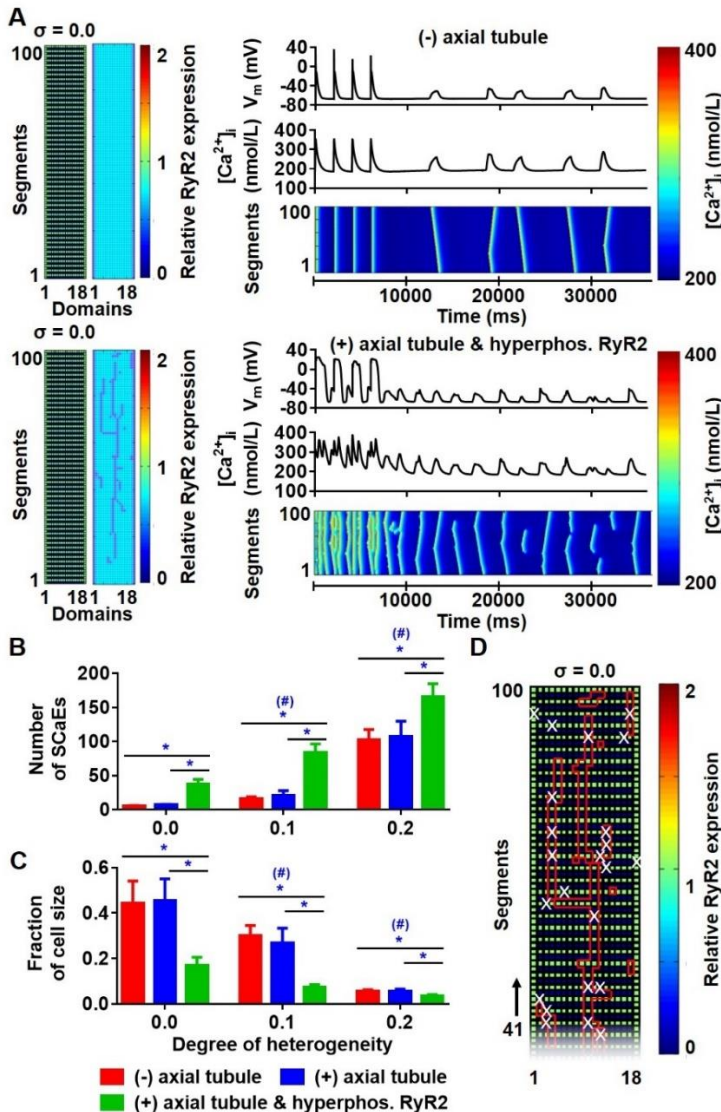


**Figure 3.18:** Effects of axial tubules on SCAEs. (A) Comparison between the model without axial tubules and model with axial tubules with uniform RyR2 expression ( $\sigma = 0.0$ ), but hyperphosphorylated RyR2 around axial tubules. (B, C) Number of calcium waves (B) and SCAE size (C) in the absence of axial tubules (red bars),

presence of axial tubules (blue bar), or presence of axial tubules with hyperphosphorylation of surrounding RyR2 (green bars). (D) Distribution of RyR2 expression and location of axial tubules (red lines) in relation to the origin of SCAEs (white crosses), showing that SCAEs primarily originated from RyR2 clusters adjacent to the axial tubules. \* indicates  $P < 0.05$  between groups and # indicates  $P < 0.05$  between a given level of heterogeneity and the group with heterogeneity 0.0;  $n = 6$  per condition.

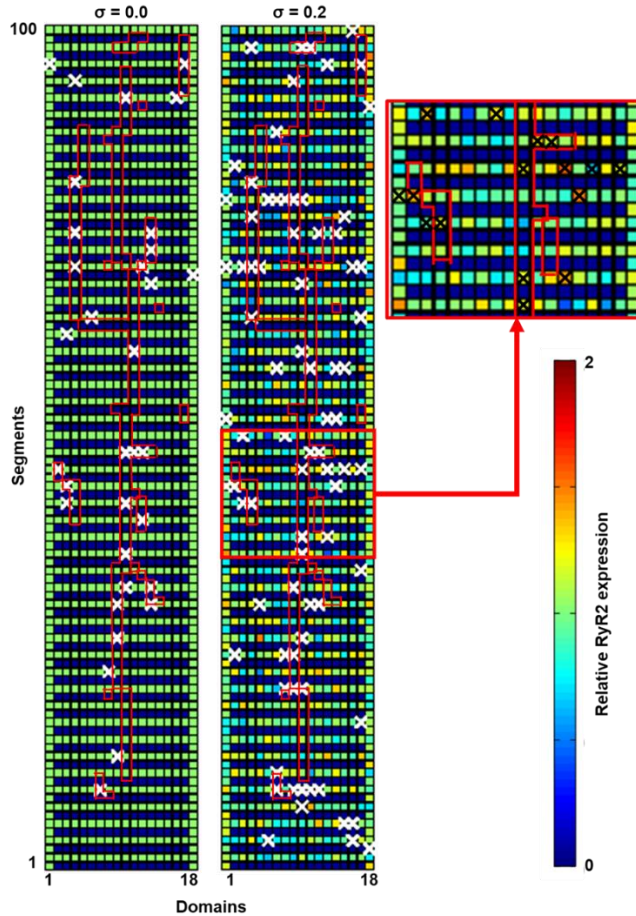


**Figure 3.19:** Distribution of RyR2 expression and location of axial tubules (red lines) in relation to the origin of SCAEs (white crosses) for simulations with uniform ( $\sigma=0.0$ ) or heterogeneous ( $\sigma=0.2$ ) RyR2 expression. SCAEs originated primarily from RyR2 clusters adjacent to the axial tubules or (in the case of heterogeneous RyR2 expression) clusters with high local RyR2 expression (e.g., see inset in which black crosses indicate the origin of SCAEs).

### 3.3.6 Predicting the effects of $\beta$ -adrenergic stimulation on SCAEs

$\beta$ -adrenergic stimulation is an accepted promoter of SCAE-mediated triggered activity (296). Here, we investigated the functional consequences of three established downstream targets of  $\beta$ -adrenergic stimulation. Chronic AF is associated with a hyperphosphorylation-mediated 100 – 500% increase in RyR2 open probability (124). Therefore, we first implemented a 100% increase of RyR2 open probability to simulate the effect of  $\beta$ -adrenergic stimulation. This resulted in smaller and more frequent SCAEs

compared to baseline (incidence of  $2.03 \pm 0.09 \text{ s}^{-1}$  in the increased RyR2 open probability group vs.  $0.19 \pm 0.02 \text{ s}^{-1}$  in the baseline group,  $n = 6$ ,  $p < 0.05$ ; **Figure 3.20**). Second, we implemented an increased SERCA2a affinity for cytosolic calcium to reflect phospholamban phosphorylation. In the presence of increased SERCA2a function, the incidence of SCAEs was increased without any statistically significant change in the size of SCAEs (**Figure 3.21**). In addition, an increase in longitudinal and transversal velocities of SCAEs was observed. Third, we implemented a homogenous increase of LTCC function by doubling the maximum conductance of the channel, which resulted in an increased SCAE incidence without any statistically significant changes in the size and velocities of SCAEs (**Figure 3.22**). The combination of all three modifications, reflecting maximal  $\beta$ -adrenergic stimulation, produced a dramatic increase in SCAEs (incidence of  $27.77 \pm 14.92 \text{ s}^{-1}$  vs.  $0.19 \pm 0.02 \text{ s}^{-1}$  in the baseline group,  $n = 6$ ,  $p < 0.05$ ), including proarrhythmic triggered activity (**Figure 3.23**).

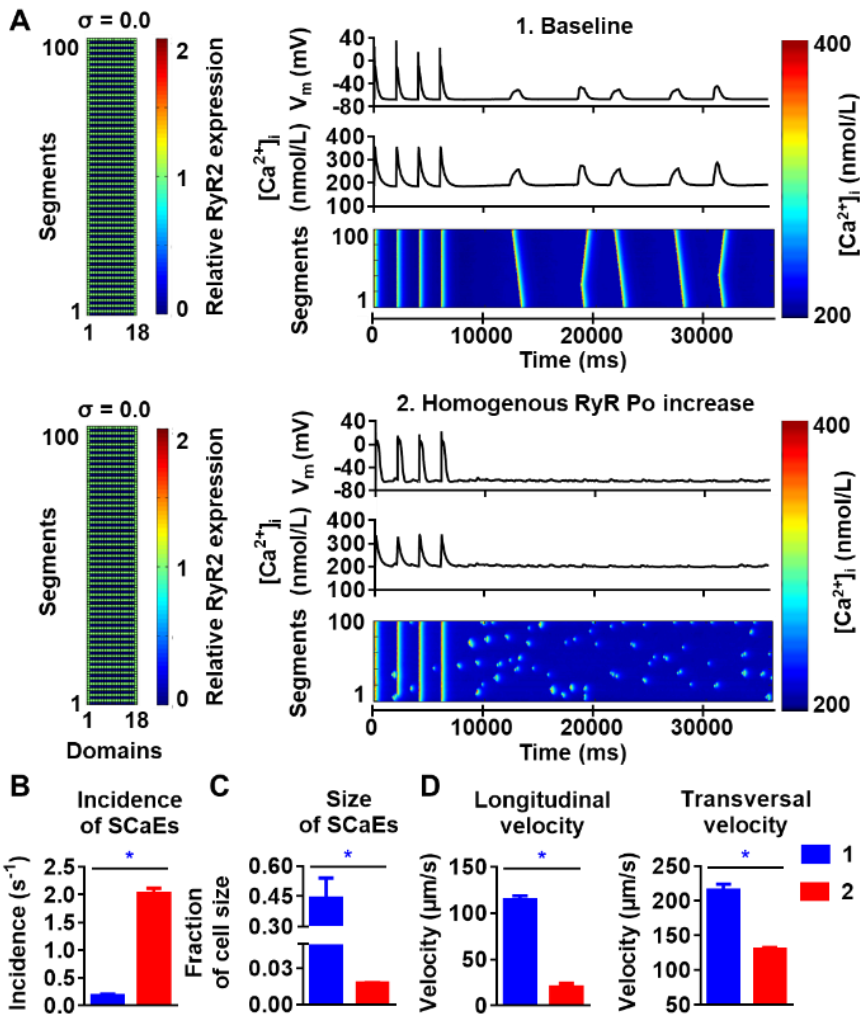


**Figure 3.20:** Effects of homogenous increase in RyR open probability. A) Membrane potential ( $V_m$ ), intracellular calcium and longitudinal line scan (top to bottom) for the baseline model (A.1) and the model in which RyR2 open probability was increased by 100%, by altering parameters as follows:  $P[0]_{RyR} = 0.2 \rightarrow 0.4$  (+100%);  $P[1]_{RyR} = 0.22 \rightarrow 0.24$  (+9%);  $P[5]_{RyR} = 0.0035 \rightarrow 0.00805$  (+130%). B-D) incidence, size and velocity of SCAEs in both models. \* indicates  $P < 0.05$  between both groups ( $n=6$  per condition).

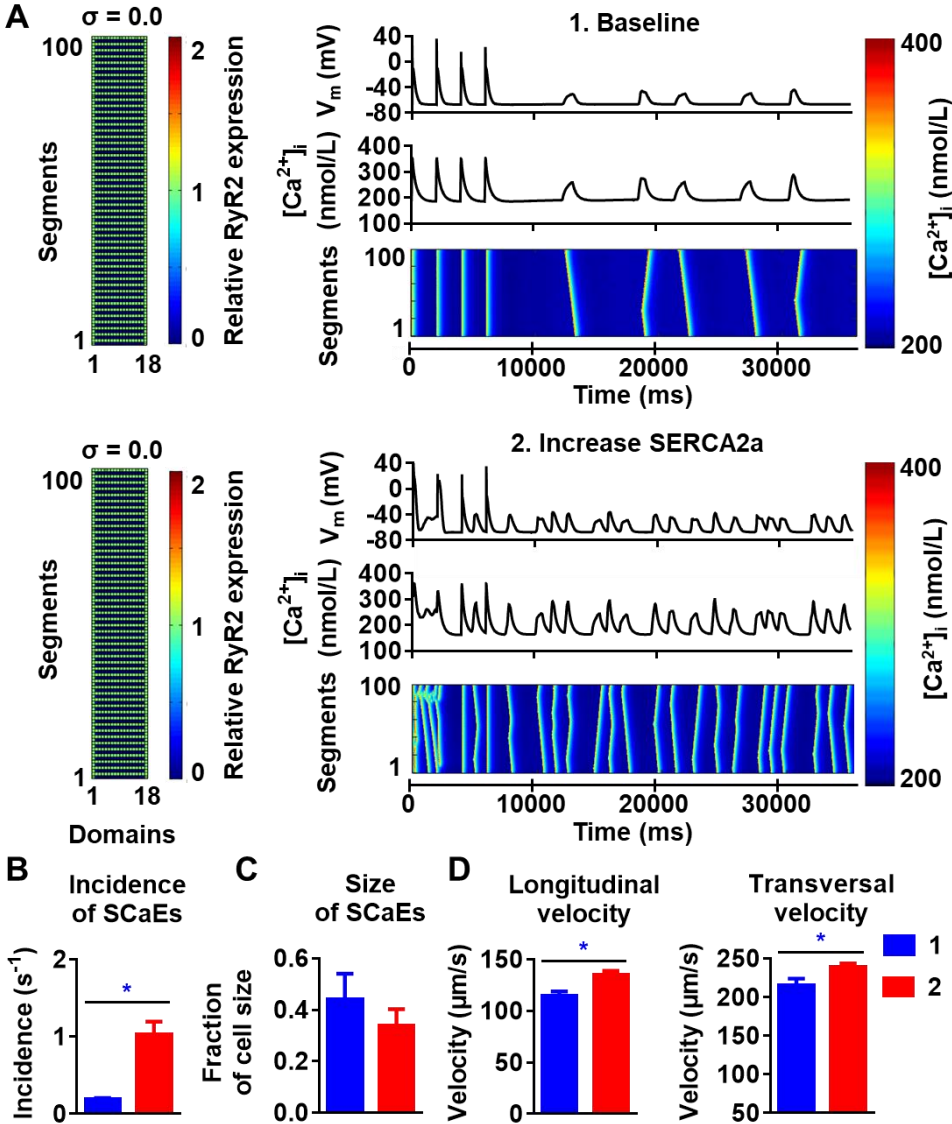


**Figure 3.21:** Increase of SERCA2a function and the propensity of SCAEs. A) Membrane potential ( $V_m$ ), intracellular calcium and longitudinal line scan (top to bottom) for the baseline model (A.1) and the model with increased SERCA2a activity as achieved by reduction of  $K_{mf}$  value by 25% (A.2). B-D) incidence, size and velocity of SCAEs in both models. The increase in SERCA2a activity resulted in an increased incidence of SCAEs with no significant change in size but significant increase in longitudinal and transversal velocities. \* indicates  $P < 0.05$  between both groups ( $n=6$  per condition).

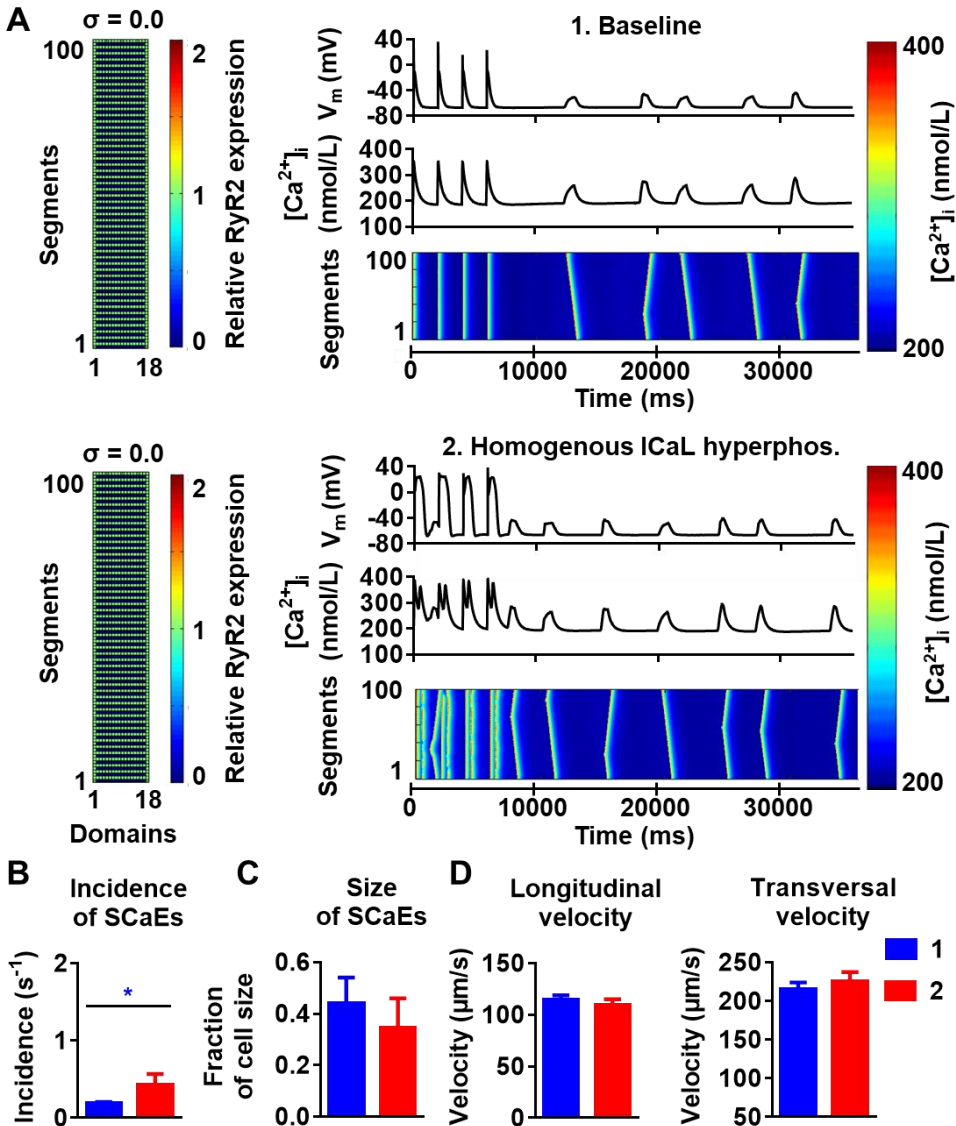


**Figure 3.22:** Effects of homogenous LTCC/ $I_{CaL}$  hyperphosphorylation on the behavior of SCaEs. A) Membrane potential ( $V_m$ ), intracellular calcium and longitudinal line scan (top to bottom) for the baseline model (A.1) and the model with doubled maximum conductance of LTCC (from  $1.7 \times 10^{-4}$  as reported before to  $3.4 \times 10^{-4}$ ) (A.2). B-D) incidence, size and velocity of SCaEs in both models. The increase in  $I_{CaL}$  resulted in increased SCaE incidence without any significant change in other SCaE parameters. \* indicates  $P < 0.05$  between both groups ( $n=6$  per condition).

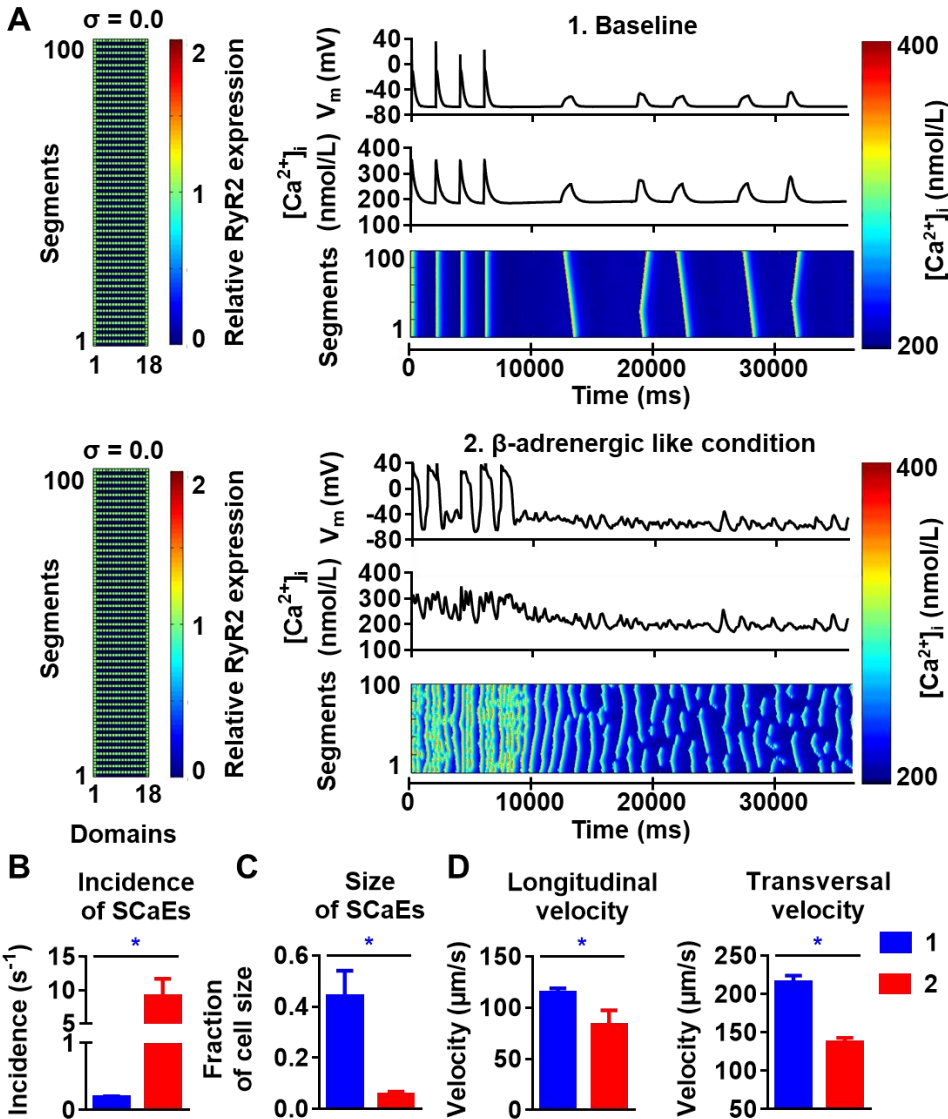


**Figure 3.23:** The effect of simulated  $\beta$ -adrenergic stimulation on the behavior of SCAEs. A) Membrane potential ( $V_m$ ), intracellular calcium and longitudinal line scan (top to bottom) for the baseline model (A.1) and the model with increased RyR2 open probability, increased SERCA2a activity and increased  $I_{Ca,L}$  (A.2.) B-D) incidence, size and velocity of SCAEs in both models. The simulated  $\beta$ -adrenergic stimulation markedly increases the incidence of SCAEs and reduces the size of SCAEs, longitudinal and transversal velocities of the spontaneous waves. \* indicates  $P < 0.05$  between both groups ( $n = 6$  per condition).

### 3.3.7 A computational model incorporating physiological RyR2 and LTCC distributions

Finally, we combined both the experimentally observed RyR2 distribution (Figure 3.7) and axial tubule network with LTCC in a novel model of the human atrial cardiomyocyte.

When using the parameters established for the model with uniform RyR2 distribution and no axial tubules, this model showed a non-physiological number of small SCAEs, in line with the effects of the experimental RyR2 distribution in **Figure 3.10A**. As such, we performed a parameter optimization to reproduce the experimentally observed calcium handling properties in the combined model (**Figure 3.24**).

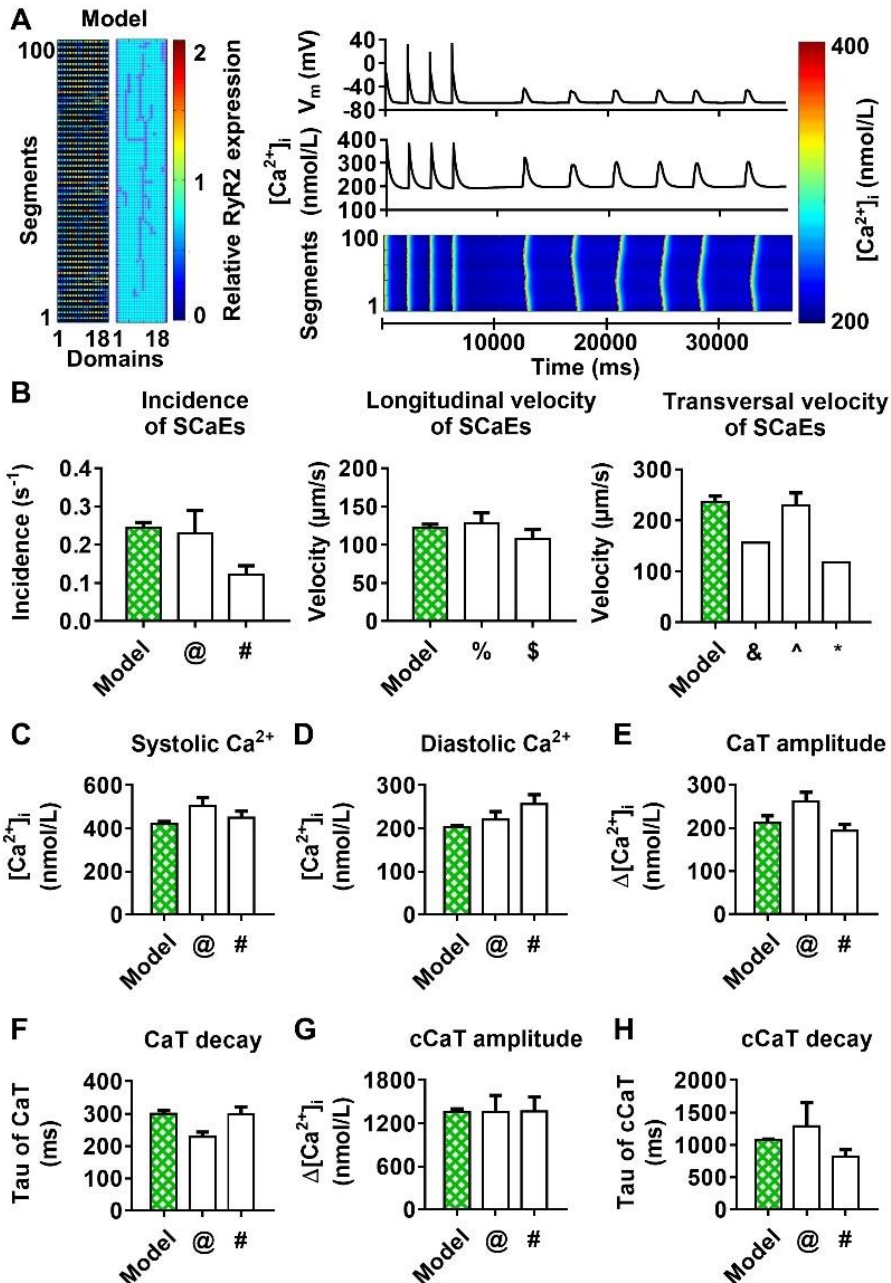


**Figure 3.24:** 100-segment model with experimental RyR2 distribution and LTCC expression based on experimentally observed axial tubules, with RyR2 hyperphosphorylation around axial tubules. (A) Model structure (left panel) and longitudinal line scan of the optimized 100-segment model ("Model"). (B–H) Comparison of SCaE characteristics (B) and whole-cell CaT properties (C–H) of the model to previously published experimental data \$ = (290); ^ = (291); & = (285); % = (292); @ = (124); # = (32); \* = (130).

## 3.4 Discussion

Recent studies have identified a major role for cardiomyocyte calcium handling abnormalities in cardiac arrhythmias and have provided insight into the underlying molecular mechanisms (2, 6). However, the impact of the subcellular distribution of RyR2 and LTCC on cardiomyocyte calcium handling remains largely unknown. It is currently experimentally challenging to study both (sub)cellular structure and functional calcium handling in the same cardiomyocyte. Here, we extended a computational model of the human atrial cardiomyocyte with a more physiological subcellular structure, including heterogeneous RyR2 distributions and axial tubules with LTCC. Our computational analyses showed that increasing RyR2 heterogeneity resulted in more, smaller SCaEs arising from regions with high local RyR2 expression. LTCC located in axial tubules produced a faster, more synchronous CICR, which was modulated by the location and extent of the axial tubular network. Moreover, hyperphosphorylation of RyR2 surrounding axial tubules increased the incidence of SCaEs and DADs. Finally, we developed and validated a novel human atrial cardiomyocyte model with physiological RyR2 distribution and axial tubules with LTCC based on experimental observations, which can serve as a tool for future studies.

### 3.4.1 Role of subcellular structure in cardiomyocyte calcium handling

An increased SCaE incidence in atrial cardiomyocytes from patients with AF contributes to the initiation of DADs and cellular triggered activity (32, 124, 138), which, when occurring at the tissue level, may act as initiators of AF or may sustain the arrhythmia when occurring repetitively at high frequency (32, 297). SCaEs are promoted by increased SR calcium load leading to store-overload-induced SR calcium release (298). In agreement, SERCA2a activity is increased in patients with paroxysmal AF and is associated with increased SR calcium load and a higher incidence of SCaEs (32). In addition, RyR2 dysfunction can increase the incidence of SCaEs even in the absence of increased SR calcium load. RyR2 mutations leading to catecholaminergic polymorphic ventricular tachycardia have been associated with familial AF (299) and genetic mouse models with these mutations show pronounced atrial calcium handling abnormalities (25). Moreover, RyR2 open probability is increased, likely due to hyperphosphorylation of the RyR2 channel, in patients with long-standing persistent AF (124). Besides changes in cardiomyocyte calcium handling, AF produces structural remodeling at the level of the single cardiomyocyte (atrial cellular hypertrophy, myolysis, alterations in size and distribution of mitochondria and SR) (300-302), suggesting a potential role for changes in subcellular structure in regulating cardiomyocyte calcium handling. Indeed, Macquaide et al. (158) reported that ultrastructural reorganization of RyR2 clusters in atrial cardiomyocytes of sheep with persistent AF is associated with overactive calcium release. In addition, Lenaerts et al. (303) reported that in sheep with persistent AF,

there was loss of T-tubule organization, fewer calcium channel-RyR couplings, and reduced efficiency of the coupling at subsarcolemmal sites, which led to a reduction in SR calcium release despite preserved SR calcium content. Thus, there is substantial indirect evidence for a role of subcellular structure in cardiomyocyte calcium handling. However, a systematic analysis of the impact of changes in calcium handling protein distributions on whole-cell proarrhythmic calcium handling is lacking.

Consistent with previous publications (287, 304), our confocal images of rabbit atrial cardiomyocytes showed a banded RyR2 expression with inter-band distance of  $\approx 1.9 \mu\text{m}$ . Moreover, there appears to be a substantial heterogeneity of RyR2 density along the z-bands. We increased the spatial resolution of our computational model to enable simulations of the banded RyR2 pattern and incorporated the experimentally observed RyR2 distribution in our model. In line with the work by Macquaide et al. (158), our simulations showed a pronounced impact of RyR2 distribution on SCAE incidence and size. Indeed, physiologically observed degrees of RyR2 heterogeneity had a larger impact on SCAEs than differences in total RyR2 expression observed between patients with sinus rhythm and paroxysmal AF (32). Of note, our simulations identified regions with high local RyR2 expression as foci for SCAEs, which is in line with recent experimental work by Galice et al. (159).

In ventricular cardiomyocytes, LTCC are primarily (but not exclusively, (305)) located in T-tubules, promoting synchronous SR calcium release throughout the cell. Recent studies have identified a similar role for axial tubules in atrial cardiomyocytes (286). For example, Brandenburg et al. (160) reported the importance of axial tubules in atrial cardiomyocytes in maintaining calcium handling and calcium wave propagation to the center of atrial cardiomyocytes. Similarly, Yue et al. (287) observed synchronous SR calcium release in mouse atrial cells, which was ascribed to the presence of transverse-axial tubules. We employed the perfect control provided by computational models to study the exact effects of different locations, numbers, and distributions of such axial tubules on whole-cell calcium handling. Incorporation of axial tubules produced a more synchronous SR calcium release, as evident from a W-shaped instead of V-shaped pattern in simulated transversal line scans. The W-shaped patterns varied with different locations of the axial tubules, consistent with experimental findings (285, 287) noting that the presence and location of the transverse-axial tubular system determined the shape of the whole-cell CaT and transversal calcium waves. Our simulations showed that more centrally located and/or higher number of axial tubules reduced the local time-to-peak. However, in order to affect the global time-to-peak and global CaT amplitude, the length of the axial tubules had to be sufficiently long to affect a large part of the virtual cardiomyocyte. Brandenburg et al. (160) reported that instead of an increase in the number of RyR2 adjacent to the axial tubules, there was a selective local RyR2 hyperphosphorylation, which led to a faster calcium release at axial tubule locations residing inside the cell. Our simulations showed that the presence of axial tubules per se did not affect SCAEs, but that simulation of local hyperphosphorylation of RyR2 increased the number of SCAEs. Furthermore, we confirmed that regions with local hyperphosphorylation acted

as the origins of SCaEs. However, these results depended on the amount of RyR2 heterogeneity and the number of axial tubules, with SCaEs also arising from regions with high local RyR2 expression independent of RyR2 hyperphosphorylation. Taken together, these findings underline the importance of the subcellular distribution of calcium handling proteins in atrial cardiomyocytes for cardiac arrhythmogenesis.

Previous publications (160, 293-295) have reported an increased RyR2 density at the lateral membrane using confocal microscopy. However, the role of these lateral RyR2 clusters remains unknown. Here, we employed a computational model with no expression of lateral RyR2s to investigate their role in the propagation of SCaEs. Our data show that lateral RyR2s hold a very important role as “bridges” that facilitate calcium wave propagation. Removal of lateral RyR2 clusters impaired calcium wave propagation and resulted in more, but smaller SCaEs, effectively converting proarrhythmic calcium waves to calcium sparks.

### **3.4.2 Comparison to previous models**

Several computational models have been developed to study cardiomyocyte calcium handling abnormalities. These include, on the one hand, highly detailed models of a single CRU to study the molecular determinants of SR calcium release. For example, Hake et al. (306) developed a computational model with a highly detailed, electron microscopy-based computational geometry of a CRU from a mouse ventricular cardiomyocyte to simulate local calcium sparks. Walker et al. (89) developed a detailed 3D model of a CRU incorporating diffusion, intracellular buffering systems, and stochastically gated RyRs and LTCCs to simulate local calcium dynamics with a high spatial resolution. This work showed that perturbations to subspace dimensions strongly alter calcium spark dynamics. Similarly, Zahradnikova and Zahradnik (307) constructed virtual CRUs composed of a variable number of RyRs distributed in clusters in line with the experimentally observed cluster-size distribution to provide a description of calcium spark properties for spontaneous and triggered calcium sparks. These studies strongly suggest that the organization of the CRU plays a critical role in determining the characteristics of microscopic calcium release events (sparks) but have not simulated whole-cell calcium handling abnormalities, which would be relevant to study arrhythmogenesis.

On the other hand, a number of models have been developed to study whole-cell calcium handling: Walker et al. (90) developed a biophysically detailed 3D model of the ventricular cardiomyocyte with stochastic gating of RyR2 channels and determined the impact of cytosolic and SR calcium concentrations, basal inward-rectifier potassium current density, and gap junction conductance on DADs and triggered activity using this model. Likewise, Wescott et al. (308) developed a mathematical whole-cell model, incorporating realistic stochastic gating of LTCCs and RyRs to investigate excitation-contraction coupling and calcium spark fidelity. Recently, Colman et al. (103) developed a detailed 3D multiscale model of a ventricular cardiomyocyte based on scanning electron microscopy data to examine the effects of a realistic SR structure on proarrhythmic calcium dynamics, alternans, and SCaEs. Song et al. (309) also investigated

the influence of subcellular structure on calcium handling in a model with a 3D network of CRUs representing different transverse tubule network structures, including uniform and random distribution of transverse tubules, to investigate calcium sparks, DADs, and triggered activities. However, these studies were primarily done in ventricular cardiomyocytes, which have well-established differences in subcellular structures, notably the configuration and number of axial tubules and a different composition of ion channels from atrial cardiomyocytes.

Here, we developed an atrial cardiomyocyte model with atrial-specific subcellular structure and electrophysiology that can simulate multiple physiological properties of cardiomyocyte calcium handling, as well as proarrhythmic calcium handling abnormalities. This model has an intermediate level of detail, incorporating heterogeneous distributions of calcium handling proteins with micrometer resolution, a level that is of the same order of magnitude as the experimental information about the distributions obtained with confocal imaging. This level of detail is highly suitable to study the structural determinants of whole-cell calcium handling abnormalities that are relevant for arrhythmogenesis. Moreover, because of its relatively modest computational complexity, this model can also be employed in future studies to investigate the determinants of triggered activity at the tissue level, something that is not possible with the previously developed, highly detailed, 3D models.

### **3.4.3 Potential limitations**

Our model with local calcium handling strongly suggested that the subcellular distribution of RyR2 and LTCC has a major impact on cardiomyocyte calcium handling. However, the model only considered a 2D representation of the cardiomyocyte, equivalent to a single slice from a z-stack. Previous computational studies using simpler 3D models have identified that persistent calcium waves can be generated through specific patterns of 3D calcium wave propagation (so-called “ping waves”) (310), suggesting a need to consider the 3D structure of cardiomyocytes. Furthermore, although we increased the spatial resolution of our previously published model (32) in order to simulate the banded pattern of RyR2 expression, the resolution of the current model (units of  $1 \mu\text{m}^2$ ) was insufficient to simulate local calcium dynamics around a single CRU (e.g., (sub)sparks). Detailed CRU models have been developed (89, 306, 307) and could potentially be integrated in the present cell-level model in future studies, although this would significantly increase the computational complexity. Additionally, we acknowledge that our investigations into the effects of  $\beta$ -adrenergic stimulation represent a highly simplified approach. Implementing a complete signaling pathway and its downstream effects on atrial electrophysiology, such as previously described for ventricular cardiomyocytes (78) would be of interest, but was beyond the scope of the present study.

The resolution and quality of confocal imaging is limited by physical properties and quality of cell-isolation and antibody staining (particularly in rabbit samples). The use of super-resolution microscopy would be beneficial to obtain a more detailed overview of the 3D RyR2 distribution. In this case, dual staining of RyR2 and axial

tubules should be performed to obtain information on both distributions in a single cardiomyocyte, which was not performed in the current study. Instead, a representative experimental axial tubule geometry from previously published work (160) was used. Ideally, future experiments would be performed in human atrial cardiomyocytes to obtain a human-specific RyR2 distribution, rather than the rabbit atrial cardiomyocytes employed here, although their availability and cell-quality is generally much lower. Indeed, the experimental RyR2 distribution that formed the basis for the model with physiological RyR2 and LTCC distribution (**Figure 3.24**) was based on a limited number of rabbit atrial cardiomyocytes and may not be representative for diseased human atrial cardiomyocytes. Likewise, the current model requires stretching of the observed RyR2 expression pattern to match the 100x18 rectangular shape of the virtual cardiomyocyte. Finally, heterogeneous distributions of other calcium handling proteins such as NCX1 or SERCA2a may also impact whole-cell calcium handling and could be studied using the computational framework developed in the present study.

### 3.5 Conclusions

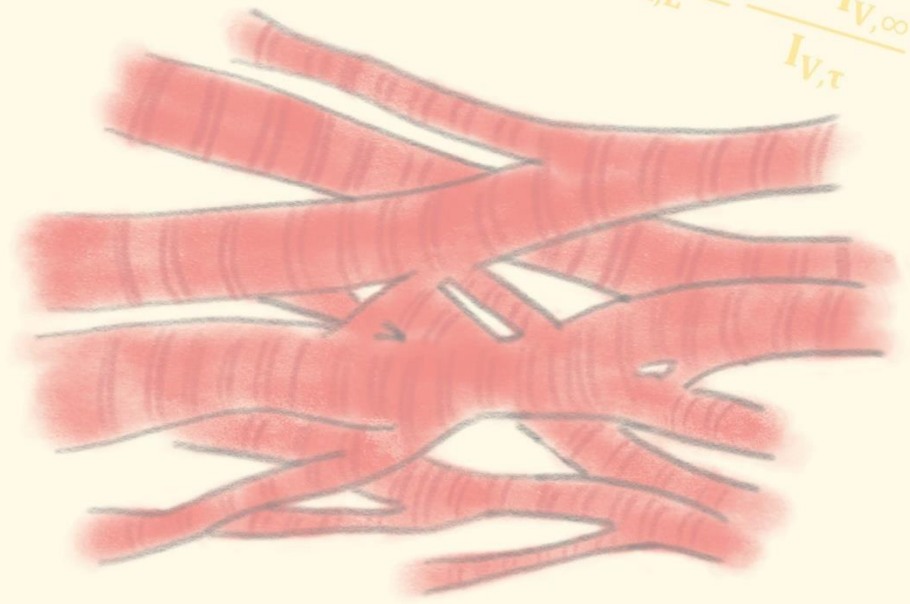
We employed the perfect control and observability provided by computer models to overcome experimental challenges in the analysis of the subcellular determinants of cardiomyocyte calcium handling. Our findings highlight the importance of atrial subcellular structures, especially RyR2 and LTCC distributions, in the genesis of SCaEs and DADs, which are well-known triggers of cardiac arrhythmias. Importantly, whole-cell calcium handling properties are determined by non-linear interactions between heterogeneities in the properties (expression, phosphorylation) of both LTCC and RyR2, highlighting the need for detailed immunocytochemistry and functional studies to explain differences in whole-cell calcium handling properties between conditions.





$$\frac{dV_m}{dt} = -\frac{1}{C_m} * I$$

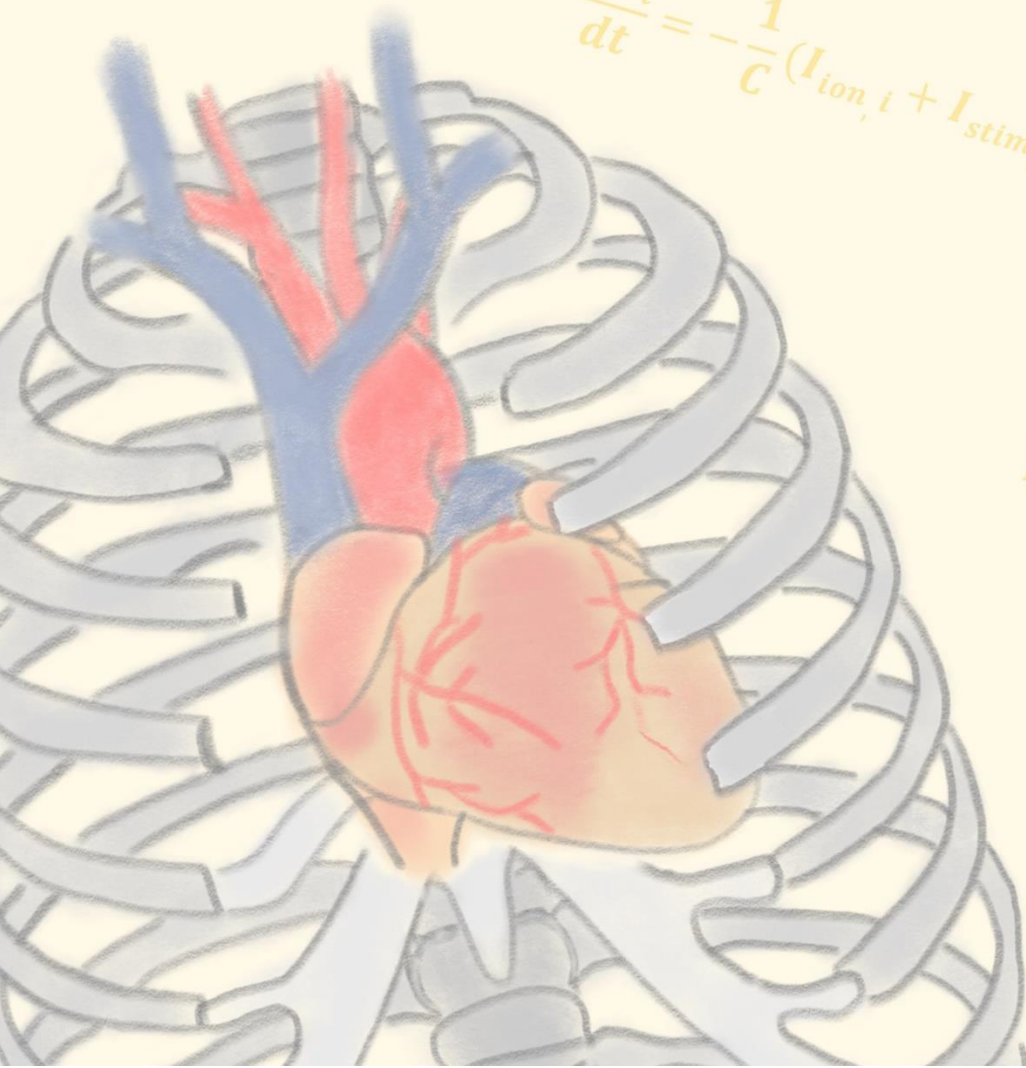
$$y_{Ca,L} = \frac{1 - I_{V,\infty}}{I_{V,\tau}}$$



$$x_{Ca,L} = \frac{I_{V,\infty}}{I_{V,\tau}}$$

$$\delta I_{Ca,L}^{s,m} =$$

$$\frac{dV_i}{dt} = -\frac{1}{C} (I_{ion,i} + I_{stim,i} + I_{diff,i})$$



$$\bar{I}_{Ca,L}^{s,m} = P_{Ca,L} \cdot (z$$

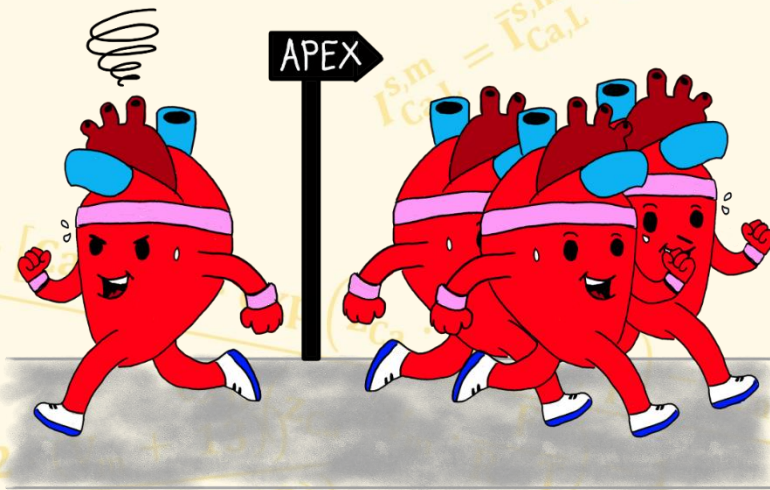
$$ACT_{\tau} = 0.59$$

# Chapter 4

## Computational modeling of subcellular calcium-handling identified calcium-handling abnormalities in patients with post-operative atrial fibrillation

Adapted from: *Atrial Myocyte NLRP3/CaMKII Nexus Forms a Substrate for Post-Operative Atrial Fibrillation*

J. Heijman, A. P. Muna, T. Veleva, C.E. Molina, **H. Sutanto**, M. Tekook, Q. Wang, I.H. Abu-Taha, M. Gorka, S. Künzel, A. El-Armouche, H. Reichenspurner, M. Kamler, V. Nikolaev, U. Ravens, N. Li, S. Nattel, X.H.T. Wehrens and D. Dobrev  
*Circ. Res.* 127:1036-1055.



$$\frac{dV}{dt} = \frac{I_{stim} - (I_K + I_{Na} + I_{leak})}{C_m}$$

## ABSTRACT

Post-operative atrial fibrillation (POAF) is a common post-surgical complication, likely resulting from the interaction between pre-existing arrhythmogenic substrate and transient peri- and post-operative triggers (e.g., inflammation). However, data on pre-existing electrical and structural remodeling in POAF patients are inconclusive. Calcium-handling abnormalities are closely associated with other types of AF (e.g., paroxysmal and persistent AF), but have not been studied in sinus-rhythm patients who subsequently develop POAF. Here, we performed a computational study to evaluate the potential proarrhythmic electrophysiological consequences of pre-existing calcium-handling abnormalities and post-operative inflammation in the generation of POAF.

Our model was based on recent experimental data in atrial cardiomyocytes from patients undergoing open heart surgery without (Ctl group) or with subsequent POAF. In particular, we optimized our previously published *in silico* model of human atrial cardiomyocyte calcium-handling (Chapter 3) to reproduce the baseline calcium-handling properties observed in these experiments. Subsequently, we developed a new POAF model variant by incorporating major differences in calcium handling between Ctl and POAF patients and investigated spontaneous sarcoplasmic reticulum calcium-release events (SCaEs) under conditions similar to experimental protocols. Under voltage-clamp conditions, the POAF model showed an increased SCaE incidence compared to the Ctl model. Simulated IL-1 $\beta$  application further exaggerated the differences in SCaE incidence between POAF and Ctl (+509% vs +122% with and without simulated IL-1 $\beta$ , respectively), consistent with experimental data. The POAF model also showed an increased SCaE incidence (+45%) during action potential simulations, but in the absence of IL-1 $\beta$ , these SCaEs were small and too dispersed to produce clear DADs. By contrast, the presence of simulated IL-1 $\beta$  (mimicking post-operative conditions) resulted in a large increase in SCaEs (+84%) and more large-amplitude DADs (+47%) in the POAF-model, which disappeared with simulated RyR2-block.

In conclusion, computational modeling supports the notion that post-operative inflammation acting on a pre-existing arrhythmogenic substrate may elicit proarrhythmic responses leading to POAF.

## 4.1 Introduction

Post-operative atrial fibrillation (POAF) is a common post-surgical complication, affecting approximately 30% of patients undergoing open-heart surgery (311). Although it is traditionally considered a transient phenomenon with a peak incidence less than a week post-surgery (312, 313), POAF is also associated with increased short- and long-term morbidity and mortality (312-314). Despite a range of proposed preventive approaches, POAF management remains challenging, partly due to incomplete understanding of the underlying mechanisms (314, 315).

Conceptually, POAF is considered a result of the interaction between transient peri- or post-operative triggers and a pre-existing arrhythmogenic substrate (314). Several potential components of the pre-existing POAF substrate have been studied in human atrial samples obtained during cardiac surgery, but results have been inconclusive. For example, while pre-operative left atrial (LA) fibrosis has been noted in some studies (316, 317), atrial fibrosis has not been consistently observed in right-atrial (RA) samples (314, 316-318). Furthermore, to date, there is no evidence for pre-existing electrical remodeling in human atrial cardiomyocytes of POAF patients (316, 319). Calcium-handling abnormalities are an accepted trigger for arrhythmogenesis present in both paroxysmal and long-standing persistent ('chronic') AF (pAF and cAF, respectively) (32, 124), as well as in systolic heart failure patients with increased AF susceptibility (121), but have not yet been studied in sinus-rhythm patients who subsequently develop POAF.

Inflammation is a major transient post-operative factor that may also trigger POAF. The time course of AF after surgery parallels changes in inflammatory markers (320-322) and a few studies have identified associations between POAF and the systemic level of pre-operative inflammatory biomarkers, notably interleukin (IL)-2 and IL-6 (320, 323), although several other studies found no correlation between POAF and pre- or post-operative C-reactive protein (CRP), IL-2, or IL-6 (314, 318, 324). Such inconsistent results for blood biomarkers might be due to a primary role for local atrial, rather than systemic, inflammation (314). Abnormal NACHT, LRR, and PYD domains containing protein-3 (NLRP3) inflammasome signaling within human atrial cardiomyocytes has recently been implicated in the pathogenesis of pAF and cAF, partly by induction of abnormal calcium-handling (224). In turn, abnormal calcium-signaling can also trigger cardiomyocyte NLRP3 inflammasome activation (325, 326); thus the coexistence of low-grade chronic inflammatory changes and abnormal calcium-signaling in the atria of patients predisposed to POAF might, particularly in the context of superimposed post-operative inflammatory and autonomic nervous system changes, initiate a positive feedback loop between abnormal atrial calcium-handling and enhanced NLRP3 inflammasome signaling that results in POAF.

Here, we performed a computational study to evaluate the possible cause-effect relationships and potential proarrhythmic electrophysiological consequences of a pre-existing vulnerable substrate interacting with post-operative inflammation in the generation of POAF. We showed that acute stimulation of this pre-existing substrate with inflammatory stimuli, as would occur during the post-operative period, resulted in proarrhythmic delayed afterdepolarizations (DADs) with the potential to form the basis for POAF.

## 4.2 Methods

We incorporated the *state-of-the-art* experimental data from Heijman et al. (327), which assessed comprehensively different aspects of atrial remodeling in RA samples from sinus rhythm patients without (Ctl) or with POAF. Heijman et al. (327) identified a discrete pre-existing proarrhythmic substrate in patients who went on to develop POAF, including increased priming and triggering of the NLRP3 inflammasome in human atrial cardiomyocytes and calcium-handling abnormalities characterized by L-type calcium-current ( $I_{Ca,L}$ ) alternans (an index of reentry-supporting repolarization heterogeneity), reduced calcium-transient (CaT) amplitude, ryanodine-receptor channel type-2 (RyR2) dysfunction with enhanced sarcoplasmic reticulum (SR) calcium leak and frequency of spontaneous SR calcium-release events (SCaEs). In addition, there was a trend towards increased SR calcium-ATPase (SERCA) function, which may have contributed to the largely maintained SR calcium load.

	Parameter	Published model (4)	Ctl (+IL-1 $\beta$ ) model	poAF (+IL-1 $\beta$ ) model
Calcium-diffusion and buffering	$\tau_{diff,SRS} \leftrightarrow cyt$ (ms)	10	12 (7.5)	10
	$\tau_{diff,seg,SRS}$ (ms)	0.220	0.150	0.150 (0.100)
	$\tau_{diff,dom,SRS}$ (ms)	0.160	0.050	0.050 (0.040)
	Calcium-buffer factor	1.000	0.850	0.850
SERCA	$J_{SERCA,max}$ (mmol/L ms <sup>-1</sup> )	3.187e-3	2.124e-3	2.762e-3
	SERCA2a $K_{m,r}$ (mmol/L)	1.250	1.750	1.750
	SERCA2a $K_{m,f}$ (mmol/L)	6.250e-4	5.000e-4	5.000e-4
NCX	$INCX,max$ (pA/pF)	4.253	1.842	1.842
	$[Ca^{2+}]_o$ observed (mmol/L)	1.0*[Ca <sup>2+</sup> ] <sub>o</sub>	0.1*[Ca <sup>2+</sup> ] <sub>o</sub>	0.1*[Ca <sup>2+</sup> ] <sub>o</sub>
RyR2	$N_{RyRs}$	2,772,000	9,900,000	9,900,000
	$P[0]_{RyR}$	0.200	0.620	0.85374
	$P[5]_{RyR}$	0.0035	0.0147 (0.018375)	0.06581 (0.08226)
	$P[7]_{RyR}$	9.000e-4	1.000e-3	1.000e-3
	$P[8]_{RyR}$	8.000e-5	7.000e-5	7.000e-5
	$G_{K1,max}$ (mS/ $\mu$ F)	6.563e-2	9.188e-2	9.188e-2
	$INaK,max$ (pA/pF)	1.260	0.630	0.630

<b>Other ion channels</b>	$I_{CaL}$	<p>Ctl and POAF as in Voigt et al.(32) with</p> $ACT_{\infty} = \frac{1}{\left(1 + \exp\left(-\frac{V_M - 13.56}{7.0}\right)\right)} \cdot \frac{1}{\left(1 + \exp\left(-\frac{V_M + 25}{5.0}\right)\right)}$
---------------------------	-----------	---------------------------------------------------------------------------------------------------------------------------------------------------------------------------------------------------------------

**Table 4.1:** Changes in model parameters compared to the reference model of the human atrial cardiomyocyte with spatial calcium handling (4). Grey shaded rows highlight parameters that are different between Ctl and POAF model version. Bold numbers in red represent parameter values during simulated IL-1 $\beta$  stimulation.

#### 4.2.1 Baseline (Ctl) model

Our recent model of human atrial cardiomyocyte calcium-handling (4) was used as the basis for all simulations. The current model consists of 101 longitudinal segments of 1  $\mu\text{m}$ , each containing 18 1- $\mu\text{m}$  wide transverse domains. In each of these spatial units, local ion concentrations, including cytosolic and SR calcium concentrations are simulated. RyR2 were incorporated in a banded pattern with RyR2 in every other segment, resulting in a 2  $\mu\text{m}$  distance between RyR2 bands, in line with experimental observations (4). We employed homogeneous expression of RyR2 within a band. Stochastic opening of individual RyR2 was simulated using a 4-state Markov model that reproduces single-channel recordings, as previously described (32). All RyR2 gate independently but are connected through a local subspace (the SR calcium-release space; SRS), representing the microdomain in the vicinity of the RyR2 with high local calcium concentrations during systole.

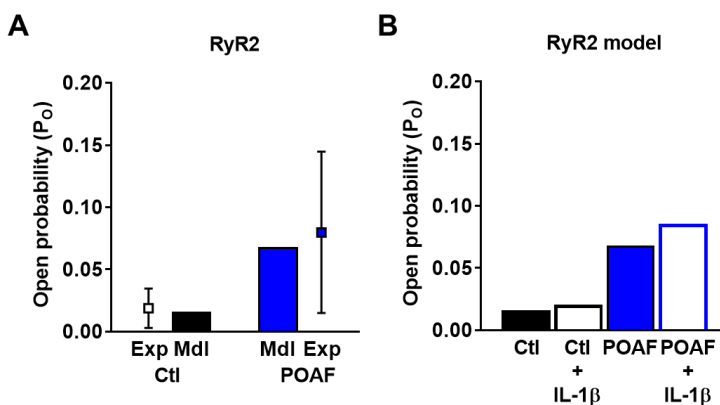


**Figure 4.1:** Simulated single-channel properties of ryanodine receptor channel type-2 (RyR2) in Ctl and POAF model variants. (A) Comparison of simulated RyR2 single-channel open probability in Ctl and POAF models with experimental data from Heijman et al. (327) under diastole-like conditions (150 nmol/L free cytosolic calcium). (B) Comparison of RyR2 open probability in Ctl and POAF in the absence or presence of simulated IL-1 $\beta$  application. Simulated effects of IL-1 $\beta$  included a 25% increase in RyR2 open probability based on experimental data showing increased calcium-spark frequency during IL-1 $\beta$  application (328).

Parameter optimization was performed to minimize the quantitative differences between the Ctl model and the experimentally observed calcium-handling properties using the published values as a starting point. These optimizations in calcium diffusion, SERCA, NCX and RyR2 (Table 4.1) allowed the model to quantitatively reproduce all major calcium-handling properties observed under voltage-clamp conditions (RyR2 open probability, CaT amplitude and decay, SR calcium content and SERCA activity; Figure 4.1-4.3). Finally, the extracellular calcium dependence of NCX was adjusted to prevent excessive calcium overload during simulations with 5 mmol/L extracellular calcium and maximal conductance of two ion channels ( $I_{K1}$  and  $I_{NaK}$ ) were adjusted based on experimental data obtained under current clamp conditions (Table 4.1).

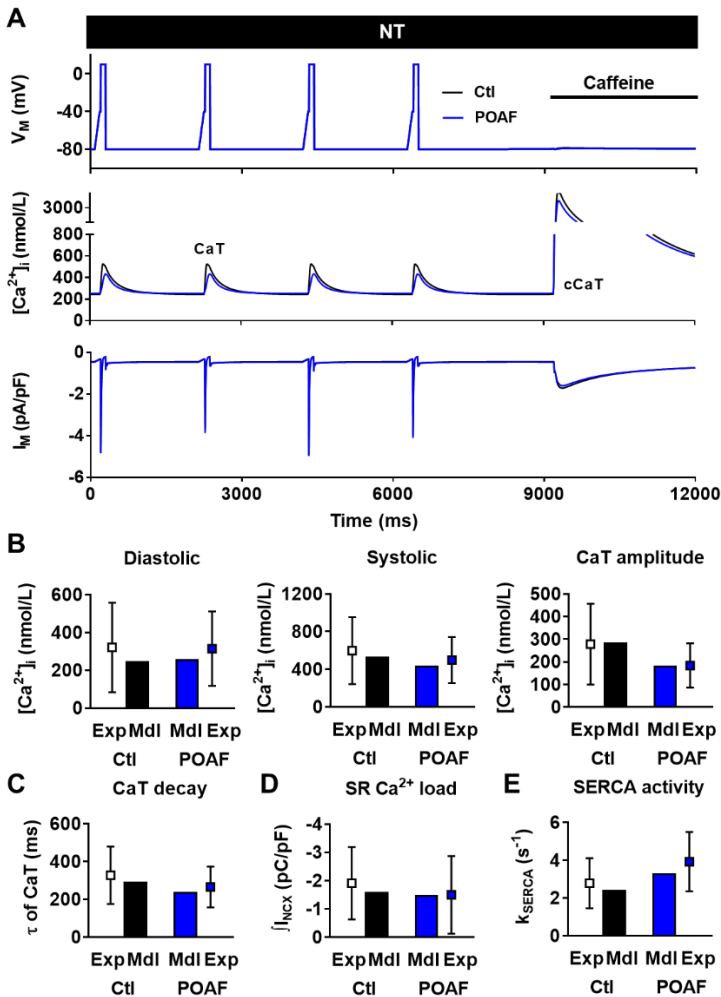


**Figure 4.2: Validation of computational models.** (A) Simulated voltage-clamp protocol (top), whole-cell calcium transient (CaT, middle) and total membrane current (bottom) in Ctl and POAF model variants. (B) Comparison of diastolic and systolic calcium levels, and CaT amplitude; (C) Time constant ( $\tau$ ) of CaT decay;

(D) Sarcoplasmic reticulum (SR) calcium load measured as integrated NCX current ( $I_{NCX}$ ) during the caffeine-induced CaT (cCaT); (E) SERCA activity estimated as the difference in decay rates between the CaT and cCaT, in Ctl and POAF model variants (bars) with experimental data (symbols).

#### 4.2.2 POAF model variant

We subsequently developed a new POAF model variant by incorporating the major differences in calcium handling between Ctl and POAF patients: numerically higher SERCA activity and RyR2 open probability. In particular, maximal SERCA2a activity ( $J_{SERCA,max}$ ) was increased by 30%, and RyR2 open probability was increased by adjusting  $P[0]_{RyR}$  (+37.7%) and  $P[5]_{RyR}$  (+348%), in line with our simulations of higher RyR2 open probability in paroxysmal AF (32). Finally, the interaction between RyR2 was adjusted by lowering the diffusion of calcium from the SRS to the cytosol ( $\tau_{diff,SRS \leftrightarrow cyt}$ , -16.67%) in order to maintain normal SR calcium release in the presence of altered RyR2 gating. With the changes in these 4 parameters (Table 4.1, grey rows), the model accurately reproduced the higher SERCA activity and RyR2 open probability (Figure 4.1A, Figure 4.2E and Figure 4.4A). Moreover, simulated diastolic and systolic calcium concentrations, CaT amplitude, time constant of CaT decay and SR calcium load (Figure 4.2), as well as relative SR calcium leak (Figure 4.3) in the POAF model variant were quantitatively similar to our experimental data, further establishing the validity of this novel model variant.

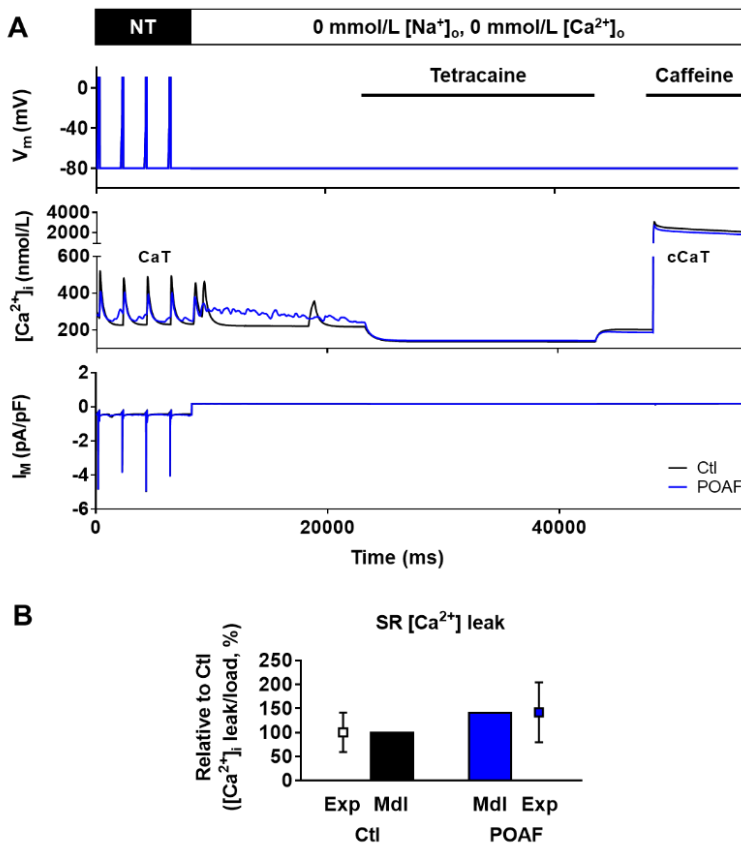


**Figure 4.3:** Simulated sarcoplasmic reticulum (SR) calcium leak protocol in Ctl and POAF model variants. (A) Voltage-clamp protocol (top), whole-cell calcium (middle) and membrane current (bottom) during simulated application of the Shannon protocol (329) to measure SR calcium leak and SR calcium load. The effects of tetracaine and caffeine were simulated by blocking the RyR2 by >99% and setting RyR2 open probability to 1.0, respectively. SR calcium leak was quantified as the decrease in cytosolic calcium during tetracaine application and SR calcium load was quantified as the amplitude of the caffeine-induced calcium transient. (B) Relative [load normalized] SR calcium leak in Ctl and POAF compared to experimental data from Heijman et al. (327).

### 4.2.3 Simulating experimental protocols

Extracellular ionic concentrations and voltage-clamp protocols were set to match experimental conditions for each simulation. During ruptured-patch voltage-clamp simulations, intracellular sodium levels were clamped to 8.5 mmol/L as previously described (32). The effects of tetracaine and caffeine on RyR2 were simulated by acutely setting RyR2 open probability to 1.0 (in the case of caffeine) or blocking the RyR2 by >99% (in the case of tetracaine). After the application of tetracaine or caffeine, RyR2 gating was released and open probability was again determined by cytosolic and SR calcium concentrations.

Experimental data on the acute effects of (post-operative) inflammation on cardiomyocyte calcium-handling are scarce, particularly for human atrial cardiomyocytes. Accordingly, we opted for a parsimonious approach with a minimal number of parameter changes to simulate IL-1 $\beta$  application. Reduced CaT amplitude is a highly consistent finding in response to acute (5 min – 24 hours) stimulation with IL-1 $\beta$ , IL-6 or tumor necrosis factor- $\alpha$  (TNF $\alpha$ ) (328, 330-333). In several (but not all (333)) studies the reduced CaT amplitude is accompanied by a reduced SR calcium content and increased incidence of SCaEs (328, 331). Furthermore, conflicting evidence exists about SERCA function, with reports of both unchanged (333) and decreased (331, 332) SERCA2a expression, as well as decreased expression of the SERCA2a inhibitory subunit phospholamban (334), which could potentially normalize SERCA function in the presence of decreased expression. Similarly, both unchanged (330) and reduced (331)  $I_{Ca,L}$  in response to IL-1 $\beta$ , IL-6 or tumor necrosis factor- $\alpha$  (TNF) stimulation have been reported. Taking into account differences in inflammatory factors and stimulus durations, these data suggest increased RyR2-mediated SR calcium leak as a potential mechanism underlying reduced CaT amplitude and increased incidence of SCaEs. Accordingly, we simulated IL-1 $\beta$  stimulation as an additional 25% increase in RyR2 open probability (**Figure 4.1**) and slower diffusion of calcium from the SRS to the cytosol ( $\tau_{diff,SRS \leftrightarrow cyt}$ ) to promote SCaEs (**Table 4.1**). With this minimal set of changes in 3 parameters, the model could quantitatively reproduce the experimentally observed difference in SCaE incidence between Ctl and POAF during acute stimulation with 40 ng/mL IL-1 $\beta$  (**Figure 4.4**). Since the effects of IL-1 $\beta$  application are associated with a slight delay due to the activation of the intracellular signaling cascades that eventually lead to alterations in calcium-handling proteins, the parameter changes were implemented gradually over a period of 10 seconds.

## 4.3 Results

We employed computational modeling to examine potential cause-effect relationships and predict arrhythmogenic consequences of previously observed POAF-associated remodeling. We adjusted our previously-developed human atrial cardiomyocyte model

with spatial calcium-handling (4, 32) to reproduce key calcium-handling properties observed in Ctl cardiomyocytes (**Figure 4.1-4.3**). We developed a POAF version by incorporating altered RyR2-gating and increased SERCA function, based on experimental data in Heijman et al. (327) (**Figure 4.4A**). With this limited set of experimentally-guided changes, the POAF model fully recapitulated the reduction in CaT amplitude despite unaltered SR calcium-load (assessed by integrated  $I_{NCX}$  during simulated caffeine) and the increase in SR calcium-leak (**Figure 4.4B**). The POAF-model also validated the increased SCaE incidence in POAF (**Figure 4.4C-D**), with simulated IL-1 $\beta$  causing a large increase in SCaE-incidence in POAF vs. Ctl (+509% vs +122% with and without simulated IL-1 $\beta$ , respectively; **Figure 4.4C-D**). These findings indicate that increased SR calcium-leak and enhanced SERCA activity are sufficient to recapitulate the altered calcium-handling observed in POAF.

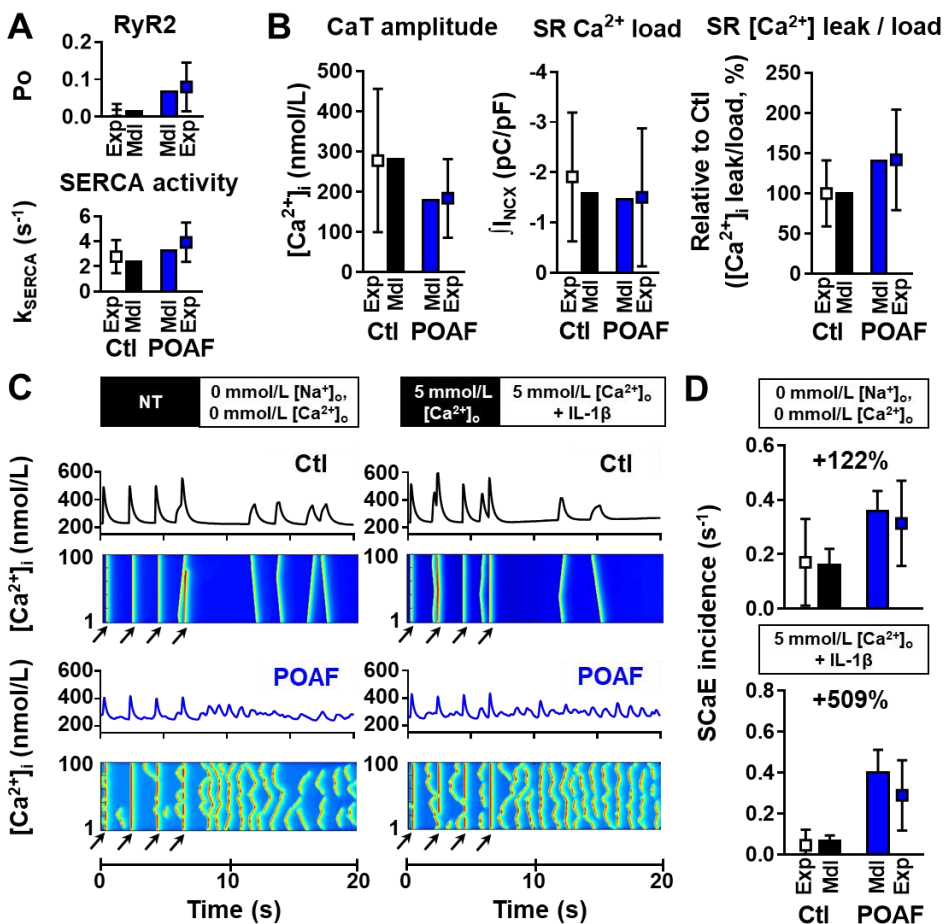


**Figure 4.4:** Computational modeling of calcium-handling abnormalities, consequences of inflammatory signaling and cellular arrhythmogenesis. (A) The novel POAF version of the human atrial cardiomyocyte model was developed by implementing the experimentally observed increases in RyR2 open-probability (top) and SERCA function (bottom). Full model parameters are provided in Table 1. (B) Calcium-handling properties (CaT-amplitude, SR calcium-load and SR calcium-load-normalized SR calcium-leak) in Ctl and

POAF models (bars) compared to experimental data (symbols). (C) Whole-cell CaT and longitudinal line-scan of depolarization-induced (arrows) or spontaneous SR calcium-release events (SCaEs) in Ctl (top row) and POAF (bottom row) models under voltage-clamp conditions with 0 mmol/L sodium and 0 mmol/L calcium (left; experimental conditions in Heijman et al. (327)) or 5 mmol/L calcium followed by acute application of IL-1 $\beta$  (experimental conditions in Heijman et al. (327)). (D) Validation of SCaE-incidence in both model variants (bars) compared to experimental data obtained under the same condition (symbols).

We then employed the model to predict the potential occurrence of proarrhythmic DADs during current-clamp simulations. The Ctl model showed a limited number of SCaEs with corresponding DADs, both in the absence or presence of simulated IL-1 $\beta$  (Figure 4.5A and Figure 4.6). Although the incidence of SCaEs was reduced in the Ctl-model following IL-1 $\beta$  stimulation, total SR calcium-leak was increased (Figure 4.7), suggesting that IL-1 $\beta$ -mediated SR calcium-leak does not translate into proarrhythmic calcium-waves without pre-existing RyR2 dysfunction. DADs, but not SCaEs, were abolished after removal of extracellular calcium and sodium, whereas SCaEs disappeared during simulated RyR2-inhibition (Figure 4.6), confirming the causal roles of RyR2-mediated SR calcium-leak and the generated depolarizing  $I_{NCX}$  in the proarrhythmic response. The model with the pre-existing POAF substrate also showed an increased SCaE incidence (+45%), but in the absence of IL-1 $\beta$ , the SCaEs were small and too dispersed to produce clear DADs (Figure 4.5). The presence of simulated IL-1 $\beta$ , mimicking post-operative conditions, in the POAF-model resulted in a large increase in SCaEs (+84%) and more large-amplitude DADs (+47%), which disappeared with simulated RyR2-block (Figure 4.5B and Figure 4.6).

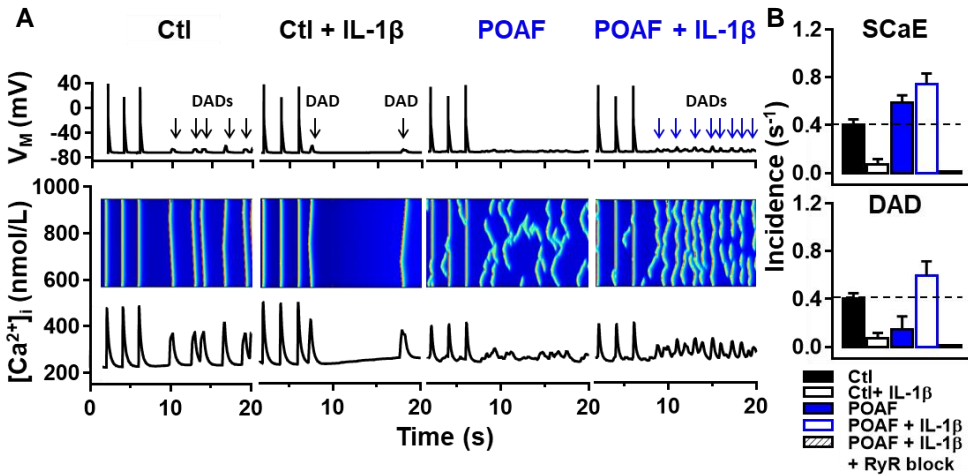


**Figure 4.5:** Computational modeling of calcium-handling abnormalities, consequences of inflammatory signaling and cellular arrhythmogenesis during current-clamp protocol. (A) Simulated action potentials (top panels), longitudinal line-scans (middle panels) and whole-cell CaTs (bottom panels) at 0.5-Hz and follow-up showing SCaEs and corresponding delayed afterdepolarizations (DADs) in Ctl, Ctl+IL-1 $\beta$ , POAF, and POAF+IL-1 $\beta$  models. (B) Quantification of SCaE (top) and DAD (bottom) incidence in Ctl, Ctl+IL-1 $\beta$ , POAF, POAF+IL-1 $\beta$  and POAF+IL-1 $\beta$ +RyR2 block models.

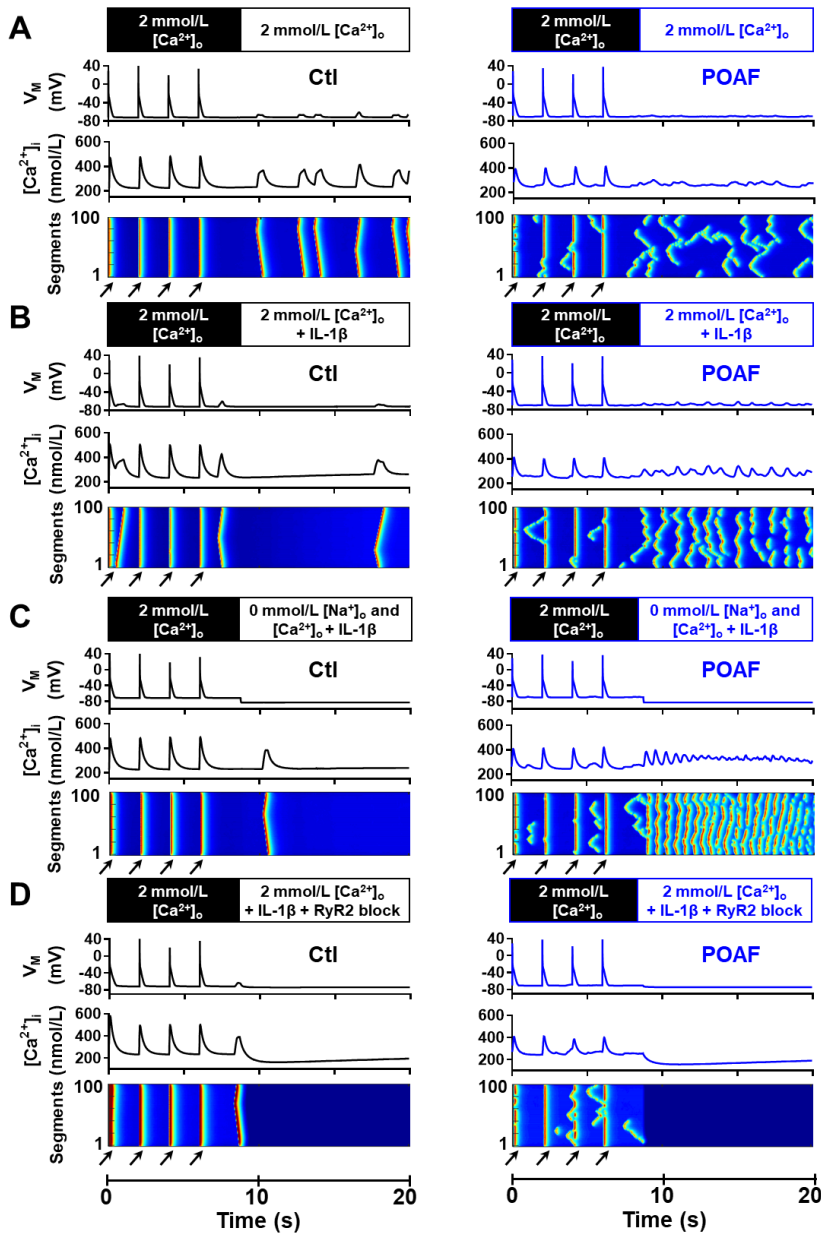


**Figure 4.6:** Current-clamp simulations during 0.5 Hz pacing (arrows) and post-pacing follow-up period to assess spontaneous sarcoplasmic reticulum calcium-release events (SCaEs) and corresponding delayed afterdepolarizations (DADs) in the Ctl (left) and POAF (right) model variants. (A) Membrane potential ( $V_M$ , top), whole-cell calcium-transient (middle) and longitudinal line scan through the center of the virtual cardiomyocyte (bottom) under control conditions (2.0 mmol/L extracellular calcium). (B) Similar to panel A in the presence of simulated IL-1 $\beta$  application during the follow-up. (C) Similar to panel B, but in the absence of extracellular calcium and sodium to inhibit transmembrane calcium fluxes. (D) Similar to panel B with inhibition of ryanodine receptor channel type-2 (RyR2)-mediated calcium release.

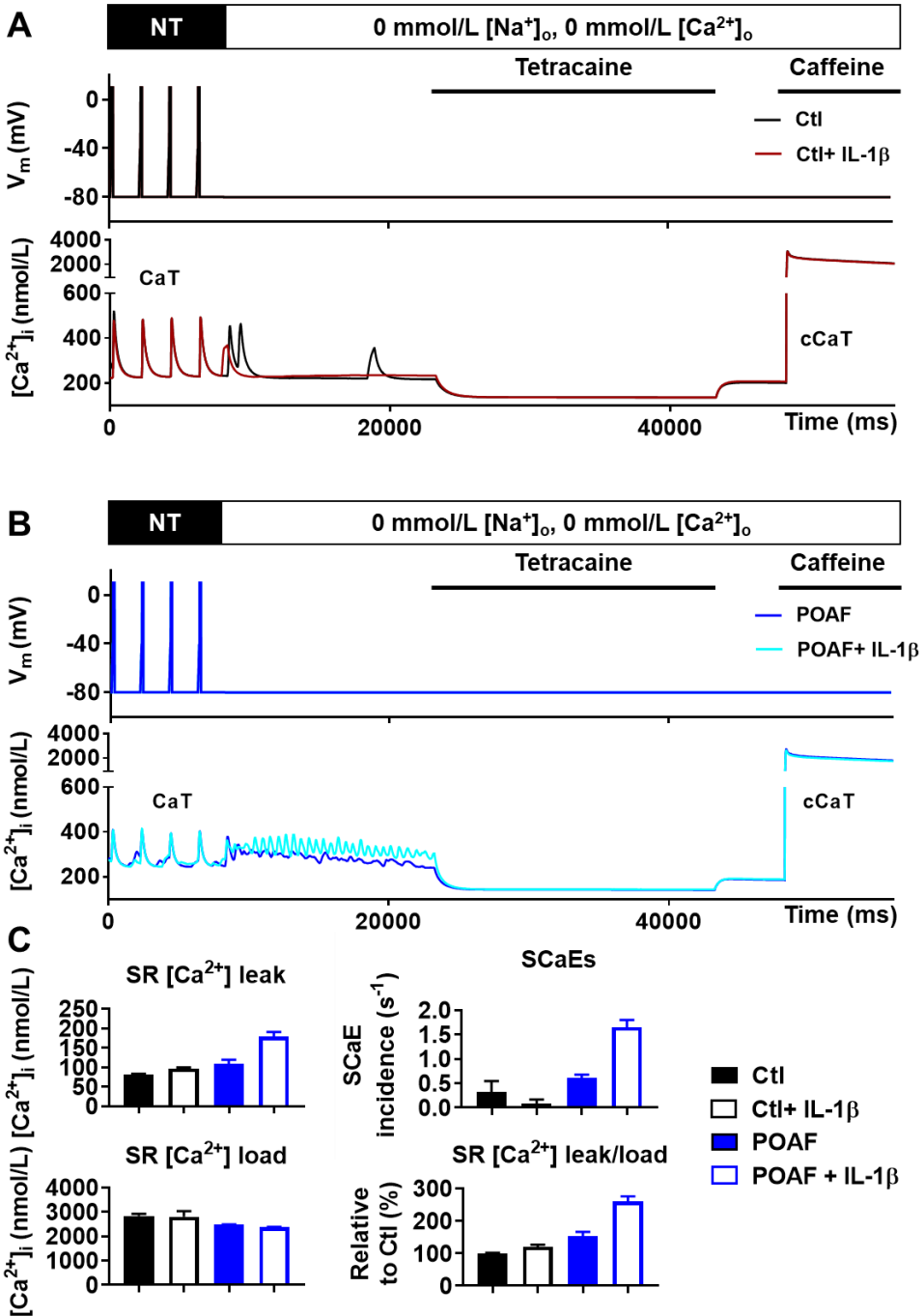


**Figure 4.7:** Simulated sarcoplasmic reticulum (SR) calcium-leak protocol in the absence or presence of interleukin-1β (IL-1β) stimulation. (A) Voltage-clamp protocol (top) and whole-cell calcium (bottom) during simulated application of the Shannon protocol (329) to measure SR calcium-leak and SR calcium-load in the

Ctl model in the absence (black line) or presence (red line) of IL-1 $\beta$ . The effects of tetracaine and caffeine were simulated by blocking the RyR2 by >99% and setting RyR2 open probability to 1.0, respectively. (B) Similar to panel A for the POAF model version. (C) Top: Quantification of SR calcium-leak and incidence of spontaneous SR calcium-release events (SCaEs). Bottom: SR calcium-load (amplitude of the caffeine-induced calcium transient, cCaT) and SR calcium-leak/load in Ctl and POAF with and without IL-1 $\beta$  stimulation.

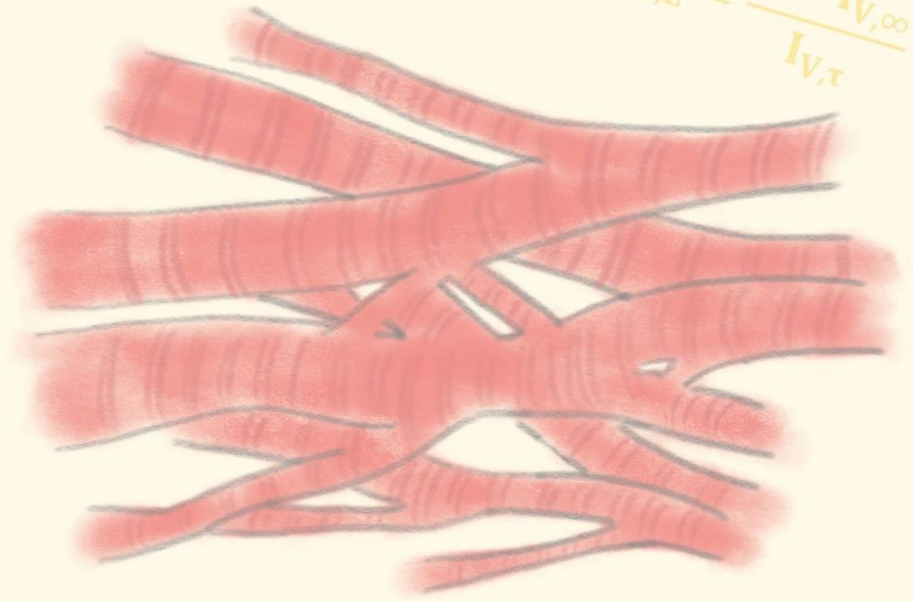
#### 4.4 Conclusion

Overall, computational modeling supports the notion that post-operative inflammation acting on a pre-existing arrhythmogenic substrate may elicit proarrhythmic responses leading to POAF.



$$\frac{dV_m}{dt} = -\frac{1}{C_m} * I$$

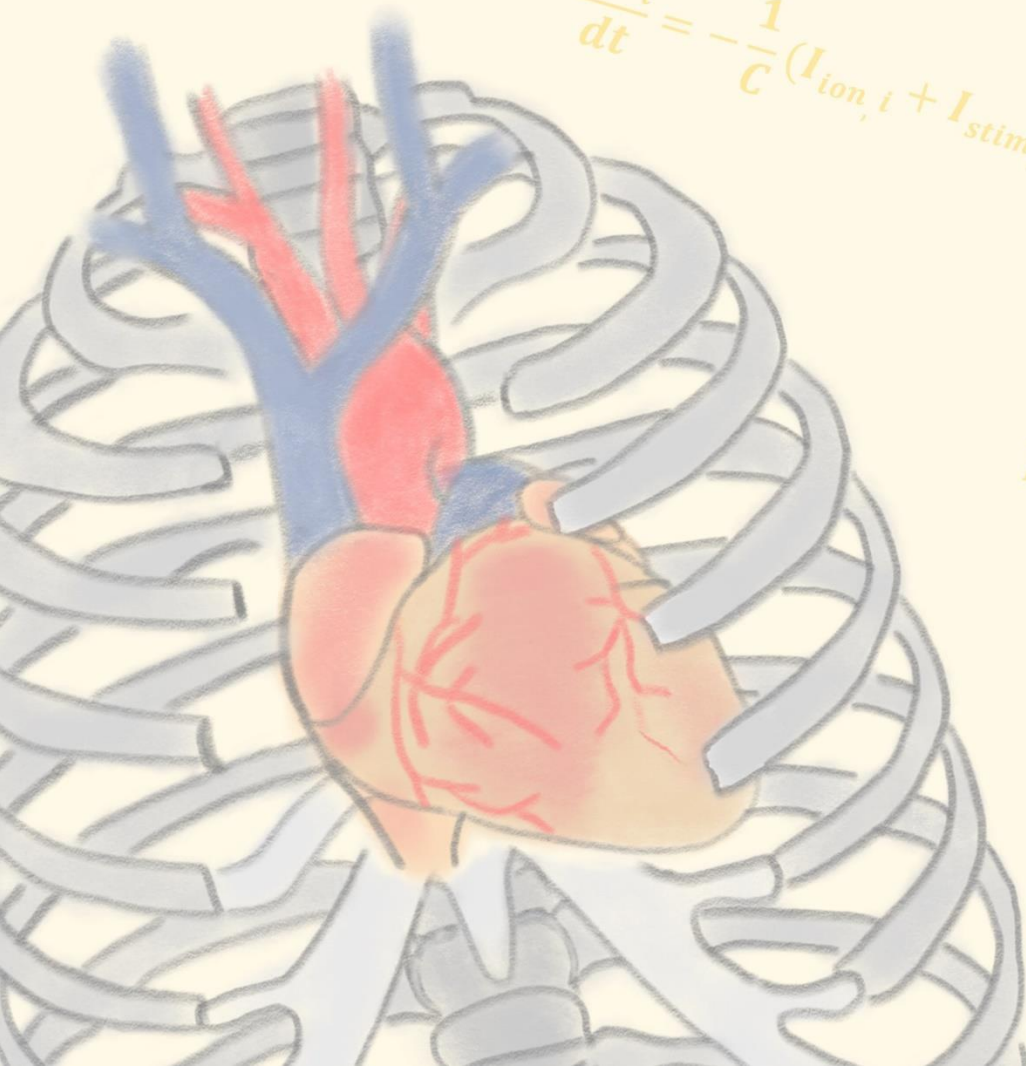
$$y_{Ca,L} = \frac{1 - I_{V,\infty}}{I_{V,\tau}}$$



$$x_{Ca,L} = \frac{I_{V,\infty}}{I_{V,\tau}}$$

$$\delta I_{Ca,L}^{s,m} =$$

$$\frac{dV_i}{dt} = -\frac{1}{C} (I_{ion,i} + I_{stim,i} + I_{diff,i})$$



$$\bar{I}_{Ca,L}^{s,m} = P_{Ca,L} \cdot (z$$

$$ACT_{\tau} = 0.59$$

# Chapter 5

Calcium-dependent regulation of cardiac ionic currents modulates atrial electrophysiology and arrhythmogenesis: insights from computational modeling

H. Sutanto, D. Dobrev, E. Grandi, P.G.A. Volders and J. Heijman.

*In Preparation*



$$\frac{dV}{dt} = \frac{I_{stim} - (I_K + I_{Na} + I_{leak})}{C_m}$$

## ABSTRACT

Calcium is essential for cardiac excitation-contraction coupling. Under pathological conditions, calcium-handling abnormalities can promote cardiac arrhythmias through several pathways, including direct regulation of cardiac ion channels. The calcium-dependent regulation of cardiac ionic currents, including the inward-rectifying potassium current ( $I_{K1}$ ), slow delayed-rectifier potassium current ( $I_{Ks}$ ), small-conductance calcium-activated potassium current ( $I_{SK}$ ) and calcium-activated chloride current ( $I_{ClCa}$ ) has been demonstrated experimentally, but its consequences for atrial electrophysiology are unknown. Here, we perform multiscale *in silico* studies to reveal the role of this regulation in atrial electrophysiology and arrhythmogenesis under physiological and pathological conditions.

We incorporated calcium-dependent regulation of  $I_{K1}$  and  $I_{Ks}$  based on published experimental data in the *state-of-the-art* 2020 version of the Grandi human atrial cardiomyocyte model, which also includes  $I_{SK}$  and  $I_{ClCa}$ . We then investigated the role of calcium-dependent regulation of these ion channels on the action potential (AP) and the genesis of delayed afterdepolarizations (DADs). A phenomenological model of stochastic ryanodine receptor gating was implemented to simulate spontaneous calcium releases and DADs. Finally, two-dimensional tissue simulations were performed to study the role of calcium-dependent regulation of ionic currents on ectopic activity and the behavior of reentrant waves.

Calcium-dependent ion-channel regulation synergistically reduced the atrial AP duration, primarily at slow pacing rates, which was diminished following progressive L-type calcium current inhibition. Calcium-dependent regulation also reduced DAD amplitude and the vulnerable window for reentry under physiological conditions. However, in the presence of atrial fibrillation-related electrical remodeling, calcium-dependent ion-channel regulation stabilized reentry and increased the vulnerable window, mainly via  $I_{K1}$  and  $I_{SK}$ .

In conclusion, calcium-dependent regulation of atrial ionic currents has substantial impact on arrhythmogenesis by inhibiting triggered activity. On the other hand, under disease conditions, this regulation stabilizes reentrant arrhythmias. Altering calcium-dependent regulation of ion channels might represent a future therapeutic strategy for atrial arrhythmias.

## 5.1 Introduction

As extensively discussed in **Chapter 2**, calcium is a key regulator of cardiac electromechanical function that interacts with many proteins and signaling molecules to regulate excitation-contraction coupling (335). Calcium enters the cardiomyocyte through L-type calcium channels (LTCC), triggering a more abundant calcium release from the sarcoplasmic reticulum (SR) through a process called calcium-induced calcium release (CICR). Subsequently, calcium interacts with contractile machineries to initiate cardiomyocyte contraction. In addition, calcium activates various signaling cascades within the cardiomyocyte, such as calcium/calmodulin-dependent protein kinase-II (CaMKII) and calcineurin/NFAT. During diastole, calcium is transported back into the SR via the SR calcium-ATPase (SERCA) and partly extruded from the cell via the sodium-calcium exchanger (NCX) (335).

Under pathological conditions, calcium-handling abnormalities can promote cardiac arrhythmias through at least 3 processes: the formation of delayed afterdepolarizations (DADs), ion-channel modulation, and structural remodeling (335). In addition to activating calcium-dependent signaling cascades, calcium also directly modulates several cardiac ion channels (55, 56, 336, 337). Some of these, such as small-conductance calcium-activated potassium (SK or K<sub>Ca</sub>) channels, are now considered as potential therapeutic targets for cardiac arrhythmias (45, 338). Calcium-dependent regulation of the inward-rectifying potassium current ( $I_{K1}$ ) results in increased systolic  $I_{K1}$  and reduced diastolic  $I_{K1}$  in the presence of low calcium (56). Similarly,  $I_{K1}$  was significantly increased in isolated canine cardiomyocytes following a rise of intracellular calcium (55). Meanwhile, intracellular calcium also enhanced rabbit ventricular slow delayed-rectifier potassium current ( $I_{Ks}$ ) by negatively shifting its voltage-dependent activation and slowing channel deactivation (336), whereas the rapid delayed-rectifier potassium current ( $I_{Kr}$ ) was unaffected by high intracellular calcium. Finally, the calcium-dependent chloride current ( $I_{ClCa}$ ) is activated in response to increased intracellular calcium concentrations, via alteration of the electrostatic properties of the ion-conduction path and conformational changes of the  $\alpha$ -helix, enabling calcium to interact with the binding site in the transmembrane domain (339). The role of  $I_{ClCa}$  in arrhythmogenesis is not fully understood. It was reported to contribute to action potential (AP) alternans in atrial cardiomyocytes (337) and implicated in DADs. Inhibition of  $I_{ClCa}$  prevented the transformation of DADs into triggered activities (TAs) (337). Due to the large number of calcium-sensitive processes and the simultaneous interaction between calcium-regulated ion channels via changes in membrane potential, it is experimentally challenging to study the impact of calcium-dependent ion-channel regulation on cardiac electrophysiology.

Employing the perfect control and observability provided by computational modeling (4), we aimed to investigate the role of calcium-dependent regulation of these ionic currents, focusing on their impact on atrial electrophysiology and arrhythmogenesis. We show that calcium-dependent regulation of atrial ionic currents modulates AP duration and DADs. Using a novel simplified model of stochastic

ryanodine receptor (RyR) gating, we next investigated the consequences of subcellular spontaneous SR calcium releases (SCaEs) and their effects on calcium-dependent ion-channel gating on tissue-level ectopy. Together, our multiscale *in silico* study provides insight on the impact of calcium-dependent ion-channel regulation on atrial electrophysiology, under both physiological and pathological conditions.

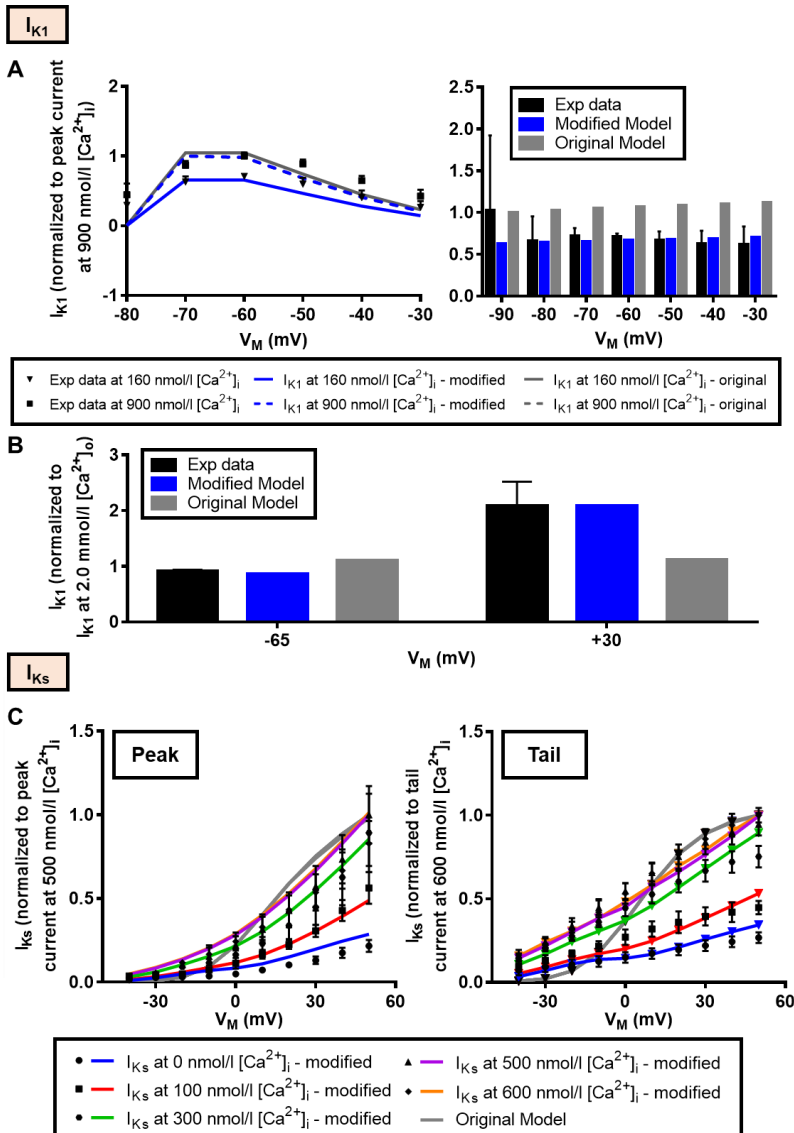


**Figure 5.1:** Incorporation and optimization of calcium-dependent regulation of  $I_{K1}$  and  $I_{Ks}$  in the Grandi human atrial cardiomyocyte model. A,B) Calcium-dependent regulation of  $I_{K1}$  optimized to experimental data by Nagy et al. (55) for membrane voltages from -90 mV to -30 mV (A) and by Zaza et al. (56) at -65 mV and +30 mV (B). C) Calcium-dependent regulation of peak (left) and tail (right)  $I_{Ks}$  optimized to experimental data by Bartos et al. (336).

## 5.2 Methods

In this study, we employed the *state-of-the-art* 2020 version of Grandi human atrial cardiomyocyte model (340, 341), which incorporated several newly-investigated channels, such as the 4-transmembrane 2-pore-region potassium ( $K_{2P}$ ) channels and SK channels (342, 343). We extended this model with calcium-dependent regulation of  $I_{K1}$  and  $I_{Ks}$  based on previously published experimental data (55, 56, 336) (Figure 5.1). All simulations in this study were performed using Myokit (344). The cellular AP simulations were performed in two groups: the control model in which the calcium observed by the current of interest was clamped to the diastolic value of 190 nmol/l to nullify calcium dependence and the dynamic model (with active calcium-dependent regulation). Zero-dimensional (single-cell) simulations were performed at various pacing frequencies to assess the rate-dependence of calcium-dependent regulation. Two-dimensional tissue simulations were performed in 4x4 cm of virtual tissue (simulated using 200x200 units). An  $S_1S_2$  induction protocol was used to induce reentrant spiral waves. In the  $S_1S_2$  protocol, the first stimulus ( $S_1$ ) is applied to generate a normal excitation wave. The second stimulus ( $S_2$ ) is then applied to part of the tissue, generating an additional wave-front that can interact with the tail of the preceding wave, producing reentry in a vulnerable substrate. In this study, the  $S_1$  was initiated from left to right and the  $S_2$  was applied to the upper-left quadrant of the tissue. The isotropic conduction velocity was set to 50 cm/s.

To study the effect of calcium-dependent regulation of atrial ionic currents on DADs, we employed both a deterministic approach (by inducing a predefined amount of SR calcium release at a specific moment), as well as a simplified stochastic RyR gating model that captures the behavior observed in more complex models with spatial calcium handling based on the approach by Colman (97). In brief, at the start of every AP, a time point for SCaE initiation was stochastically generated using a function controlled by the SR calcium concentration. If this random time point occurred before the next stimulus, SR calcium release was initiated by temporarily increasing RyR2 open probability. The properties of this SR calcium release (amplitude and duration) were similarly randomly-assigned through stochastic functions at the start of each AP. Parameters for the stochastic functions were chosen to qualitatively reproduce experimentally observed SCaE properties. Using this new method, SCaEs were simulated and their effect on DAD properties was studied in the absence or presence of calcium-dependent ion-channel regulation. Furthermore, we incorporated the models with simplified stochastic RyR gating in two-dimensional tissue models to enable the simulation of DADs and ectopic activities at the tissue level during a long observation periods of 8 s following pacing at 2 Hz. The model is freely accessible in Myokit format at our GitHub page ([www.github.com/jordiheijman](http://www.github.com/jordiheijman)). Statistical analyses were performed using Mann-Whitney test for non-normally distributed data and results were considered statistically significant for  $P < 0.05$ .

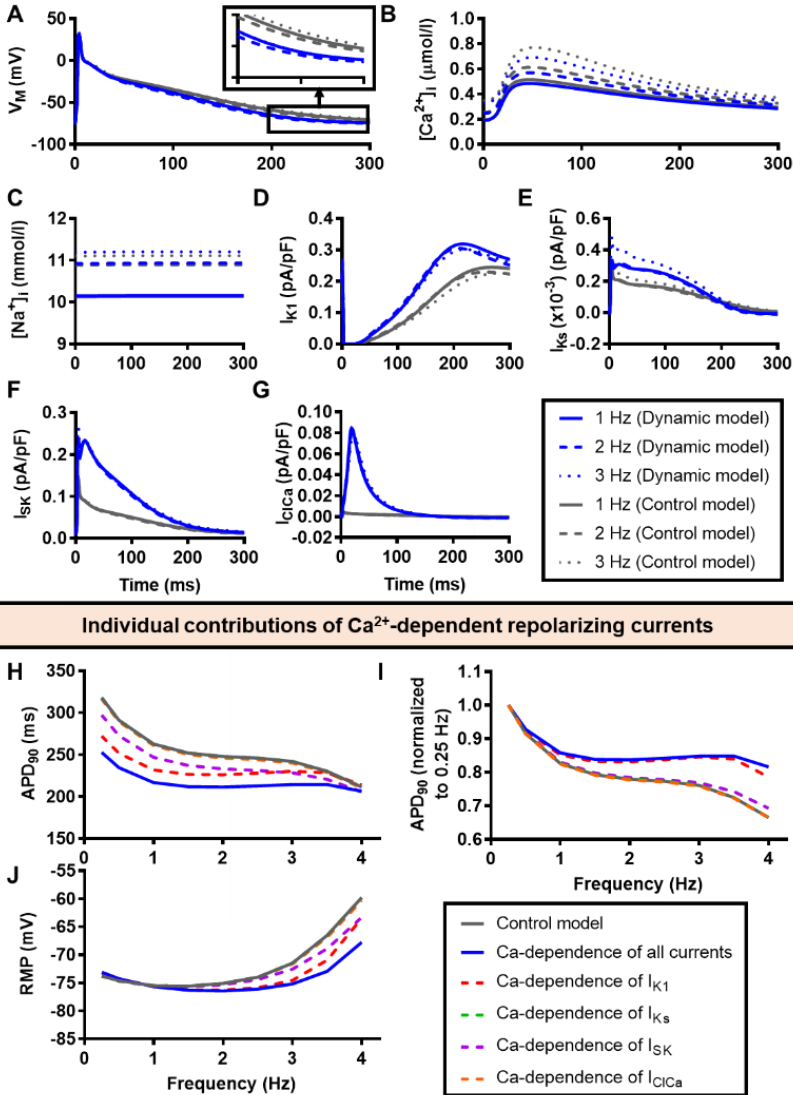


**Figure 5.2:** Rate-dependent effects of calcium-dependent ion-channel regulation on the human atrial action potential. A-G) The effects of calcium-dependent modulation on AP, calcium transient, calcium-dependent currents, and intracellular sodium level for different pacing frequencies, from 1 Hz to 3 Hz. H-J) Parameter sensitivity analysis of the individual contributions of calcium-dependent currents. The relationship between pacing rate and absolute APD<sub>90</sub> (H), relative APD<sub>90</sub> (I, normalized to 0.25 Hz) and RMP (J) are shown. (APD = action potential duration; RMP = resting membrane potential)

### 5.3 Results

#### 5.3.1 The effects of calcium-dependent ion-channel regulation on atrial action potentials

First, we simulated the effects of calcium-dependent regulation of 4 atrial ionic currents ( $I_{K1}$ ,  $I_{Ks}$ ,  $I_{SK}$ , and  $I_{CaCa}$ ) on AP properties during 1 Hz pacing. The dynamic model displayed

a 46 ms (17.4%) shorter AP duration (APD) at 1 Hz pacing than the control model due to a substantial calcium-dependent increase in all 4 currents (Figure 5.2A-G). Accelerating the pacing frequency from 0.25 Hz to 4 Hz reduced APD by 33% and 19% in control and dynamic models, respectively (Figure 5.2H). Accordingly, calcium-dependent APD regulation was augmented at slow pacing rates (20.5% APD reduction at 0.25 Hz compared to 11.4% APD reduction at 3 Hz), highlighting the predominance of calcium-dependent ion-channel regulation at slow pacing frequencies (Figure 5.2H-I) despite the rate-dependent increase in intracellular calcium concentrations. By contrast, the dynamic model hyperpolarized the resting membrane potential (RMP) primarily at fast pacing rates (Figure 5.2J). Parameter sensitivity analyses revealed that calcium-dependent regulation of  $I_{K1}$  and  $I_{SK}$  were the major determinants of APD and RMP changes, with minor contribution from  $I_{CaL}$  and negligible support from  $I_{Ks}$ .

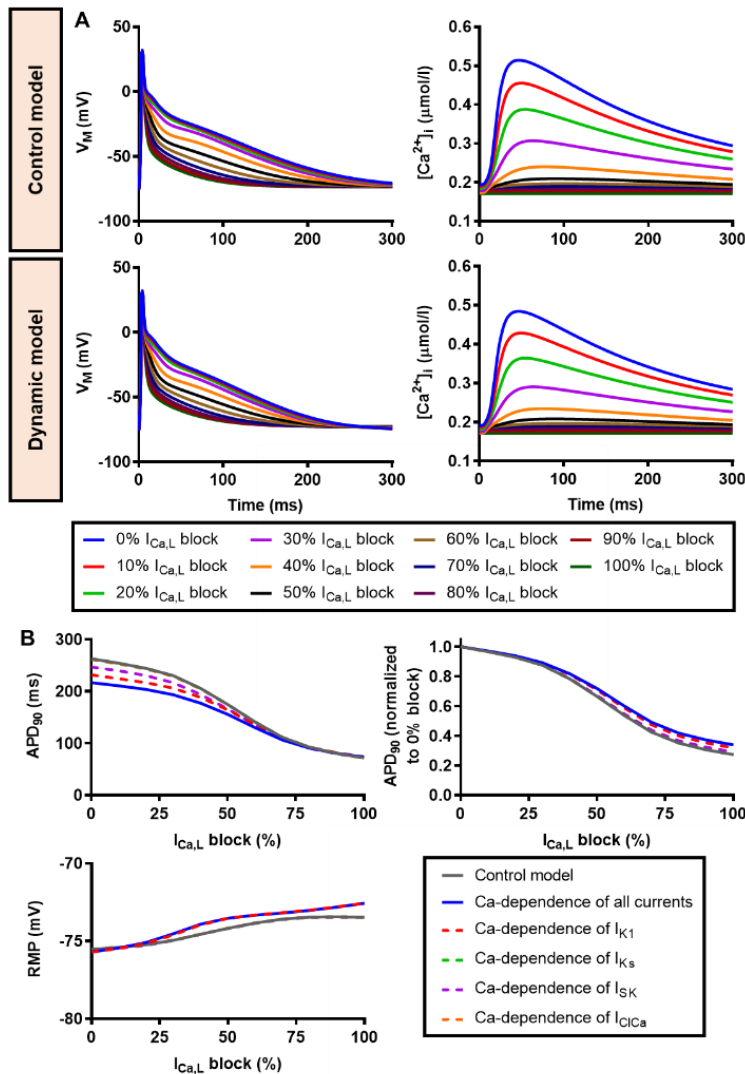


**Figure 5.3:** Calcium-dependent regulation of atrial ionic currents under L-type calcium current ( $I_{Ca,L}$ ) block. A) The AP and calcium transient of control and dynamic models for increasing levels of  $I_{Ca,L}$  block from 0% to 100%. B) The individual contributions of calcium-dependent currents to the relationship between the degree of LTCC block and AP properties ( $APD_{90}$  and RMP). ( $APD$  = action potential duration;  $RMP$  = resting membrane potential)

Next, we investigated the effect of calcium-dependent ion-channel regulation under altered intracellular calcium concentrations. These alterations were achieved 1) by limiting calcium-influx into atrial cardiomyocytes by blocking LTCC and 2) by limiting calcium-efflux from cardiomyocytes by blocking the sodium-potassium-ATPase (NKA), which indirectly inhibits calcium extrusion via NCX. Increasing LTCC block from 0% to 100% resulted in progressive APD reduction (73% in control and 66% in the dynamic model) and calcium-transient amplitude in both models (**Figure 5.3**). The shorter APD in the dynamic model at baseline (**Figure 5.2H**) was diminished with 100% LTCC block (**Figure 5.3B**), confirming the involvement of calcium in the observed APD reduction in the dynamic model. Blocking LTCC up to 100% also depolarized the RMP due to a reduction in calcium-dependent regulation of  $I_{K1}$ . The impact of LTCC block on calcium-dependent currents and calcium-handling proteins are depicted in **Figures 5.4-5.5**.

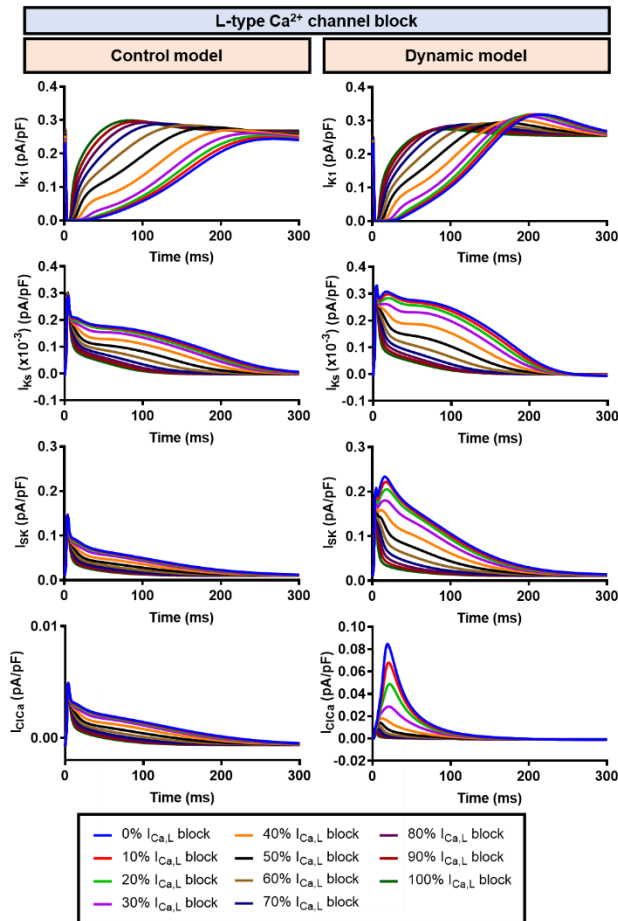


**Figure 5.4:** Calcium-dependent currents in the presence of L-type calcium current ( $I_{Ca,L}$ ) block. The effects of incremental  $I_{Ca,L}$  block from 0% to 100% on the calcium-dependent  $I_{K1}$ ,  $I_{Ks}$ ,  $I_{Sk}$ , and  $I_{ClCa}$  in the dynamic model was compared to the control model.

Next, we increased intracellular calcium by blocking NKA, which limits the efflux of calcium via NCX. Progressive NKA block from 0% to 100% had minor effects on APD (**Figures 5.6-5.8**). Up to 70% NKA block, APD in both control and dynamic models were slightly prolonged (by 5% and 6%, respectively; **Figure 5.6B**). With higher levels of NKA block, RMP became strongly depolarized, significantly altering AP morphology and duration, and several episodes of DADs and TAs were documented. In the dynamic model, RMP depolarization was slightly less pronounced due to calcium-dependent augmentation of  $I_{K1}$ .

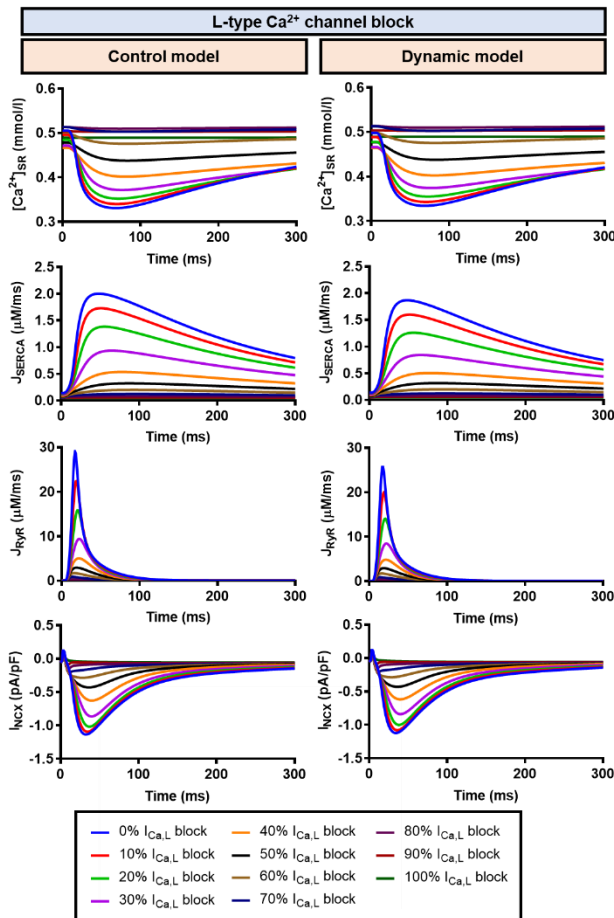


**Figure 5.5:** Calcium-handling properties of control and dynamic models during L-type calcium current ( $I_{Ca,L}$ ) block. The effects of incremental  $I_{Ca,L}$  block from 0% to 100% on calcium-handling in the dynamic model was compared to the control model.

Finally, we assessed the role of calcium-dependent regulation of atrial ionic currents under pathological conditions, i.e., in the presence of atrial remodeling related to long-standing persistent “chronic” atrial fibrillation (cAF). With cAF-related

remodeling, the dynamic model similarly exhibited shorter APD than the control model at 1 Hz pacing (by 28 ms; 25%), with an increase in all 4 calcium-dependent currents (Figure 5.9A-G). In the presence of cAF-related remodeling, the difference between APD-rate dependence in the control and dynamic models was blunted (25% and 27% APD reduction between 0.25 and 4.0 Hz, respectively). The calcium-dependent APD-shortening effect observed in the dynamic cAF model was similar for all pacing rates, reflecting the absence of rate-dependence in calcium handling in the presence of cAF-related remodeling. Parameter sensitivity analysis revealed  $I_{K1}$  and  $I_{SK}$  as the primary mediators of APD shortening, similar to what we observed in the non-diseased atrium. The dynamic cAF model also hyperpolarized RMP, with predominance at fast pacing frequencies (Figure 5.9J), controlled mainly by calcium-dependent regulation of  $I_{K1}$ .

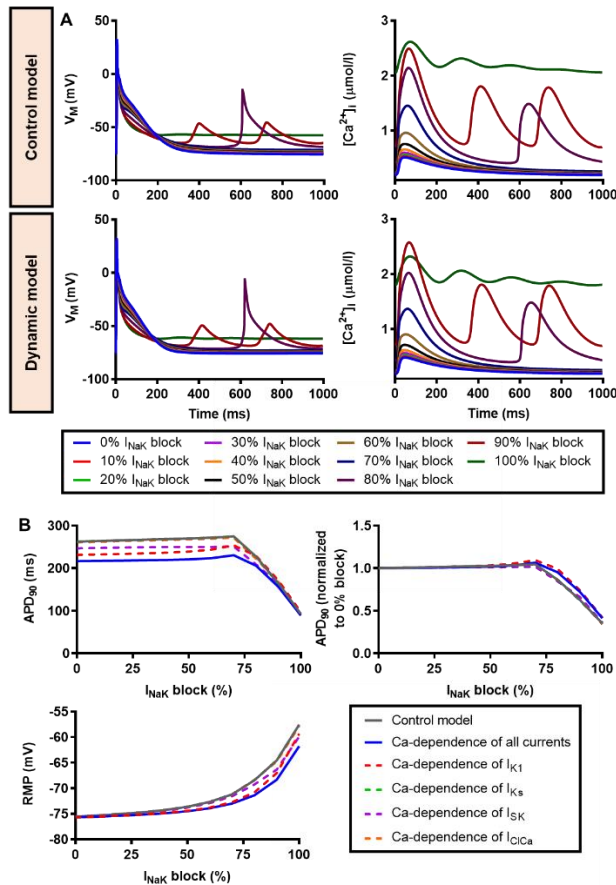


**Figure 5.6:** Calcium-dependent regulation of atrial ionic currents under NKA block. A) The AP and calcium transient of control and dynamic models under incremental NKA ( $I_{NaK}$ ) block from 0% to 100%. B) The individual contributions of calcium-dependent currents to the relationship between the degree of NKA block and AP properties (APD<sub>90</sub> and RMP). (APD = action potential duration; RMP = resting membrane potential)

### 5.3.2 Calcium-dependent ion-channel regulation alters DAD properties

DADs are a major mechanism of ectopic activity, occurring as a consequence of diastolic SCAEs (4, 345). DAD properties are modulated by many factors, including the balance

between repolarizing  $I_{K1}$  and depolarizing NCX. In case of hypokalemia, when the RMP is hyperpolarized, a larger stimulus is needed to activate  $I_{Na}$  and trigger an AP (345). In the previous section and in **Figure 5.2J**, we observed a slightly lower RMP in the dynamic model compared to the control model due to calcium-dependent regulation of  $I_{K1}$ . These data suggest that calcium-dependent regulation of atrial ionic currents during SCAEs may also affect DAD properties. We employed two approaches to trigger DADs in the Grandi human atrial cardiomyocyte model. First, we altered RyR flux ( $J_{RyR}$ ) in the model in a predefined, deterministic manner, similar to a caffeine-induced calcium-release effect observed in experiments. Second, we implemented a *state-of-the-art* approach that phenomenologically reflects subcellular stochastic RyR gating, as proposed by Colman (97).

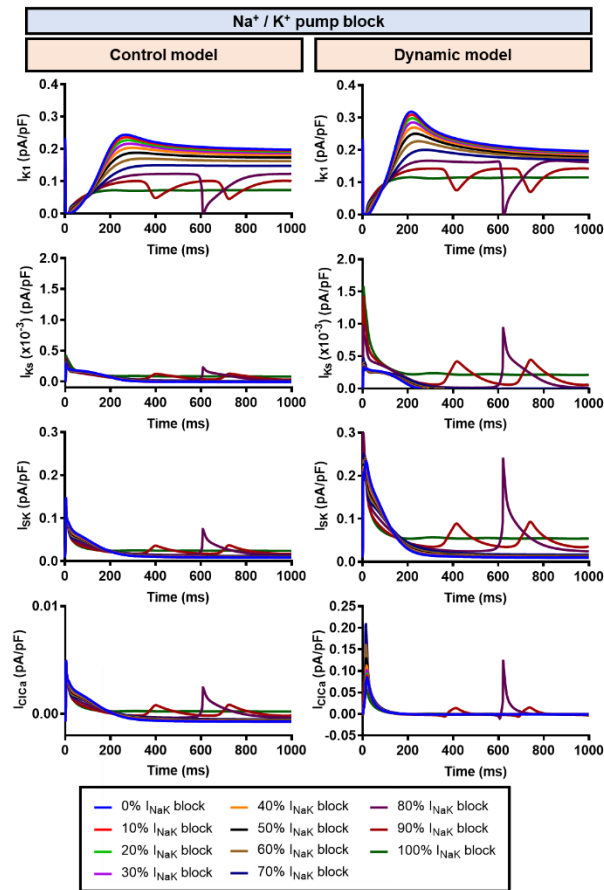


**Figure 5.7:** Calcium-dependent currents under NKA block. The effects of incremental NKA block from 0% to 100% on the calcium-dependent  $I_{K1}$ ,  $I_{Ks}$ ,  $I_{SK}$ , and  $I_{CaCa}$  in the dynamic model was compared to the control model.

Using the predefined, deterministic approach, we demonstrated that calcium-dependent regulation of atrial ionic currents in the dynamic model lowered the DAD amplitude, preventing the occurrence of TA for an SR calcium release that did trigger an AP in the control model (**Figure 5.10A**, green line). As such, a slight rightward-shift was observed in the  $\Delta CaT-\Delta V_M$  curve (**Figure 5.10B**). Traces of calcium-dependent

currents and calcium-handling parameters during simulated DADs are shown in **Figures 5.11-5.12**.

To investigate the effects of calcium-dependent ion-channel modulation on the behavior of dynamic DADs occurring after the cessation of pacing, we extended the human atrial model by incorporating a simplified stochastic RyR model. We calculated the DAD incidence as previously reported using a more complex and detailed spatial subcellular calcium-handling model (4) for various amplitude, latency and duration of RyR-mediated SR calcium release. As depicted in **Figure 5.13A-C**, using this stochastic approach ( $N=60$  simulations), the model with dynamic calcium-dependent ion-channel regulation had a lower TA incidence with a slight increase in DAD incidence compared to the control model. Consistent with the phenomenological approach, the average and maximum DAD amplitudes were also reduced in the dynamic model (**Figure 5.13D-E**), highlighting the RMP-stabilizing role of calcium-dependent modulation of ionic currents.

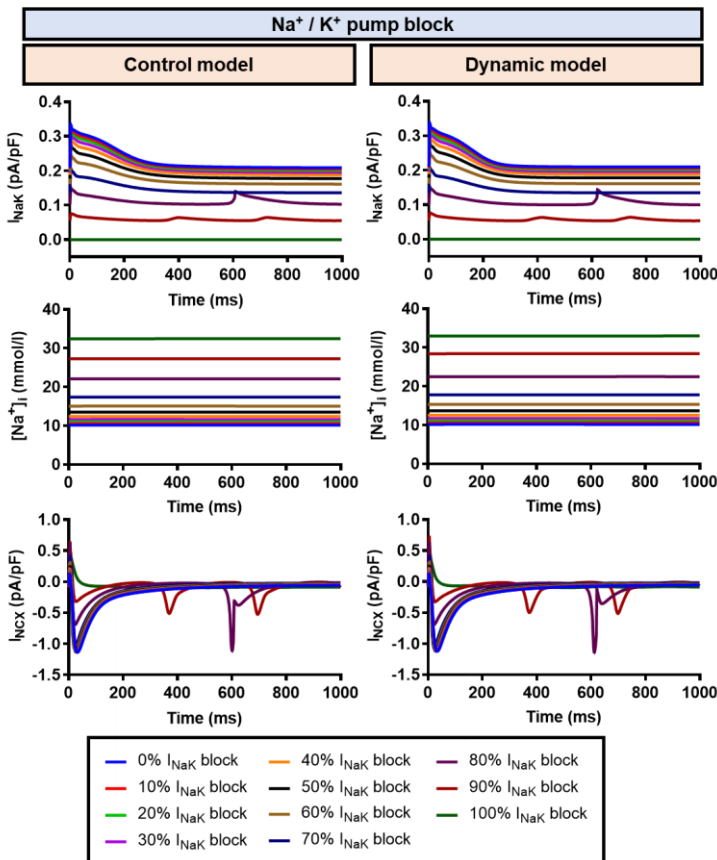


**Figure 5.8:** Calcium-handling properties of control and dynamic models under NKA block. The effects of incremental NKA block from 0% to 100% on calcium handling in the dynamic model was compared to the control model.

Next, we investigated the impact of calcium-dependent ion-channel regulation on DAD properties in cAF, incorporating the AF-induced electrical remodeling and previously documented AF-associated changes in calcium-handling properties (**Table 5.1; Figure 5.14A-B**) (94). The cAF model showed a substantial increase in the incidence of DADs in the absence and presence of calcium-dependent regulation compared to the non-diseased model (**Figure 5.14C**), consistent with the increased RyR open probability in AF. The dynamic model produced a statistically significant reduction in DAD incidences and maximum DAD amplitudes, without significant differences in TA incidences and the average DAD amplitudes compared to the control model (**Figure 5.14D-E**). These findings suggest an attenuation of the membrane-stabilizing effect of calcium-dependent ion-channel regulation under pathological conditions.

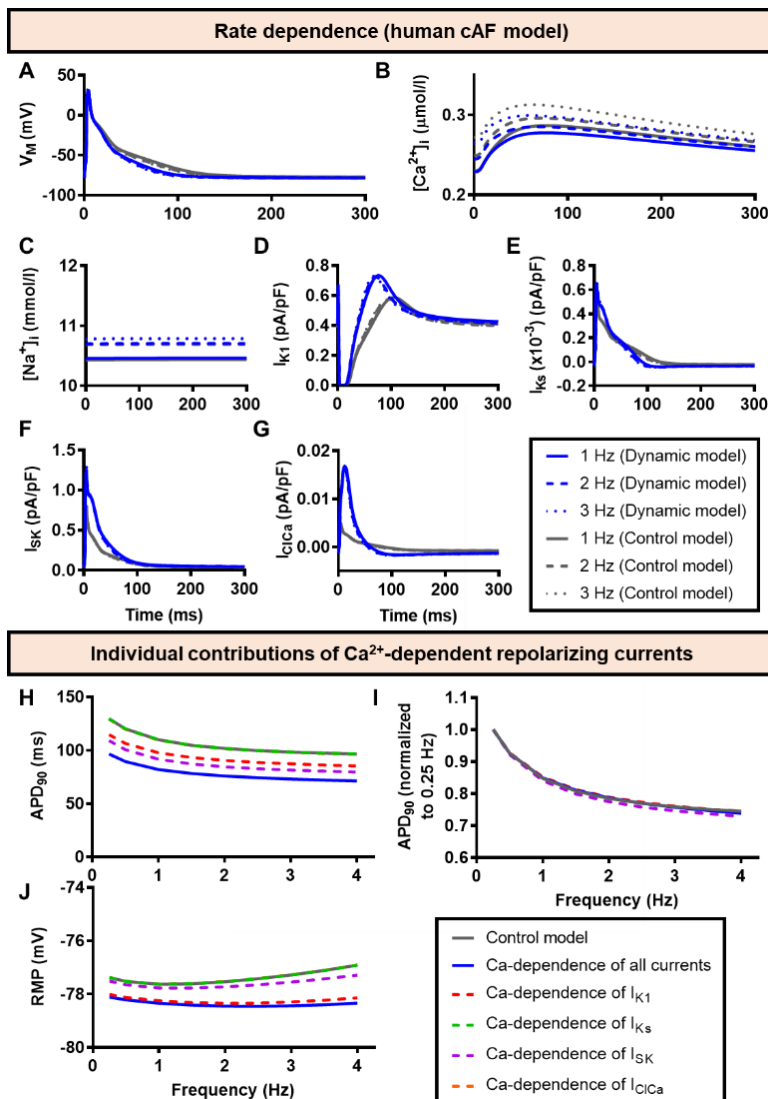


**Figure 5.9:** Rate-dependent effects of calcium-dependent regulation of atrial ionic currents on action potential in chronic AF. A-G) The effects of calcium-dependent ion-channel modulation on AP, calcium transient, calcium-dependent currents, and intracellular sodium level for different pacing frequencies (1 Hz to 3 Hz). H-J) Parameter sensitivity analysis revealing the individual contributions of calcium-dependent currents on the relationship between pacing rate and absolute APD<sub>90</sub> (H), relative APD<sub>90</sub> (I) and RMP (J). (APD = action potential duration; RA = right atrium; RMP = resting membrane potential)

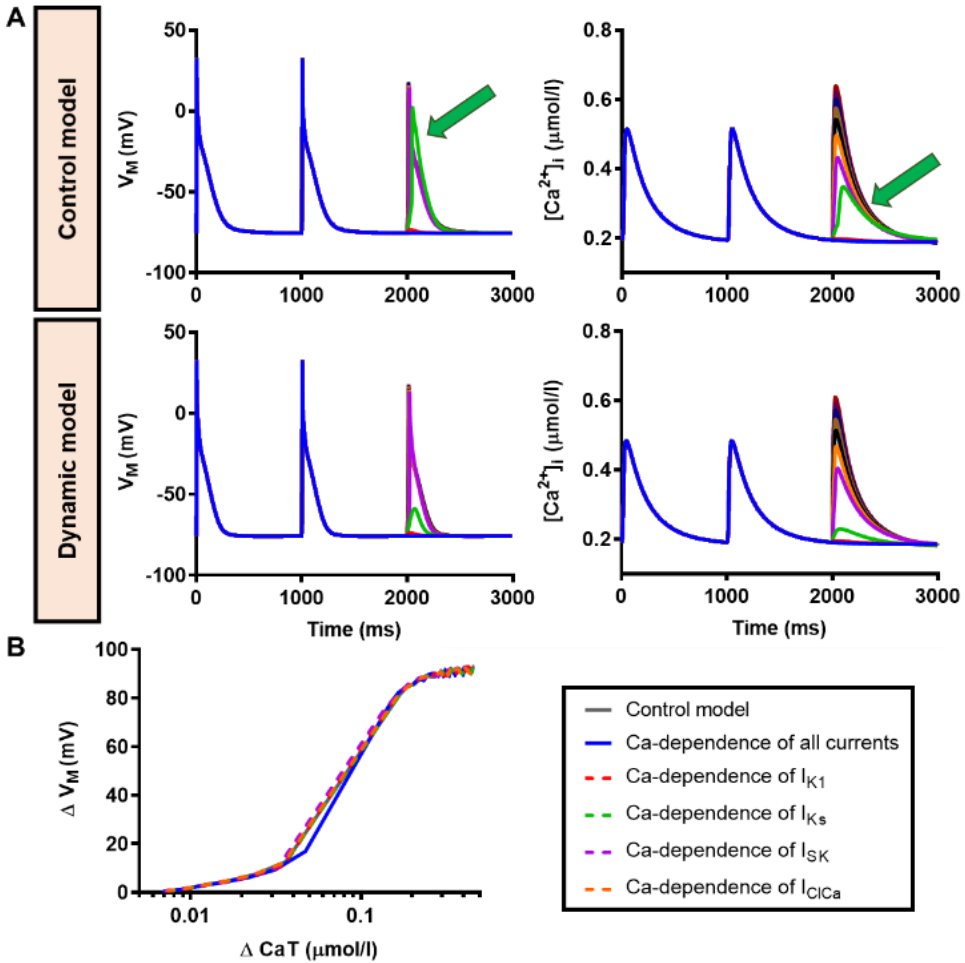


**Figure 5.10:** The impact of calcium-dependent regulation of atrial ionic currents on DAD amplitude. A) Membrane potential and intracellular calcium of both control and dynamic models for predefined degrees of SR calcium release due to alterations in RyR flux. Green traces represent conditions producing triggered activity in the control model (arrows), but not in the dynamic model. B) The individual contribution of calcium-dependent currents on DAD amplitude, shown as  $\Delta CaT$ - $\Delta V_M$  curves. ( $CaT$  = calcium transient;  $V_M$  = membrane potential)

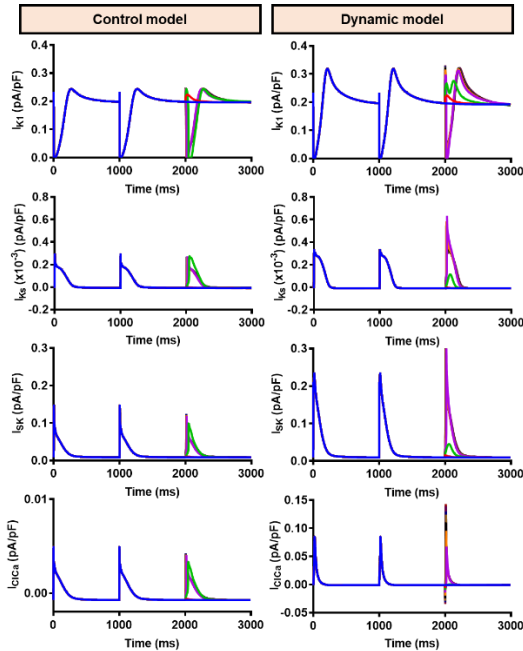


**Figure 5.11:** Calcium-dependent currents during pre-defined, controlled SR calcium-release simulations. The calcium-dependent  $I_{K1}$ ,  $I_{Ks}$ ,  $I_{SK}$ , and  $I_{CaCa}$  in the dynamic model during simulations with various amounts of SR calcium release were compared to the control model.

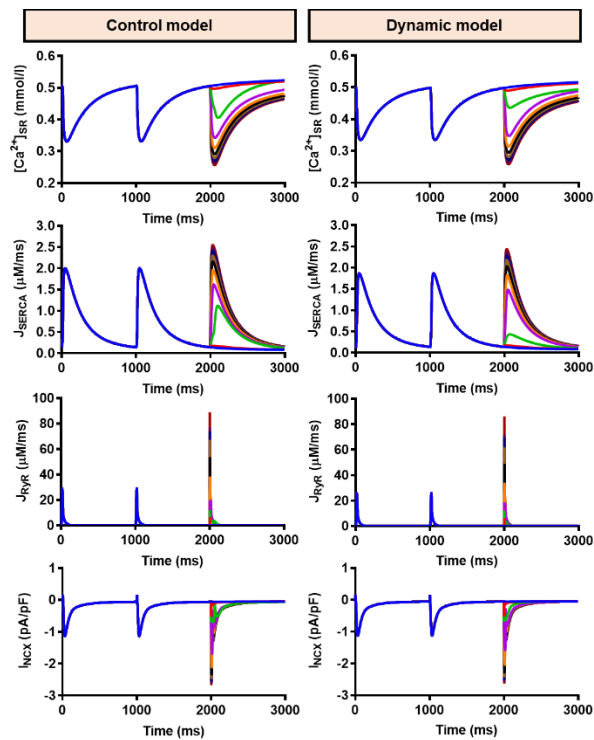


**Figure 5.12:** Calcium-handling proteins during pre-defined, controlled SR calcium-release simulations. The calcium-handling proteins in the dynamic model during simulations with various amounts of SR calcium release were compared to the control model.

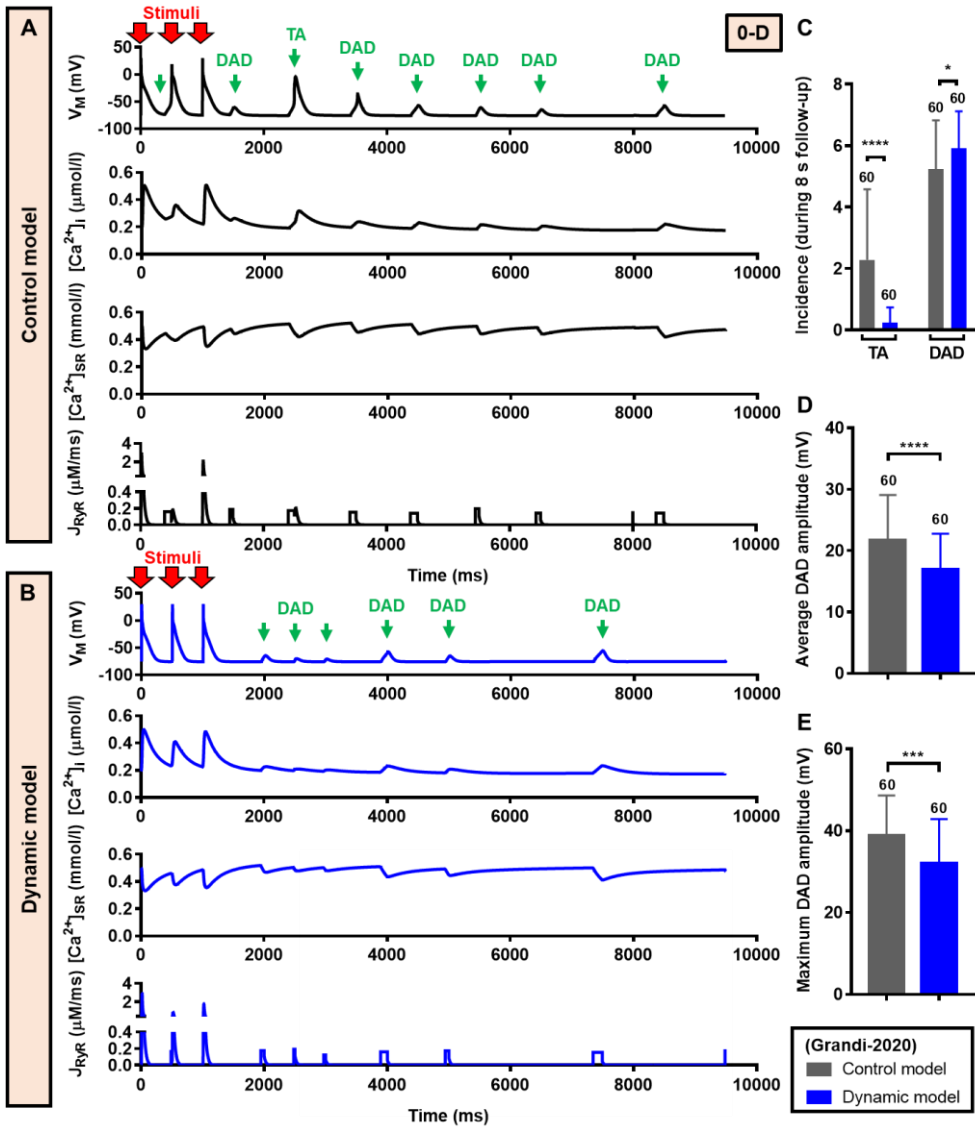


**Figure 5.13:** The cellular consequences of calcium-dependent regulation of ionic currents on DAD properties (stochastic RyR gating approach). A-B) Membrane potential, cytosolic and sarcoplasmic reticulum calcium levels and RyR calcium flux (top to bottom) showing 3 paced beats followed by simulated spontaneous calcium releases and consequent DADs and TAs in the control (A) and dynamic (B) models. C) The comparison of DAD and TA incidence between control and dynamic models. D-E) The comparison of average (D) and maximum (E) DAD amplitude between control and dynamic models. (\*) indicates statistical significance ( $p < 0.05$ ) (DAD = delayed afterdepolarization; SR = sarcoplasmic reticulum; TA = triggered activity)

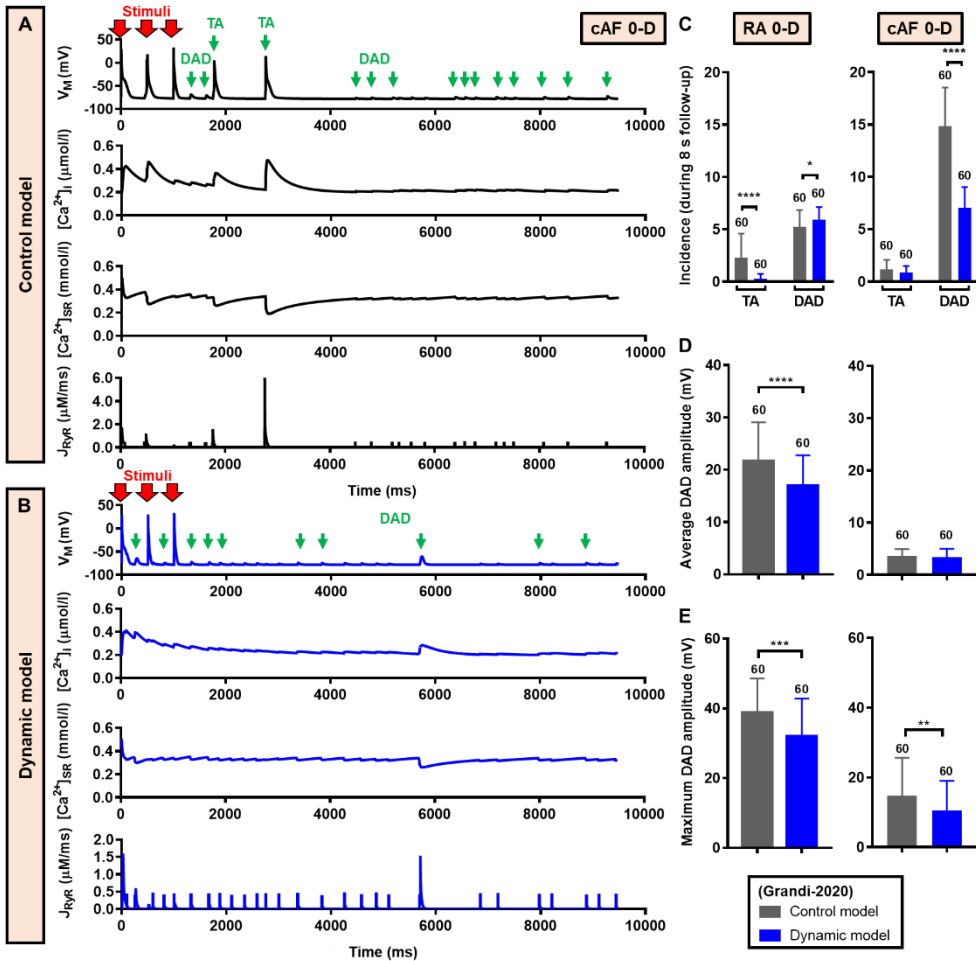


**Figure 5.14:** The cellular consequences of calcium-dependent regulation of cardiac ion channels on DAD properties in cAF (stochastic RyR gating approach). A-B) Simulated DADs and TAs by the simplified stochastic RyR gating approach in the control cAF model as compared to the dynamic cAF model. C) The comparison of DAD and TA incidence between control and dynamic models in normal right atrium and cAF. D-E) The comparison of (average and maximum) DAD amplitude between control and dynamic models. (\*) indicated the statistical significance ( $p < 0.05$ ) (DAD = delayed afterdepolarization; RA = right atrium; SR = sarcoplasmic reticulum; TA = triggered activity)

RyR gating parameter	Non-diseased RA model	cAF model
Mean latency of calcium release	1.5 s	1.5 s
Latency SD	0.1 s	0.1 s
Calcium-release threshold	0.45 mmol/l	0.2 mmol/l
Amplitude of calcium release	2.0	5.0
Duration of calcium release	0.15 s	0.15 s
Interval of RyR Po	0.5 s	0.25 s
SERCA function	100%	75%

**Table 5.1:** The RyR gating parameters employed in the simplified subcellular stochastic RyR gating model. Several changes on the RyR gating parameters were made to fit in the experimental DADs shown in non-diseased atria (4) and AF (32, 94).

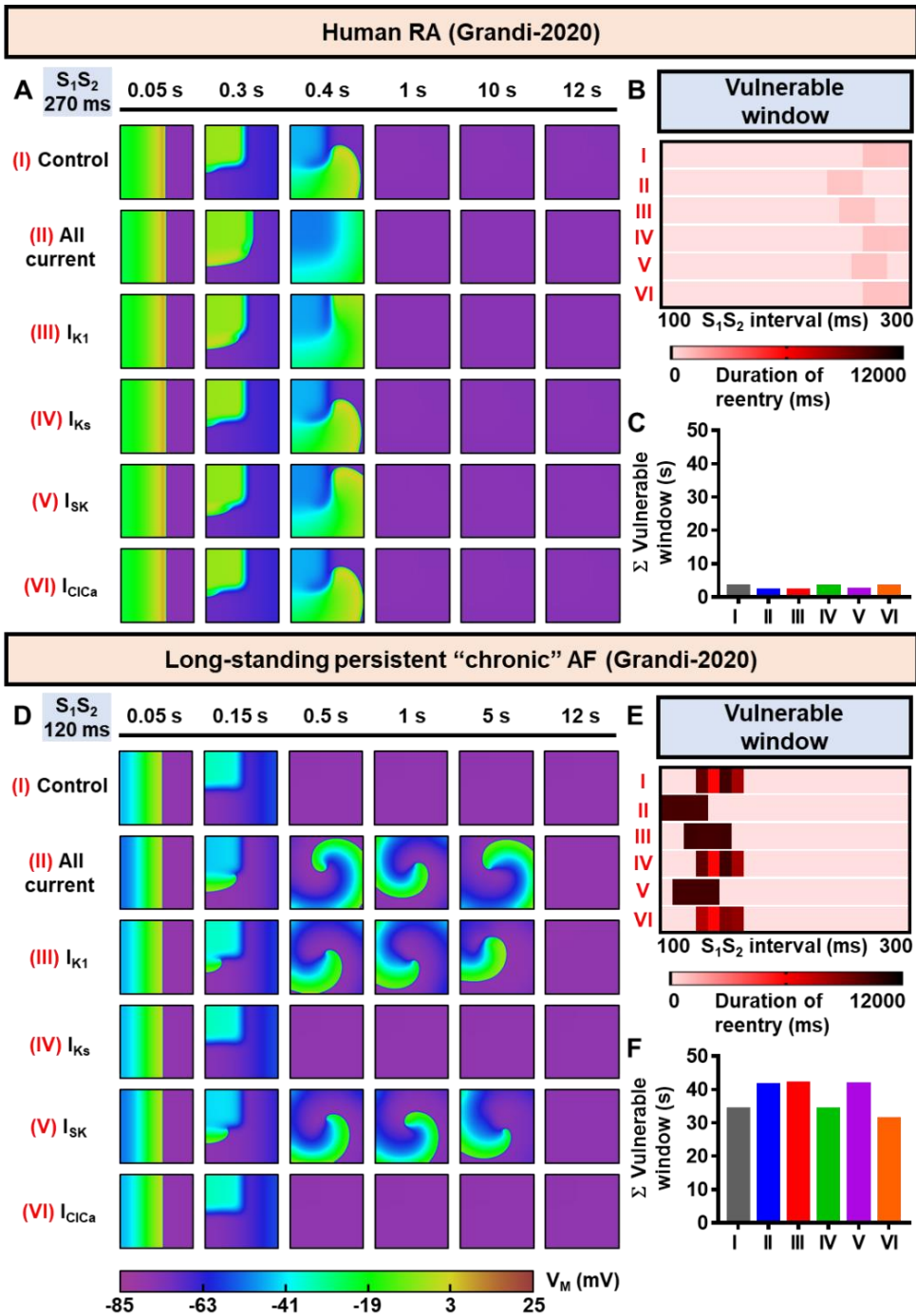


**Figure 5.15:** Calcium-dependent regulation of atrial ionic currents and reentrant arrhythmias. A, D) The snapshots of reentrant spiral waves in non-diseased right atrium (RA, panel A) and cAF model (D) at specific  $S_1S_2$  intervals, comparing the control, dynamic (all 4 calcium-dependent currents), calcium-dependent  $I_{K1}$  only, calcium-dependent  $I_{Ks}$  only, calcium-dependent  $I_{SK}$  only and calcium-dependent  $I_{CaCa}$  only models. B, E) The vulnerable windows of the reentry for different  $S_1S_2$  interval. The span of the window represents inducibility of reentry, while the color of the heatmap defines the stability of reentry. C, F) The sum ( $\Sigma$ ) of vulnerable windows as a quantitative assessment of total arrhythmogenic risk.

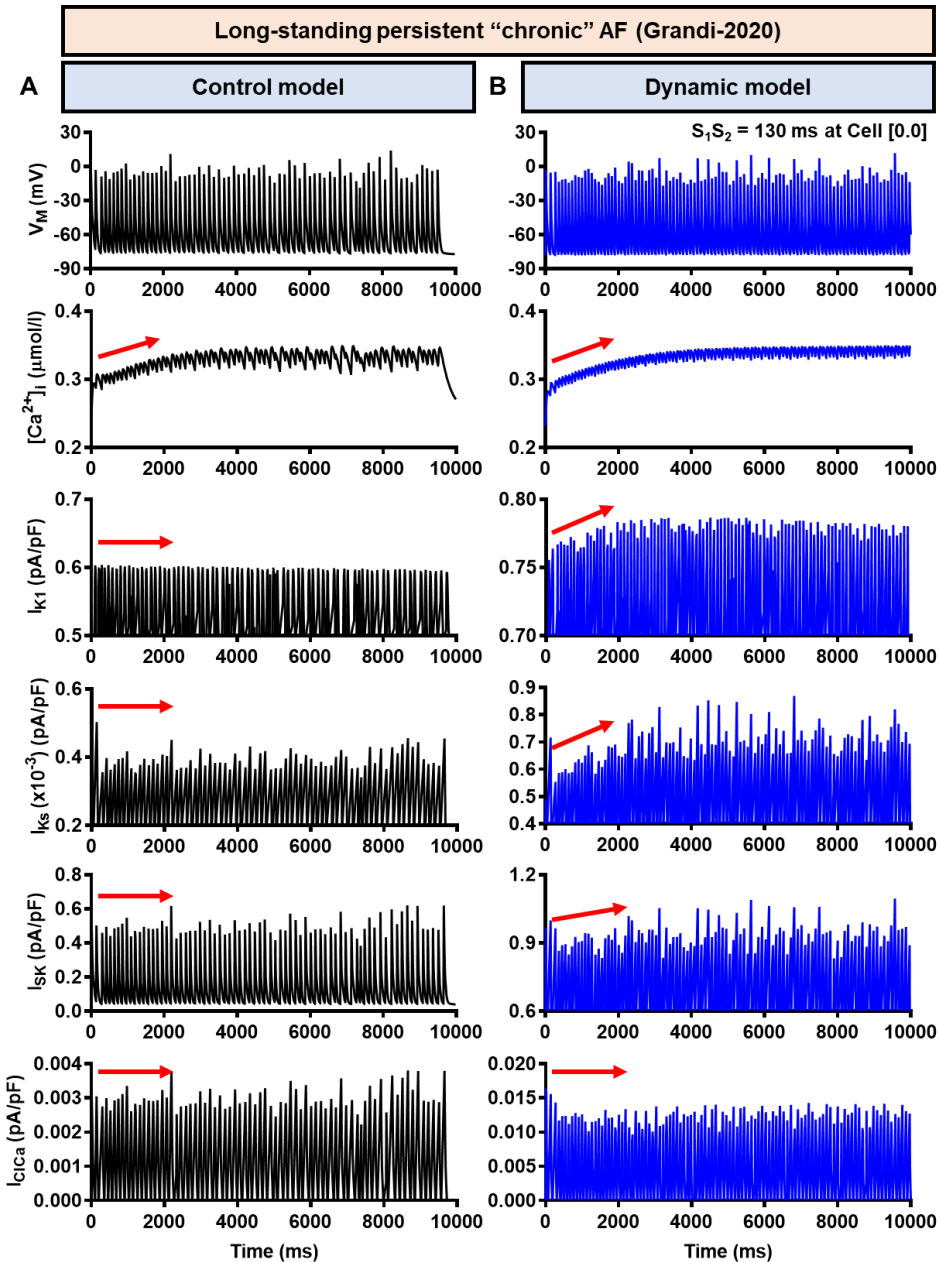


**Figure 5.16:** Dynamic changes in calcium-dependent ionic currents during reentrant spiral waves in the cAF model. The membrane potential ( $V_M$ ), calcium transient, and all 4 calcium-dependent currents in the dynamic model (right panels) were compared to the control model (left panels). The red arrows indicate the changes in corresponding current density over time.

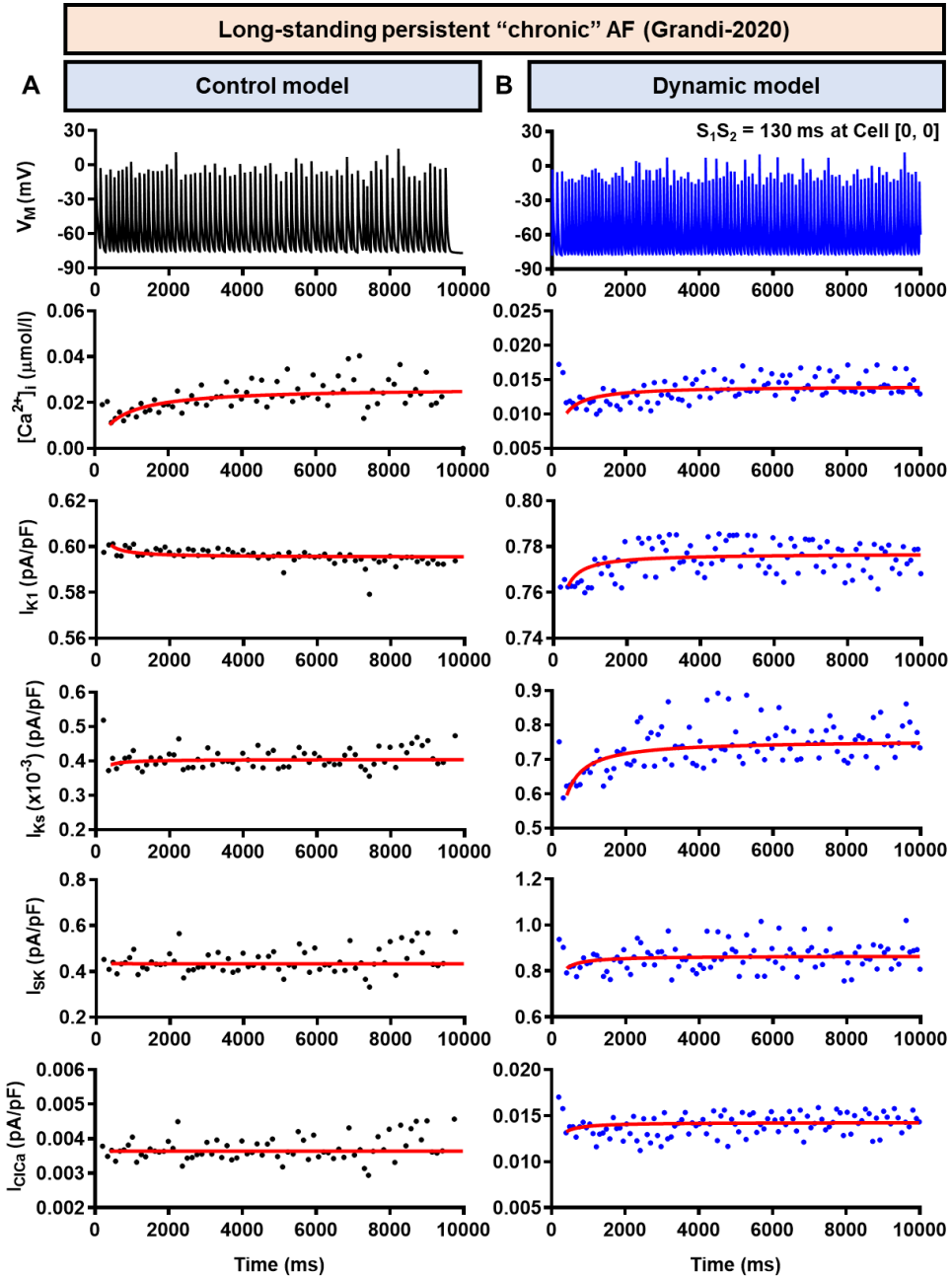


**Figure 5.17:** Dynamic changes in the maximum amplitude of calcium-dependent ionic currents during reentrant spiral waves in the cAF model. The membrane potential ( $V_M$ ) and the amplitudes of calcium

transient and all 4 calcium-dependent currents in the dynamic model (right panels) were compared to the control model (left panels). The red lines represent a non-linear regression fit and reflect the changes in amplitude of ionic currents over time.

### 5.3.3 Calcium-dependent ion-channel regulation affects reentrant arrhythmia maintenance

As described in **Chapter 2**, calcium-handling abnormalities can promote reentry through several pathways, including direct ion-channel modulation (335). Therefore, we investigated the role of calcium-dependent ion-channel regulation on the inducibility and maintenance of reentrant arrhythmias in two-dimensional tissue simulations. The vulnerable windows, reflecting the duration of reentry induced for different  $S_1S_2$  intervals, were evaluated to assess both the inducibility and stability of reentrant arrhythmias under different conditions. The size of the vulnerable windows indicates the inducibility of reentry (i.e., the number of  $S_1S_2$  intervals producing reentry) and the duration of reentry within the vulnerable windows reflects the stability of reentrant arrhythmias. Since reentry durations can be distinct for different  $S_1S_2$  intervals, both factors were combined into a total arrhythmogenic risk parameter by summing the reentry durations over the entire vulnerable window to provide a single quantitative assessment. Consistent with our previous study using the Courtemanche human atrial model (346), no stable reentry could be induced in the non-diseased Grandi human right atrial model (**Figure 5.15A-B**). However, reentrant spiral waves persisting for multiple seconds could be induced in the presence of cAF-induced ion channel remodeling (**Figure 5.15C-D**). In the non-diseased atrium, calcium-dependent ion-channel regulation in the dynamic model shifted the vulnerable windows to earlier  $S_1S_2$  intervals and slightly reduced the total arrhythmogenic risk (**Figure 5.15B-C**). By contrast, in the cAF model, the calcium-dependent regulation of atrial ionic currents stabilized the reentrant waves and shifted the vulnerable windows to earlier  $S_1S_2$  intervals. As a consequence, the total arrhythmogenic risk was increased in the dynamic cAF model (**Figure 5.15E-F**). The effects observed both in the presence and absence of cAF-related remodeling were due to calcium-dependent regulation of  $I_{K1}$  and  $I_{SK}$ , similar to our results at the cellular level. The dynamic changes in calcium-dependent regulation of ionic currents during reentry in the cAF model can be seen in **Figures 5.16-5.17**. During reentry, the intracellular calcium rose due to the increased activation rate in both control and dynamic models (**Figure 5.16**, red arrows). In the presence of calcium-dependent regulation this dynamic increase was paralleled by ionic currents. As such, the dynamic model resulted in larger ionic current densities, shortening the refractory period and stabilizing the reentrant waves (**Figure 5.17**).

Next, we investigated the impact of calcium-dependent ion-channel regulation on TA at the tissue level by simulating several  $S_1$  stimuli followed by a long observation period of 8 s in 2 Hz pacing in our two-dimensional tissue model with stochastic RyR (**Figure 5.18**). Random SCaEs and DADs occurred at the cellular level, which under particular conditions resulted in ectopic activities at the tissue level. This transformation from cell-level SCaEs/DADs to tissue-level ectopic activities depended on RyR-gating properties, such as the duration of calcium release, the amplitude of calcium release, and the mean latency of calcium release, as well as the standard deviation (SD) of calcium release latency between cells. As shown in **Figure 5.18B**, reducing the latency SD 10-fold synchronized the SCaEs throughout the tissue, thereby

initiating TAs in the control model. However, a 10-fold reduction in the latency SD alone was insufficient to initiate TA in the dynamic model (Figure 5.18D) due to the RMP-stabilizing effect of calcium-dependent regulation of atrial ionic currents, in line with our results at the cellular level. In some cases, especially during higher calcium-release amplitude and reduced latency SD, these SCaE-mediated ectopic activities could induce reentrant spiral waves (Online Video 1, Figure 5.19) although those modifications were not adequate to maintain a stable reentry.

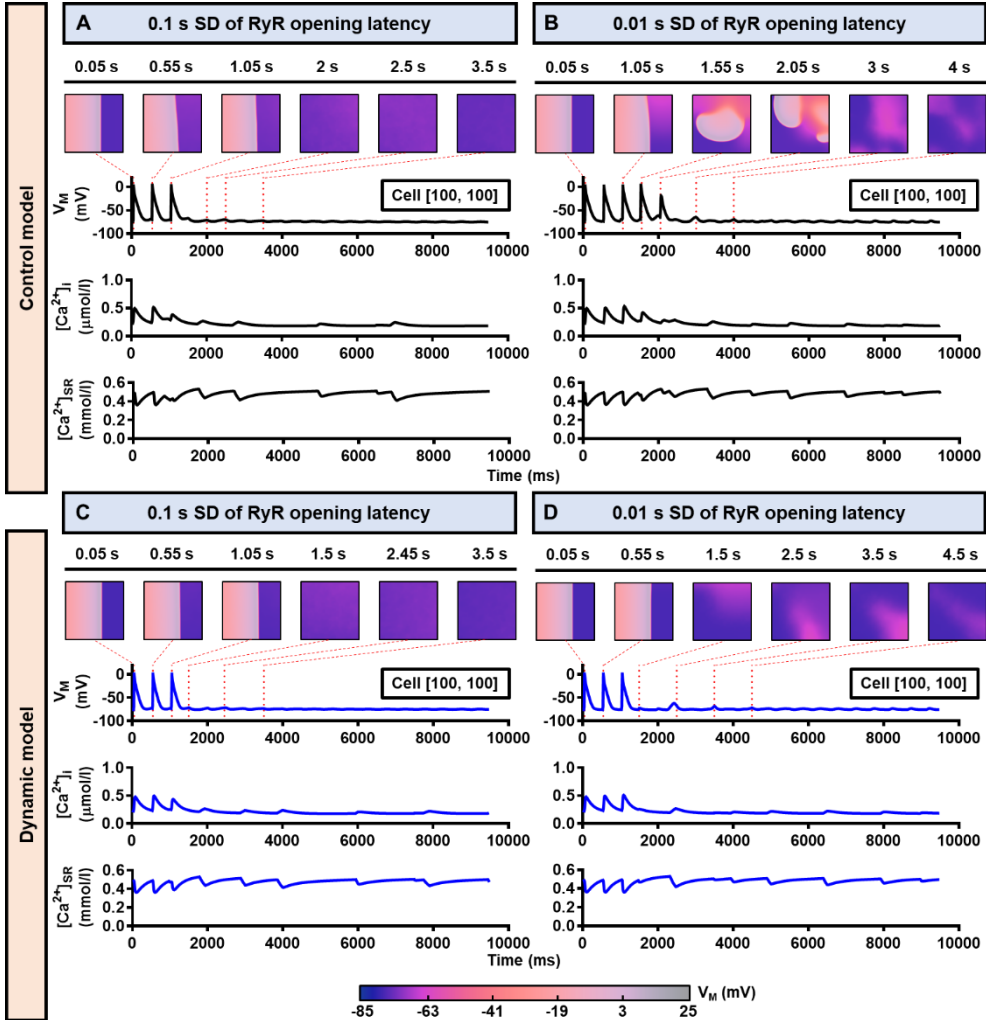


**Figure 5.18:** Impact of calcium-dependent regulation of atrial ionic currents on DAD properties and triggered activity in tissue-level simulations (stochastic RyR gating approach). A,B) Membrane potential ( $V_M$ ), cytosolic and sarcoplasmic reticulum calcium for 3 stimulated beats and an 8-second follow-up period in the control model with 100 ms (A) or 10 ms (B) standard deviation (SD) of RyR latency. Smaller latency SD produces a more synchronous calcium release in the tissue. C,D) Similar to panels A,B for the dynamic model. All traces were recorded at the center of the virtual tissue (i.e., coordinate  $x=100, y=100$ ) of the 2-dimensional tissue. Snapshot of the entire virtual tissue at specific moments in time are shown above the traces.

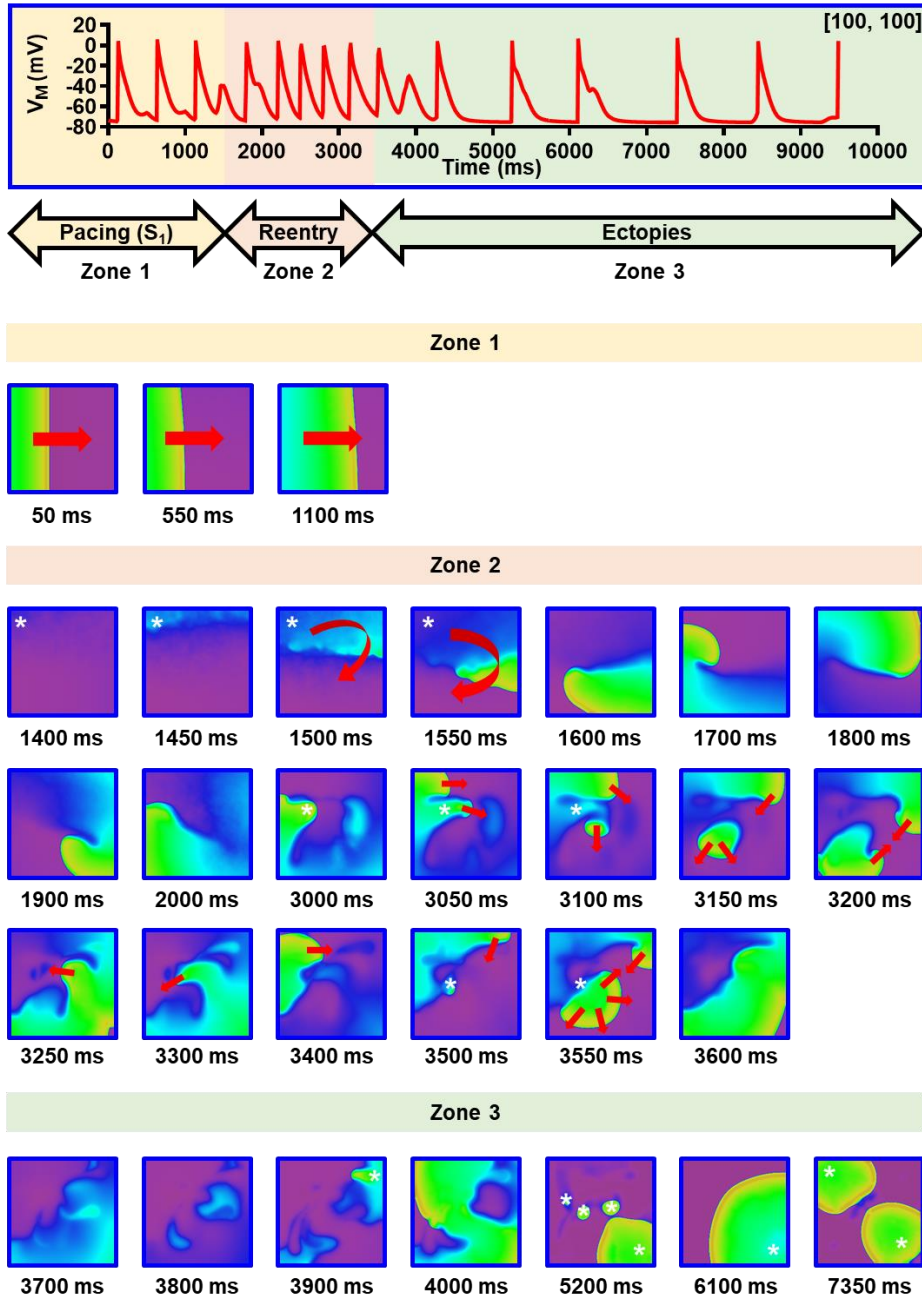


**Figure 5.19:** Synchronization of cellular DADs leads to the initiation of non-sustained reentrant arrhythmias. The upper panel of the figure shows the membrane potential ( $V_M$ ) of control model and the snapshots of reentry as presented in [Online Video 1](#) were displayed on the lower panels. To induce reentrant spiral wave, the SD of the latency of calcium release was set to 0.01 s and the amplitude of calcium release was increased to 5. To maintain the sustainability of reentrant wave, the conduction velocity was reduced to 30 cm/s. The white (\*) signs indicate the origin of ectopy and the red arrows denote the direction of propagating waves.

Finally, we varied the duration, amplitude, mean latency and latency SD of calcium release to further compare and characterize the effects of calcium-dependent ion-channel regulation with different RyR-gating properties (Figure 5.20). The dynamic model consistently showed a lower average and maximum DAD amplitudes, while inducing higher numbers of DADs. Increasing the amplitude of calcium release (Figure 5.20A) increased the number of DADs, amplified the average and maximum DAD amplitudes in both control and dynamic models. However, an increased amplitude alone was insufficient to trigger TA. Similarly, the reduction of latency SD (resulting in more synchronous SCaEs between cells) increased the average and maximum DAD amplitudes. In this subset of simulations, TA could only be induced in the control model with very low latency (Figure 5.20B). However, the combination of both RyR gating properties (amplitude and latency) had synergistic effects, initiating stronger and more synchronous calcium releases, permitting several episodes of TAs to occur in both control and dynamic models (Figure 5.20C). Additionally, the alteration of mean latency of calcium release lowered the average and maximum DAD amplitudes in both control and dynamic models without producing TA (Figure 5.20D). Increasing the duration of RyR opening to allow more calcium release produced a slightly larger average and maximum DAD amplitudes (Figure 5.20E). In general, employing tissue level simulations with stochastic RyR, we demonstrated that large, synchronous calcium releases are required for TA and that calcium-dependent regulation of atrial ionic currents stabilized the RMP and reduced the likelihood of TA.

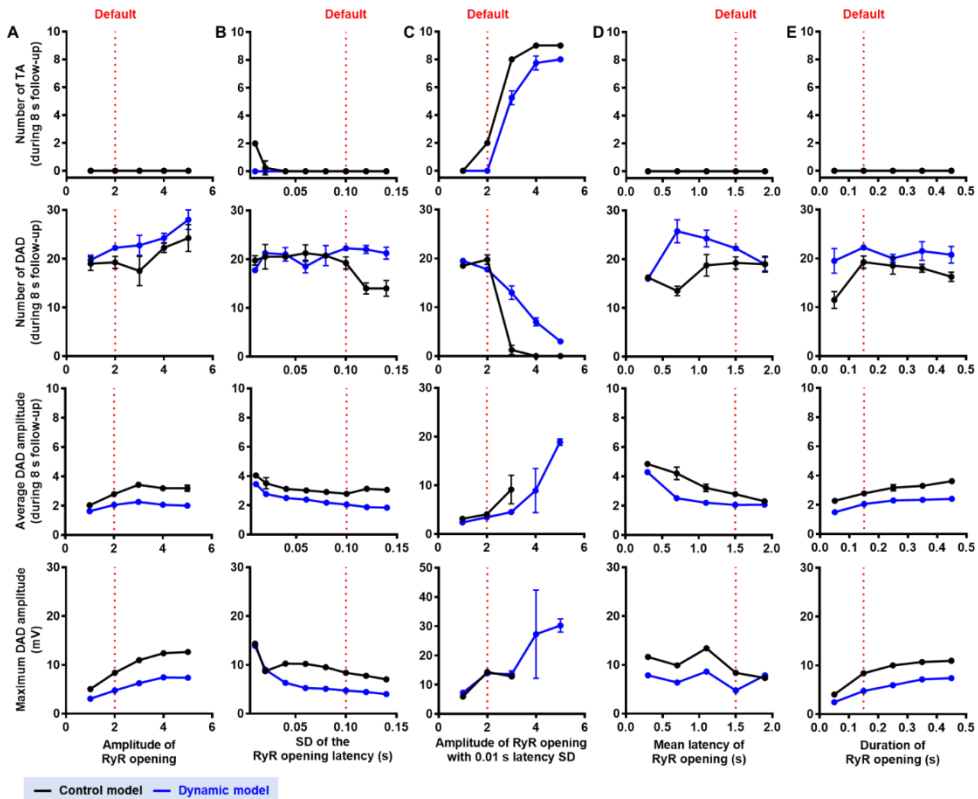


**Figure 5.20:** Properties of spontaneous calcium releases, DADs and TA in control (black) and dynamic (blue) models for different RyR-gating properties. A-E) Number of TA and DAD, average and maximum DAD amplitude (top to bottom) in response to increasing calcium-release amplitude (A), alteration of latency SD of RyR opening (B), highlighting the synergy between amplitude and latency SD in producing stronger and more synchronous calcium release (C), alterations in mean latency of RyR opening (D) and altered duration of RyR opening (E). Default values are indicated by red dotted lines (also provided in [Table 5.1](#)). (DAD = delayed afterdepolarization; RyR = ryanodine receptor; SD = standard deviation; TA = triggered activity)

## 5.4 Discussion

Our multiscale *in silico* study aimed to improve the understanding of the impact of calcium-dependent ion-channel regulation on atrial electrophysiology under physiological and pathological conditions. To achieve this goal, we modified the 2020 version of the Grandi human atrial cardiomyocyte model, enabling the simulation of calcium-dependent regulation of 4 ionic currents:  $I_{K1}$ ,  $I_{Ks}$ ,  $I_{SK}$ , and  $I_{Ca}$ . The computational modeling study was performed under various experimental conditions and from cell to tissue level. We developed a simplified subcellular model of stochastic RyR gating to study how calcium-dependent ion-channel modulation alters DAD properties. To the best of our knowledge, our study was the first to investigate the consequences of altered subcellular RyR gating properties in the presence of calcium-dependent ion-channel regulation on tissue-level ectopic activities. Using the advantages offered by this computational modeling approach, we show that calcium-dependent regulation of cardiac ionic currents shortened APD, hyperpolarized RMP and increased all 4 calcium-dependent currents. Calcium-dependent ion-channel regulation also stabilized RMP and therefore reduced the DAD amplitude in the non-diseased atrium. At the tissue level, the arrhythmogenic effects of calcium-dependent ion-channel modulation depended on the presence of concomitant disease. In the absence of AF-related remodeling, calcium-dependent ion-channel regulation slightly reduced the total arrhythmogenic risk, while in cAF, it increased arrhythmogenic risk. Both effects were due to the contributions of  $I_{K1}$  and  $I_{SK}$ . Finally, a stronger, more synchronous calcium release was required to initiate tissue-level ectopic activities in the presence of calcium-dependent ion-channel regulation compared to the control model.

### 5.4.1 Calcium-dependent regulation of cardiac ionic currents and cardiac arrhythmias

For more than a decade, calcium-dependent regulation of cardiac ion channels has been documented experimentally. In 1998, Zaza et al. (56) demonstrated that systolic  $I_{K1}$  was increased and diastolic  $I_{K1}$  was reduced in the presence of low calcium. Although calcium-induced effects only represented a small fraction of total  $I_{K1}$  rectification, they were adequately large to affect excitability and repolarization. Another study in canine cardiomyocytes similarly reported that high intracellular calcium led to the augmentation of  $I_{K1}$ , which was partly mediated by a CaMKII-dependent pathway and might function as a protective mechanism against cardiac arrhythmias due to calcium overload (55). These findings are consistent with our multiscale *in silico* study. In [Figure 5.2](#), we have shown that calcium-dependent regulation shortened atrial APD in the dynamic model and hyperpolarized the RMP, requiring a stronger stimulus to activate the fast sodium channel and providing a protective effect against DADs and TAs,

as shown in **Figures 5.10, 5.13**. Altering the intracellular calcium concentrations by blocking LTCC and NKA revealed that the RMP-hyperpolarizing effect was diminished with full LTCC block and augmented by full NKA block, in line with their effects on intracellular calcium levels (**Figures 5.3, 5.6**). At the tissue level, we also investigated the effect of calcium-dependent regulation on reentrant arrhythmias. In the non-diseased atrium, the dynamic model slightly reduced the total arrhythmogenic risk. However, these protective tissue-level effects were cancelled by cAF-induced ion-channel remodeling, resulting in an increased total arrhythmogenic risk in the presence of calcium-dependent ion-channel regulation. This finding is consistent with previous publications highlighting the significance of  $I_{K1}$  (347) and  $I_{SK}$  (348) in reentry stabilization.

In addition to  $I_{K1}$ , our study also underlined the contribution of  $I_{SK}$  to the cellular- and tissue-level effects. SK channels are solely activated by intracellular calcium and found more abundantly in the atria than in the ventricles. SK channels alter cardiac repolarization and their inhibition prolongs atrial APD. SK2 knockout mice demonstrated a significant APD prolongation prominently in the late phase of repolarization in atrial cardiomyocytes (47). Moreover, SK channels are upregulated in heart failure and (in some studies) atrial fibrillation, and are therefore considered a potential therapeutic target against AF (45). Overexpression of SK3 in mouse models resulted in significant shortening of atrial APD and effective refractory period, together with an increased susceptibility to AF (47). Furthermore, pharmacological inhibition of SK channel in AF animal models have shown promising antiarrhythmic properties (45), although its proarrhythmic potential has also been documented (47, 335). Our findings demonstrated that the atrial APD-shortening effect observed in the dynamic model was partly due to  $I_{SK}$ , aligned with the aforementioned role of SK channel in atrial repolarization. The role of  $I_{SK}$  in reentry stabilization (**Figure 5.15**) has also been reported (348).

#### **5.4.2 The limited contributions of calcium-dependent regulation $I_{Ks}$ and $I_{ClCa}$**

In contrast, we observed very minor contributions of calcium-dependent  $I_{Ks}$  and  $I_{ClCa}$  on atrial electrophysiology. Experiments in rabbit ventricular cardiomyocytes provided direct evidence that intracellular calcium was critical for  $I_{Ks}$  function. In its physiological range, intracellular calcium dynamically regulated  $I_{Ks}$ , increasing its amplitude, negatively shifting voltage-dependent activation and lowered deactivation. Such effects were augmented during  $\beta$ -adrenergic stimulation (336). Our result revealed an elevated  $I_{Ks}$  amplitude (almost doubling of  $I_{Ks}$  current density in the dynamic model following  $\sim 200$ nM increase of intracellular calcium; **Figure 5.2E**), consistent with experimental findings (336). However, we observed minimal changes in repolarization due to the calcium-dependent effect, likely due to the very low basal  $I_{Ks}$  density in human atrium compared to the ventricle (340, 349). We observed similar calcium-dependent regulation of  $I_{Ks}$  in cAF. Although  $I_{Ks}$  was upregulated in cAF, the much lower calcium-transient in cAF also produced lower calcium-dependent augmentation and therefore, resulted in a negligible change on AP (**Figure 5.9**).

The role of  $I_{ClCa}$  in atrial arrhythmogenesis remains unclear.  $I_{ClCa}$  was reported to contribute to AP alternans in rabbit atrial cardiomyocytes. Furthermore, in sheep Purkinje fibers and ventricular cardiomyocytes, it was implicated in DAD formation,

with its inhibition preventing the transformation of DADs into TAs (337). However, to date, there is no documented data on the effect of  $I_{\text{ClCa}}$  on arrhythmogenesis in humans, although the gene encoding the ClCa channel (hTMEM16A), is expressed in multiple human tissues, including the heart (350). Although  $I_{\text{ClCa}}$  contributes to transient outward rectification in rabbit atrial cardiomyocytes (351), available data do not support a role of  $I_{\text{ClCa}}$  in the human transient outward current (352). The role of  $I_{\text{ClCa}}$  in phase-1 repolarization and the generation of afterdepolarizations of either normal or failing human heart was also very limited, limiting the clinical relevance of  $I_{\text{ClCa}}$  inhibition (350). In agreement, our computational study also showed that the calcium-dependent regulation of  $I_{\text{ClCa}}$  had a minor impact on the AP properties, both under physiological and pathological conditions (Figures 5.2, 5.9).

### 5.4.3 Potential applications of calcium-dependent regulation of atrial ionic currents

Our results suggest that calcium-dependent regulation of atrial ionic currents could be an adaptive mechanism of the non-diseased atrium against intracellular calcium overload, by stabilizing the membrane potential and lowering DAD amplitude, preventing TA. Moreover, we show that such protective effects could be diminished in pathological situations, such as AF, even producing potentially proarrhythmic behavior by stabilizing reentrant arrhythmias. Therefore, a pharmacological intervention that can alter this direct calcium-dependent regulation (or its remodeling) might be beneficial in atrial pathology. Several publications have reported the association of calcium-dependent ion-channel regulation with CaMKII-dependent pathways and  $\beta$ -adrenergic stimulation (55, 336), therefore CaMKII inhibition, either directly or via  $\beta$ -blockers might be effective. Indeed, inhibition of CaMKII-mediated phosphorylation of RyR2 prevented AF induction in FKBP12.6-/- mice by suppressing SR calcium leak and DADs (353). Moreover, calmodulin / CaMKII inhibition improved intercellular communication and impulse propagation in the heart, destabilizing and terminating reentrant spiral waves in Langendorff-perfused rabbit hearts (354). Similarly,  $\beta$ -blockers are also effective in AF, preventing afterdepolarizations and atrial reentry (355). Nevertheless, a more specific pharmacological agent may be needed to prevent unwanted effects of the inhibition of such vast and complex pathways (356).

### 5.4.4 Study limitations

Our study employed the *state-of-the-art* 2020 version of Grandi human atrial cardiomyocyte model, which was well-validated and, to the best of our knowledge, has the most accurate common-pool representation of atrial calcium handling. However, model-dependent effects cannot be ruled out, because the variability of ion channel distributions across different *in silico* models could affect the result, particularly the sensitivity of membrane potential to SCaEs, which determines the incidence of DAD and TA. Similarly, intra- and inter-subject variability can also affect the results. We have partly overcome this limitation with the application of our novel simplified subcellular stochastic RyR gating, which produces random calcium releases depending on its SR calcium concentration. However, more extensive validation of SCaE properties obtained with this phenomenological approach is warranted.

Due to the limited availability of experimental data, we optimized the calcium-dependent regulation of  $I_{Ks}$  based on rabbit ventricular data, which might be different compared to the human atria. Since the basal magnitude of  $I_{Ks}$  in the human atrial model was almost negligible, this interspecies diversity is unlikely to affect our results and conclusions. However, such differences may become relevant under conditions with increased  $I_{Ks}$  (e.g., during sympathetic stimulation). Similarly, we optimized the calcium-dependent regulation of  $I_{K1}$  based on two animal models data: guinea-pig and canine ventricular cardiomyocytes, due to limited available data. Due to the larger  $I_{K1}$  density in dogs compared to human (357), we cannot rule out the potential influence of such interspecies diversity on our findings.

Additionally, in this study, tissue-level simulations were performed in isotropic virtual tissue in the absence of structural remodeling. Such structural remodeling can potentially modulate the proarrhythmic consequences of (subtle) electrophysiological remodeling, as already demonstrated in **Chapter 6** of this thesis (346).

## 5.5 Conclusions

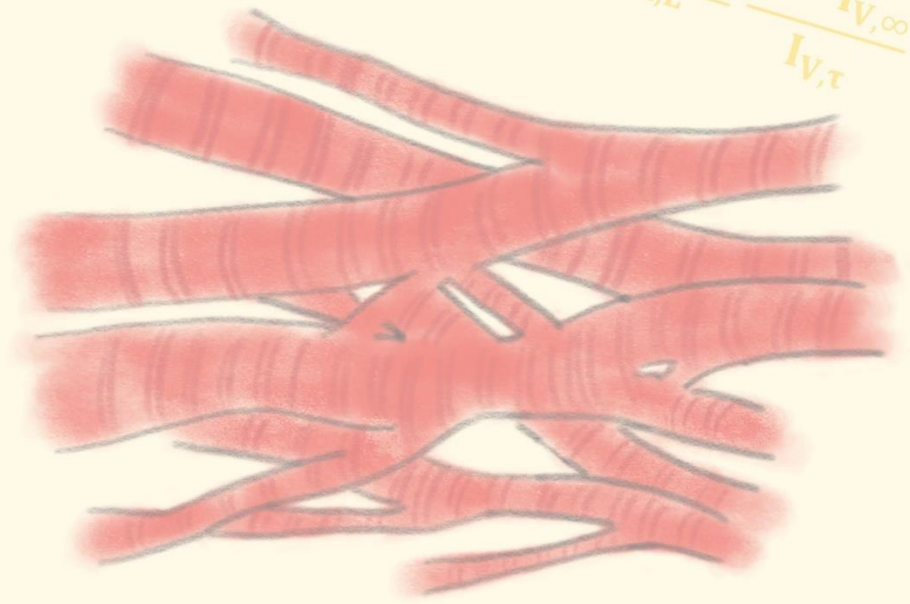
Our multiscale *in silico* study demonstrated that calcium-dependent regulation of atrial ionic currents alters human atrial electrophysiology at the cellular and tissue level. It has protective effects in non-diseased atrium by stabilizing the membrane potential and lowering DAD amplitude, preventing the occurrence of TA. However, in the presence of cAF-related remodeling, the calcium-dependent regulation of atrial ionic currents is proarrhythmic due to its APD-shortening and RMP-hyperpolarizing effects, stabilizing reentrant waves. Parameter sensitivity analyses revealed that  $I_{K1}$  and  $I_{SK}$  are the major contributing factors to our findings and future pharmacological interventions to alter calcium-dependent regulation of  $I_{K1}$  and  $I_{SK}$  might constitute novel therapeutic strategies for AF.





$$\frac{dV_m}{dt} = -\frac{1}{C_m} * I$$

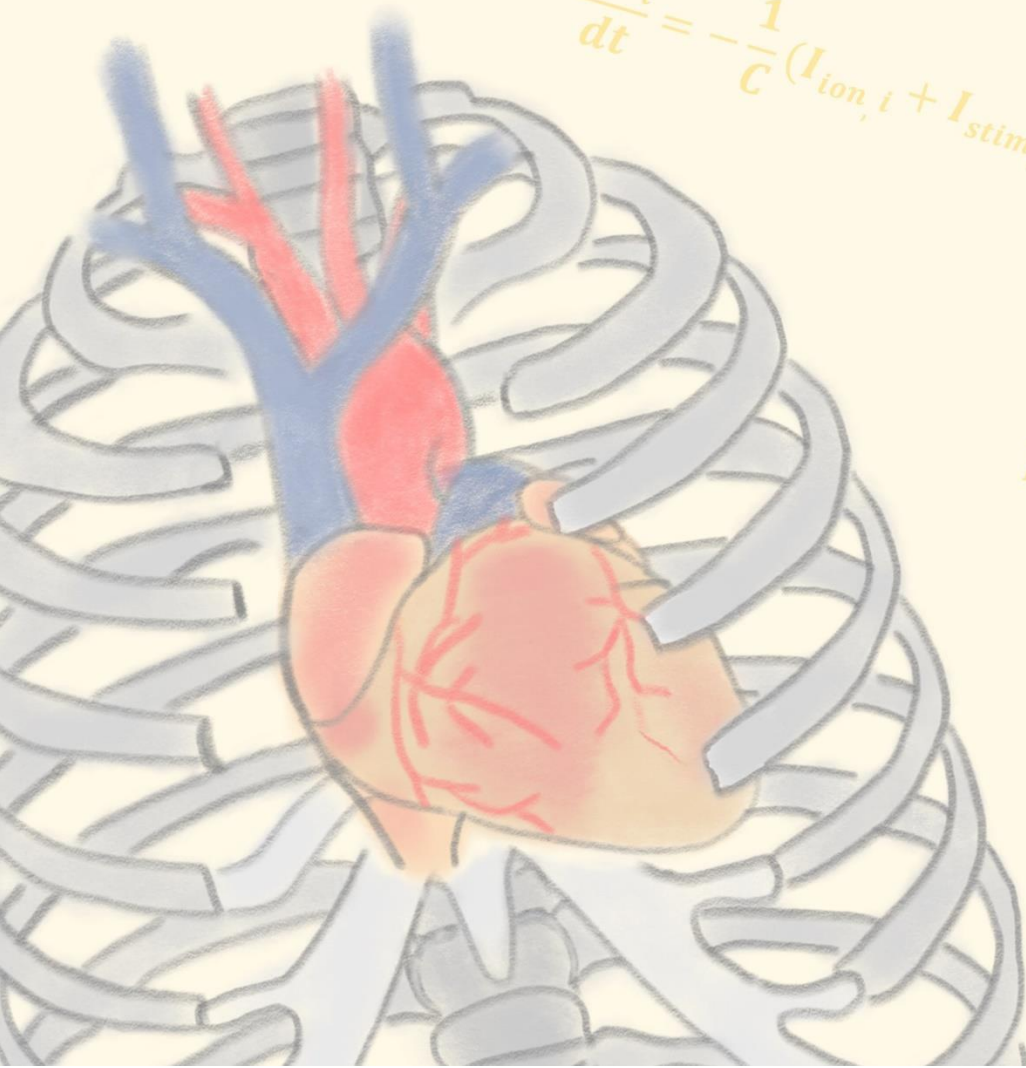
$$y_{Ca,L} = \frac{1 - I_{V,\infty}}{I_{V,\tau}}$$



$$x_{Ca,L} = \frac{I_{V,\infty}}{I_{V,\tau}}$$

$$\delta I_{Ca,L}^{s,m} =$$

$$\frac{dV_i}{dt} = -\frac{1}{C} (I_{ion,i} + I_{stim,i} + I_{diff,i})$$



$$\bar{I}_{Ca,L}^{s,m} = P_{Ca,L} \cdot (z$$

$$ACT_{\tau} = 0.59$$

# Chapter 6

## Acute effects of alcohol on cardiac electrophysiology and arrhythmogenesis: insights from multiscale *in silico* analyses

H. Sutanto, M.J.M. Cluitmans, D. Dobrev, P.G.A. Volders, M. Bébarová and J. Heijman.  
*J Mol Cell Cardiol.* 146:69-83.



$$\frac{dV}{dt} = \frac{I_{stim} - (I_K + I_{Na} + I_{leak})}{C_m}$$

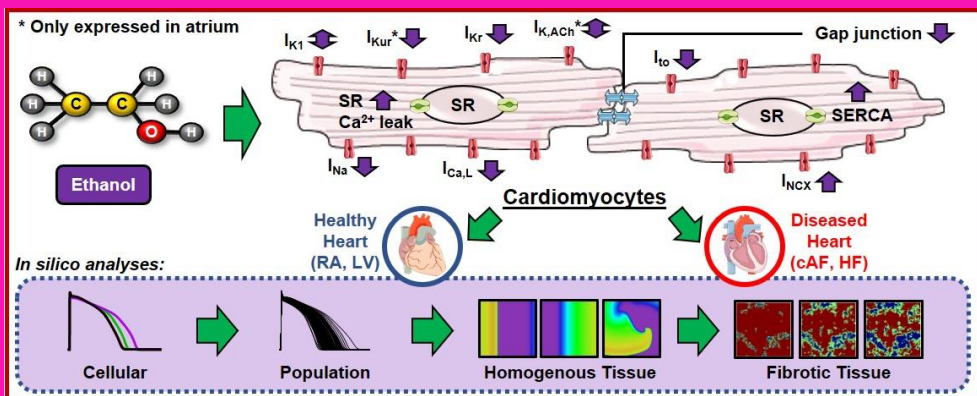
## ABSTRACT

Acute excessive ethyl alcohol (ethanol) consumption alters cardiac electrophysiology and can evoke cardiac arrhythmias, e.g. in 'holiday heart syndrome'. Ethanol acutely modulates numerous targets in cardiomyocytes, including ion channels, calcium-handling proteins and gap junctions. However, the mechanisms underlying ethanol-induced arrhythmogenesis remain incompletely understood and difficult to study experimentally due to the multiple electrophysiological targets involved and their potential interactions with preexisting electrophysiological or structural substrates. Here, we employed cellular- and tissue-level *in-silico* analyses to characterize the acute effects of ethanol on cardiac electrophysiology and arrhythmogenesis.

Acute electrophysiological effects of ethanol were incorporated into human atrial and ventricular cardiomyocyte computer models: reduced  $I_{Na}$ ,  $I_{Ca,L}$ ,  $I_{to}$ ,  $I_{Kr}$  and  $I_{Kur}$ , dual effects on  $I_{K1}$  and  $I_{K,ACh}$  (inhibition at low and augmentation at high concentrations), and increased  $I_{NCX}$  and SR calcium leak. Multiscale simulations in the absence or presence of preexistent atrial fibrillation or heart-failure-related remodeling demonstrated that low ethanol concentrations prolonged atrial action-potential duration (APD) without effects on ventricular APD. Conversely, high ethanol concentrations abbreviated atrial APD and prolonged ventricular APD. High ethanol concentrations promoted reentry in tissue simulations, but the extent of reentry promotion was dependent on the presence of altered intercellular coupling, and the degree, type, and pattern of fibrosis.

Taken together, these data provide novel mechanistic insight into the potential proarrhythmic interactions between a preexisting substrate and acute changes in cardiac electrophysiology. In particular, acute ethanol exposure has concentration-dependent electrophysiological effects that differ between atria and ventricles, and between healthy and diseased hearts. Low concentrations of ethanol can have anti-fibrillatory effects in atria, whereas high concentrations promote the inducibility and maintenance of reentrant atrial and ventricular arrhythmias, supporting a role for limiting alcohol intake as part of cardiac arrhythmia management.

## Graphical Abstract



## 6.1 Introduction

Acute and chronic alcohol (i.e., ethanol) consumption are major risk factors for cardiovascular diseases, particularly cardiac arrhythmias and sudden cardiac death (358). (Heavy) Episodic alcohol drinking is a major public health issue, affecting 1 in 6 adults and more than 30% of college-age individuals in the United States and Europe (359, 360). Acute excessive ethanol intake can promote cardiac arrhythmias, a phenomenon known as ‘holiday heart syndrome’ (361). For example, the MunichBREW study performed at the 2015 Munich Oktoberfest showed that acute ethanol consumption led to cardiac arrhythmias in 30.5% of individuals, with a prevalence of atrial fibrillation (AF) of 0.8% (362). Abstinence from excessive ethanol intake reduced AF recurrence and lowered AF burden over 6-months follow-up in a multicenter study of 140 patients (363). Numerous cases of ventricular arrhythmias and sudden cardiac death have also been reported following acute excessive ethanol intake, further highlighting its proarrhythmic potential (361, 364).

Acute ethanol exposure alters multiple cardiac ion channels and calcium-handling proteins, including the fast sodium current ( $I_{Na}$ ), L-type calcium current ( $I_{Ca,L}$ ), transient-outward potassium current ( $I_{to}$ ), rapid delayed-rectifier potassium current ( $I_{Kr}$ ), inward-rectifier potassium current ( $I_{K1}$ ), ultra-rapid delayed-rectifier potassium current ( $I_{Kur}$ ), acetylcholine-activated inward-rectifier potassium current ( $I_{KACh}$ ), sodium/calcium-exchange current ( $I_{NCX}$ ), and sarcoplasmic reticulum (SR) calcium leak (365-370). Ethanol induces these effects in a dose-dependent manner through a variety of pathways, including reactive oxygen species and downstream signaling cascades like c-Jun N-terminal kinase and calcium/calmodulin-dependent kinase-II (CaMKII) (371, 372). These acute electrophysiological effects exhibit complex interactions via intracellular ion concentrations and membrane potential, and are accompanied by changes in gap-junction coupling and associated intercellular coupling disturbances. In addition, the effects of ethanol-dependent alterations in ion-channel function may depend on the preexisting structural or electrophysiological substrate, e.g., disease-related ion-channel remodeling or the amount of fibrosis.

Because of these complex (sub)cellular and tissue-level effects of acute ethanol exposure, its exact proarrhythmic mechanisms remain incompletely understood. Moreover, the complex interactions between preexisting substrate, altered ionic currents and gap-junction remodeling pose a challenge for experimental studies into the mechanisms and consequences of ethanol-induced arrhythmogenesis. Here, we employ multiscale computational modeling to characterize potential anti- and proarrhythmic effects of ethanol and their underlying ionic mechanisms. These data provide novel insights in a common cause of cardiac arrhythmias and provide a framework to study the complex interactions between preexisting substrate and dynamic triggers of atrial and ventricular arrhythmias.

## 6.2 Methods

Experimentally observed ethanol-induced acute electrophysiological changes were incorporated in two *in-silico* models: the Courtemanche human atrial cardiomyocyte model (373) and the Passini human ventricular cardiomyocyte model (374). Multiscale (cellular and tissue) simulations were performed in Myokit (344) and model code is available from [www.github.com/jordiheijman](http://www.github.com/jordiheijman). Concentration-dependent effects of

ethanol on cardiac ion channels ( $I_{Na}$ ,  $I_{Ca,L}$ ,  $I_{to}$ ,  $I_{K1}$ ,  $I_{Kr}$  and  $I_{NCX}$  for atrium and ventricle, as well as  $I_{Kur}$  and  $I_{K,ACh}$  for atrium) and SR calcium leak were implemented (Figure 6.1, Figure 6.2) based on published experimental data, as shown in the Appendix C. To simulate the effects of ethanol in the setting of long-standing persistent ('chronic') AF (cAF) and heart failure (HF), cAF- and HF-associated remodeling of cardiac ion channels and calcium-handling proteins were implemented as previously described (340, 375). Reentrant spiral waves were simulated using an  $S_1S_2$  induction protocol in homogeneous tissue of 8x8 cm (400x400 units) and in the presence of structural remodeling (fibrosis). In the  $S_1S_2$  protocol, the first stimulus ( $S_1$ ) is applied to generate a normal excitation wave. The second stimulus ( $S_2$ ) is then applied to part of the tissue, generating an additional wave-front that can interact with the tail of the preceding wave, producing reentry in a vulnerable substrate. In this study, the  $S_1$  was initiated from left to right and the  $S_2$  was applied to the upper-left quadrant of the tissue. The patterns of fibrosis were generated randomly using a Gaussian Random Field approach (376), with or without border-zone (BZ)-associated remodeling. In the presence of BZ, both previously reported cellular electrophysiological changes and alterations in conduction velocity were applied to the HF cardiomyocyte model (375, 377, 378).

To evaluate the robustness of our findings and assess potential consequences of intra- and inter-subject variability on the electrophysiological effect of ethanol, the maximum conductance of 10 major ionic currents ( $I_{Na}$ ,  $I_{NaL}$ ,  $I_{Ca,L}$ ,  $I_{to}$ ,  $I_{K1}$ ,  $I_{Kr}$ ,  $I_{Ks}$ ,  $I_{NCX}$  and  $I_{NaK}$  in both atrial and ventricular models, as well as  $I_{Kur}$  in the atrial model) were scaled based on a normal distribution with mean 1.0 and standard deviation 0.2, to create populations of models, as previously described (379, 380). In brief, 1000 variants of both models were created and the variants displaying "non-physiological" AP properties (defined as  $APD_{90}$  or RMP outside the range of 3 standard deviations of experimental  $APD_{90}$  and RMP from (381, 382)) were excluded. In total, 40 out of 1000 atrial models and none of the ventricular models were excluded. The non-normally distributed data are presented as median and inter-quartile ranges (IQR).

## 6.3 Results

### 6.3.1 Acute concentration-dependent effects of ethanol on cardiomyocyte ion channels and action potentials

Ethanol reduces  $I_{Na}$ ,  $I_{Ca,L}$ ,  $I_{to}$ ,  $I_{Kur}$ , and  $I_{Kr}$  (365, 368, 369) and exhibits dual effects on  $I_{K1}$  and  $I_{K,ACh}$  (366, 367), with inhibition of these latter currents at low concentrations and augmentation at high concentrations. Moreover, ethanol also enhanced  $I_{NCX}$ , sarco/endoplasmic reticulum calcium-ATPase (SERCA) function and SR calcium leak, increasing proarrhythmic spontaneous calcium release events (370). These experimental findings were reproduced in human right atrial (RA) (373) and left ventricular (LV) (374) cardiomyocyte models (Figure 6.1A-B, Figure 6.2). The SR calcium leak was calculated using a simulated tetracaine protocol in the presence of 0 mmol/L extracellular sodium and calcium to prevent trans-sarcolemmal calcium fluxes. The ethanol-induced augmentation of SR calcium leak in atrial and ventricular models was comparable to the experimental data (Figure 6.1B, Figure 6.2B). Finally, concentration-dependent effects of ethanol on cardiac ion channels were incorporated based on published experimental data (Figure 6.1C).

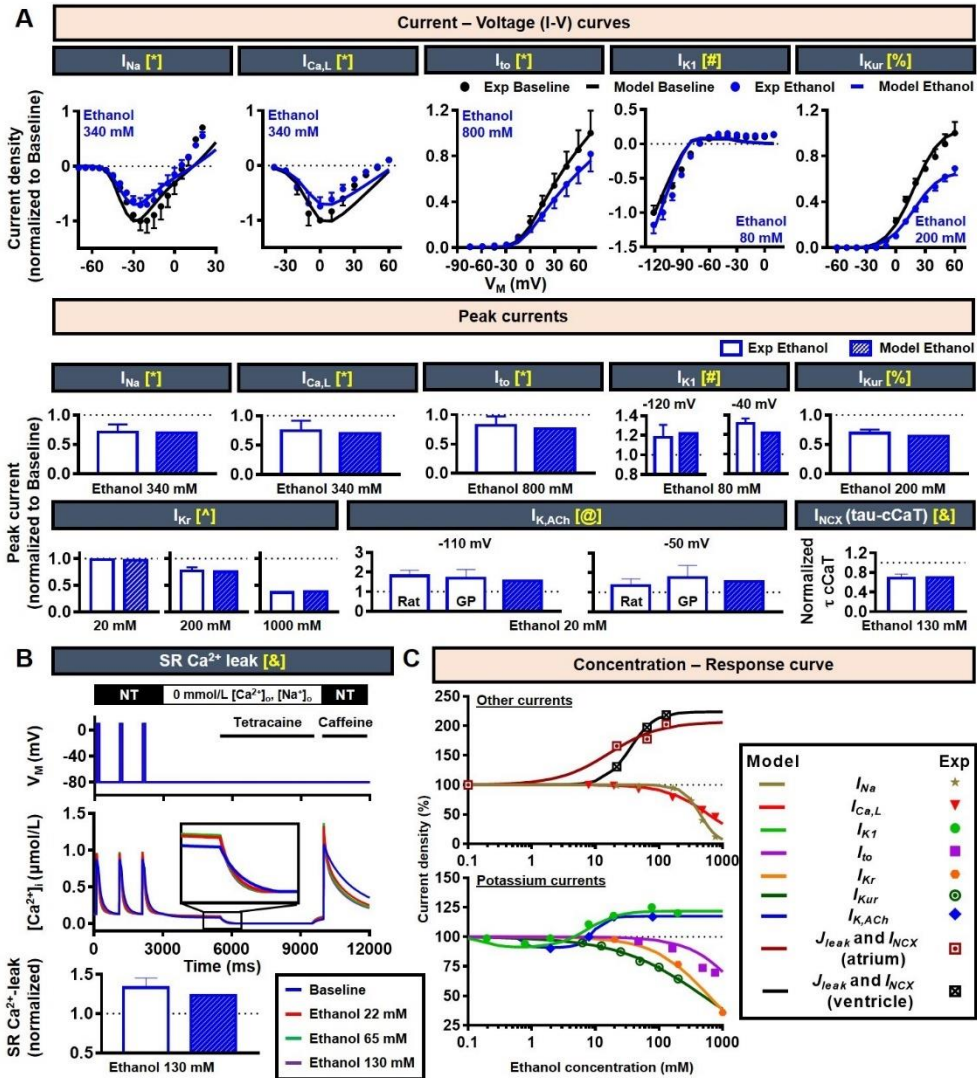


**Figure 6.1:** Concentration-dependent effects of ethanol on human atrial cardiomyocyte ion channels. The Courtenanche human atrial cardiomyocyte model reproduced the experimentally-observed acute effects of ethanol on cardiac ion channels. A) Top row: The normalized current-voltage relationship ( $I$ - $V$  curves) of  $I_{Na}$ ,  $I_{Ca,L}$ ,  $I_{to}$ ,  $I_{K1}$  and  $I_{Kur}$  at baseline (0 mM ethanol; black lines) or in the presence of ethanol (blue lines) in the human atrial cardiomyocyte model compared to experimental data (black and blue dots) from several publications ([\*] = (365), [#] = (366), [%] = (368)). Bottom panels: peak currents of different ion channels relative to the baseline condition (not shown) with 0mM ethanol. Experimental data are shown in white bars ([\*] = (365), [#] = (366), [%] = (368), [^] = (369), [Ⓜ] = (367), [Ⓜ] = (370)), and simulated counterparts in blue bars. For  $I_{K1}$  and  $I_{K,ACh}$  the relative change is shown for both the inward current (at -120 mV and -110 mV) and the outward current at (-40 mV and -50 mV) through these channels. The ethanol-induced effect on  $I_{NCX}$  was assessed using the relative change in the time-constant of the caffeine-induced transient (tau-cCaT), as reported experimentally (370). A decrease in tau-cCaT represents an increase in NCX-mediated calcium extrusion. B) The tetracaine-caffeine protocol, involving inhibition of SR calcium leak with tetracaine in the absence of extracellular sodium and calcium to block trans-sarcolemmal calcium fluxes and caffeine-induced calcium release to assess SR calcium load, was simulated (top panels). The relative change in SR calcium leak in the presence of 130 mM ethanol in the model (blue bar) was compared to experimental data (white bar)

(370). C) Concentration-dependent effect of ethanol on relative current densities of potassium currents (bottom panel) and other ionic targets (top panel) in the model (lines) and experiments (symbols). (Exp = experiment; GP = guinea-pig;  $I_{Na}$  = fast sodium current;  $I_{Ca,L}$  = L-type calcium current;  $I_{to}$  = transient-outward potassium current;  $I_{K1}$  = inward-rectifier potassium current;  $I_{Kur}$  = ultra-rapid delayed-rectifier potassium current;  $I_{Kr}$  = rapid delayed-rectifier potassium current;  $I_{K,ACh}$  = acetylcholine-activated inward-rectifier potassium current;  $I_{NCX}$  = sodium/calcium-exchange current; NT = normal Tyrode)

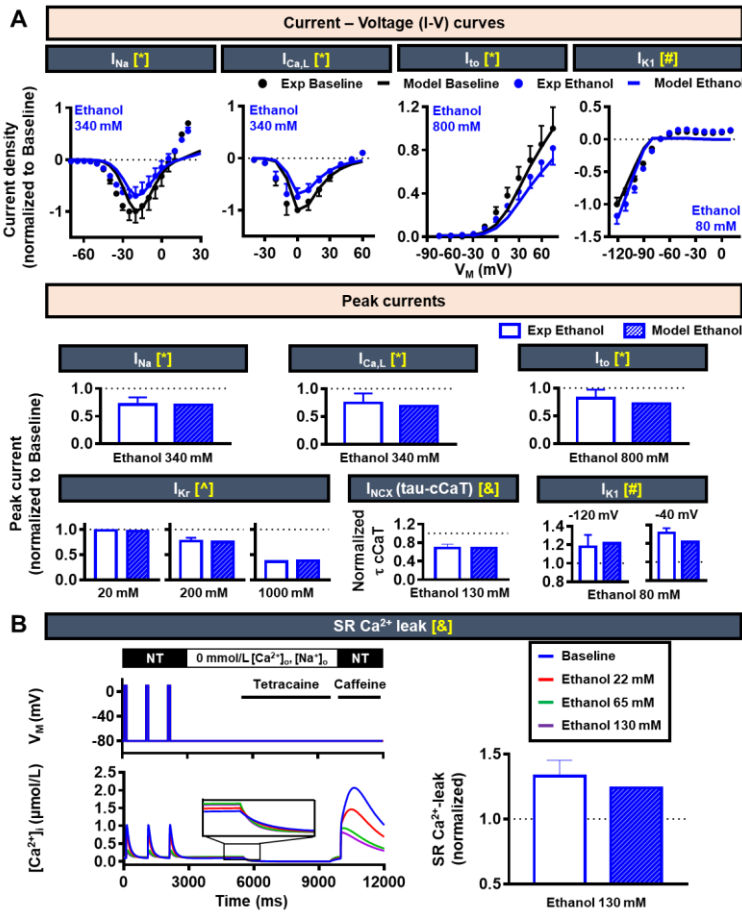


**Figure 6.2:** The concentration-dependent effects of ethanol on human ventricular cardiomyocyte ion channels. The Passini human ventricular cardiomyocyte model reproduced the experimentally-observed acute effects of ethanol on cardiac ion channels. A) Top panel: The current-voltage relationship (I-V curves) of ethanol-dependent regulation of  $I_{Na}$ ,  $I_{Ca,L}$ ,  $I_{to}$  and  $I_{K1}$  of the ventricular model (blue lines) relative to baseline (0 mM ethanol; black lines) were compared to the experimental data (black and blue dots) from several publications ([\*] = (365), [#] = (366)). Bottom panel: The peak currents of ion channels derived from experiments (white bars; [\*] = (365), [#] = (366), [^] = (369), [&] = (370)), relative to the baseline condition with 0mM ethanol (not shown), compared to the simulated counterparts (blue bars). The  $I_{NCX}$  was calculated from the time-constant of the caffeine-induced transient (tau cCaT) as reported experimentally (370). A decrease in tau-cCaT represents an increase in NCX-mediated calcium extrusion. B) The tetracaine-caffeine protocol was simulated to evaluate SR calcium leak in the model and compared to experimental data (370). (Exp = experiment;  $I_{Na}$  = fast sodium current;  $I_{Ca,L}$  = L-type calcium current;  $I_{to}$  = transient-outward potassium current;  $I_{K1}$  = inward-rectifier potassium current;  $I_{Kr}$  = rapid delayed-rectifier potassium current;  $I_{NCX}$  = sodium/calcium-exchange current; NT = normal Tyrode)

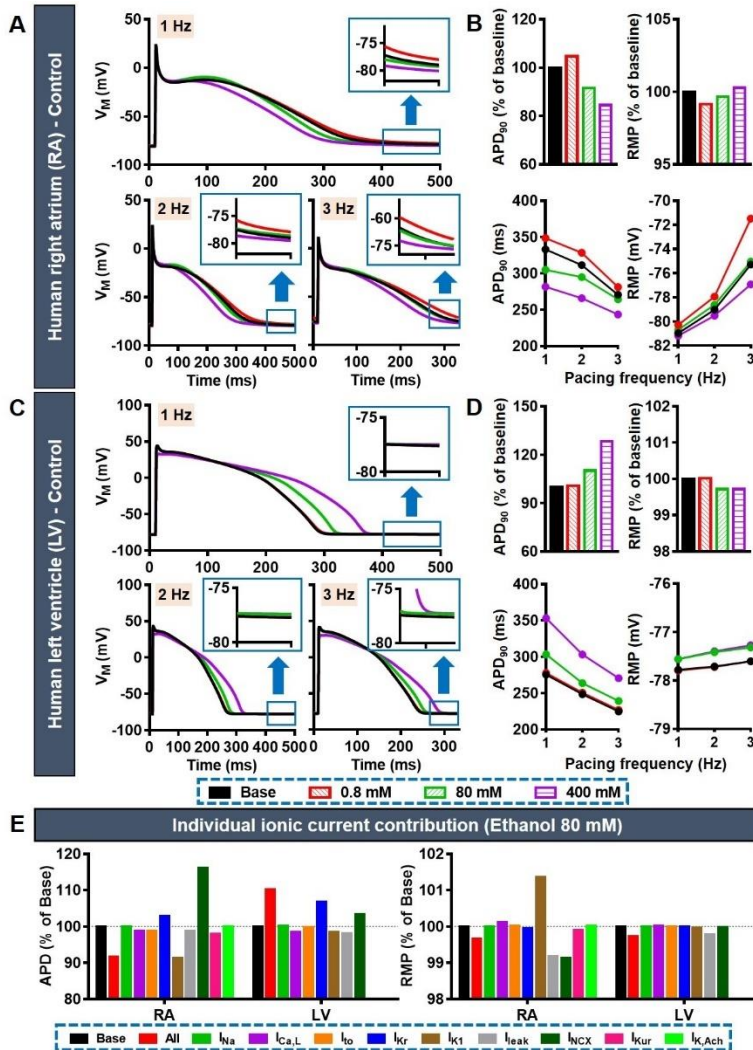


**Figure 6.3:** The effect of ethanol on atrial and ventricular cardiomyocyte action potentials (APs). A) Acute effect of ethanol on APs in human right atrial (RA) cardiomyocyte model for 1, 2 and 3 Hz pacing. B) AP duration (APD) and resting membrane potential (RMP) at baseline and for 0.8, 80 and 400 mM ethanol during 1-Hz pacing (top), as well as APD and RMP rate dependence (bottom). C, D) Similar to panels A-B for the human left ventricular (LV) cardiomyocyte model. E) Impact of ethanol (80 mM)-dependent regulation of individual ion currents on APD and RMP in RA (left) and LV (right) models. Dotted horizontal line represents values of the baseline model (100%), for comparison. (APD = action potential duration;  $I_{Na}$  = fast sodium current;  $I_{Ca,L}$  = L-type calcium current;  $I_{to}$  = transient-outward potassium current;  $I_{K1}$  = inward-rectifier potassium current;  $I_{Kur}$  = ultra-rapid delayed-rectifier potassium current;  $I_{Kr}$  = rapid delayed-rectifier potassium current;  $I_{K,ACh}$  = acetylcholine-activated inward-rectifier potassium current;  $I_{NCX}$  = sodium/calcium-exchange current; LV = left ventricle; RA = right atrium; RMP = resting membrane potential)

Subsequently, single-cell simulations incorporating ethanol-dependent regulation of all these cardiac ion channels were performed using both the Courtemanche human RA and Passini human LV cardiomyocyte models. Binge alcohol drinking is defined as blood alcohol concentrations above 0.8‰, with values exceeding

5‰ resulting in a high possibility of coma or death (383). Blood alcohol concentrations in the MunichBREW study ranged from 0 to 2.94‰ with a mean of 0.85‰. Accordingly, we analyzed low (0.8 mM, corresponding to ~0.04‰) and high (80 mM, corresponding to ~3.64‰) ethanol concentrations. In addition, 400 mM ethanol was applied to study the maximal cellular effect (**Figure 6.1C**). Compared to the baseline atrial model without ethanol effects, 0.8 mM ethanol prolonged APD at 90% of repolarization (APD<sub>90</sub>) by 15 ms (4.6%) at 1 Hz pacing and slightly depolarized the resting membrane potential (RMP) by 0.7 mV (0.9%) in the human RA cardiomyocyte model, without affecting ventricular APs. Meanwhile, 80 and 400 mM ethanol reduced APD<sub>90</sub> in the atrial model by 28 ms and 52 ms (8.4% and 15.4%), but prolonged the APD<sub>90</sub> in the ventricle by 28 and 78 ms (10.2% and 28.3%; **Figure 6.3**). The potential influence of ethanol-induced heart-rate changes were assessed by simulating elevated pacing rates (2 and 3 Hz). The ethanol-induced alterations in atrial and ventricular APDs were reduced compared to 1-Hz pacing for all cellular concentrations. By contrast, the effects of ethanol on RMP in the human RA model were slightly augmented at fast rates (**Figure 6.3**).

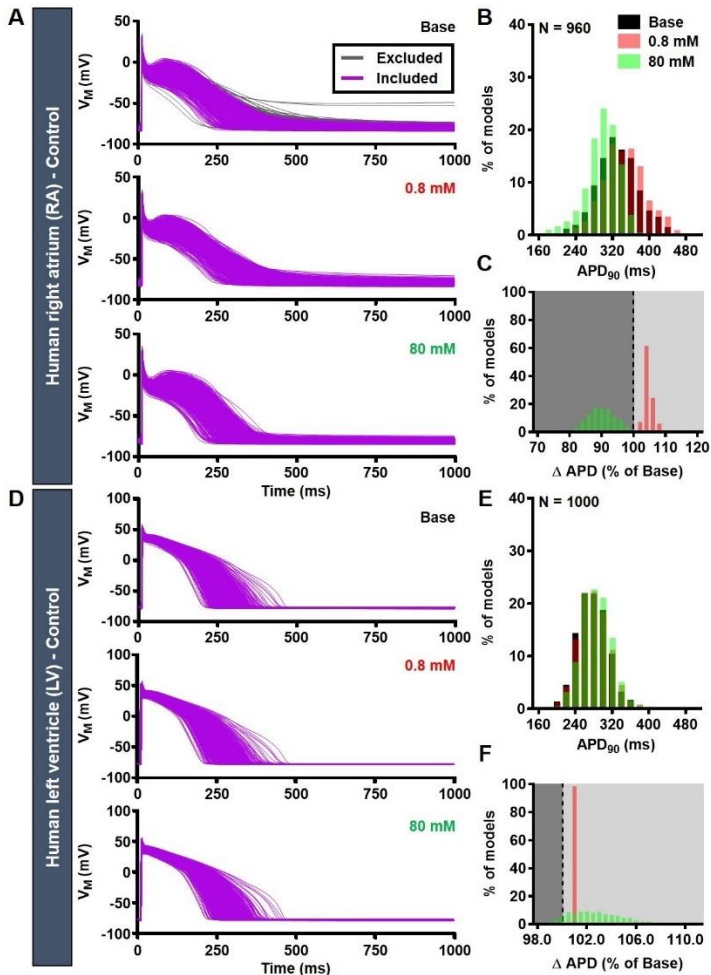


**Figure 6.4:** Effects of ethanol on a population of models reflecting intra- and inter-subject variability. The population was built from 1000 models by scaling the maximum conductance of 10 major ionic currents ( $I_{Na}$ ,  $I_{Ca,L}$ ,  $I_{NaL}$ ,  $I_{to}$ ,  $I_{K1}$ ,  $I_{Kr}$ ,  $I_{Ks}$ ,  $I_{NCX}$ ,  $I_{NaK}$  and  $I_{Kur}$ ) based on a normal distribution with sigma = 0.2. A) Action potentials (APs) for the 1000 human right atrial (RA) models at baseline (0 mM ethanol) and in the presence of 0.8 or 80 mM ethanol. Non-physiological APs with APD<sub>90</sub> shorter or longer than 3 standard deviations of experimental data obtained from (381, 382) (shown in grey), were excluded. B) Histogram of absolute APD<sub>90</sub> for the 3 ethanol concentrations (0, 0.8 and 80 mM) of the 960 included models. C) Histogram of  $\Delta$ APD<sub>90</sub> (relative to baseline). The dark grey shaded area represents APD reduction, while light grey corresponds to APD prolongation. D-F) Similar to panels A-C for the human left ventricular (LV) cardiomyocyte model based on 1000 included models.

To address the effects of intra- and inter-subject variability, populations of 1000 RA and LV models were simulated and analyzed. Following the exclusion of “non-physiological” APs, 960 atrial models and 1000 ventricular models were used (**Figure 6.4A**). The frequency distributions of APD<sub>90</sub> with 0, 0.8 and 80 mM ethanol (**Figure 6.4B**) and the histogram of relative ethanol-induced APD<sub>90</sub> changes (**Figure 6.4C**) revealed consistent atrial APD-prolonging effect at low concentrations (Median: 104.3% of baseline, IQR: 103.6-105.2) and atrial APD-shortening at high concentrations (Median: 90% of baseline, IQR: 87-93). In the ventricles, low concentrations of ethanol produced consistent minor APD prolongation (Median: 100.9%, IQR: 100.8-100.9), while high concentrations of ethanol demonstrated a wide range of effects on APD (Median: 102.5%, IQR: 101.1-104.2; **Figure 6.4E-F**). Thus, the results obtained with the default models appear representative for a wide range of ion-current densities, representing different virtual genotypes.

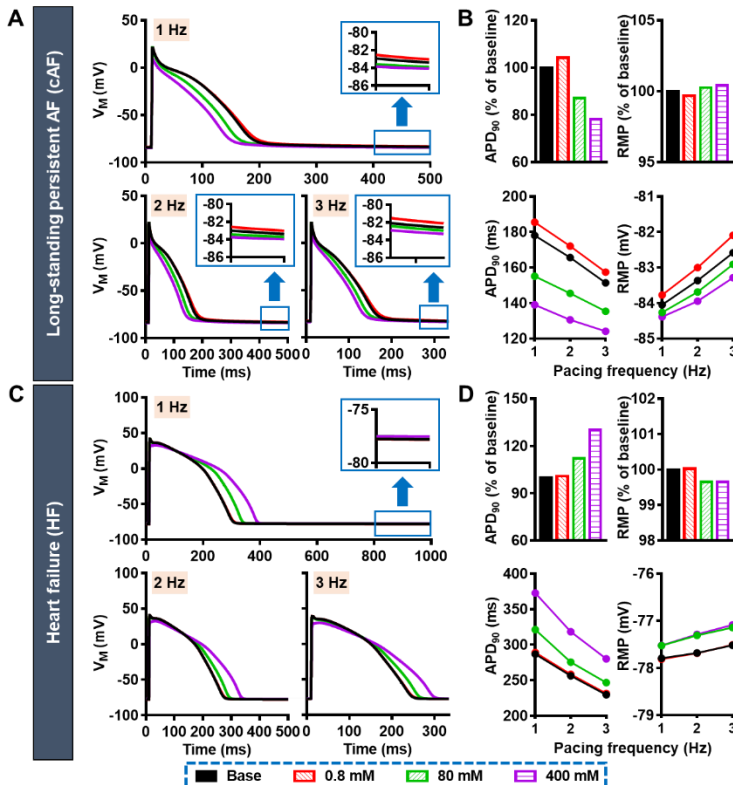


**Figure 6.5:** The effect of ethanol on cardiac action potentials (APs) of the diseased heart. A) Acute effect of ethanol on APs in long-standing persistent atrial fibrillation (cAF) cardiomyocyte model for 1, 2 and 3 Hz pacing. B) AP duration (APD) and resting membrane potential (RMP) for 0.8, 80 and 400 mM ethanol during 1-Hz pacing (top), as well as APD and RMP rate dependence (bottom). C, D) Similar to panels A and B for the heart failure (HF) cardiomyocyte model. (APD = action potential duration; RMP = resting membrane potential)

To investigate the effects of ethanol in remodeled cardiomyocytes, electrophysiological remodeling observed in cAF (340) and HF (375) were incorporated into the Courtemanche RA and Passini LV model, respectively. Cellular simulations using these remodeled cardiomyocyte models showed qualitatively similar ethanol-induced electrophysiological changes as the control models: low concentrations of ethanol prolonged APD in the cAF model, while high concentration of ethanol shortened the APD in the cAF and prolonged APD in the HF model (Figure 6.5). The ethanol-induced changes in relative APD were slightly larger in the presence of disease-related remodeling than in the control models. These results indicate that the cellular effects of ethanol are robust and may potentially have proarrhythmic consequences under a wide range of conditions.

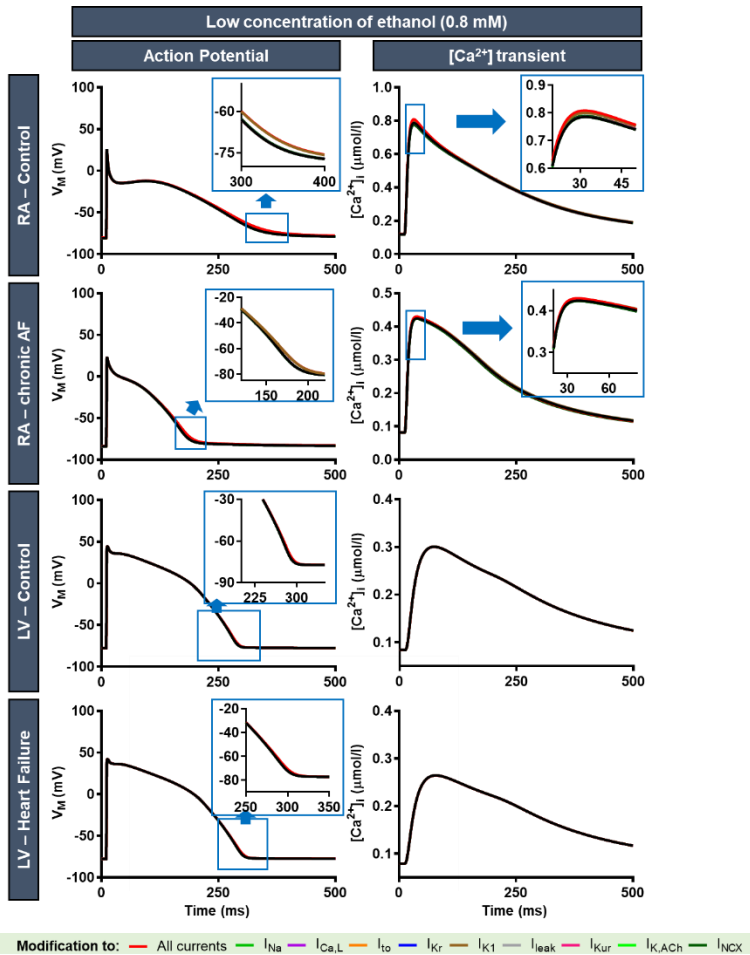


**Figure 6.6:** Individual contributions of ethanol-induced ion channel remodeling on cardiac cellular electrophysiology (focused on low concentration of ethanol). Each line represented the acute effect of ethanol on all currents (red) and single current (other colors, see legends), compared to the baseline with no ethanol-induced ion-channel remodeling (black).

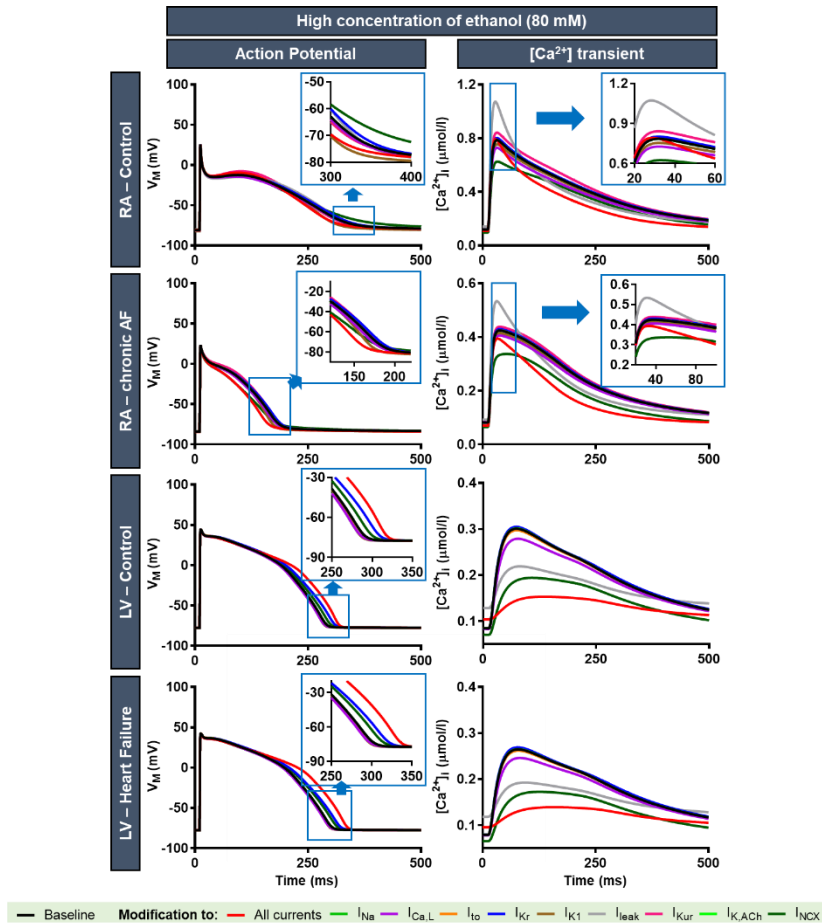


**Figure 6.7:** Individual contributions of ethanol-induced ion channel remodeling on cardiac cellular electrophysiology (focused on high concentration of ethanol). Each line represented the acute effect of ethanol on all currents (red) and single current (other colors, see legends), compared to the baseline with no ethanol-induced ion-channel remodeling (black).

Exploiting the perfect control offered by computational modeling, the individual contribution of each ethanol-dependent ion-channel alteration to the change in cardiomyocyte AP was assessed. The APD prolongation and slight RMP depolarization observed with 0.8 mM ethanol in the atrial cardiomyocyte model were entirely due to the inhibition of  $I_{K1}$  (Figure 6.6). At high ethanol concentrations, a complex, cell-type-specific interplay among ionic currents was identified. For example, the APD prolongation in the human LV model resulted from the interaction between  $I_{NCX}$  and  $I_{Kr}$ . On the other hand, the atrial APD shortening was mainly due to the ethanol-induced increase in  $I_{K1}$ , opposed by the APD-prolonging effects of  $I_{NCX}$  and  $I_{Kr}$  (Figure

6.3E, lower panel). The complete overview of the individual ionic contributions to ethanol-induced AP changes is provided in **Figures 6.6-6.8**.

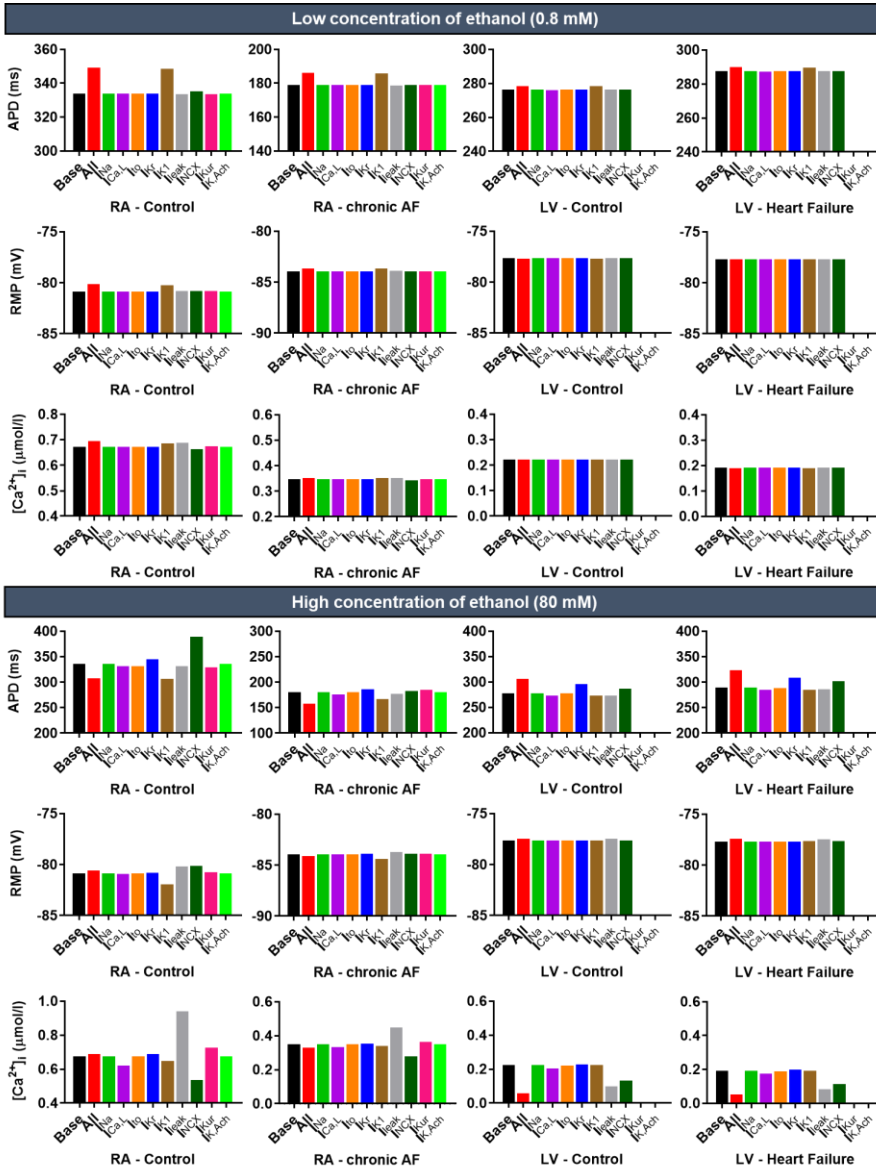


**Figure 6.8:** The sensitivity analysis of ethanol-induced ion channel remodeling. The cellular effect of ethanol on cardiac ion channels were evaluated independently and compared to the base model and the model with combined effect. The APD, RMP and calcium transient amplitude for both low and high concentration of ethanol are shown.

**6.3.2 The acute effects of ethanol on reentrant arrhythmias**

Two-dimensional tissue simulations were performed using both atrial and ventricular models to investigate the acute effects of ethanol on reentrant arrhythmias induced

using an  $S_1S_2$  pacing protocol (Figure 6.9). Previously described ethanol-induced reductions in intercellular coupling (364, 384, 385) were incorporated into the models based on a Hill equation with an  $IC_{50}$  of 320 mM and Hill coefficient of 1 (see Appendix C). The vulnerable windows, reflecting the duration of reentry induced for different  $S_1S_2$  intervals, were evaluated to assess both the inducibility and stability of reentrant arrhythmias under different conditions (Figure 6.9). The size of the vulnerable windows indicates the inducibility of reentry (i.e., the number of  $S_1S_2$  intervals producing reentry) and the duration of reentry within the vulnerable windows indicates the stability of reentrant arrhythmias. Since reentry durations can be distinct for different  $S_1S_2$  intervals, both factors were combined into a total arrhythmogenic risk parameter by summing the reentry durations over the entire vulnerable window (Figure 6.9) to provide a single quantitative assessment of the proarrhythmic effects of ethanol under a given condition.

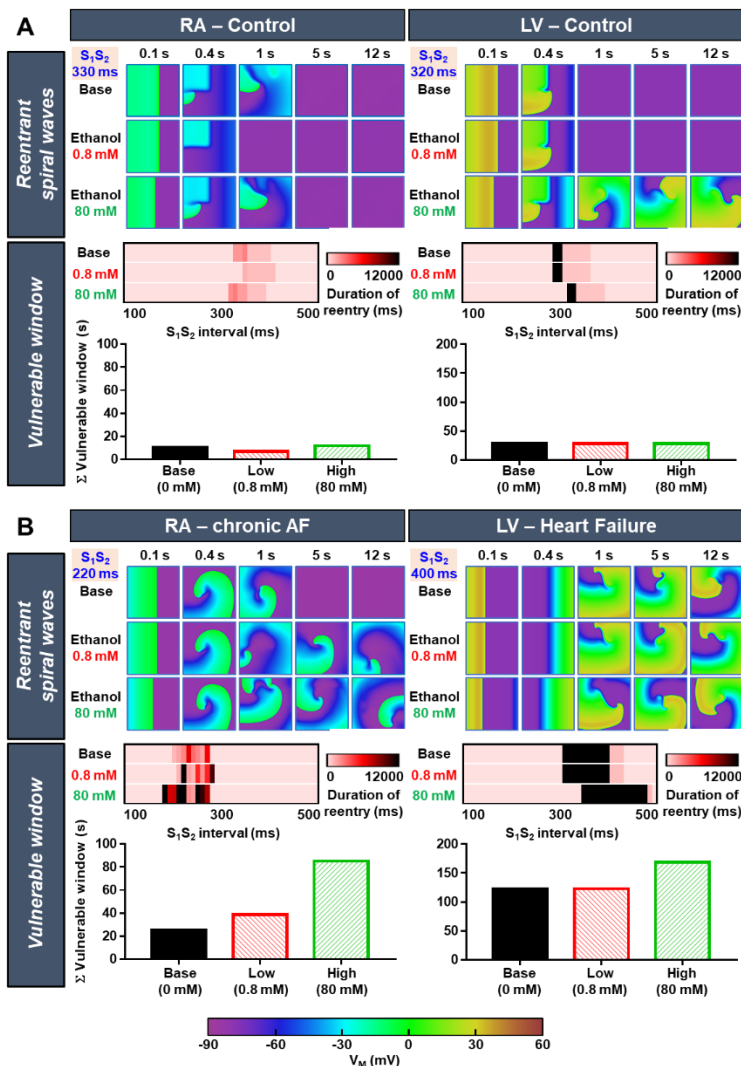


**Figure 6.9:** Acute effects of ethanol on reentrant arrhythmias. The 2-dimensional *in-silico* studies were performed in homogenous 8x8 cm tissue of 4 different models: the human right atrial (A, left), the human left ventricular (A, right), the long-standing persistent (“chronic”) AF and the heart failure models (B, left and right, respectively). Reentrant spiral waves were assessed in the presence of 0, 0.8 and 80 mM ethanol for various  $S_1S_2$  intervals, where the first stimulus ( $S_1$ ) was initiated from left to right, and the second stimulus ( $S_2$ ) excited the upper left quadrant of the tissue. The top panels show snapshots of reentrant waves at designated  $S_1S_2$  intervals (330 ms in RA-control, 320 ms in LV-control, 220 ms in RA-chronic AF, and 400 ms in LV-Heart Failure), while the bottom panels show the complete vulnerable windows and the sum ( $\Sigma$ ) of reentry duration for all  $S_1S_2$  intervals tested, quantifying the total arrhythmogenic risk. Reentry persisting for more than 12 s was considered stable (colored as black in the heatmap of the vulnerable windows). (Ctl = control; LV = left ventricle; RA = right atrium)

In the control human RA model, 0.8 mM ethanol reduced the duration of reentry and shifted the vulnerable window for reentry induction towards longer  $S_1S_2$  intervals (**Figure 6.9A, left panel**). On the other hand, 80 mM ethanol produced a slight increase in reentry duration and shifted the vulnerable window to shorter  $S_1S_2$  intervals (**Figure 6.9A, left panel**). Stable reentry (i.e., reentry that persists after 12 s) could not be induced in the control RA model. In the control LV model, 0.8 mM ethanol did not have any effect on either the vulnerable window or the duration of reentry (**Figures 6.9A, right panels**), consistent with the cellular results (**Figure 6.3C-D**). However, 80 mM ethanol shifted the vulnerable window to longer  $S_1S_2$  intervals, without a noticeable effect on reentry duration (**Figure 6.9A, right panel**). In general, reentry was more stable with a less meandering rotor core in the ventricular compared to the atrial model (**Figure 6.10**).

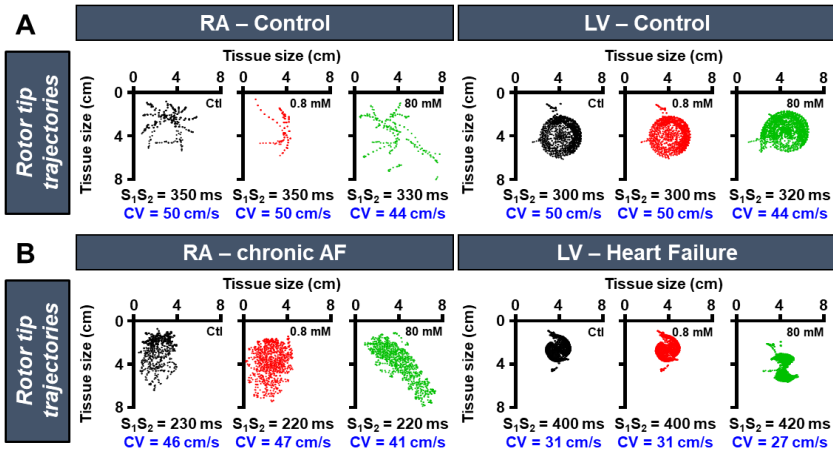


**Figure 6.10:** Acute effects of ethanol on rotor tip trajectories of the reentrant waves. The 2-dimensional *in-silico* studies were performed in homogenous 8x8 cm tissue of 4 different models: the human right atrial (RA) control model (A, left), the human left ventricular (LV) control model (A, right), the RA model with long-standing persistent (“chronic”) AF and the LV model with heart failure (B, left and right, respectively). Reentrant spiral waves were assessed in the presence of 0, 0.8 and 80 mM ethanol for the indicated  $S_1S_2$  intervals, corresponding to the longest duration of reentry in each model. CV = conduction velocity.

Compared to the control atrial model, the cAF model exhibited a more variable pattern of reentry durations for different  $S_1S_2$  intervals: for some intervals, reentry was short, whereas for others, it was long (**Figure 6.9B, left panel**). Both low and high concentrations of ethanol increased reentry duration in the cAF model, with several  $S_1S_2$  intervals producing stable reentry for both ethanol concentrations, suggesting an

ethanol-induced promotion of arrhythmia maintenance. Furthermore, the larger vulnerable window for high ethanol concentrations indicates an ethanol-induced increase in reentry inducibility in the cAF model. At high ethanol concentrations, the rotors of the cAF model also exhibited a more meandering core, highlighting the dynamicity of the reentrant waves (**Figure 6.10B, left panel**).

To simulate the effect of ethanol on reentrant arrhythmias in the setting of HF, a 40% reduction in intercellular coupling was applied to simulate HF-related gap-junction remodeling (386, 387), in addition to the ion-channel remodeling (375). Consequently, the conduction velocity was reduced from 50 cm/s in the control LV model to 31 cm/s in the HF model (**Figure 6.10A-B, right panels**), consistent with previous experimental data (386). HF-associated remodeling increased reentry duration at baseline and for all ethanol concentrations and produced a larger window of stable reentry (**Figure 6.9B, right panel**). Consistent with the control LV model, low ethanol concentrations did not affect reentry in the HF model, whereas high ethanol concentrations resulted in a larger window of stable reentry (**Figure 6.9B, right panel**), highlighting the proarrhythmic role of high ethanol concentrations in HF. Thus, at the tissue level, ethanol's proarrhythmic effects are more outspoken in the presence of disease-related remodeling.

To investigate if these proarrhythmic effects also occur in the presence of ethanol concentrations closer to the cut-off value for heavy episodic drinking (0.8‰), we investigated the consequence of 20 and 40 mM ethanol (~0.91‰ and ~1.82‰, respectively) on reentrant arrhythmias in the cAF and HF models. In cAF, ethanol produced a concentration-dependent increase in the duration of reentry with several episodes of stable reentries at 20 and 40 mM (**Figure 6.11**). In HF, both 20 and 40 mM ethanol produced a larger window of stable reentry compared to the baseline HF model (**Figure 6.11**). These results confirm the potential proarrhythmic effects of ethanol at these concentrations.

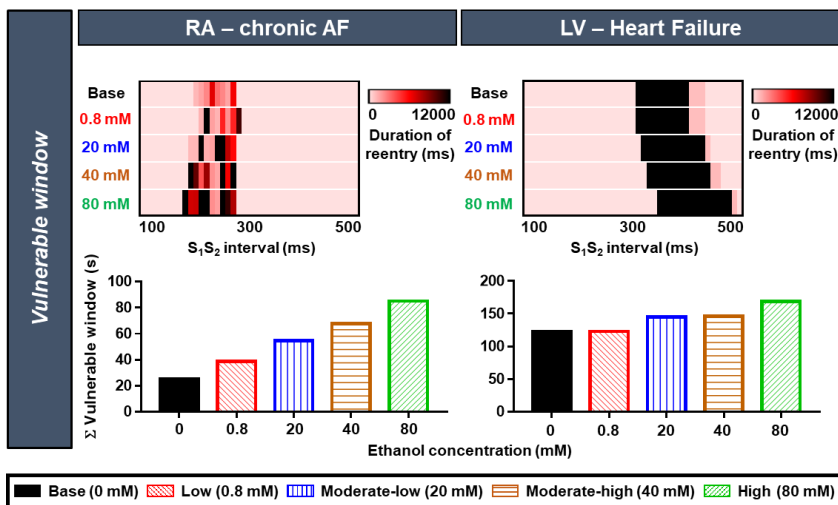


**Figure 6.11:** The concentration-dependent effects of ethanol on vulnerable windows for reentrant arrhythmias. Two ethanol concentrations were added to represent the moderate-low (20 mM) and moderate-high (40 mM) concentrations of ethanol. The  $S_1S_2$  induction protocol was performed in cAF and HF models

*Acute effects of alcohol on cardiac electrophysiology and arrhythmogenesis*

without structural remodeling. The vulnerable windows (upper panels) and the sum ( $\Sigma$ ) of vulnerable windows (lower panels) were shown and compared with base, low and high ethanol concentrations. (RA = right atrium; LV = left ventricle)

To study the effect of intra- and inter-subject variability on the ethanol-dependent promotion of reentrant arrhythmias, models with the shortest and longest APD<sub>90</sub> were selected from both the atrial and ventricular populations (**Figure 6.12**). As expected, vulnerable windows were shifted to longer S<sub>1</sub>S<sub>2</sub> intervals and stability of reentrant waves was reduced in the models with long APDs, while short APDs promoted reentry. In general, the ethanol-induced effects on reentry in the maximum APD models (**Figure 6.12A-B, middle panels**) and minimum APD models (**Figure 6.12A-B, right panels**) were consistent with the default models, displaying proarrhythmic effects in the presence of high concentrations of ethanol.

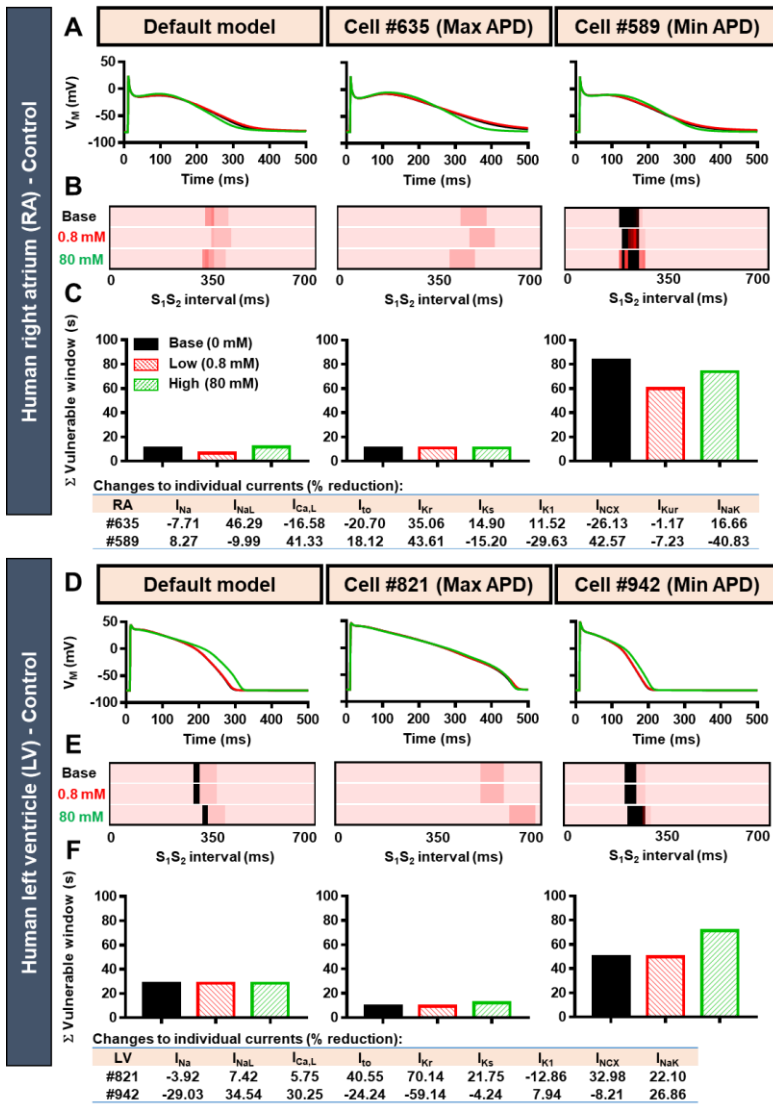


**Figure 6.12:** The effect of variability of the ionic currents on ethanol-associated reentrant arrhythmias. We extended the analysis of intra- and inter-subject variability using the populations of models depicted in Figure 6.4 to 2-dimensional homogenous tissue simulations. The shortest and the longest action potential duration (APD<sub>90</sub>) in the population were chosen and reentries were simulated for three different ethanol concentrations (0, 0.8, and 80 mM). A) Action potentials of the default model, model with longest APD and model with the shortest APD in the presence of 0 (black), 0.8 (red) or 80 (green) mM ethanol. B) Vulnerable windows for the three different ethanol concentrations for the default model, the model with longest APD<sub>90</sub> and the model with shortest APD<sub>90</sub>. C) The sum ( $\Sigma$ ) of atrial vulnerable windows, quantifying the total arrhythmogenic risk for the three models and three different concentrations of ethanol. D, E, F) Similar to panels A-C for the human LV model. The changes (in %) in the ionic current maximum conductances for the models with shortest and longest APD are shown in the small tables below the bar charts.

### 6.3.3 The role of gap-junction remodeling in ethanol-induced promotion of reentrant arrhythmias

Altered intercellular coupling is an important feature of HF (386, 387). Therefore, we investigated how ethanol- and HF-induced altered intercellular coupling interact. The comparison of HF models with (Figure 6.13, left panel) and without (Figure 6.13, middle panel) ethanol-induced gap-junction remodeling revealed no significant differences in reentry inducibility or stability for the baseline model and 0.8 mM ethanol. However, with 80 mM ethanol, the absence of ethanol-induced gap-junction remodeling reduced the occurrence of stable reentry and shortened the vulnerable window (Figure 6.13, left and middle panels), highlighting the critical role of reduced intercellular communication in ethanol-induced reentry promotion in HF. Conversely, the absence of ethanol-induced remodeling of intercellular coupling in both the control and cAF RA models did not significantly alter the effect of ethanol on atrial reentrant arrhythmias (Figure 6.14).

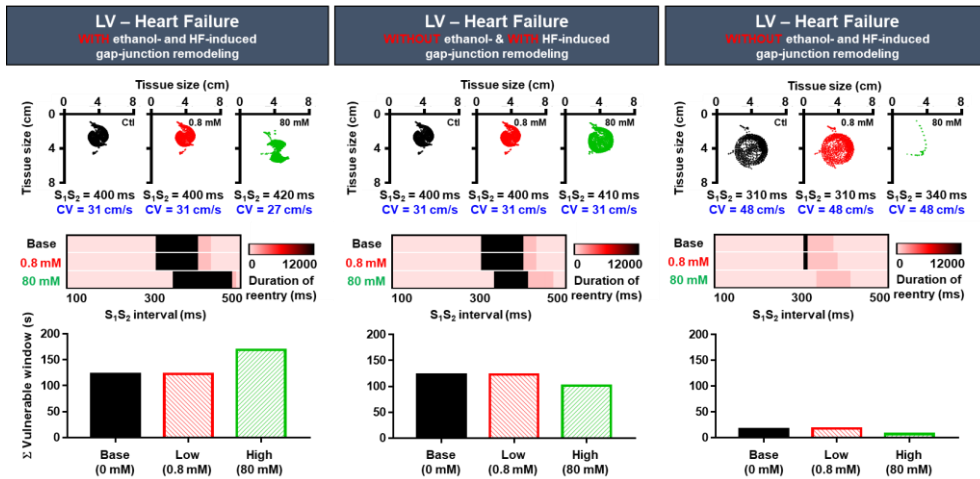


**Figure 6.13:** The role of gap-junction remodeling in ethanol-induced reentry promotion in heart failure. Human LV models representing the setting of heart failure with both ethanol- and HF-induced (left panels), without ethanol-induced (middle panels) and without both ethanol- and HF-induced (right panels) gap-junction remodeling in the presence of different concentrations of ethanol. For each condition, the rotor tip trajectories (top), vulnerable windows (middle) and the sum ( $\Sigma$ ) of vulnerable windows (bottom), were determined. (Ctl = control; CV = conduction velocity; LV = left ventricle)

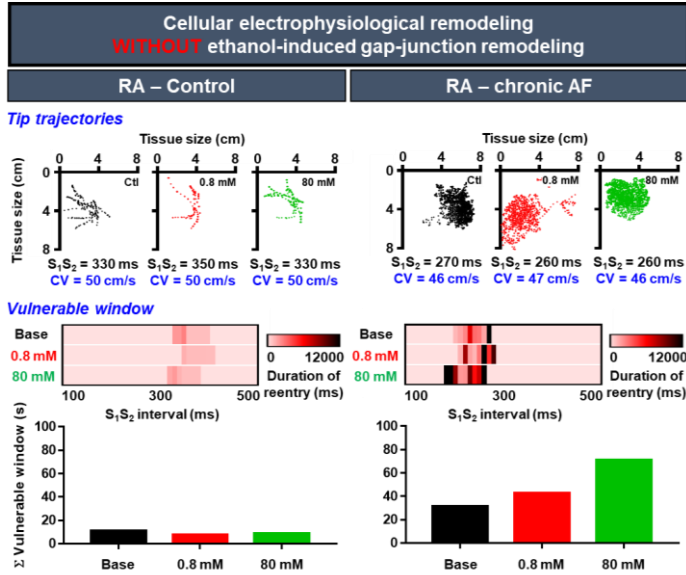


**Figure 6.14:** Acute effects of ethanol on reentrant arrhythmias in the absence of ethanol-induced intercellular coupling abnormalities. The 2-dimensional *in-silico* studies were performed in homogenous 8x8 cm tissue of human right atrial (left panel) and long-standing persistent (“chronic”) AF models (right panel). The tip trajectories are shown in the upper panels. The vulnerable windows were assessed for 0, 0.8 and 80 mM ethanol (middle panels) and bottom panels quantify total arrhythmogenic risk as the sum ( $\Sigma$ ) of vulnerable windows (i.e., the sum of reentry duration for all  $S_1S_2$  intervals tested). Reentry persisting for more than 12 s was considered stable (black bars in the vulnerable windows). (Ctl = control; CV = conduction velocity; LV = left ventricle; RA = right atrium)

The absence of HF-related gap-junction remodeling also drastically reduced the episodes of stable reentry in two-dimensional simulations of the HF model for all concentrations of ethanol (compare **Figure 6.13, middle and right panels**). Strikingly, no stable reentry could be induced in the HF model without gap-junction remodeling (by either HF or ethanol) in the presence of simulated high ethanol concentrations (**Figure 6.13**). The inability to induce stable reentry in the LV model without gap-junction-associated remodeling was due to the APD-prolonging effect of ethanol-induced  $I_{Kr}$  inhibition and  $I_{NCX}$  augmentation (**Figure 6.15**).

### 6.3.4 The interaction between ethanol and structural remodeling modulates reentrant arrhythmia stability

Structural remodeling, notably cardiac fibrosis, is a key feature of cAF and HF and may act as a substrate for cardiac arrhythmias, favoring reentrant waves to occur and persist (64, 388). In addition, long-term ethanol abuse can produce structural remodeling, promoting alcoholic cardiomyopathy (364, 372, 389). As such, we assessed the acute effects of ethanol in the presence of mild (4% fibrotic tissue), moderate (11% fibrotic tissue) and extensive (20% fibrotic tissue) structural remodeling (**Figure 6.16A**). In the cAF models with 0 or 0.8 mM ethanol, extensive fibrosis slightly reduced the duration of reentry compared to mild fibrosis, whereas in the presence of high ethanol concentrations, moderate and extensive fibrosis resulted in a substantial reduction of stable reentry (**Figure 6.16B, green bars**). By contrast, in the ventricle, extensive

fibrosis increased the duration and improved the stability of reentry for all ethanol concentrations tested (Figure 6.16C, Online Videos 1-2). Subsequent analyses revealed that the differences between atrial and ventricular models were likely due to the stronger meandering of rotors in the atrial model compared to the ventricle, which increases the likelihood of wave break, collisions and subsequent termination of reentrant waves in the presence of extensive fibrosis. Overall, these data show that the proarrhythmic effects of ethanol depend on ethanol concentration, cell-type, as well as underlying structural remodeling.

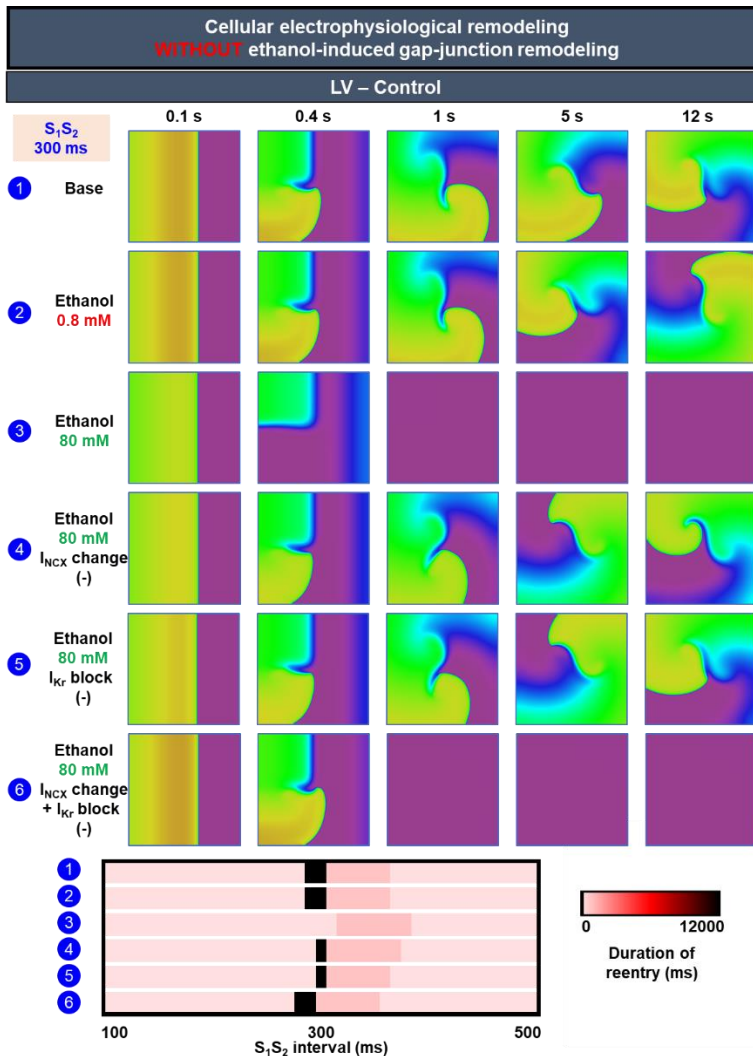


**Figure 6.15:** The analysis of the potential antiarrhythmic effect of high concentration of ethanol in the Passini human left ventricular model without ethanol-associated gap-junction remodeling. 1) Baseline model, 2) Low concentration of ethanol, 3) High concentration of ethanol with all documented ion channel remodeling 4) High concentration of ethanol without ethanol-induced  $I_{NCX}$  change 5) High concentration of ethanol without ethanol-induced  $I_{Kr}$  inhibition 6) High concentration of ethanol without both ethanol-induced  $I_{NCX}$  change and  $I_{Kr}$  inhibition.

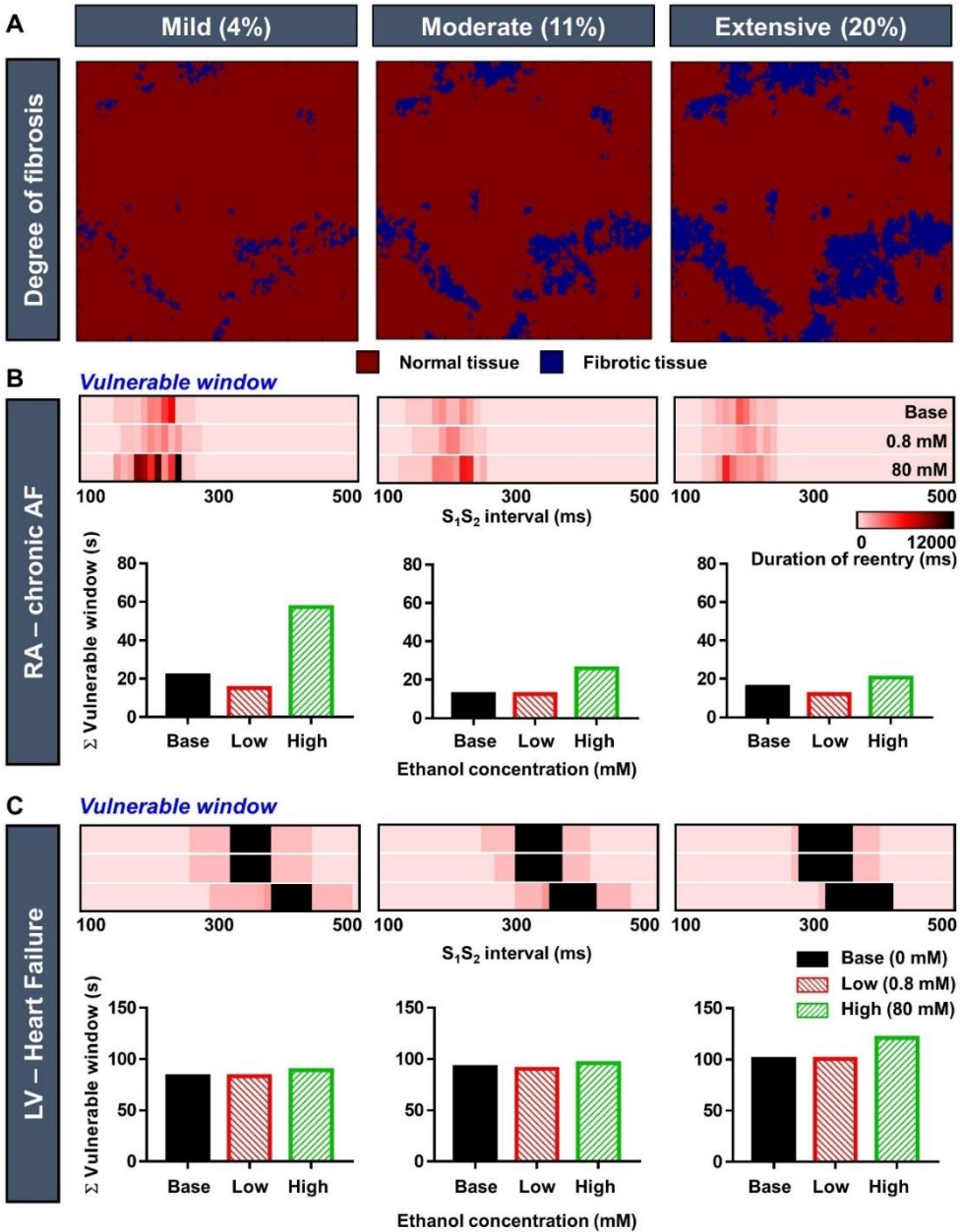
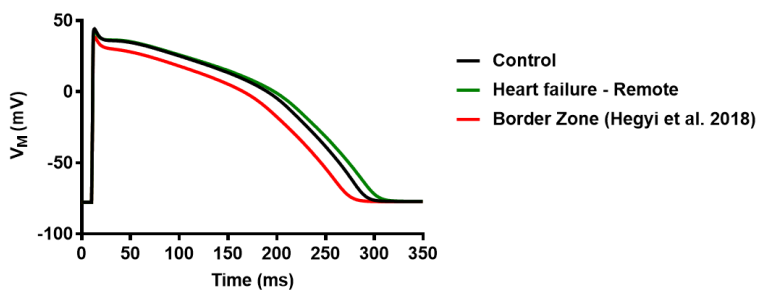


**Figure 6.16:** Impact of fibrosis on reentrant arrhythmias in the absence or presence of ethanol. Three degrees of fibrosis (mild, moderate and extensive) were simulated and the effects of ethanol in the presence of such structural remodeling were simulated. A) Random patterns of mild, moderate and extensive fibrosis. B) The vulnerable windows for reentry for the three degrees of fibrosis in baseline (0 mM), low (0.8 mM) and high (80 mM) ethanol concentrations in the right-atrial (RA) model with chronic atrial fibrillation (AF)-related remodeling. Bottom panels quantify total arrhythmogenic risk as the sum ( $\Sigma$ ) of vulnerable windows (i.e., the sum of reentry duration for all  $S_1S_2$  intervals tested). C) Similar to panel B for the human left-ventricular (LV) cardiomyocyte model with heart failure-related remodeling. (LV = left ventricle; RA = right atrium)

Subsequently, we investigated the potential impact of border-zone cardiomyocytes in HF after myocardial infarction (MI) on reentry in the presence of different concentrations of ethanol. Border-zone-associated electrical remodeling of cardiac ion channels (**Figure 6.17**) and a 50% reduction in intercellular coupling with border-zone cardiomyocytes was simulated as previously reported (375, 377, 378). The effect of ethanol was subsequently investigated when the border zone was applied to the fibrotic tissue for the three different degrees of fibrosis presented in **Figure 6.16A**. The mild fibrosis model contained 7% border zone, the moderate fibrosis model contained 21% border zone and the extensive fibrosis model contained 27% border zone (**Figure 6.18A**). Surprisingly, the presence of border-zone cardiomyocytes did not have a significant impact on reentry in the presence of mild or moderate fibrosis, independent of the absence or presence of ethanol. With extensive fibrosis, the presence of border-zone cells even reduced the duration of reentry and resulted in fewer episodes of stable reentry, particularly in the presence of ethanol (**Figure 6.18B**). Under these conditions, electrical conduction through a number of conduits between patches of fibrosis was blocked in the presence of border zone-related conduction abnormalities, thus reducing the likelihood of stable reentry (**Online Video 3**).



Ionic current	Control	Heart failure (remote)	Border Zone (Hegyi et al. 2018)
$I_{Na}$	100%	91%	79%
$I_{NaL}$		145%	106%
$I_{NCX}$		139%	114%
$I_{Ca,L}$		104%	51%
$I_{Ks}$		116%	79%
$I_{Kr}$		103%	100%
$I_{K1}$		91%	86%

\*Net charge

**Figure 6.17:** The simulated cardiomyocyte APs comparing the control model, the heart failure model (remote area) and the border zone. The Passini human left ventricular model was employed and subsequent ionic changes as reported by Hegyi et al. (375) were applied. The ionic changes employed to the model were shown in the table. The border-zone ionic changes were displayed relative to control.

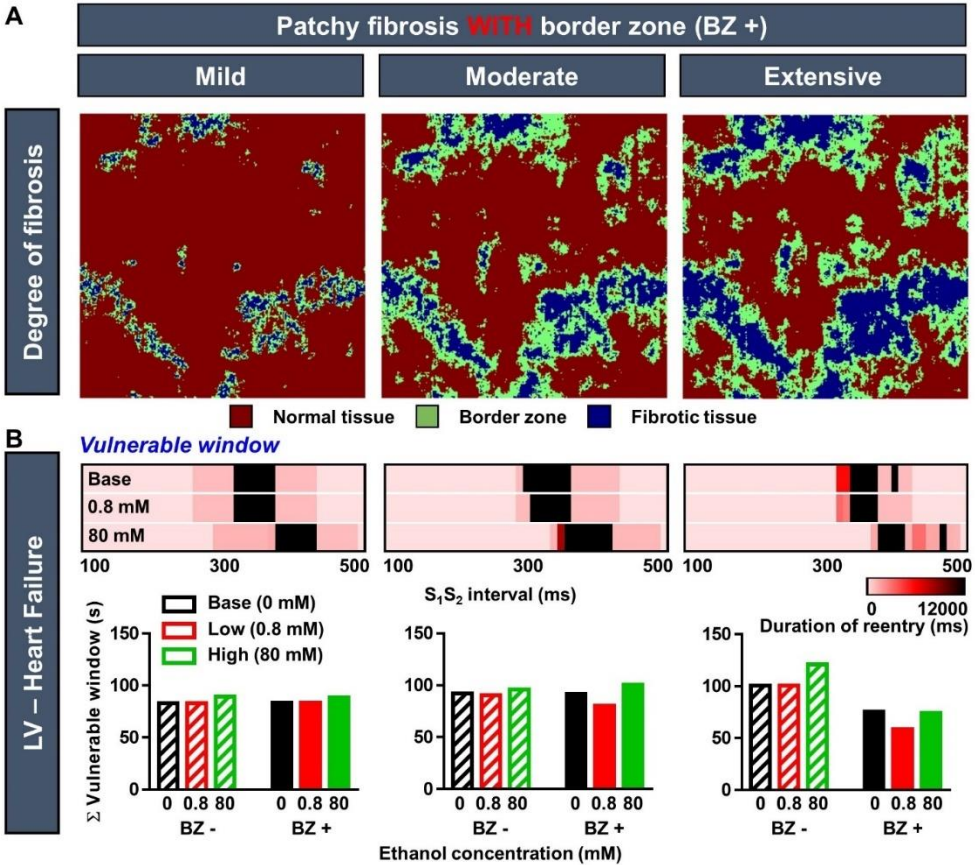


**Figure 6.18:** The impact of border-zone-associated remodeling on ethanol-dependent modulation of reentrant arrhythmias. A) Random patterns of mild, moderate and extensive fibrosis with border zone (light green color). Border zone was incorporated by applying both cellular remodeling and 50% reduction of intercellular coupling, as previously reported (375, 377, 378). B) Reentry vulnerable windows of conditions with border zone, as well as the sum ( $\Sigma$ ) of vulnerable windows comparing conditions without (hatched bars, from Figure 6.16C) and with border zone, for baseline, low (0.8 mM) and high concentration (80 mM) of ethanol. (BZ = border zone; LV = left ventricle)

Besides the degree of fibrosis, we also investigated the effects of different types of randomly generated fibrosis (patchy, compact and diffuse (390)) on ethanol-associated reentrant arrhythmias (Figure 6.19A). We initially simulated a mild degree of fibrosis (4-5% fibrosis) for all three fibrosis types. However, as previously reported (391), the 4% diffuse fibrosis significantly impaired wave propagation. Therefore, we had to reduce the amount of fibrosis to 1.2% to maintain wave propagation throughout the tissue. Nevertheless, the effects of ethanol on reentry were consistent among the three types of fibrosis, with a reduction of total arrhythmogenic risk for low ethanol concentrations and an increased risk with high ethanol concentrations in the atria (Figure 6.19B). In the ventricles, low ethanol concentrations did not affect arrhythmogenic risk, whereas high concentrations increased the risk substantially (Figure 6.19C). The three fibrosis patterns produced different behaviors of reentrant waves, which was partly influenced by the rotor tip stability (Figure 6.10) and ethanol-

induced ion channel remodeling (**Online Video 4-6**). **Online Video 5** displays three types of reentrant waves that can occur with different ethanol concentrations in the presence of compact fibrosis: stable reentry anchored to the fibrosis, functional reentry occurring independent from the fibrosis and unstable reentry with multiple wavelets. The latter two only occurred in the presence of high concentrations of ethanol.

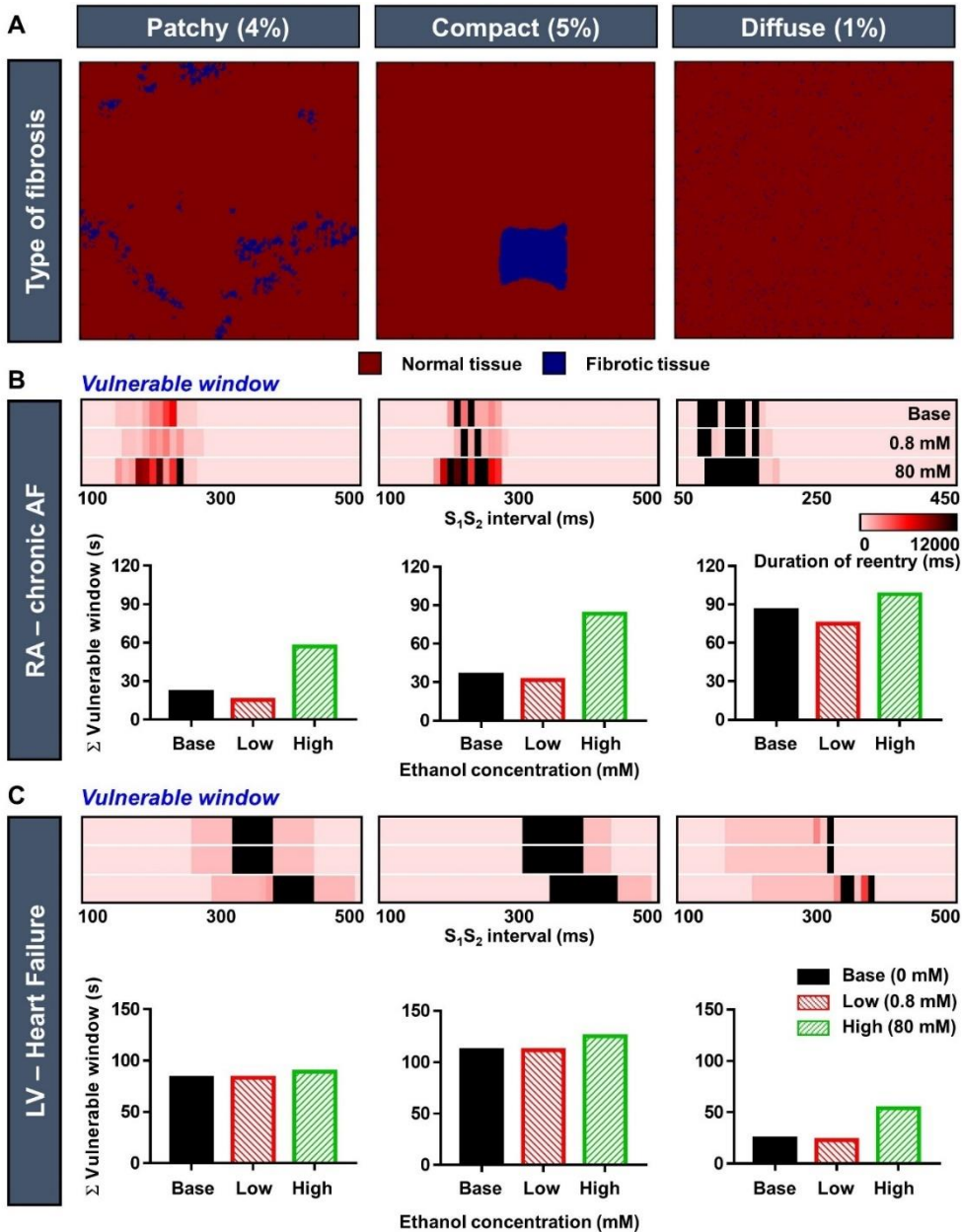


**Figure 6.19:** Ethanol-induced reentrant arrhythmias in the presence of different types of fibrosis. A) Three types of fibrosis: patchy, compact and diffuse fibrosis, all representing mild structural remodeling. B) The

vulnerable windows for reentry for the three types of mild fibrosis at baseline (0 mM) and for low (0.8 mM) and high (80 mM) ethanol concentrations in the right-atrial (RA) model with chronic atrial fibrillation (AF)-related remodeling. Bottom panels quantify total arrhythmogenic risk as the sum ( $\Sigma$ ) of reentry duration for each vulnerable window. C) Similar to panel B for the human left-ventricular (LV) cardiomyocyte model with heart failure-related remodeling. (LV = left ventricle; RA = right atrium)

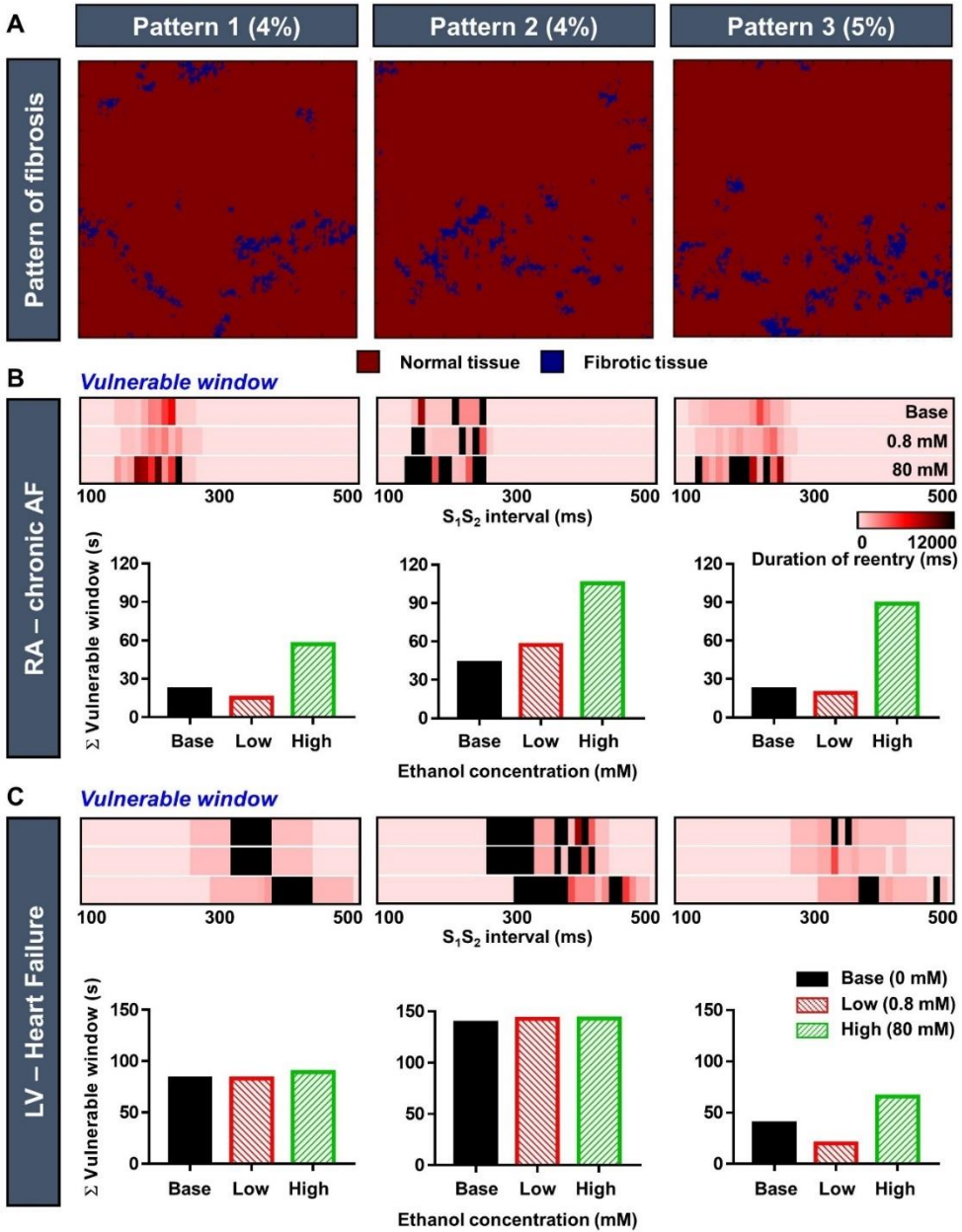


**Figure 6.20:** Fibrosis pattern and ethanol-induced reentrant arrhythmias. A) Three random patterns of fibrosis, all representing mild structural remodeling. B) The vulnerable windows for reentry for the three patterns of mild patchy fibrosis in baseline (0 mM), low (0.8 mM) and high (80 mM) ethanol concentrations

in the right-atrial (RA) model with chronic atrial fibrillation (AF)-related remodeling. Bottom panels quantify total arrhythmogenic risk as the sum ( $\Sigma$ ) of reentry duration for each vulnerable window. C) Similar to panel B for the human left-ventricular (LV) cardiomyocyte model with heart failure-related remodeling. (LV = left ventricle; RA = right atrium)

Finally, we investigated whether the configuration of patchy fibrosis also affected reentry behavior in the absence or presence of ethanol. Three different random patterns of patchy fibrosis with similar mild degrees of fibrosis (4-5%) were generated (**Figure 6.20A**). As shown in **Figure 6.20B**, all patterns demonstrated markedly different reentry behavior with pattern 2 being the most proarrhythmic pattern of the three random fibrosis patterns tested, exhibiting stable reentries for all ethanol concentrations, even in the baseline cAF model (0 mM ethanol). Consistent with our simulations in the absence of structural remodeling, high concentrations of ethanol increased the stability of reentrant waves and led to more episodes of stable reentry in all patterns (**Figure 6.20B**), highlighting the proarrhythmic effects of ethanol in high concentrations, independent of the pattern of fibrosis. However, the electrophysiological effects of low ethanol concentrations were pattern dependent, with proarrhythmic effects in some patterns (**Figure 6.20B, pattern 2**) similar to the results in homogeneous cAF tissue (**Figure 6.9B**), and antiarrhythmic effects in other patterns.

In the HF model, pattern 2 also presented the most proarrhythmic behavior, resulting in several isolated  $S_1S_2$  intervals with stable reentry surrounded by intervals with unstable or no reentry (**Figure 6.20C, Online Video 7-8**). By contrast, pattern 3, which numerically has the largest amount of fibrosis (5%), resulted in the lowest total reentry vulnerability. In line with the effects in homogeneous tissue, ethanol shifted the vulnerable window towards longer  $S_1S_2$  intervals in all patterns. However, the effect of ethanol on total reentry vulnerability was pattern dependent, with limited concentration-dependent effects in pattern 1, but a strong concentration-dependent effect in pattern 3 (**Figure 6.20C**).

## 6.4 Discussion

In this study, we evaluated the acute effects of ethanol on cardiac electrophysiology and reentrant arrhythmias using a multiscale computational modeling approach. To the best of our knowledge, our study is the first to exploit the perfect control and observability offered by a multiscale *in-silico* approach to unravel the arrhythmogenic consequences of ethanol-induced ion-channel and gap-junction regulation in the absence and presence of a preexisting substrate. Using this approach, we demonstrated that ethanol had concentration-dependent electrophysiological effects, with high concentrations of ethanol promoting both the inducibility and stability of reentrant arrhythmias, particularly in the presence of disease-associated remodeling. The exact proarrhythmic effects were cell-type dependent and influenced by disease-related gap-junction remodeling, as well as the degrees, types, and patterns of structural remodeling commonly accompanying underlying pathologies.

### 6.4.1 Ethanol and cardiac ion channels

Ethanol dose-dependently affects multiple cardiac ion channels, including  $I_{Na}$ ,  $I_{Ca,L}$ ,  $I_{to}$ ,  $I_{K1}$ ,  $I_{Kr}$  and  $I_{NCX}$  in both atrium and ventricle, as well as  $I_{Kur}$  and  $I_{K,ACh}$  in atrium (**Figure**

**6.1A).** Although the exact molecular mechanisms of ethanol-dependent ion-channel regulation have not been fully elucidated, several publications have shown that ethanol can alter ionic-current gating properties, leading to changes in channel open probabilities. For example, ethanol reduced the open probability and availability of cardiac sodium channel at moderate to high concentrations (392). The family of G-protein coupled inward-rectifier potassium channels is activated by alcohols through a hydrophobic alcohol-binding pocket in the cytoplasmic domain in a phosphatidylinositol-4,5-bisphosphate (PIP<sub>2</sub>)-dependent manner. However, mutations in the proposed alcohol-binding pocket of Kir2.1 channels did not affect ethanol-dependent inhibition of I<sub>K1</sub>, suggesting potentially different binding sites for activation and inhibition of I<sub>K1</sub> by ethanol (393).

In addition to direct ion-channel modifications, ethanol can activate intracellular signaling pathways, e.g., through oxidative stress and CaMKII, altering calcium-handling proteins, including SERCA2a activity and SR calcium leak, as well as reducing calcium-transient amplitude and myofilament calcium sensitivity (370, 371). These calcium-handling abnormalities may then affect transmembrane ion channels via their calcium-dependent regulation (394) and therefore, contribute to ethanol-induced AP changes.

By reproducing whole-cell ion-currents measured in cardiomyocytes in the presence of different concentrations of ethanol, our computational approach incorporates all functional consequences of ethanol on these ion channels, independent of the exact underlying molecular mechanism.

#### **6.4.2 The potential cardioprotective effects of low ethanol concentrations**

The potential protective effects of low and moderate alcohol intake on cardiovascular health has been studied for decades. Moderate alcohol consumption lowered the morbidity and mortality risks from cardiovascular diseases, and led to more favorable cardiovascular health profiles (358, 395). Moreover, although ethanol consumption was associated with an increased risk of AF, the attributable risk of ethanol consumption within recommended limits without acute excessive episode (binge) drinking was insignificant (396).

Our *in-silico* study employing both human RA and LV models demonstrated the antiarrhythmic effect of acute low concentrations of ethanol in the RA model. Low ethanol concentrations slightly prolonged the atrial APD, depolarized the RMP and reduced the reentry duration, without significantly affecting ventricular electrophysiology. The atrial APD prolonging effect is retained in the presence of cAF-related remodeling, although in the two-dimensional tissue simulations, the antiarrhythmic effect was diminished. Ethanol-induced I<sub>K1</sub> inhibition was responsible for the effects on atrial APD and reentry, consistent with previous experimental and computational studies highlighting the importance of I<sub>K1</sub> in rotor stabilization and fibrillation termination (347, 397). However, the reduction in I<sub>K1</sub> by low concentrations of ethanol could not overcome the cAF-induced increase in I<sub>K1</sub> (340), which removed the protective effects of ethanol at the tissue level and led to an increased stability of reentrant waves in cAF. In addition, differences in ion-channel properties and distribution (e.g., higher availability of I<sub>Na</sub>, lower expression of the ancillary subunit β<sub>1</sub>

of Nav1.5 and greater  $I_{K1}$ ) in the LV compared to RA may explain the absence of protective effects of low ethanol concentrations in the LV model (398). In general, extrapolation of these findings to long-term cardioprotective effects of low alcohol intake is challenging given ethanol's many systemic effects.

Our computer simulations also suggested potential protective effects of high concentrations of ethanol in the LV models without ethanol-induced gap-junction remodeling (**Figure 6.13**). This effect was achieved due to APD prolongation derived from ethanol-induced  $I_{Kr}$  block and  $I_{NCX}$  augmentation (**Figure 6.15**). Although epidemiological data have suggested possible benefits of moderate drinking on the risk of HF and mortality after onset of HF (399), our *in-silico* study indicates that acute antiarrhythmic effects were only present in the absence of substantial alterations to the intercellular coupling, which would only apply to the earliest stage of HF (386). These data are consistent with known antiarrhythmic effects of class-III antiarrhythmic drugs, as well as with their proarrhythmic potential in the presence of structural remodeling.

#### 6.4.3 The detrimental effects of high ethanol concentrations

The detrimental effects of acute excessive ethanol consumption have been described in many studies (358, 362, 363, 372, 395). Ethanol alters cardiac cellular electrophysiology, acutely slowing the conduction velocity (364, 385). Chronically, ethanol further impairs excitation-contraction coupling and promotes structural remodeling, including LV dilatation, reduced LV wall thickness and increased LV mass. In advanced stages, this leads to a reduction in LV ejection fraction and the development of an alcoholic cardiomyopathy (372, 389). Here, we confirmed the acute detrimental effects of high ethanol concentrations and provide new insights on the underlying mechanisms. In particular, high ethanol concentrations shortened APD and hyperpolarized the RMP in the atrial model, promoting reentry. These effects resulted mainly from the ethanol-induced increase of  $I_{K1}$ , opposed partially by increased  $I_{NCX}$  and decreased  $I_{Kr}$ . The ethanol-induced hyperpolarization of the RMP in the atria is vital, as it may increase the availability of  $I_{Na}$  and further enhances cardiac excitability (397). By contrast, ethanol-induced augmentation of  $I_{NCX}$  and inhibition of  $I_{Kr}$  prolonged APD in the ventricle, both in the control and HF models. The ethanol-induced conduction velocity slowing in cardiac tissue further increased the propensity for reentrant arrhythmias. Particularly in HF, the combination of disease- and ethanol-induced  $I_{Na}$  and gap-junction remodeling produced substantial conduction slowing, consistent with experimental observations (387).

Ethanol also promotes SR calcium leak and increases SERCA uptake and NCX function, promoting diastolic SR calcium release events and reduces the calcium-transient amplitude (370). The latter then alters excitation-contraction coupling and impairs cardiac contractility. Although more detailed, spatial calcium-handling models are required to simulate spontaneous SR calcium release events (394), in our *in-silico* study, the Passini human LV model similarly showed an ethanol-dependent reduction of calcium-transient amplitude (**Figures 6.7-6.8**). Despite similar concentration-dependent regulation of  $I_{NCX}$  and SR calcium leak by ethanol in the atrial and ventricular models (**Figure 6.1C**), the ethanol-dependent reduction in calcium-transient amplitude was not present in the RA model, likely due to baseline differences in calcium handling between both models and the complex interplay and counteracting effects of ethanol-

dependent regulation of SERCA, NCX and SR calcium leak (Figure 6.21). The larger calcium-transient amplitude in the RA model than in the LV model (Figure 6.21) also contributes to the large effect of ethanol-dependent  $I_{NCX}$  regulation in the RA model (Figure 6.3E).

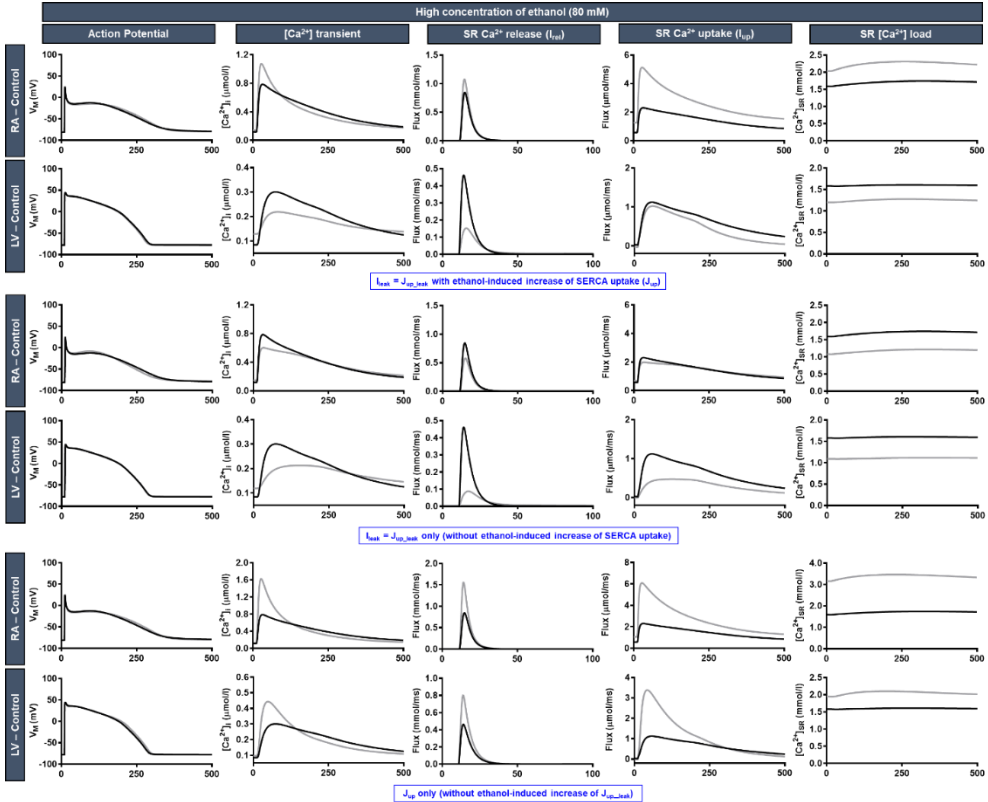


**Figure 6.21:** The acute effects of ethanol on calcium-handling proteins. As reported by Mustroph et al. (370), in addition to the increase of  $I_{NCX}$ , ethanol also increased the SERCA uptake and SR calcium leak. The implication of ethanol-induced remodeling of SERCA and SR calcium leak on calcium-handling proteins was analyzed. The upper panel showed the combination of both increased SERCA uptake and SR calcium leak. The middle panel showed the effect of increasing SR calcium leak only. The lower panel displayed the effect of increasing SERCA uptake only. All simulations were performed under high concentration of ethanol (80 mM) in both control human right atrial and human left ventricular models.

#### 6.4.4 The role of multiscale computational modeling in predicting the impact of ethanol-induced arrhythmias

Despite the strong clinical association between excessive alcohol consumption and cardiovascular morbidity and mortality, the interaction between disease-related cardiac remodeling and ethanol-induced changes in cardiac electrophysiology has not been fully elucidated. Using the perfect control and observability provided by computational modeling, we were able to predict the acute effect of ethanol in the presence of cAF or HF-related ion-channel and calcium-handling remodeling, as well as in the presence of different degrees, types and patterns of structural remodeling (i.e., fibrosis). We show that the degree, type and pattern of fibrosis play an important role

in the proarrhythmic effects of ethanol. In particular, our analyses reveal that the impact of fibrosis depends significantly on the baseline rotor behavior. For example, extensive fibrosis has a smaller effect on a stable rotor core compared to a meandering core, because collisions with fibrotic tissue and subsequent wave break occur more frequently in the latter condition. This effect can be seen in **Figure 6.16**, where the high concentration of ethanol reduced the duration of reentry in cAF model (which exhibited a more meandering core) yet increased it in HF model (which showed a more stable core) with extensive fibrosis. Thus, at the tissue level, the potential proarrhythmic effects of high ethanol concentrations strongly depend on the preexisting substrate. This highlights the potential benefit of a personalized computational modeling approach to accurately address the clinical implication of ethanol-induced arrhythmias. Cardiac imaging modalities, such as magnetic resonance imaging (MRI) can provide personalized scar patterns, including the border zone area. Such imaging information may function as an input for modeling work, replacing the randomly assigned fibrosis that was used in the present study. However, the spatial resolution of MRI is still relatively limited and may not be sufficient to capture detailed fibrotic patterns, although specialized sequences with improved resolution are being developed (400).

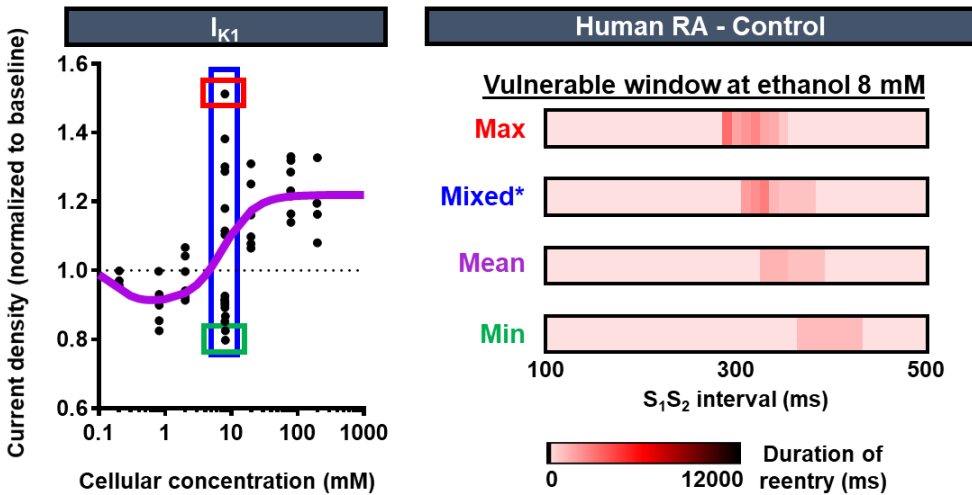
#### 6.4.5 Study limitations

We investigated the effects of ethanol using extensively validated and well accepted human atrial and ventricular cardiomyocyte models. However, the available *in-vitro* data for the acute effects of ethanol on cardiac ion channels were obtained in different animal models. We assumed that the relative changes were similar across species. Furthermore, significant cell-to-cell variability in the acute effects of ethanol have been described (366, 367) and may result in diverse effects at higher scales (**Figure 6.22**) (401). For example, although one study showed a dual effect of ethanol on  $I_{K1}$  (366), another study failed to show any significant effect of ethanol on the channel formed by Kir2.1 subunits (402), which prevail in the ventricles. Some of the variability may be due to differences in the stoichiometry of the ion channels (403), although the exact mechanism needs to be further investigated. Our simulations using populations of models show that cell-to-cell variability in ion-channel expression (**Figure 6.12**), as well as variability in ethanol-dependent  $I_{K1}$  regulation can principally affect reentry vulnerability (**Figure 6.22**), but since the pattern of variability in ethanol-dependent regulation in tissue is unknown, this aspect was not elaborated further.

In this study, we primarily simulated low (0.8 mM) and high (80 mM) cellular ethanol concentrations. However, *in vivo*, the local ethanol concentrations observed by cardiomyocytes depend on a variety of dynamic pharmacokinetic factors. Pharmacokinetics/-dynamics models exist and, in the future, could be implemented to obtain a more precise simulation of the electrophysiological consequences of different ethanol consumption patterns.

In our models, the disease- and border zone-associated, as well as the ethanol-induced alterations of intercellular coupling were equal in the transversal and longitudinal directions. However, anisotropy is acknowledged as an important determinant of reentry (347). Together with the structural heterogeneity of the cardiac tissue (e.g., fibrosis / scar), it alters the initiation and maintenance of reentrant waves. Similarly, the complex electrophysiological effects of ethanol may also be supported by

autonomic remodeling including acute activation of the sympathetic nervous system and vagal inhibition (364), which can produce spatial heterogeneous alterations in cardiac electrophysiology that have not been taken into account in our model. However, both components are expected to exacerbate the potential proarrhythmic effects that we characterized here. Finally, the role of potential atrioventricular interactions in generating cardiac arrhythmias has not been accommodated in our cell and tissue simulations. In the future, such interactions could be studied using whole-heart modeling approaches.



\*) Mixed  $I_{K1}$  densities from -20% (min) to +65% (max) was applied randomly and uniformly distributed.

**Figure 6.22:** The consequence of cell-to-cell variability of  $I_{K1}$  on the ethanol-induced reentrant arrhythmias. The experimental cell-to-cell variability of  $I_{K1}$  is shown on the left as black dots. The purple line indicates the mean  $IC_{50}$  values used as a modeling input. Two-dimensional tissue simulations were performed at 8mM ethanol and divided into 4 groups: The group incorporating only the maximum value of ethanol-induced  $I_{K1}$  remodeling, i.e., +65% (red box), the minimum only, i.e., -20% (green box), the mean value (purple) and the heterogeneous group, incorporating mixed  $I_{K1}$  densities from -20% to +65% (min to max) that were applied randomly and distributed uniformly (blue).

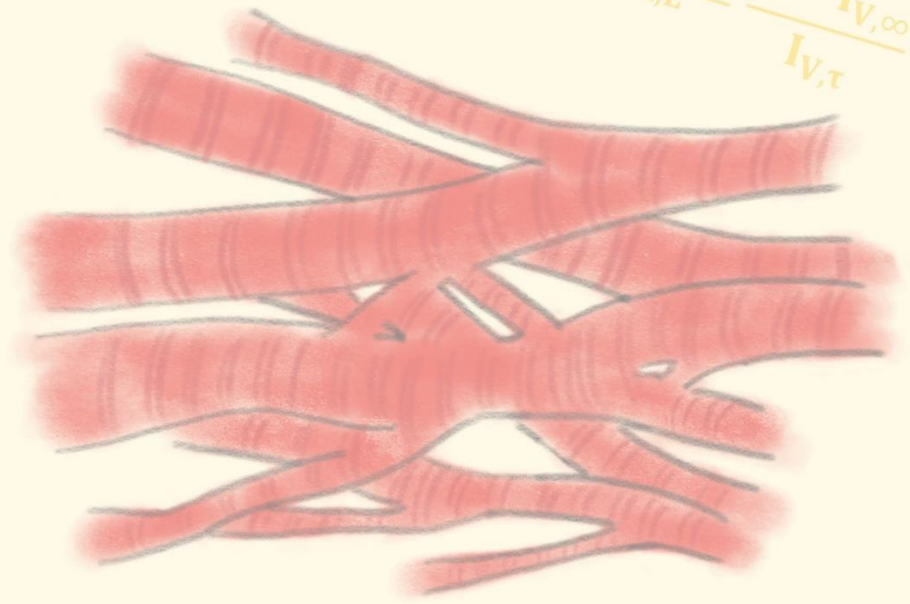
## 6.5 Conclusions

Our multiscale *in-silico* study provides new insights into the acute effects of ethanol on cardiac electrophysiology and arrhythmogenesis, demonstrating that ethanol has concentration-dependent electrophysiological effects that differ between atria and ventricles, and in the absence or presence of disease-related remodeling. Low concentrations of ethanol could have antiarrhythmic effects in the atria whereas high concentrations may promote reentrant arrhythmias. Ethanol-induced gap-junction remodeling is an important determinant of ethanol-induced reentrant arrhythmias. The exact proarrhythmic risk depends on the degree, type and pattern of disease-associated structural remodeling, and may be modulated by other co-factors, including autonomic nervous influences. Together, these findings highlight the necessity for a personalized multiscale computational modeling approach to better predict the consequences of ethanol on cardiac electrophysiology in humans.



$$\frac{dV_m}{dt} = -\frac{1}{C_m} * I$$

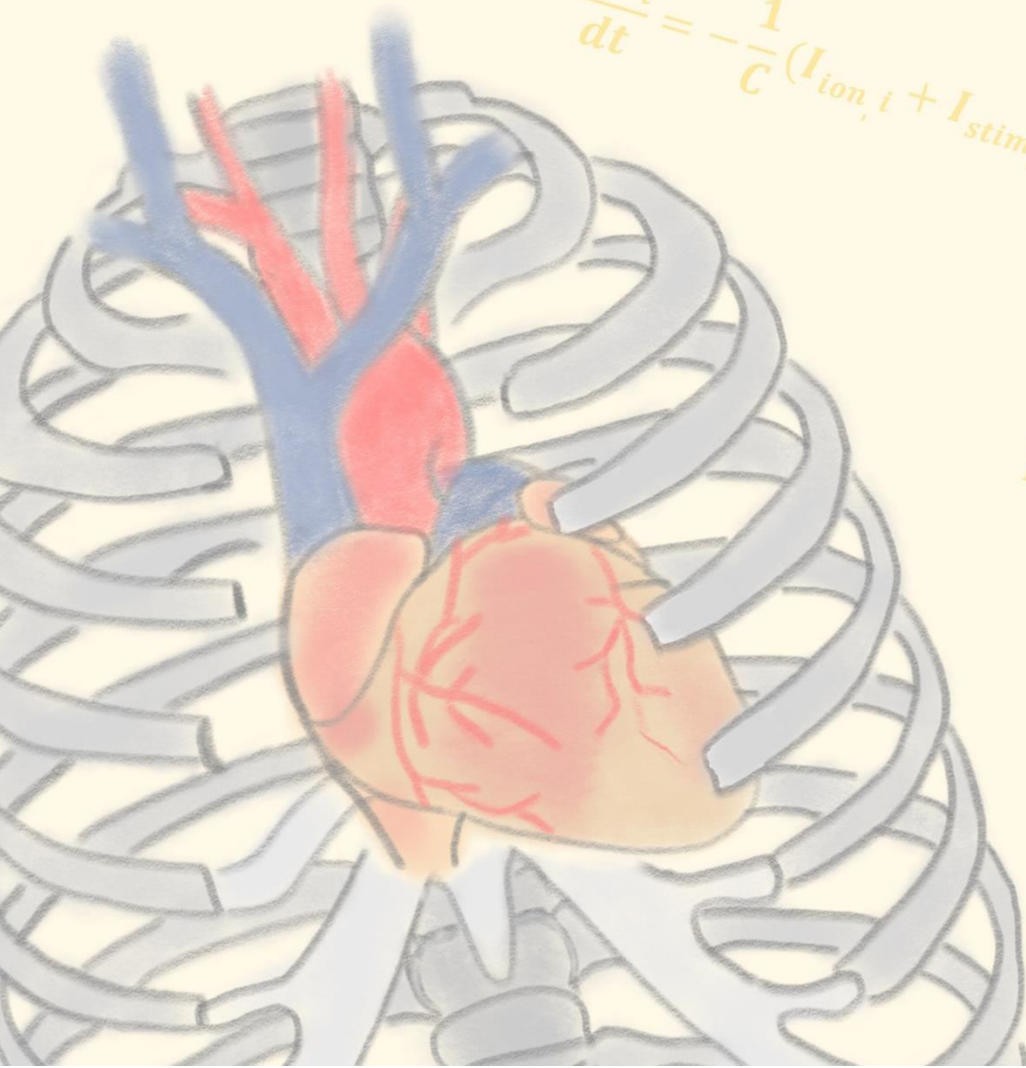
$$y_{Ca,L} = \frac{1 - I_{V,\infty}}{I_{V,\tau}}$$



$$x_{Ca,L} = \frac{I_{V,\infty}}{I_{V,\tau}}$$

$$\delta I_{Ca,L}^{s,m} =$$

$$\frac{dV_i}{dt} = -\frac{1}{C} (I_{ion,i} + I_{stim,i} + I_{diff,i})$$



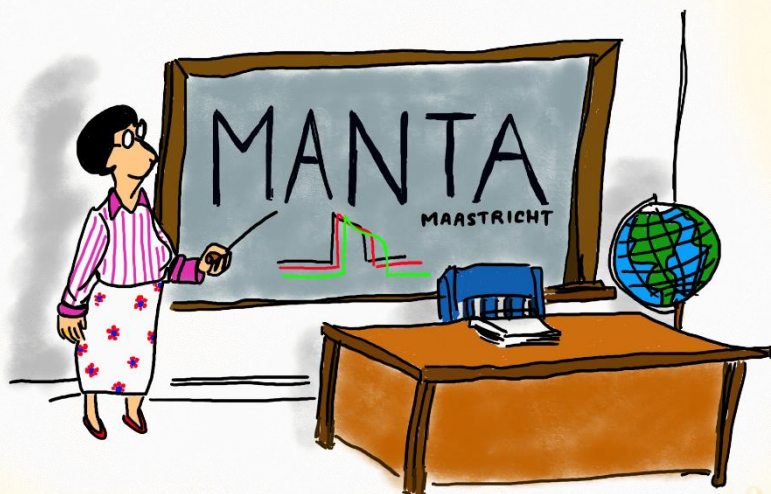
$$\bar{I}_{Ca,L}^{s,m} = P_{Ca,L} \cdot (z$$

$$ACT_{\tau} = 0.59$$

# Chapter 7

## Maastricht ANTIarrhythmic drug evAluator (MANTA): A computational tool for better understanding of antiarrhythmic drugs

H. Sutanto, L. Laudy, M. Clerx, D. Dobrev, H.J.G.M. Crijns and J. Heijman  
*Pharmacol Res.* 148:104444.



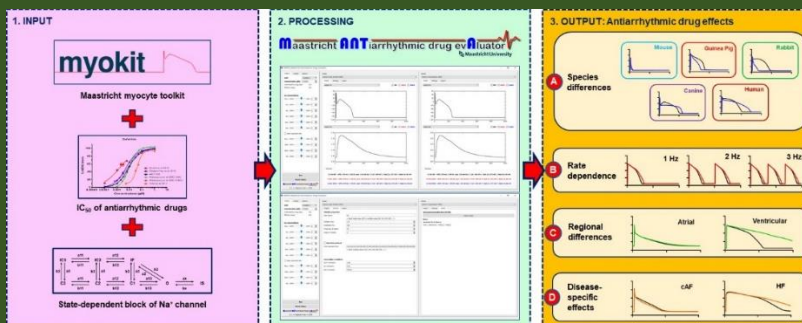
$$\frac{dV}{dt} = \frac{I_{stim} - (I_K + I_{Na} + I_{leak})}{C_m}$$

## ABSTRACT

Cardiac arrhythmias are a global health burden, contributing significantly to morbidity and mortality worldwide. Despite technological advances in catheter ablation therapy, AADs remain a cornerstone for the management of cardiac arrhythmias. Experimental and translational studies have shown that commonly used AADs exert multiple effects in the heart, the manifestation of which strongly depends on the exact experimental or clinical conditions. This diversity makes the clinical application of AADs challenging.

Here, we present a novel computational tool designed to facilitate a better understanding of the complex mechanisms of action of AADs (the Maastricht ANTIarrhythmic drug evAluator, MANTA). In this tool, we integrated published computational cardiomyocyte models from different species (mouse, guinea pig, rabbit, dog, and human), regions (atrial, ventricular, and Purkinje cells) and disease conditions (atrial fibrillation- and heart failure-related remodeling). Subsequently, we investigated the effects of clinically available AADs (Vaughan-Williams Classes I, III, IV and multi-channel blockers) on AP properties and the occurrence of proarrhythmic effects such as early afterdepolarizations. Steady-state drug effects were simulated based on a newly compiled overview of published  $IC_{50}$  values for each cardiac ion channel and by integrating state-dependent block of the cardiac sodium current by Class I AADs using a Markov-model approach. Using MANTA, we demonstrated and characterized important species-, rate-, cell-type-, and disease-state-specific AAD effects, including 1) a stronger effect of Class III AADs in large mammals than in rodents; 2) a rate-dependent decrease in upstroke velocity with Class I AADs and reverse rate-dependent effects of Class III AADs on action potential duration; 3) ventricular-predominant effects of pure  $I_{Kr}$  blockers; 4) preferential reduction in atrial AP upstroke velocity with vernakalant; and 5) excessive AP prolongation with Class III AADs other than amiodarone under heart failure conditions.

In conclusion, the effects of AADs are highly complex and strongly dependent on the experimental or clinical conditions. MANTA is a powerful and freely available tool reproducing a wide range of AAD characteristics that enables analyses of the underlying ionic mechanisms. Use of MANTA is expected to improve our understanding of AAD effects on cellular electrophysiology under a wide range of conditions, which may provide clinically-relevant information on the safety and efficacy of AAD treatment.



## 7.1 Introduction

Cardiovascular diseases are the leading cause of death and disability worldwide, with cardiac arrhythmias significantly contributing to cardiovascular deaths (404). Despite advances in catheter ablation therapy, AADs remain widely used for the treatment of arrhythmias. However, currently available AADs have limited efficacy and important safety limitations, notably an increased risk of ventricular proarrhythmia and extra-cardiac toxicity (405-407). Traditionally, AADs have been classified into Vaughan Williams Classes I-IV, targeting sodium channels,  $\beta$ -adrenoceptors, potassium channels and LTCC for Classes I, II, III and IV, respectively. However, experimental and translational research performed over the last 30 years has revealed that most AADs exert effects on multiple molecular targets and alternative classifications have been developed (5, 408, 409). In addition, the effects of AADs strongly depend on experimental/clinical conditions. For example, AADs exhibit species-dependent effects due to the distinct contribution of ion currents to the cardiac AP across species (410), which hinder the clinical translation of animal studies (411). Moreover, many AADs block ion channels in a rate- (or use-) dependent manner (412, 413). Some AADs (e.g. vernakalant and ranolazine) have preferential effects on atrial versus ventricular cardiomyocytes by targeting ion channels that are only expressed in the atria or preferentially inhibiting atrial sodium channels through state-selective blocking properties (414). Finally, disease-related remodeling can also influence the effects of AADs. These condition-dependent effects make a detailed understanding of the clinical efficacy of AADs highly challenging and contribute to the suboptimal use of currently available AADs under dynamic clinical conditions. Moreover, such effects may hinder the development of novel, more effective and safer AADs.

Computational models can integrate experimental and pharmacological findings, and provide perfect control and observability of parameters, enabling *in silico* experiments in a controlled setting (10, 12, 94). Several software tools have been developed to enhance the understanding of cardiovascular (patho) physiology, ranging from cellular electrophysiology to hemodynamics in the entire cardiovascular system (12). For example, the CircAdapt® model simulates cardiovascular mechanics and hemodynamics to study (patho)physiology of heart and circulation (415) and ECGSIM solves the forward problem of electrocardiology to compute electrograms at the body surface that result from user-defined electrical activity at the heart surface (416). Both have also been used for educational purposes. However, to simulate AAD effects, detailed models of cardiac cellular electrophysiology are needed. Several relatively user-friendly tools have been developed to simulate cardiac cellular electrophysiology (417-421). However, these tools often focus on a single model and are limited in their ability to compare (state-dependent) AAD effects. Thus, despite the relevance of understanding the complex effects of AADs under various conditions, there is, to the best of our knowledge, no software tool available that addresses this critical issue.

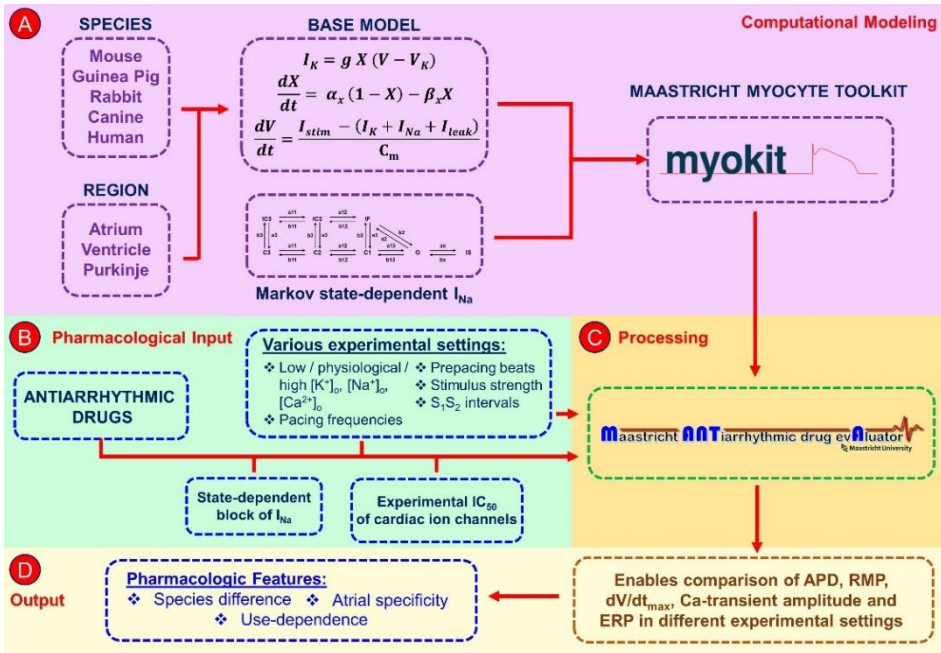


**Figure 7.1:** Maastricht Antiarrhythmic Drug Evaluator (MANTA) and its components. MANTA is developed as an extension of Myokit, a software tool designed for cardiac AP simulations (344). MANTA enables analyses of the effects of AADs on the AP under user-defined experimental settings by integrating a large number of *in silico* cardiomyocyte models of various species with a newly compiled overview of pharmacodynamic properties of AADs from different Vaughan-Williams Classes. (APD: action potential duration, RMP: resting membrane potential,  $dV/dt_{max}$ : upstroke velocity, ERP: effective refractory period,  $IC_{50}$ : half-maximal inhibitory concentration;  $I_{Na}$ : sodium current)

Here, we present a novel, user-friendly software tool (the Maastricht ANTIarrhythmic drug evAluator; MANTA) that enables analyses of species- and condition-dependent effects of a wide range of clinically relevant AADs on cardiac ion currents, as well as their downstream effects on AP and CaT properties (Figure 7.1). MANTA may facilitate a better understanding of the complex effects of AADs, thereby promoting improved use of these drugs during experiments as well as increased awareness of their limitations under specific clinical conditions. Finally, it can provide insight into the proarrhythmic side-effects of some AADs. In addition to its research use, MANTA can be employed to teach students about the mechanism-of-action of currently available AADs.

## 7.2 Methods

### 7.2.1 The Maastricht antiarrhythmic drug evaluator (MANTA)

MANTA was developed as an extension of Myokit, a python-based software tool designed for cardiac AP simulations (344). MANTA integrates a wide range of published cardiomyocyte models and AADs (based on their affinity for different cardiac ion channels, including state-dependent block of sodium channels, as detailed below). A graphical user interface was created, which provides easy access to settings, enabling

simulations of AAD effects under different conditions. A Python package was generated to facilitate installation of MANTA from the Python Package Index (PyPI) on Microsoft Windows-based platforms.

MANTA displays simulation results of two *in silico* cardiomyocyte models side-by-side (**Figure 7.2A**). By default, the AP and CaT are shown for both models, but drop-down lists enable visualization of all model variables, including intracellular ion concentrations and ion currents. Simulation of up to two clinically available AADs at user-defined concentrations enables comparison of the electrophysiological effects of these agents. In “custom” mode, the activity of individual ion channels can be adjusted to study the effect of these changes on the AP, enabling simulations of novel AADs. Moreover, in the “options” panel, several properties of the experimental environment can be adjusted (**Figure 7.2B**), including the number of pre-paced beats, pacing frequency and extracellular ionic concentrations ( $[K^+]_o$ ,  $[Na^+]_o$ , and  $[Ca^{2+}]_o$ ). The AP duration (APD), maximum AP upstroke velocity ( $dV/dt_{max}$ ) and CaT amplitude are automatically calculated for each model and condition. MANTA also enables the user to perform an  $S_1S_2$  protocol simulation to calculate the frequency-dependent effective refractory period (ERP), which is defined as the shortest interval after the start of the last stimulus allowing the generation of a new AP. We considered a new AP to be generated when maximal membrane potential after 75% of the current  $APD_{90}$  exceeded 80% of the peak of the current AP. Since this threshold may not be appropriate for all models and/or stimuli, manual confirmation of ERP detection is recommended. Subsequently, the results can be exported as comma-separated value (.csv) or text (.txt) files for further analysis (**Figure 7.2B**).

### 7.2.2 Incorporation of computational models of cardiac cellular electrophysiology

To investigate the effects of AADs at the cellular level, 17 previously published and validated *in silico* cardiomyocyte models (78, 263, 374, 422-430), reflecting different species, regions of the heart and disease-related remodeling, were incorporated into MANTA. Each model contains a number of ion currents and transporters with various degrees of complexity, ranging from basic Hodgkin-Huxley mathematical models to more complex Markov models. An overview of the computational cardiomyocyte models is provided in **Table 7.1**.

### 7.2.3 AADs available in the current version of MANTA

In total, 25 AADs belonging to Vaughan-Williams Classes I, III and IV, and exhibiting diverse cardiac ion-channel-blocking properties were included in MANTA (**Table 7.2**). AADs commonly used in clinical practice (flecainide, amiodarone) as well as more recent multi-channel blockers (e.g., vernakalant), were incorporated, but Class II AADs ( $\beta$ -blockers) were excluded from the tool due to the absence of  $\beta$ -adrenoceptor-signaling components in most of the available cardiomyocyte models. To model the effect of an AAD on a cardiac ion channel, its maximal conductance was scaled based on the given drug concentration and a sigmoidal Hill curve based on previously reported  $IC_{50}$ , as summarized in **Table 7.2**. Validation of each drug based on an overview of

*Maastricht antiarrhythmic drug evaluator (MANTA)*

published IC<sub>50</sub> values and dose-response curves is provided in **Table 7.3** and **Figure 7.3A-Y**. Moreover, based on these IC<sub>50</sub> values, AAD-induced changes in APD were largely consistent with experimental data in most models (**Figure 7.4**).

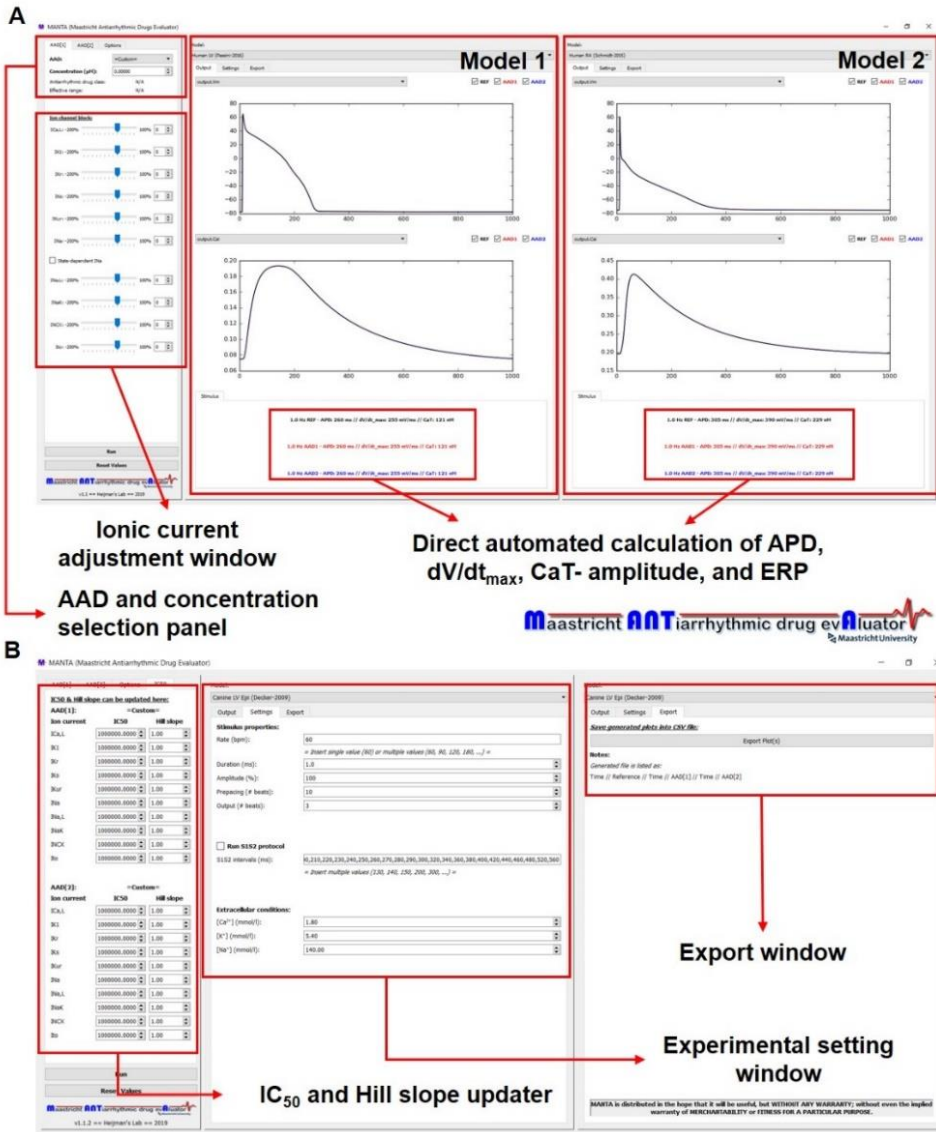


**Figure 7.2:** The MANTA graphical user interface. MANTA displays two cardiomyocyte models side-by-side and enables comparison of up to two AADs at a user-defined concentration. A) Main MANTA screen, comparing the simulation results of two different computational models side-by-side, whilst automatically calculating the APD,  $dV/dt_{max}$ , and CaT amplitude. B) Additional tabs in the MANTA interface enabling alterations in simulation settings (including pacing frequency and different extracellular ionic concentrations), alterations in the IC<sub>50</sub> and/or Hill coefficients of the selected drug for each ion-channel target, as well as allowing users to export the simulation results to comma-separated values (.csv) files for further analysis or data extraction.

No	Species	Region	First Author	Year	Citation
1	Mouse	LV	Bondarenko	2004	(422)
2	Guinea Pig		Luo	1991	(423)
3			Faber	2000	(424)
4	Rabbit		Mahajan	2008	(425)
5	Canine		Decker	2009	(426)
6			Heijman	2011	(78)
7	Human	LV (Endo)	O'Hara	2011	(263)
8			Passini	2016	(374)
9		LV(Mid)	O'Hara	2011	(263)
10		LV (Epi)	O'Hara	2011	(263)
11		HF LV (Endo)	Passini	2016	(374)
12		RA	Courtemanche	1998	(427)
13			Schmidt	2015	(428)
14		cAF RA	Courtemanche	1998	(427)
15			Schmidt	2015	(428)
16		Purkinje	Stewart	2009	(429)
17			Sampson	2010	(430)

**Table 7.1:** The computational cardiomyocyte models available in MANTA. LV: left ventricle, RA: right atrium, Endo: Endocardium, Mid: Midmyocardium, Epi: Epicardium, HF: heart failure, cAF: long-standing persistent ('chronic') atrial fibrillation.

	I <sub>Ca,L</sub>	I <sub>K1</sub>	I <sub>Kr</sub>	I <sub>Ks</sub>	I <sub>Kur</sub>	I <sub>to</sub>	I <sub>Na</sub>	I <sub>Na,L</sub>	I <sub>NaK</sub>	I <sub>NCX</sub>
<b>Class Ia</b>										
Ajmaline	70		1		1.7	14	28			
Cibenzoline	20	33.7	15				15	45		
Disopyramide	1037		11			21	168.4			
Procainamide	340	33	300	810			646			
Quinidine	10		0.7	5	5	3.5	12	10		
Quinine	27		5	37		79	24	11 (h=0.4)		
<b>Class Ib</b>										
Lidocaine							20	10.8		
Phenytoin	22.07		120				80.41			
Ranolazine	250		12	100			200	8		91

Class Ic										
Flecainide	27.1		1.6		2.9	10 (h=0.8)	6.5	20 (h=0.6)		
Propafenone	1.55		0.44	16		7.2	2.5	4		
Class III										
Ambasilide			3.6		35	23				
Acute amiodarone	1.5 (h=0.6)		3.0	100		3.8 (h=0.4)	5	9 (h=0.4)		3.4
Chronic amiodarone	1.5 (h=0.6)		0.8 (h=0.6)	20 (h=0.6)		3.8 (h=0.4)	5	9 (h=0.4)		3.4
Bepriidil	2.8		0.16	6.1			2.2	1.8		
Dofetilide	26.7		0.008	415			150			
Dronedarone	4		2	10			1 (h=1.7)			
E-4031			0.008							
Ibutilide	62.5		0.02				42.5			
Niferidil	100	203	0.0382	28	60	203				
Sotalol	2100	2500	100	3500			7000			
Vernakalant	84		20		15	15	90	14		
Class IV										
Diltiazem	0.45		13				22			
Nitrendipine	0.025	417	20	19.5			21.5			
Verapamil	0.2		0.5		2.2		35			

**Table 7.2:** List of AADs and their IC<sub>50</sub> values (in μM) and Hill coefficients for individual drug targets incorporated into MANTA. In total, MANTA includes 25 AADs, corresponding to Classes I, III and IV of the Vaughan-Williams classification, which can affect 10 major ion currents. Results are presented as IC<sub>50</sub> and Hill coefficient or IC<sub>50</sub> value only in case of a Hill coefficient of 1.0.

### 7.2.4 Incorporation of state-dependent sodium current block in cardiomyocyte models

Since Class I AADs have markedly different affinities for individual states of the sodium channel (open, closed, and inactivated) (431-433), we introduced a state-of-the-art sodium channel Markov model enabling simulation of state-dependent sodium channel block (Figure 7.5) (431) in each of the 17 cardiomyocyte models. The parameters of the baseline sodium current (I<sub>Na</sub>) Markov models were optimized to produce similar peak amplitude, non-inactivating late current, voltage dependence of activation and inactivation, time constants of inactivation and recovery from inactivation of I<sub>Na</sub>, along with upstroke velocity during current-clamp simulations as the original Hodgkin-Huxley models in the absence of AADs. Details of the I<sub>Na</sub> Markov model and the results of the optimization procedure are provided in Figure 7.5, 7.6.

The baseline Markov model was extended with drug-blocked states for neutral and charged fractions of Class I AADs, which have distinct affinities for open, closed and inactivated states (**Figure 7.5**) (431). In line with the approach by Moreno et al. (431), the parameters representing the affinities of flecainide and lidocaine for open, closed and inactivated states were fixed and parameters reflecting state transitions within blocked states were subsequently numerically optimized to reproduce experimentally observed drug-block properties for individual baseline  $I_{Na}$  Markov models (**Appendix B**). In particular, drug-induced shifts in steady-state availability, tonic block and rate-dependent block at 5 Hz for various AAD concentrations, as well as frequency dependence from 1 to 10 Hz and recovery from rate-dependent block by flecainide and lidocaine could be reproduced using this Markov model (**Figure 7.7**). Parameters for vernakalant were similarly optimized to reproduce the tonic, rate-dependent and voltage-dependent block observed in experimental studies (434).

**Table 7.3:** Published experimental  $IC_{50}$  values of antiarrhythmic drugs and final values used in MANTA

DRUG	SAMPLE ORIGIN	$IC_{50}$ OF CARDIAC ION CHANNELS ( $\mu M$ )										REF
		$I_{Ca,L}$	$I_{K1}$	$I_{Kr}$	$I_{Ks}$	$I_{Kur}$	$I_{to}$	$I_{Na}$	$I_{Na,L}$	$I_{NaK}$	$I_{NCX}$	
AJMALINE	Rat (V)	70.8± 0.09			61.0± 1.10		25.9± 2.91	27.8± 1.1 (holding - 75 mV), 47.2± 1.1 (holding - 120 mV)				(435)
	Oocytes					186± 31.4	292± 2.85					(436)
	CHO					1.70± 0.82	2.66± 2.8					(436)
	HEK293	71		1.04				8.2				(437)
	<b>MANTA</b>	<b>70</b>		<b>1</b>		<b>1.7</b>	<b>14</b>	<b>28</b>				
AMBASILIDE	Human (A)					34.2± 2.9	22.6± 1.9					(438)
	Canine (A)					37.5± 1.6						(439)
	Human (A)						23.3					(440)
	CHO			3.6								(441)
	<b>MANTA</b>			<b>3.6</b>		<b>35</b>	<b>23</b>					
ACUTE AMIODARONE	Rabbit (V)			2.8	minimal							(442)
	Oocytes			38	300							(442)
	Oocytes			9.8								(443)

Maastricht antiarrhythmic drug evaluator (MANTA)

	MANTA	1.5	3.0	100	3.8	5	9	3.4
CHRONIC AMIODARONE	HEK/CHO	1.28	0.94		3.76	4.58	9.423	(444)
	HEK/CHO	1.9	0.86			15.9		(445)
	HEK293	0.27	0.03			4.8		(437)
	Human (A)					59% at 3 $\mu$ M (4.3)		(446)
	Rabbit (A)					1.8 $\pm$ 1.1		(447)
	Rabbit (V)					40.4 $\pm$ 11.9		(447)
	Guinea pig (A)							3.3- 3.6 (448)
	N/A		1					(449)
	ChanTest	1.903	342.9	0.863	47.20		15.85	(450)
		<b>MANTA</b>	<b>1.5</b>	<b>0.8</b>	<b>20</b>	<b>3.8</b>	<b>5</b>	<b>9</b>
BEPRIDIL	ChanTest	1.048	87.72	0.159	6.156		2.271	(450)
	HEK/CHO	2.8	0.2			2.9	1.814	(444)
	HEK/CHO	1	0.16			2.3		(445)
	HEK293	0.211	0.033			3.7		(437)
	N/A		0.6					(449)
	HEK/CHO	0.175	0.074			0.517	0.411	(451)
		<b>MANTA</b>	<b>2.8</b>	<b>0.16</b>	<b>6.1</b>		<b>2.2</b>	<b>1.8</b>
CIBENZOLINE	Guinea pig (V)	30						(452)
	HEK/CHO		2.097			21.75	46.58	(444)
	N/A		23					(449)
	HEK293	30	22.6			7.8		(437)
	Guinea pig (V)	14.4	33.7	23		7.8		(453)
		<b>MANTA</b>	<b>20</b>	<b>33.7</b>	<b>15</b>		<b>15</b>	<b>45</b>
DILTIAZEM	HEK/CHO	0.112	6.569			>12.5		(444)
	Native heart cell		17.3					(454)
	N/A		10					(449)
	HEK/CHO	0.76	13.2			22.4		(445)

	HEK293	0.45		17.3				(437)	
	ChanTest	0.763	900	13.18	68.99		22.44	(450)	
	<b>MANTA</b>	<b>0.45</b>		<b>13</b>			<b>22</b>		
DISOPYRAMIDE	N/A			1.8				(449)	
	Rat (V)			37.2± 0.17		20.9± 0.13		(455)	
	CHO			7.23± 0.72				(456)	
	Model	1037		10.66 ±0.04		259	168.4	(457)	
	HEK/CHO	1037		14.4			168.4	(445)	
	<b>MANTA</b>	<b>1037</b>		<b>11</b>		<b>21</b>	<b>168.4</b>		
DOFETILIDE	HEK/CHO	>0.01	>0.01	0.002	>0.01	>0.01	>0.01	>0.01	(444)
	HEK/CHO	26.7		0.03			162.1	(445)	
	HEK/CHO	26.7		0.005	415.8		147.9	(451)	
	Oocytes			0.11± 0.01				(458)	
	Guinea pig (V)			0.009 ± 0.002				(458)	
	CHO			0.01± 0.002				(458)	
	HEK293			0.036				(459)	
	AT1-cells			11.2± 1.9				(460)	
	AT1-cells			0.012				(461)	
	N/A			0.005				(449)	
	HEK293			0.039				(462)	
	HEK293	60		0.005			300	(437)	
	<b>MANTA</b>	<b>26.7</b>		<b>0.008</b>	<b>415</b>			<b>150</b>	
DRONEDARONE	Human (A)						I <sub>Na</sub> 77% at 0.3 μM, 3% at 3 μM (0.55)	(446)	
	Guinea pig (V)	0.18	>30	2	10			(463)	
	Canine (V)	24% at 10 μM (3.2)						(464)	
	<b>MANTA</b>	<b>4</b>		<b>2</b>	<b>10</b>			<b>1</b>	

*Maastricht antiarrhythmic drug evaluator (MANTA)*

E-4031	Human (A)			N.S.	N.S.			(438)
	Oocytes		0.17± 0.03					(458)
	Guinea pig (V)		0.010					(458)
	CHO		0.006					(458)
	Model		0.016					(457)
	<b>MANTA</b>		<b>0.008</b>					
FLECAINIDE (★)	HEK/CHO	>20	0.7	>20	9.27	6.7	18.9	(444)
	Oocytes					41		(465)
	HEK/CHO	27.1	1.5			6.2		(445)
	HEK293		3.91± 0.68					(466)
	Human (A)			N.S.	12			(467)
	HEK293		1.7			11		(459)
	RVW					10.7		(468)
	Canine (A)				2.9± 0.24			(439)
	N/A		3.91					(449)
	HEK293				38.14 ±1.06			(469)
	<b>MANTA</b>	<b>27.1</b>	<b>1.6</b>	<b>2.9</b>	<b>10</b>	<b>6.5</b>	<b>20</b>	
IBUTILIDE	Oocytes		0.028					(470)
	Mouse AT-1 cell		0.02					(461)
	N/A		0.010					(449)
	HEK/CHO	62.5	0.018			42.5		(445)
	ChanTest	62.5	75.6	0.018	192.4		42.42	(450)
	<b>MANTA</b>	<b>62.5</b>	<b>0.02</b>			<b>42.5</b>		
LIDOCAINE (★)	HEK/CHO					>15	10.8	(444)
	Oocytes					521		(465)
	HEK293		N.S.					(466)
	Human					Resting = 96.21, Inact state = 17.12		(471)

	hNav1.5-CW							Resting = 606±15, Open = 35.3±2.7	(472)
	<b>MANTA</b>							<b>20 10.8</b>	
NIFERDIL	Guinea pig (A)			0.001					(473)
	Guinea pig (V)			0.038					(473)
	Mouse (V)	100	203		28	60	203		(474)
	<b>MANTA</b>	<b>100</b>	<b>203</b>	<b>0.038</b>	<b>28</b>	<b>60</b>	<b>203</b>		
NITREN-DIPINE	ChanTest	0.025	417.1	20.09	19.52			21.58	(450)
	HEK293	0.002		10				36	(437, 475)
	HEK/CHO	0.025		24.6				21.6	(445)
	N/A			10					(449)
	<b>MANTA</b>	<b>0.025</b>	<b>417</b>	<b>20</b>	<b>19.5</b>			<b>21.5</b>	
PHENYTOIN	N/A			100					(449)
	HEK293	103		100				49	(437)
	HEK/CHO	21.9		147				72.4	(445)
	ChanTest	22.07	470.6	147.2	227.5			80.41	(450)
	<b>MANTA</b>	<b>22.07</b>		<b>120</b>				<b>80.41</b>	
PROCAINAMIDE	Guinea pig							13700	(476)
	HEK/CHO			310					(449)
	N/A	389.5		272.4				746.6	(445)
	ChanTest	341.3	33.51	272.9	813.2			646.3	(450)
	<b>MANTA</b>	<b>340</b>	<b>33</b>	<b>300</b>	<b>810</b>			<b>646</b>	
PROPAPENONE	HEK293			0.44±0.07					(466)
	Ionworks							1.2	(477)
	N/A			0.44					(449)
	HEK/CHO	1.55		0.481	16		35.76	3.886 4.036	(444)
	HEK293	1.8		0.44				1.19	(437)
	Rabbit			0.80±0.14				7.27±0.53	(478)

*Maastricht antiarrhythmic drug evaluator (MANTA)*

	Human (A)				4.8± 0.4			(479)
	<b>MANTA</b>	<b>1.55</b>	<b>0.44</b>	<b>16</b>	<b>7.2</b>	<b>2.5</b>	<b>4</b>	
QUINIDINE	HEK/CHO	>5.4	0.34	4.9	3.49	>5.4	>5.4	(444)
	Guinea pig						560	(476)
	Oocytes					198		(465)
	HEK/CHO	6.4	0.72			14.6		(445)
	HEK293	15.6	0.3			16.6		(437)
	HEK293		0.41± 0.04					(466)
	tsA201		0.32	6.0				(480)
	HEK293					12		(459)
	Human (A)				~5.0	~7.0		(467)
	Oocytes		16.8± 2.2					(458)
	Guinea pig (V)		1.4± 0.2					(458)
	CHO		1.0± 0.2					(458)
	AT-1		1.0± 0.4					(460)
	Canine (A)				5.03± 0.34			(439)
	hiPSC-CM	15.2				16.6		(481)
	N/A		0.3					(449)
	Model	14.9 ±1.5	0.62± 0.03	4.899		3.487	14.6	12.0± 0.7
ChanTest	6.364	574.1	0.716	48.51		14.62		(450)
	<b>MANTA</b>	<b>10</b>	<b>0.7</b>	<b>5</b>	<b>5</b>	<b>3.5</b>	<b>12</b>	<b>10</b>
QUININE	HEK/CHO	27.18	5.17	37.45	79.25	24.15	11.05	(444)
	<b>MANTA</b>	<b>27</b>	<b>5</b>	<b>37</b>	<b>79</b>	<b>24</b>	<b>11</b>	
RANOLAZINE	HEK/CHO		6.49		>69	7.88		(444)
	Canine (V)	296	12	<20% at 30 µM		6	91	(482)
	ChanTest	215.1	2267	10.7	1038	101.8		(450)
	Canine (V)					294	6.5	(483)
	KPQ murine CM					135	15	(484)

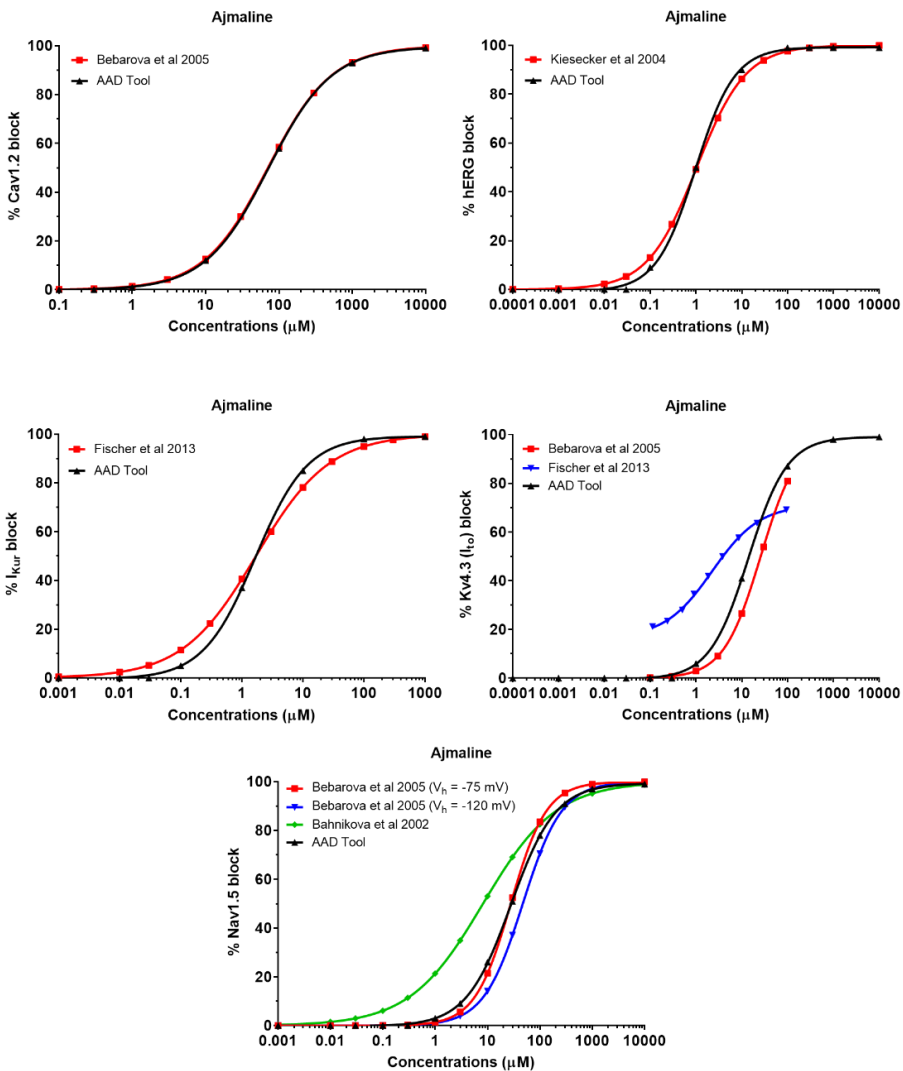
	HEK293					259.3			(485)
	HEK293					259			(486)
	HEK293		14.4				6.9		(487)
	Rabbit (V)						16.5		(488)
	tsA201							1.7	(489)
	Rabbit (V)							> 100	(490)
	<b>MANTA</b>	<b>250</b>	<b>12</b>	<b>100</b>		<b>200</b>	<b>8</b>	<b>91</b>	
SOTALOL	Human (A)					N.S.	N.S.		(438)
	HEK/CHO	2100	2100	86.3	2100				(444)
	HEK/CHO	193.3		111.4			7014		(445)
	HEK293			1200					(459)
	N/A			74					(449)
	ChanTest	360.0	2504	111.4	3569		1180		(450)
	<b>MANTA</b>	<b>2100</b>	<b>2500</b>	<b>100</b>	<b>3500</b>		<b>7000</b>		
VERAPAMIL	HEK/CHO	0.202		0.5				>1	(444)
	HEK/CHO	0.2		0.25				32.5	(445)
	Canine (A)					2.2± 0.3			(439)
	HEK293			0.68					(459)
	HEK293	0.1		0.143				41.5	(437)
	Guinea pig (V)	0.6							(452)
	Ionworks							9.3	(477)
	Native heart cells			0.143					(454)
	N/A			0.140					(449)
	HEK/CHO	0.079		0.813			7.221	6.093	(451)
	ChanTest	0.108	9034	0.250	69.96		32.45		(450)
	<b>MANTA</b>	<b>0.2</b>		<b>0.5</b>		<b>2.2</b>	<b>35</b>		
VERAKALANT	Rat (V)	220					15		(434)
	HEK293			21		13	30	30- 200	(434)
	Human (A)	84				15	15	90	(491)

HEK293	42	21						(491)
HEK293				13.35 ±0.93				(469)
FDA N/A	>100	7-21	>100	3-13	5-30	31- 107	14	(492)
<b>MANTA</b>	<b>84</b>	<b>20</b>	<b>15</b>	<b>15</b>	<b>90</b>	<b>14</b>		

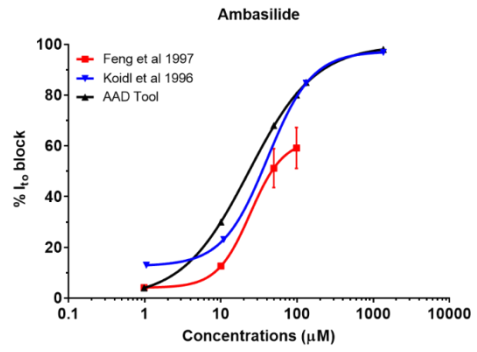
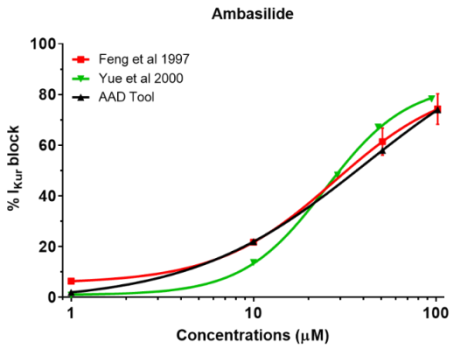
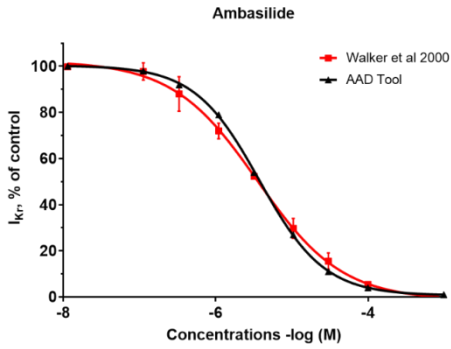
State-dependent block of  $I_{Na}$  is available for flecainide and lidocaine.

Figure 7.3A-Y: Comparison of experimental dose-response curves of antiarrhythmic drugs with dose-response curve used in MANTA for different antiarrhythmic drugs. (Hill coefficient of MANTA (h) = 1, unless stated differently)

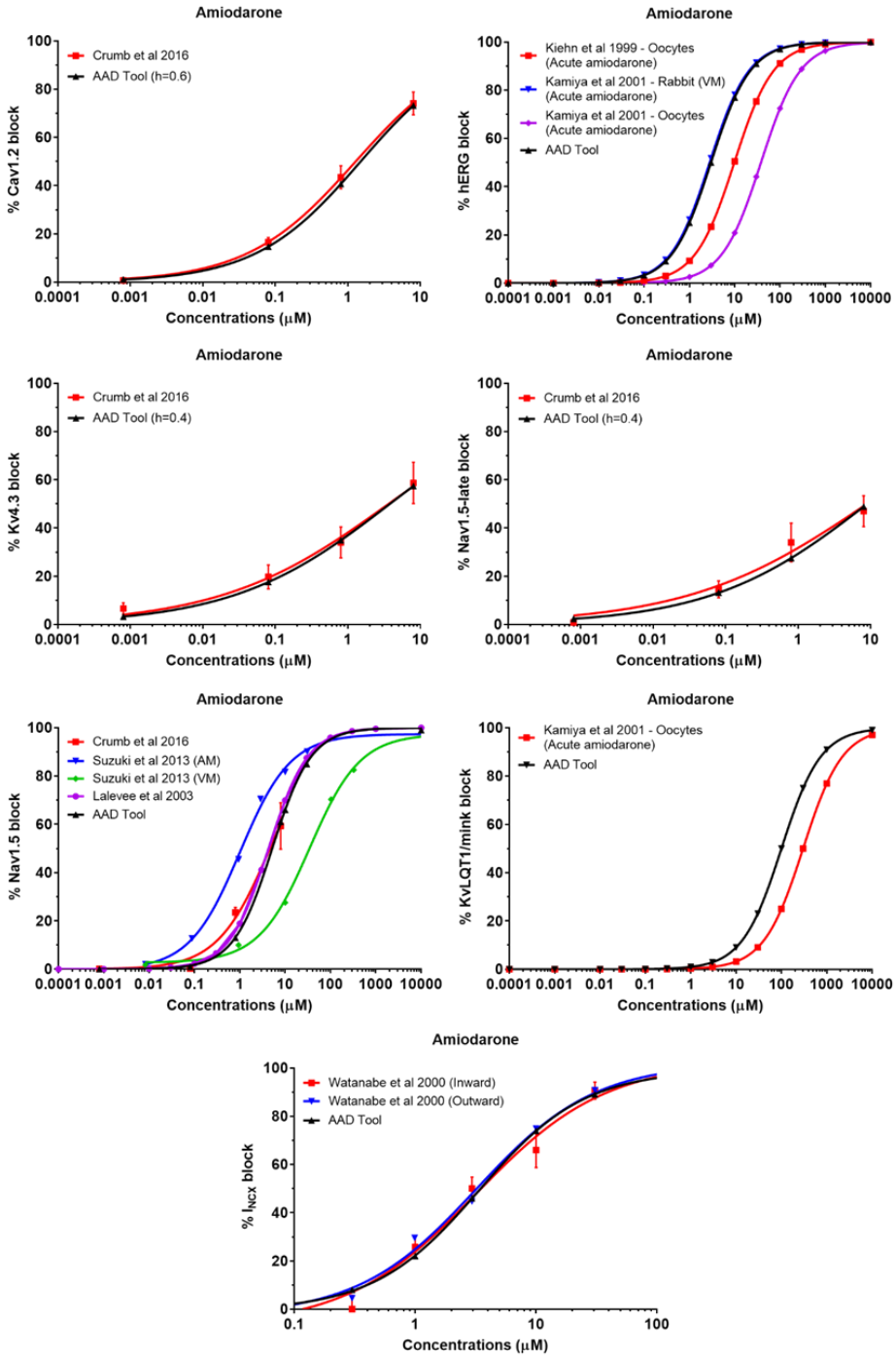
A. Ajmaline



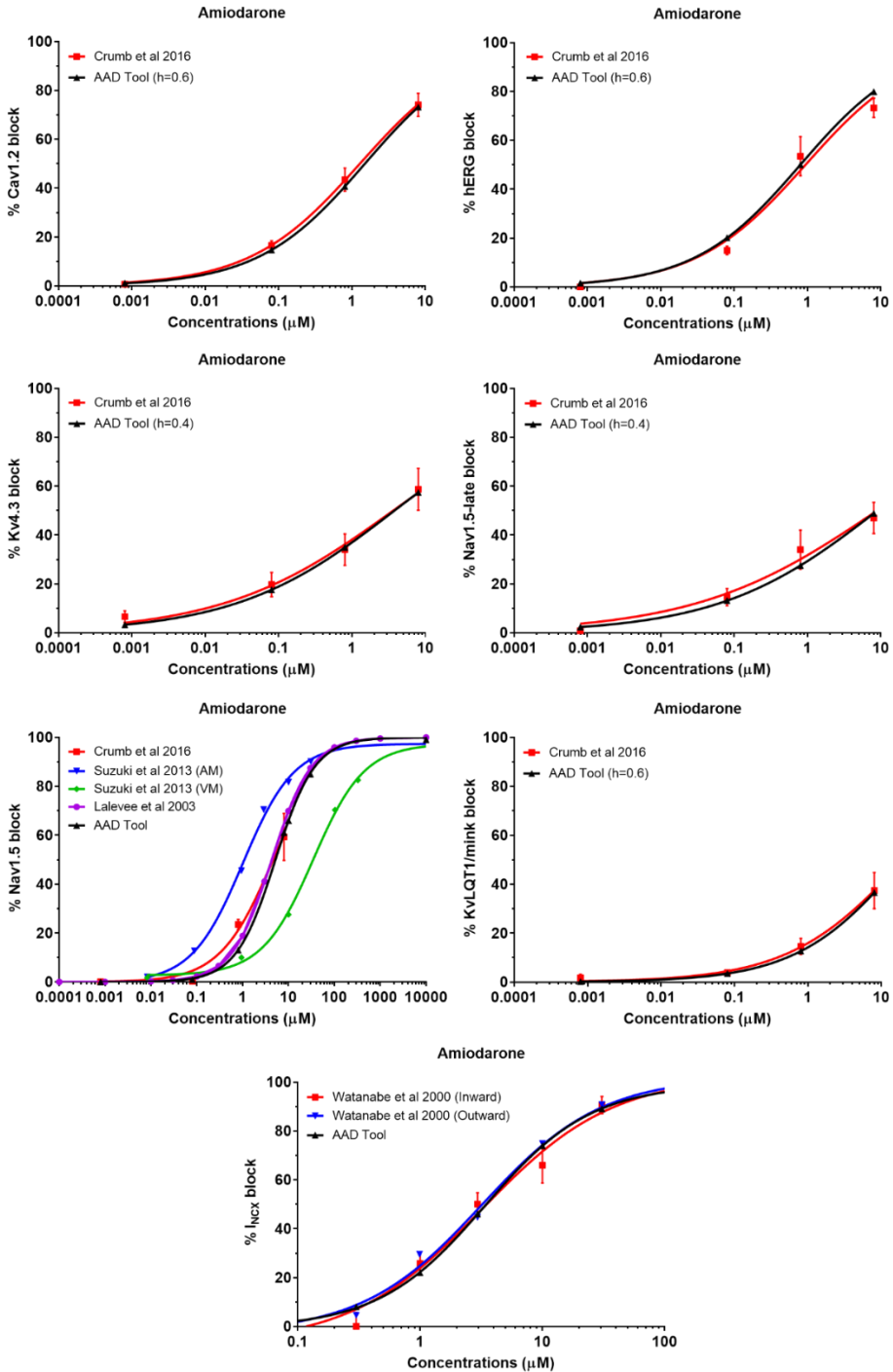
B. Ambasilide



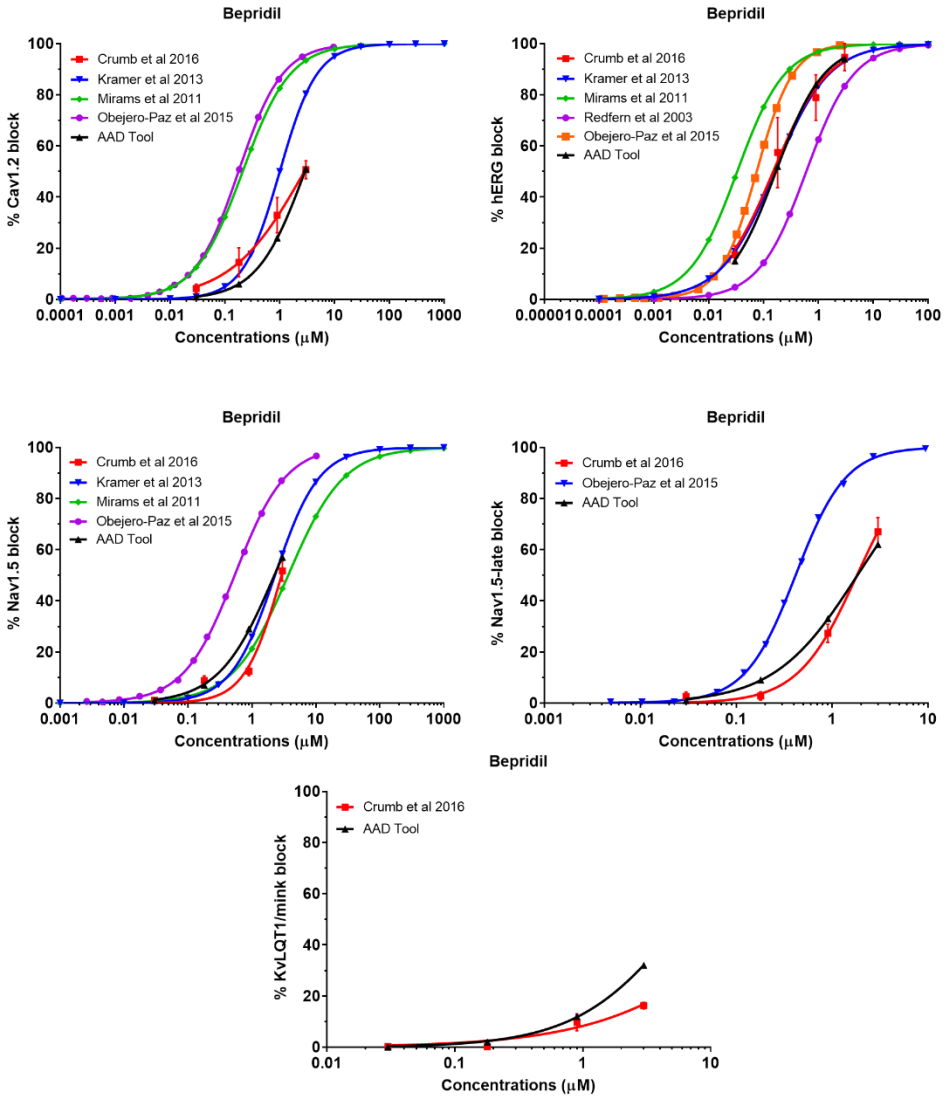
C. Acute amiodarone



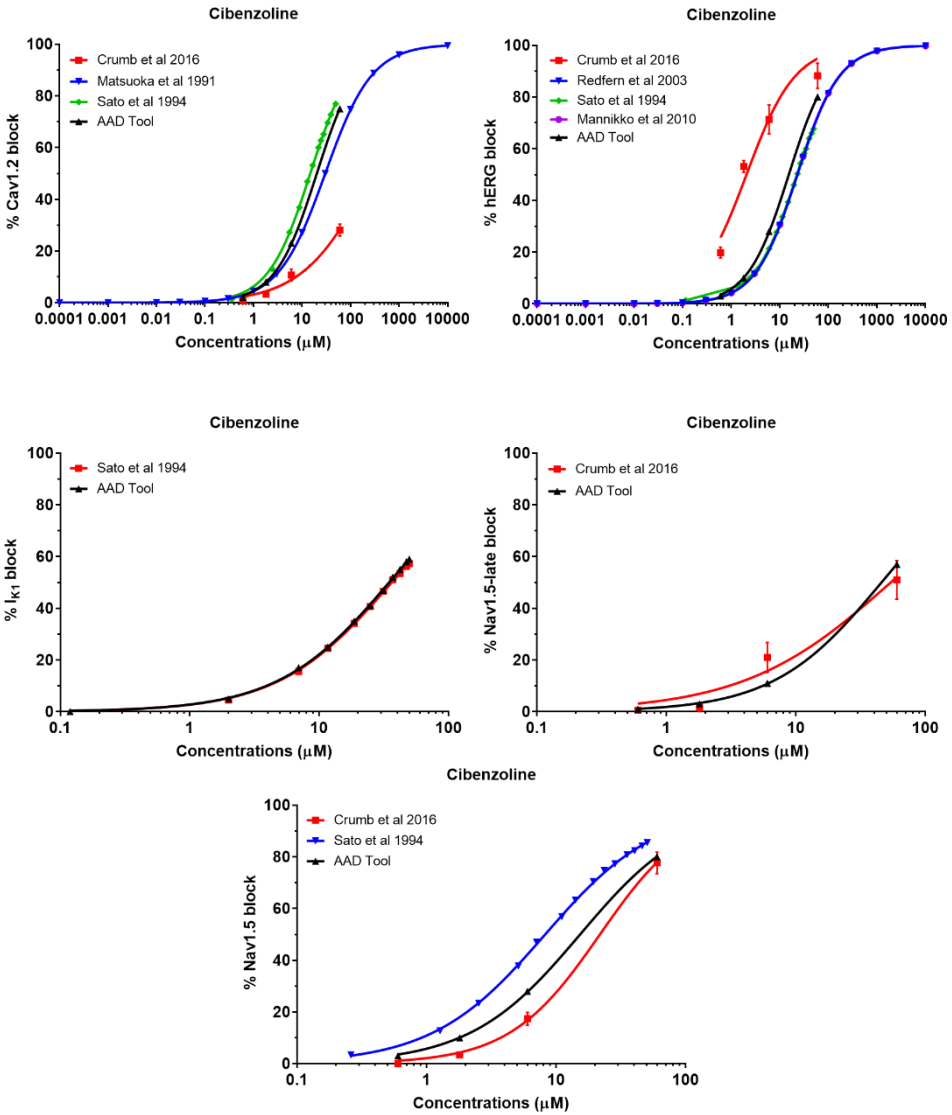
D. Chronic amiodarone



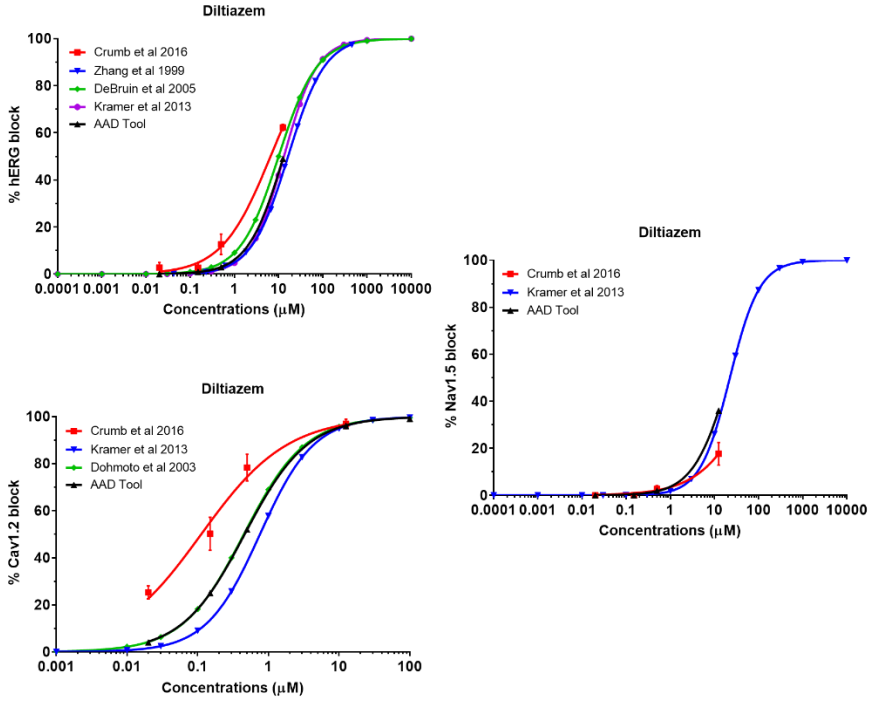
E. Bepridil



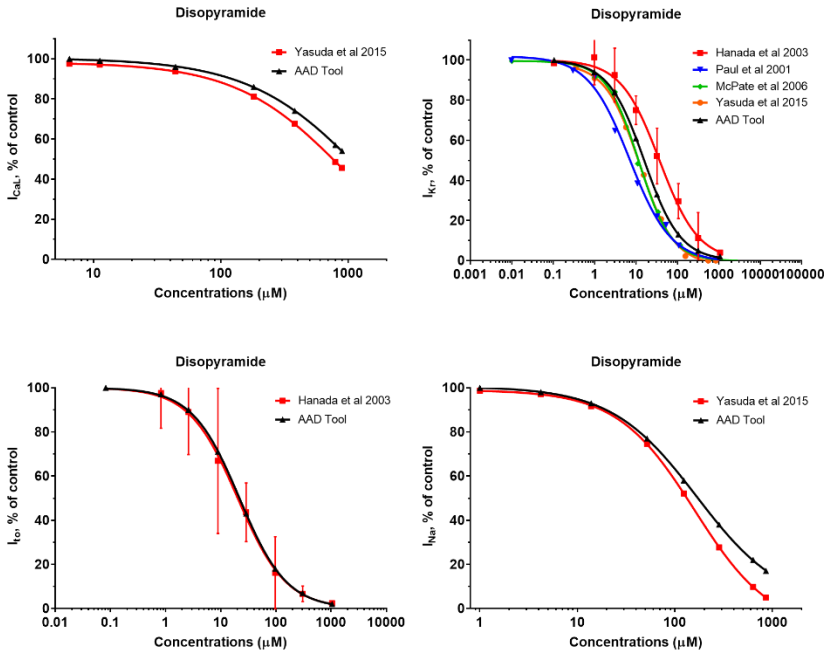
F. Cibenzoline



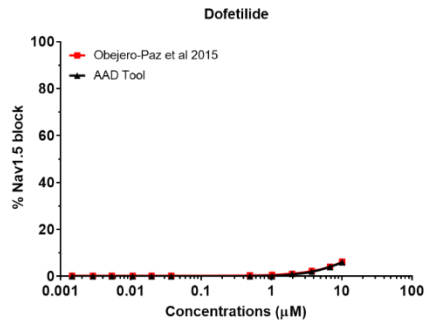
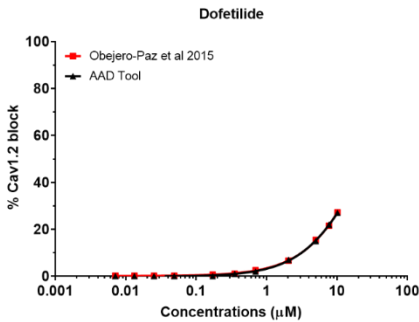
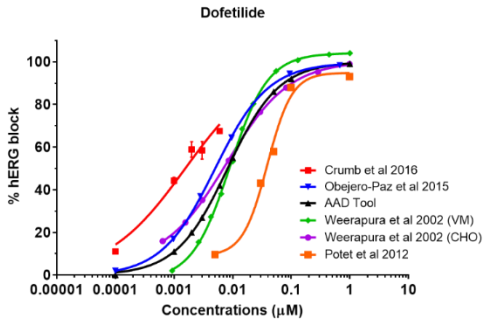
G. Diltiazem



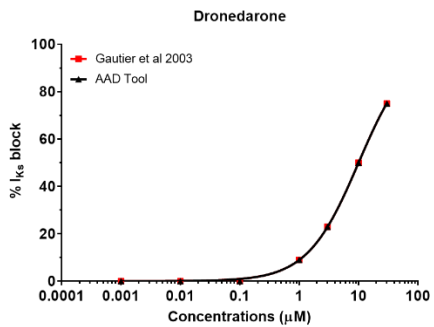
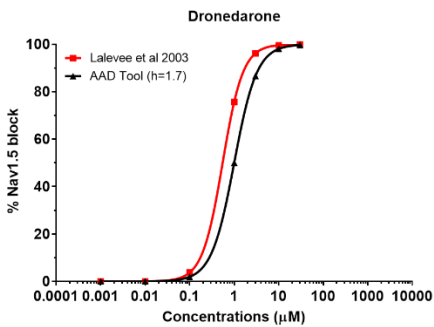
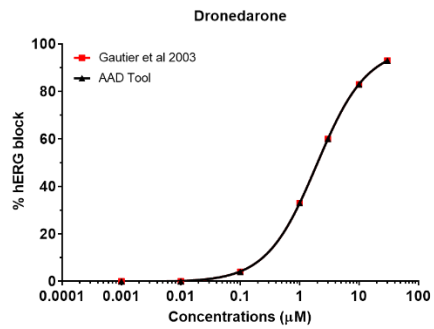
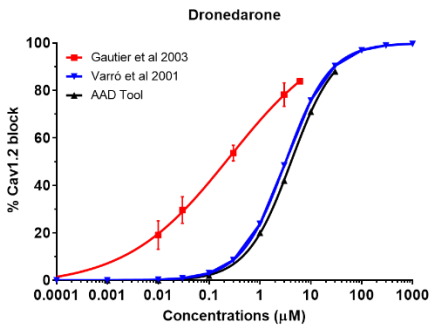
H. Disopyramide



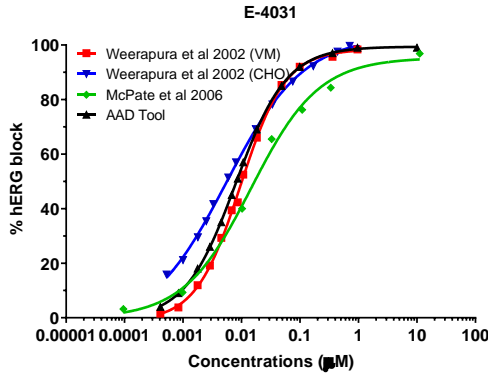
I. Dofetilide



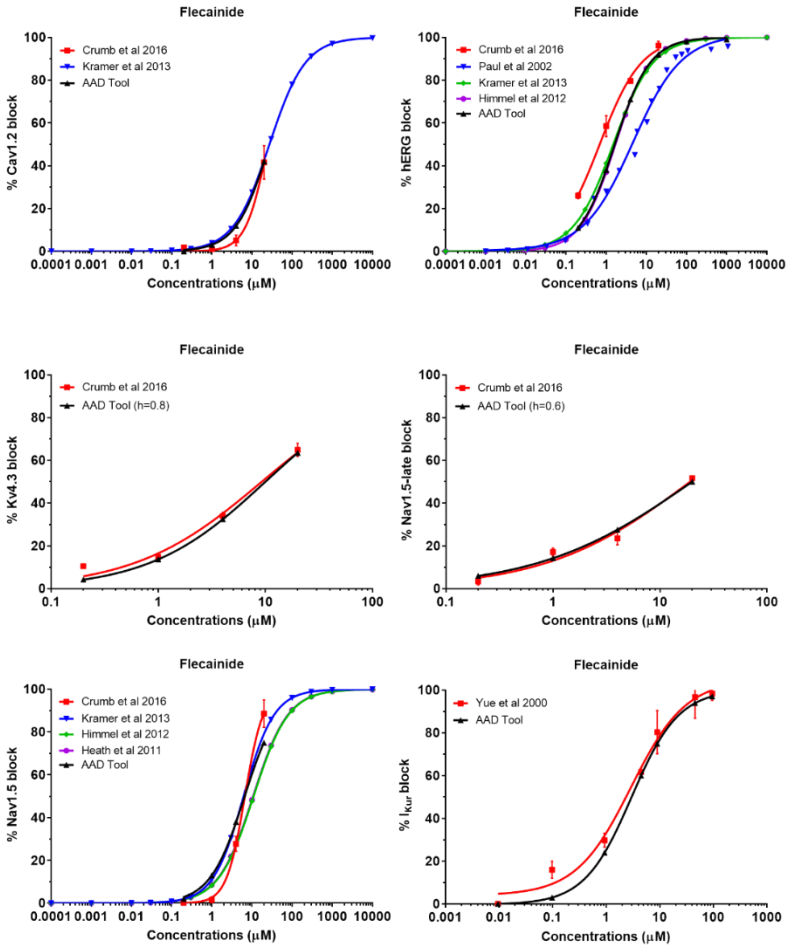
J. Dronedaron



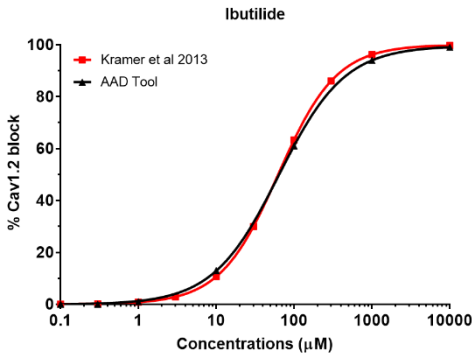
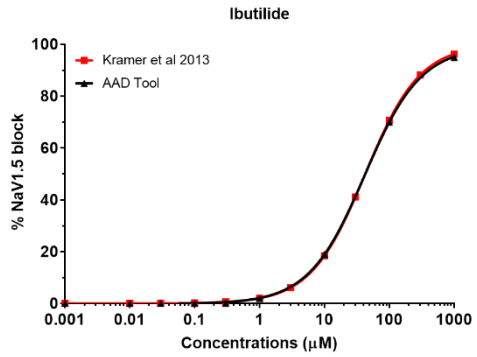
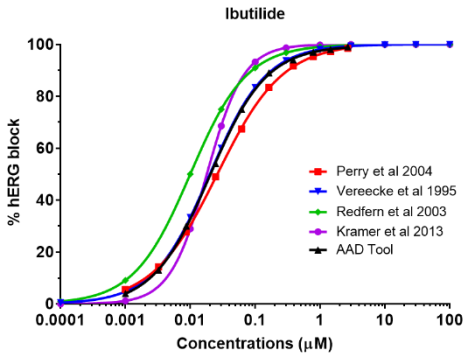
K. E-4031



L. Flecainide

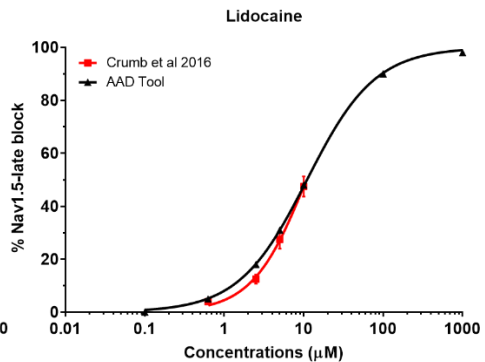
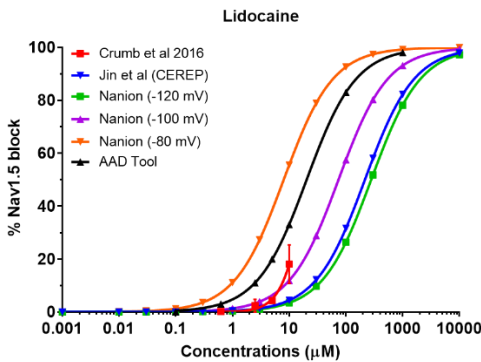


M. Ibutilide

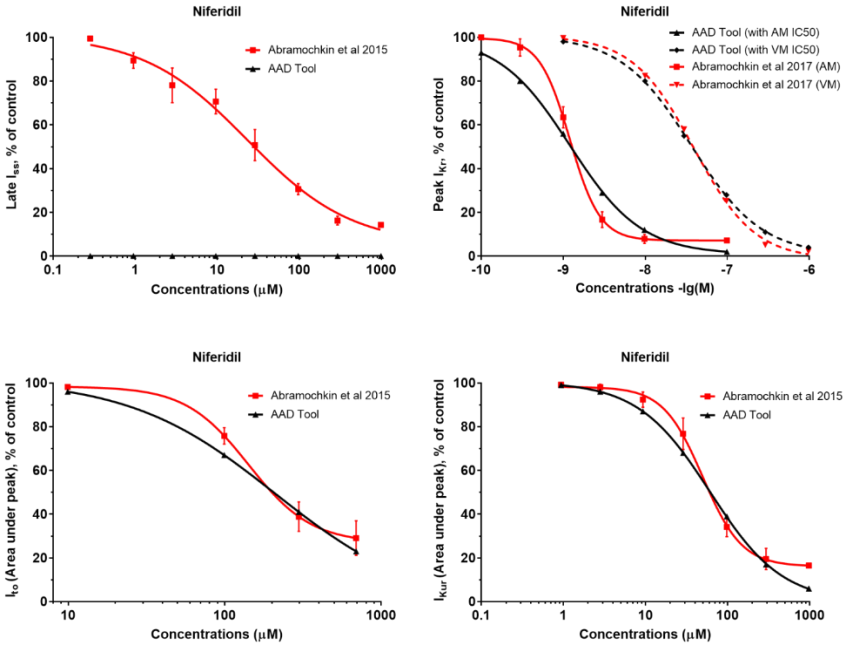


Chapter 7

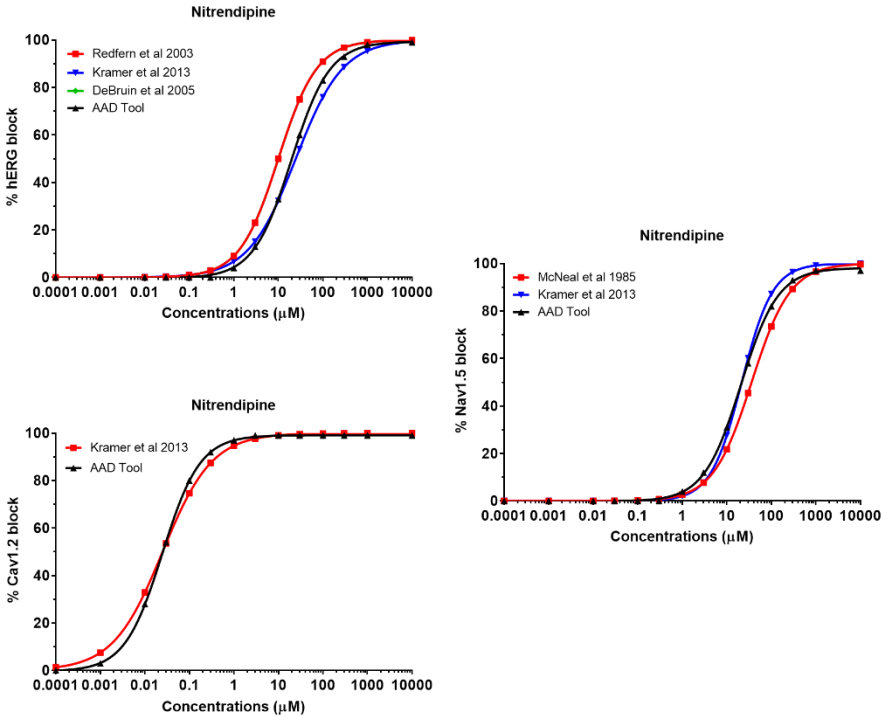
N. Lidocaine



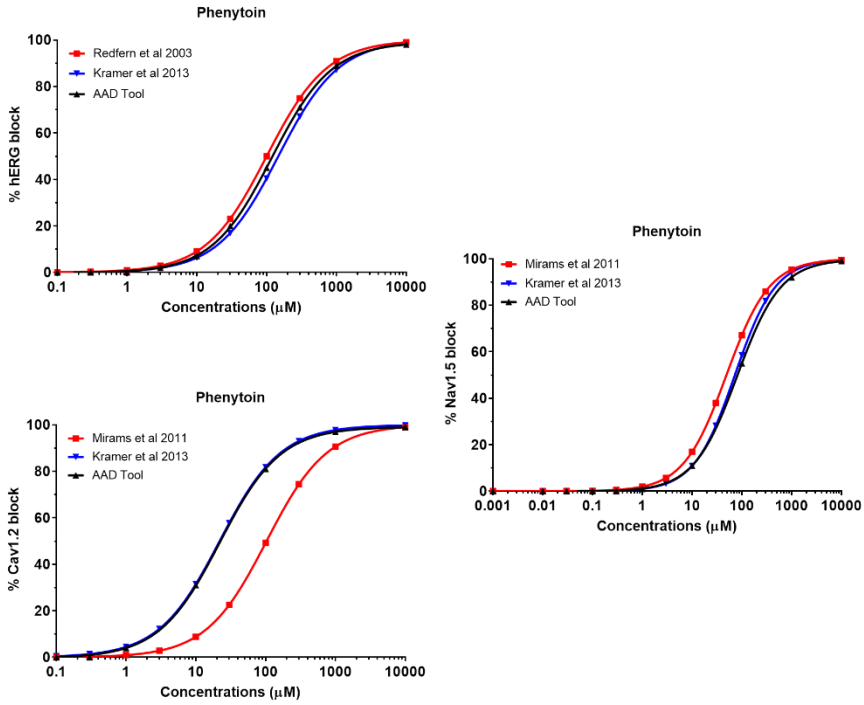
O. Nifedidil



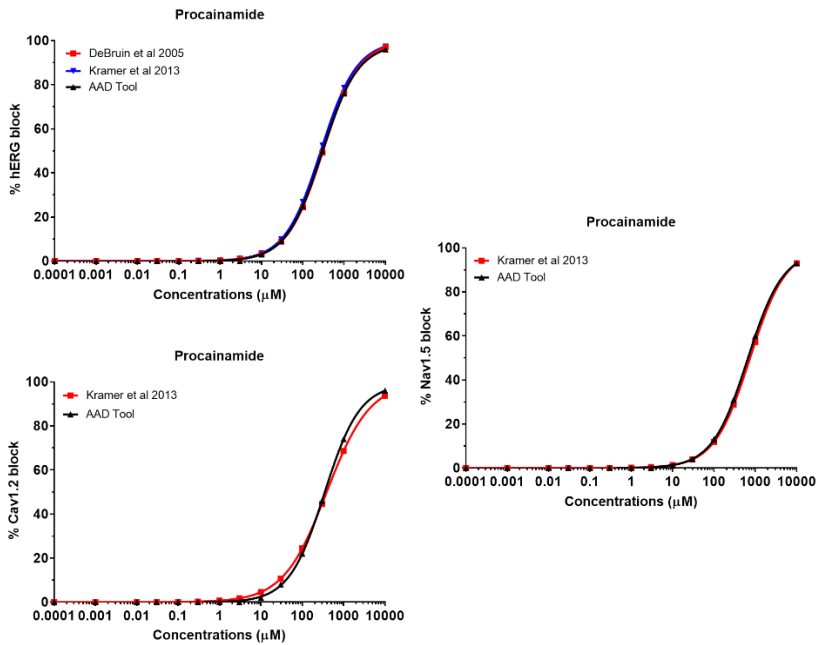
P. Nitrendipine



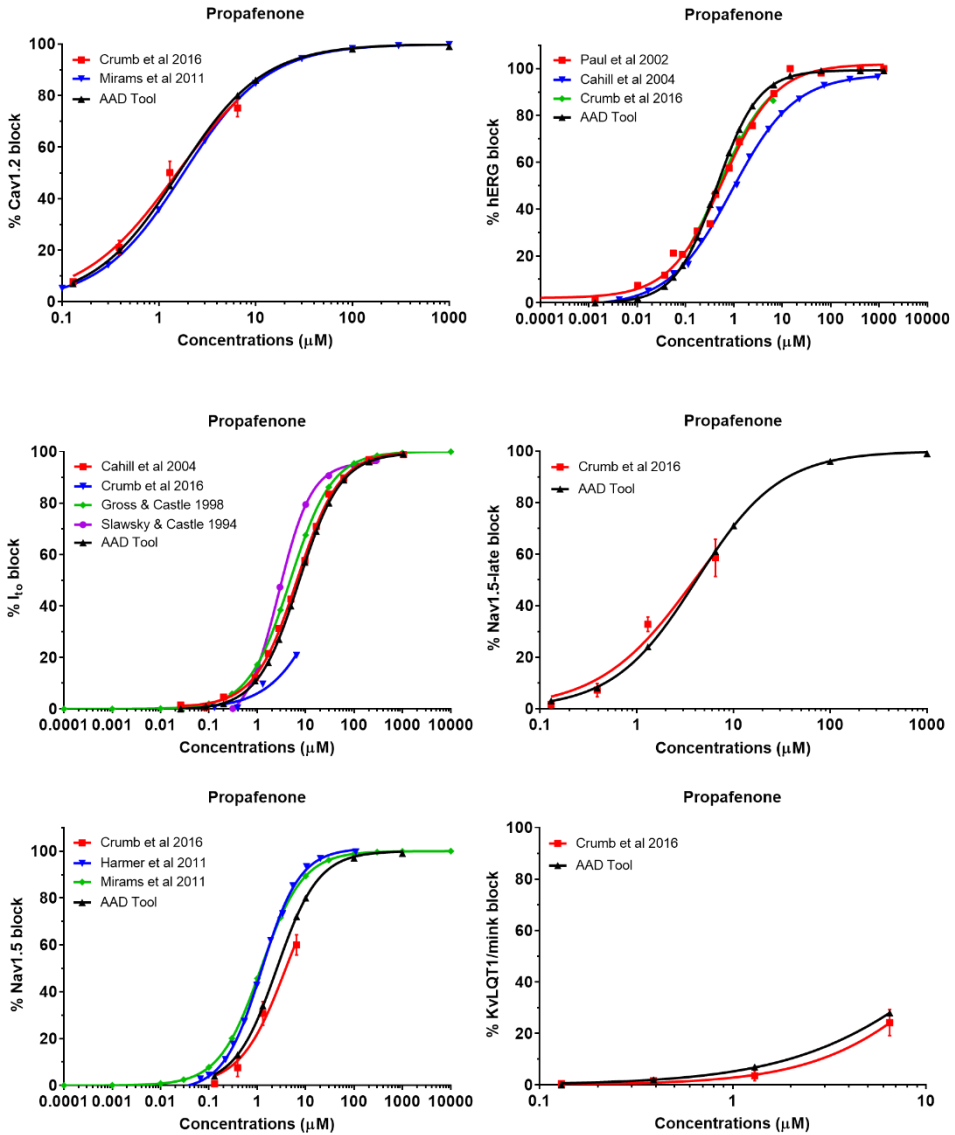
Q. Phenytoin



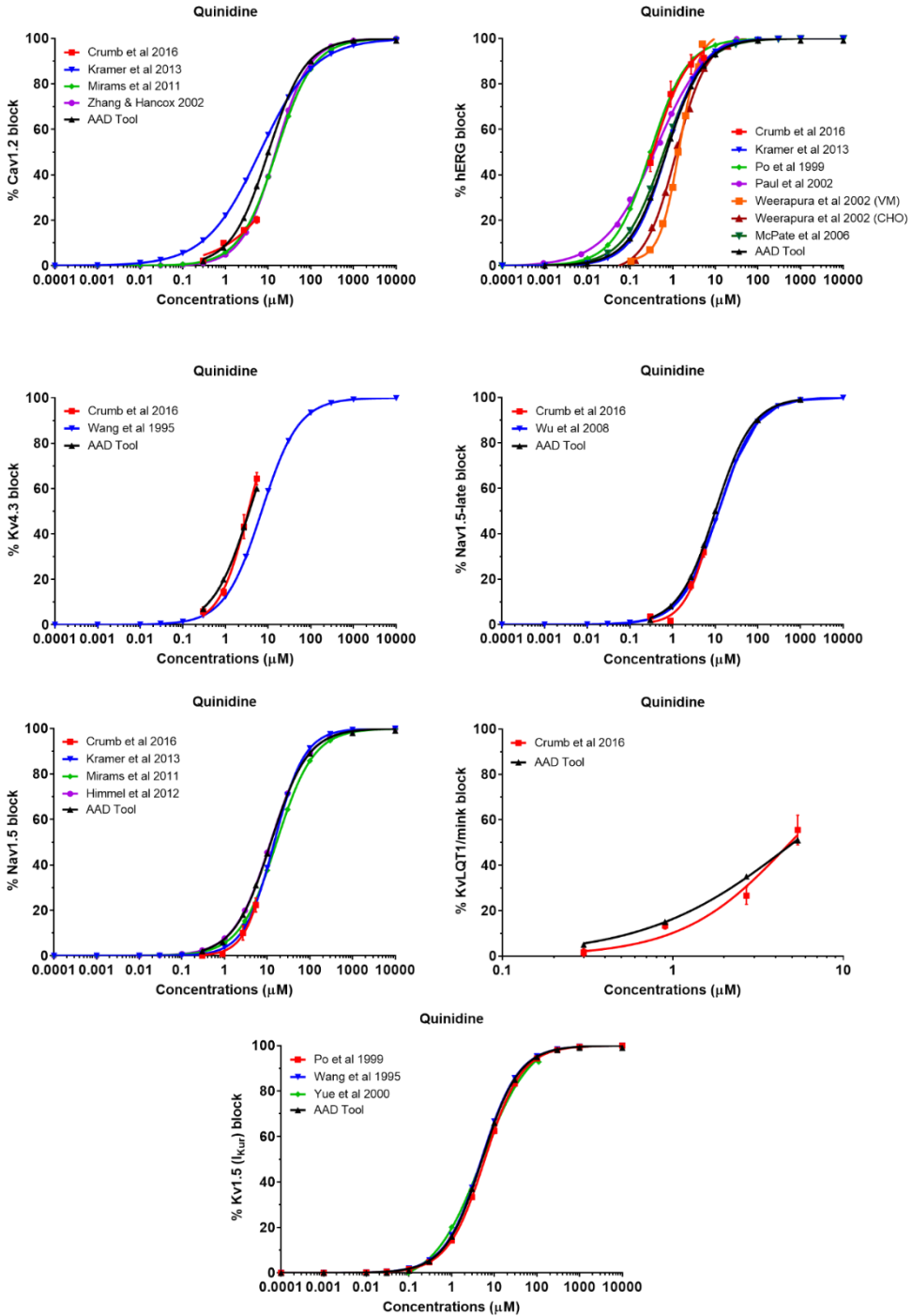
R. Procainamide



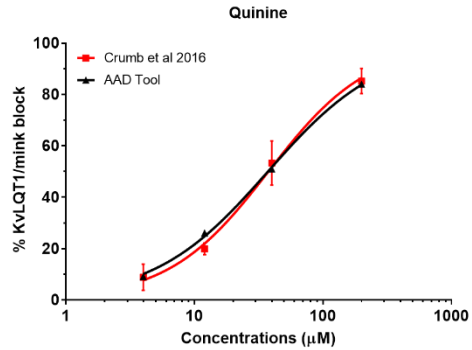
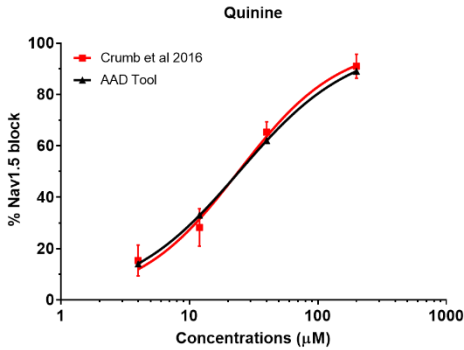
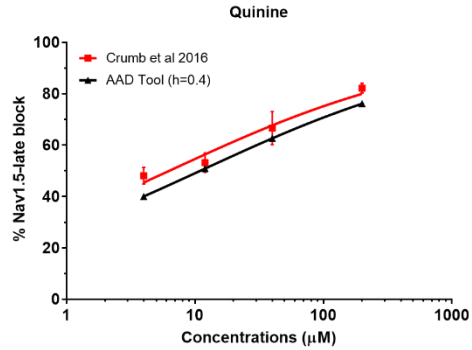
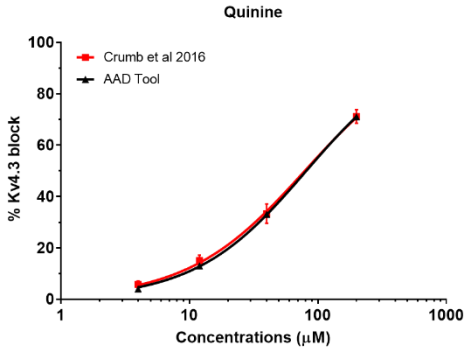
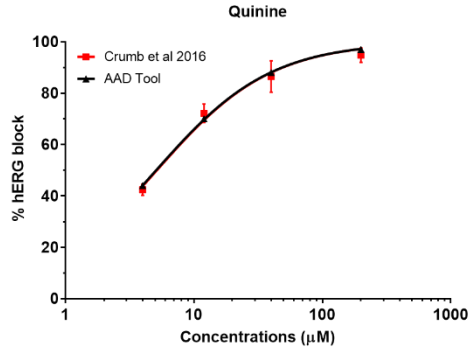
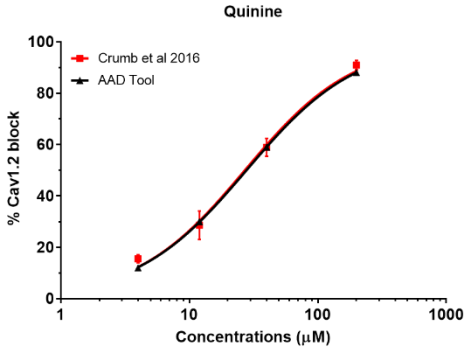
S. Propafenone



T. Quinidine

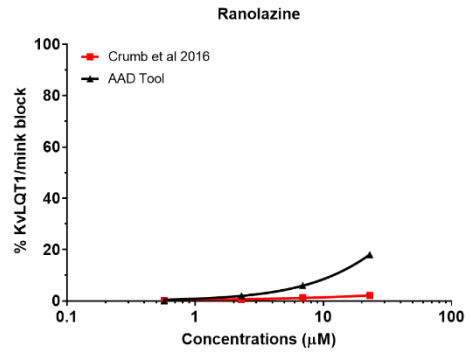
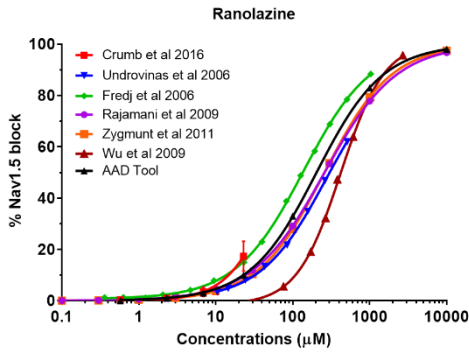
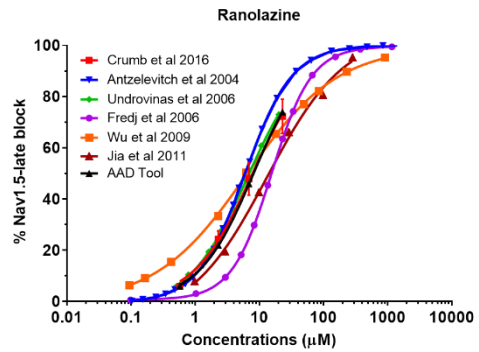
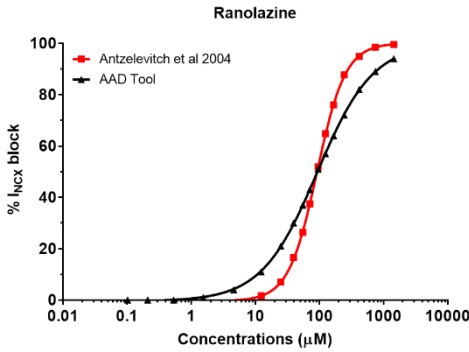
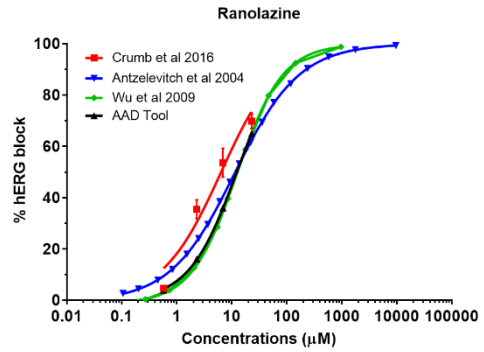
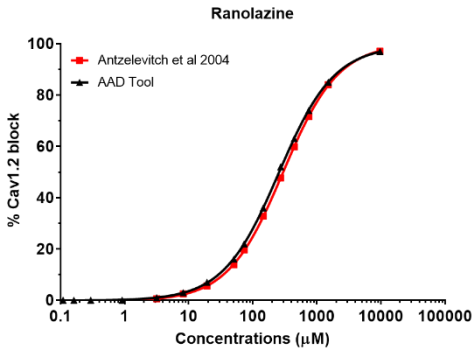


U. Quinine

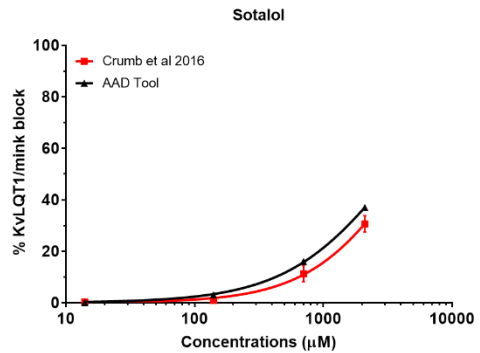
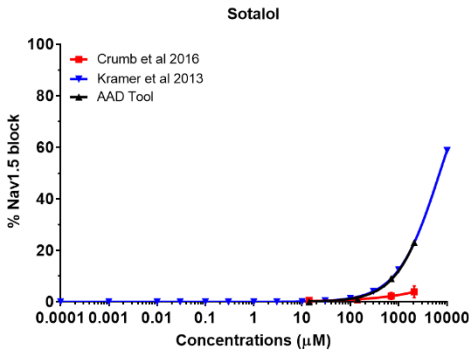
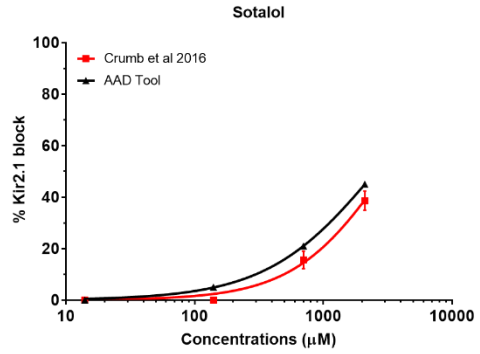
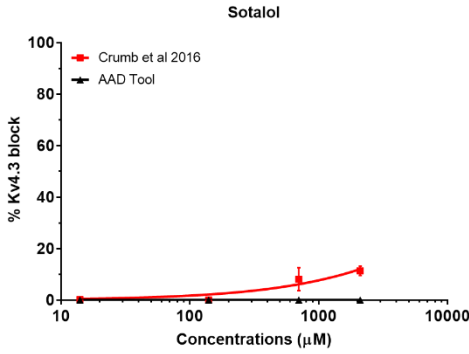
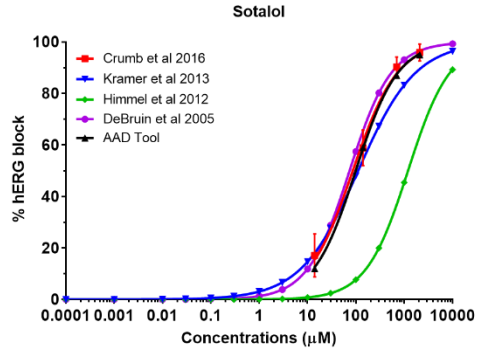
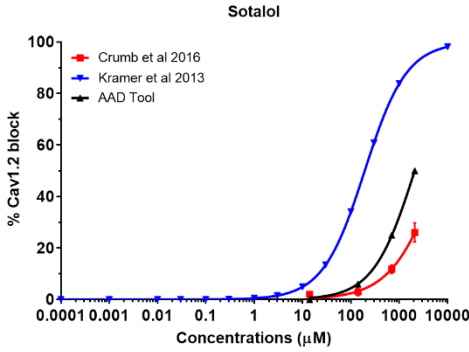


Chapter 7

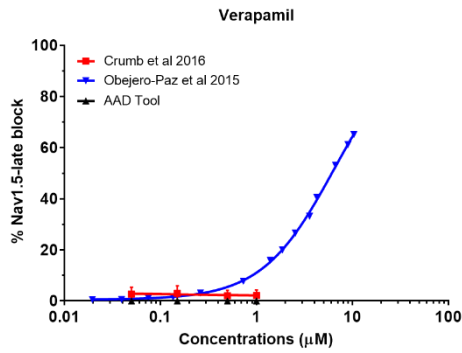
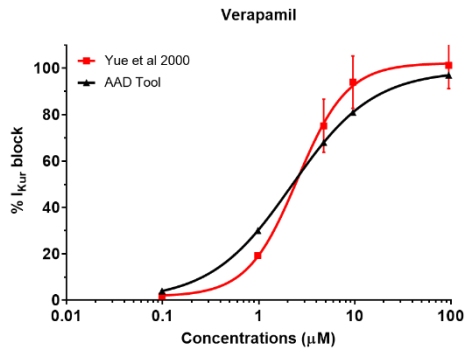
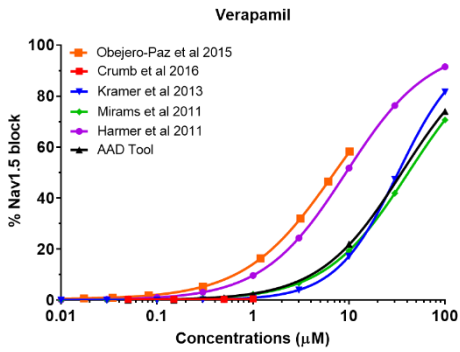
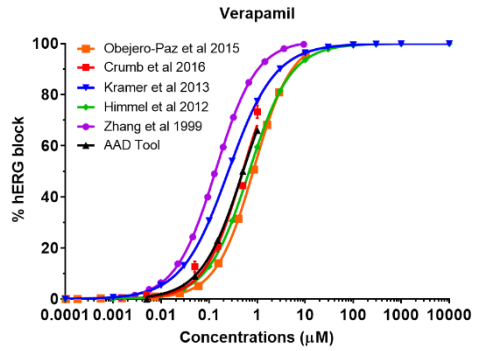
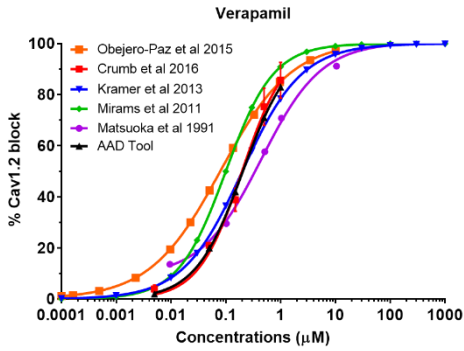
V. Ranolazine



W. Sotalol



X. Verapamil



Y. Vernakalant

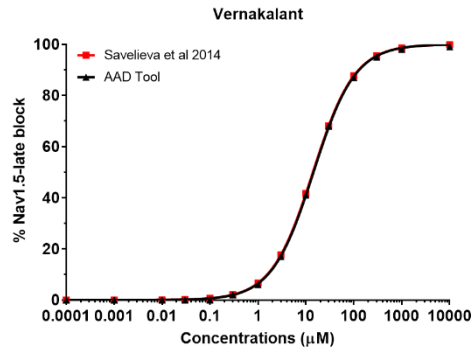
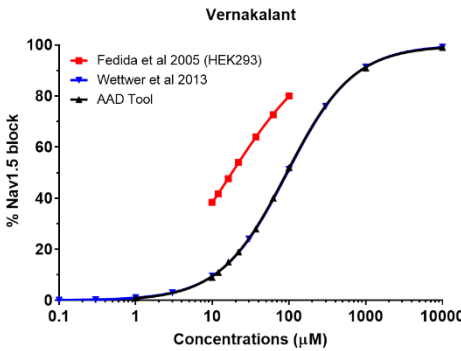
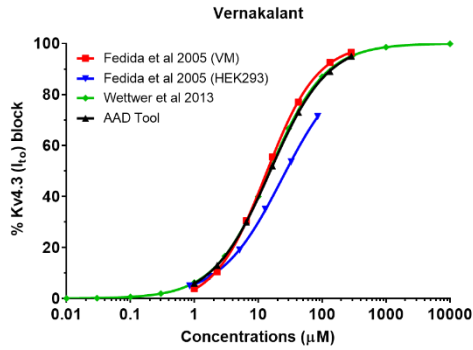
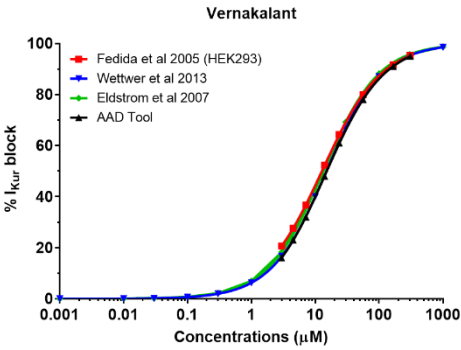
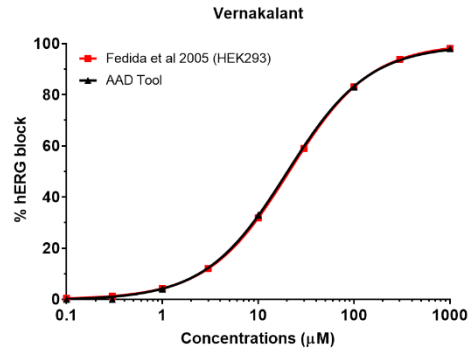
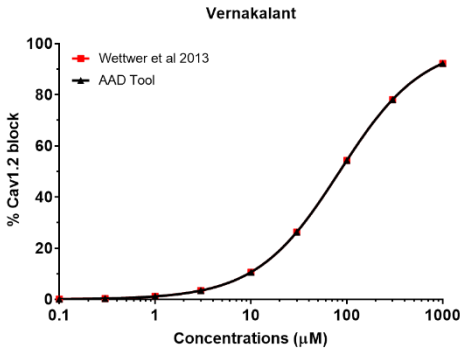
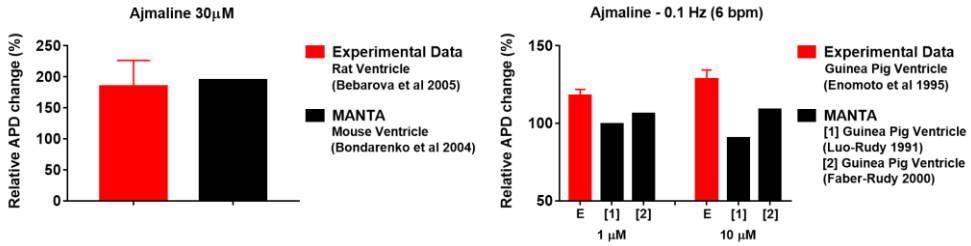
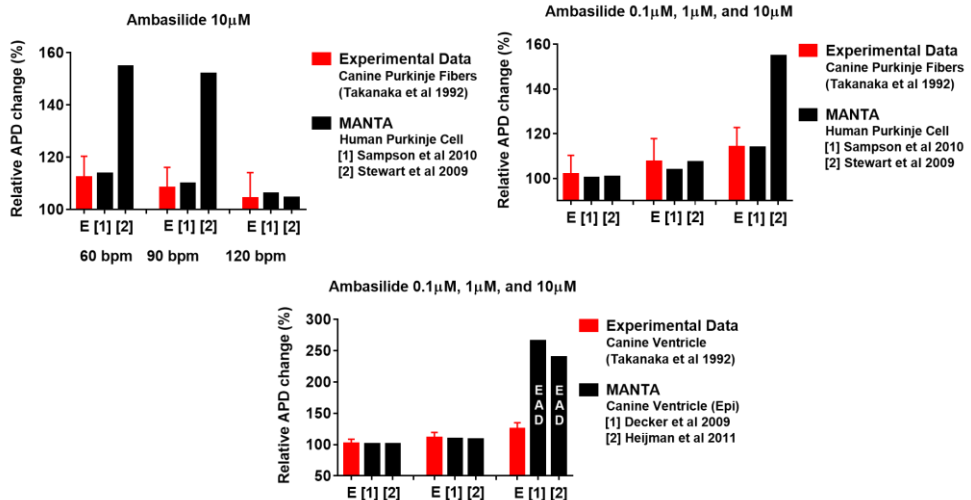


**Figure 7.4:** Comparison of relative APD changes produced by different antiarrhythmic drugs between previously published experimental data and computational models available in MANTA.

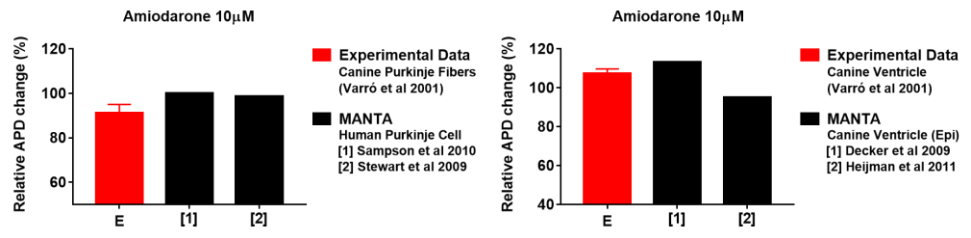
**Ajmaline (435, 493)**



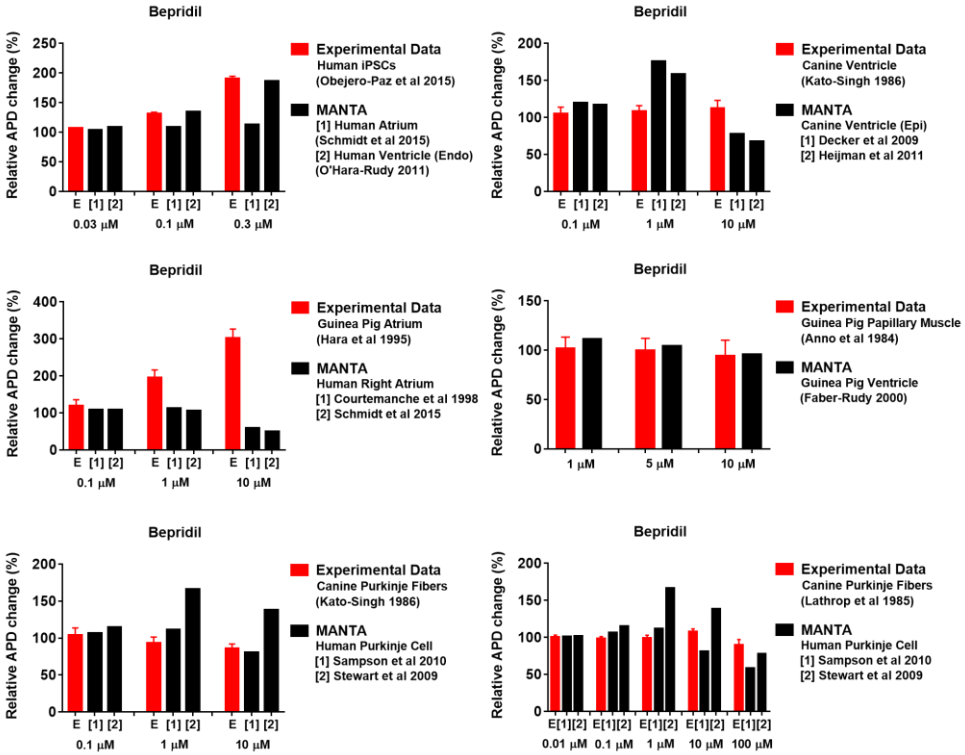
**Ambasilide (494)**



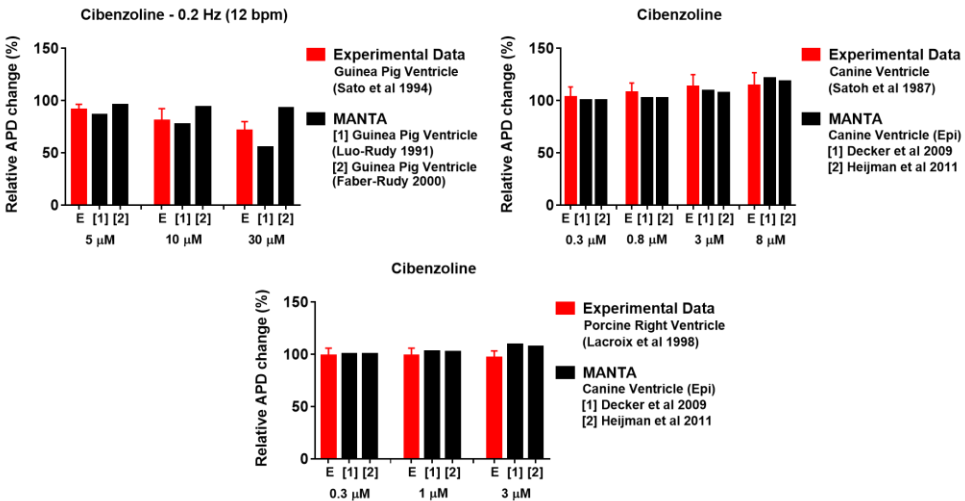
**Amiodarone (464)**



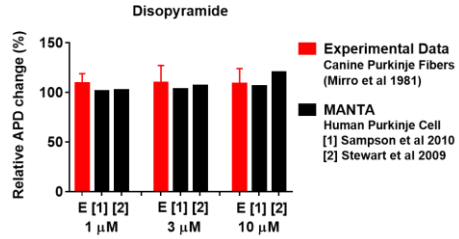
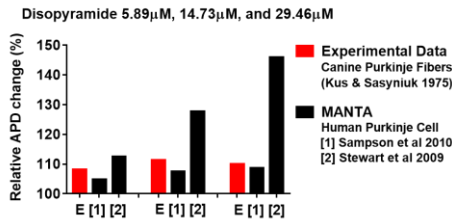
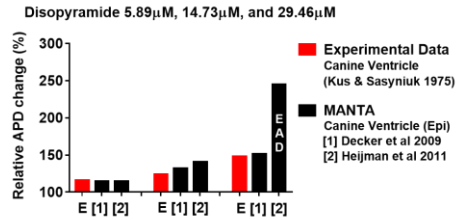
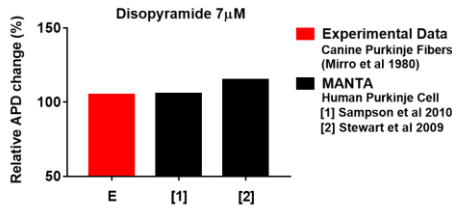
Bepidil (451, 495-498)



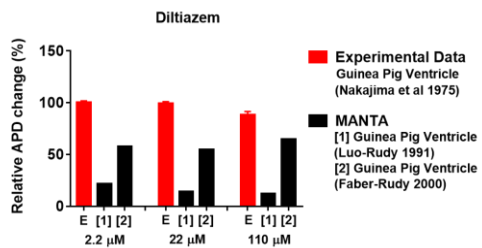
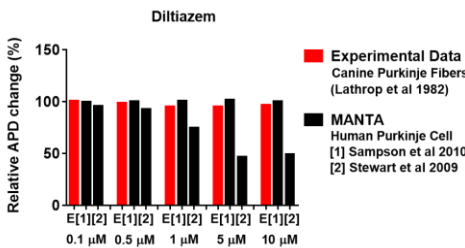
Cibenzoline (453, 499, 500)



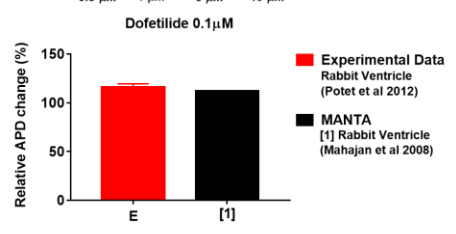
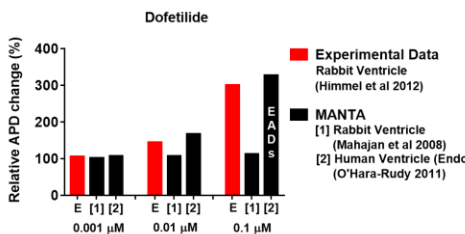
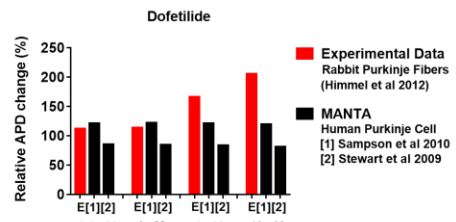
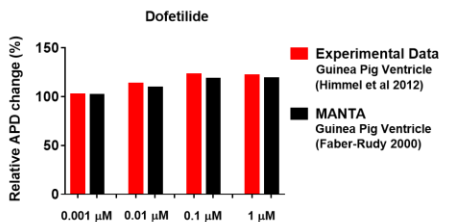
## Disopyramide (501-503)



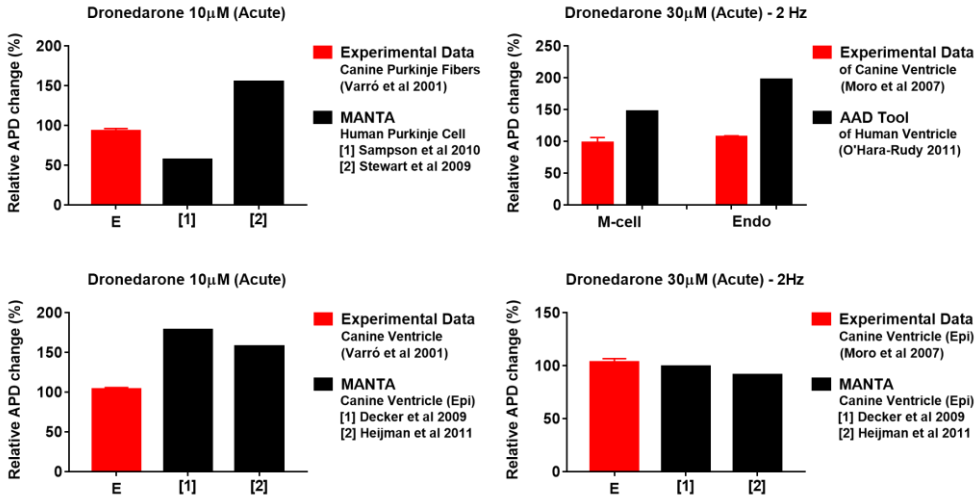
## Diltiazem (504, 505)



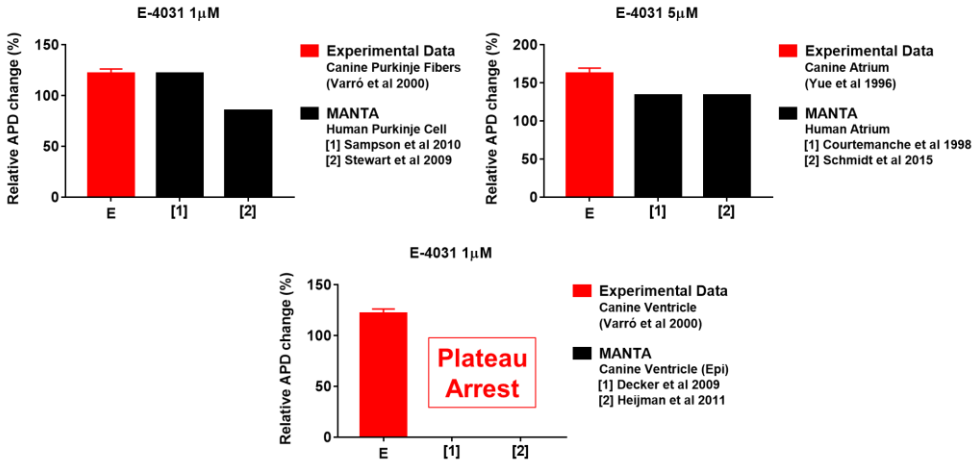
## Dofetilide (459, 462)



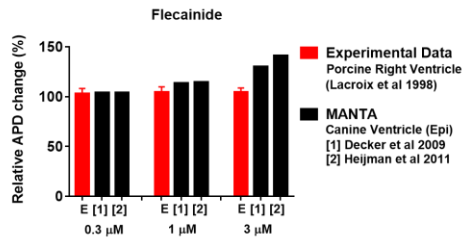
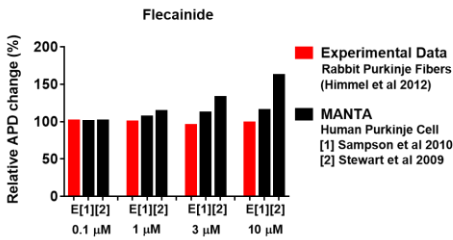
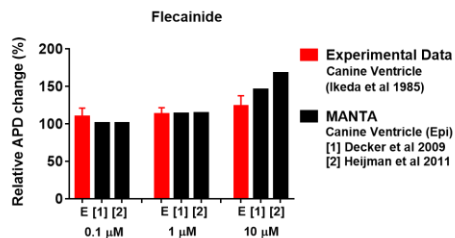
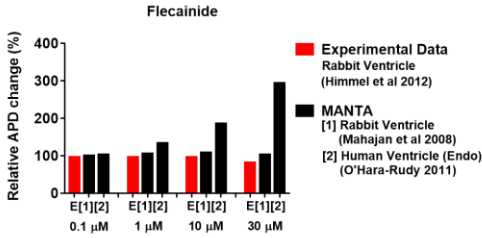
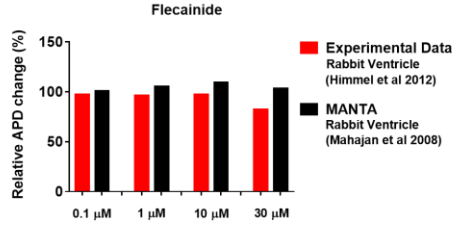
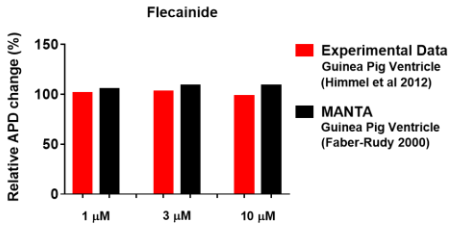
Dronedaron (464, 506)



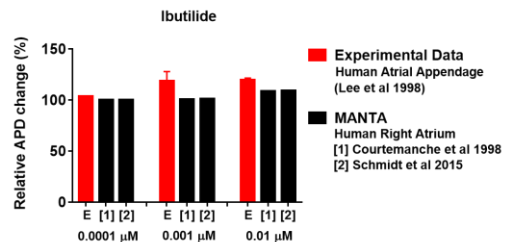
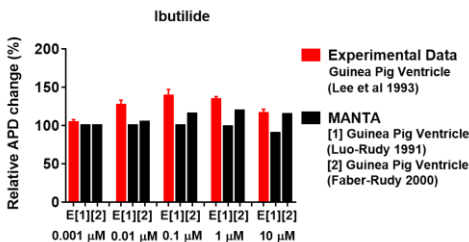
E-4031 (507, 508)



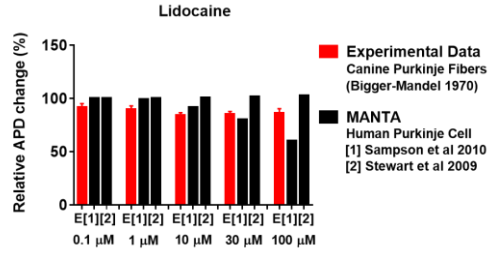
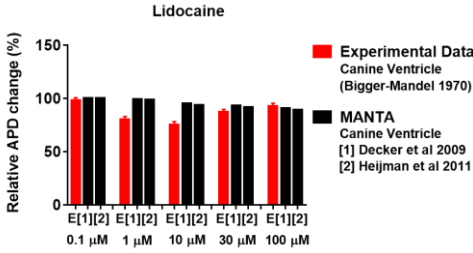
## Flecainide (459, 500, 509)



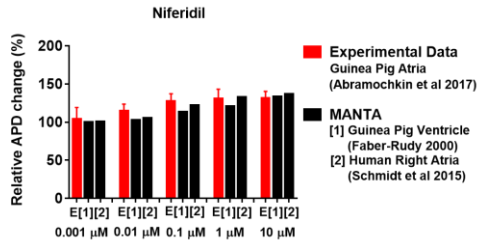
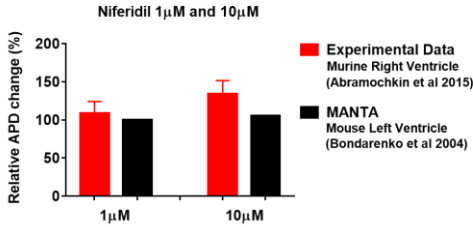
## Ibutilide (510, 511)



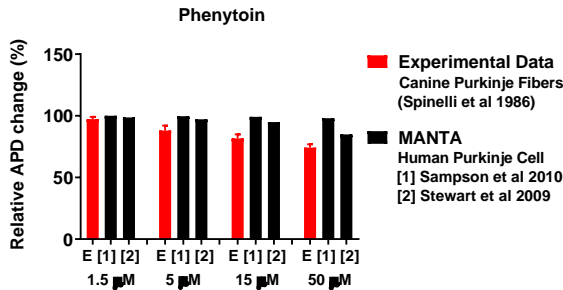
Lidocaine (512)



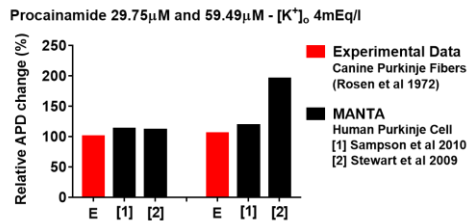
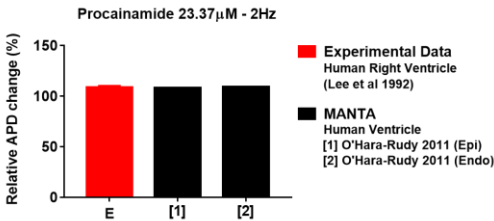
Nifedipil (473, 474)



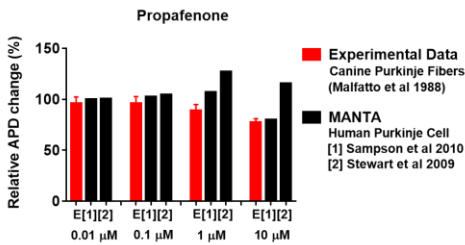
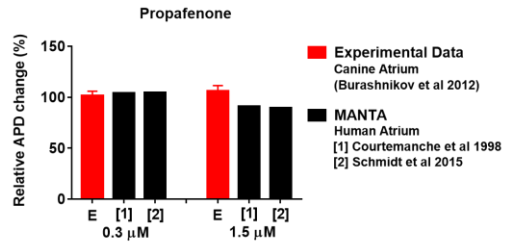
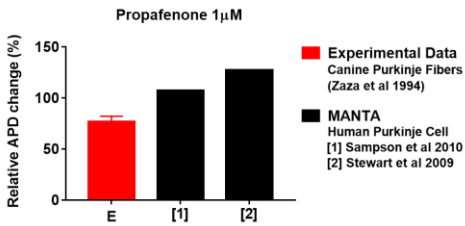
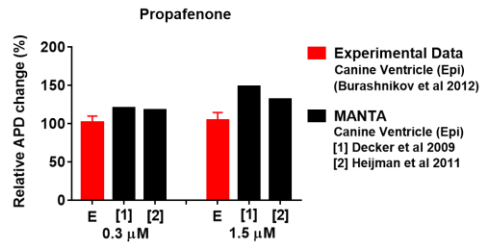
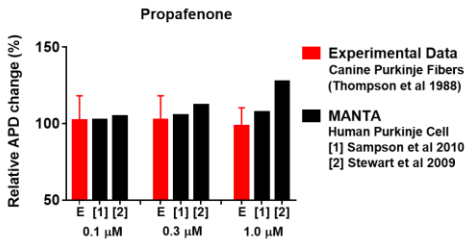
Phenytoin (513)



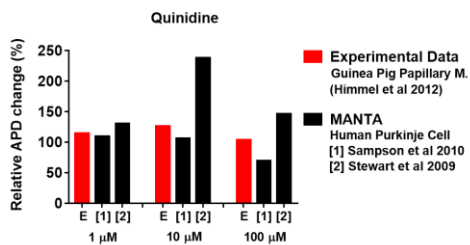
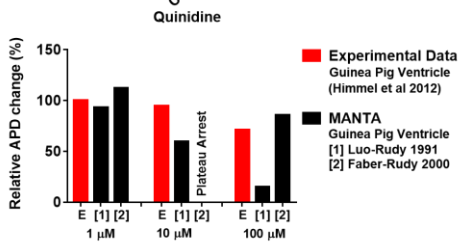
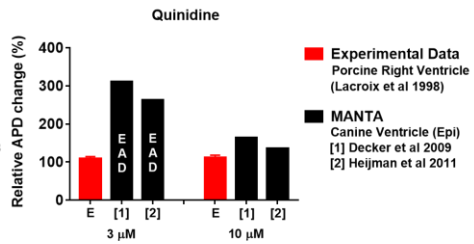
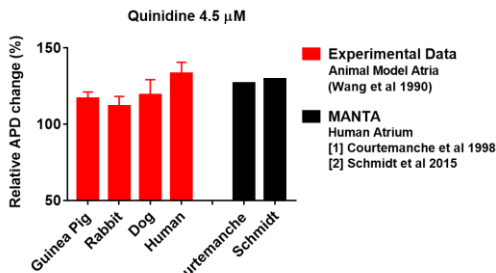
Procainamide (514, 515)



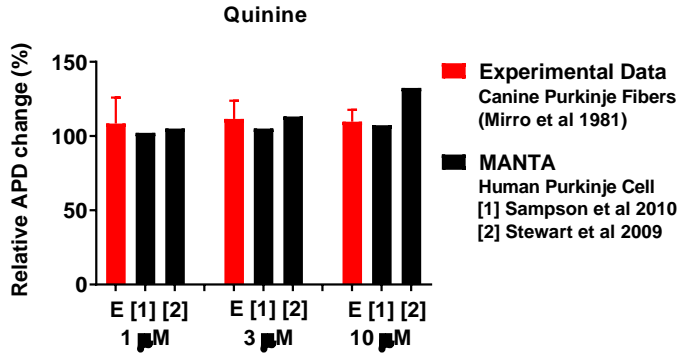
Propafenone (516-519)



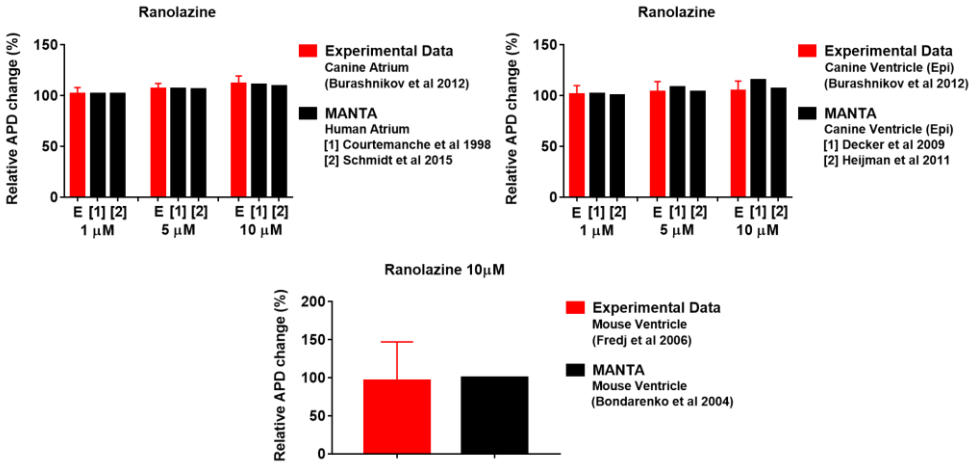
Quinidine (459, 500, 520)



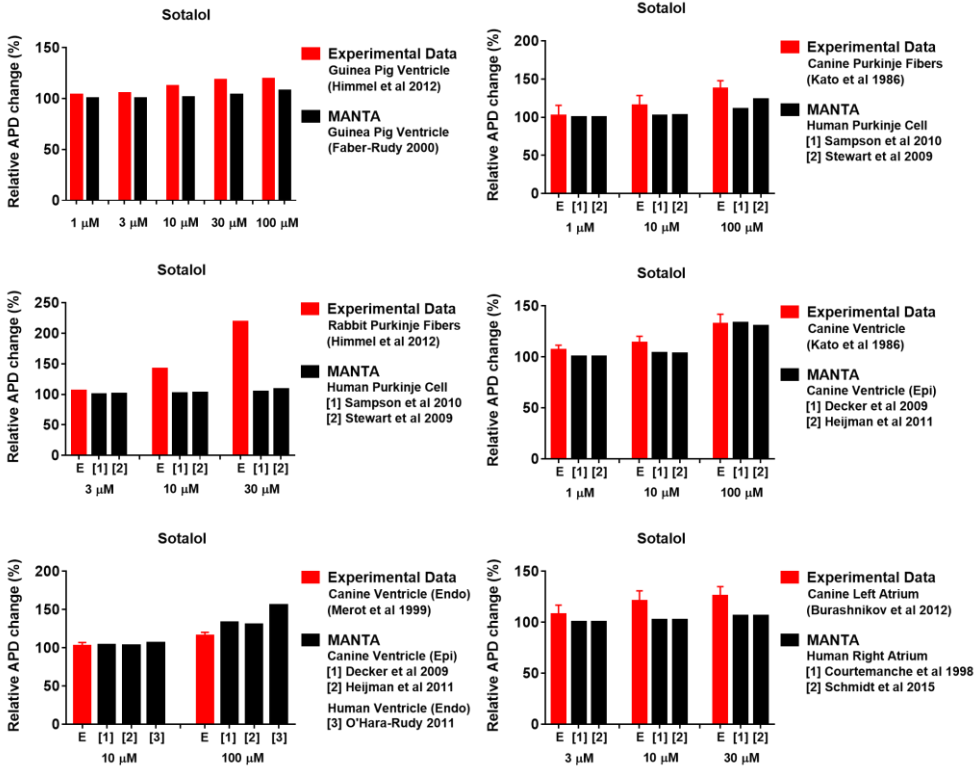
Quinine (503)



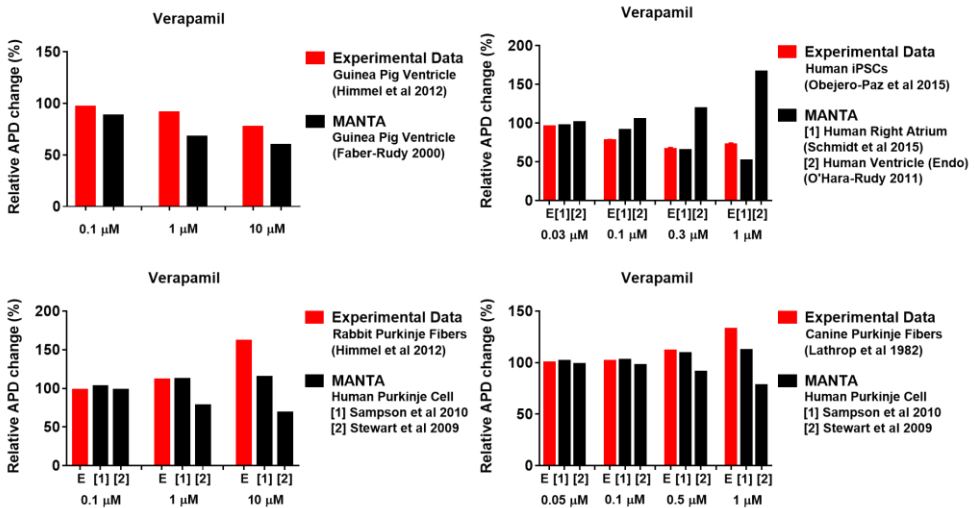
Ranolazine (484, 519)



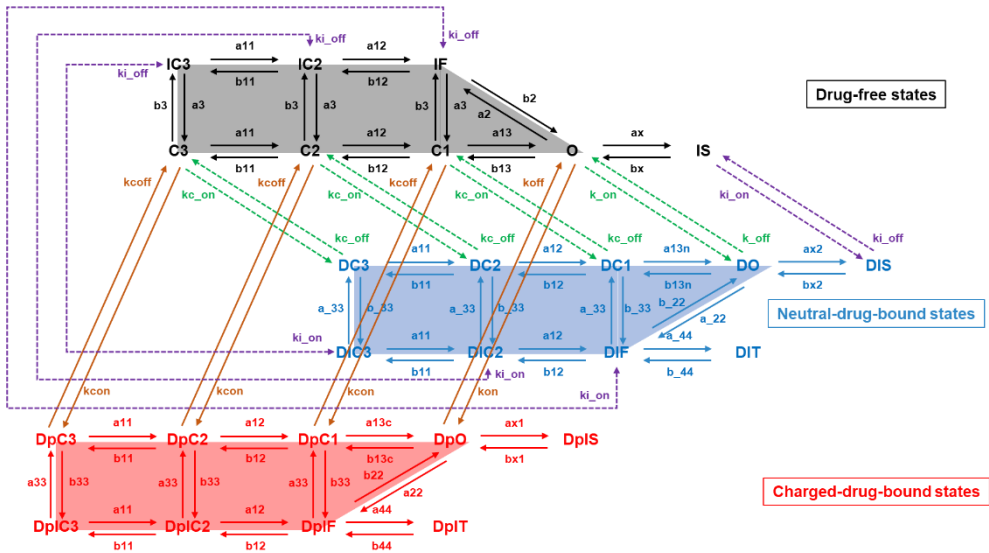
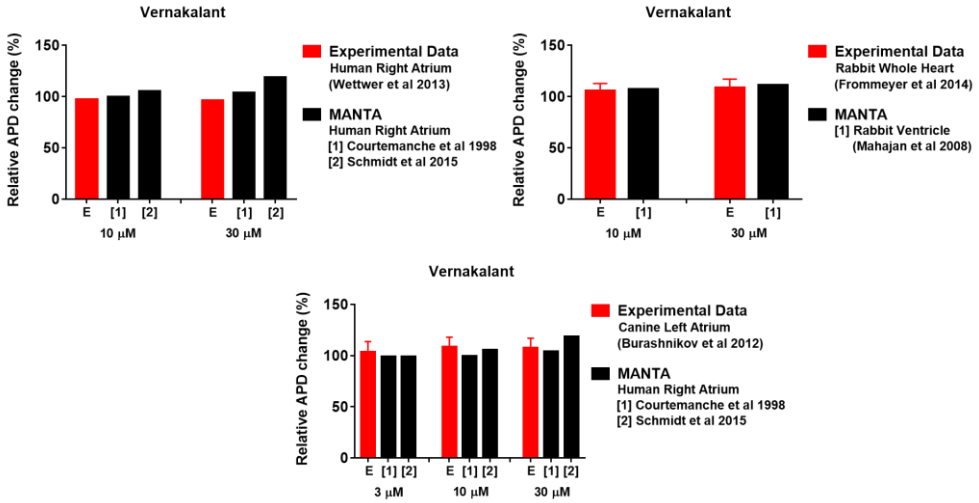
Sotalol (459, 521-523)



Verapamil (451, 459, 505)

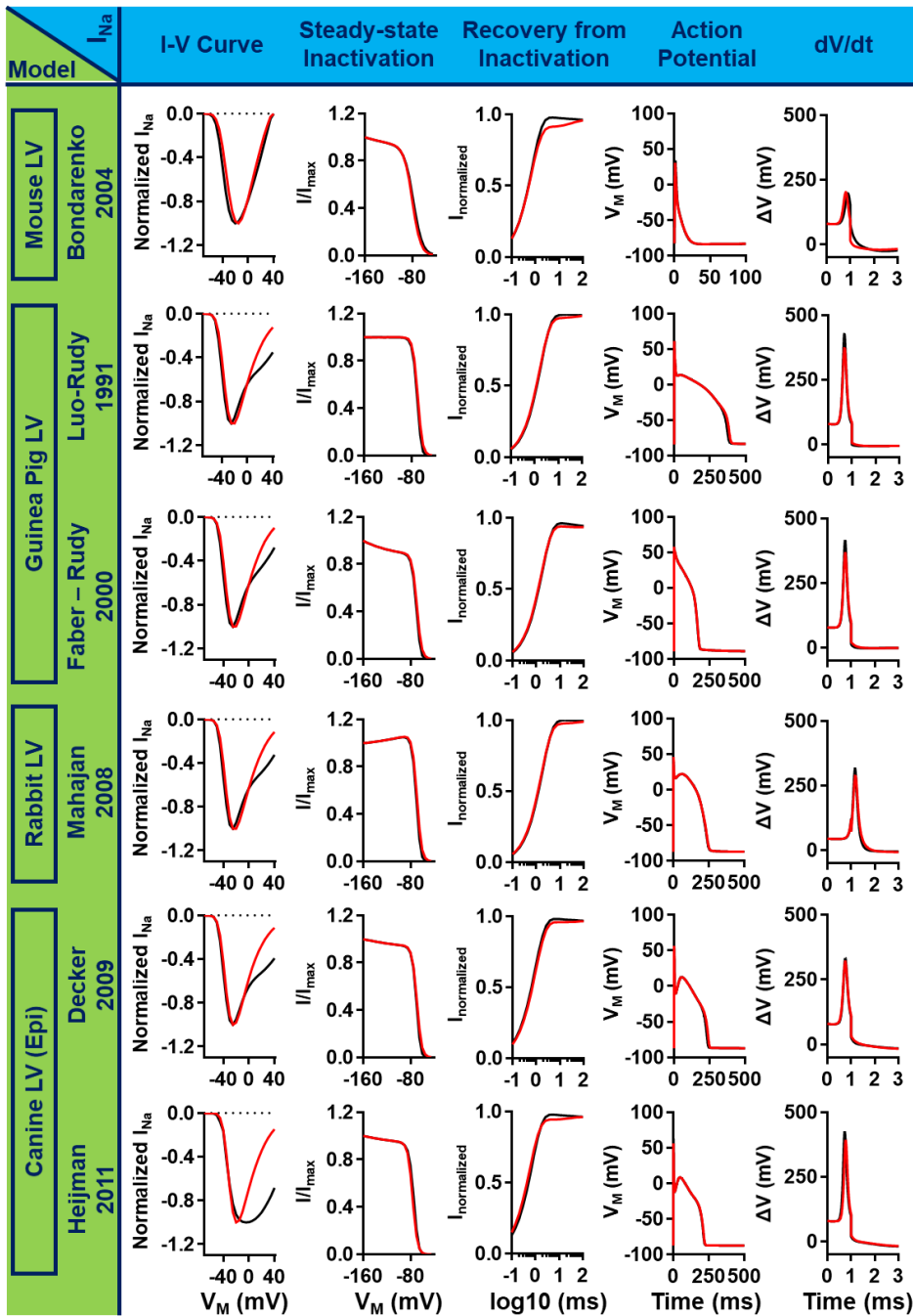


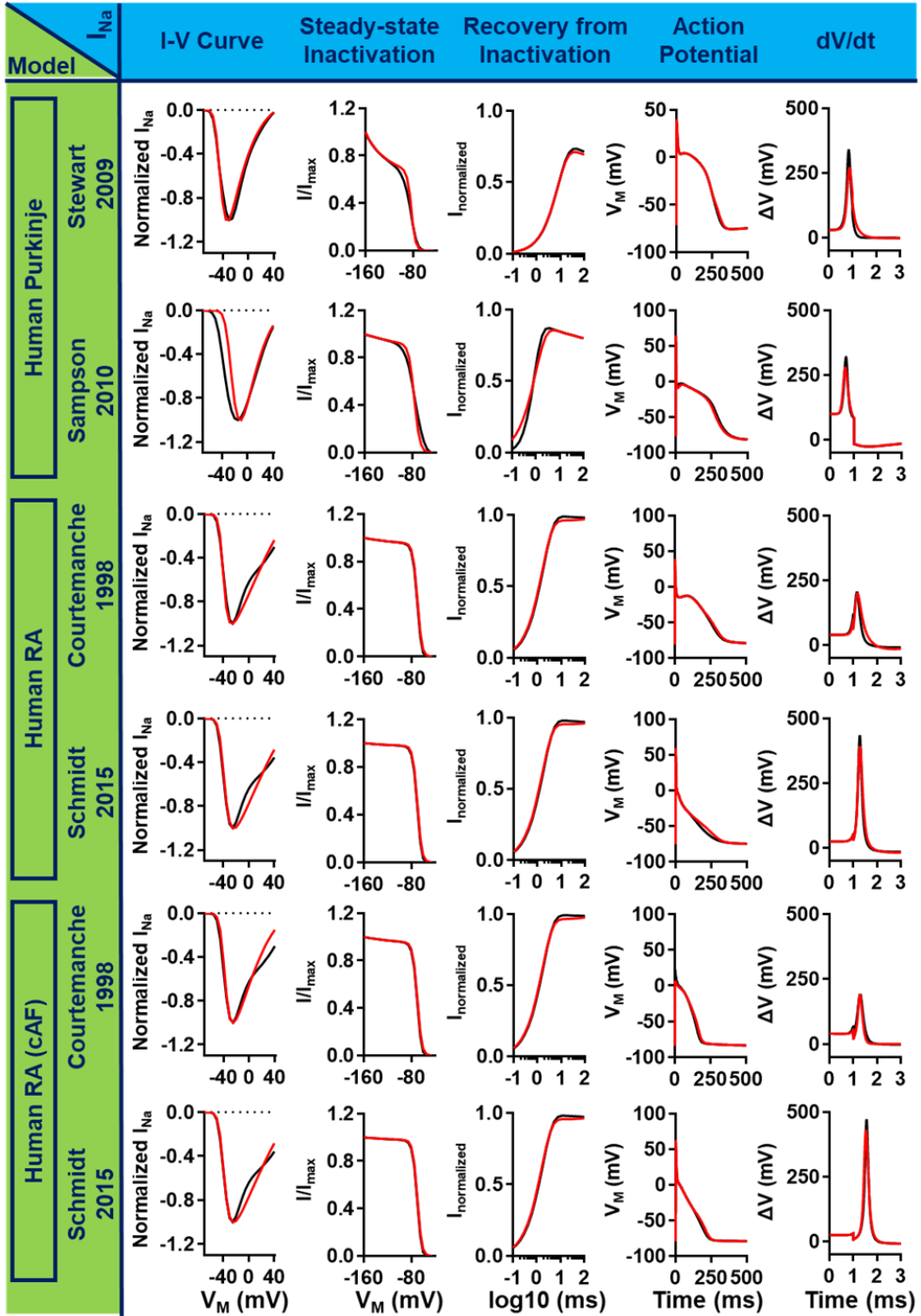
Vernakalant (491, 523, 524)

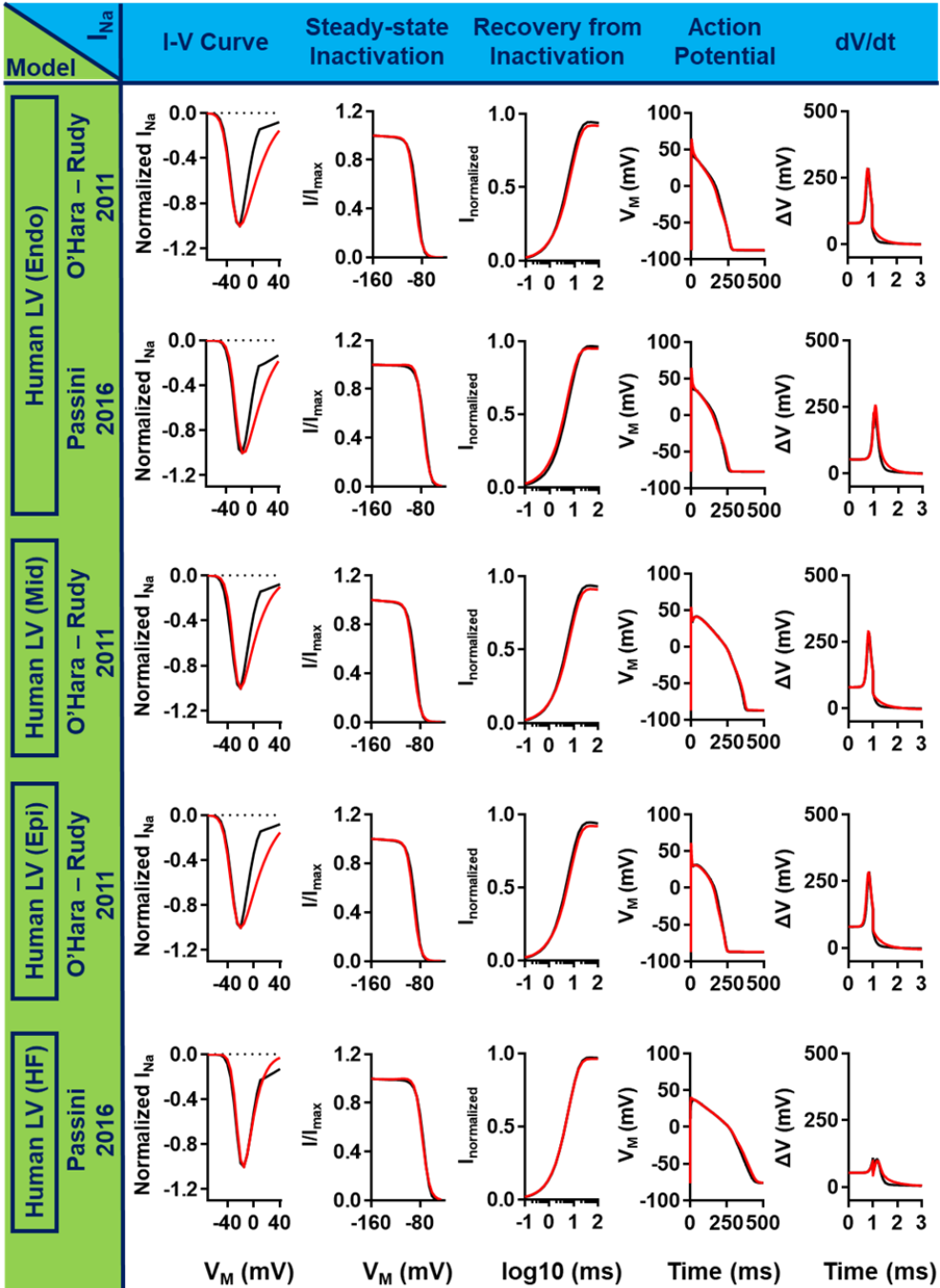


**Figure 7.5:** Structure of the  $I_{Na}$  Markov model (adapted from Moreno et al (431)) incorporated into all action potential models. The markov  $I_{Na}$  consists of three parts: the drug-free states (**black**), the neutral-drug-bound states (**blue**) and the charged-drug-bound states (**red**). The inactivated, trapped states (DpIT / DIT) are active in the presence of flecainide, but not for lidocaine, in line with Moreno et al. (431).

**Figure 7.6: Optimization of  $I_{Na}$  properties** (I-V curve, steady-state inactivation, recovery from inactivation, action potential and upstroke velocity; left to right) in the drug-free component of the Markov model (**red lines**) compared to the original models'  $I_{Na}$  formulation (**black lines**) for different action potential models.







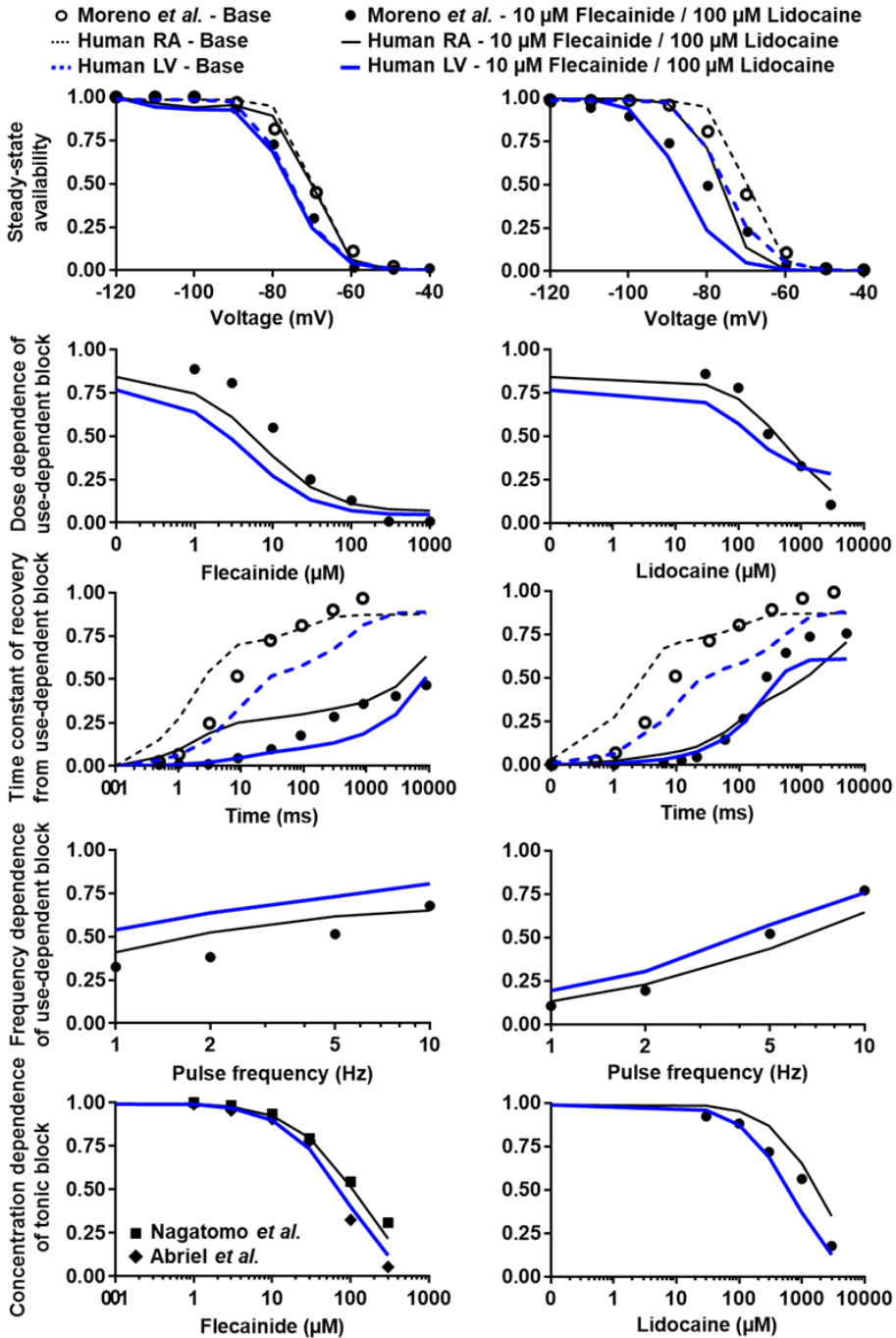


Figure 7.7: Simulated inhibition of relative  $I_{Na}$  by flecainide and lidocaine compared to published experimental results for various voltage-clamp protocols (details in Moreno *et al.* (431)).

## 7.3 Results

### 7.3.1 Species differences in AAD effects

Numerous animal models have been used to study AADs and species differences in AAD effects may hinder the clinical translation of experimental findings (525). Therefore, we investigated the species-dependent effects of AADs on the APs of mouse, guinea pig, rabbit, dog and human left ventricular (LV) cardiomyocyte models using MANTA. Application of the Class Ic AAD flecainide resulted in a concentration-dependent prolongation of APD and reduction in  $dV/dt_{max}$  in all species. However, the extent of APD prolongation and  $dV/dt_{max}$  reduction were species dependent, with the largest APD prolongation in the Passini human LV cardiomyocyte model (29% increase with 1  $\mu$ M and 72% increase with 3  $\mu$ M flecainide) and the smallest APD prolongation in the Faber guinea pig LV and Mahajan rabbit LV model (+5% with 1  $\mu$ M and +9% with 3  $\mu$ M). On the other hand, the biggest reduction of  $dV/dt_{max}$  was achieved by the Faber guinea pig LV model (51 mV/ms (-14%) and 116 mV/ms reduction (-32%) with 1  $\mu$ M and 3  $\mu$ M flecainide; **Figure 7.8A**).

Similarly, the effects of dofetilide, a Class III AAD with primarily  $I_{Kr}$ -blocking properties, were highly species dependent. Low (6 nM) and high (12 nM) concentrations of dofetilide did not prolong APD in the Bondarenko mouse LV model (**Figure 7.8B**) and produced minor prolongation in the Faber guinea pig LV model (+7% and +11%) and the Mahajan rabbit LV model (+5% and +8%). In dog and human models, the same concentrations of dofetilide led to a much larger APD prolongation, with 38% and 84% increase in APD in the Passini human LV model and the occurrence of proarrhythmic EADs in the Decker canine LV model with 12 nM dofetilide. No change in  $dV/dt_{max}$  was observed with dofetilide (**Figure 7.8B**), consistent with  $I_{Kr}$  inhibition as primary mechanism of action.

Verapamil is a Class IV AAD (calcium channel blocker) with additional  $I_{Kr}$ ,  $I_{Kur}$  and  $I_{Na}$ -blocking effects (437, 439, 444, 445, 451, 452, 454, 459, 477). In the Bondarenko mouse LV model, a 17% increase in APD was observed with 2.0  $\mu$ M Verapamil, while in the Faber guinea pig LV model, APD decreased by 25% and 35% with 0.4  $\mu$ M and 2.0  $\mu$ M verapamil, respectively (**Figure 7.8C**). An APD reduction (of 60% and 73%) was also obtained in the Mahajan rabbit LV model. On the other hand, in the canine and human models, verapamil showed various degrees of APD prolongation depending on the proportional balance between  $I_{Ca,L}$ - and  $I_{Kr}$ -block. For example, in the Decker canine LV model, low concentrations of verapamil resulted in 42% APD prolongation, while high concentrations only slightly increased APD, with  $I_{Ca,L}$  inhibition offsetting APD-prolonging effects with higher concentrations of verapamil. By contrast, the Passini human LV model showed a larger APD prolongation with 2.0  $\mu$ M verapamil (+137%) compared to 0.4  $\mu$ M (+28%). These results highlight the complex concentration- and species-dependent effects of AADs.

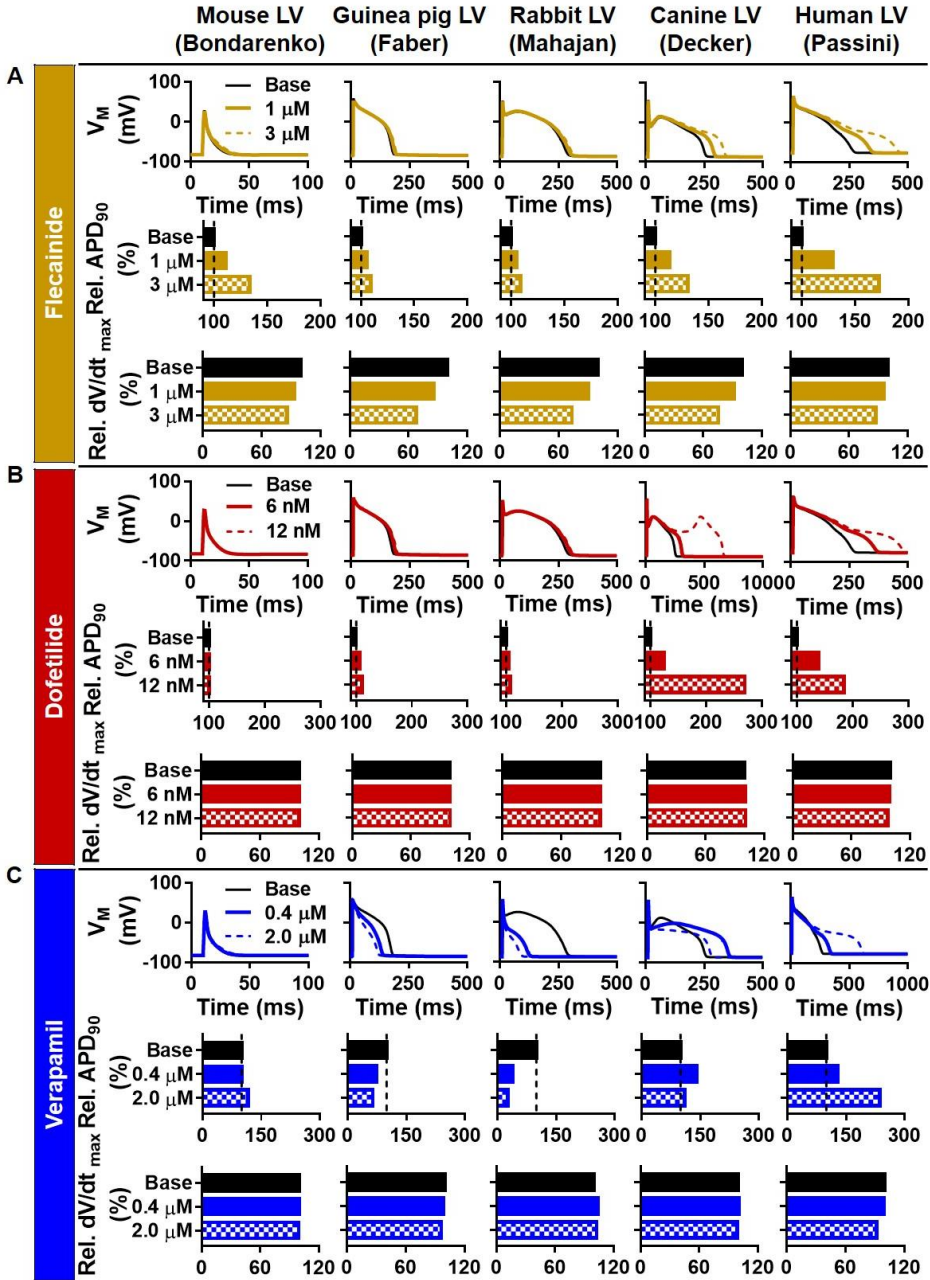
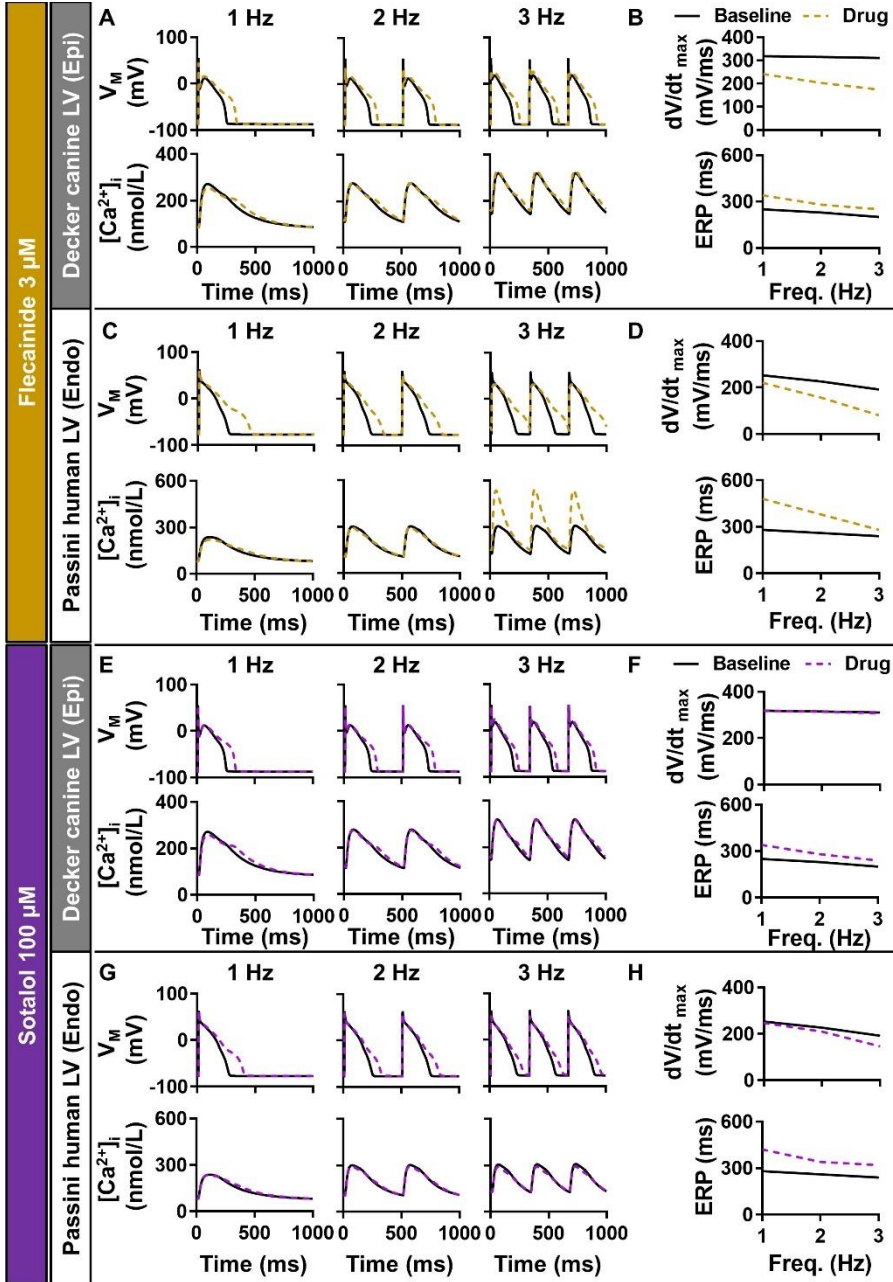


**Figure 7.8:** The effects of flecainide, dofetilide and verapamil on APD and  $dV/dt_{\text{max}}$  of various species. A) APs at baseline and with 1 and 3  $\mu\text{M}$  flecainide (top) and quantification of APD and  $dV/dt_{\text{max}}$  changes relative to baseline (bottom) for mouse, guinea pig, rabbit, dog and human left-ventricular (LV) cardiomyocyte models. B) Similar to panel A for baseline, 6 nM and 12 nM dofetilide. C) Similar to panel A for 0.4  $\mu\text{M}$  and 2.0  $\mu\text{M}$  verapamil.

### 7.3.2 Rate-dependence and reverse rate-dependence of AADs

Class I AADs have pronounced rate-dependent properties due to state-dependent sodium channel block. Most Class I AADs primarily block the sodium channel during open and inactivated states, leading to increased inhibition at faster pacing rates (412). In the closed state, the drug unbinds, losing its ability to block the sodium channel (526, 527). At slow rates, the channel spends more time in the closed state, promoting greater drug unbinding. By contrast, Class III AADs exhibit the strongest APD-prolonging effect at slow rates, a concept termed reverse rate-dependence (412, 528). Reverse rate-dependence can potentially increase the risk of ventricular proarrhythmia, particularly during bradycardia. Several mechanisms may contribute to this property of Class III drugs, including state-dependent interactions with potassium channels (432); rate-dependent changes in the contribution of potassium channels to repolarization (529), e.g., accumulation of incompletely deactivated  $I_{Ks}$  during fast pacing frequencies (412, 530); or accumulation of potassium in the sarcolemmal cleft during fast pacing, reducing the APD-prolonging effect of potassium channel blockers (460). Finally, reverse rate-dependence is not restricted to pacing rates, but is an intrinsic property of the AP resulting from the interaction between APD and net membrane current, whereby a fixed reduction in membrane current results in a stronger APD-prolonging effect when the initial/baseline APD is long enough (as is the case at slow rates) (413, 531).

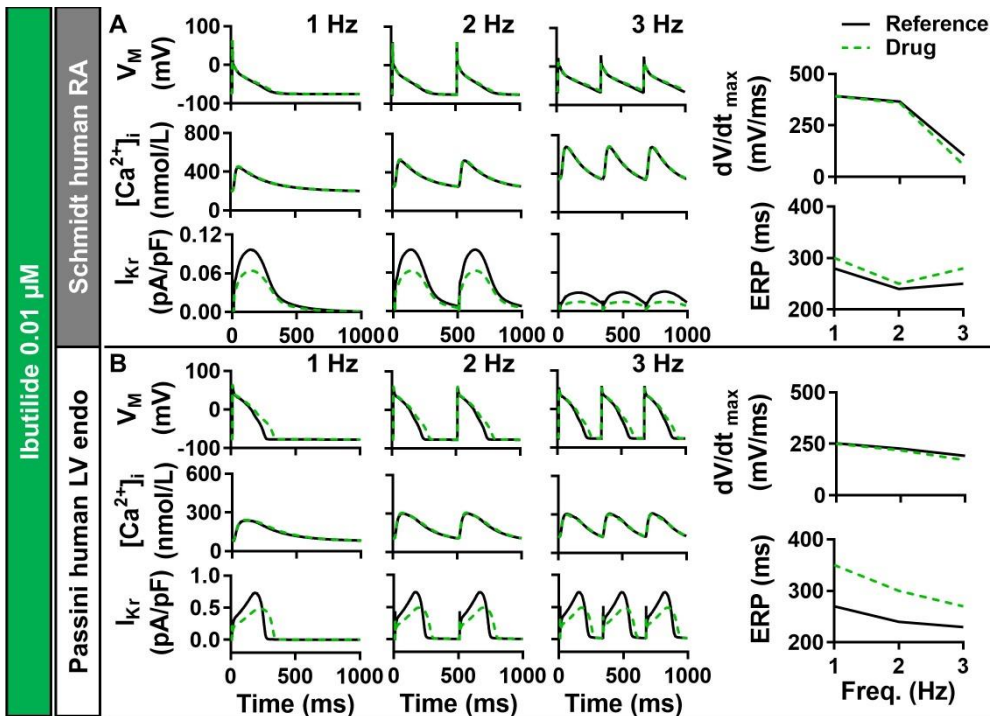
We employed MANTA to demonstrate the (reverse) rate-dependence of Class I and III AADs in the canine and human LV cardiomyocyte models (Figure 7.9). Simulated application of 3  $\mu\text{M}$  flecainide decreased  $dV/dt_{\text{max}}$  the most at higher pacing frequencies in both canine and human LV models, highlighting the rate-dependent behavior of Class I AADs. The  $I_{Kr}$ -blocking property of flecainide also resulted in prolongation of APD, which was most pronounced at slower pacing rates, consistent with the reverse rate-dependence of traditional  $I_{Kr}$ -blocking drugs (Figure 7.9A, C). Together, the reverse rate-dependent APD prolongation and rate-dependent reduction of excitability, leading to post-repolarization refractoriness, resulted in a prolongation of ERP in both models, with the largest effect at slow pacing frequencies (Figure 7.9B, D). On the other hand, simulated application of 100  $\mu\text{M}$  sotalol (simulated without  $\beta$ -blocking effects) resulted in a clear reverse rate-dependent pattern in both models, with more pronounced APD prolongation with decreasing pacing frequency (Figure 7.9E-H). Sotalol did not directly affect  $dV/dt_{\text{max}}$  in the canine model and had a minor indirect effect on  $dV/dt_{\text{max}}$  in the human model at fast rates due to a shorting of the diastolic interval and less time for recovery from inactivation of  $I_{Na}$  (Figure 7.9G-H).



**Figure 7.9:** The effect of flecainide and sotalol on upstroke velocity ( $dV/dt_{max}$ ) and effective refractory period (ERP) of canine and human LV models. A–D) APs and CaTs during steady-state pacing at 1, 2, or 3 Hz in the absence (black solid lines) or presence (dashed lines) of  $3 \mu\text{M}$  flecainide in the Decker canine LV model (A) and Passini human LV model (C). Panels B and D show frequency dependence of  $dV/dt_{max}$  and ERP in both models, highlighting a rate-dependent reduction in  $dV/dt_{max}$ . E–H) Similar to panels A–D for  $100 \mu\text{M}$  sotalol, a Class III AAD, showing a reverse rate-dependence of ERP prolongation, without significant effects on  $dV/dt_{max}$ .

### 7.3.3 Atrial specificity of AADs

AF is the most common clinically relevant heart rhythm disorder and despite advances in catheter ablation therapy, pharmacological management with anticoagulants and AADs remains a cornerstone for the treatment of symptomatic AF (532-534). However, the use of currently available AADs is limited by an increased risk of ventricular proarrhythmia (535). The development of atrial-specific AADs has been proposed to enable a safer, more effective pharmacological treatment of AF (405, 414). We employed MANTA to compare AAD effects on atrial and ventricular APs and assessed potential proarrhythmic side effects. The Class III AAD ibutilide (0.01  $\mu\text{M}$ ) prolonged the APD of the human RA model by 27 ms (**Figure 7.10A**), while in the human LV endocardium model, APD was increased by 68 ms at 1 Hz pacing (**Figure 7.10B**), suggesting a ventricular-predominant effect with associated risk for drug-induced “torsade-de-pointes” arrhythmias. On the other hand, vernakalant has been shown to exhibit atrial predominant effects (414, 469, 492) by blocking  $I_{\text{Kur}}$ , which is found exclusively in atrial cardiomyocytes, and favoring inhibition of  $I_{\text{Na}}$  at fast rates, as would occur during rapid atrial rhythms like AF. Simulated application of 10  $\mu\text{M}$  vernakalant in both atrial and ventricular models at 3 Hz pacing frequency prolonged the ERP by 50 ms and 40 ms, respectively (**Figure 7.10C, D**). Similarly, the reduction in maximum upstroke velocity was more pronounced in atrial compared to ventricular cardiomyocyte models (185 mV/ms vs. 91 mV/ms reduction at 2 Hz), suggesting a slight atrial-predominant effect of vernakalant in these models, although this effect was less pronounced than observed experimentally (434, 491, 523).



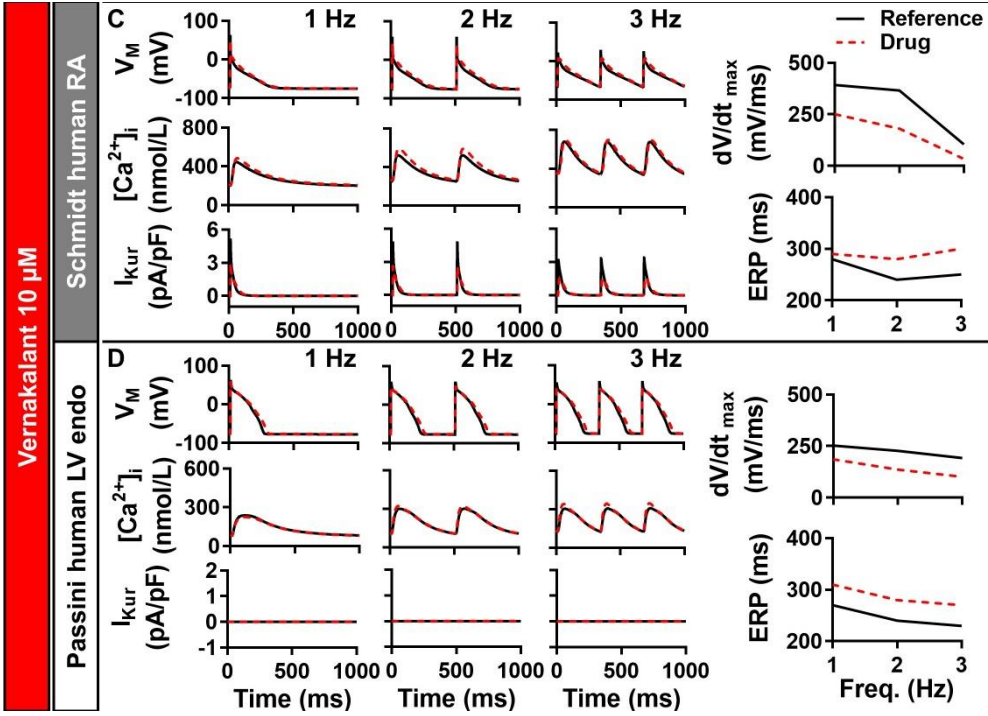


**Figure 7.10:** The effects of ibutilide and vernakalant on upstroke velocity ( $dV/dt_{max}$ ) and effective refractory period (ERP) of human RA and LV cardiomyocyte models. A–B) APs, CaTs and  $I_{Kur}$  during steady-state pacing at 1, 2, or 3 Hz in the absence (black solid lines) or presence (dashed lines) of  $0.1 \mu\text{M}$  ibutilide in the Schmidt human RA model (A) and Passini human LV model (B). Rightmost panels show frequency dependence of  $dV/dt_{max}$  and ERP in both models, highlighting a ventricle-predominant effect of ibutilide. C–D) Similar to panels A–B for  $10 \mu\text{M}$  vernakalant. In these models, vernakalant exhibits a slight atrial-predominant effect, with larger reduction of  $dV/dt_{max}$  and more ERP prolongation in the human RA model during 3 Hz pacing.

### 7.3.4 Changes in AAD effects in cardiovascular diseases

Cardiovascular diseases such as AF and HF produce extensive ion channel (electrical) remodeling, which may modulate the effect of AADs. For example, all Class III AADs except amiodarone are contraindicated for rhythm control of AF in patients with concomitant HF due to increased risk of ventricular proarrhythmia under these conditions (408). Amiodarone has differential acute and chronic electrophysiological effects (Table 7.3). We compared the steady-state effects of chronic amiodarone, as would be used for long-term rhythm control, dofetilide and sotalol on APD in Passini human LV cardiomyocyte models with and without HF-related electrical remodeling, as reported by (536) (Figure 7.11). HF-related electrical remodeling resulted in reduced  $I_{Kur}$ , prolonged APD and CaT duration, reduced CaT amplitude, and increased diastolic calcium levels (Figure 7.11A, B) (374). Inhibition of  $I_{Kur}$  by sotalol and dofetilide produced a concentration-dependent increase in APD, which was more pronounced in the heart failure compared to the control model. For example, simulated application of sotalol ( $125 \mu\text{M}$ ) resulted in a larger APD prolongation (286 ms) in the HF model compared to the control model (169 ms). Similarly, dofetilide ( $8 \text{ nM}$ ) prolonged APD by

222 ms and 136 ms in the HF and control models, respectively. This excessive concentration-dependent APD prolongation in the setting of HF-related remodeling was less pronounced during simulated application of chronic amiodarone (Figure 7.11C), consistent with its lower proarrhythmic risk in heart failure patients.

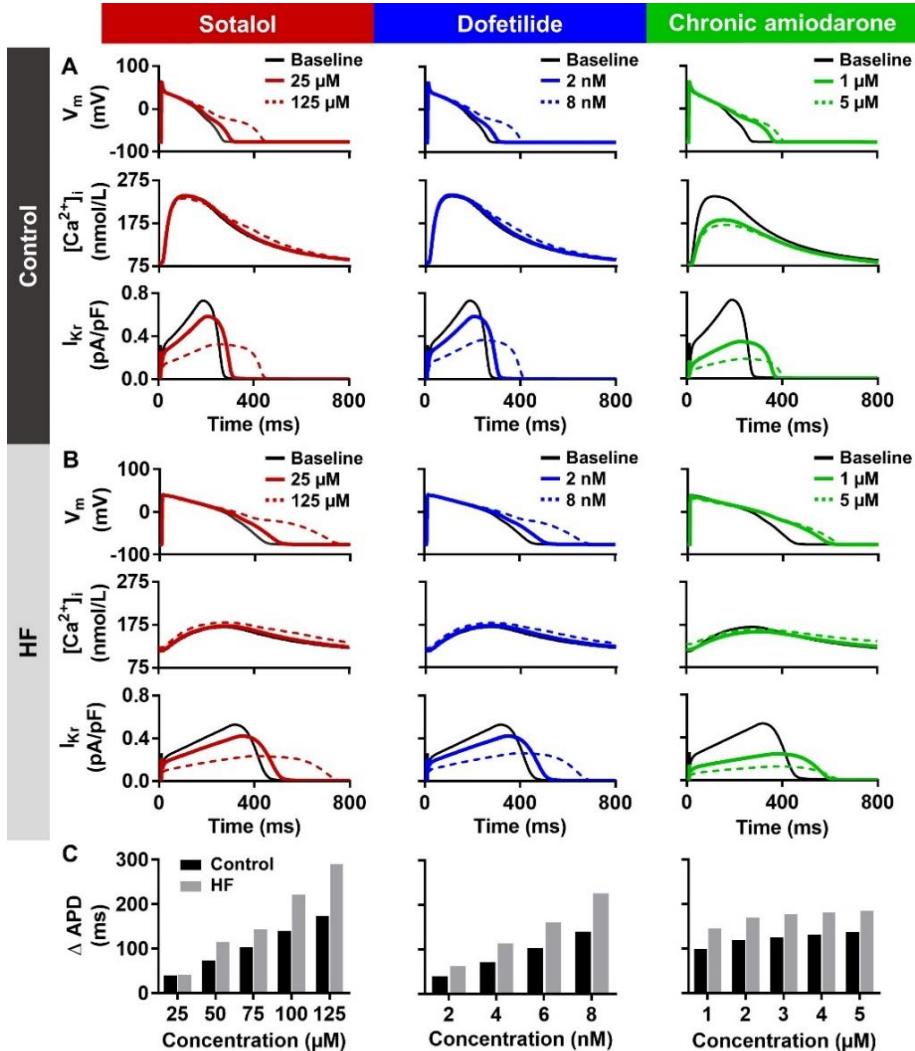


**Figure 7.11:** The effects of sotalol, dofetilide and chronic amiodarone on the APD of Passini human ventricular cardiomyocyte models with or without HF-related electrical remodeling. Degree of HF-related electrical remodeling was based on (536). A–B) APs, CaTs and  $I_{Kr}$  in models without (control, A) and with (B) HF-related electrical remodeling in the absence or presence of sotalol, dofetilide or chronic amiodarone (left to right). Sotalol, dofetilide and chronic amiodarone prolonged APD in all models by blocking  $I_{Kr}$ . C) Quantification of APD changes induced by various concentrations of sotalol, dofetilide and chronic amiodarone in control (black bars) and HF (grey bars) models. Sotalol and dofetilide produced a more pronounced concentration-dependent APD prolongation in the HF model compared to the control (non-HF) model, which was not observed with chronic amiodarone.

We also employed MANTA to investigate the steady-state electrophysiological effects of AADs in the Schmidt human RA cardiomyocyte model with and without long-standing persistent ('chronic') AF (cAF)-related remodeling (Figure 7.12). Simulated application of sotalol during 2 Hz pacing resulted in a similar concentration-dependent prolongation of APD in both the model with and without cAF-related remodeling (18 ms and 53 ms increase with 50  $\mu\text{M}$  or 400  $\mu\text{M}$  sotalol in cAF vs. 19 ms and 47 ms in control). High concentrations of sotalol also reduced  $dV/dt_{\text{max}}$  due to inhibition of  $I_{K1}$ , leading to depolarization of resting membrane potential, as well as slight  $I_{\text{Na}}$  inhibition. This effect was less pronounced in the presence of cAF-related remodeling (21 mV/ms vs. 45 mV/ms), which reduces the resting membrane potential. The effects of the Class Ic AAD flecainide also depended on the disease condition. In the model with cAF-related remodeling paced at 2 Hz, APD prolongation was smaller (46 ms and 81 ms increase with 2  $\mu\text{M}$  or 8  $\mu\text{M}$  flecainide, respectively) compared to the control model (53 ms and 95 ms). In addition, the flecainide-induced reduction of  $dV/dt_{\text{max}}$  was smaller (11 mV/ms and 35 mV/ms reduction with 2  $\mu\text{M}$  and 8  $\mu\text{M}$  flecainide) compared to the control model (27 mV/ms and 76 mV/ms) due to hyperpolarization of the resting membrane potential, further highlighting the disease-specific effects of AADs. By contrast, simulated application of 0.5  $\mu\text{M}$  chronic amiodarone had similar effects on  $dV/dt_{\text{max}}$  in the cAF model and the control model (22 mV/ms reduction), although the APD-prolonging effects at this concentration were minimal. These observations are consistent with in vivo measurements in AF patients showing unaltered monophasic APD but reduced intra-atrial conduction velocity in the presence of amiodarone (537), although APD-prolonging effects have also been described (538). The fact that amiodarone-induced electrophysiological effects are preserved in cAF may contribute to the superior clinical effectiveness of this AAD for long-term rhythm control in AF patients compared to sotalol and flecainide (407).

## 7.4 Discussion

Understanding the effect of AADs in the heart can often be challenging yet is needed for better arrhythmia management. In this study, we presented MANTA, a novel computational tool to predict the cellular effects of AADs in various species, regions of the heart and experimental settings. Our simulations reproduce a number of key characteristics: 1) species-specific effects of AADs, 2) rate-dependent effects of AADs, 3) the atrial specificity of vernakalant, and 4) the superiority of chronic amiodarone as an antiarrhythmic therapy in the setting of heart failure and cAF. Our data establish MANTA as a useful tool to analyze the mechanisms underlying a wide range of AAD properties and to illustrate the distinct properties of AADs for educational purposes.

### 7.4.1 Diversity of AAD actions

AAD therapy plays a major role in cardiac arrhythmia management but choosing the optimal AAD for an individual patient is highly challenging. Several AADs, including quinidine, flecainide, dofetilide and sotalol can promote ventricular proarrhythmia (532). Since quinidine was introduced as one of the first AADs more than a century ago (539), significant efforts have therefore been made to develop new AADs with increased

efficacy and fewer adverse side-effects. However, progress has been limited, likely in part due to an incomplete understanding of both the underlying arrhythmia mechanisms and complex electrophysiological effects of AADs (540). Using MANTA, we could demonstrate that AADs have pronounced species-dependent effects, which were due to the differential expression of cardiac ion channels, resulting in distinct APD/ERP prolongation across species (410, 541), as well as in different regions of the heart (1, 542). Such species-dependent effects make the selection of appropriate animal models for AAD testing essential. In addition, simulated application of Class I and III AADs resulted in rate-dependent electrophysiological effects due to their (reverse) rate-dependent behavior (413). Cardiovascular diseases such as AF and HF produce abnormalities in cardiac electrophysiology and calcium handling (3, 32, 121), which may change the pharmacodynamics of AADs. We demonstrated preserved electrophysiological effects during simulated application of chronic amiodarone in cardiomyocyte models with cAF- or HF-related electrical remodeling, illustrating how MANTA can be used to assess disease-specific AAD effects.

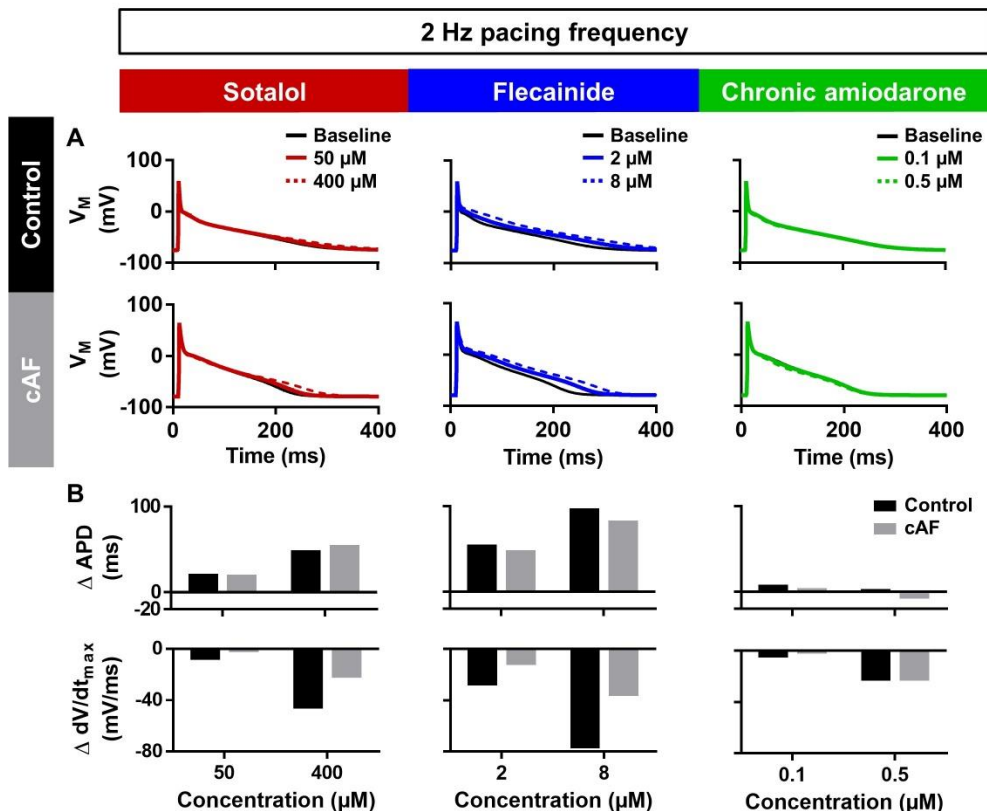


**Figure 7.12:** The effects of sotalol, flecainide and chronic amiodarone on APD and upstroke  $dV/dt_{max}$  of Schmidt human RA models with and without long-standing persistent ('chronic') atrial fibrillation (cAF)-related electrical remodeling. A) APs at baseline and with 50 and 400  $\mu$ M sotalol (left), 2 and 8  $\mu$ M flecainide (center) and 0.1 and 0.5  $\mu$ M chronic amiodarone for control (top) and cAF (bottom) cardiomyocyte models.

## *Maastricht antiarrhythmic drug evaluator (MANTA)*

B) Quantification of APD changes compared to baseline (top) and difference in  $dV/dt_{max}$  compared to baseline (bottom) for control (black) and cAF (grey) cardiomyocyte models.

Nonetheless, the wide spectrum of comorbidities associated with these cardiovascular diseases may also affect the pharmacokinetics of AADs, potentially altering drug absorption, metabolism or excretion and making it more difficult to develop AADs with strong efficacy without evoking major adverse events. Together, these complex interactions between AAD properties and actual clinical conditions make it challenging to intuitively predict whether the antiarrhythmic actions of AADs would outweigh their potential proarrhythmic tendencies (412). AADs with atrial-predominant effects might provide safer options for pharmacological treatment of AF. In general, the atrial specificity of these AADs is achieved by their  $I_{Kur}$  blocking effect, a higher affinity for the inactivated state of the cardiac sodium channel and fast sodium channel dissociation kinetics (543). Atrial cardiomyocytes have a more depolarized resting membrane potential compared to ventricular cardiomyocytes, particularly at fast rates such as during AF, which promotes the atrial-predominant effect of these AADs (434, 523, 543). In agreement, we could demonstrate ventricular-predominant effects of Class III AADs and a slight atrial-predominant effect of simulated vernakalant. Moreover, MANTA makes it easy to adjust the affinity of an AAD for individual targets, enabling investigations of the optimal AAD properties for a given clinical condition, for example to achieve AF-predominant effects.

### **7.4.2 Role of computational modeling in cardiac arrhythmia management**

In the last few decades, computational modeling of cardiac electrophysiology has contributed to a better understanding of cardiac arrhythmogenesis. Until now, more than 50 computational cardiomyocyte models of different species and regions of the heart have been developed to investigate cardiac electrophysiology and (patho)physiology. Based on these advances, *in silico* modeling has also become a central element in the Comprehensive *in vitro* Proarrhythmia Assay (CiPA) initiative to assess the safety profile of new drugs (544). For example, the Virtual Assay (421) provides a framework for *in silico* proarrhythmic toxicity trials in a population of calibrated human ventricular cardiomyocyte models and can predict clinical risk of 62 reference compounds with high accuracy. In addition, the U.S. Food and Drug Administration (FDA) aims to transform computational modeling from a scientific tool into a valuable regulatory instrument in which digital evidence is being used instead of other types of evidence (545). Moreover, whole-heart modeling has recently been employed to support the decision-making process prior to catheter ablation of AF (546). Thus, several novel clinical and regulatory applications of computational modeling are starting to emerge.

In addition, several educational tools have been developed to teach cardiac (cellular) electrophysiology. For example, LabHEART® provides a user-friendly tool to simulate ion currents and calcium transport proteins in a rabbit ventricular myocyte (417), the MioLab® simulator describes calcium dynamics and contractile forces during contraction and relaxation of cardiomyocytes (418), and the web-based

simulation platform eSolv enables teachers to load a cardiomyocyte CellML model and generate simulations adapted to the students' level by defining whether and to what extent model parameters can be changed (419). Although it is possible to perform simulations with ion-channel blockers in both eSolv and MioLab®, as well as in the more generic cardiomyocyte simulation tools Myokit (344) and LongQt (420), these computational tools are limited in their ability to compare the effects of AADs on the AP under various conditions in a user-friendly way. They do not contain a library of cardiomyocyte models, nor do they come with multiple AADs, which effects can be simulated simultaneously in a reasonably short period of time. Moreover, these tools do not incorporate the state-dependent effects of AADs, which are particularly relevant for Class I AADs. MANTA was developed to facilitate analyses of the cellular effects of currently available AADs under user-defined experimental settings. It also serves as a library of commonly used cardiomyocyte models and AADs, with a capability to simulate the cellular effects of AADs using either state-dependent regulation or IC<sub>50</sub>-based inhibition of cardiac ion channels. MANTA also enables a direct comparison of the effects of two AADs on two different cardiomyocyte models. Finally, MANTA combines these features in a user-friendly interface, so that the users can operate MANTA without extensive guidance and/or modeling skills. As such, MANTA can function as an educational tool to help students understand the cellular mechanism of AADs, as well as their species- and condition-dependent effects. As MANTA facilitates comparison between two AADs under user-defined experimental/environmental settings, including heart rate / pacing frequency and electrolyte concentrations, it enables simulations to dissect, for example, why AADs are contraindicated under certain simulated pathophysiological conditions such as hypo/hyperkalemia or bradycardia.

### 7.4.3 Potential limitations

We employed 17 previously published cellular cardiomyocyte models, each with their own limitations, which likely affect the outcome of AAD simulations. For example, the original Luo-Rudy Guinea pig model (423) does not consider different potassium channel subtypes, precluding reliable analyses of Class III AADs in this particular model. Similarly, we enable the users to change the extracellular calcium, potassium, and sodium to observe the effects of different extracellular ionic concentrations on the AP. However, the effects might not be representative if the range of applicability of a particular model is exceeded, as previously shown by Severi et al (150) for changes in extracellular calcium. Such model limitations should be considered when interpreting simulation results. On the other hand, the ability to quickly compare drug effects in two models of the same species/region in MANTA may help to highlight such limitations.

We simulated the effects of AADs on individual cardiac ion channels based on previously published experimental IC<sub>50</sub> values, which may be influenced by various experimental conditions, including the cell type, temperature, ionic concentrations and voltage-clamp protocols (547-549). Indeed, as seen in **Figure 7.3**, there are differences in the reported IC<sub>50</sub> values between studies and the availability of data in human cardiomyocytes is rather limited. As such, some validation of the state-dependent I<sub>Na</sub>

inhibition was adapted from non-human experimental data, which may bias the results. In addition, there is evidence that dynamic state-dependent block may also be relevant for other ion channels (e.g.  $I_{Kur}$ ,  $I_{Kr}$  and  $I_{SK}$ ) (10, 76, 380, 550, 551), so as more experimental data become available, future work might consider replacing the  $IC_{50}$ -based inhibition of ion currents with state-dependent inhibition using detailed Markov models. Nevertheless, the cellular electrophysiological response (e.g., APD prolongation) of several AADs and models was consistent with experimental data (Figure 7.4), strongly suggesting that the current approach provides a reasonable approximation. Finally, in the current version of MANTA, we incorporated drug effects on 10 major cardiac ion currents. However, data about AAD effects on several additional cardiac ion channels is emerging, including the acetylcholine-activated inward-rectifier potassium channel and two-pore domain potassium channel (428), hyperpolarization-activated cyclic nucleotide-gated (HCN) channel (552), transient receptor potential (TRP) channels (553) and voltage-gated  $Kv1.1$  channels (554), which are not included in most current cardiomyocyte models. Therefore, it is currently not possible to simulate the effect of AADs such as ivabradine (552), BMS914392 (555), NIP-151 (556) and tertiapin (557), which exert their function mainly through those channels. Similarly, the absence of  $\beta$ -adrenoceptor-signaling components in almost all cardiomyocyte models precludes simulation of the effects of Class II AADs and makes it difficult to simulate exercise, which is a well-known proarrhythmic trigger (3, 78, 558, 559), although MANTA allows users to simulate the effects of AADs during higher pacing frequencies.

Importantly, although MANTA can provide useful general information about species- and condition-specific AAD effects, there is pronounced inter-individual variability in cardiac electrophysiology and pharmacokinetics that can influence AAD effects. Although population-based approaches have been proposed to simulate inter-individual variability (421), patient-specific risk assessment or recommendation of AAD therapy is currently not feasible.

#### **7.4.4 Future outlook and potential contributions of MANTA**

We have shown that MANTA can reproduce a large number of clinically relevant AAD characteristics at the cellular level and can be used to investigate the underlying ionic mechanisms. However, various publications have shown that the cellular effects of an AAD can be different from organ-level effects due to cell-to-cell interactions, spatial heterogeneities in electrical properties and additional factors, such as autonomic innervation (409, 541, 560-562). Importantly, arrhythmias are inherently tissue-level phenomena and to study pro- or antiarrhythmic actions of AADs the tool would have to be extended to tissue or whole-heart simulations. At present, these simulations are computationally demanding, limiting the educational use of the tool. However, as processor speeds increase, future versions of MANTA may be able to accommodate such simulations, significantly increasing the clinical relevance of the tool. Additionally, MANTA simulates the effects of AADs based on a given cellular concentration. At the moment, it is hard to determine the appropriate concentration based on the clinical drug dose due to the different pharmacokinetics of each AAD. Pharmacokinetic models

for different cardiovascular drugs have been established that enable simulation of plasma concentrations over time (563, 564). In the future, MANTA could incorporate such pharmacokinetic models to investigate the electrophysiological effects of various dosing strategies for different AADs.

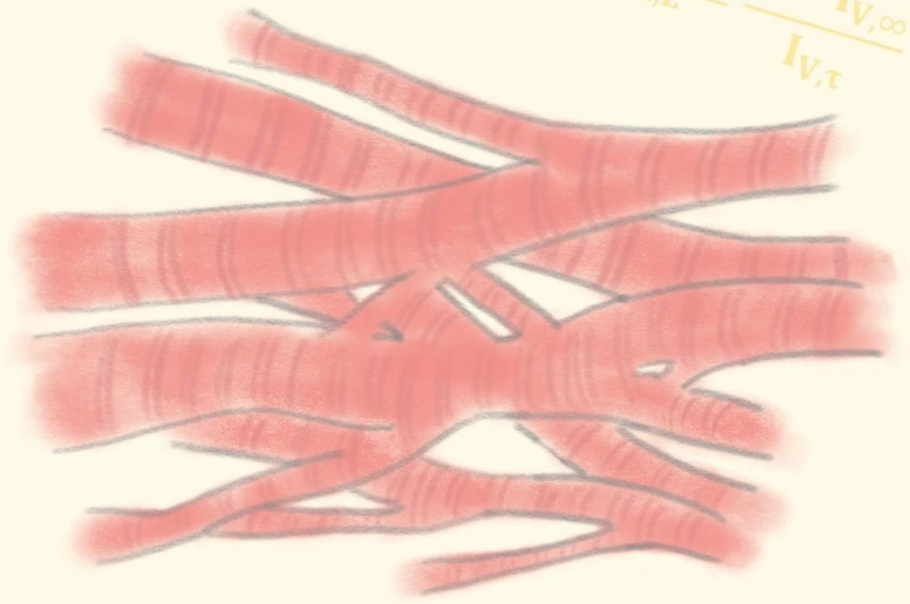
### **7.5 Conclusions**

The effects of AADs are complex and highly dependent on the experimental or clinical conditions. MANTA is a powerful, freely available tool able to reproduce a wide range of AAD characteristics including species-, rate-, and disease-dependent effects. MANTA enables analyses of the underlying ionic mechanisms as well as investigations of novel AADs with specific affinities for one or more targets. MANTA can facilitate a better understanding of AAD effects on cellular electrophysiology under a wide range of conditions, which may provide educational and/or clinically-relevant information on the safety and efficacy of AAD treatment.



$$\frac{dV_m}{dt} = -\frac{1}{C_m} * I$$

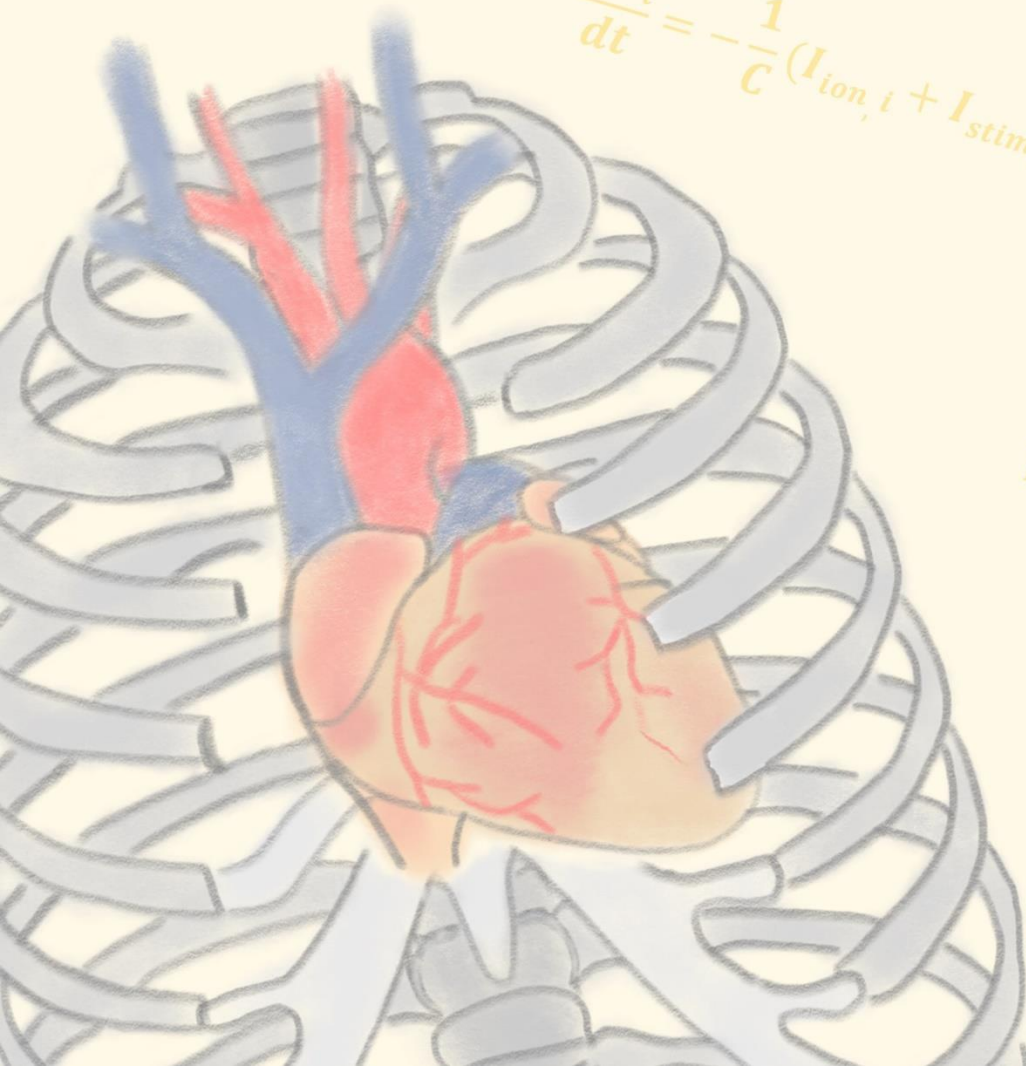
$$y_{Ca,L} = \frac{1 - I_{V,\infty}}{I_{V,\tau}}$$



$$x_{Ca,L} = \frac{I_{V,\infty}}{I_{V,\tau}}$$

$$\delta I_{Ca,L}^{s,m} =$$

$$\frac{dV_i}{dt} = -\frac{1}{C} (I_{ion,i} + I_{stim,i} + I_{diff,i})$$



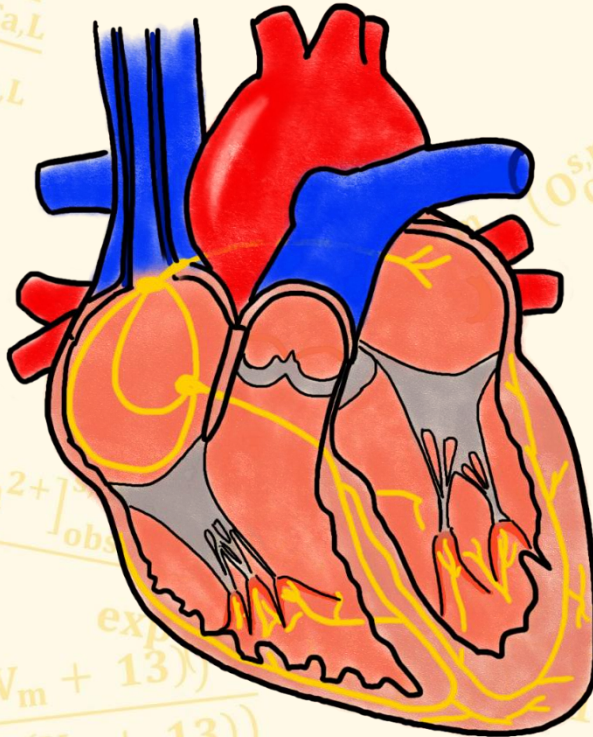
$$\bar{I}_{Ca,L}^{s,m} = P_{Ca,L} \cdot (z$$

$$ACT_{\tau} = 0.59$$

# Chapter 8

**Beta-adrenergic receptor stimulation modulates the cellular proarrhythmic effects of chloroquine and azithromycin**

H. Sutanto and J. Heijman.  
*Front Physiol.* 11:587709.



$$\frac{dV}{dt} = \frac{I_{stim} - (I_K + I_{Na} + I_{leak})}{C_m}$$

## ABSTRACT

The antimalarial drug chloroquine and antimicrobial drug azithromycin have received significant attention during the COVID-19 pandemic. Both drugs can alter cardiac electrophysiology and have been associated with drug-induced arrhythmias. Meanwhile, sympathetic activation is commonly observed during systemic inflammation and oxidative stress (e.g., in SARS-CoV-2 infection), and may influence the electrophysiological effects of chloroquine and azithromycin.

Here, we investigated the effect of  $\beta$ -adrenergic stimulation on proarrhythmic properties of chloroquine and azithromycin using detailed *in silico* models of ventricular electrophysiology. Concentration-dependent alterations in ion-channel function were incorporated into the Heijman canine and O'Hara-Rudy human ventricular cardiomyocyte models. Single and combined drug effects on action-potential (AP) properties were analyzed using a population of 1000 models accommodating inter-individual variability. Sympathetic stimulation was simulated by increasing pacing rate and experimentally validated isoproterenol-induced changes in ion-channel function.

In the canine ventricular model at 1 Hz pacing, therapeutic doses of chloroquine and azithromycin (5 and 20  $\mu$ M, respectively) individually prolonged AP duration (APD) by 33% and 13%. Their combination produced synergistic APD prolongation (+161%) with incidence of proarrhythmic early afterdepolarizations in 53.5% of models. Increasing the pacing frequency to 2 Hz shortened APD and together with 1  $\mu$ M isoproterenol counteracted the drug-induced APD prolongation. No afterdepolarizations occurred following increased rate and simulated application of isoproterenol. Similarly, chloroquine and azithromycin individually prolonged APD by 43% and 29% in the human ventricular cardiomyocyte model, while their combination prolonged APD by 76% without causing early afterdepolarizations. Consistently, 1  $\mu$ M isoproterenol at 2 Hz pacing counteracted the drug-induced APD prolongation. Increasing the  $I_{Ca,L}$  window current produced afterdepolarizations, which were exacerbated by isoproterenol. In both models, reduced extracellular potassium reduced the repolarization reserve and increased drug effects.

In conclusion, chloroquine- and azithromycin-induced proarrhythmia is promoted by conditions with reduced repolarization reserve. Sympathetic stimulation limits drug-induced APD prolongation, suggesting the potential importance of heart rate and autonomic status monitoring in particular conditions (e.g., COVID-19).

## 8.1 Introduction

Nine-months after its first identification in Wuhan, China in December 2019, Severe Acute Respiratory Syndrome-associated Coronavirus type-2 (SARS-CoV-2) infection (i.e., Coronavirus Disease 2019 / COVID-19) has contributed to more than 850,000 deaths worldwide and has been declared a pandemic with significant global socioeconomic impact (565). At the moment, the exact pathophysiology of the disease remains unclear and no definitive therapy is available. Several drugs are considered effective in preclinical studies and are currently being tested against SARS-CoV-2 in the clinic (e.g., the antivirals lopinavir, ritonavir, and remdesivir; the antimicrobial azithromycin; the antimalarial drugs chloroquine and hydroxychloroquine, and more recently antiparasitic ivermectin) (566-568). Of those, chloroquine (CQ) and azithromycin (AZM) have gained significant attention due to their high accessibility and low cost. Nonetheless, their effectivity against COVID-19 has not been confirmed by any large clinical trial and their use is controversial. Some studies reported the benefit of those drugs (569-572), while others reported no effect (573-575). This controversy is further complicated by the retraction of papers demonstrating the absence of benefit of these drugs in COVID-19 (573), potential issues with study design and analysis (576, 577), and the termination of their emergency use by the United States Food and Drug Administration (FDA) due to their potential proarrhythmic effects (578).

CQ is a widely-used antimalarial drug that inhibits multiple cardiac ion-channels (444). It has been suggested to prevent the viral entry, transport and post-entry events in COVID-19, most likely via its effects on endosomal pH and the resulting under-glycosylation of angiotensin-converting enzyme 2 (ACE2) receptors that are required for viral entry, although the exact mechanisms remain incompletely understood (579, 580). Meanwhile, AZM is a broad-spectrum macrolide antibiotic that is believed to potentiate the effect of CQ, reducing the replication capabilities of SARS-CoV-2 (579). Similar to CQ, AZM also inhibits multiple cardiac ion-channels in a dose-dependent manner (444). Therefore, the administration of CQ and AZM, alone or in combination, can prolong the ventricular cardiomyocyte action potential (AP) duration (APD) and thereby the QT interval on the electrocardiogram. Experimentally, the APD-prolonging effect of CQ and AZM, alone and in combination, has been shown in anaesthetized guinea-pig model (581). Moreover, excessive QT-interval prolongation has been implicated in drug-induced malignant arrhythmias such as Torsade de Pointes, by promoting early afterdepolarizations (EADs) and a heterogeneous repolarization substrate, and consistently observed in COVID-19 patients with CQ and AZM (578, 582-585).

Although the cardiac pathophysiology of COVID-19 remains incompletely understood, several aspects point towards increased incidence of cardiac arrhythmias (586). SARS-CoV-2 induces systemic inflammation, leading to cytokine storm (587), which is expected to increase oxidative stress by releasing reactive oxygen species (ROS). Moreover, CQ may itself promote oxidative stress (588). Both inflammation and oxidative stress have been associated with increased arrhythmogenic risk (589), e.g., through activation of calcium/calmodulin-dependent protein kinase II (CaMKII) (590, 591) and NLRP3 inflammasome (592), as observed in COVID-19 (593). Troponin-T, a marker for myocardial injury, has been shown to increase in groups of COVID-19 patients with malignant arrhythmias, denoting the major detrimental impact of SARS-

CoV-2 on the cardiovascular system (594). Moreover, COVID-19 may activate the  $\beta$ -adrenergic signaling cascade in cardiomyocytes via the stimulation of the sympathetic nervous system (587). Palpitation, which is commonly associated with the activation of  $\beta$ -adrenergic response, has been reported to be the main symptom of COVID-19 (594). Altogether, these processes may increase the propensity for cardiac arrhythmias by altering cardiomyocyte calcium-handling and modulating ion-channel properties (Figure 8.1) (335).

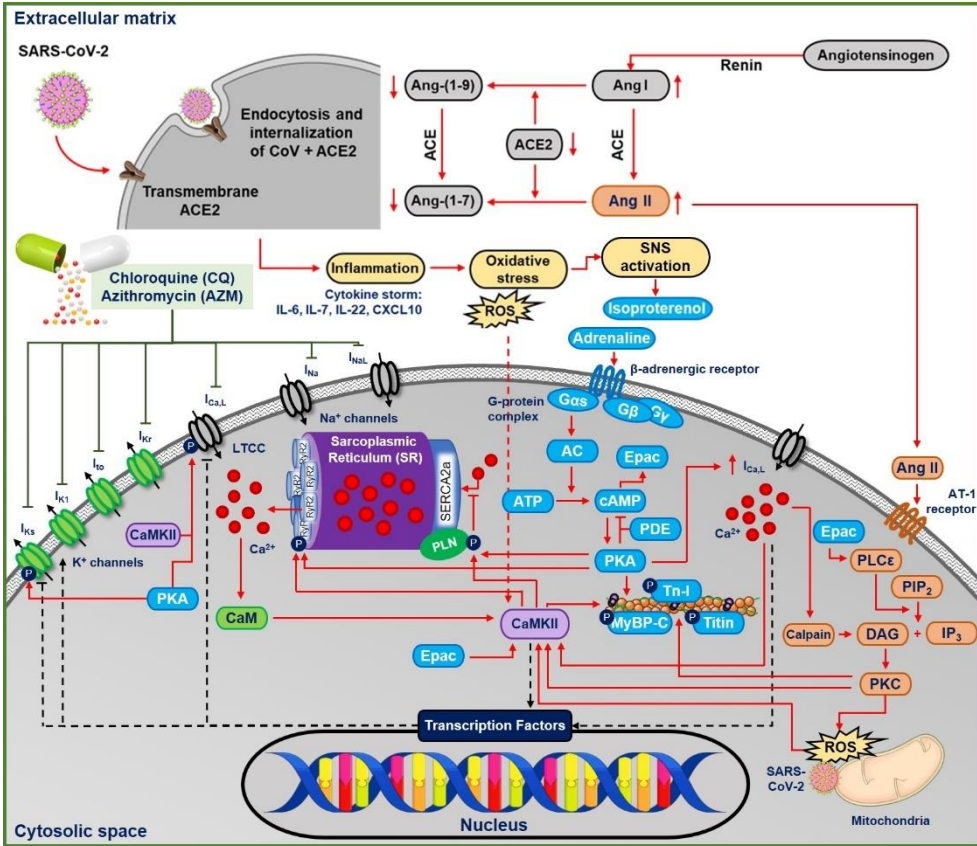


**Figure 8.1:** The multifactorial effects of COVID-19 in the ventricular cardiomyocyte and the ionic targets of chloroquine and azithromycin. The SARS-CoV-2 virus leads to the endocytosis and internalizations of the transmembrane ACE2 receptors, preventing the conversion of angiotensin I and II into their metabolites. Thus, angiotensin II binds to the AT-II receptor, initiating PKC-dependent pathways, which may further activate CaMKII-dependent signaling cascades. In COVID-19, the systemic inflammation and cytokine storm can also increase oxidative stress, leading to ROS-mediated CaMKII activation. CQ and AZM alter action potential properties through inhibition of multiple cardiac ion channels ( $I_{Na}$ ,  $I_{NaL}$ ,  $I_{Kr}$ ,  $I_{Ks}$ ,  $I_{K1}$ ,  $I_{to}$ ,  $I_{CaL}$ ). (AC = adenylyl cyclase; ACE = angiotensin converting enzyme; Ang II = angiotensin II; ATP = adenosine triphosphate; CaM = calmodulin; CaMKII = calcium/calmodulin-dependent protein kinase II; cAMP = cyclic adenosine monophosphate; DAG = diacyl glycerol; IL = interleukin; IP<sub>3</sub> = inositol triphosphate; PDE = phosphodiesterase; PIP<sub>2</sub> = phosphatidylinositol biphosphate; PKA = protein kinase A; PKC = protein kinase C; PLC = phospholipase C; ROS = reactive oxygen species; Tn-I = troponin-I)

To the best of our knowledge, previous experimental and observational studies of the potential proarrhythmic effects of CQ and AZM have not considered the role of  $\beta$ -

adrenergic receptor stimulation. Computational modeling has increasingly been used in cardiac safety pharmacology to predict the proarrhythmic effect of novel compounds (595-597). Therefore, this study aimed to assess the potential cellular proarrhythmic effects of CQ and AZM in both the absence and presence of  $\beta$ -adrenergic receptor stimulation using a population of detailed *in silico* models of ventricular electrophysiology.

## 8.2 Methods

Concentration-dependent CQ and AZM-induced alterations in 7 ion-channels (fast sodium current ( $I_{Na}$ ), late sodium current ( $I_{NaL}$ ), L-type calcium current ( $I_{CaL}$ ), transient-outward potassium current ( $I_{to}$ ), inward-rectifier potassium current ( $I_{K1}$ ), rapid delayed-rectifier potassium current ( $I_{Kr}$ ) and slow delayed-rectifier potassium current ( $I_{Ks}$ )) (444) (**Figure 8.2**) were incorporated into the Heijman canine ventricular cardiomyocyte model (78) with  $\beta$ -adrenergic receptor signaling and O'Hara-Rudy (ORd) human ventricular epicardial cardiomyocyte model (263). The Heijman canine ventricular model was employed in this study because it is one of the few cardiomyocyte models of a large mammal incorporating detailed  $\beta$ -adrenergic signaling cascades, including PKA- and CaMKII-mediated phosphorylation of cardiac ion channels. Meanwhile, the ORd human ventricular model was chosen because it is the most widely used human ventricular cardiomyocyte model that works over a wide range of experimental conditions. To simulate the electrophysiological effects of  $\beta$ -adrenergic stimulation in the human ventricular model, the experimentally validated changes in ionic current properties in response to 1  $\mu$ M isoproterenol (ISO, (598)) were applied to the ORd model and further calibrated based on recent data (599) to improve the model accuracy during maximal ISO stimulation (1  $\mu$ M).

A drug concentration within the therapeutic range of CQ and AZM was selected (5 and 20  $\mu$ M, respectively (600, 601)) and cellular simulations were performed in Myokit (344). The effects of the drugs alone and in combination (assuming independent drug-binding sites) on AP properties were assessed. Sympathetic stimulation was simulated by an increase in pacing rate and experimentally validated ISO-induced changes in ion-channel function (78, 81). All results are presented during steady-state pacing at the indicated pacing frequencies (after 1000 beats of prepacing). To evaluate the robustness of our findings and assess potential consequences of intra- and inter-subject variability on the electrophysiological effect of CQ and AZM, the maximum conductance of 9 major ionic currents ( $I_{Na}$ ,  $I_{NaL}$ ,  $I_{CaL}$ ,  $I_{Kr}$ ,  $I_{Ks}$ ,  $I_{K1}$ ,  $I_{to}$ ,  $I_{NCX}$  and  $I_{NaK}$ ) were scaled based on a normal distribution with mean 1.0 and standard deviation 0.2, to create populations of models, as previously described (346, 379). In brief, 1000 variants of the model were created and the variants displaying “non-physiological” AP properties were excluded. Non-physiological was defined as  $APD_{90}$  or RMP outside the range of 3 standard deviations of experimental  $APD_{90}$  and RMP from (382, 602), based on previous studies (381, 382). In total, 592 out of 1000 canine ventricular models and all 1000 human ventricular models were included. The non-normally distributed data are presented as median and inter-quartile ranges (IQR). The model code is available at [www.github.com/jordiheijman](http://www.github.com/jordiheijman).

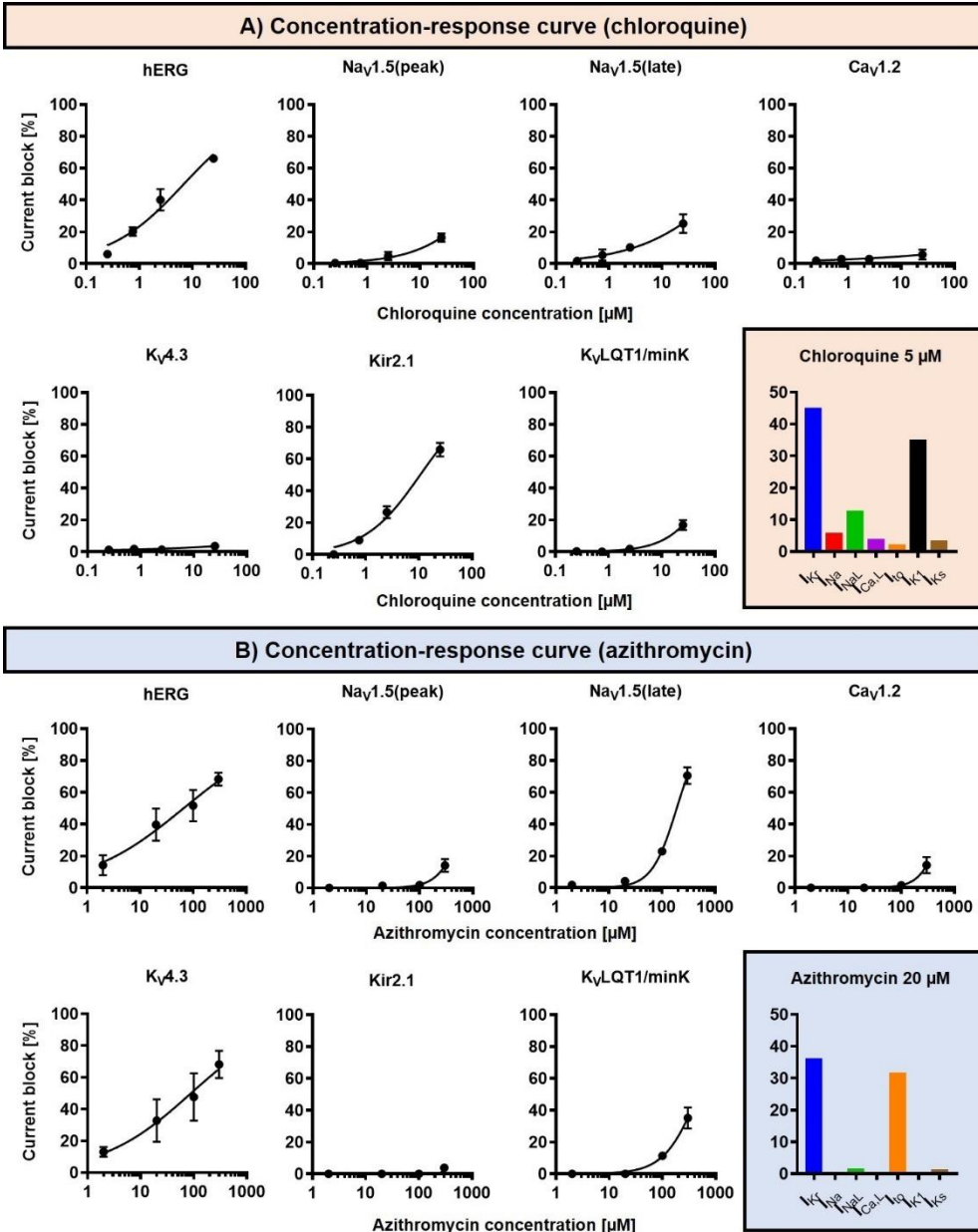


**Figure 8.2:** The concentration-dependent effects of chloroquine and azithromycin on cardiac ion channels. A) chloroquine mainly blocks  $I_{K_r}$  and  $I_{K_1}$ , with minor effects on  $I_{Na}$ ,  $I_{NaL}$ ,  $I_{to}$ ,  $I_{CaL}$  and  $I_{Ks}$ . B) azithromycin mainly blocks  $I_{K_r}$  and  $I_{to}$ , with minimal effects on  $I_{Na}$ ,  $I_{NaL}$ ,  $I_{CaL}$ ,  $I_{K_1}$  and  $I_{Ks}$ . The experimental data (black symbols) were obtained from previous experiments (444) and were fitted using Hill equations in the model (black lines). Bar charts show percentage inhibition of different ion channels using the clinically relevant concentrations employed in subsequent simulations.

## 8.3 Results

### 8.3.1 The effects of chloroquine and azithromycin on canine ventricular electrophysiology

During 1 Hz pacing, application of 5  $\mu\text{M}$  CQ in the Heijman canine ventricular epicardial cardiomyocyte model prolonged APD by 70 ms (+33%), while 20  $\mu\text{M}$  AZM prolonged APD by 27 ms (+13%). The combination of both drugs showed a synergistic effect with an APD prolongation of 339 ms (+161%) and the occurrence of an EAD, as shown in **Figure 8.3A, upper panels**. Subsequently, the contributions of  $\beta$ -adrenergic-dependent signaling cascades were assessed in two ways: by increasing the pacing frequency and through the simulated application of a maximal concentration of the  $\beta$ -adrenergic receptor agonist isoproterenol (ISO; 1  $\mu\text{M}$ ) in combination with the escalation of pacing rate. Increasing the pacing rate from 1 to 2 Hz reduced the APD in all groups, with APD reduction of 14 ms (-7%) in the non-treated, 28 ms (-10%) in the CQ, 21 ms (-9%) in the AZM and 261 ms (-47%) in the combined groups. The previously observed EAD in the combined group was not observed following the increase in pacing rate (**Figure 8.3A, middle panels**). The combination of simulated ISO application and increased pacing rate further reduced APD, with APD reduction of 40 ms (-19%) in the non-treated, 84 ms (-30%) in the CQ, 53 ms (-22%) in the AZM and 341 ms (-62%) in the combined groups compared to APD during 1 Hz pacing (**Figure 8.3A, lower panels**). Increasing the pacing rate up to 4 Hz further reduced APD and lowering the pacing rate from 1 to 0.25 Hz prolonged the APD and resulted in EADs in the combined CQ+AZM group (**Figure 8.3B, left and middle panels**). At 4 Hz, calcium transient and AP alternans was observed in the non-treated, CQ alone and AZM alone groups, and its occurrence was prevented in the presence of ISO (**Figure 8.4**). Furthermore, at pacing rates >1 Hz, AZM slightly hyperpolarized the RMP, which was opposed by the RMP-depolarizing effect of  $\beta$ -adrenergic activation, while CQ with or without ISO consistently showed a slight depolarization of RMP, likely due to its inhibition of  $I_{K1}$  (**Figure 8.2**). The RMP modulating effect was attenuated at slow pacing rates (**Figure 8.3B, right panel**).

The  $\beta$ -adrenergic-induced modification of 9 ionic currents ( $I_{Na}$ ,  $I_{NaL}$ ,  $I_{Ca,L}$ ,  $I_{to}$ ,  $I_{Kr}$ ,  $I_{Ks}$ ,  $I_{K1}$ ,  $I_{NCX}$  and  $I_{NaK}$ ) can be seen in **Figure 8.5**, highlighting the significantly increased  $I_{Ks}$  during  $\beta$ -adrenergic stimulation. Indeed, ISO-induced phosphorylation of  $I_{Ks}$  and  $I_{Ca,L}$  was key for the observed APD reduction in the model, as previously documented (78) and preventing such phosphorylation resulted in repolarization failure (RF) in the CQ+AZM group in the presence of simulated  $\beta$ -adrenergic stimulation (**Figure 8.6**).

Next, we investigated concentration-dependent effects of ISO on APD in both non-treated (control) and CQ+AZM groups at 1 Hz pacing. In the control group, ISO produced a mild APD shortening at concentrations >10 nM, as previously demonstrated (78). In the combined CQ+AZM group, low concentrations of ISO up to 0.3 nM did not prevent EADs. At 0.3-1.0 nM ISO abbreviated APD and diminished the occurrence of EADs. Further increasing the ISO concentration to 50 nM produced a progressive reduction in APD from 378 ms at 1 nM to 250 ms at 50 nM (-34%). ISO concentrations >50 nM produced minor additional changes in APD (**Figure 8.7**). The cellular effect of 1 nM ISO in all 4 treatment groups can be seen in **Figure 8.8, upper panels**.

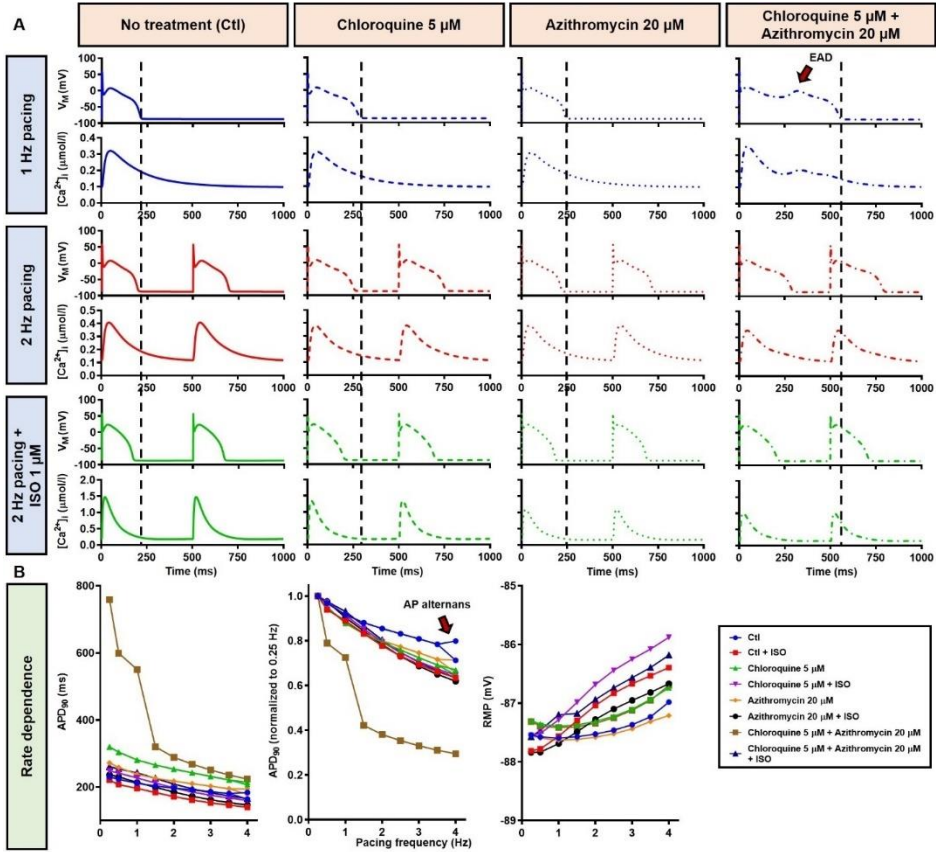


**Figure 8.3:** The effects of chloroquine and azithromycin on AP properties of canine ventricular epicardium. A) The AP and calcium transient of non-treated, chloroquine 5  $\mu\text{M}$ , azithromycin 20  $\mu\text{M}$  and combined groups. The dashed vertical lines indicate the end of the AP with 1 Hz pacing to provide a clearer depiction of the effects of increasing pacing rate and ISO on APD. The EAD is indicated with an arrow. B) APD and RMP for different pacing rates in the four groups with and without simulated  $\beta$ -adrenergic stimulation. The occurrence of alternans at 4 Hz pacing is marked with an arrow. (AP = action potential; APD = action potential duration; Ctl = control; ISO = isoproterenol; RMP = resting membrane potential)

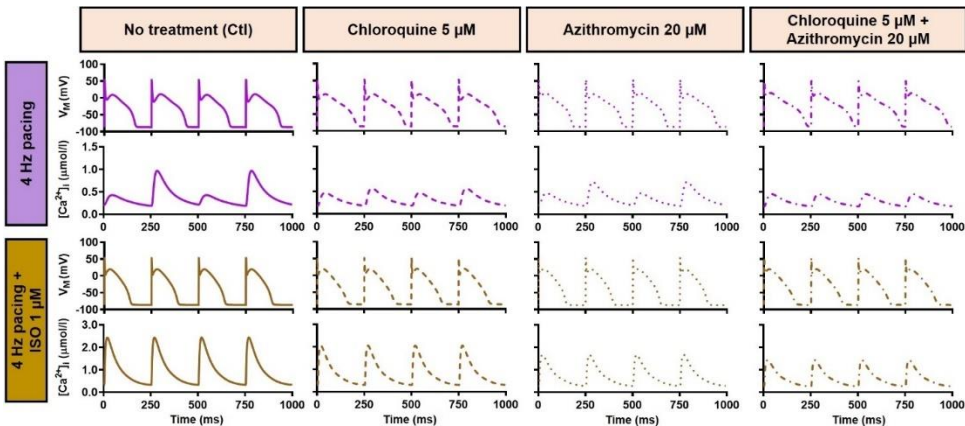


**Figure 8.4:** Action potential and calcium-transient alternans at 4 Hz pacing. The upper panels exemplify the AP and calcium-transient alternans at 4 Hz pacing in non-treated, CQ alone and AZM alone groups. The application of 1  $\mu\text{M}$  ISO abolishes the alternans, as shown in the lower panels. (AP = action potential; AZM = azithromycin; Ctl = control; CQ = chloroquine; ISO = isoproterenol)

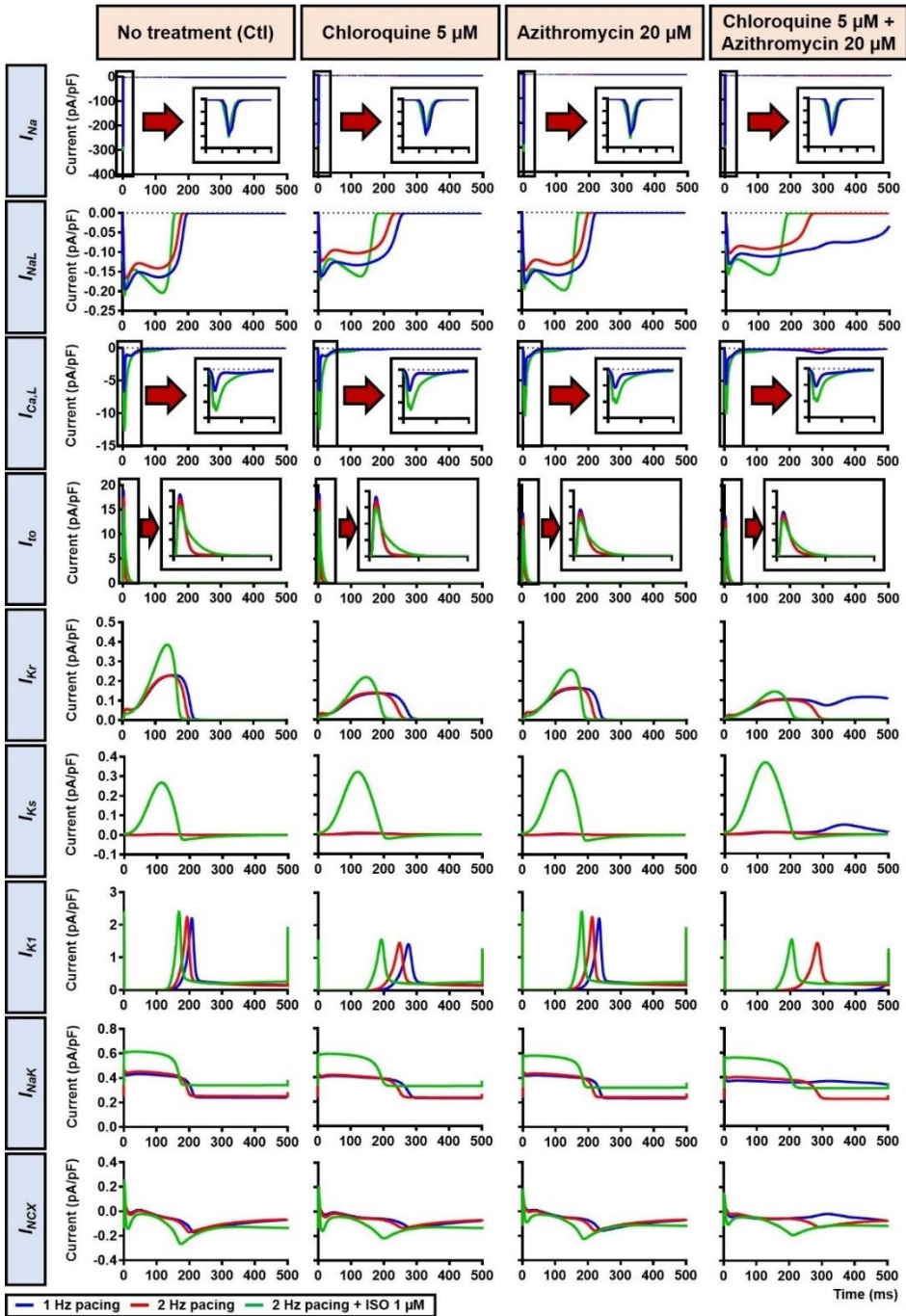


**Figure 8.5:** The effects of  $\beta$ -adrenergic stimulation on cardiac ion channels of canine ventricular epicardium. The effects were assessed in 4 groups: non-treated, chloroquine, azithromycin and combined groups. The blue lines represent the ionic currents during 1 Hz pacing, the red lines represent the ionic currents during 2 Hz pacing and the green lines represent the currents during 2 Hz pacing with ISO 1  $\mu$ M. The fast sodium current ( $I_{Na}$ ), L-type calcium current ( $I_{Ca,L}$ ) and transient-outward potassium current ( $I_{to}$ ) are shown at an expanded scale in the insets. (Ctl = control; ISO = isoproterenol)

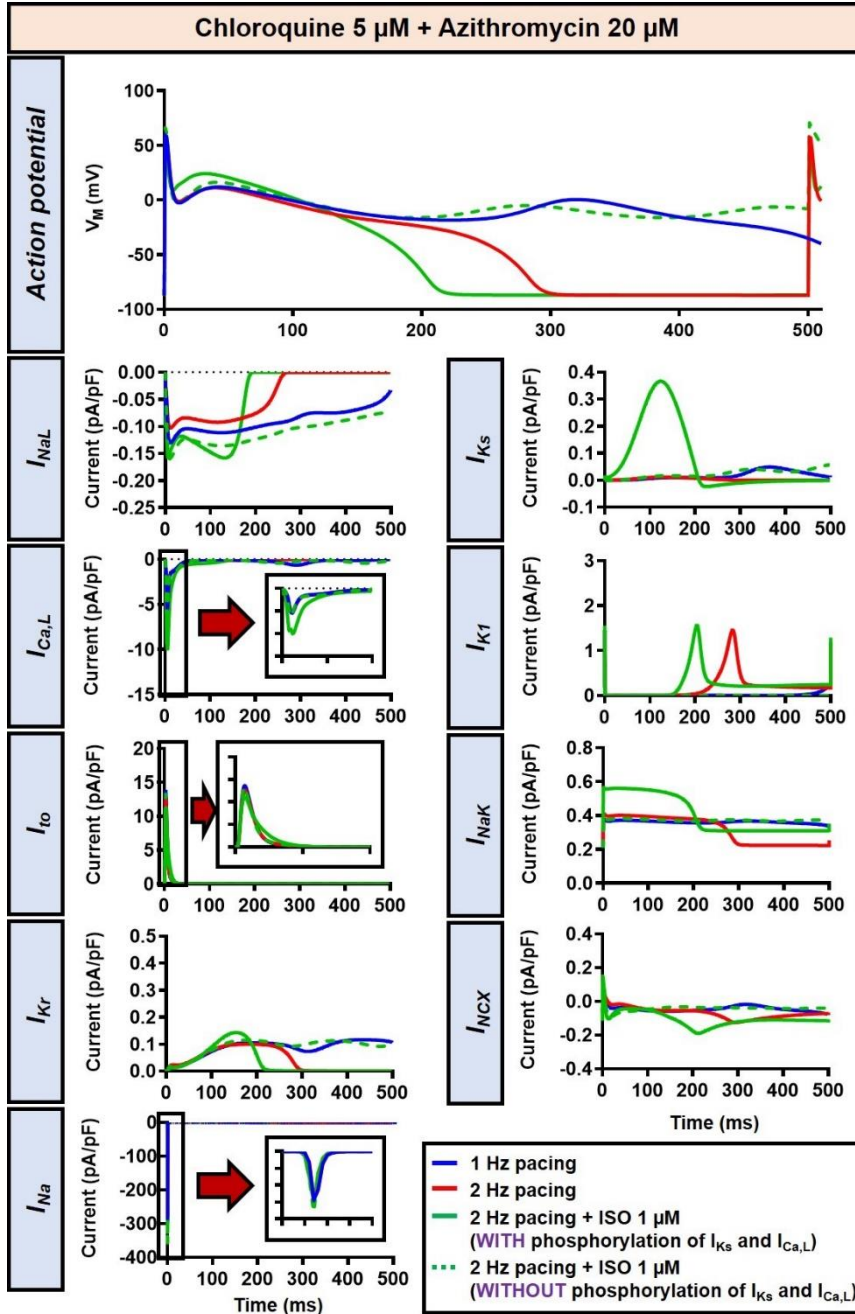


**Figure 8.6:** The impact of  $I_{K_S}$  and  $I_{Ca,L}$  phosphorylation on the action potential of canine ventricular epicardium in the presence of chloroquine (CQ) and azithromycin (AZM). The effect of CQ 5  $\mu\text{M}$  in combination with AZM 20  $\mu\text{M}$  in the presence of ISO-induced  $I_{K_S}$  and  $I_{Ca,L}$  phosphorylation is shown in solid green lines. The green dashed lines represent the effect of CQ 5  $\mu\text{M}$  in combination with AZM 20  $\mu\text{M}$  in the absence of ISO-induced  $I_{K_S}$  and  $I_{Ca,L}$  phosphorylation.

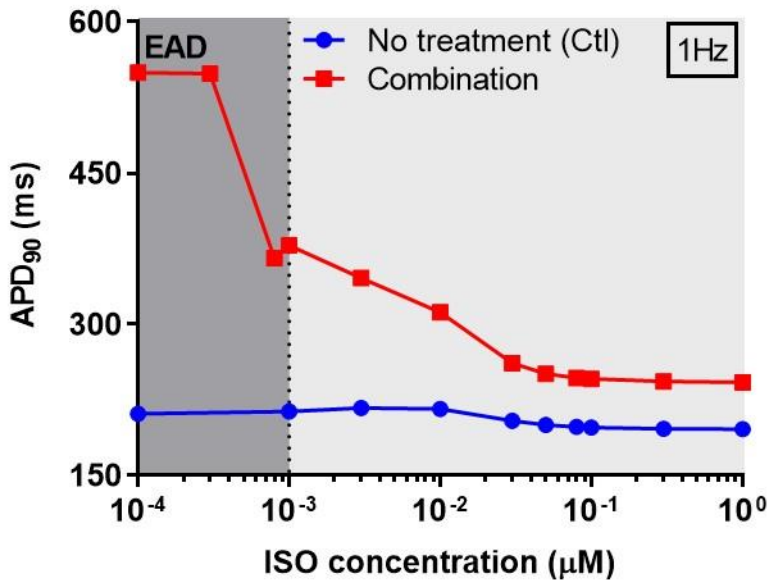


**Figure 8.7:** The concentration-dependent effect of ISO on APD of canine ventricular epicardium. The APD in the presence of various concentrations of ISO from 0.1 nM to 1  $\mu\text{M}$  in non-treated group (blue line) was compared to the combined group (Chloroquine 5  $\mu\text{M}$  + Azithromycin 20  $\mu\text{M}$ ; red line). The simulations were performed with 1 Hz pacing. (APD = action potential duration; Ctl = control; ISO = isoproterenol)

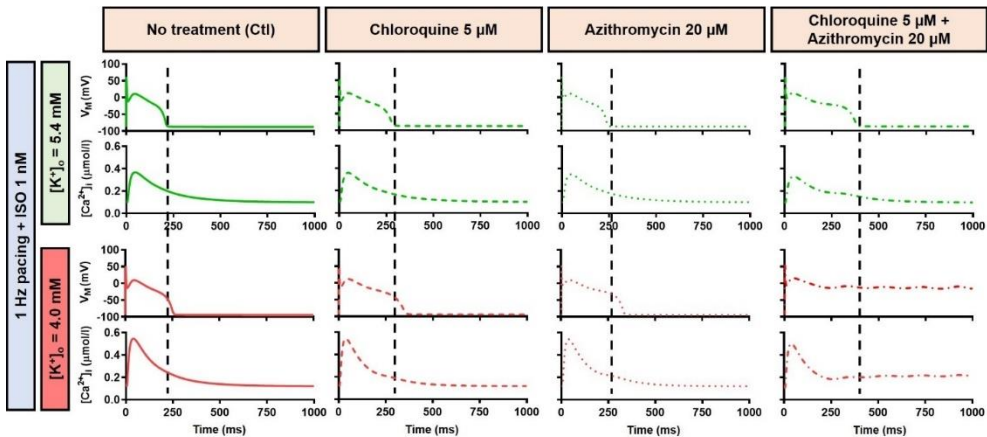


**Figure 8.8:** The effects of chloroquine and azithromycin on canine AP in the presence of an intermediate concentration of ISO. The AP and calcium transient of non-treated, chloroquine 5  $\mu\text{M}$ , azithromycin 20  $\mu\text{M}$  and combined groups with 1 Hz pacing and 1 nM ISO in the presence of low extracellular potassium ( $[\text{K}^+]_o = 4.0 \text{ mM}$ ) were compared to  $[\text{K}^+]_o = 5.4 \text{ mM}$ . The dashed vertical lines indicate the end of AP in models with

$[K^+]_o = 5.4$  mM to provide a clearer depiction of the effects of reduced extracellular potassium on APD. (AP = action potential; APD = action potential duration; Ctl = control; ISO = isoproterenol)

Alteration of cardiac repolarization by a pharmacological agent is frequently observed. However, sole administration of a drug rarely induces arrhythmias unless other predisposing factors aggravate the proarrhythmic risk by challenging the repolarization reserve (e.g., preexisting disease, concomitant drugs, or hypokalemia). We employed the Heijman canine ventricular cardiomyocyte model to investigate the effect of alterations to repolarization reserve, particularly in the setting of low extracellular potassium (hypokalemia). As shown in **Figure 8.9**, the simulated application of CQ+AZM with  $[K^+]_o$  of 4.0 mM (instead of the default 5.4 mM) prolonged APD and caused RF in the absence of ISO and slight APD prolongation with 1  $\mu$ M ISO. Moreover, the RMP was slightly hyperpolarized in the presence of hypokalemia. With 4.0 mM extracellular potassium, higher concentrations of ISO are needed to restore these repolarization abnormalities: 1 nM ISO prevents EADs and RF with 5.4 mM extracellular potassium, but not with 4.0 mM (**Figure 8.8**). These data highlight the importance of baseline repolarization reserve for the cellular proarrhythmic effects of CQ and AZM.

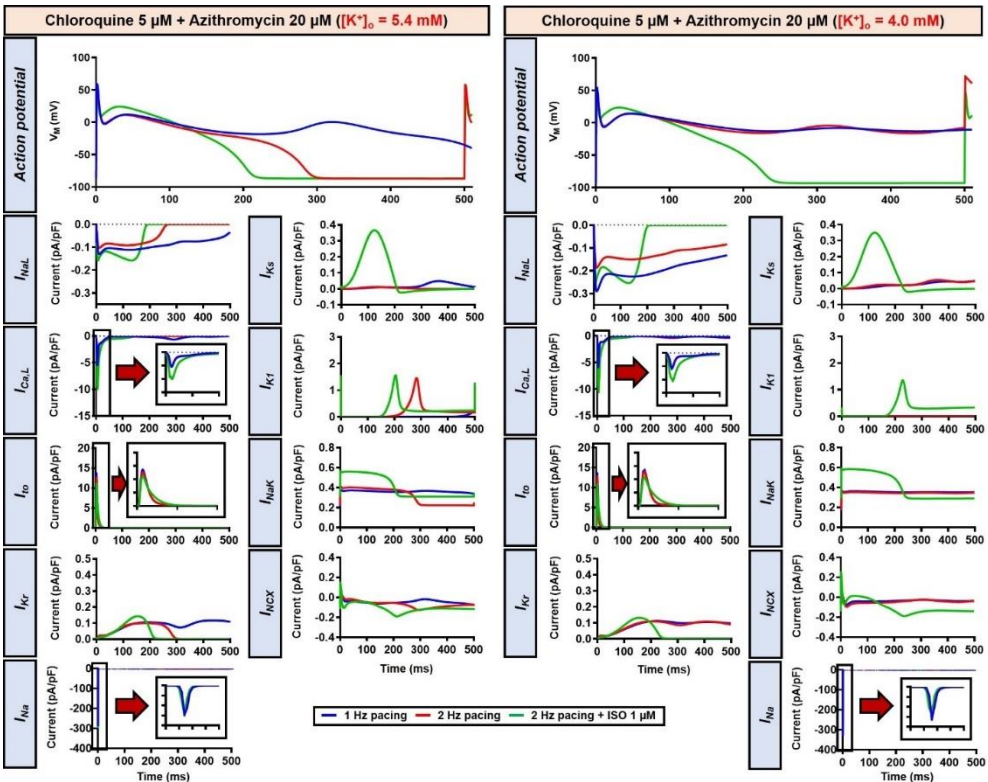


**Figure 8.9:** The impact of reduced extracellular potassium on the action potential of canine ventricular epicardium in the presence of chloroquine and azithromycin. The left panels show the effect of CQ 5  $\mu$ M in combination with AZM 20  $\mu$ M with 5.4 mM  $[K^+]_o$ . The right panels show the effect of CQ 5  $\mu$ M in combination with AZM 20  $\mu$ M in the presence of reduced  $[K^+]_o$  (4.0 mM).

Next, a population-based study was conducted to accommodate intra- and inter-individual variability. A population of 1000 models was created by varying the conductances of 9 ionic currents as described in the **Methods**. After the exclusion of models with non-physiological baseline APs, 592 models were included in the population (**Figure 8.10A, upper panels, blue lines** and **Figure 8.10G**). To simulate  $\beta$ -adrenergic activation, various concentrations of ISO that produced maximum  $\beta$ -adrenergic response were assigned to each model. Consistent with the default model without variability, at 1 Hz pacing, CQ ( $5 \mu\text{M}$ ) prolonged the APD by a median 73.3 ms (IQR 67.5-82.3). Similarly, AZM  $20 \mu\text{M}$  prolonged the APD by a median 28.7 ms (IQR 25.5-36.3) and the combination of CQ and AZM prolonged the APD with median 146.5 ms (IQR 92.1-334.7). During 2 Hz pacing, CQ, AZM and CQ+AZM prolonged the APD with median 59 ms (IQR 56.7-62), 22.7 ms (IQR 20.8-25.5), and 95.2 ms (IQR 84.2-109.3), respectively. Finally, following the addition of ISO, the APD prolongation was further reduced with median prolongation of 26.5 ms (IQR 25.3-27.9) in CQ, 13.5 ms (IQR 13.1-14.2) in AZM and 37.6 ms (IQR 35.7-40.7) in combined groups (**Figure 8.10A-E**).

Finally, the incidence of EADs and RF in the population of models was calculated (**Figure 8.10F**). During 1 Hz pacing, no EAD/RF was documented in the non-treated group, while 6.4% of models in the CQ group, 2.4% of models in the AZM group, and 53.5% of models in the combined group exhibited EADs/RFs. Following the increase in pacing rate to 2 Hz, the incidence of EAD/RF was reduced to 0.5%, 0.7% and 11.5%, respectively. No EAD/RF was observed in any of the groups following the application of ISO during 2 Hz pacing.

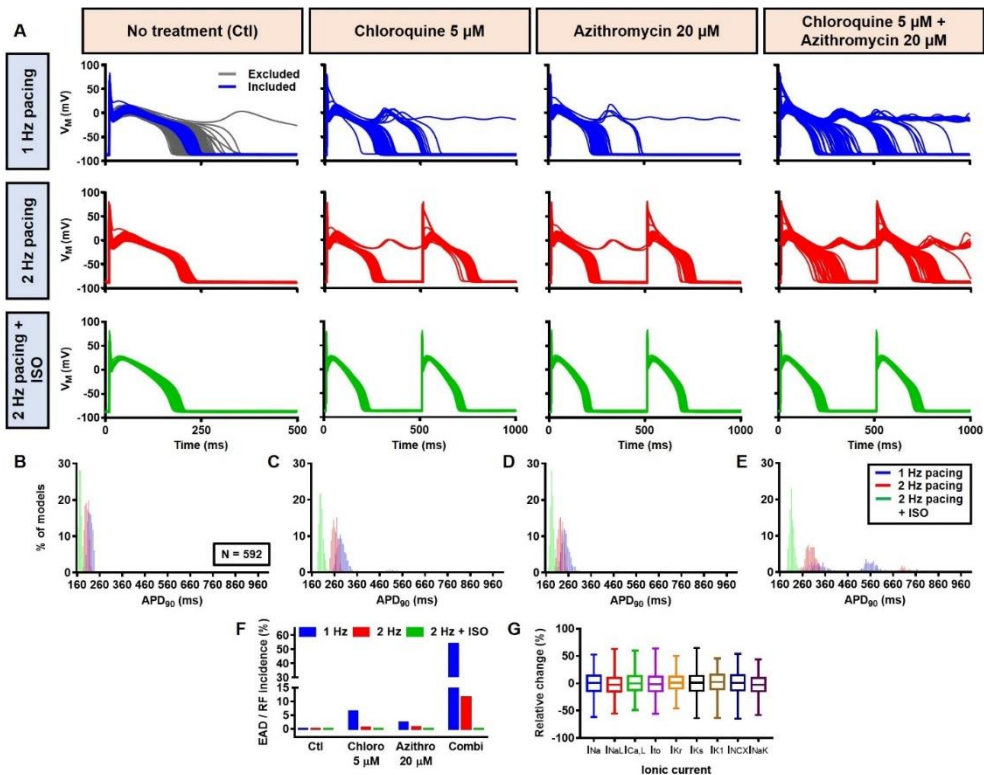


**Figure 8.10:** The cellular effects of chloroquine and azithromycin in the population of 1000 canine ventricular epicardial myocyte models. A) The APs of 592 models included in the study, with the 408 excluded non-physiological APs shown as grey lines. B-E) The frequency distribution of APD in non-treated, chloroquine, azithromycin and combined groups. F) The incidence of EAD/RF observed in the population-based study (as percentage of models). G) Boxplot showing the distribution of relative changes in ionic currents to accommodate the interindividual variability. (AP = action potential; APD = action potential duration; Ctl = control; EAD = early afterdepolarization; ISO = isoproterenol; RF = repolarization failure)

### **8.3.2 The effects of chloroquine and azithromycin on human ventricular electrophysiology**

Although the dog is a commonly used animal model with relatively similar electrophysiological properties to humans, some differences in ion-channel expression and AP profile exist, which may modulate drug effects (603, 604). As such, we also studied the impact of CQ and AZM on the human ventricular AP. During 1 Hz pacing, application of 5  $\mu\text{M}$  CQ in the ORd human ventricular epicardium model prolonged APD by 100 ms (+43%), while 20  $\mu\text{M}$  AZM prolonged APD by 68 ms (+29%). The combination of both drugs showed a synergistic effect with an APD prolongation of 177 ms (+76%; **Figure 8.11A, upper panels**), similar to the canine ventricular model. Likewise, increasing the pacing rate from 1 to 2 Hz reduced the APD in all groups (by 11%, 14%, 14% and 16% in the non-treated, CQ, AZM and combined groups, respectively; **Figure 8.11A, middle panels**). The combination of simulated ISO application and increased pacing rate reduced APD by 49 ms (-21%) in the non-treated, 106 ms (-32%) in the CQ, 95 ms (-32%) in the AZM and 164 ms (-40%) in the combined groups compared to APD during 1 Hz pacing (**Figure 8.11A, lower panels**). At fast pacing rates, the RMP in the CQ and CQ+AZM groups without ISO displayed a marked depolarization due to incomplete repolarization within a single cycle length (**Figure 8.11B, right panel**). Overall, no EAD or RF was observed on ORd human ventricular model. Similar to the canine ventricular model, ISO-induced phosphorylation of  $I_{Ks}$  and  $I_{Ca,L}$  contributed to the previously observed APD reduction in the model and preventing such phosphorylation resulted in similar APDs in the CQ+AZM group with 1  $\mu\text{M}$  ISO and the CQ+AZM group at 2 Hz pacing (**Figure 8.12**).

In the population-based study, all 1000 models were included in the study (**Figure 8.13A, left panels, blue lines**). Consistent with the default model without variability, at 1 Hz pacing, APD prolonged by a median 99.4 ms (IQR 94.7-104.8) with CQ (5  $\mu\text{M}$ ), 65.4 ms (IQR 61.5-68.9) with AZM (20  $\mu\text{M}$ ) and 175.5 ms (IQR 166.2-184.2) with the combination. During 2 Hz pacing, CQ, AZM and CQ+AZM prolonged the APD with median 79.9 ms (IQR 75.9-83.7), 51.2 ms (IQR 48.8-53.9), and 139.8 ms (IQR 132.9-147.1), respectively. Finally, following the addition of ISO, the APD prolongation was further reduced with median prolongation of 42.4 ms (IQR 39.6-45.3) in CQ, 21.5 ms (IQR 19.7-23.6) in AZM and 62.3 ms (IQR 57.6-67.6) in combined groups (**Figure 8.13A-E**).

To investigate the effect of CQ+AZM on the human AP in the presence of altered repolarization reserve during severe hypokalemia, we lowered the  $[K^+]_o$  to 2.0 mM. Severe hypokalemia prolonged the APD while hyperpolarizing the RMP. However, no EAD was induced by this reduction in repolarization reserve (**Figure 8.14**). Therefore, we extended the analysis using a population modeling approach to evaluate whether EADs could be induced during hypokalemia in the population of models with variations in ionic current conductance. However, as shown in **Figure 8.13F-G**, no EAD was

documented in the population of 1000 models despite the extremely long APD (>600 ms) in some models.

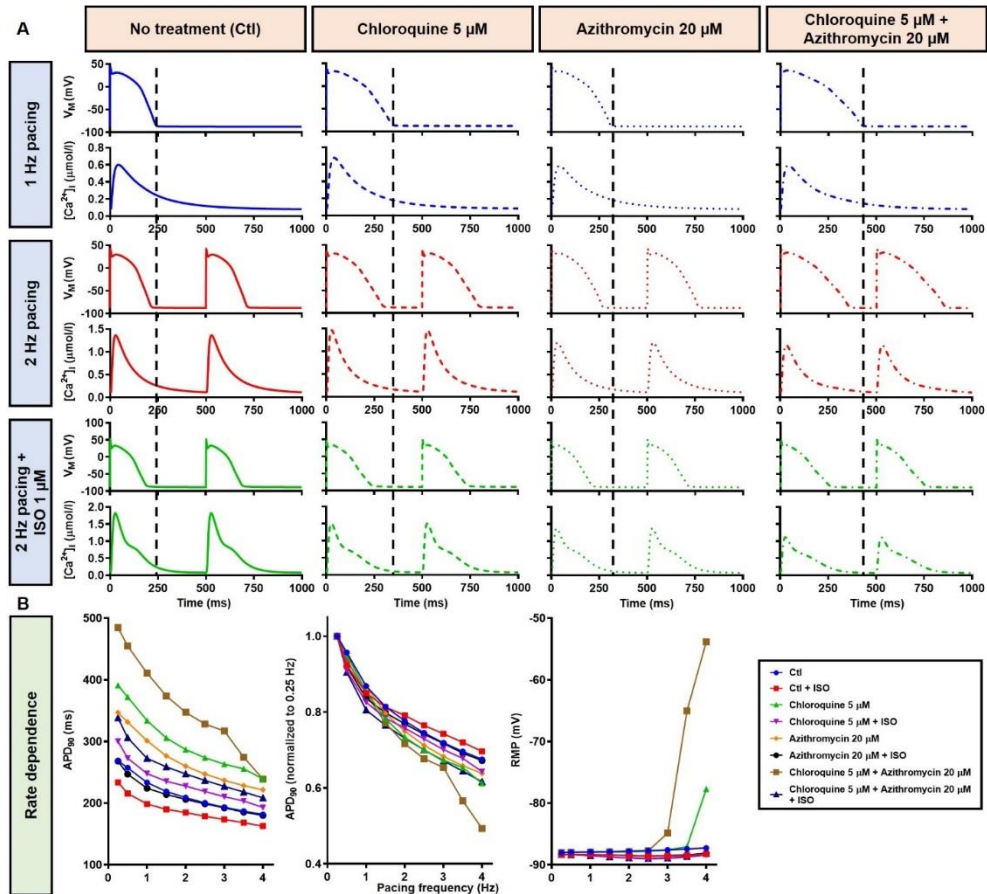


**Figure 8.11:** The effects of chloroquine and azithromycin on AP properties of human ventricular epicardium. A) The AP and calcium transient of non-treated, chloroquine 5  $\mu\text{M}$ , azithromycin 20  $\mu\text{M}$  and combined groups with 1 Hz pacing (blue), 2 Hz pacing (red) or 2 Hz pacing with electrophysiological effects of maximal  $\beta$ -adrenergic stimulation (green). The dashed vertical lines indicate the end of AP with 1 Hz pacing to provide a clearer depiction of the effects of increasing pacing rate and ISO on APD. B) APD and RMP for different pacing rates in the four groups with and without simulated  $\beta$ -adrenergic stimulation. (AP = action potential; APD = action potential duration; Ctl = control; ISO = isoproterenol; RMP = resting membrane potential)

Since EAD formation has been attributed to the reactivation of  $I_{\text{Ca,L}}$  (605), we increased the  $I_{\text{Ca,L}}$  window current by leftward shifting the steady-state activation so that the channels get activated at more negative potentials and rightward shifting the steady-state inactivation so that channels start to recover from inactivation at more positive potentials. Using this approach, we were able to induce EADs in the population of models, both in the absence and presence of severe hypokalemia (Figure 8.15A-B). Interestingly, in contrast with the EADs resulting from reduced repolarization reserve seen in the canine ventricular model, the EADs generated by the increased  $I_{\text{Ca,L}}$  window could not be prevented by  $\beta$ -adrenergic stimulation. As depicted in Figure 8.15C, while

the 2 Hz pacing alone reduced the incidence of EADs and RFs, the application of 1  $\mu\text{M}$  ISO resulted in a marked increase in the EAD/RF incidence, affecting more than 50% of the models. Interestingly, this phenomenon occurred in the presence of ISO-induced APD reduction, highlighting the significance of the  $I_{\text{Ca,L}}$  window for the generation of EADs.

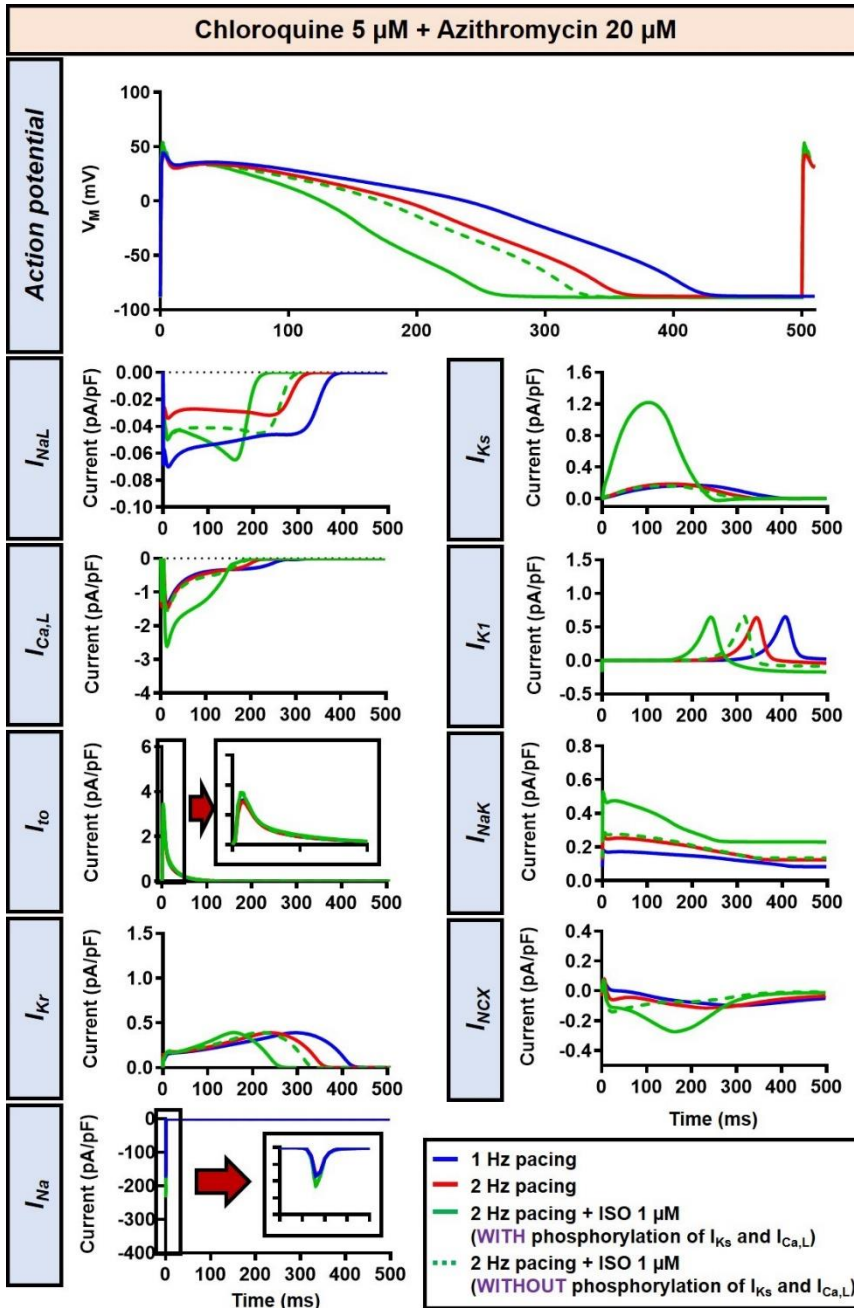


**Figure 8.12:** The impact of  $I_{Ks}$  and  $I_{Ca,L}$  phosphorylation on the action potential of human ventricular epicardium in the presence of chloroquine (CQ) and azithromycin (AZM). The effect of CQ 5  $\mu\text{M}$  in combination with AZM 20  $\mu\text{M}$  in the presence of ISO-induced  $I_{Ks}$  and  $I_{Ca,L}$  phosphorylation is shown in solid green lines. The green dashed lines represent the effect of CQ 5  $\mu\text{M}$  in combination with AZM 20  $\mu\text{M}$  in the absence of ISO-induced  $I_{Ks}$  and  $I_{Ca,L}$  phosphorylation.

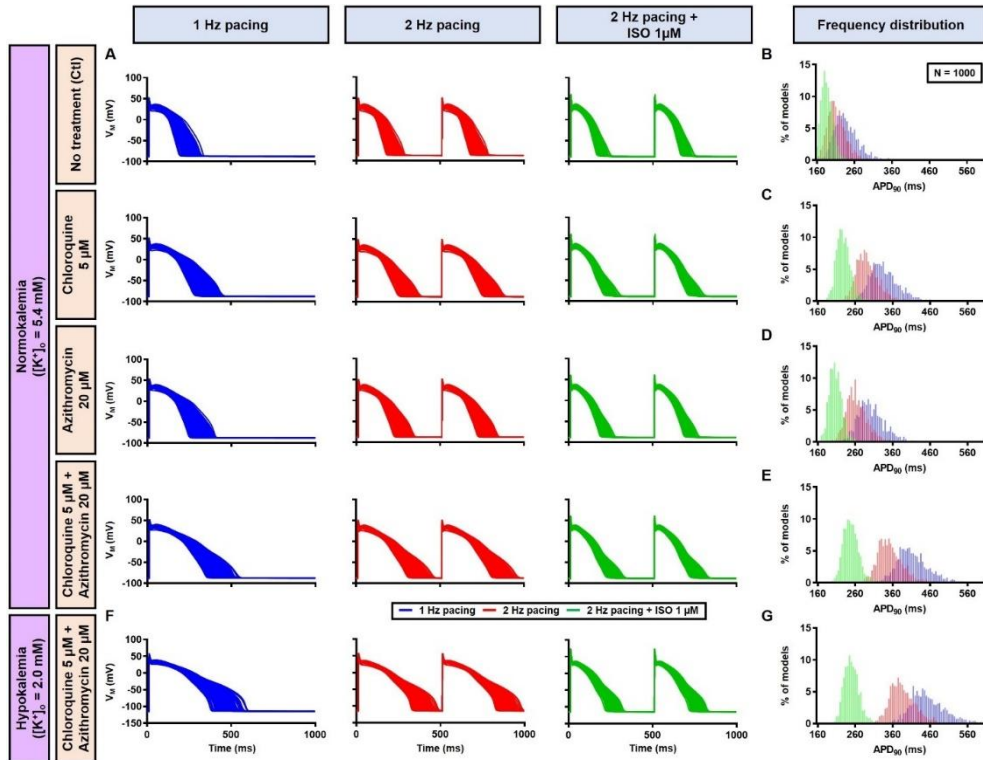


**Figure 8.13:** The cellular effects of chloroquine and azithromycin in the population of 1000 human ventricular epicardial myocyte models in the absence and presence of hypokalemia. [A-E] The effects of CQ and AZM on the human ventricular myocyte AP in normokalemia ( $[K^+]_o = 5.4 \text{ mM}$ ). A) The APs of 1000 models included in the study under Ctl conditions, with 5  $\mu\text{M}$  chloroquine, 20  $\mu\text{M}$  azithromycin, or a combination (top to bottom) at 1 Hz pacing, 2 Hz pacing or 2 Hz pacing with electrophysiological effects of maximal  $\beta$ -adrenergic stimulation (left to right). B-E) The frequency distribution of APD in non-treated, chloroquine, azithromycin and combined groups. F-G) The effects of CQ and AZM in the presence of severe hypokalemia ( $[K^+]_o = 2.0 \text{ mM}$ ), on human ventricular APs (F) and the frequency distributions of APD (G). (AP = action potential; APD = action potential duration; Ctl = control; ISO = isoproterenol)

## 8.4 Discussion

Here, we investigated the potential proarrhythmic effects of CQ and AZM in the ventricular cardiomyocyte in the absence or presence of  $\beta$ -adrenergic stimulation using an *in silico* approach. First, both our canine and human models indicate that CQ and AZM can significantly prolong the APD even within their therapeutic range. Moreover, their combination resulted in a synergistic APD prolongation, leading to the initiation of proarrhythmic EADs, which was more pronounced in the presence of reduced repolarization reserve due to reduced extracellular potassium. Second,  $\beta$ -adrenergic stimulation reduced APD prolongation in both canine and human models, and prevented EAD formation in the canine model via the upregulation of  $I_{Ks}$  and  $I_{Ca,L}$ . Third,

our population-based study confirmed the robustness of these findings and showed that  $\beta$ -adrenergic stimulation completely cancelled the initiation of EADs and RFs in canine model variants. Finally, we presented the interesting observation that  $\beta$ -adrenergic stimulation could increase the incidence of EADs and RFs in the human model with increased  $I_{Ca,L}$  window current, highlighting a potential important role for  $\beta$ -adrenergic activity in modulating drug-induced proarrhythmia by CQ and AZM.

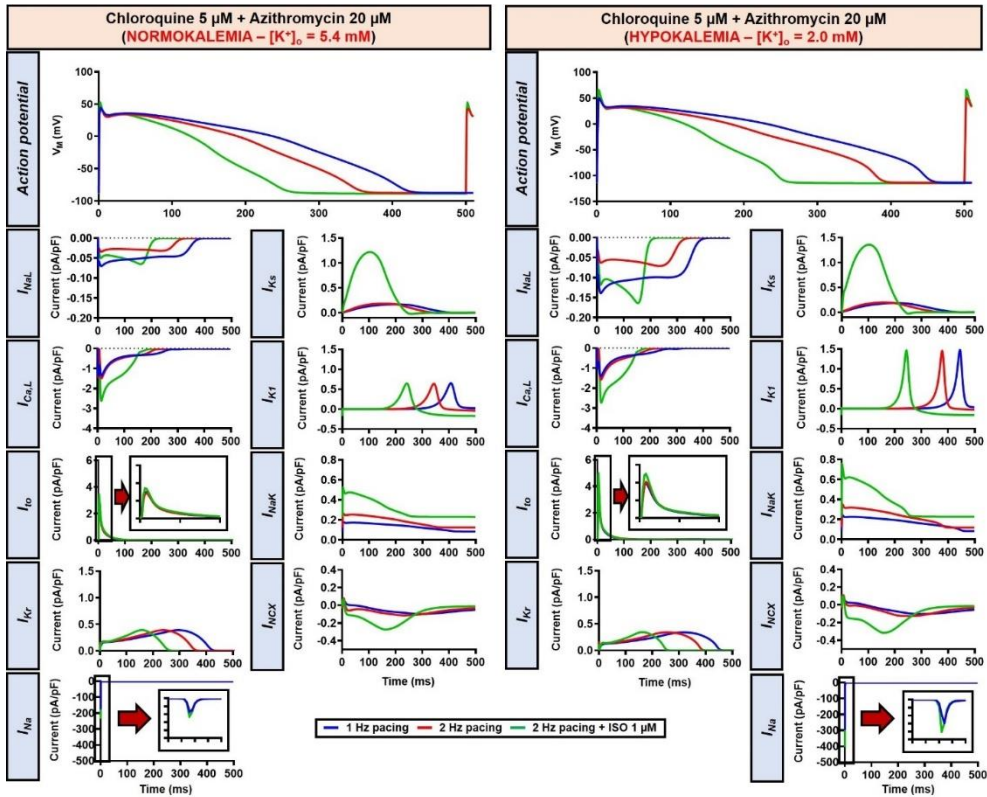


**Figure 8.14:** The impact of severe hypokalemia on the action potential of human ventricular epicardium in the presence of chloroquine and azithromycin. The left panels show the effect of CQ 5  $\mu$ M in combination with AZM 20  $\mu$ M in the absence of hypokalemia ( $[K^+]_o = 5.4$  mM). The right panels show the effect of CQ 5  $\mu$ M in combination with AZM 20  $\mu$ M in the presence of severe hypokalemia ( $[K^+]_o = 2.0$  mM).

### 8.4.1 Chloroquine and azithromycin exhibit a synergistic APD-prolonging effect

CQ and AZM block multiple ion channels, including the rapid delayed-rectifier potassium current ( $I_{Kr}$ ) (444), which dose-dependently prolongs the APD and increases the propensity for EADs, creating a substrate for cardiac arrhythmias. In the clinic, they are known to prolong the QT interval, increasing the susceptibility for life-threatening arrhythmias such as Torsade de Pointes. Anaesthetized guinea-pig experiment revealed that CQ indeed has an APD-prolonging effect, while the combination with AZM did not cause further APD prolongation (581). This finding is different from a recent prospective observational study which showed that the maximum corrected QT interval during treatment was significantly longer in the combination group compared to the monotherapy group, highlighting the synergy between CQ and AZM (583), in

agreement with our results. Several studies have also reported the potential proarrhythmic effects of CQ and AZM in COVID-19 patients (578, 582, 583, 585). This discrepancy might be due to differences in heart or pacing rate at which the APD-prolonging effects were evaluated as well as interspecies differences in cardiac ion-channel properties, as previously discussed (603, 604). Nonetheless, further experiments are needed to confirm the origin of the inconsistency.

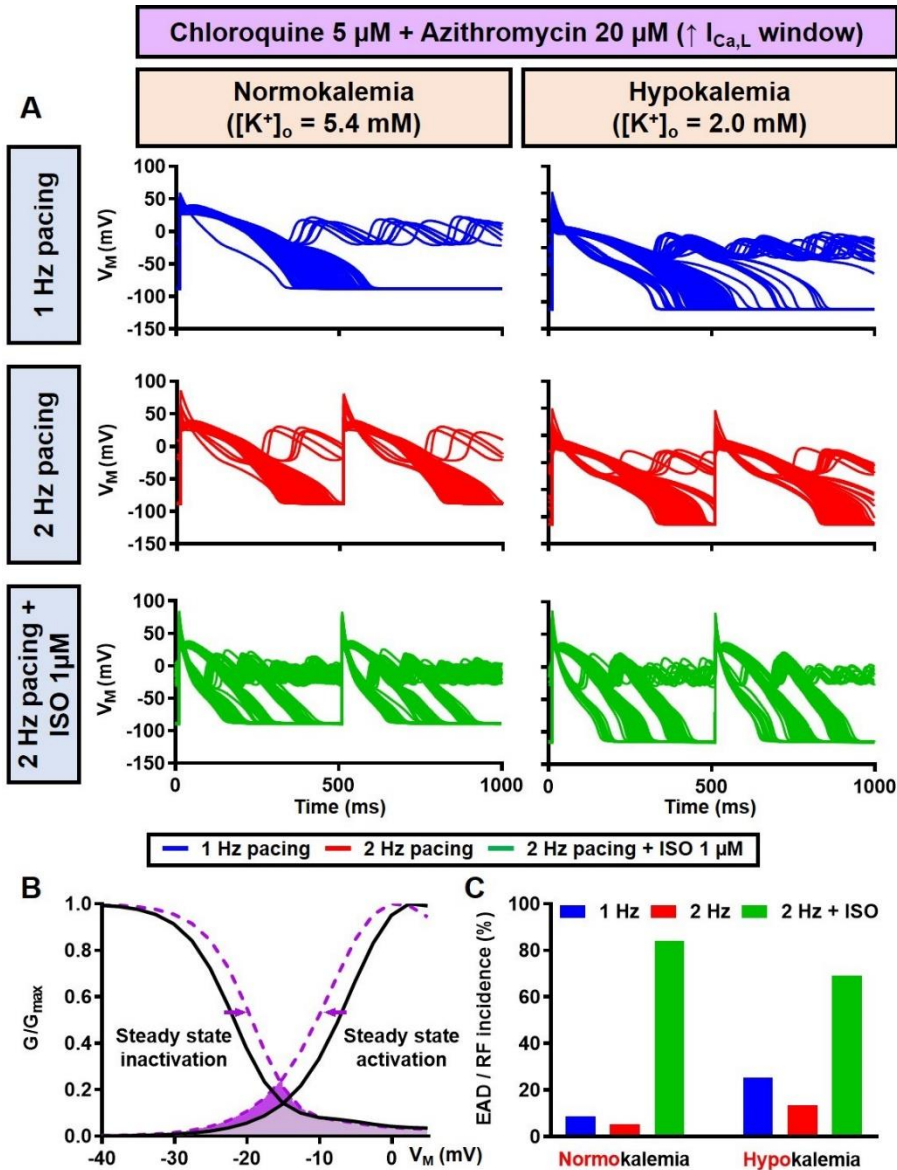


**Figure 8.15:** The impact of severe hypokalemia on the population of 1000 human ventricular epicardium APs with increased  $I_{Ca,L}$  window in the presence of chloroquine and azithromycin. A) The effect of CQ 5  $\mu\text{M}$  in combination with AZM 20  $\mu\text{M}$  in the absence of hypokalemia ([K<sup>+</sup>]<sub>o</sub> = 5.4 mM; left panel) and in the presence

of severe hypokalemia ( $[K^+]_o = 2.0$  mM; right panel). B) A 3 mV shift in the steady-state activation and inactivation of  $I_{Ca,L}$  were introduced in the human ventricular epicardium model to increase the  $I_{Ca,L}$  window (shift from black to purple lines). C) The incidence of EAD/RF observed in the population-based study (as percentage of models). (EAD = early afterdepolarization;  $I_{Ca,L}$  = L-type calcium current; ISO = isoproterenol; RF = repolarization failure;  $V_M$  = membrane potential)

Employing a computational canine ventricular cardiomyocyte model, we confirmed the potentially harmful ventricular APD-prolonging effect of CQ and AZM. Within the therapeutic range, the incidence of EADs was relatively low (6.4% in CQ group and 2.4% in AZM group). Nonetheless, the combination of both drugs, as proposed in the treatment of COVID-19, produced a synergistic APD-prolonging effect that further increased the likelihood of EADs, particularly at slow heart rates, suggesting the need for close monitoring of the QT interval during the administration of these drugs in the clinic. The simulations using a human ventricular model also showed a significant APD prolongation, although no EADs were documented. This was in agreement with recent data that reported trivial instances of drug-induced Torsade de Pointes or arrhythmogenic death following the administration of CQ+AZM despite significant QT prolongation (583, 584, 606).

Our results also revealed that hypokalemia further augmented the drug-induced APD prolongation and reduced repolarization reserve. Lowering the  $[K^+]_o$  to 4.0 mM produced RF in the canine model without  $\beta$ -adrenergic stimulation (Figure 8.9). Similarly, the simulation of severe hypokalemia also prolonged the APD in the human ventricular model, highlighting the importance of baseline repolarization reserve for the proarrhythmic effects of CQ and AZM and the potential for hypokalemia correction to minimize arrhythmia risk in COVID-19 patients under CQ and AZM therapy (580).

#### ***8.4.2 Beta-adrenergic activation reduces the APD and modulates the cellular proarrhythmic risk of chloroquine and azithromycin***

Beta-adrenergic agonists have been used as an antidote against CQ intoxication for a long time (607, 608). Their benefit in the management of CQ-induced arrhythmia has been experimentally demonstrated in anaesthetized rats, showing that the CQ-infused group treated with isoprenaline (a selective  $\beta$ -adrenergic receptor agonist) displayed longer time to the onset of arrhythmias and death (609). Conversely, the administration of propranolol (a  $\beta$ -adrenergic receptor blocker) potentiated the electrocardiographic effects of CQ, indicating that  $\beta$ -adrenergic receptor blockade might render the heart more vulnerable to the actions of CQ (610).

In this study, we demonstrated that  $\beta$ -adrenergic stimulation could be a potential protective factor against CQ- and AZM-induced proarrhythmia by lowering the APD prolongation and therefore, preventing the occurrence of afterdepolarizations. Our population-based study using cellular models of canine ventricular electrophysiology showed that the protective effects of  $\beta$ -adrenergic stimulation are robust, reducing the incidence of EADs and RFs for a large number of virtual genotypes and with a relatively wide range of simulated isoproterenol concentrations. Similar APD-reducing effects of  $\beta$ -adrenergic stimulation were also demonstrated in the population of human ventricular models, restoring the drug-induced reduction in repolarization reserve. We also showed that the APD-reducing effect of  $\beta$ -adrenergic stimulation was due to the PKA-mediated phosphorylation of  $I_{Ca,L}$  and  $I_{Ks}$ . Phosphorylation of  $I_{Ks}$  increases the current density during  $\beta$ -adrenergic stimulation,

promoting repolarization. Meanwhile, phosphorylation of  $I_{Ca,L}$  abbreviated APD through the elevation of the plateau potential due to increased  $I_{Ca,L}$ , promoting additional voltage-dependent activation of repolarizing potassium currents (e.g.,  $I_{Ks}$ ; (611)), as demonstrated in **Figure 8.6**. Moreover, stronger calcium-dependent  $I_{Ca,L}$  inactivation (CDI) during  $\beta$ -adrenergic stimulation due to increased calcium loading (**Figure 8.3A** and **8.11A, lower panels**), together with  $I_{Ca,L}$  phosphorylation, may give larger peak  $I_{Ca,L}$  current density but also a reduction in the persistent, APD-prolonging component. Genetic mutations altering  $I_{Ks}$  phosphorylation, as reported in long-QT syndrome type 1, may be responsible for prolonging the AP with  $\beta$ -adrenergic stimulation, especially at slower cycle lengths (598, 612, 613). Although extrapolation of these findings to the clinical setting is challenging, they suggest that the concomitant sympathetic stimulation in COVID-19 patients may reduce the likelihood of drug-induced Torsade de Pointes, or arrhythmogenic death in COVID-19 patients despite the presence of marked QT interval prolongation, in line with observational studies (583).

On the other hand, our results suggest that  $\beta$ -adrenergic stimulation might also be harmful in the presence of increased  $I_{Ca,L}$  window current. Such conditions may arise from gain-of-function mutations in the L-type calcium channel (LTCC)-encoding genes, underlying e.g., long-QT syndrome type 8 (Timothy syndrome; (614)). Increased  $I_{Ca,L}$  window current has also been reported in failing human and rat ventricular myocytes, where a redistribution of functional LTCCs, increased open probability, and CaMKII-mediated phosphorylation of the channel occurred (172). In our *in silico* analyses, isoproterenol-induced EAD promotion occurred irrespective of the APD-reducing effect of  $\beta$ -adrenergic stimulation, indicating the importance of  $I_{Ca,L}$  reactivation in maintaining EAD. This finding suggests the need for careful consideration of  $\beta$ -adrenergic stimulation under disease conditions that potentially enlarge the  $I_{Ca,L}$  window. Moreover, long-term  $\beta$ -adrenergic stimulation promotes cardiac remodeling, including hypertrophy, fibrosis and the downregulation of several ion channels via transcriptional and post-translational modifications, potentially creating a substrate for cardiac arrhythmias (335, 615, 616). The present study revealed that transient activation of the  $\beta$ -adrenergic response may be beneficial against drug-induced proarrhythmia and  $\beta$ -blockers might not be appropriate under such circumstances. On the other hand,  $\beta$ -blockers could be used to reduce the detrimental effect of long-term  $\beta$ -adrenergic stimulation or to reduce the complications of COVID-19-induced systemic inflammation in the absence of medications with proarrhythmic behavior.

#### 8.4.3 Limitations of the study

Here, we performed a computational study using an established canine ventricular cardiomyocyte model with  $\beta$ -adrenergic signaling (78, 81) and a human ventricular cardiomyocyte model (263) phenomenologically incorporating the maximum electrophysiological effect of  $\beta$ -adrenergic stimulation (598, 599). Despite similarities between canine and human electrophysiology, future studies integrating all signaling components of  $\beta$ -adrenergic cascades in a human cardiomyocyte model are warranted. Although EADs are an established proarrhythmic mechanism, extrapolation of the current findings to tissue- or organ-level simulations, taking into account the heterogeneous nature of sympathetic innervation, would be required to confirm the pro- and antiarrhythmic effects identified at the cellular level and to identify potential markers of proarrhythmic risk. These were not performed due to the computational

costs associated with the complexity of the cardiomyocyte model and the relatively slow time-course of  $\beta$ -adrenergic stimulation-induced electrophysiological modulation (requiring long simulations).

In this study, we used cellular concentrations of CQ and AZM, i.e., concentrations employed during *in vitro* experiments where specific drugs produce certain measured effects at the cellular level. However, it can be challenging to correlate these cellular concentrations to the clinically relevant doses due to variability in the pharmacokinetics and -dynamics of the drugs, particularly in severely ill patients. Pharmacokinetics/-dynamics models exist and, in the future, could be implemented to obtain a more precise simulation of the electrophysiological consequences of the drugs.

The drug-induced ion-channel modifications incorporated in this study (**Figure 8.2**) were derived from a previous publication using heterologous expression systems (in Chinese hamster ovary / human embryonic kidney cells), which could display different results from human cardiomyocytes (444). Since these data are the only available data to date, we assumed that the relative drug effects are retained across species and cell types.

## 8.5 Conclusions

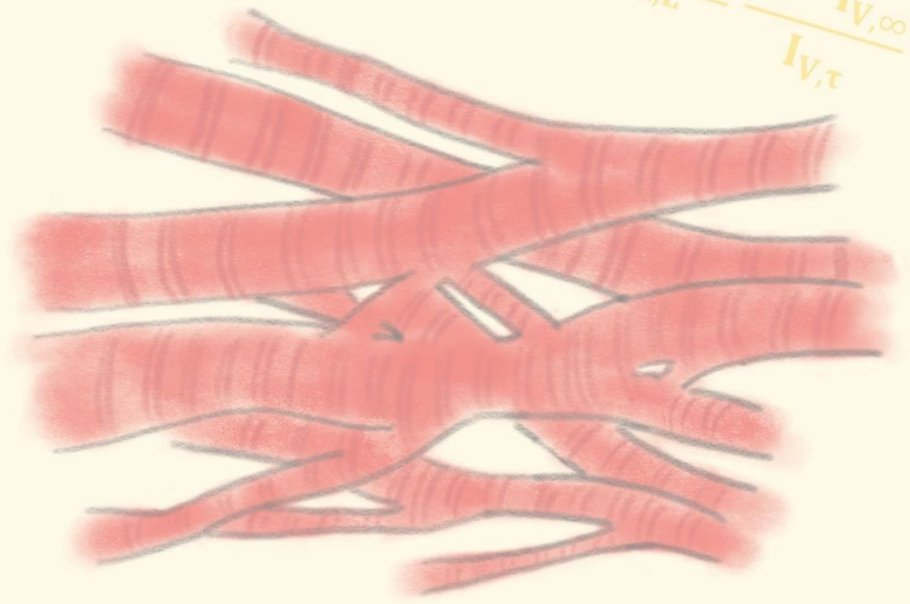
CQ and AZM exhibit synergistic APD-prolonging effects, potentially resulting in increased proarrhythmic risk, although the severity of the electrophysiological effects depends on the baseline repolarization reserve. Transient activation of the sympathetic nervous system may prevent CQ- and AZM-induced proarrhythmia by reducing their APD-prolonging effect, highlighting the importance of preserving  $\beta$ -adrenergic response in the presence of such proarrhythmic medications and the potential significance of heart-rate and autonomic-status monitoring in particular conditions such as COVID-19.





$$\frac{dV_m}{dt} = -\frac{1}{C_m} * I$$

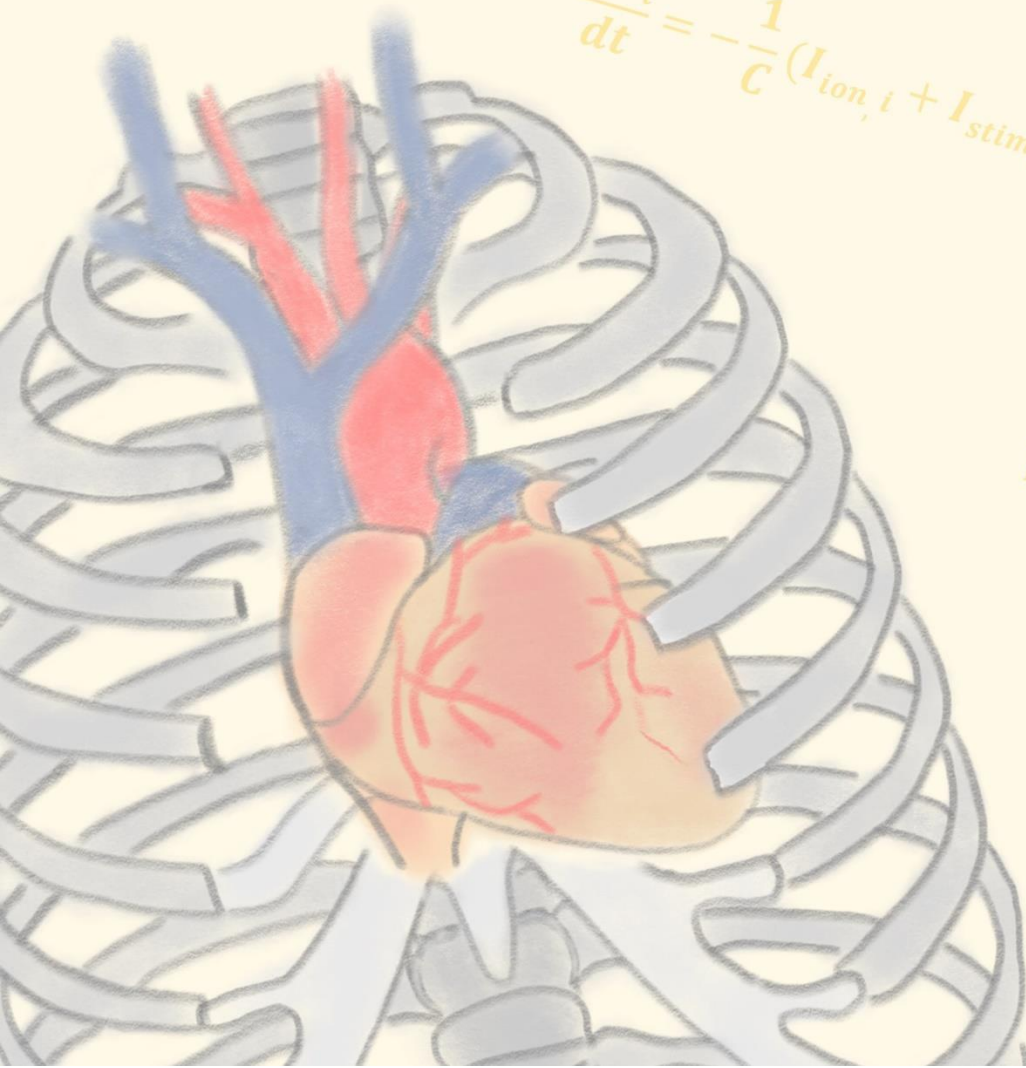
$$y_{Ca,L} = \frac{1 - I_{V,\infty}}{I_{V,\tau}}$$



$$x_{Ca,L} = \frac{I_{V,\infty}}{I_{V,\tau}}$$

$$\delta I_{Ca,L}^{s,m} =$$

$$\frac{dV_i}{dt} = -\frac{1}{C} (I_{ion,i} + I_{stim,i} + I_{diff,i})$$



$$\bar{I}_{Ca,L}^{s,m} = P_{Ca,L} \cdot (z$$

$$ACT_{\tau} = 0.59$$

# Chapter 9

## Discussion



$$g_X(V - V_K)$$

$$\frac{dX}{dt} = \alpha_x(1 - X) - \beta_x X$$

$$\delta I_{Ca,L}^{s,m} = \theta_{Ca,L} \cdot \frac{X_{Ca,L} \cdot Y_{Ca,L}^{s,m} \cdot \delta_{Ca,L}^{s,m}}{Y_{Ca,L} \cdot X_{Ca,L} \cdot \theta_{Ca,L}}$$

$$\frac{X_{Ca,L} \cdot Y_{Ca,L}^{s,m} \cdot \delta_{Ca,L}^{s,m}}{Y_{Ca,L} \cdot X_{Ca,L} \cdot \theta_{Ca,L}}$$

$$I_{Ca,L}^{s,m} (O_{Ca,L}^{s,m} + O_{Ca,L}^{s,m})$$

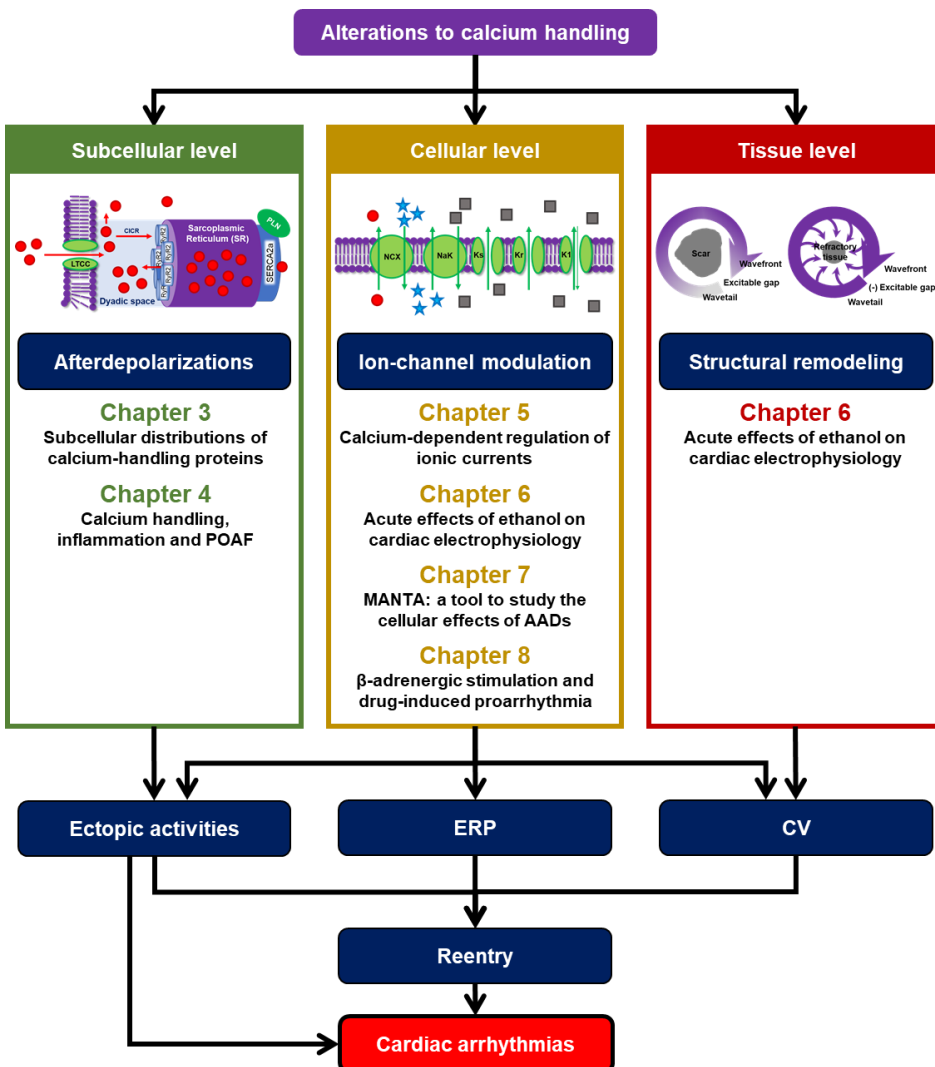
$$\frac{V_m \cdot F^2}{R \cdot T} \cdot \frac{Y_{Ca,i} \cdot [Ca^{2+}]_{obs} \cdot \exp(z_{Ca} \cdot \frac{V_m}{R \cdot T}) - Y_{Ca,o} \cdot [Ca^{2+}]_o}{1 + \exp(0.052 \cdot (V_m + 13))} \cdot \frac{\exp(z_{Ca} \cdot \frac{V_m}{R \cdot T}) - 1}{1 + \exp(0.132 \cdot (V_m + 13))}$$

$$\frac{dV}{dt} = \frac{I_{stim} - (I_K + I_{Na} + I_{leak})}{C_m}$$



## 9.1 Introduction

Cardiomyocyte calcium handling is the key mediator of cardiac excitation-contraction coupling. In the healthy heart, calcium controls both electrical impulse propagation by shaping the cardiac action potential and myofilament cross-bridge cycling, providing synchronous and adequate contraction of cardiac muscles (**Chapters 1-2**). Due to the complex and tight interactions between calcium and other molecules within a cardiomyocyte (335), it remains experimentally challenging to study the exact contributions of calcium-handling abnormalities to arrhythmogenesis. Therefore, multiscale computational studies are increasingly being used together with laboratory experiments to unravel the exact mechanisms of calcium-mediated arrhythmogenesis. This thesis describes various examples of how integrative computational modeling makes it possible to unravel the arrhythmogenic consequences of alterations to cardiac calcium handling at subcellular, cellular and tissue levels (**Figure 9.1**).



Chapter 9

**Figure 9.1: Alterations to calcium handling as a key determinant of cardiac arrhythmias.** Subcellular calcium-handling abnormalities may initiate delayed afterdepolarizations (DADs) and triggered activity. At the cellular level, modifications of calcium-handling proteins can directly or indirectly affect cardiac ion-channel function, leading to substantial changes in AP properties. At higher spatial scales, calcium-handling abnormalities may promote structural remodeling, allowing the generation of reentrant waves. Together, those processes may create vulnerable substrates for cardiac arrhythmias.

First, **Chapter 2** of this thesis summarized the numerous roles of cardiomyocyte calcium handling in health and disease, and showed the potential synergy between *in vitro* experiments and *in silico* models of cardiomyocyte calcium handling (335). **Chapter 3** discussed our *state-of-the-art* subcellular model of human atrial cardiomyocyte calcium handling to investigate the impact of subcellular distributions of calcium-handling proteins (e.g., RyR2 and LTCC) on atrial electrophysiology (4). **Chapter 4** demonstrated the application of the previously developed subcellular model to elucidate the mechanisms and cause-effect relationship between calcium-handling abnormalities, acute transient inflammation and POAF (327). **Chapter 5** revealed the significance of direct calcium-dependent regulation of atrial ionic currents on cardiac electrophysiology under physiological and pathological conditions (61). **Chapter 6** illustrated a multiscale computational framework to investigate complex arrhythmias (i.e., ethanol-associated reentrant arrhythmia), incorporating the *in vitro* electrophysiological data of acute ethanol-induced electrical remodeling into multiscale *in silico* simulations under different conditions (346). **Chapter 7** presented MANTA (603), a novel, easy-to-use educational tool to better understand the cellular effects of AADs, incorporating the currently available *in silico* models of cardiac cellular electrophysiology and various classes of AADs (Vaughan-William I, III, IV and multi-channel blockers). Finally, **Chapter 8** exemplified the role of computational models of canine and human ventricular cardiomyocytes to study the effect of  $\beta$ -adrenergic receptor stimulation in the presence of repolarization reserve-reducing medications (e.g., chloroquine and azithromycin) (617).

## 9.2 Cardiomyocyte calcium handling: The complex hub of excitation and contraction

As extensively discussed in **Chapters 2**, calcium plays a major role in both excitation and contraction of a cardiomyocyte. The influx of calcium via LTCC mediates a much larger SR calcium release through CICR, which initiates myriads of processes within a cardiomyocyte, including activation of calcium-dependent signaling molecules (e.g., calmodulin, calcineurin, calpain, etc.), transmembrane ion channels, calcium-handling proteins and, last but not least, contractile machineries of the cardiomyocyte. During diastole, calcium ions are partly stored back in the SR and partly extruded from the cell via NCX. Under pathological conditions, these complex processes can be disrupted, creating substrates and triggers for cardiac arrhythmias (335). There are three major calcium-dependent arrhythmogenic mechanisms: initiation of afterdepolarizations (i.e., EADs and DADs leading to TA), direct and indirect ion-channel modulation, and the promotion of structural remodeling (335). Those pathological processes can modify AP properties (e.g., APD, RMP and ERP) and cell-to-cell coupling, further altering tissue-

level conduction velocity. In turn, these electrophysiological alterations may promote ectopic activity, reentrant waves and cardiac arrhythmias (**Figure 9.1**).

Due to the complex interacting and tightly-controlled calcium-mediated processes within the heart, it is experimentally challenging to study the exact role of calcium in arrhythmogenesis. There are several controversial topics related to the roles of calcium and calcium-handling proteins in cardiac pathologies. For example, SERCA upregulation has been considered proarrhythmic by increasing calcium leak and SCAEs due to store overload-induced calcium release (SOICR) (26). However, at the same time, evidence suggests that SERCA stimulation may reduce the likelihood of SCAEs and triggered activity by impairing the communication between RyR2 clusters, elevating the intra-SR threshold for the generation of calcium waves and slowing calcium-wave propagation (33). This antiarrhythmic behavior of SERCA stimulation was documented in several studies using HF rats (34) and ischemia-reperfusion porcine models (35). Similarly, in atrial cardiomyocytes from patients with long-standing persistent AF, some studies reported RyR2 dysfunction and increased SCAE incidence (121, 124, 137-139), while the others showed reduced SCAE incidence and calcium-signaling silencing (**Figure 9.2**) (130, 140-142). These two examples highlight the complexity of calcium-mediated processes within a cardiomyocyte, which laboratory experiments have not been able to fully resolve.

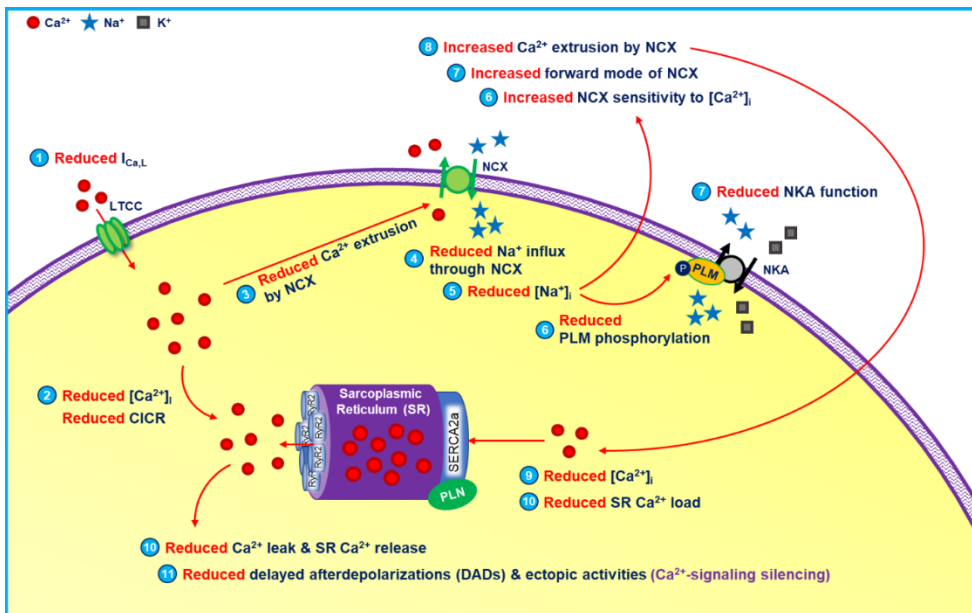


**Figure 9.2:** The proposed mechanisms involved in low intracellular sodium-induced calcium silencing. The reduction of LTCC function following rapid atrial pacing / persistent AF has been proposed as the cause of low intracellular sodium, which further induced the calcium extrusion via NCX and lowered the frequency of SR calcium leak and SCAEs, ultimately leading to calcium-signaling stabilization / silencing in the long term.

### 9.3 Integrative experimentation: Is it necessary?

There are at least three types of laboratory experiments in cardiovascular research: *in vitro*, *ex vivo* (e.g., the whole-heart Langendorff setup) and *in vivo* experiments. Although these experiments have been instrumental in investigating different aspects of calcium-mediated arrhythmogenesis, each of them has their own limitations. *In vitro* experiments are widely used to study the arrhythmogenic consequences of calcium-handling abnormalities at the subcellular and cellular levels. Due to the limited availability of human cardiomyocytes, heterologous expression systems and, more recently, human induced pluripotent stem cells, have been widely used (618). However, these systems are not identical to human cardiomyocytes, and may present potentially different calcium-dependent effects. Moreover, the absence of complete and mature signaling pathways within those cells may also affect the findings. However, even when using adult human cardiomyocytes, several limitations have to be considered. The availability of undiseased donor hearts is limited, so, samples from patients undergoing cardiac surgery who have an extensive history of cardiovascular disease, are commonly used. In addition, isolated cardiomyocytes lack regulation by systemic modulators, such as the autonomic nervous and humoral systems, which have been shown to hold an important role in calcium-mediated arrhythmogenesis. Furthermore, single-cell experiments also lack intercellular coupling, which might modify the observed cellular effects. The role of electrotonic coupling has previously been studied in canine wedge preparation, in which cells close to the site of pacing experienced the greatest electrotonic load and therefore had the maximum attenuation of action potential upstroke amplitude. When electrotonic load due to propagation was reduced, upstroke amplitude was markedly enhanced (619). Similarly, the inhibition of  $I_{to}$  significantly reduced calcium-transient amplitude in single-cell simulations, while the reduction of calcium-transient amplitude following  $I_{to}$  blockade was minimal in tissue simulations due to electrotonic load (426).

Although *ex vivo* experiments could potentially solve some of the aforementioned limitations of *in vitro* experiments, several challenges remain. Because the examined heart has to be detached from the body, it has to be denervated and therefore might lose some of the autonomic nervous control. Moreover, this type of experiment does not allow to study the underlying cause of the calcium-dependent arrhythmia, which are commonly found at more microscopic scales, at the exact timescale when the arrhythmia occur or in the same cells. Simultaneous optical mapping can be performed in Langendorff-perfused hearts to capture the membrane potential and the intracellular free calcium at the same time (620-622). However, at the moment, this approach is limited to these two parameters (membrane potential and bulk calcium transient), has limited spatial and temporal resolution, and is unable to image the depth of the cardiac walls. Therefore, it is often unable to unravel the causality of calcium-dependent cardiac arrhythmias. Moreover, it is currently challenging to non-invasively visualize calcium *in vivo*. Some efforts using multiphoton microscopy technique (623) and optical mapping (624) have enabled recordings of membrane potential and calcium in an autonomically intact heart. However, they required surgical access to the heart, hindering the application of the techniques in humans. In the future, noninvasive photoacoustic imaging (625) might be useful to

visualize and quantify the electrophysiological determinants at molecular and cellular levels (411). Despite the ability of *in vivo* experiments to show the contribution of autonomic nervous system to various calcium-dependent processes, several limitations remain, including ethical considerations, cost and preparation time. These limitations typically preclude the use of large numbers of samples, which potentially reduces the significance of the findings. Therefore, currently available non-integrative laboratory experiments are not adequate to fully elucidate the mechanisms underlying calcium-mediated arrhythmogenesis and another means of integrative experimentation is required to unravel the exact pathophysiology of calcium-induced arrhythmia.

#### 9.4 Why do we need integrative computational modeling?

For more than 40 years, computational modeling of cardiac cellular electrophysiology has been shown to be beneficial in identifying the drivers of cardiac arrhythmias at the cellular scale. Employing the perfect control and observability of *in silico* models, the key determinants of arrhythmogenesis can be identified and managed. Computational modeling is also cost-effective, and with the advancement of computational power and the development of *in silico* tools such as Myokit (344), computational modeling enables the simulations of complex cellular models in a fairly short timeframe. In this thesis, we demonstrated some of the benefits of computational modeling to better understand the pathophysiology of calcium-dependent arrhythmia. First, in **Chapter 3**, employing our *state-of-the-art* spatial calcium-handling model, we showed that heterogeneity of the distributions of calcium-handling proteins has a significant impact on the propensity of SCAEs. Moreover, using our model, we were able to manipulate the arrangement of the axial tubules, attach and detach the concomitant RyR2 hyperphosphorylation, and selectively modify the subcellular distributions of these calcium-handling components, which at present cannot be done experimentally. With this approach, we could show, for the first time, the consequences of different locations and number of axial tubules for atrial calcium wave propagation, the magnitude of the contribution of RyR2 hyperphosphorylation, and the role of lateral RyR2 bands and inter-band RyR2 clusters in calcium wave propagation and how they may contribute to the susceptibility of SCAEs and DADs. Second, in **Chapter 4**, we employed this spatial calcium-handling model to investigate the consequences of both calcium-handling abnormalities and acute transient inflammation on the propensity of SCAEs in the setting of POAF. Our findings confirmed that inflammation is a prerequisite to trigger cellular proarrhythmicity in the vulnerable preexisting substrate of POAF patients. Third, in **Chapter 7**, we showed using our novel tool (MANTA) that interspecies differences in ion-channel function may significantly affect the cellular response to AADs. Furthermore, our tool may also provide a hint on the potential drug-induced proarrhythmia exhibited by various classes of AAD. Similarly, **Chapter 8** also demonstrated the difference between canine and human ventricular cardiomyocytes in facilitating EAD generation in the presence of reduced repolarization reserve. Furthermore, using population of 1000 models, we also showed that  $\beta$ -adrenergic stimulation may limit the proarrhythmic behavior of APD-prolonging drugs by restoring the repolarization reserve, although in the presence of increased  $I_{Ca,L}$  window,  $\beta$ -adrenergic stimulation could be detrimental.

Despite the benefits of subcellular or cellular *in silico* models, the clinical applicability of such findings is limited. Although we showed an increase in SCAEs at the

(sub)cellular level, their effects at higher levels, such as tissue and organ levels, are unknown. Likewise, although our tool was able to demonstrate potential drug-induced arrhythmia at the cellular level, the effect might be eliminated by strong intercellular electrotonic coupling or cell-to-cell variability at higher scales (Figure 9.3). Therefore, the integration of *in silico* models into a multiscale modeling approach is needed. In this thesis, we dedicated Chapter 5 and 6 to highlight the advantage of such an integrative modeling approach. In Chapter 5, we demonstrated that the incorporation of a simplified stochastic RyR2-gating model reproducing behavior from detailed spatial calcium-handling models into an atrial cellular electrophysiological model was able to provide new insight into calcium-mediated arrhythmogenesis. In particular, we showed that calcium-dependent regulation of atrial ionic currents could stabilize the resting membrane potential, increasing the threshold for DADs in healthy atria. However, in an electrically-remodeled atrium, such membrane-stabilizing effects were attenuated. The integration of subcellular, cellular and tissue-level atrial models in Chapter 5 further showed that synchronization of diastolic SR calcium release across cells is needed to transform the cellular-level DADs into tissue-level ectopic activities. Moreover, employing our integrative modeling approach, we directly demonstrated that calcium-induced ectopic activity is able to develop into a non-sustained reentrant arrhythmia. Chapter 6 has also demonstrated the benefits of integrative modeling in investigating complex arrhythmias. Ethanol is known to alter multiple cardiac ion channels, calcium-handling proteins and gap-junction coupling. Using our multiscale model, we could show that ethanol-induced remodeling of  $I_{K1}$  contributed to the protective effects produced by low ethanol concentrations by slightly prolonging atrial APD and lowering the total arrhythmogenic risk at the tissue level. We also showed the consequences of disease-associated electrical and structural remodeling on the ethanol-induced arrhythmogenesis. Finally, we showed that cell-to-cell variability in ethanol-induced  $I_{K1}$  remodeling was an important determinant for the tissue phenotype. Therefore, characterization of such variability is needed to accurately predict the effect of ethanol in cardiac electrophysiology.

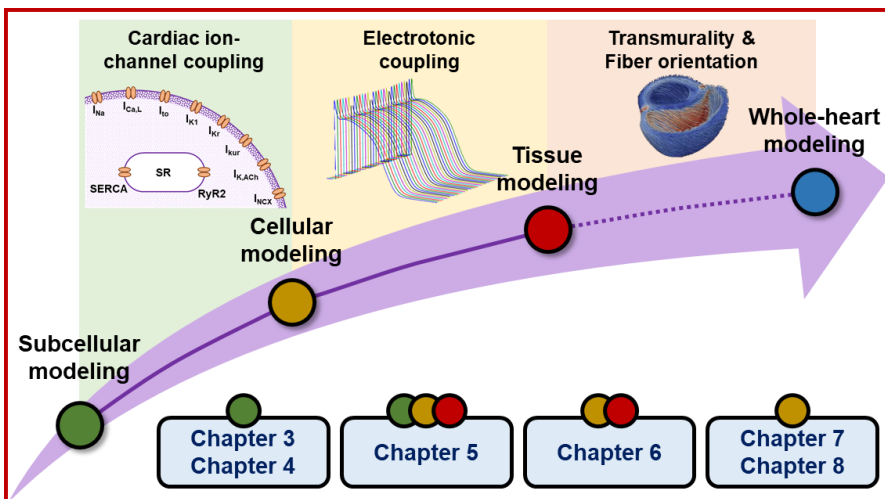


**Figure 9.3:** Schematic illustration of multiscale computational modeling and positioning of the chapters in this PhD thesis. To integrate individual modeling scales into a holistic model, a subcellular model of cardiomyocyte calcium handling is coupled with other cardiac ion channels to form a cellular model. Subsequently, cell models propagate the electrical impulse through gap junctions to form a 1-dimensional strand or 2-dimensional tissue model. At the organ level, different types of tissues, representing different regions and layers of the heart (e.g., epicardium, mid-myocardium, endocardium, Purkinje fibers, etc.) are combined with fiber orientation and structural remodeling.

## 9.5 All models are wrong, but some are useful

George E.P. Box, a British statistician, once said “*all models are wrong, but some are useful*”, which indicates that no *in silico* model is perfect and that each model has its own limitations and uncertainties. Indeed, models can become irrelevant over time, e.g., due to the discoveries of new experimental findings, allowing newer and more advanced models to develop. However, all existing cardiomyocyte models have been constructed based on the available experimental data at the moment when the models were developed and they have been useful to address the specific research questions that they were intended to answer. Moreover, the most interesting lessons are learned when a model is discovered to be incorrect, as this reflects a gap in knowledge or error in our underlying assumptions. As such, one could consider that the statement “*All models are imperfect, but they are nonetheless useful*” would be more appropriate. Nevertheless, several areas for improvement remain. Here, we describe three common limitations of integrative *in silico* models, which require additional attention in future research: interspecies diversity, temperature dependence and intra-/inter-individual heterogeneities.

### 9.5.1 Interspecies diversity

The availability of human cardiomyocyte samples is often limited. Therefore, experimental cardiac cellular electrophysiological research may benefit from the use of heterologous expression system (e.g., HEK293, CHO, *Xenopus laevis* oocytes, etc.), in which a specific ion-channel of interest can be analyzed using patch-clamp experiments. Alternatively, cardiomyocytes can be obtained from various animal models, including mouse, rat, rabbit, guinea-pig, pig, and dog. However, each species has a different composition of cardiac ion channels that may affect the observations and experimental results. For example, mice express little  $I_{Kr}$  and  $I_{Ks}$ , which limits their use for drug-induced proarrhythmia research (604, 626). In **Chapter 7**, we demonstrated such interspecies difference on the AP response to AADs using MANTA. Following the application of dofetilide (a class III AAD, primarily blocking  $I_{Kr}$ ), canine LV and human LV models revealed the biggest APD prolongation, while the mouse LV model showed no effect on AP properties. Similarly, the calcium-channel blocker verapamil (a class IV AAD) displayed species-specific responses in the models. In mouse models, the drug slightly prolonged the APD, while in the guinea-pig and rabbit, it shortened APD. Interestingly, in the canine model, the drug demonstrated an opposing effect at low and high concentrations, with low concentrations prolonging APD and high concentrations shortening APD. Thus, understanding the characteristics (i.e., ion-channel compositions) of the species / models of interest is essential.

Unfortunately, the availability of experimental data from humans (or even from the same animal model) for computational analysis are often limited. Therefore, most *in silico* models are optimized using experimental data from multiple animal models, which could potentially influence the behavior of *in silico* models (627, 628). In these models, we often assume that the observed effects are conserved across species. Although in some cases this assumption is valid, prudent interpretation of the results is necessary.

### 9.5.2 Temperature dependence

It is essential for *in vitro* experiments to be conducted at body temperature (approx. 34-37 degrees Celsius) to produce results closest to physiological conditions. However, sometimes it is challenging due to the increased cell instability at higher temperatures, which forces the experiments to be done at much lower temperature (e.g., room temperature). It has been shown that temperature differences alter the function of several calcium-handling proteins. For example, an increase in temperature from 24 to 37 degrees Celsius increased the rate-constant of decay of the calcium-transient (CaT) and caffeine-induced calcium-transient (cCaT) in both rat and guinea-pig cardiomyocytes, reflecting altered NCX and SERCA function at higher temperature (629). Similarly, temperature changes have been reported to affect the properties of calcium-sparks in rat cardiomyocytes. A reduction of experimental temperature from 35 to 10 degrees Celsius increased the frequency of calcium sparks and reduced their amplitude, while prolonging the time-to-peak and decay of calcium sparks (630). Such findings emphasize the need to carefully observe the data prior to the incorporation into *in silico* models.

To accommodate thermodynamic effects, several computational models have incorporated scaling factors, typically based on a  $Q_{10}$  factor (the change in rate for a 10-degree increase in temperature), into the ionic-current equations. However, the data to validate these factors are scarce and thus may affect the robustness of computational studies when simulations are performed at temperatures other than those at which the data were obtained. Moreover, the temperature-dependent effects may be distinct for different model components and experimental data from different sources may be obtained at different temperatures, making their integration in computational models challenging.

### 9.5.3 Intra- and inter-individual heterogeneities

The pathogenesis of cardiac arrhythmias has not been fully elucidated due to the complex interaction between signaling molecules, calcium-handling proteins, ion channels and other proarrhythmic substrates within the heart. In particular, there are considerable intra- and inter-individual heterogeneities in cardiac electrophysiological properties, which limit the effectiveness and safety of currently available one-size-fits-most therapeutic strategies for cardiac arrhythmias (5). Inter-individual variability is evident even among healthy individuals. However, the clinically observed magnitude of such inter-individual heterogeneities might be overestimated due to the considerable overlap with unexplored intra-individual heterogeneity. Intra-individual variation can be the result of distinct interactions between electrical impulse determinants at the cellular, tissue (e.g., gap-junction coupling and anisotropy) and organ levels (e.g., fiber arrangement, wall thickness and structural remodeling). At the molecular level, the

heterogeneity of the distribution and expression of ion channels and signaling molecules, as well as the interactions between two or more tightly co-expressed genes and the integration of multiple proteins in macromolecular complexes may contribute to the functional variability observed at the cellular and tissue levels (631). In the healthy heart, the effect of single-cell variability may be cancelled out by strong electrotonic coupling (632), while in the diseased heart with altered intercellular coupling, the effect of such variability is unknown and yet to be investigated. Comprehensive characterizations of this molecular and cellular heterogeneity have so far not been performed.

Computationally, inter-individual heterogeneity is (partly) addressed by employing a population of models, incorporating variability of specific parameters of interests (typically the maximum conductance of ionic currents, reflecting differences in the expression level of ion channels) (382). Using this population-based approach, the inter-individual variability of ionic currents can be accommodated and more representative results can be obtained. However, the exact magnitude of such variability is unknown and therefore relies on predefined assumptions. In **Chapter 6**, in addition to the population modeling approach to confirm our cellular findings, we also performed multiscale *in silico* simulations to study the role of cell-to-cell variability at the tissue level. We aimed to study whether the ethanol-associated increase in reentrant arrhythmia vulnerability is affected by the variability of ethanol-induced  $I_{K1}$  remodeling. Our simulations revealed that the proportion of cells incorporating an ethanol-induced increase or decrease of  $I_{K1}$  in the virtual tissue modulated the behavior of the reentrant arrhythmias (346). This finding highlights the need for considering cell-to-cell variability to improve the accuracy of the computational model at the higher scale (e.g., tissue or organ level).

## 9.6 The future outlook of integrative *in silico* modeling

### 9.6.1 Organ-level modeling

In specific cases, 2-dimensional tissue simulations may be adequate to address the arrhythmogenic consequences of calcium handling abnormalities. By employing such tissue simulations, the significance of cell-to-cell interaction can be elucidated with a fairly reasonable computational cost (633). However, the results may not be representative of the actual condition in the organ level due to the absence of other supporting components, such as extracellular matrices, Purkinje fibers, muscle-fiber orientation and spatial gradients in electrophysiological properties (e.g., between left and right, or between endocardial, mid-myocardial and epicardial layers) (634). Those organ-level components might also play an important role in wave propagation within the heart (635). Therefore, organ-level modeling incorporating detailed structures of cardiac electrophysiology may ultimately be needed for studying cardiac arrhythmias.

However, despite its potential benefit for arrhythmia research, organ-level modeling is computationally intense and requires supercomputing clusters to operate, which hinders its broad application (634). To overcome this issue, (sub)cellular models have had to be significantly simplified. As an illustration, on a normal personal computer, a simulation using the detailed spatial calcium-handling model as described

in **Chapter 3** could take more than 12 hours to complete, while a cellular simulation using a common-pool AP model would only take less than two minutes to compute. Meanwhile, a simulation of 400x400 cells with detailed ionic currents could last for more than 8 hours. This definitely limits the use of such detailed models at tissue- and organ-level scales. Simpler alternatives have been proposed at the cost of losing realism in the mathematical description, e.g., using phenomenological models, which reduce the number of state-variables substituting the actual ionic current descriptions by simple mathematical equations (634). In this thesis (**Chapter 5**), we have applied a similar simplification to bypass the complexity of subcellular components of cardiomyocyte calcium handling to investigate the consequences of SCaEs at the cellular and tissue levels. However, such simplifications may limit the ability of the organ-level model to mimic the precise conditions observed experimentally, particularly in the presence of genetic mutations altering the gating components of specific cardiac ion channels or calcium-handling proteins. Therefore, until now, the application of organ-level modeling in pathologies requiring complex biophysical details has been limited to a few studies by a handful of labs worldwide. Moreover, the models in these studies are often used to address issues in which the changes to the ion channels or calcium-handling proteins can be implemented by modifying the maximum conductance of the currents (e.g., to simulate arrhythmogenic consequences of myocardial infarction / ischemia). Nonetheless, computing power continues to advance and organ-level modeling will likely become feasible to investigate the arrhythmogenic consequences of calcium-handling abnormalities.

### 9.6.2 Integrative personalized modeling

Despite the limitations of current integrative computational modeling approaches, there is a growing demand for more personalized modeling approaches that accommodate interindividual heterogeneities to unravel patient-specific mechanisms and develop tailored therapy of cardiac arrhythmias. Although for now this is still far from reality, in the future, arrhythmia research would benefit from such a personalized approach. Ideally, a patient-specific “bottom-up” framework can be initiated by extracting cardiomyocytes from a patient, in which a comprehensive *in vitro* characterization of cardiac ion-channels can be made. Advances in induced pluripotent stem cell and automated patch-clamp technologies have provided first steps in this direction. Subsequently, such experimental data could be used as input for computational studies at the cellular level. Next, patient-specific intercellular / gap-junction conduction can be assessed and incorporated in a personalized tissue model. Using advanced imaging techniques, the detailed geometry of the heart, as well as patient-specific fibrosis patterns can be mapped to create a personalized cardiac mesh for the 3-dimensional organ-level model. Combined with database-derived human Purkinje network and fiber orientation from diffusion tensor imaging, a patient-specific 3-dimensional heart model can be developed and employed for patient-specific research. Finally, the standard 12-lead electrocardiogram, as well as invasive electrophysiological studies and non-invasive electrocardiographic mapping may provide important functional data to personalize the model’s electrophysiological properties at the organ level (**Figure 9.4**).

Such comprehensive personalized approaches have been partially performed, for example to guide catheter ablation in atrial fibrillation (636) and ventricular fibrillation (637). In these translational studies, the patient-specific fibrotic regions were incorporated into organ-level models and the appropriate target ablation site was identified in the model, which was then confirmed during a clinical electrophysiological study. Using this personalized modeling approach, lengthy electrical mapping procedure could potentially be avoided and the accuracy of targeted ablation could be improved. Conceptually, the future management of complex inherited arrhythmia syndromes, for example arrhythmogenic cardiomyopathy (AC), may similarly benefit from a personalized modeling approach. The cardiomyocytes from an AC patient could be extracted and characterized. Then, the results could be incorporated in a cellular electromechanical model. Meanwhile, advanced imaging and tissue optical mapping could be performed to identify fibrotic regions and assess the intercellular conduction and anisotropy. At the organ level, the fibrofatty infiltration, trabeculation and fiber arrangement could be assessed. All of those findings could then be incorporated into the whole-heart electromechanical and hemodynamic model and subsequently, the predisposing factors for arrhythmogenesis in this particular patient could be identified, the pathophysiology of the disease could be explained and the best treatment strategy, either pharmacological, interventional, or a combination of those two, could be applied.

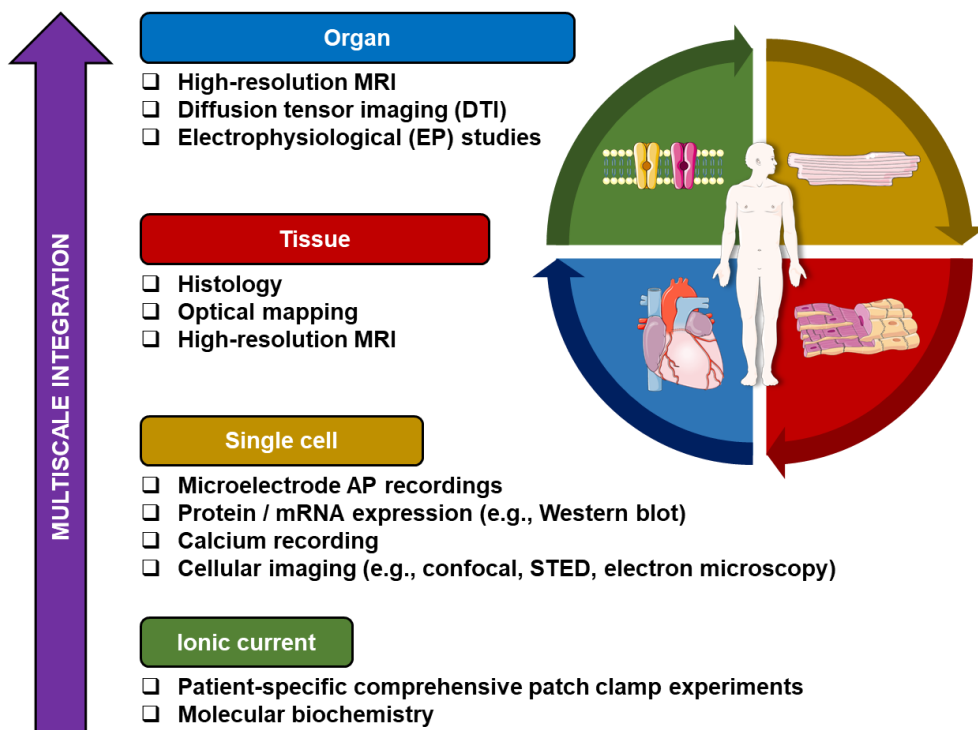


**Figure 9.4:** A schematic illustration summarizing multiscale integration of patient-specific data. The “bottom-up” approach starts from the ionic current / molecular level up to the organ level. At each scale, the acquired

## *Discussion*

data can be utilized as an input for computational modeling. Ultimately, a personalized 3-dimensional computational model can be developed and used for patient-specific arrhythmia research.

## **9.7 Conclusions**

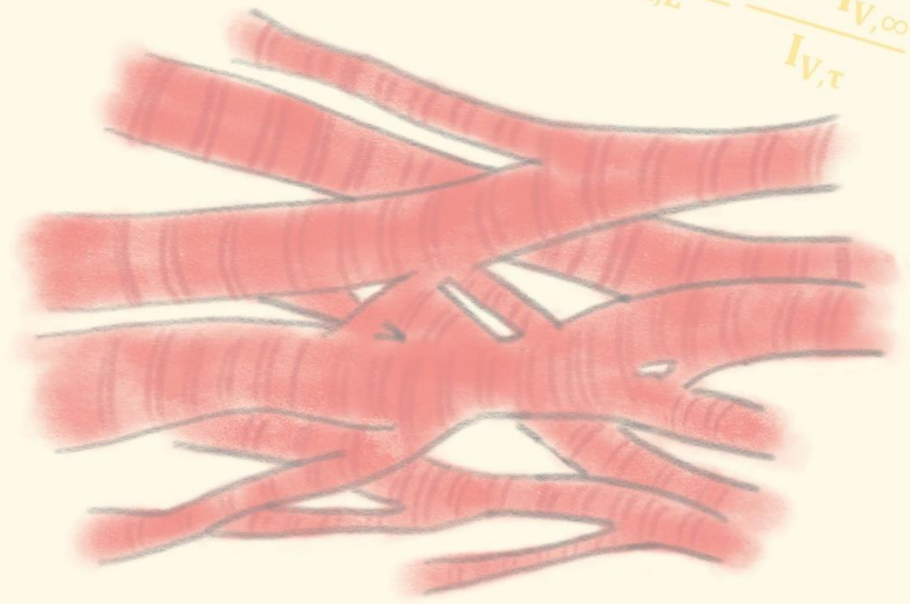
Calcium-handling abnormalities have multiscale implications that may promote cardiac arrhythmias. Computational modeling is a powerful tool to investigate the arrhythmogenic mechanisms and consequences of alterations in cardiac calcium handling. In this thesis, we demonstrated how integrative computational modeling of calcium handling can provide new insights into arrhythmia mechanisms, although some challenges remain. Future arrhythmia research will benefit from organ-level modeling of calcium-handling abnormalities, and, more importantly, an integrative patient-specific modeling approach. Such advances will certainly improve the accuracy and predictability of computational models and increase their clinical relevance. John von Neumann stated that “*With four parameters I can fit an elephant, and with five I can make him wiggle his trunk*”. In the end, one extra sentence deserves to be added to this statement: “... *but even with thousands of parameters, I cannot make him alive.*”, indicating that *in silico* models will always be *in silico* and therefore, synergy between modeling, biological experiments and clinical research remains an absolute prerequisite.





$$\frac{dV_m}{dt} = -\frac{1}{C_m} * I$$

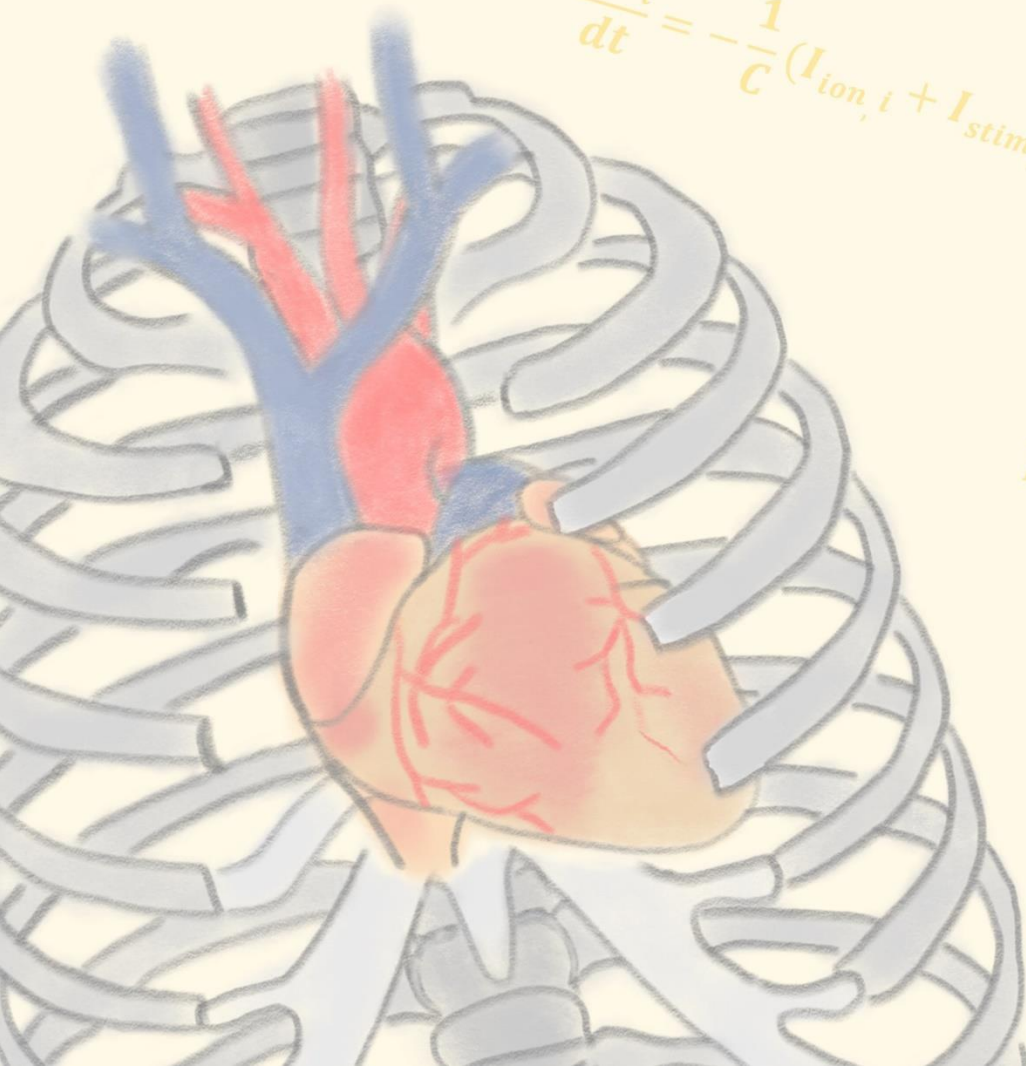
$$y_{Ca,L} = \frac{1 - I_{V,\infty}}{I_{V,\tau}}$$



$$x_{Ca,L} = \frac{I_{V,\infty}}{I_{V,\tau}}$$

$$\delta I_{Ca,L}^{s,m} =$$

$$\frac{dV_i}{dt} = -\frac{1}{C} (I_{ion,i} + I_{stim,i} + I_{diff,i})$$



$$\bar{I}_{Ca,L}^{s,m} = P_{Ca,L} \cdot (z$$

$$ACT_{\tau} = 0.59$$

# Summary

$$\frac{dX}{dt} = \alpha_x (1 - X) - \beta_x X$$

$$\delta I_{Ca,L}^{s,m} = \theta_{Ca,L} \cdot \frac{X_{Ca,L} \cdot y_{Ca,L}^{s,m} \cdot \delta_{Ca,L}^{s,m}}{y_{Ca,L} \cdot X_{Ca,L}^{s,m} \cdot \theta_{Ca,L}}$$

$$\frac{X_{Ca,L} \cdot y_{Ca,L}^{s,m} \cdot \delta_{Ca,L}^{s,m}}{y_{Ca,L} \cdot X_{Ca,L}^{s,m} \cdot \theta_{Ca,L}}$$

$$I_{Ca,L}^{s,m} = \bar{I}_{Ca,L}^{s,m} \cdot (O_{Ca,L}^{s,m} + O_{Ca,L}^{s,m})$$

$$\frac{V_m \cdot F^2}{R \cdot T} \cdot \frac{y_{Ca,i} \cdot [Ca^{2+}]_{obs}^{s,m} \cdot \exp\left(z_{Ca} \cdot V_m \cdot \frac{F}{R \cdot T}\right) - y_{Ca,o} \cdot [Ca^{2+}]_o}{1 + \exp(0.052 \cdot (V_m + 13))} \cdot \frac{\exp\left(z_{Ca} \cdot V_m \cdot \frac{F}{R \cdot T}\right) - 1}{1 + \exp(0.132 \cdot (V_m + 13))}$$

$$\frac{dV}{dt} = \frac{I_{stim} - (I_K + I_{Na} + I_{leak})}{C_m}$$



## Summary

Cardiomyocyte calcium handling is a major determinant of excitation-contraction coupling. Alterations in one or more calcium-handling proteins may induce arrhythmias through the formation of ectopic activity, direct and indirect ion-channel regulation, and structural remodeling. Due to the complex and tight interactions between calcium and other molecules within a cardiomyocyte, it remains experimentally challenging to study the exact contributions of calcium-handling abnormalities to arrhythmogenesis. Multiscale computational studies performed in close collaboration with laboratory experiments create new opportunities to unravel the mechanisms of arrhythmogenesis. This thesis describes the roles of integrative computational modeling in unraveling the arrhythmogenic consequences of calcium-handling abnormalities.

In **Chapter 2**, we reviewed the complex mechanisms and proarrhythmic consequences of calcium-dependent ion-channel regulation, SCaEs, post-translational calcium-signaling pathways, and long-term transcriptional regulation of calcium handling. We also discussed potential advantages of combined *in vitro* and *in silico* studies to address such complexities.

In **Chapter 3**, we employed the perfect control and observability provided by computer models to elucidate the subcellular determinants of cardiomyocyte calcium handling. Our findings highlighted the importance of subcellular RyR2 and LTCC distributions in the genesis of SCaEs and DADs, which are well-known triggers of cardiac arrhythmias. Importantly, whole-cell calcium handling properties are determined by non-linear interactions between heterogeneities in the expression and phosphorylation of both LTCC and RyR2, highlighting the need for detailed immunocytochemistry and functional studies to explain differences in whole-cell calcium handling between conditions.

**Chapter 4** illustrated the application of the spatial calcium-handling model from **Chapter 3** to support the notion that post-operative inflammation acting on a pre-existing arrhythmogenic substrate may elicit SCaEs and DADs that could initiate POAF.

Meanwhile, in **Chapter 5**, our multiscale *in silico* study demonstrated that calcium-dependent regulation of atrial ionic currents alters human atrial electrophysiology at the cellular and tissue level. It has protective effects in non-diseased atrium by stabilizing the membrane potential, lowering DAD amplitude and preventing TA. However, in the presence of cAF-related remodeling, calcium-dependent ion-channel regulation has proarrhythmic APD-shortening and RMP-hyperpolarizing effects, stabilizing reentrant waves. We identified  $I_{K1}$  and  $I_{SK}$  as the major ionic contributing factors.

**Chapter 6** of this thesis showed how our multiscale *in-silico* study provides new insights into the acute effects of ethanol on cardiac electrophysiology and arrhythmogenesis, demonstrating that ethanol has concentration-dependent

## Summary

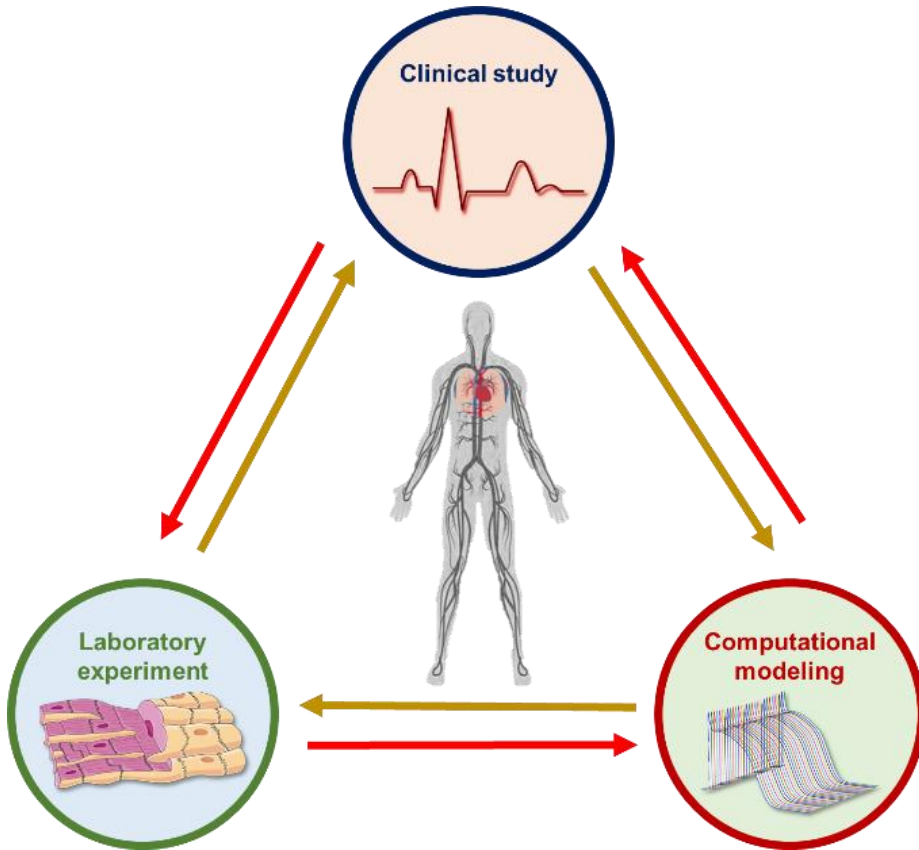
electrophysiological effects that differ between atria and ventricles, and in the absence or presence of disease-related remodeling. Low concentrations of ethanol had antiarrhythmic effects in the atria, whereas high concentrations promoted reentrant arrhythmias. In this chapter, we also showed that the exact proarrhythmic risk depends on ethanol-induced gap-junction remodeling and the degree, type and pattern of disease-associated structural remodeling, highlighting the need for personalized multiscale computational modeling to better predict the consequences of ethanol on cardiac electrophysiology in humans.

**Chapter 7** introduced MANTA, a powerful, freely available tool to reproduce a wide range of AAD characteristics including species-, rate-, and disease-dependent effects. MANTA enables analyses of the underlying ionic mechanisms as well as investigations of novel AADs with specific affinities for one or more targets. MANTA can facilitate a better understanding of the complex effects of AADs on cellular electrophysiology under a wide range of conditions, which may provide educational and/or clinically-relevant information on the safety and efficacy of AAD treatment.

**Chapter 8** demonstrated the synergistic APD-prolonging effect of CQ and AZM, which potentially increases the proarrhythmic risk, although the severity of the electrophysiological effects depends on the baseline repolarization reserve. Additionally, we showed that transient activation of the sympathetic nervous system may prevent CQ- and AZM-induced proarrhythmia by reducing their APD-prolonging effect, highlighting the importance of preserving  $\beta$ -adrenergic response in the presence of such proarrhythmic medications, and the potential significance of heart-rate and autonomic-status monitoring in conditions such as COVID-19.

Finally, **Chapter 9** wrapped up this thesis with an *aide-mémoire* that calcium-handling abnormalities have multiscale implications that may promote cardiac arrhythmias. Integrative computational modeling enables investigations into the arrhythmogenic mechanisms and consequences of alterations in cardiac calcium handling, although some challenges remain. Future arrhythmia research would benefit from organ-level, and, more importantly, integrative personalized / patient-specific modeling approaches, which will certainly improve the accuracy and clinical applicability of computational models.

In the end, *in silico* models will always be *in silico*. Therefore, synergistic interactions with clinical studies and biological experiments are an absolute prerequisite to address unmet needs of current arrhythmia research.

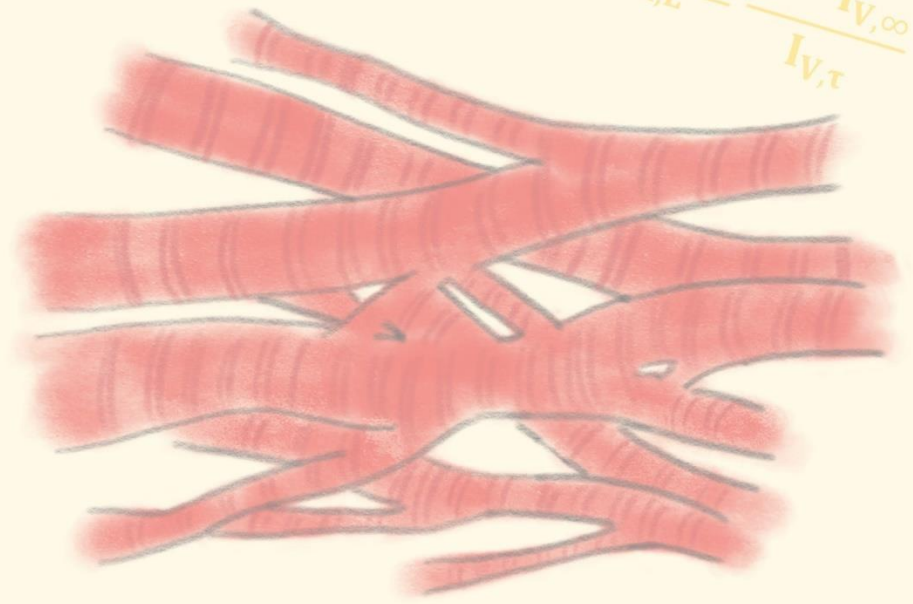


**Summary figure:** Three pillars of cardiovascular research. In the future, an integrative synergy between clinical studies, laboratory experiments and computational modeling would be beneficial in addressing the knowledge gaps and unmet needs of current arrhythmia research.



$$\frac{dV_m}{dt} = -\frac{1}{C_m} * I$$

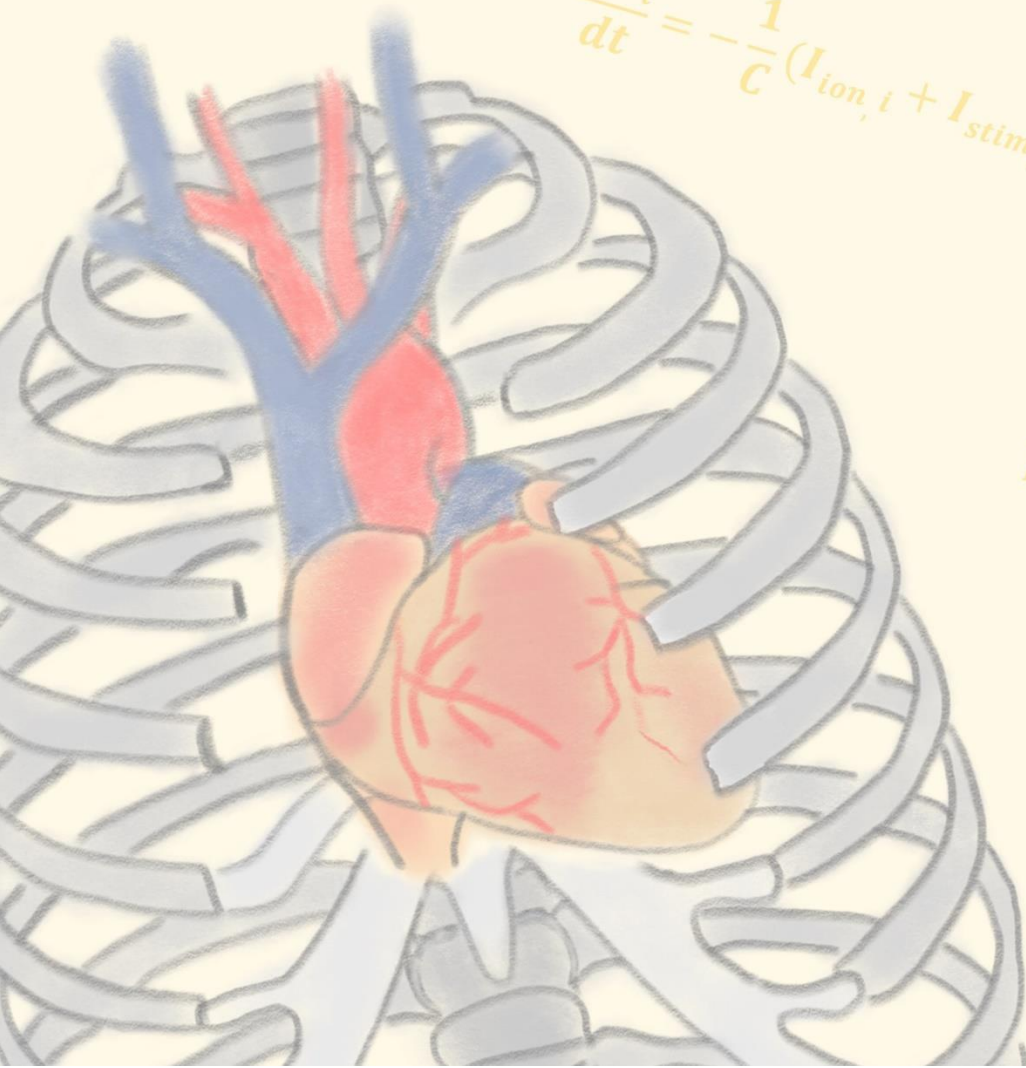
$$y_{Ca,L} = \frac{1 - I_{V,\infty}}{I_{V,\tau}}$$



$$x_{Ca,L} = \frac{I_{V,\infty}}{I_{V,\tau}}$$

$$\delta I_{Ca,L}^{s,m} =$$

$$\frac{dV_i}{dt} = -\frac{1}{C} (I_{ion,i} + I_{stim,i} + I_{diff,i})$$



$$\bar{I}_{Ca,L}^{s,m} = P_{Ca,L} \cdot (z$$

$$ACT_{\tau} = 0.59$$

# Impact

$$\frac{dX}{dt} = \alpha_x (1 - X) - \beta_x X$$

$$\delta I_{Ca,L}^{s,m} = \theta I_{Ca,L} \cdot \frac{X_{Ca,L} \cdot y_{Ca,L}^{s,m} \cdot \delta_{Ca,L}^{s,m}}{y_{Ca,L} \cdot X_{Ca,L}^{s,m} \cdot \theta_{Ca,L}}$$

$$\frac{X_{Ca,L} \cdot y_{Ca,L}^{s,m} \cdot \delta_{Ca,L}^{s,m}}{y_{Ca,L} \cdot X_{Ca,L}^{s,m} \cdot \theta_{Ca,L}}$$

$$I_{Ca,L}^{s,m} = \bar{I}_{Ca,L}^{s,m} \cdot (O_{Ca,L}^{s,m} + OS_{Ca,L}^{s,m})$$

$$\frac{V_m \cdot F^2}{R \cdot T} \cdot \frac{Y_{Ca,i} \cdot [Ca^{2+}]_{obs}^{s,m} \cdot \exp\left(z_{Ca} \cdot V_m \cdot \frac{F}{R \cdot T}\right) - Y_{Ca,o} \cdot [Ca^{2+}]_o}{1 + \exp(0.052 \cdot (V_m + 13))} \cdot \frac{\exp\left(z_{Ca} \cdot V_m \cdot \frac{F}{R \cdot T}\right) - 1}{1 + \exp(0.132 \cdot (V_m + 13))}$$

$$\frac{dV}{dt} = \frac{I_{stim} - (I_K + I_{Na} + I_{leak})}{C_m}$$



## Impact

Cardiovascular disease is a leading global cause of death, contributing to approximately 17.8 million deaths in 2017. This number is expected to grow to more than 22.2 million by 2030 (638). In accordance, the prevalence of atrial fibrillation (AF) is estimated to be 1-2% of the general population in developed countries (e.g. North America, Europe and Japan) and about 0.5-1% in developing countries, turning AF into the most commonly found arrhythmia in the clinic, affecting more than 33 million people worldwide (639). Despite decades of research, a large number of unmet needs and knowledge gaps remain, preventing more effective management of patients at risk of arrhythmias (540). At the moment, the insights on the pathophysiology of arrhythmias in an individual patient are incomplete, affecting our available approaches to identify the actionable patient-specific molecular arrhythmia mechanisms, to detect and target key dynamic modulators of cardiac arrhythmias, to achieve atrial targeting of specific molecular arrhythmic mechanisms with drugs, and to integrate studies of specific molecular/cellular AF pathophysiology (411, 540).

The chapters in this thesis aimed to address a number of current knowledge gaps by employing the perfect control and observability of computational modeling to better understand the role of cardiomyocyte calcium handling in arrhythmogenesis.

### **Scientific impact**

To recapitulate, **Chapters 1** and **2** of this thesis summarized the roles of cardiomyocyte calcium handling in health and disease. **Chapter 3** discussed our *state-of-the-art* subcellular model of the human atrial cardiomyocyte to investigate the impact of subcellular distributions of calcium-handling proteins on atrial electrophysiology. **Chapter 4** employed this subcellular model to elucidate the cause-effect relationship between calcium-handling abnormalities, acute transient inflammation and POAF. **Chapter 5** evaluated the consequences of calcium-dependent ion-channel regulation on atrial electrophysiology under physiological and pathological conditions. **Chapter 6** presented a multiscale computational framework to investigate ethanol-associated reentrant arrhythmia in both healthy and remodeled hearts. **Chapter 7** presented MANTA, a novel, easy-to-use educational tool to better understand the cellular effects of AADs. Finally, **Chapter 8** highlighted the significance of  $\beta$ -adrenergic receptor stimulation in modulating the cellular proarrhythmic effects of chloroquine and azithromycin.

Of the 8 scientific chapters in this thesis, 7 have been published in international peer-reviewed journals and 1 is still in the process of submission. **Chapter 1** has been published in *Frontiers for Young Minds* in 2019 (640), and due to its unique concept and reasonably high societal impact, this chapter will be discussed separately in the next section. **Chapter 2** has been published in *Progress in Biophysics and Molecular Biology* in 2020 (335). This publication was the first that extensively discussed the potential synergy between *in vitro* and *in silico* studies of cardiomyocyte calcium handling on cardiac cellular electrophysiology. It has been accessed >1500 times in the first 6-months since its publication. **Chapter 3** has been published in *Frontiers in Physiology* in 2018 (4) and the subcellular calcium handling model has been used to address specific molecular/cellular AF pathophysiology as illustrated in **Chapter 4**. **Chapter 4** has been published in *Circulation Research* in 2020 (327) as part of a comprehensive study

## *Impact*

involving both *in vitro* and *in silico* experiments. **Chapter 6** of this thesis was published in *Journal of Molecular and Cellular Cardiology* in 2020 (346), and during its first month of publication, it has become the journal's most read publication, with a high interest from the general community. This study was the first that employed multiscale computational modeling to study the acute effects of ethanol in cardiac electrophysiology. Moreover, this extensive *in silico* study provides a general framework to computationally investigate other complex arrhythmias. **Chapter 7** was published in *Pharmacological Research* in 2019 (603), and was the first easy-to-use educational tool to better understand the effects of antiarrhythmic drugs (AADs) on cardiac cellular electrophysiology. MANTA has been used in several other unpublished projects to give an overview on how AADs may behave in specific *in silico* models and it is currently used as part of the Master Systems Biology program at Maastricht University. Finally, **Chapter 8** of this thesis was published in *Frontiers in Physiology* in 2020 (617). The study was the first to identify the role of  $\beta$ -adrenergic stimulation in the presence of altered repolarization reserve, for example during the administration of chloroquine and azithromycin. The study was conducted during the COVID-19 pandemic, a disease state in which the sympathetic nervous and  $\beta$ -adrenergic response activation were expected to occur, and thus might interact with such proarrhythmic medications. Of note, all of our (Maastricht-led) publications and models are freely accessible, reflecting our commitment and support to the open science initiative.

One way through which computational models can have scientific impact is the identification of arrhythmia mechanisms based on the perfect control of model parameters. For example, the study in **Chapter 3** was the first to employ computational modeling of subcellular calcium handling to investigate the role of the distributions of calcium-handling proteins in atrial electrophysiology. It is at present not possible to selectively modulate the location of individual proteins experimentally. Using our *state-of-the-art* subcellular model of cardiomyocyte calcium handling, we could show that increased heterogeneity of RyR2 clusters contributed to the propensity for SCaEs and DADs, and future targeting of this arrhythmogenic substrate might be advantageous to treat arrhythmia, for example in heart failure and AF, where increased heterogeneity of RyR2 clusters size has been documented (158, 159). Employing the perfect control of computational modeling, we also unraveled the significance of lateral RyR2 bands and interbands on the atrial wave propagation, something that could also only be addressed by *in silico* modeling. Although there are at present no therapeutic options to target these factors involved in arrhythmogenesis, altering the localization of proteins might be possible in the future, e.g., by modulating targeting of trafficking mechanisms through existing gene-editing technologies, including CRISPR-Cas9.

In addition to its strong educational impact, **Chapter 7** of this thesis also helps the scientific community on highlighting the interspecies diversity of AAD effects and therefore, the importance of selecting the most appropriate animal model for particular arrhythmia research. In the future, MANTA, as well as the other computer models developed in this thesis, can be used as a preliminary screening tool to reduce unnecessary animal experimentations, in line with the spirit of World Medical Association Declaration of Helsinki.

Meanwhile, **Chapter 6** illustrated the future use of multiscale integrative computational modeling to investigate specific risk factors (in this particular case,

alcohol consumption) under different conditions (e.g., the absence or presence of heart failure or AF-related remodeling). We could show that the degree, type and pattern of fibrosis had a significant impact on the behavior of reentrant arrhythmias, therefore indicating the need for a more personalized modeling approach. Such personalized modeling is expected to become increasingly used in patient care, as already demonstrated in for computationally guided catheter ablation (636, 637). This, together with the FDA-approved comprehensive *in vitro* proarrhythmia assay (CiPA) initiative (444, 595) to develop safer future pharmacological agents, are steadily bringing computational modeling towards clinically relevant applications. The work presented in this thesis underscores the importance of model personalization (**Chapters 6 and 7**) and provides novel approaches to simulate patient-specific triggers (e.g., post-operative triggers in **Chapter 4**).

Lastly, computational modeling in general and the publications in this thesis in particular have enriched internal and external research collaborations. Computational modeling is inherently collaborative work since the models are built together and improved by computer modelers all over the world and rely on experimental data from many research. For example, the original O'Hara-Rudy dynamic model developed at Washington University in St. Louis, MO (263) has been modified, recalibrated and widely employed by modelers across the globe, highlighting such vast collaborations in the field of computational modeling. As part of this thesis, collaborations were established between the Departments of Cardiology, Physiology, Biomedical Engineering, and Genetics & Cell Biology at Maastricht University. Externally, among others, international partnerships were built with University Duisburg-Essen (DE), Masaryk University (CZ), and University of California Davis (CA).

### ***Societal impact***

During the PhD, we also put emphasis on the potential societal impact of our projects and publications. We intentionally designed our projects to not only provide specific scientific insights to the field, but also to improve the basic understanding of calcium handling and the relevance of its dysfunction in the general community. **Chapter 1** of this thesis is one of the examples of these efforts. *Frontiers for Young Minds* is an international journal that aims to disseminate science and new scientific findings to general audiences, especially the future scientists. It is peer-reviewed by children in the range of 8-15 years to stimulate their curiosity and expose them to the world of science, guided by a science mentor. To support this initiative, the author of this thesis has become a science mentor for the journal during his PhD. In the first year after its publication, **Chapter 1** of this thesis has received a huge interest from people around the world, reflected by its high read index (more than 20,000 reads to date; see the map below), turning the paper into one of the top 2% of all *Frontiers* publications. Moreover, it has received a reasonably good response on social media platforms, such as Twitter, Reddit, Facebook and Mendeley.

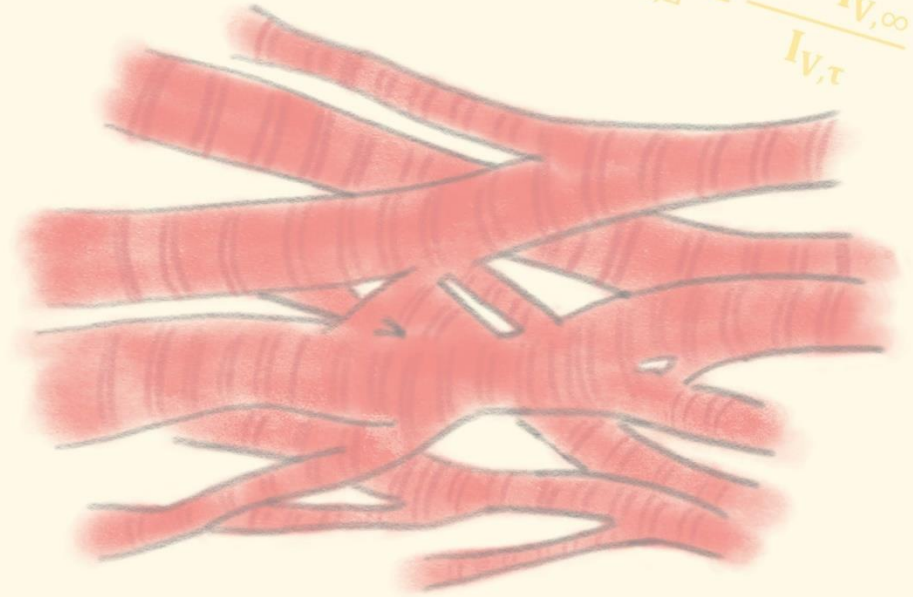
In addition to **Chapter 1**, almost all of our publications have received high interests from both scientific and general communities on social media, supporting our aforementioned commitment in disseminating our research. The most interesting example is **Chapter 6** of this thesis that touched on a very sensitive issue: alcohol





$$\frac{dV_m}{dt} = -\frac{1}{C_m} * I$$

$$y_{Ca,L} = \frac{1 - I_{V,\infty}}{I_{V,\tau}}$$



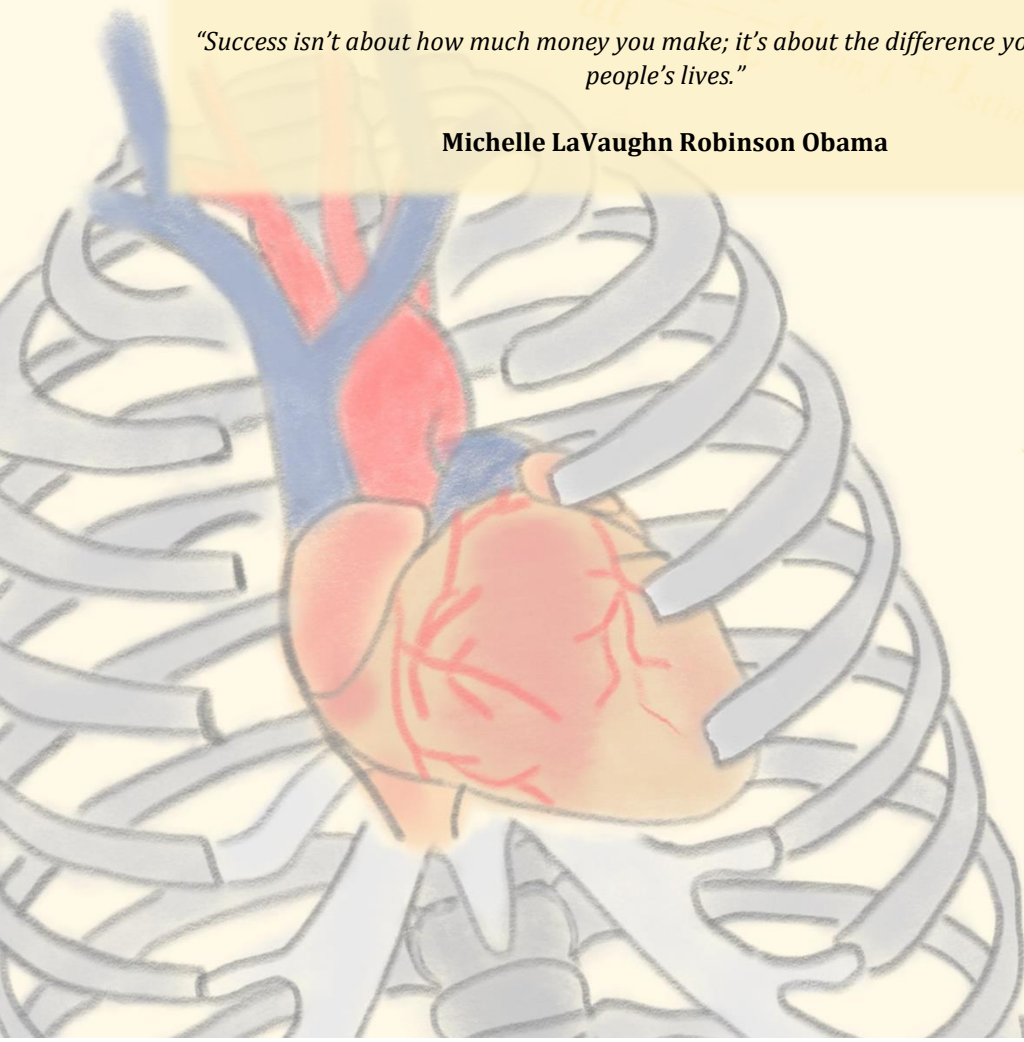
$$x_{Ca,L} = \frac{I_{V,\infty}}{I_{V,\tau}}$$



*"Success isn't about how much money you make; it's about the difference you make in people's lives."*

**Michelle LaVaughn Robinson Obama**

$$\delta I_{Ca,L}^{s,m} =$$



$$\bar{I}_{Ca,L}^{s,m} = P_{Ca,L} \cdot (z$$

$$ACT_{\tau} = 0.59$$

# Acknowledgement

$$\frac{dX}{dt} = \alpha_x (1 - X) - \beta_{Ca} X$$

$$\delta I_{Ca,L}^{s,m} = \theta I_{Ca,L} \cdot \frac{X_{Ca,L} \cdot y_{Ca,L}^{s,m} \cdot \delta_{Ca,L}^{s,m}}{y_{Ca,L} \cdot X_{Ca,L}^{s,m} \cdot \theta_{Ca,L}}$$

$$\frac{X_{Ca,L} \cdot y_{Ca,L}^{s,m} \cdot \delta_{Ca,L}^{s,m}}{y_{Ca,L} \cdot X_{Ca,L}^{s,m} \cdot \theta_{Ca,L}}$$

$$I_{Ca,L}^{s,m} = \bar{I}_{Ca,L}^{s,m} \cdot (O_{Ca,L}^{s,m} + O_{Ca,L}^{s,m})$$

$$\frac{V_m \cdot F^2}{R \cdot T} \cdot \frac{y_{Ca,i} \cdot [Ca^{2+}]_{obs}^{s,m} \cdot \exp\left(z_{Ca} \cdot V_m \cdot \frac{F}{R \cdot T}\right) - y_{Ca,o} \cdot [Ca^{2+}]_o}{1 + \exp(0.052 \cdot (V_m + 13))} \cdot \frac{\exp\left(z_{Ca} \cdot V_m \cdot \frac{F}{R \cdot T}\right) - 1}{1 + \exp(0.132 \cdot (V_m + 13))}$$

$$\frac{dV}{dt} = \frac{I_{stim} - (I_K + I_{Na} + I_{leak})}{C_m}$$



## **Acknowledgement**

First and foremost, I would like to thank **God** who has put me into this PhD position through a very unique and complicated way. Being a PhD student was never on my wish list and the way He amazingly brought this opportunity to me was beyond my expectations. The second tier of my acknowledgement goes to **my family** who has supported me unconditionally during my PhD, both in my sunny and gloomy days. My parents **Hadiman** and **Jeny**, my brother **Andryanto**, my sister **Caroline** and my uncle **Stevanus** have been so caring. I still remember the day when I had to depart from my hometown Surabaya to Maastricht in February 2017. Despite my unfit physical condition due to laparotomy I had a month before, my uncle accompanied and stayed with me for a week in Maastricht, just to make sure that everything was okay. Without you all, I would not be here and I would not have had the strength needed to finish this PhD.

Next, I would like to thank **Jordi**. I have to say that I don't know exactly how I should introduce him. He is my supervisor, teacher, mentor, senior, brother, friend, and many more. The only thing I can say is that he is my "family" in a faraway land. He always takes care of me both in the scientific and non-scientific occasions. Thank you for your trust in me in the last 4 years and thank you for your immense support when I was feeling blue. I think people deserve to know how amazing you are as a person and a supervisor, apart from your infamous scientific excellence. Without Jordi, I would not be writing this thesis today and my PhD would not even exist. The image is still clear in my mind when I first came here as a visitor, and despite my zero knowledge in computational modeling, even zero coding experience, he trusted me and said something that he probably has forgotten by now, which was pretty much like: "*As long as you are motivated, I can help you learn anything you want to learn.*" As the only supervisor I have, you gave all of the efforts and time I needed, 7 days a week, both during and out of working hours. Thank you for showing me the personal and scientific quality I have never seen in a person, which have challenged myself not to be too far from your quality. I want to let people know that you deserve all the credits for what we have achieved in the last 4 years. I think this quote fits your trait very well: "*The good teacher makes the poor student good and the good student superior*". Although we often disagree on things, I will surely miss the moment when we work together. If time allows, I would love to learn many more things from you and see more of your "walking PubMed" brain in the future. If not, I will always keep your advices in mind for my future career, whatever it will be.

The next appreciation goes to my promotors, **Prof. Harry Crijns** and especially **Prof. Paul Volders**, who has allowed me to join his team and has treated me very well as part of his team. From Paul, I have learnt a lot about cardiac cellular electrophysiology and I now realize how I actually missed the Vlaai sessions we have had during our working meetings. Next, I would like to express my full gratitude to the chair and members of the assessment committee of this 'oversized' PhD thesis: **Prof. Frits Prinzen**, **Prof. Ralf Peeters**, **Dr. Dominik Linz**, **Prof. Antonio Zaza** and **Prof. Stefano Severi** for their time and efforts, also to the esteemed 'opponents' in my PhD

## *Acknowledgement*

defense, who are working hard to keep everything in equilibrium/homeostasis. Then, of course to current and previous members of Paul's team: **Rachel, Roel, Sandrine, Matthijs, Michael, Joyce, Gudrun, Dan, Antonio, Henk, Monique** and **Cristina Moreno**. Thank you for making my day during the last 4 years, and for supporting me personally and scientifically. For **Roel**, special thanks to you for being the nurturing father of the pack and especially for being my paranymp. Furthermore, I would like to thank Paul's PhD students squad: **Cristina Altrocchi, Beatrice, Alberto, Bianca, Job**, and **Anna Savchenko** for helping me a lot during my PhD. Special thanks to **Cristina**, my informal "co-supervisor", who has guided me during my first PhD year. It seems that at the end, I am the first to defend, but I am sure your time will come soon as well and I am looking forward to it. Then **Job**, the world's grumpiest man, thank you for being my office mate for the last 3 years. It was a great time being with you in the legendary 3.106 and seeing you munching a box full of sandwiches alone all the time (PS: I think the lonely bifi will still be on my desk by now). Thanks for always keeping your role as my opposition and for being my paranymp. I wish you all the best of luck for the rest of your PhD trajectories and beyond.

I would also like to acknowledge all the people whom I have interacted and collaborated with during the last 4 years. **Prof. Dobromir Dobrev** from Essen, thank you for the excellent suggestions I obtained from you on all of our publications, which motivated me to read about things that I did not know before. **Joost** and **Aurore**, I learned a lot from you, especially **Aurore**, my electro-mechanical modeling guru. Also, thanks to **Patrick, Giulia, Vladimir, Marcia, Ben, Bart, Lian, Cristian, Yvonne, Nikki, Su Min, Melania** and other (former / PhD) students whom I have interacted with. I have learnt something useful from you all. This acknowledgement would not be complete without my thanks to all of my Simula Summer School supervisors (**Hermenegild, Valeriya** and **Per Magne**), friends and colleagues, especially **Ana, Savannah, Teo** and **Luca**. Without you all, I would have had no idea how I could enjoy my first summer school ever (although my impression about ML remains the same whatsoever).

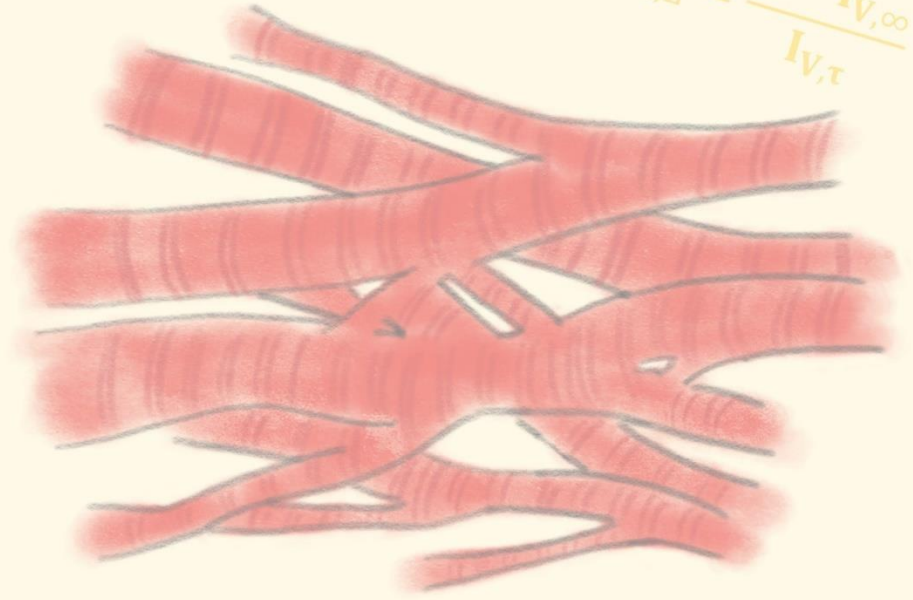
Lastly, to those that I did not mention explicitly here: it does not mean that you are less important to me than the others. I always appreciate all your supports and kindness to me and I would not be able to describe how blessed I am with your presence in my life. As people always say: "*when there is a beginning, there will always an end*". Unfortunately, our path might be separated from now on, but we will surely meet again sometime soon.





$$\frac{dV_m}{dt} = -\frac{1}{C_m} * I$$

$$y_{Ca,L} = \frac{1 - I_{V,\infty}}{I_{V,\tau}}$$



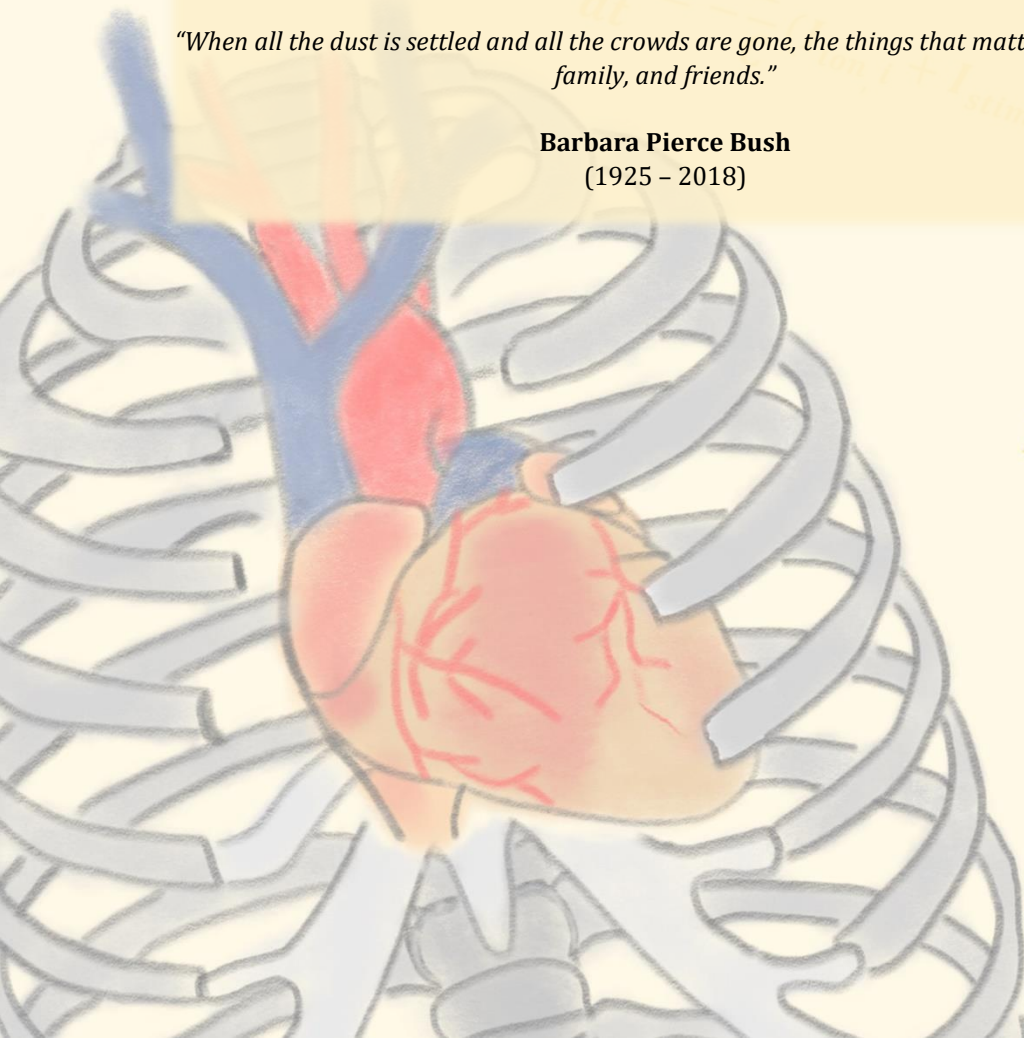
$$x_{Ca,L} = \frac{I_{V,\infty}}{I_{V,\tau}}$$



*"When all the dust is settled and all the crowds are gone, the things that matter are faith, family, and friends."*

**Barbara Pierce Bush**  
(1925 - 2018)

$$\delta I_{Ca,L}^{s,m} =$$



$$\bar{I}_{Ca,L}^{s,m} = P_{Ca,L} \cdot (z$$

$$ACT_{\tau} = 0.59$$

# Curriculum vitae, publications and awards

$$\frac{dX}{dt} = \alpha_x (1 - X) - \beta X$$

$$\delta I_{Ca,L}^{s,m} = \theta I_{Ca,L} \cdot \frac{X_{Ca,L} \cdot y_{Ca,L}^{s,m} \cdot \delta_{Ca,L}^{s,m}}{y_{Ca,L} \cdot X_{Ca,L}^{s,m} \cdot \theta_{Ca,L}}$$

$$\frac{X_{Ca,L} \cdot y_{Ca,L}^{s,m} \cdot \delta_{Ca,L}^{s,m}}{y_{Ca,L} \cdot X_{Ca,L}^{s,m} \cdot \theta_{Ca,L}}$$

$$I_{Ca,L}^{s,m} = \bar{I}_{Ca,L}^{s,m} \cdot (O_{Ca,L}^{s,m} + O_{Ca,L}^{s,m})$$

$$\frac{V_m \cdot F^2}{R \cdot T} \cdot \frac{y_{Ca,i} \cdot [Ca^{2+}]_{obs}^{s,m} \cdot \exp\left(z_{Ca} \cdot V_m \cdot \frac{F}{R \cdot T}\right) - y_{Ca,o} \cdot [Ca^{2+}]_o}{1 + \exp(0.052 \cdot (V_m + 13))} \cdot \frac{\exp\left(z_{Ca} \cdot V_m \cdot \frac{F}{R \cdot T}\right) - 1}{1 + \exp(0.132 \cdot (V_m + 13))}$$

$$\frac{dV}{dt} = \frac{I_{stim} - (I_K + I_{Na} + I_{leak})}{C_m}$$



## Curriculum vitae

---



Henry Sutanto, MD, MSc, MRSB was born in Surabaya, East Java, Indonesia on December 20<sup>th</sup> 1988. He spent his childhood being an ordinary child who liked nature and life science. His passion on natural sciences and his desire to contribute to the community made him pursue a degree in Medicine at Faculty of Medicine, Airlangga University, Indonesia in 2006-2011. After completing medical school, he worked in several clinical positions, such as an intern doctor in a remote area and a general practitioner in a community health center (2011-2015). He also volunteered for Indonesian Red Cross before he decided to follow his passion to pursue further education in cardiovascular research at the Institute of Cardiovascular Sciences, University College London (UCL), the United Kingdom (2015-2016). Following his graduation (with distinction) from the master degree at UCL, he was appointed a PhD student in the Department of Cardiology, Maastricht University, the Netherlands, under the supervision of Assoc. Prof. Jordi Heijman (2017-2021).

During his PhD track, he took part actively as a member in some renowned societies, including the European Society of Cardiology, the Heart Rhythm Society, the Physiological Society, the American Physiological Society, the Biophysical Society and the Royal Society of Biology. He also participated actively as a presenter in several prominent conferences across the globe. Additionally, he continuously devotes himself to science by being a science mentor for Frontiers for Young Minds and a journal reviewer for the International Journal of Cardiology: Heart and Vasculature.

## Publications

---

### Original Research Article

**2020**      **Electrophysiological and calcium-handling maturation during long-term culture of human induced pluripotent stem cell-derived cardiomyocytes**

*Fitzwilliam Seibertz\*, Henry Sutanto\*, Rebekka Dülk, Julius Ryan D. Pronto, Robin Springer, Luisa Huesgen, Marie Klopp, Tony Rubio, Funsho E. Fakuade, Fleur E. Mason, Nico Hartmann, Steffen Pabel, Katrin Strekfuß-Bomeke, Lukas Cyganek, Samuel Sosalla, Wolfram Hubertus Zimmermann, Jordi Heijman, Niels Voigt (\* equally contributed)*

Basic Research in Cardiology, in preparation

**2020**      **Functional stabilization of the lactate-Proton shuttle McT1 requires isoform-specific caveolin interactions in cardiomyocytes**

Jonas Peper, Daniel Kownatzki-Danger, Gunnar Weninger, Fitzwilliam Seibertz, Julius Ryan Pronto, **Henry Sutanto**, David Pacheu Grau, Robin Hindmarsh, Sören Brandenburg, Tobias Kohl, Gerd Hasenfuß, Michael Gotthardt, Eva A Rog-Zielinska, Bernd Wollnik, Peter Rehling, Henning Urlaub, Jörg W Wegener, Jordi Heijman, Niels Voigt, Lukas Cyganek, Christof Lenz, Stephan Lehnart

Circulation Research, accepted

**2020 Treatment of atrial fibrillation with doxapram: TASK-1 potassium channel inhibition as a novel pharmacological strategy**

Felix Wiedmann, Christoph Beyersdorf, Xiao-Bo Zhou, Manuel Kraft, **Henry Sutanto**, Antonius Büscher, Kathrin I Foerster, Antje Blank, Ibrahim El-Battrawy, Xin Li, Siegfried Lang, Ursula Tochtermann, Jamila Kremer, Rawa Arif, Matthias Karck, Niels Decher, Gunther van Loon, Ibrahim Akin, Martin Borggreffe, Stefan Kallenberger, Jordi Heijman, Walter E. Haefeli, Hugo A. Katus, Constanze Schmidt

Cardiovascular Research, in revision

**2020 Beta-adrenergic receptor stimulation modulates the cellular proarrhythmic effects of chloroquine and azithromycin**

**Henry Sutanto** and Jordi Heijman

Frontiers in Physiology, September 2020, 11:587709.

**2020 Atrial myocyte NLRP3/CaMKII nexus forms a substrate for post-operative atrial fibrillation**

Jordi Heijman, Azinwi Phina Muna, Tina Veleva, Cristina E Molina, **Henry Sutanto**, Marcel A. Tekook, Qionglng Wang, Issam Abu-Taha, Marcel Gorka, Stephan Künzel, Ali El-Armouche, Hermann Reichenspurner, Markus Kamler, Viacheslav O Nikolaev, Ursula Ravens, Na Li, Stanley Nattel, Xander HT Wehrens, Dobromir Dobrev

Circulation Research, July 2020, 127:1036-1055.

**2020 Acute effects of alcohol on cardiac electrophysiology and arrhythmogenesis: insights from multiscale in silico analyses**

**Henry Sutanto**, Matthijs JM Cluitmans, Dobromir Dobrev, Paul GA Volders, Markéta Bébarová, Jordi Heijman

Journal of Molecular and Cellular Cardiology, July 2020, 146:69-83.

**2019 Maastricht antiarrhythmic drug evaluator (MANTA): a computational tool for better understanding of antiarrhythmic drugs**

**Henry Sutanto**, Lian Laudy, Michael Clerx, Dobromir Dobrev, Harry JGM Crijns, Jordi Heijman

Pharmacological Research, September 2019, 148:104444.

**2018 The Subcellular Distribution of Ryanodine Receptors and L-type Ca<sup>2+</sup> Channels Modulates Ca<sup>2+</sup>-transient Properties and Spontaneous Ca<sup>2+</sup>-release Events in Atrial Cardiomyocytes**

*Henry Sutanto\**, Bart van Sloun\*, Patrick Schönleitner, Marc van Zandvoort, Gudrun Antoons, Jordi Heijman (\* equally contributed)

Frontiers in Physiology, August 2018, 9:1108.

- 2018**      **Frequency of genetic variants associated with arrhythmogenic right ventricular cardiomyopathy in the genome aggregation database**

Charlotte L Hall, *Henry Sutanto*, Chrysoula Dalageorgou, William John McKenna, Petros Syrris, Marta Futema

European Journal of Human Genetics, May 2018, 26:1312–1318.

#### Review Article

- 2020**      **Cardiomyocyte calcium handling in health and disease: insights from *in vitro* and *in silico* studies.**

*Henry Sutanto*, Aurore Lyon, Joost Lumens, Ulrich Schotten, Dobromir Dobrev, Jordi Heijman

Progress in Biophysics and Molecular Biology, March 2020

- 2019**      **The Role of Calcium in the Human Heart: With Great Power Comes Great Responsibility**

*Henry Sutanto* and Jordi Heijman

Frontiers for Young Minds, May 2019, 7:65.

#### Editorial

- 2019**      **Genome-wide association studies of atrial fibrillation: Finding meaning in the life of risk loci**

*Henry Sutanto*, Dobromir Dobrev, Jordi Heijman

International Journal of Cardiology: Heart and Vasculature, July 2019, 24:100397.

- 2018**      **Resveratrol: an effective pharmacological agent to prevent inflammation-induced atrial fibrillation?**

*Henry Sutanto*, Dobromir Dobrev, Jordi Heijman

Naunyn-Schmiedeberg's Archives of Pharmacology, September 2018, 391(11):1163-1167.

#### Conference Abstract

- 2019**      **A computational framework facilitating analyses of fundamental cellular electrophysiological features of clinically-used antiarrhythmic drugs**

*Henry Sutanto*, Lian Laudy, Michael Clerx, Dobromir Dobrev, Harry Crijns, Jordi Heijman

Journal of Arrhythmia Volume 35, Issue S1

- 2019**      **In silico prediction of the effects of ethanol on cardiac cellular electrophysiology and reentrant arrhythmias**

*Henry Sutanto*, Markéta Bébarová, Dobromir Dobrev, Paul Volders, Jordi Heijman

- 2018 Journal of Arrhythmia Volume 35, Issue S1  
**Calcium-dependent regulation of potassium channels in cardiac electrophysiology: A computational study**  
*Henry Sutanto, Dobromir Dobrev, Eleonora Grandi, Paul GA Volders, Jordi Heijman*
- 2018 Biophysical Journal Volume 114, Issue 3  
**I<sub>Na</sub> Loss-of-Function by Compound Variants in SCN5A from a Large Founder Population with Excess Sudden Cardiac Death**  
*Cristina Altrocchi, Roel RL Spätjens, Henry Sutanto, Rachel MA ter Bekke, Sandrine Seyen, Jordi Heijman, Cristina Moreno, Paul GA Volders*  
Biophysical Journal Volume 114, Issue 3

## Presentations

---

### Oral presentations

- 2019 **Understanding species-, atrial-, disease- and rate-specific effects of clinically used antiarrhythmic drugs using computational models**, presented in Karlsruhe Institute of Technology (KIT) Workshop: Towards an integrated numerical heart model, Bad Herrenalb, Germany.
- 2018 **Subcellular organization of ryanodine receptors and Ca<sup>2+</sup> channels modulates the propensity of spontaneous Ca<sup>2+</sup> waves and cardiac arrhythmias**, presented in Early Career Physiologists' Symposium (ECPS) – Europhysiology 2018, London, the United Kingdom.

### Poster presentations

- 2019 **A computational framework facilitating analyses of fundamental cellular electrophysiological features of clinically-used antiarrhythmic drugs**, presented in Asia-Pacific Heart Rhythm Society (APHRS) annual meeting, Bangkok, Thailand.
- 2019 **In silico prediction of the effects of ethanol on cardiac cellular electrophysiology and reentrant arrhythmias**, presented in Asia-Pacific Heart Rhythm Society (APHRS) annual meeting, Bangkok, Thailand.
- 2019 **Understanding species-, atrial-, disease- and rate-specific effects of clinically used antiarrhythmic drugs using computational models**, presented in EHRA-EWGCCE 2019, Lisbon, Portugal.
- 2018 **Subcellular organization of ryanodine receptors and Ca<sup>2+</sup> channels modulates the propensity of spontaneous Ca<sup>2+</sup> waves and cardiac arrhythmias**, presented in Europhysiology 2018, London, the United Kingdom.
- 2018 **Calcium-dependent regulation of potassium channels in cardiac electrophysiology: A computational study**, presented in 2018 Biophysical Society annual meeting, San Francisco, California.

## Awards

---

- 2019**      **Simula Summer School of Computational Physiology (SSCP) 2019 Travel Grant**, Oslo – Norway & San Diego – California (15.000 NOK)
- 2018**      **Best oral presentation, European Early Career Physiologists' Symposium – Europhysiology 2018**, London, the United Kingdom (£ 500)
- 2018**      **The Physiological Society travel grant award for Europhysiology 2018** (£ 500)

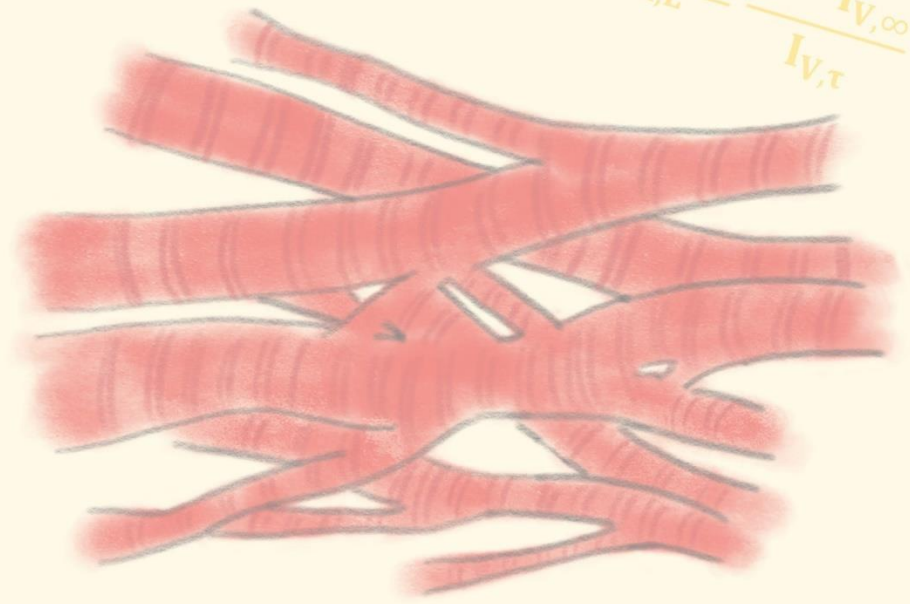
## ORCID, ResearchGate and Twitter

---



$$\frac{dV_m}{dt} = -\frac{1}{C_m} * I$$

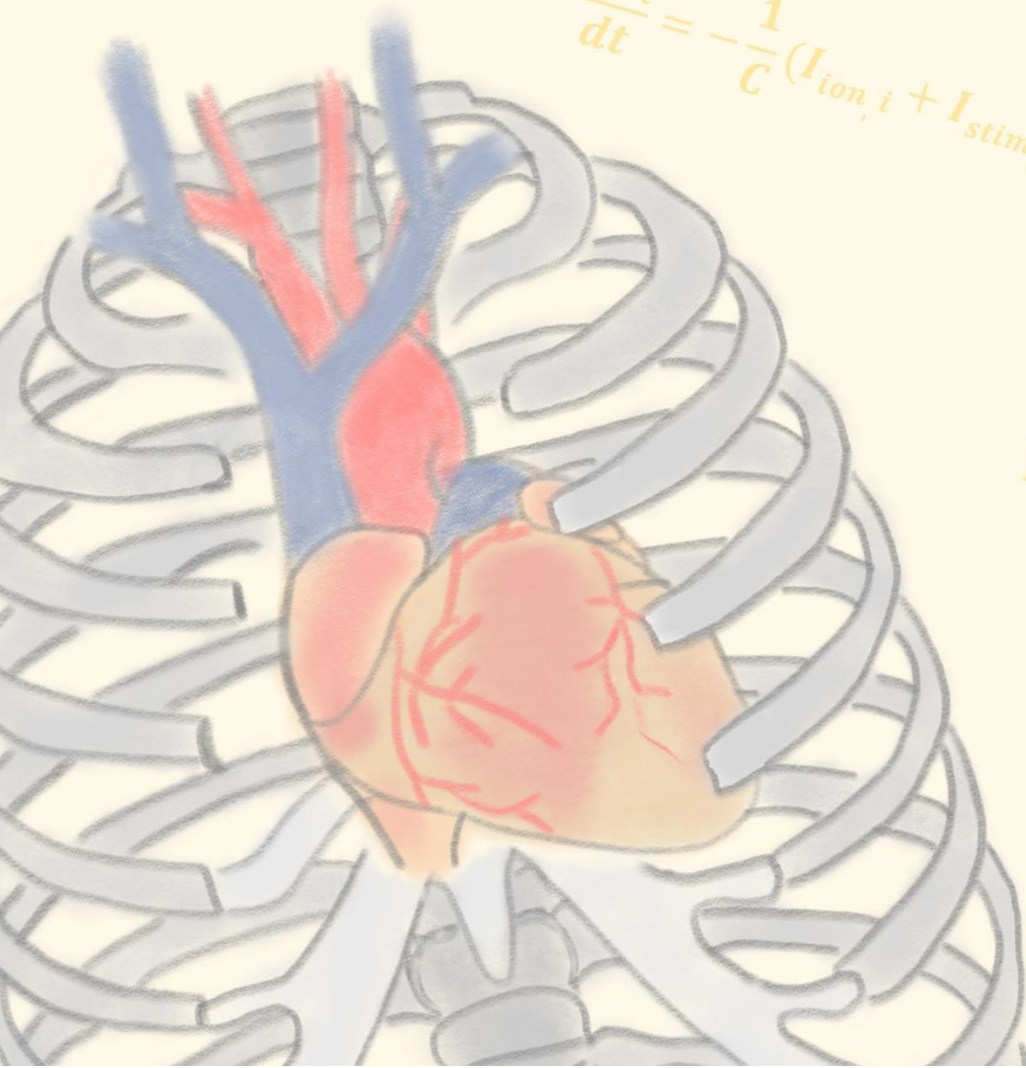
$$y_{Ca,L} = \frac{1 - I_{V,\infty}}{I_{V,\tau}}$$



$$x_{Ca,L} = \frac{I_{V,\infty}}{I_{V,\tau}}$$

$$\delta I_{Ca,L}^{s,m} =$$

$$\frac{dV_i}{dt} = -\frac{1}{C} (I_{ion,i} + I_{stim,i} + I_{diff,i})$$



$$\bar{I}_{Ca,L}^{s,m} = P_{Ca,L} \cdot (z$$

$$ACT_{\tau} = 0.59$$

# Appendices

$$\frac{dX}{dt} = \alpha_x(1 - X) - \beta_x X$$

$$\delta I_{Ca,L}^{s,m} = \theta I_{Ca,L} \cdot \frac{X_{Ca,L} \cdot y_{Ca,L}^{s,m} \cdot \delta_{Ca,L}^{s,m}}{y_{Ca,L} \cdot X_{Ca,L}^{s,m} \cdot \theta_{Ca,L}}$$

$$\frac{X_{Ca,L} \cdot y_{Ca,L}^{s,m} \cdot \delta_{Ca,L}^{s,m}}{y_{Ca,L} \cdot X_{Ca,L}^{s,m} \cdot \theta_{Ca,L}}$$

$$I_{Ca,L}^{s,m} = \bar{I}_{Ca,L}^{s,m} \cdot (O_{Ca,L}^{s,m} + O_{Ca,L}^{s,m})$$

$$\frac{V_m \cdot F^2}{R \cdot T} \cdot \frac{y_{Ca,i} \cdot [Ca^{2+}]_{obs}^{s,m} \cdot \exp\left(z_{Ca} \cdot V_m \cdot \frac{F}{R \cdot T}\right) - y_{Ca,o} \cdot [Ca^{2+}]_o}{1 + \exp(0.052 \cdot (V_m + 13))} \cdot \frac{\exp\left(z_{Ca} \cdot V_m \cdot \frac{F}{R \cdot T}\right) - 1}{1 + \exp(0.132 \cdot (V_m + 13))}$$

$$\frac{dV}{dt} = \frac{I_{stim} - (I_K + I_{Na} + I_{leak})}{C_m}$$



## Appendix A

$$ACT_{\tau} = 0.59 + 0.8 \cdot \frac{\exp(0.052 \cdot (V_m + 13))}{1 + \exp(0.132 \cdot (V_m + 13))}$$

$$ACT_{\infty} = \frac{1}{\left(1 + \exp\left(-\frac{V_m - 13.56}{P_1}\right)\right) \cdot \left(1 + \exp\left(-\frac{V_m + 25}{5}\right)\right)}$$

$$\alpha_{Ca,L} = \frac{ACT_{\infty}}{ACT_{\tau}}, \quad \beta_{Ca,L} = \frac{1 - ACT_{\infty}}{ACT_{\tau}}$$

$$I_{V,\infty} = \frac{1}{1.2474} \cdot \left(0.2474 + \frac{1}{1 + \exp((V_m + P_5)/P_6)}\right)$$

$$IS_{V,\infty} = \frac{1}{1.001} \cdot \left(0.001 + \frac{1}{1 + \exp((V_m + P_5)/P_6)}\right)$$

$$I_{V,\tau} = \frac{1}{\frac{1}{70.0 \cdot \left(1 + \exp((V_m + P_2)/P_3)\right)} + \frac{1}{P_4 \cdot \left(1 + \exp(-(V_m + 0.213)/10.807)\right)}}$$

$$IS_{Ca}^{s,m} = P_7 - \frac{P_8}{1 + \left(\frac{3.500 \cdot 10^{-4}}{[Ca^{2+}]_{obs}^{s,m}}\right)^4}$$

$$IS_{V,\tau}^{s,m} = \frac{1}{\frac{1}{70.0 \cdot \left(1 + \exp((V_m + 49.10)/10.349)\right)} + \frac{1}{IS_{Ca}^{s,m} \cdot \left(1 + \exp(-(V_m + 0.213)/10.807)\right)}}$$

$$x_{Ca,L} = \frac{I_{V,\infty}}{I_{V,\tau}}, \quad y_{Ca,L} = \frac{1 - I_{V,\infty}}{I_{V,\tau}}$$

$$xS_{Ca,L}^{s,m} = \frac{IS_{V,\infty}}{IS_{V,\tau}}, \quad yS_{Ca,L}^{s,m} = \frac{1 - IS_{V,\infty}}{IS_{V,\tau}}$$

$$\delta_{Ca,L}^{s,m} = \frac{P_9}{1 + \left(\frac{P_{10} \cdot 10^{-3}}{[Ca^{2+}]_{obs}^{s,m}}\right)^4}, \quad \theta_{Ca,L} = 1$$

$$\theta_{Ca,L} = 1.0 \cdot 10^{-6}, \quad \delta I_{Ca,L}^{s,m} = \theta_{Ca,L} \cdot \frac{x_{Ca,L} \cdot yS_{Ca,L}^{s,m} \cdot \delta_{Ca,L}^{s,m}}{y_{Ca,L} \cdot xS_{Ca,L}^{s,m} \cdot \theta_{Ca,L}}$$

$$P_{Ca,L} = 1.7 \cdot 10^{-4} \frac{\text{cm}}{\text{s}}, \quad \gamma_{Ca,i} = 1.0, \quad \gamma_{Ca,o} = 0.341$$

## Appendix

$$\bar{I}_{Ca,L}^{s,m} = P_{Ca,L} \cdot (z_{Ca})^2 \cdot \frac{V_m \cdot F^2}{R \cdot T} \cdot \frac{\gamma_{Ca,i} \cdot [Ca^{2+}]_{obs}^{s,m} \cdot \exp\left(z_{Ca} \cdot V_m \cdot \frac{F}{R \cdot T}\right) - \gamma_{Ca,o} \cdot [Ca^{2+}]_o}{\exp\left(z_{Ca} \cdot V_m \cdot \frac{F}{R \cdot T}\right) - 1}$$

$$I_{Ca,L}^{s,m} = \bar{I}_{Ca,L}^{s,m} \cdot (O_{Ca,L}^{s,m} + O_{S_{Ca,L}}^{s,m})$$



## Appendix B

All cardiomyocyte models were extended with a state-of-the-art Markov model allowing simulation of state-dependent sodium channel block. Optimized parameters for the baseline part of the model as well as for the drug-specific transition rates in the drug-bound states are shown below for two human cardiomyocyte models; the Passini human left ventricular endocardium (374) and Schmidt human right atrium model (428). The parameters were optimized using Nelder-Mead optimization protocol and have been incorporated into each MANTA model. In brief, experimental voltage-clamp protocols were reproduced in the models and a sum-of-squares error criterion incorporating the difference between Markov model and original  $I_{Na}$  formulation (for the baseline model), and between simulated and experimental data (431) (in the case of drug-induced  $I_{Na}$  inhibition) was minimized.

Param.	Passini human LV model			Schmidt human RA model		
	Flecainide	Lidocaine	Vernakalant	Flecainide	Lidocaine	Vernakalant
diffusion	5500	500	170.867	5500	500	3.104e+3
gNa	241.1554			13.4338		
pKa	9.3	7.6	5.4	9.3	7.6	5.4
d1	11.2e-6	318e-6	340e-6	11.2e-6	318e-6	111.3e-6
d2	400e-6	400e-6	484e-6	400e-6	400e-6	206.3e-6
d3	5.4e-6	3.4e-6	9.6e-6	5.4e-6	3.4e-6	1.7e-6
d4	800e-6	900e-6	46.2e-6	800e-6	900e-6	39.9e-6
d5	1	1	1	1	1	1
actshift	-2.8424			-32.2217		
h1	4.8746			1.6000		
p1	1.6442			9.3467		
p2	3.0690e-2			1.4800e-1		
p3	15.7108			9.7715		
p4	11.2671			18.6939		
p5	5.2551			10.3420		
p6	7.6230e-1			5.9074e-1		
p7	826.5339			227.7919		
p8	4.4492e-2			7.9261e-2		
p9	38.4111			8.2196		
p10	3.9229e-1			3.3248		
p11	4.9252			5.9433		
p12	6.2475e-1			6.0556e-1		
p13	13.8297			13.6961		
p14_new	-77.2417			-69.9611		
p15_new	5.3593			3.5994		
p16_new	1.0499e-1			1.4914e-1		
p17_new	2.4121e-1			2.5403e-1		
p18	13.8089			1.3906		
p19	43.5223			44.7185		
p20	3.4316e-2			3.5427e-2		
p21	1.8094e-2			1.8070e-2		
p01	49.8798			41.2656		

## Appendix

p22	57.4011	78.0104	124.6093	57.7163	78.0104	10.1425
p23	2.9659e+4	1.1578e+6	1.2723e+6	2.9173e+4	1.1578e+6	1.0116e+5
p24	6.2665e-5	6.2444e-7	6.6659e-7	6.1653e-5	6.2444e-7	1.8922e-7
p25	7.8794e-8	6.4698	4.8201	7.7977e-8	6.4698	1.7325
p26	3.1056e-1	127.9276	33.1729	3.1198e-1	1.2793e-1	2.5909
p27	1.6768e+3	6.5611e-6	7.4354e-6	1.7691e+3	6.5611e-6	3.1667e-6
p28	41.8116	1.6713e-5	2.1151e-5	41.5737	1.6713e-5	5.0896e-6
p29	9.4642e-7	1.7842e-5	1.9869e-5	8.8738e-7	1.7842e-5	2.1747e-5
p30	2.1620	4.3909	4.8477e-2	2.1543	4.3909	6.0619
p31	1.7963e-4	15.9639	12.6802	1.9328e-4	15.9639	3.3801
p32	2.7543	0	0	2.9155	0	0
p33	2.6235e-1	0	0	2.6661e-1	0	0
p34	1.0624e-3	0	0	1.0711e-3	0	0
p35	2.1450e-2	0	0	2.1258e-2	0	0

### **Equations for Markov $I_{Na}$ formulations:**

F = Faraday constant (96485 C/mol)

R = Universal gas constant (8314 J/kmol/K)

T = Temperature (295 K)

pH = 7.4

[D] = Drug concentration (mol)

$kd\_open = d1 * \exp(-0.7 * V * F/R*T)$

$portion = 1/(1+10^{(pH-pKa)})$

$[D^+] = portion * [D]$

$[D^n] = portion * [D]$

$kon = [D^+] * diffusion$

$kcon = kon$

$koff = kd\_open * diffusion$

$kcoff = koff$

$k\_on = [D^n] * diffusion$

$k\_off = d2 * diffusion$

$ki\_on = k\_on / 2$

$ki\_off = d3 * diffusion$

$kc\_on = k\_on / 2$

$kc\_off = d4 * diffusion$

$Tfactor = 1 / (d5 ^ ((37 - (T - 273)) / 10))$

### **Transition rates :**

$a11 = Tfactor * p1 / (p2 * \exp(-(V - actshift) / p3) + p6 * \exp(-(V - actshift) / p7))$

$a12 = Tfactor * p1 / (p2 * \exp(-(V - actshift) / p4) + p6 * \exp(-(V - actshift) / p7))$

$a13 = Tfactor * p1 / (p2 * \exp(-(V - actshift) / p5) + p6 * \exp(-(V - actshift) / p7))$

$b11 = Tfactor * p8 * \exp(-(V - actshift) / p9)$

$b12 = Tfactor * p10 * \exp(-(V - actshift - p11) / p9)$

$b13 = Tfactor * p12 * \exp(-(V - actshift - p13) / p9)$

```

a3_ss = 1/(1+exp((V - p14_new) / p15_new))
a3_tau = h1 + p01 * exp(p16_new * (V - p14_new)) / (1 + exp(p17_new * (V - p14_new)))
a3 = Tfactor * a3_ss / a3_tau
b3 = Tfactor * (1 - a3_ss) / a3_tau
a2 = Tfactor * p18 * exp(V / p19)
b2 = (a13*a2*a3) / (b13*b3)
ax = p20 * a2
bx = p21 * a3
a13c = p22 * a13
b13c = if(kon>0, (b13 * kcon * koff * a13c) / (kon * kcoff * a13), 0)
a13n = p23 * a13
b13n = if(k_on>0, (b13 * kc_on * a13n * k_off) / (kc_off * a13 * k_on), 0)
ax1 = p24 * ax
bx1 = p25 * bx
ax2 = p26 * ax
bx2 = if(ki_on>0, (bx * k_on * ax2 * ki_off) / (ax * ki_on * k_off), 0)
a22 = p27 * a2
a_22 = p28 * a2
b22 = if(b13c>0, (a13c * a22 * a33) / (b13c * b33), 0)
b_22 = if(b13n>0, (a_33 * a13n * a_22) / (b_33 * b13n), 0)
b33 = p29 * b3
b_33 = p30 * b3
a33 = p31 * a3
a_33 = if(ki_on>0, (ki_off * a3 * kc_on * b_33) / (ki_on * kc_off * b3), 0)
a44 = p32 * a2
b44 = p33 * a3
a_44 = p34 * a2
b_44 = p35 * a2

```



## Appendix C

Published  $I_{K,ACh}$  formulation from (641) was incorporated into the Courtemanche human atrial model to study the acute effects of ethanol on the channel, as previously reported (367). To simulate the concentration-dependent effects of ethanol on cardiac electrophysiology, several  $IC_{50}$  and  $EC_{50}$  values were extrapolated based on previously published data. The details are as following:

**$I_{Na}$ ,  $I_{Ca,L}$ ,  $I_{to}$ ,  $I_{Kr}$  and  $I_{Kur}$ :**

$$\text{Current block} = \frac{\text{drug}^{Hill}}{\text{drug}^{Hill} + IC_{50}^{Hill}}$$

Ionic current	$IC_{50}$ (mM)	Hill coefficient
$I_{Na}$	446	3.1
$I_{Ca,L}$	600	1.3
$I_{to}$	2188	1.1
$I_{Kr}$	608	0.99
$I_{Kur}$	494.6	0.6437

**$I_{K1}$  and  $I_{K,ACh}$  (accommodating the dual effects):**

$$I_{K1} \text{ block} = \left( \left( 0.0919 * \frac{\text{drug}^3}{\text{drug}^3 + 0.1854^3} \right) - \left( 0.3112 * \frac{\text{drug}^{1.8}}{\text{drug}^{1.8} + 7.461^{1.8}} \right) \right)$$

$$I_{K,ACh} \text{ block} = \left( \left( 0.0906 * \frac{\text{drug}^{8.281}}{\text{drug}^{8.281} + 0.7442^{8.281}} \right) - \left( 0.2651 * \frac{\text{drug}^{4.064}}{\text{drug}^{4.064} + 9.186^{4.064}} \right) \right)$$

**$I_{NCX}$  and  $I_{leak}$ :**

$$\text{Current factor} = 1 + \left( (\text{drug}^{Hill}) * \frac{\text{Variable}}{\text{drug}^{Hill} + EC_{50}^{Hill}} \right)$$

Ionic current	$EC_{50}$ (mM)	Hill coefficient	Variable
$I_{NCX} / I_{leak}$ (Atria)	16.43	1.088	1.067
$I_{NCX} / I_{leak}$ (Ventricle)	35.32	2.282	1.238

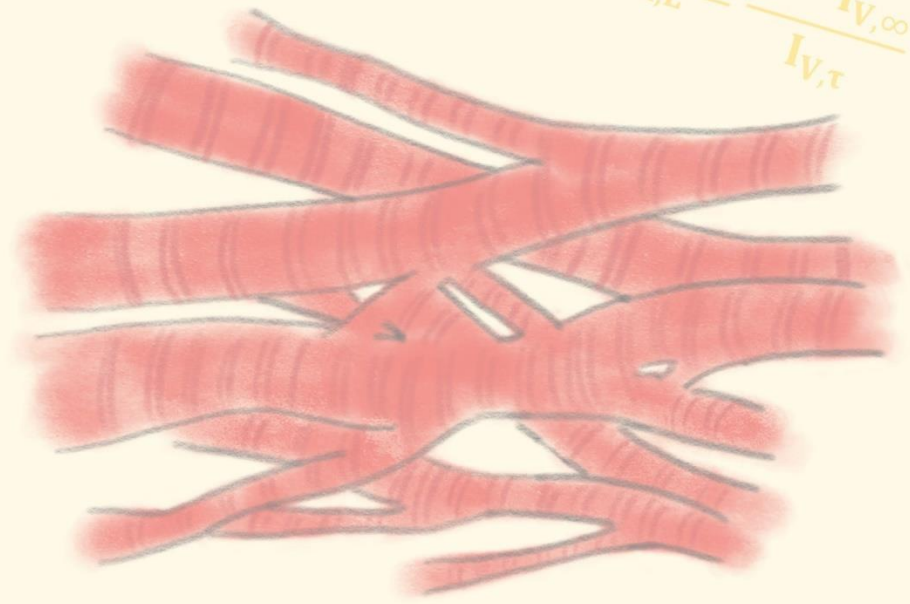
**Ethanol-induced gap-junction remodeling** =  $\frac{\text{drug}^{Hill}}{\text{drug}^{Hill} + IC_{50}^{Hill}}$ , with  $IC_{50} = 320$  mM and Hill coefficient = 1





$$\frac{dV_m}{dt} = -\frac{1}{C_m} * I$$

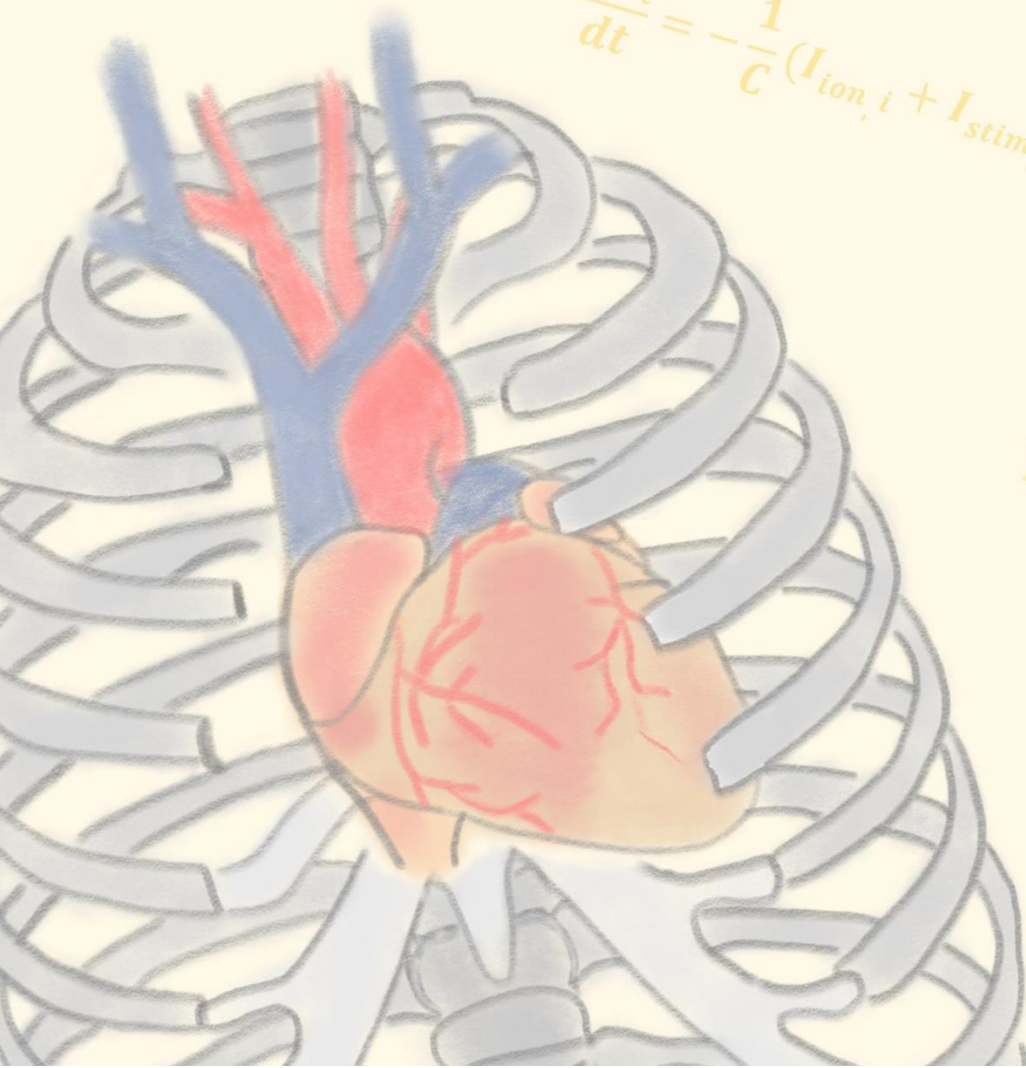
$$y_{Ca,L} = \frac{1 - I_{V,\infty}}{I_{V,\tau}}$$



$$x_{Ca,L} = \frac{I_{V,\infty}}{I_{V,\tau}}$$

$$\delta I_{Ca,L}^{s,m} =$$

$$\frac{dV_i}{dt} = -\frac{1}{C} (I_{ion,i} + I_{stim,i} + I_{diff,i})$$



$$\bar{I}_{Ca,L}^{s,m} = P_{Ca,L} \cdot (z$$

$$ACT_{\tau} = 0.59$$

# References

$$\frac{dX}{dt} = \alpha_x (1 - X) - \beta_x X$$

$$\delta I_{Ca,L}^{s,m} = \theta_{Ca,L} \cdot \frac{X_{Ca,L} \cdot y_{Ca,L}^{s,m} \cdot \delta_{Ca,L}^{s,m}}{y_{Ca,L} \cdot X_{Ca,L}^{s,m} \cdot \theta_{Ca,L}}$$

$$\frac{X_{Ca,L} \cdot y_{Ca,L}^{s,m} \cdot \delta_{Ca,L}^{s,m}}{y_{Ca,L} \cdot X_{Ca,L}^{s,m} \cdot \theta_{Ca,L}}$$

$$I_{Ca,L}^{s,m} = \bar{I}_{Ca,L}^{s,m} \cdot (O_{Ca,L}^{s,m} + OS_{Ca,L}^{s,m})$$

$$\frac{V_m \cdot F^2}{R \cdot T} \cdot \frac{Y_{Ca,i} \cdot [Ca^{2+}]_{obs}^{s,m} \cdot \exp\left(z_{Ca} \cdot V_m \cdot \frac{F}{R \cdot T}\right) - Y_{Ca,o} \cdot [Ca^{2+}]_o}{1 + \exp(0.052 \cdot (V_m + 13))} \cdot \frac{\exp\left(z_{Ca} \cdot V_m \cdot \frac{F}{R \cdot T}\right) - 1}{1 + \exp(0.132 \cdot (V_m + 13))}$$

$$\frac{dV}{dt} = \frac{I_{stim} - (I_K + I_{Na} + I_{leak})}{C_m}$$



## References

1. Bartos DC, Grandi E, Ripplinger CM. Ion Channels in the Heart. *Compr Physiol*. 2015;5(3):1423-64.
2. Heijman J, Schirmer I, Dobrev D. The multiple proarrhythmic roles of cardiac calcium-handling abnormalities: triggered activity, conduction abnormalities, beat-to-beat variability, and adverse remodelling. *Europace*. 2016;18(10):1452-4.
3. Johnson DM, Antoons G. Arrhythmogenic Mechanisms in Heart Failure: Linking beta-Adrenergic Stimulation, Stretch, and Calcium. *Front Physiol*. 2018;9:1453.
4. Sutanto H, van Sloun B, Schonleitner P, van Zandvoort M, Antoons G, Heijman J. The Subcellular Distribution of Ryanodine Receptors and L-Type Ca<sup>2+</sup> Channels Modulates Ca<sup>2+</sup>-Transient Properties and Spontaneous Ca<sup>2+</sup>-Release Events in Atrial Cardiomyocytes. *Front Physiol*. 2018;9:1108.
5. Heijman J, Ghezelbash S, Dobrev D. Investigational antiarrhythmic agents: promising drugs in early clinical development. *Expert Opin Investig Drugs*. 2017;26(8):897-907.
6. Landstrom AP, Dobrev D, Wehrens XHT. Calcium Signaling and Cardiac Arrhythmias. *Circ Res*. 2017;120(12):1969-93.
7. van Opbergen CJ, Delmar M, van Veen TA. Potential new mechanisms of proarrhythmia in arrhythmogenic cardiomyopathy: focus on calcium sensitive pathways. *Neth Heart J*. 2017;25(3):157-69.
8. Bachmann M, Fiederling F, Bastmeyer M. Practical limitations of superresolution imaging due to conventional sample preparation revealed by a direct comparison of CLSM, SIM and dSTORM. *J Microsc-Oxford*. 2016;262(3):306-15.
9. Eisner DA, Caldwell JL, Kistamas K, Trafford AW. Calcium and Excitation-Contraction Coupling in the Heart. *Circ Res*. 2017;121(2):181-95.
10. Grandi E, Dobrev D, Heijman J. Computational modeling: What does it tell us about atrial fibrillation therapy? *Int J Cardiol*. 2019.
11. Gray RA, Pathmanathan P. Patient-Specific Cardiovascular Computational Modeling: Diversity of Personalization and Challenges. *J Cardiovasc Transl Res*. 2018;11(2):80-8.
12. Niederer SA, Lumens J, Trayanova NA. Computational models in cardiology. *Nat Rev Cardiol*. 2019;16(2):100-11.
13. Bers DM. Calcium cycling and signaling in cardiac myocytes. *Annu Rev Physiol*. 2008;70:23-49.
14. Dewenter M, von der Lieth A, Katus HA, Backs J. Calcium Signaling and Transcriptional Regulation in Cardiomyocytes. *Circ Res*. 2017;121(8):1000-20.
15. Bonilla IM, Belevych AE, Baine S, Stepanov A, Mezache L, Bodnar T, et al. Enhancement of Cardiac Store Operated Calcium Entry (SOCE) within Novel Intercalated Disk Microdomains in Arrhythmic Disease. *Sci Rep*. 2019;9(1):10179.
16. Chung JH, Biesiadecki BJ, Ziolo MT, Davis JP, Janssen PM. Myofilament Calcium Sensitivity: Role in Regulation of In vivo Cardiac Contraction and Relaxation. *Front Physiol*. 2016;7:562.
17. Orini M, Nanda A, Yates M, Di Salvo C, Roberts N, Lambiase PD, et al. Mechano-electrical feedback in the clinical setting: Current perspectives. *Prog Biophys Mol Biol*. 2017;130(Pt B):365-75.

## References

18. Pfeiffer ER, Tangney JR, Omens JH, McCulloch AD. Biomechanics of cardiac electromechanical coupling and mechanoelectric feedback. *J Biomech Eng.* 2014;136(2):021007.
19. Antzelevitch C, Burashnikov A. Overview of Basic Mechanisms of Cardiac Arrhythmia. *Card Electrophysiol Clin.* 2011;3(1):23-45.
20. Heijman J, Voigt N, Nattel S, Dobrev D. Cellular and Molecular Electrophysiology of Atrial Fibrillation Initiation, Maintenance, and Progression. *Circulation Research.* 2014;114(9):1483-99.
21. Li N, Chiang DY, Wang S, Wang Q, Sun L, Voigt N, et al. Ryanodine receptor-mediated calcium leak drives progressive development of an atrial fibrillation substrate in a transgenic mouse model. *Circulation.* 2014;129(12):1276-85.
22. Stern MD, Capogrossi MC, Lakatta EG. Spontaneous calcium release from the sarcoplasmic reticulum in myocardial cells: mechanisms and consequences. *Cell Calcium.* 1988;9(5-6):247-56.
23. Cheng H, Lederer WJ, Cannell MB. Calcium sparks: elementary events underlying excitation-contraction coupling in heart muscle. *Science.* 1993;262(5134):740-4.
24. Beard NA, Laver DR, Dulhunty AF. Calsequestrin and the calcium release channel of skeletal and cardiac muscle. *Prog Biophys Mol Biol.* 2004;85(1):33-69.
25. Shan J, Xie W, Betzenhauser M, Reiken S, Chen BX, Wronska A, et al. Calcium leak through ryanodine receptors leads to atrial fibrillation in 3 mouse models of catecholaminergic polymorphic ventricular tachycardia. *Circ Res.* 2012;111(6):708-17.
26. Venetucci LA, Trafford AW, O'Neill SC, Eisner DA. The sarcoplasmic reticulum and arrhythmogenic calcium release. *Cardiovasc Res.* 2008;77(2):285-92.
27. Kim JC, Perez-Hernandez M, Alvarado FJ, Maurya SR, Montnach J, Yin Y, et al. Disruption of  $[Ca^{2+}]_i$  Homeostasis and Connexin 43 Hemichannel Function in the Right Ventricle Precedes Overt Arrhythmogenic Cardiomyopathy in Plakophilin-2-Deficient Mice. *Circulation.* 2019;140(12):1015-30.
28. van Opbergen CJM, Noorman M, Pfenniger A, Copier JS, Vermij SH, Li Z, et al. Plakophilin-2 Haploinsufficiency Causes Calcium Handling Deficits and Modulates the Cardiac Response Towards Stress. *Int J Mol Sci.* 2019;20(17).
29. Mohamed BA, Hartmann N, Tirilomis P, Sekeres K, Li W, Neef S, et al. Sarcoplasmic reticulum calcium leak contributes to arrhythmia but not to heart failure progression. *Sci Transl Med.* 2018;10(458).
30. Shaw RM, Colecraft HM. L-type calcium channel targeting and local signalling in cardiac myocytes. *Cardiovascular Research.* 2013;98(2):177-86.
31. Mattiazzi A, Kranias EG. The role of CaMKII regulation of phospholamban activity in heart disease. *Front Pharmacol.* 2014;5:5.
32. Voigt N, Heijman J, Wang Q, Chiang DY, Li N, Karck M, et al. Cellular and molecular mechanisms of atrial arrhythmogenesis in patients with paroxysmal atrial fibrillation. *Circulation.* 2014;129(2):145-56.
33. Fernandez-Tenorio M, Niggli E. Stabilization of  $Ca^{2+}$  signaling in cardiac muscle by stimulation of SERCA. *J Mol Cell Cardiol.* 2018;119:87-95.
34. Lyon AR, Bannister ML, Collins T, Pearce E, Sepehrpour AH, Dubb SS, et al. SERCA2a gene transfer decreases sarcoplasmic reticulum calcium leak and reduces ventricular arrhythmias in a model of chronic heart failure. *Circ Arrhythm Electrophysiol.* 2011;4(3):362-72.

35. Prunier F, Kawase Y, Gianni D, Scapin C, Danik SB, Ellinor PT, et al. Prevention of ventricular arrhythmias with sarcoplasmic reticulum  $\text{Ca}^{2+}$  ATPase pump overexpression in a porcine model of ischemia reperfusion. *Circulation*. 2008;118(6):614-24.
36. van der Zwaag PA, van Rijsingen IAW, de Ruiter R, Nannenbergh EA, Groeneweg JA, Post JG, et al. Recurrent and founder mutations in the Netherlands-Phospholamban p.Arg14del mutation causes arrhythmogenic cardiomyopathy. *Neth Heart J*. 2013;21(6):286-93.
37. Wagner M, Weber S, El-Armouche A. Linking superinhibitory PLN mutations to CaMKII activation: a new arrhythmogenic mechanism in genetic DCM? *Cardiovasc Res*. 2015;107(1):5-6.
38. Dick IE, Joshi-Mukherjee R, Yang W, Yue DT. Arrhythmogenesis in Timothy Syndrome is associated with defects in  $\text{Ca}^{2+}$ -dependent inactivation. *Nat Commun*. 2016;7:10370.
39. Limpitikul WB, Dick IE, Joshi-Mukherjee R, Overgaard MT, George AL, Jr., Yue DT. Calmodulin mutations associated with long QT syndrome prevent inactivation of cardiac L-type  $\text{Ca}^{2+}$  currents and promote proarrhythmic behavior in ventricular myocytes. *J Mol Cell Cardiol*. 2014;74:115-24.
40. Chang PC, Chen PS. SK channels and ventricular arrhythmias in heart failure. *Trends Cardiovasc Med*. 2015;25(6):508-14.
41. Li N, Timofeyev V, Tuteja D, Xu D, Lu L, Zhang Q, et al. Ablation of a  $\text{Ca}^{2+}$ -activated  $\text{K}^{+}$  channel (SK2 channel) results in action potential prolongation in atrial myocytes and atrial fibrillation. *J Physiol*. 2009;587(Pt 5):1087-100.
42. Zhang XD, Timofeyev V, Li N, Myers RE, Zhang DM, Singapuri A, et al. Critical roles of a small conductance  $\text{Ca}^{2+}$ -activated  $\text{K}^{+}$  channel (SK3) in the repolarization process of atrial myocytes. *Cardiovasc Res*. 2014;101(2):317-25.
43. Diness JG, Skibsbye L, Simo-Vicens R, Santos JL, Lundegaard P, Citerni C, et al. Termination of Vernakalant-Resistant Atrial Fibrillation by Inhibition of Small-Conductance  $\text{Ca}^{2+}$ -Activated  $\text{K}^{+}$  Channels in Pigs. *Circ Arrhythm Electrophysiol*. 2017;10(10).
44. Qi XY, Diness JG, Brundel BJ, Zhou XB, Naud P, Wu CT, et al. Role of small-conductance calcium-activated potassium channels in atrial electrophysiology and fibrillation in the dog. *Circulation*. 2014;129(4):430-40.
45. Skibsbye L, Bengaard AK, Uldum-Nielsen AM, Boddum K, Christ T, Jespersen T. Inhibition of small conductance calcium-activated potassium (SK) channels prevents arrhythmias in rat atria during beta-adrenergic and muscarinic receptor activation. *Front Physiol*. 2018;9:510.
46. Diness JG, Bentzen BH, Sorensen US, Grunnet M. Role of Calcium-activated Potassium Channels in Atrial Fibrillation Pathophysiology and Therapy. *J Cardiovasc Pharmacol*. 2015;66(5):441-8.
47. Zhang XD, Lieu DK, Chiamvimonvat N. Small-conductance  $\text{Ca}^{2+}$ -activated  $\text{K}^{+}$  channels and cardiac arrhythmias. *Heart Rhythm*. 2015;12(8):1845-51.
48. Bonilla IM, Long VP, 3rd, Vargas-Pinto P, Wright P, Belevych A, Lou Q, et al. Calcium-activated potassium current modulates ventricular repolarization in chronic heart failure. *PLoS One*. 2014;9(10):e108824.
49. Chang PC, Hsieh YC, Hsueh CH, Weiss JN, Lin SF, Chen PS. Apamin induces early afterdepolarizations and torsades de pointes ventricular arrhythmia from failing

## References

- rabbit ventricles exhibiting secondary rises in intracellular calcium. *Heart Rhythm*. 2013;10(10):1516-24.
50. Terentyev D, Rochira JA, Terentyeva R, Roder K, Koren G, Li W. Sarcoplasmic reticulum  $\text{Ca}^{2+}$  release is both necessary and sufficient for SK channel activation in ventricular myocytes. *Am J Physiol Heart Circ Physiol*. 2014;306(5):H738-46.
  51. Chua SK, Chang PC, Maruyama M, Turker I, Shinohara T, Shen MJ, et al. Small-conductance calcium-activated potassium channel and recurrent ventricular fibrillation in failing rabbit ventricles. *Circ Res*. 2011;108(8):971-9.
  52. Gui L, Bao Z, Jia Y, Qin X, Cheng ZJ, Zhu J, et al. Ventricular tachyarrhythmias in rats with acute myocardial infarction involves activation of small-conductance  $\text{Ca}^{2+}$ -activated  $\text{K}^+$  channels. *Am J Physiol Heart Circ Physiol*. 2013;304(1):H118-30.
  53. Morotti S, Ellinwood N, Ni H, Koivumäki JT, Maleckar MM, Heijman J, et al. Effects of modulation of small-conductance calcium-activated potassium current on atrial electrophysiology and arrhythmogenesis: a population-based computational study. *Biophysical Journal*. 2018;114(3):473a.
  54. Bartos DC, Morotti S, Ginsburg KS, Grandi E, Bers DM. Quantitative analysis of the  $\text{Ca}^{2+}$ -dependent regulation of delayed rectifier  $\text{K}^+$  current  $\text{I}_{\text{Ks}}$  in rabbit ventricular myocytes. *J Physiol*. 2017;595(7):2253-68.
  55. Nagy N, Acsai K, Kormos A, Sebok Z, Farkas AS, Jost N, et al.  $[\text{Ca}^{2+}]_i$ -induced augmentation of the inward rectifier potassium current ( $\text{I}_{\text{K1}}$ ) in canine and human ventricular myocardium. *Pflugers Arch*. 2013;465(11):1621-35.
  56. Zaza A, Rocchetti M, Brioschi A, Cantadori A, Ferroni A. Dynamic  $\text{Ca}^{2+}$ -induced inward rectification of  $\text{K}^+$  current during the ventricular action potential. *Circ Res*. 1998;82(9):947-56.
  57. Shah VN, Wingo TL, Weiss KL, Williams CK, Balsler JR, Chazin WJ. Calcium-dependent regulation of the voltage-gated sodium channel hH1: Intrinsic and extrinsic sensors use a common molecular switch. *P Natl Acad Sci USA*. 2006;103(10):3592-7.
  58. Tan HL, Kupersmidt S, Zhang R, Stepanovic S, Roden DM, Wilde AAM, et al. A calcium sensor in the sodium channel modulates cardiac excitability. *Nature*. 2002;415(6870):442-7.
  59. Johnson CN. Calcium modulation of cardiac sodium channels. *J Physiol*. 2019.
  60. Gong D, Chi X, Wei J, Zhou G, Huang G, Zhang L, et al. Modulation of cardiac ryanodine receptor 2 by calmodulin. *Nature*. 2019;572(7769):347-51.
  61. Sutanto H, Dobrev D, Grandi E, Volders PGA, Heijman J. Calcium-Dependent Regulation of Potassium Channels in Cardiac Electrophysiology: A Computational Study. *Biophysical Journal*. 2018;114(3):473a.
  62. Wagner S, Maier LS, Bers DM. Role of sodium and calcium dysregulation in tachyarrhythmias in sudden cardiac death. *Circ Res*. 2015;116(12):1956-70.
  63. Engelhardt S, Boknik P, Keller U, Neumann J, Lohse MJ, Hein L. Early impairment of calcium handling and altered expression of junctin in hearts of mice overexpressing the beta(1)-adrenergic receptor. *Faseb J*. 2001;15(12):2718-+.
  64. Heijman J, Voigt N, Nattel S, Dobrev D. Cellular and molecular electrophysiology of atrial fibrillation initiation, maintenance, and progression. *Circ Res*. 2014;114(9):1483-99.
  65. Numaga-Tomita T, Oda S, Shimauchi T, Nishimura A, Mangmool S, Nishida M. TRPC3 Channels in Cardiac Fibrosis. *Front Cardiovasc Med*. 2017;4:56.

66. Nattel S. Electrical coupling between cardiomyocytes and fibroblasts: experimental testing of a challenging and important concept. *Cardiovasc Res.* 2018;114(3):349-52.
67. Ongstad E, Kohl P. Fibroblast-myocyte coupling in the heart: Potential relevance for therapeutic interventions. *J Mol Cell Cardiol.* 2016;91:238-46.
68. Moccia F, Lodola F, Stadiotti I, Pilato CA, Bellin M, Carugo S, et al. Calcium as a Key Player in Arrhythmogenic Cardiomyopathy: Adhesion Disorder or Intracellular Alteration? *Int J Mol Sci.* 2019;20(16).
69. Hodgkin AL, Huxley AF. Currents carried by sodium and potassium ions through the membrane of the giant axon of *Loligo*. *J Physiol.* 1952;116(4):449-72.
70. Schwiening CJ. A brief historical perspective: Hodgkin and Huxley. *J Physiol.* 2012;590(11):2571-5.
71. Beeler GW, Reuter H. Reconstruction of the action potential of ventricular myocardial fibres. *J Physiol.* 1977;268(1):177-210.
72. DiFrancesco D, Noble D. A model of cardiac electrical activity incorporating ionic pumps and concentration changes. *Philos Trans R Soc Lond B Biol Sci.* 1985;307(1133):353-98.
73. Noble D, Varghese A, Kohl P, Noble P. Improved guinea-pig ventricular cell model incorporating a diadic space,  $I_{Kr}$  and  $I_{Ks}$ , and length- and tension-dependent processes. *Can J Cardiol.* 1998;14(1):123-34.
74. Luo CH, Rudy Y. A dynamic model of the cardiac ventricular action potential. II. Afterdepolarizations, triggered activity, and potentiation. *Circ Res.* 1994;74(6):1097-113.
75. Rice JJ, Jafri MS. Modelling calcium handling in cardiac cells. *Philos T R Soc A.* 2001;359(1783):1143-57.
76. Vagos M, van Herck IGM, Sundnes J, Arevalo HJ, Edwards AG, Koivumaki JT. Computational Modeling of Electrophysiology and Pharmacotherapy of Atrial Fibrillation: Recent Advances and Future Challenges. *Front Physiol.* 2018;9:1221.
77. Greenstein JL, Tanskanen AJ, Winslow RL. Modeling the actions of beta-adrenergic signaling on excitation--contraction coupling processes. *Ann NY Acad Sci.* 2004;1015:16-27.
78. Heijman J, Volders PG, Westra RL, Rudy Y. Local control of beta-adrenergic stimulation: Effects on ventricular myocyte electrophysiology and  $Ca^{2+}$ -transient. *J Mol Cell Cardiol.* 2011;50(5):863-71.
79. Onal B, Unudurthi SD, Hund TJ. Modeling CaMKII in cardiac physiology: from molecule to tissue. *Front Pharmacol.* 2014;5:9.
80. Saucerman JJ, Brunton LL, Michailova AP, McCulloch AD. Modeling beta-adrenergic control of cardiac myocyte contractility in silico. *J Biol Chem.* 2003;278(48):47997-8003.
81. Tomek J, Rodriguez B, Bub G, Heijman J. beta-Adrenergic receptor stimulation inhibits proarrhythmic alternans in postinfarction border zone cardiomyocytes: a computational analysis. *Am J Physiol Heart Circ Physiol.* 2017;313(2):H338-H53.
82. Stern MD. Theory of excitation-contraction coupling in cardiac muscle. *Biophys J.* 1992;63(2):497-517.
83. Greenstein JL, Winslow RL. An integrative model of the cardiac ventricular myocyte incorporating local control of  $Ca^{2+}$  release. *Biophys J.* 2002;83(6):2918-45.

## References

84. Rice JJ, Jafri MS, Winslow RL. Modeling gain and gradedness of  $\text{Ca}^{2+}$  release in the functional unit of the cardiac diadic space. *Biophys J*. 1999;77(4):1871-84.
85. Chu L, Greenstein JL, Winslow RL. Modeling  $\text{Na}^+$ - $\text{Ca}^{2+}$  exchange in the heart: Allosteric activation, spatial localization, sparks and excitation-contraction coupling. *J Mol Cell Cardiol*. 2016;99:174-87.
86. Chu L, Greenstein JL, Winslow RL.  $\text{Na}^+$  microdomains and sparks: Role in cardiac excitation-contraction coupling and arrhythmias in ankyrin-B deficiency. *J Mol Cell Cardiol*. 2019;128:145-57.
87. Restrepo JG, Weiss JN, Karma A. Calsequestrin-mediated mechanism for cellular calcium transient alternans. *Biophys J*. 2008;95(8):3767-89.
88. Song Z, Xie LH, Weiss JN, Qu Z. A Spatiotemporal Ventricular Myocyte Model Incorporating Mitochondrial Calcium Cycling. *Biophys J*. 2019.
89. Walker MA, Williams GS, Kohl T, Lehnart SE, Jafri MS, Greenstein JL, et al. Superresolution modeling of calcium release in the heart. *Biophys J*. 2014;107(12):3018-29.
90. Walker MA, Gurev V, Rice JJ, Greenstein JL, Winslow RL. Estimating the probabilities of rare arrhythmic events in multiscale computational models of cardiac cells and tissue. *PLoS Comput Biol*. 2017;13(11):e1005783.
91. Bootman MD, Smyrniak I, Thul R, Coombes S, Roderick HL. Atrial cardiomyocyte calcium signalling. *Biochim Biophys Acta*. 2011;1813(5):922-34.
92. Richards MA, Clarke JD, Saravanan P, Voigt N, Dobrev D, Eisner DA, et al. Transverse tubules are a common feature in large mammalian atrial myocytes including human. *Am J Physiol Heart Circ Physiol*. 2011;301(5):H1996-2005.
93. Koivumaki JT, Korhonen T, Tavi P. Impact of sarcoplasmic reticulum calcium release on calcium dynamics and action potential morphology in human atrial myocytes: a computational study. *PLoS Comput Biol*. 2011;7(1):e1001067.
94. Heijman J, Erfanian Abdoust P, Voigt N, Nattel S, Dobrev D. Computational models of atrial cellular electrophysiology and calcium handling, and their role in atrial fibrillation. *J Physiol*. 2016;594(3):537-53.
95. Brandenburg S, Pawlowitz J, Fakuade FE, Kownatzki-Danger D, Kohl T, Mitronova GY, et al. Axial Tubule Junctions Activate Atrial  $\text{Ca}^{2+}$  Release Across Species. *Front Physiol*. 2018;9:1227.
96. Ladd D, Tilunaite A, Roderick HL, Soeller C, Crampin EJ, Rajagopal V. Assessing Cardiomyocyte Excitation-Contraction Coupling Site Detection From Live Cell Imaging Using a Structurally-Realistic Computational Model of Calcium Release. *Front Physiol*. 2019;10:1263.
97. Colman MA. Arrhythmia mechanisms and spontaneous calcium release: Bi-directional coupling between re-entrant and focal excitation. *PLoS Comput Biol*. 2019;15(8):e1007260.
98. Lu L, Zheng Q, Xia L, Zhu X. Spatial remodelling of calcium release units may impair cardiac electro-mechanical function: A simulation study. *Comput Biol Med*. 2019;108:234-41.
99. Romero L, Alvarez-Lacalle E, Shiferaw Y. Stochastic coupled map model of subcellular calcium cycling in cardiac cells. *Chaos*. 2019;29(2):023125.
100. Marchena M, Echebarria B. Computational Model of Calcium Signaling in Cardiac Atrial Cells at the Submicron Scale. *Front Physiol*. 2018;9:1760.

101. Zsolnay V, Fill M, Gillespie D. Sarcoplasmic Reticulum Ca<sup>2+</sup> Release Uses a Cascading Network of Intra-SR and Channel Countercurrents. *Biophys J*. 2018;114(2):462-73.
102. Berti C, Zsolnay V, Shannon TR, Fill M, Gillespie D. Sarcoplasmic reticulum Ca<sup>2+</sup>, Mg<sup>2+</sup>, K<sup>+</sup>, and Cl<sup>-</sup> concentrations adjust quickly as heart rate changes. *J Mol Cell Cardiol*. 2017;103:31-9.
103. Colman MA, Pinali C, Trafford AW, Zhang H, Kitmitto A. A computational model of spatio-temporal cardiac intracellular calcium handling with realistic structure and spatial flux distribution from sarcoplasmic reticulum and t-tubule reconstructions. *PLoS Comput Biol*. 2017;13(8):e1005714.
104. Singh JK, Barsegyan V, Bassi N, Marszalec W, Tai S, Mothkur S, et al. T-tubule remodeling and increased heterogeneity of calcium release during the progression to heart failure in intact rat ventricle. *Physiol Rep*. 2017;5(24).
105. Qu Z, Liu MB, Nivala M. A unified theory of calcium alternans in ventricular myocytes. *Sci Rep*. 2016;6:35625.
106. Chan YH, Tsai WC, Song Z, Ko CY, Qu Z, Weiss JN, et al. Acute reversal of phospholamban inhibition facilitates the rhythmic whole-cell propagating calcium waves in isolated ventricular myocytes. *J Mol Cell Cardiol*. 2015;80:126-35.
107. Nivala M, Song Z, Weiss JN, Qu Z. T-tubule disruption promotes calcium alternans in failing ventricular myocytes: mechanistic insights from computational modeling. *J Mol Cell Cardiol*. 2015;79:32-41.
108. Thul R, Rietdorf K, Bootman MD, Coombes S. Unifying principles of calcium wave propagation - Insights from a three-dimensional model for atrial myocytes. *Biochim Biophys Acta*. 2015;1853(9):2131-43.
109. Walker MA, Kohl T, Lehnart SE, Greenstein JL, Lederer WJ, Winslow RL. On the Adjacency Matrix of RyR2 Cluster Structures. *PLoS Comput Biol*. 2015;11(11):e1004521.
110. Walker MA, Williams GSB, Kohl T, Lehnart SE, Jafri MS, Greenstein JL, et al. Superresolution modeling of calcium release in the heart. *Biophys J*. 2014;107(12):3018-29.
111. Li Q, O'Neill SC, Tao T, Li Y, Eisner D, Zhang H. Mechanisms by which cytoplasmic calcium wave propagation and alternans are generated in cardiac atrial myocytes lacking T-tubules-insights from a simulation study. *Biophys J*. 2012;102(7):1471-82.
112. Lu L, Xia L, Zhu X. Simulation of arrhythmogenic effect of rogue RyRs in failing heart by using a coupled model. *Comput Math Methods Med*. 2012;2012:183978.
113. Nivala M, de Lange E, Rovetti R, Qu Z. Computational modeling and numerical methods for spatiotemporal calcium cycling in ventricular myocytes. *Front Physiol*. 2012;3:114.
114. Thul R, Coombes S, Roderick HL, Bootman MD. Subcellular calcium dynamics in a whole-cell model of an atrial myocyte. *Proc Natl Acad Sci U S A*. 2012;109(6):2150-5.
115. Williams GS, Chikando AC, Tuan HT, Sobie EA, Lederer WJ, Jafri MS. Dynamics of calcium sparks and calcium leak in the heart. *Biophys J*. 2011;101(6):1287-96.
116. Rovetti R, Cui X, Garfinkel A, Weiss JN, Qu Z. Spark-induced sparks as a mechanism of intracellular calcium alternans in cardiac myocytes. *Circ Res*. 2010;106(10):1582-91.

## References

117. Izu LT, Means SA, Shadid JN, Chen-Izu Y, Balke CW. Interplay of ryanodine receptor distribution and calcium dynamics. *Biophys J*. 2006;91(1):95-112.
118. Campbell KL, Dicke AA. Sarcolipin Makes Heat, but Is It Adaptive Thermogenesis? *Front Physiol*. 2018;9:714.
119. Xie LH, Shanmugam M, Park JY, Zhao Z, Wen H, Tian B, et al. Ablation of sarcolipin results in atrial remodeling. *Am J Physiol Cell Physiol*. 2012;302(12):C1762-71.
120. Shimura D, Kusakari Y, Sasano T, Nakashima Y, Nakai G, Jiao Q, et al. Heterozygous deletion of sarcolipin maintains normal cardiac function. *Am J Physiol Heart Circ Physiol*. 2016;310(1):H92-103.
121. Molina CE, Abu-Taha IH, Wang Q, Rosello-Diez E, Kamler M, Nattel S, et al. Profibrotic, Electrical, and Calcium-Handling Remodeling of the Atria in Heart Failure Patients With and Without Atrial Fibrillation. *Front Physiol*. 2018;9:1383.
122. Shanmugam M, Molina CE, Gao S, Severac-Bastide R, Fischmeister R, Babu GJ. Decreased sarcolipin protein expression and enhanced sarco(endo)plasmic reticulum  $Ca^{2+}$  uptake in human atrial fibrillation. *Biochem Biophys Res Commun*. 2011;410(1):97-101.
123. Zaman JA, Harling L, Ashrafian H, Darzi A, Gooderham N, Athanasiou T, et al. Post-operative atrial fibrillation is associated with a pre-existing structural and electrical substrate in human right atrial myocardium. *Int J Cardiol*. 2016;220:580-8.
124. Voigt N, Li N, Wang Q, Wang W, Trafford AW, Abu-Taha I, et al. Enhanced sarcoplasmic reticulum  $Ca^{2+}$  leak and increased  $Na^{+}$ - $Ca^{2+}$  exchanger function underlie delayed afterdepolarizations in patients with chronic atrial fibrillation. *Circulation*. 2012;125(17):2059-70.
125. Koivumaki JT, Takalo J, Korhonen T, Tavi P, Weckstrom M. Modelling sarcoplasmic reticulum calcium ATPase and its regulation in cardiac myocytes. *Philos Trans A Math Phys Eng Sci*. 2009;367(1896):2181-202.
126. Abdoust PE, Heijman J, Dobrev D. A new computational model for SERCA2a regulation in human atrial cardiomyocytes. *Heart Rhythm*. 2016;13(5).
127. Higgins ER, Cannell MB, Sneyd J. A buffering SERCA pump in models of calcium dynamics. *Biophys J*. 2006;91(1):151-63.
128. Tran K, Smith NP, Loisel DS, Crampin EJ. A thermodynamic model of the cardiac sarcoplasmic/endoplasmic  $Ca^{2+}$  (SERCA) pump. *Biophys J*. 2009;96(5):2029-42.
129. Pavlovic D, Fuller W, Shattock MJ. Novel regulation of cardiac Na pump via phospholemman. *J Mol Cell Cardiol*. 2013;61:83-93.
130. Greiser M, Kerfant BG, Williams GS, Voigt N, Harks E, Dibb KM, et al. Tachycardia-induced silencing of subcellular  $Ca^{2+}$  signaling in atrial myocytes. *J Clin Invest*. 2014;124(11):4759-72.
131. Negroni JA, Morotti S, Lascano EC, Gomes AV, Grandi E, Puglisi JL, et al. beta-adrenergic effects on cardiac myofilaments and contraction in an integrated rabbit ventricular myocyte model. *J Mol Cell Cardiol*. 2015;81:162-75.
132. Bastug-Ozel Z, Wright PT, Kraft AE, Pavlovic D, Howie J, Froese A, et al. Heart failure leads to altered beta2-adrenoceptor/cyclic adenosine monophosphate dynamics in the sarcolemmal phospholemman/ $Na,K$  ATPase microdomain. *Cardiovasc Res*. 2019;115(3):546-55.
133. Hafver TL, Hodne K, Wanichawan P, Aronsen JM, Dalhus B, Lunde PK, et al. Protein Phosphatase 1c Associated with the Cardiac Sodium Calcium Exchanger

- 1 Regulates Its Activity by Dephosphorylating Serine 68-phosphorylated Phospholemman. *J Biol Chem.* 2016;291(9):4561-79.
134. Zhang XQ, Wang J, Song J, Rabinowitz J, Chen X, Houser SR, et al. Regulation of L-type calcium channel by phospholemman in cardiac myocytes. *J Mol Cell Cardiol.* 2015;84:104-11.
135. Abriel H, Rougier JS, Jalife J. Ion channel macromolecular complexes in cardiomyocytes: roles in sudden cardiac death. *Circ Res.* 2015;116(12):1971-88.
136. Heijman J, Dobrev D. Ion channels as part of macromolecular multiprotein complexes : Clinical significance. *Herzschrittmacherther Elektrophysiol.* 2018;29(1):30-5.
137. Beavers DL, Wang W, Ather S, Voigt N, Garbino A, Dixit SS, et al. Mutation E169K in Junctophilin-2 Causes Atrial Fibrillation Due to Impaired RyR2 Stabilization. *Journal of the American College of Cardiology.* 2013;62(21):2010-9.
138. Hove-Madsen L, Llach A, Bayes-Genis A, Roura S, Rodriguez Font E, Aris A, et al. Atrial fibrillation is associated with increased spontaneous calcium release from the sarcoplasmic reticulum in human atrial myocytes. *Circulation.* 2004;110(11):1358-63.
139. Neef S, Dybkova N, Sossalla S, Ort KR, Fluschnik N, Neumann K, et al. CaMKII-dependent diastolic SR Ca<sup>2+</sup> leak and elevated diastolic Ca<sup>2+</sup> levels in right atrial myocardium of patients with atrial fibrillation. *Circ Res.* 2010;106(6):1134-44.
140. Christ T, Rozmaritsa N, Engel A, Berk E, Knaut M, Metzner K, et al. Arrhythmias, elicited by catecholamines and serotonin, vanish in human chronic atrial fibrillation. *Proc Natl Acad Sci U S A.* 2014;111(30):11193-8.
141. Greiser M. Calcium signalling silencing in atrial fibrillation. *J Physiol.* 2017;595(12):4009-17.
142. Greiser M, Schotten U. Dynamic remodeling of intracellular Ca<sup>2+</sup> signaling during atrial fibrillation. *J Mol Cell Cardiol.* 2013;58:134-42.
143. Dobrev D, Wehrens XHT. Calcium-mediated cellular triggered activity in atrial fibrillation. *J Physiol.* 2017;595(12):4001-8.
144. Nivala M, Ko CY, Nivala M, Weiss JN, Qu Z. Criticality in intracellular calcium signaling in cardiac myocytes. *Biophys J.* 2012;102(11):2433-42.
145. Bers DM, Despa S. Na<sup>+</sup> transport in cardiac myocytes; Implications for excitation-contraction coupling. *IUBMB Life.* 2009;61(3):215-21.
146. Llach A, Molina CE, Alvarez-Lacalle E, Tort L, Benitez R, Hove-Madsen L. Detection, properties, and frequency of local calcium release from the sarcoplasmic reticulum in teleost cardiomyocytes. *PLoS One.* 2011;6(8):e23708.
147. Eiras S, Narolska NA, van Loon RB, Boontje NM, Zaremba R, Jimenez CR, et al. Alterations in contractile protein composition and function in human atrial dilatation and atrial fibrillation. *J Mol Cell Cardiol.* 2006;41(3):467-77.
148. El-Armouche A, Boknik P, Eschenhagen T, Carrier L, Knaut M, Ravens U, et al. Molecular determinants of altered Ca<sup>2+</sup> handling in human chronic atrial fibrillation. *Circulation.* 2006;114(7):670-80.
149. Sossalla S, Kallmeyer B, Wagner S, Mazur M, Maurer U, Toischer K, et al. Altered Na<sup>+</sup> currents in atrial fibrillation effects of ranolazine on arrhythmias and contractility in human atrial myocardium. *J Am Coll Cardiol.* 2010;55(21):2330-42.

## References

150. Severi S, Corsi C, Cerbai E. From in vivo plasma composition to in vitro cardiac electrophysiology and in silico virtual heart: the extracellular calcium enigma. *Philos Trans A Math Phys Eng Sci.* 2009;367(1896):2203-23.
151. Plank DM, Sussman MA. Intracellular Ca<sup>2+</sup> measurements in live cells by rapid line scan confocal microscopy: simplified calibration methodology. *Methods Cell Sci.* 2003;25(3-4):123-33.
152. Hagen BM, Boyman L, Kao JP, Lederer WJ. A comparative assessment of fluo Ca<sup>2+</sup> indicators in rat ventricular myocytes. *Cell Calcium.* 2012;52(2):170-81.
153. Lock JT, Parker I, Smith IF. A comparison of fluorescent Ca<sup>2+</sup> indicators for imaging local Ca<sup>2+</sup> signals in cultured cells. *Cell Calcium.* 2015;58(6):638-48.
154. Ito DW, Hannigan KI, Ghosh D, Xu B, Del Villar SG, Xiang YK, et al. beta-adrenergic-mediated dynamic augmentation of sarcolemmal Cav 1.2 clustering and cooperativity in ventricular myocytes. *J Physiol.* 2019;597(8):2139-62.
155. Jones PP, MacQuaide N, Louch WE. Dyadic Plasticity in Cardiomyocytes. *Front Physiol.* 2018;9:1773.
156. Louch WE. Channel surfing: new insights into plasticity of excitation-contraction coupling. *J Physiol.* 2019;597(8):2119-20.
157. Scardigli M, Ferrantini C, Crocini C, Pavone FS, Sacconi L. Interplay Between Sub-Cellular Alterations of Calcium Release and T-Tubular Defects in Cardiac Diseases. *Front Physiol.* 2018;9:1474.
158. MacQuaide N, Tuan HT, Hotta J, Sempels W, Lenaerts I, Holemans P, et al. Ryanodine receptor cluster fragmentation and redistribution in persistent atrial fibrillation enhance calcium release. *Cardiovasc Res.* 2015;108(3):387-98.
159. Galice S, Xie Y, Yang Y, Sato D, Bers DM. Size Matters: Ryanodine Receptor Cluster Size Affects Arrhythmogenic Sarcoplasmic Reticulum Calcium Release. *J Am Heart Assoc.* 2018;7(13).
160. Brandenburg S, Kohl T, Williams GS, Gusev K, Wagner E, Rog-Zielinska EA, et al. Axial tubule junctions control rapid calcium signaling in atria. *J Clin Invest.* 2016;126(10):3999-4015.
161. Pinali C, Bennett H, Davenport JB, Trafford AW, Kitmitto A. Three-Dimensional Reconstruction of Cardiac Sarcoplasmic Reticulum Reveals a Continuous Network Linking Transverse-Tubules This Organization Is Perturbed in Heart Failure. *Circulation Research.* 2013;113(11):1219-U98.
162. Manfra O, Shen X, Hell JW, Louch WE. Super-resolution (dSTORM) imaging of calcium handling proteins in cardiomyocytes. *Biophysical Journal.* 2018;114(3):620a.
163. Kolstad TR, van den Brink J, MacQuaide N, Lunde PK, Frisk M, Aronsen JM, et al. Ryanodine receptor dispersion disrupts Ca(2+) release in failing cardiac myocytes. *Elife.* 2018;7.
164. Shen X, van den Brink J, Hou Y, Colli D, Le C, Kolstad TR, et al. 3D dSTORM imaging reveals novel detail of ryanodine receptor localization in rat cardiac myocytes. *J Physiol.* 2019;597(2):399-418.
165. Guo A, Zhang C, Wei S, Chen B, Song LS. Emerging mechanisms of T-tubule remodelling in heart failure. *Cardiovasc Res.* 2013;98(2):204-15.
166. Bers DM, Shannon TR. Calcium movements inside the sarcoplasmic reticulum of cardiac myocytes. *J Mol Cell Cardiol.* 2013;58:59-66.

167. Wu X, Bers DM. Sarcoplasmic reticulum and nuclear envelope are one highly interconnected  $\text{Ca}^{2+}$  store throughout cardiac myocyte. *Circ Res.* 2006;99(3):283-91.
168. Swietach P, Spitzer KW, Vaughan-Jones RD.  $\text{Ca}^{2+}$ -mobility in the sarcoplasmic reticulum of ventricular myocytes is low. *Biophys J.* 2008;95(3):1412-27.
169. Loucks AD, O'Hara T, Trayanova NA. Degradation of T-Tubular Microdomains and Altered cAMP Compartmentation Lead to Emergence of Arrhythmogenic Triggers in Heart Failure Myocytes: An in silico Study. *Front Physiol.* 2018;9:1737.
170. Maleckar MM, Edwards AG, Louch WE, Lines GT. Studying dyadic structure-function relationships: a review of current modeling approaches and new insights into  $\text{Ca}^{2+}$  (mis)handling. *Clin Med Insights Cardiol.* 2017;11:1179546817698602.
171. Rajagopal V, Bass G, Walker CG, Crossman DJ, Petzer A, Hickey A, et al. Examination of the Effects of Heterogeneous Organization of RyR Clusters, Myofibrils and Mitochondria on  $\text{Ca}^{2+}$  Release Patterns in Cardiomyocytes. *PLoS Comput Biol.* 2015;11(9):e1004417.
172. Sanchez-Alonso JL, Bhargava A, O'Hara T, Glukhov AV, Schobesberger S, Bhogal N, et al. Microdomain-Specific Modulation of L-Type Calcium Channels Leads to Triggered Ventricular Arrhythmia in Heart Failure. *Circ Res.* 2016;119(8):944-55.
173. Harada M, Luo X, Murohara T, Yang B, Dobrev D, Nattel S. MicroRNA regulation and cardiac calcium signaling: role in cardiac disease and therapeutic potential. *Circ Res.* 2014;114(4):689-705.
174. Hu X, Li J, van Marion DMS, Zhang D, Brundel B. Heat shock protein inducer GGA\*-59 reverses contractile and structural remodeling via restoration of the microtubule network in experimental Atrial Fibrillation. *J Mol Cell Cardiol.* 2019;134:86-97.
175. Undrovinas A, Maltsev VA, Sabbah HN. Calpain inhibition reduces amplitude and accelerates decay of the late sodium current in ventricular myocytes from dogs with chronic heart failure. *PLoS One.* 2013;8(4):e54436.
176. Patterson C, Portbury AL, Schisler JC, Willis MS. Tear me down: role of calpain in the development of cardiac ventricular hypertrophy. *Circ Res.* 2011;109(4):453-62.
177. Harvey RD, Hell JW.  $\text{Ca}_v1.2$  signaling complexes in the heart. *J Mol Cell Cardiol.* 2013;58:143-52.
178. Barefield DY, McNamara JW, Lynch TL, Kuster DWD, Govindan S, Haar L, et al. Ablation of the calpain-targeted site in cardiac myosin binding protein-C is cardioprotective during ischemia-reperfusion injury. *J Mol Cell Cardiol.* 2019;129:236-46.
179. French JP, Quindry JC, Falk DJ, Staib JL, Lee Y, Wang KK, et al. Ischemia-reperfusion-induced calpain activation and SERCA2a degradation are attenuated by exercise training and calpain inhibition. *Am J Physiol Heart Circ Physiol.* 2006;290(1):H128-36.
180. Pedrozo Z, Sanchez G, Torrealba N, Valenzuela R, Fernandez C, Hidalgo C, et al. Calpains and proteasomes mediate degradation of ryanodine receptors in a model of cardiac ischemic reperfusion. *Biochim Biophys Acta.* 2010;1802(3):356-62.

## References

181. Singh RB, Chohan PK, Dhalla NS, Netticadan T. The sarcoplasmic reticulum proteins are targets for calpain action in the ischemic-reperfused heart. *J Mol Cell Cardiol.* 2004;37(1):101-10.
182. Wanichawan P, Hafver TL, Hodne K, Aronsen JM, Lunde IG, Dalhus B, et al. Molecular basis of calpain cleavage and inactivation of the sodium-calcium exchanger 1 in heart failure. *J Biol Chem.* 2014;289(49):33984-98.
183. Singh RM, Cummings E, Pantos C, Singh J. Protein kinase C and cardiac dysfunction: a review. *Heart Fail Rev.* 2017;22(6):843-59.
184. Ferreira JC, Mochly-Rosen D, Boutjdir M. Regulation of cardiac excitability by protein kinase C isozymes. *Front Biosci (Schol Ed).* 2012;4:532-46.
185. Heijman J, Voigt N, Wehrens XH, Dobrev D. Calcium dysregulation in atrial fibrillation: the role of CaMKII. *Front Pharmacol.* 2014;5:30.
186. Makary S, Voigt N, Maguy A, Wakili R, Nishida K, Harada M, et al. Differential protein kinase C isoform regulation and increased constitutive activity of acetylcholine-regulated potassium channels in atrial remodeling. *Circ Res.* 2011;109(9):1031-43.
187. Voigt N, Friedrich A, Bock M, Wettwer E, Christ T, Knaut M, et al. Differential phosphorylation-dependent regulation of constitutively active and muscarinic receptor-activated  $I_{K_{ACh}}$  channels in patients with chronic atrial fibrillation. *Cardiovasc Res.* 2007;74(3):426-37.
188. Zhu H, Xue H, Jin QH, Guo J, Chen YD. Increased expression of ryanodine receptor type-2 during atrial fibrillation by miR-106-25 cluster independent mechanism. *Exp Cell Res.* 2019;375(2):113-7.
189. Dobrev D, Friedrich A, Voigt N, Jost N, Wettwer E, Christ T, et al. The G protein-gated potassium current  $I_{K_{ACh}}$  is constitutively active in patients with chronic atrial fibrillation. *Circulation.* 2005;112(24):3697-706.
190. Baudenbacher F, Schober T, Pinto JR, Sidorov VY, Hilliard F, Solaro RJ, et al. Myofilament  $Ca^{2+}$  sensitization causes susceptibility to cardiac arrhythmia in mice. *J Clin Invest.* 2008;118(12):3893-903.
191. Hamdani N, Kooij V, van Dijk S, Merkus D, Paulus WJ, dos Remedios C, et al. Sarcomeric dysfunction in heart failure. *Cardiovascular Research.* 2008;77(4):649-58.
192. Saucerman JJ, McCulloch AD. Mechanistic systems models of cell signaling networks: a case study of myocyte adrenergic regulation. *Prog Biophys Mol Biol.* 2004;85(2-3):261-78.
193. Yang JH, Saucerman JJ. Computational models reduce complexity and accelerate insight into cardiac signaling networks. *Circ Res.* 2011;108(1):85-97.
194. Zeigler AC, Richardson WJ, Holmes JW, Saucerman JJ. Computational modeling of cardiac fibroblasts and fibrosis. *J Mol Cell Cardiol.* 2016;93:73-83.
195. Kreusser MM, Lehmann LH, Keranov S, Hoting MO, Oehl U, Kohlhaas M, et al. Cardiac CaM Kinase II genes delta and gamma contribute to adverse remodeling but redundantly inhibit calcineurin-induced myocardial hypertrophy. *Circulation.* 2014;130(15):1262-73.
196. Neef S, Heijman J, Otte K, Dewenter M, Saadatmand AR, Meyer-Roxlau S, et al. Chronic loss of inhibitor-1 diminishes cardiac RyR2 phosphorylation despite exaggerated CaMKII activity. *Naunyn Schmiedebergs Arch Pharmacol.* 2017;390(8):857-62.

197. Pereira L, Cheng H, Lao DH, Na L, van Oort RJ, Brown JH, et al. Epac2 mediates cardiac beta1-adrenergic-dependent sarcoplasmic reticulum Ca<sup>2+</sup> leak and arrhythmia. *Circulation*. 2013;127(8):913-22.
198. Hund TJ, Mohler PJ. Role of CaMKII in cardiac arrhythmias. *Trends Cardiovasc Med*. 2015;25(5):392-7.
199. Hegyi B, Bers DM, Bossuyt J. CaMKII signaling in heart diseases: Emerging role in diabetic cardiomyopathy. *J Mol Cell Cardiol*. 2019;127:246-59.
200. Zhang T, Brown JH. Role of Ca<sup>2+</sup>/calmodulin-dependent protein kinase II in cardiac hypertrophy and heart failure. *Cardiovasc Res*. 2004;63(3):476-86.
201. Hasenfuss G, Lehnart SE. Negative Adrenergic Feedback Specific to Phospholamban. *JACC Basic Transl Sci*. 2017;2(2):181-3.
202. Respress JL, van Oort RJ, Li N, Rolim N, Dixit SS, deAlmeida A, et al. Role of RyR2 phosphorylation at S2814 during heart failure progression. *Circ Res*. 2012;110(11):1474-83.
203. Uchinoumi H, Yang Y, Oda T, Li N, Alsina KM, Puglisi JL, et al. CaMKII-dependent phosphorylation of RyR2 promotes targetable pathological RyR2 conformational shift. *J Mol Cell Cardiol*. 2016;98:62-72.
204. Dobrev D, Wehrens XH. Role of RyR2 phosphorylation in heart failure and arrhythmias: Controversies around ryanodine receptor phosphorylation in cardiac disease. *Circ Res*. 2014;114(8):1311-9; discussion 9.
205. Park SJ, Zhang D, Qi Y, Li Y, Lee KY, Bezzerides VJ, et al. Insights Into the Pathogenesis of Catecholaminergic Polymorphic Ventricular Tachycardia From Engineered Human Heart Tissue. *Circulation*. 2019;140(5):390-404.
206. Bezzerides VJ, Caballero A, Wang S, Ai Y, Hylind RJ, Lu F, et al. Gene Therapy for Catecholaminergic Polymorphic Ventricular Tachycardia by Inhibition of Ca<sup>2+</sup>/Calmodulin-Dependent Kinase II. *Circulation*. 2019;140(5):405-19.
207. Di Pasquale E, Lodola F, Miragoli M, Denegri M, Avelino-Cruz JE, Buonocore M, et al. CaMKII inhibition rectifies arrhythmic phenotype in a patient-specific model of catecholaminergic polymorphic ventricular tachycardia. *Cell Death Dis*. 2013;4:e843.
208. Grandi E, Dobrev D. Non-ion channel therapeutics for heart failure and atrial fibrillation: Are CaMKII inhibitors ready for clinical use? *J Mol Cell Cardiol*. 2018;121:300-3.
209. Li N, Wang TN, Wang W, Cutler MJ, Wang QL, Voigt N, et al. Inhibition of CaMKII Phosphorylation of RyR2 Prevents Induction of Atrial Fibrillation in FKBP12.6 Knockout Mice. *Circulation Research*. 2012;110(3):465-U208.
210. Schotten U, Dobrev D, Platonov PG, Kottkamp H, Hindricks G. Current controversies in determining the main mechanisms of atrial fibrillation. *J Intern Med*. 2016;279(5):428-38.
211. Greer-Short A, Musa H, Alsina KM, Ni L, Word TA, Reynolds JO, et al. Calmodulin kinase II regulates atrial myocyte late sodium current, calcium handling and atrial arrhythmia. *Heart Rhythm*. 2019.
212. Hegyi B, Morotti S, Liu C, Ginsburg KS, Bossuyt J, Belardinelli L, et al. Enhanced Depolarization Drive in Failing Rabbit Ventricular Myocytes. *Circ Arrhythm Electrophysiol*. 2019;12(3):e007061.
213. Morotti S, Edwards AG, McCulloch AD, Bers DM, Grandi E. A novel computational model of mouse myocyte electrophysiology to assess the synergy between Na<sup>+</sup> loading and CaMKII. *J Physiol*. 2014;592(6):1181-97.

## References

214. Onal B, Gratz D, Hund TJ.  $Ca^{2+}$ /calmodulin-dependent kinase II-dependent regulation of atrial myocyte late  $Na^+$  current,  $Ca^{2+}$  cycling, and excitability: a mathematical modeling study. *Am J Physiol Heart Circ Physiol*. 2017;313(6):H1227-H39.
215. Tomek J, Hao G, Tomkova M, Lewis A, Carr C, Paterson DJ, et al. beta-Adrenergic Receptor Stimulation and Alternans in the Border Zone of a Healed Infarct: An ex vivo Study and Computational Investigation of Arrhythmogenesis. *Front Physiol*. 2019;10:350.
216. Bers DM, Grandi E. Calcium/calmodulin-dependent kinase II regulation of cardiac ion channels. *J Cardiovasc Pharmacol*. 2009;54(3):180-7.
217. Hidalgo CG, Chung CS, Saripalli C, Methawasin M, Hutchinson KR, Tsapralis G, et al. The multifunctional  $Ca^{2+}$ /calmodulin-dependent protein kinase II delta (CaMKIIdelta) phosphorylates cardiac titin's spring elements. *J Mol Cell Cardiol*. 2013;54:90-7.
218. Sadayappan S, Gulick J, Osinska H, Barefield D, Cuello F, Avkiran M, et al. A critical function for Ser-282 in cardiac Myosin binding protein-C phosphorylation and cardiac function. *Circ Res*. 2011;109(2):141-50.
219. Ljubojevic S, Bers DM. Nuclear calcium in cardiac myocytes. *J Cardiovasc Pharmacol*. 2015;65(3):211-7.
220. Hohendanner F, McCulloch AD, Blatter LA, Michailova AP. Calcium and  $IP_3$  dynamics in cardiac myocytes: experimental and computational perspectives and approaches. *Front Pharmacol*. 2014;5:35.
221. Saucerman JJ, Bers DM. Calmodulin mediates differential sensitivity of CaMKII and calcineurin to local  $Ca^{2+}$  in cardiac myocytes. *Biophys J*. 2008;95(10):4597-612.
222. Molkentin JD. Calcineurin-NFAT signaling regulates the cardiac hypertrophic response in coordination with the MAPKs. *Cardiovasc Res*. 2004;63(3):467-75.
223. Qi XY, Yeh YH, Xiao L, Burstein B, Maguy A, Chartier D, et al. Cellular signaling underlying atrial tachycardia remodeling of L-type calcium current. *Circ Res*. 2008;103(8):845-54.
224. Yao C, Veleva T, Scott L, Jr., Cao S, Li L, Chen G, et al. Enhanced Cardiomyocyte NLRP3 Inflammasome Signaling Promotes Atrial Fibrillation. *Circulation*. 2018;138(20):2227-42.
225. Luo X, Pan Z, Shan H, Xiao J, Sun X, Wang N, et al. MicroRNA-26 governs profibrillatory inward-rectifier potassium current changes in atrial fibrillation. *J Clin Invest*. 2013;123(5):1939-51.
226. He J, Xu Y, Yang L, Xia G, Deng N, Yang Y, et al. Regulation of inward rectifier potassium current ionic channel remodeling by AT1 -Calcineurin-NFAT signaling pathway in stretch-induced hypertrophic atrial myocytes. *Cell Biol Int*. 2018;42(9):1149-59.
227. Aflaki M, Qi XY, Xiao L, Ordog B, Tadevosyan A, Luo X, et al. Exchange protein directly activated by cAMP mediates slow delayed-rectifier current remodeling by sustained beta-adrenergic activation in guinea pig hearts. *Circ Res*. 2014;114(6):993-1003.
228. Liu W, Deng J, Ding W, Wang G, Shen Y, Zheng J, et al. Decreased KCNE2 Expression Participates in the Development of Cardiac Hypertrophy by Regulation of Calcineurin-NFAT (Nuclear Factor of Activated T Cells) and Mitogen-Activated Protein Kinase Pathways. *Circ Heart Fail*. 2017;10(6).

229. Rinne A, Kapur N, Molkentin JD, Pogwizd SM, Bers DM, Banach K, et al. Isoform- and tissue-specific regulation of the Ca<sup>2+</sup>-sensitive transcription factor NFAT in cardiac myocytes and heart failure. *Am J Physiol Heart Circ Physiol*. 2010;298(6):H2001-9.
230. Nie J, Duan Q, He M, Li X, Wang B, Zhou C, et al. Ranolazine prevents pressure overload-induced cardiac hypertrophy and heart failure by restoring aberrant Na<sup>+</sup> and Ca<sup>2+</sup> handling. *J Cell Physiol*. 2019;234(7):11587-601.
231. Olivares-Florez S, Czolbe M, Riediger F, Seidlmayer L, Williams T, Nordbeck P, et al. Nuclear calcineurin is a sensor for detecting Ca<sup>2+</sup> release from the nuclear envelope via IP3R. *J Mol Med (Berl)*. 2018;96(11):1239-49.
232. Cooling MT, Hunter P, Crampin EJ. Sensitivity of NFAT cycling to cytosolic calcium concentration: implications for hypertrophic signals in cardiac myocytes. *Biophys J*. 2009;96(6):2095-104.
233. Kang JH, Lee HS, Kang YW, Cho KH. Systems biological approaches to the cardiac signaling network. *Brief Bioinform*. 2016;17(3):419-28.
234. Khalilimeybodi A, Daneshmehr A, Sharif Kashani B. Ca<sup>2+</sup>-dependent calcineurin/NFAT signaling in beta-adrenergic-induced cardiac hypertrophy. *Gen Physiol Biophys*. 2018;37(1):41-56.
235. Kreusser MM, Backs J. Integrated mechanisms of CaMKII-dependent ventricular remodeling. *Front Pharmacol*. 2014;5:36.
236. Backs J, Olson EN. Control of cardiac growth by histone acetylation/deacetylation. *Circ Res*. 2006;98(1):15-24.
237. Backs J, Song K, Bezprozvannaya S, Chang S, Olson EN. CaM kinase II selectively signals to histone deacetylase 4 during cardiomyocyte hypertrophy. *J Clin Invest*. 2006;116(7):1853-64.
238. Zhao X, Sternsdorf T, Bolger TA, Evans RM, Yao TP. Regulation of MEF2 by histone deacetylase 4- and SIRT1 deacetylase-mediated lysine modifications. *Mol Cell Biol*. 2005;25(19):8456-64.
239. Backs J, Backs T, Neef S, Kreusser MM, Lehmann LH, Patrick DM, et al. The delta isoform of CaM kinase II is required for pathological cardiac hypertrophy and remodeling after pressure overload. *Proc Natl Acad Sci U S A*. 2009;106(7):2342-7.
240. Ronkainen JJ, Hanninen SL, Korhonen T, Koivumaki JT, Skoumal R, Rautio S, et al. Ca<sup>2+</sup>-calmodulin-dependent protein kinase II represses cardiac transcription of the L-type calcium channel alpha(1C)-subunit gene (*Cacna1c*) by DREAM translocation. *J Physiol*. 2011;589(Pt 11):2669-86.
241. Franz MR, Bode F. Mechano-electrical feedback underlying arrhythmias: the atrial fibrillation case. *Prog Biophys Mol Biol*. 2003;82(1-3):163-74.
242. Huke S, Knollmann BC. Increased myofilament Ca<sup>2+</sup>-sensitivity and arrhythmia susceptibility. *J Mol Cell Cardiol*. 2010;48(5):824-33.
243. Fraysse B, Weinberger F, Bardswell SC, Cuello F, Vignier N, Geertz B, et al. Increased myofilament Ca<sup>2+</sup> sensitivity and diastolic dysfunction as early consequences of Mybpc3 mutation in heterozygous knock-in mice. *J Mol Cell Cardiol*. 2012;52(6):1299-307.
244. Kohlhaas M, Nickel AG, Maack C. Mitochondrial energetics and calcium coupling in the heart. *J Physiol*. 2017;595(12):3753-63.

## References

245. Baker LC, Wolk R, Choi BR, Watkins S, Plan P, Shah A, et al. Effects of mechanical uncouplers, diacetyl monoxime, and cytochalasin-D on the electrophysiology of perfused mouse hearts. *Am J Physiol Heart Circ Physiol.* 2004;287(4):H1771-9.
246. de Tombe PP, Mateja RD, Tachampa K, Ait Mou Y, Farman GP, Irving TC. Myofilament length dependent activation. *J Mol Cell Cardiol.* 2010;48(5):851-8.
247. Peyronnet R, Nerbonne JM, Kohl P. Cardiac Mechano-Gated Ion Channels and Arrhythmias. *Circ Res.* 2016;118(2):311-29.
248. Petroff MG, Kim SH, Pepe S, Dessy C, Marban E, Balligand JL, et al. Endogenous nitric oxide mechanisms mediate the stretch dependence of  $Ca^{2+}$  release in cardiomyocytes. *Nat Cell Biol.* 2001;3(10):867-73.
249. Wakayama Y, Miura M, Stuyvers BD, Boyden PA, ter Keurs HE. Spatial nonuniformity of excitation-contraction coupling causes arrhythmogenic  $Ca^{2+}$  waves in rat cardiac muscle. *Circ Res.* 2005;96(12):1266-73.
250. Hongo K, White E, Le Guennec JY, Orchard CH. Changes in  $[Ca^{2+}]_i$ ,  $[Na^+]_i$  and  $Ca^{2+}$  current in isolated rat ventricular myocytes following an increase in cell length. *J Physiol.* 1996;491 ( Pt 3):609-19.
251. Iribe G, Ward CW, Camelliti P, Bollensdorff C, Mason F, Burton RA, et al. Axial stretch of rat single ventricular cardiomyocytes causes an acute and transient increase in  $Ca^{2+}$  spark rate. *Circ Res.* 2009;104(6):787-95.
252. Nishimura S, Kawai Y, Nakajima T, Hosoya Y, Fujita H, Katoh M, et al. Membrane potential of rat ventricular myocytes responds to axial stretch in phase, amplitude and speed-dependent manners. *Cardiovasc Res.* 2006;72(3):403-11.
253. Ward CW, Prosser BL, Lederer WJ. Mechanical stretch-induced activation of ROS/RNS signaling in striated muscle. *Antioxid Redox Signal.* 2014;20(6):929-36.
254. Jian Z, Han H, Zhang T, Puglisi J, Izu LT, Shaw JA, et al. Mechanochemotransduction during cardiomyocyte contraction is mediated by localized nitric oxide signaling. *Sci Signal.* 2014;7(317):ra27.
255. Allen DG, Kurihara S. The effects of muscle length on intracellular calcium transients in mammalian cardiac muscle. *J Physiol.* 1982;327:79-94.
256. Mulieri LA, Hasenfuss G, Leavitt B, Allen PD, Alpert NR. Altered myocardial force-frequency relation in human heart failure. *Circulation.* 1992;85(5):1743-50.
257. Balnave CD, Davey DF, Allen DG. Distribution of sarcomere length and intracellular calcium in mouse skeletal muscle following stretch-induced injury. *J Physiol.* 1997;502 ( Pt 3):649-59.
258. Jaimes R, 3rd, Walton RD, Pasdois P, Bernus O, Efimov IR, Kay MW. A technical review of optical mapping of intracellular calcium within myocardial tissue. *Am J Physiol Heart Circ Physiol.* 2016;310(11):H1388-401.
259. Christoph J, Chebbok M, Richter C, Schroder-Schetelig J, Bittihn P, Stein S, et al. Electromechanical vortex filaments during cardiac fibrillation. *Nature.* 2018;555(7698):667-72.
260. Swift LM, Asfour H, Posnack NG, Arutunyan A, Kay MW, Sarvazyan N. Properties of blebbistatin for cardiac optical mapping and other imaging applications. *Pflugers Arch.* 2012;464(5):503-12.
261. Shaw J, Izu L, Chen-Izu Y. Mechanical analysis of single myocyte contraction in a 3-D elastic matrix. *PLoS One.* 2013;8(10):e75492.
262. Mills RJ, Hudson JE. Bioengineering adult human heart tissue: How close are we? *APL Bioeng.* 2019;3(1):010901.

263. O'Hara T, Virag L, Varro A, Rudy Y. Simulation of the undiseased human cardiac ventricular action potential: model formulation and experimental validation. *PLoS Comput Biol*. 2011;7(5):e1002061.
264. ten Tusscher KH, Panfilov AV. Alternans and spiral breakup in a human ventricular tissue model. *Am J Physiol Heart Circ Physiol*. 2006;291(3):H1088-100.
265. Land S, Park-Holohan SJ, Smith NP, Dos Remedios CG, Kentish JC, Niederer SA. A model of cardiac contraction based on novel measurements of tension development in human cardiomyocytes. *J Mol Cell Cardiol*. 2017;106:68-83.
266. Niederer SA, Hunter PJ, Smith NP. A quantitative analysis of cardiac myocyte relaxation: a simulation study. *Biophys J*. 2006;90(5):1697-722.
267. Rice JJ, Wang F, Bers DM, de Tombe PP. Approximate model of cooperative activation and crossbridge cycling in cardiac muscle using ordinary differential equations. *Biophys J*. 2008;95(5):2368-90.
268. Niederer SA, Smith NP. A mathematical model of the slow force response to stretch in rat ventricular myocytes. *Biophys J*. 2007;92(11):4030-44.
269. Zile MA, Trayanova NA. Rate-dependent force, intracellular calcium, and action potential voltage alternans are modulated by sarcomere length and heart failure induced-remodeling of thin filament regulation in human heart failure: A myocyte modeling study. *Prog Biophys Mol Biol*. 2016;120(1-3):270-80.
270. Timmermann V, Dejgaard LA, Haugaa KH, Edwards AG, Sundnes J, McCulloch AD, et al. An integrative appraisal of mechano-electric feedback mechanisms in the heart. *Prog Biophys Mol Biol*. 2017;130(Pt B):404-17.
271. Healy SN, McCulloch AD. An ionic model of stretch-activated and stretch-modulated currents in rabbit ventricular myocytes. *Europace*. 2005;7 Suppl 2:128-34.
272. Pueyo E, Orini M, Rodriguez JF, Taggart P. Interactive effect of beta-adrenergic stimulation and mechanical stretch on low-frequency oscillations of ventricular action potential duration in humans. *J Mol Cell Cardiol*. 2016;97:93-105.
273. Campbell SG, Flaim SN, Leem CH, McCulloch AD. Mechanisms of transmurally varying myocyte electromechanics in an integrated computational model. *Philos Trans A Math Phys Eng Sci*. 2008;366(1879):3361-80.
274. Iribe G, Kohl P, Noble D. Modulatory effect of calmodulin-dependent kinase II (CaMKII) on sarcoplasmic reticulum  $Ca^{2+}$  handling and interval-force relations: a modelling study. *Philos Trans A Math Phys Eng Sci*. 2006;364(1842):1107-33.
275. Solovyova O, Vikulova N, Katsnelson LB, Markhasin VS, Noble P, Garny A, et al. Mechanical interaction of heterogeneous cardiac muscle segments in silico: effects on  $Ca^{2+}$  handling and action potential. *International Journal of Bifurcation and Chaos*. 2003;13(12):3757-82.
276. Markhasin VS, Solovyova O, Katsnelson LB, Protsenko Y, Kohl P, Noble D. Mechano-electric interactions in heterogeneous myocardium: development of fundamental experimental and theoretical models. *Prog Biophys Mol Biol*. 2003;82(1-3):207-20.
277. Matsuoka S, Sarai N, Kuratomi S, Ono K, Noma A. Role of individual ionic current systems in ventricular cells hypothesized by a model study. *Jpn J Physiol*. 2003;53(2):105-23.
278. Sachse FB, Seemann G, Chaisaowong K, Weiss D. Quantitative reconstruction of cardiac electromechanics in human myocardium: assembly of electrophysiologic

## References

- and tension generation models. *J Cardiovasc Electrophysiol.* 2003;14(10 Suppl):S210-8.
279. Chugh SS, Havmoeller R, Narayanan K, Singh D, Rienstra M, Benjamin EJ, et al. Worldwide epidemiology of atrial fibrillation: a Global Burden of Disease 2010 Study. *Circulation.* 2014;129(8):837-47.
280. Roth GA, Huffman MD, Moran AE, Feigin V, Mensah GA, Naghavi M, et al. Global and regional patterns in cardiovascular mortality from 1990 to 2013. *Circulation.* 2015;132(17):1667-78.
281. Morillo CA, Banerjee A, Perel P, Wood D, Jouven X. Atrial fibrillation: the current epidemic. *J Geriatr Cardiol.* 2017;14(3):195-203.
282. Houser SR. Role of RyR2 phosphorylation in heart failure and arrhythmias: protein kinase A-mediated hyperphosphorylation of the ryanodine receptor at serine 2808 does not alter cardiac contractility or cause heart failure and arrhythmias. *Circ Res.* 2014;114(8):1320-7; discussion 7.
283. Arora R, Aistrup GL, Supple S, Frank C, Singh J, Tai S, et al. Regional distribution of T-tubule density in left and right atria in dogs. *Heart Rhythm.* 2017;14(2):273-81.
284. McNutt NS, Fawcett DW. The ultrastructure of the cat myocardium. II. Atrial muscle. *J Cell Biol.* 1969;42(1):46-67.
285. Kirk MM, Izu LT, Chen-Izu Y, McCulle SL, Wier WG, Balke CW, et al. Role of the transverse-axial tubule system in generating calcium sparks and calcium transients in rat atrial myocytes. *J Physiol.* 2003;547(Pt 2):441-51.
286. Dibb KM, Clarke JD, Eisner DA, Richards MA, Trafford AW. A functional role for transverse (t-) tubules in the atria. *J Mol Cell Cardiol.* 2013;58:84-91.
287. Yue X, Zhang R, Kim B, Ma A, Philipson KD, Goldhaber JJ. Heterogeneity of transverse-axial tubule system in mouse atria: Remodeling in atrial-specific Na<sup>+</sup>-Ca<sup>2+</sup> exchanger knockout mice. *J Mol Cell Cardiol.* 2017;108:50-60.
288. Dyba M, Jakobs S, Hell SW. Immunofluorescence stimulated emission depletion microscopy. *Nat Biotechnol.* 2003;21(11):1303-4.
289. Muller T, Schumann C, Kraegeloh A. STED microscopy and its applications: new insights into cellular processes on the nanoscale. *Chemphyschem.* 2012;13(8):1986-2000.
290. Tanaka H, Masumiya H, Sekine T, Kase J, Kawanishi T, Hayakawa T, et al. Involvement of Ca<sup>2+</sup> waves in excitation-contraction coupling of rat atrial cardiomyocytes. *Life Sci.* 2001;70(6):715-26.
291. Woo SH, Cleemann L, Morad M. Ca<sup>2+</sup> current-gated focal and local Ca<sup>2+</sup> release in rat atrial myocytes: evidence from rapid 2-D confocal imaging. *J Physiol.* 2002;543(Pt 2):439-53.
292. Loughrey CM, Smith GL, MacEachern KE. Comparison of Ca<sup>2+</sup> release and uptake characteristics of the sarcoplasmic reticulum in isolated horse and rabbit cardiomyocytes. *Am J Physiol Heart Circ Physiol.* 2004;287(3):H1149-59.
293. Chen-Izu Y, McCulle SL, Ward CW, Soeller C, Allen BM, Rabang C, et al. Three-dimensional distribution of ryanodine receptor clusters in cardiac myocytes. *Biophys J.* 2006;91(1):1-13.
294. Musa H, Lei M, Honjo H, Jones SA, Dobrzynski H, Lancaster MK, et al. Heterogeneous expression of Ca<sup>2+</sup> handling proteins in rabbit sinoatrial node. *J Histochem Cytochem.* 2002;50(3):311-24.

295. Dan P, Lin E, Huang J, Biln P, Tibbits GF. Three-dimensional distribution of cardiac  $\text{Na}^+$ - $\text{Ca}^{2+}$  exchanger and ryanodine receptor during development. *Biophys J*. 2007;93(7):2504-18.
296. Chen PS, Chen LS, Fishbein MC, Lin SF, Nattel S. Role of the autonomic nervous system in atrial fibrillation: pathophysiology and therapy. *Circ Res*. 2014;114(9):1500-15.
297. Vincenti A, Brambilla R, Fumagalli MG, Merola R, Pedretti S. Onset mechanism of paroxysmal atrial fibrillation detected by ambulatory Holter monitoring. *Europace*. 2006;8(3):204-10.
298. MacLennan DH, Chen SR. Store overload-induced  $\text{Ca}^{2+}$  release as a triggering mechanism for CPVT and MH episodes caused by mutations in RYR and CASQ genes. *J Physiol*. 2009;587(Pt 13):3113-5.
299. Enriquez A, Antzelevitch C, Bismah V, Baranchuk A. Atrial fibrillation in inherited cardiac channelopathies: From mechanisms to management. *Heart Rhythm*. 2016;13(9):1878-84.
300. Morillo CA, Klein GJ, Jones DL, Guiraudon CM. Chronic rapid atrial pacing. Structural, functional, and electrophysiological characteristics of a new model of sustained atrial fibrillation. *Circulation*. 1995;91(5):1588-95.
301. Brundel BJ, Henning RH, Kampinga HH, Van Gelder IC, Crijns HJ. Molecular mechanisms of remodeling in human atrial fibrillation. *Cardiovasc Res*. 2002;54(2):315-24.
302. Goette A, Kalman JM, Aguinaga L, Akar J, Cabrera JA, Chen SA, et al. EHRA/HRS/APHRS/SOLAECE expert consensus on atrial cardiomyopathies: definition, characterization, and clinical implication. *Europace*. 2016;18(10):1455-90.
303. Lenaerts I, Bito V, Heinzl FR, Driesen RB, Holemans P, D'Hooge J, et al. Ultrastructural and functional remodeling of the coupling between  $\text{Ca}^{2+}$  influx and sarcoplasmic reticulum  $\text{Ca}^{2+}$  release in right atrial myocytes from experimental persistent atrial fibrillation. *Circ Res*. 2009;105(9):876-85.
304. Hiess F, Vallmitjana A, Wang R, Cheng H, ter Keurs HE, Chen J, et al. Distribution and Function of Cardiac Ryanodine Receptor Clusters in Live Ventricular Myocytes. *J Biol Chem*. 2015;290(33):20477-87.
305. Best JM, Kamp TJ. Different subcellular populations of L-type  $\text{Ca}^{2+}$  channels exhibit unique regulation and functional roles in cardiomyocytes. *J Mol Cell Cardiol*. 2012;52(2):376-87.
306. Hake J, Edwards AG, Yu Z, Kekenus-Huskey PM, Michailova AP, McCammon JA, et al. Modelling cardiac calcium sparks in a three-dimensional reconstruction of a calcium release unit. *J Physiol*. 2012;590(18):4403-22.
307. Zahradnikova A, Zahradnik I. Construction of calcium release sites in cardiac myocytes. *Front Physiol*. 2012;3:322.
308. Wescott AP, Jafri MS, Lederer WJ, Williams GS. Ryanodine receptor sensitivity governs the stability and synchrony of local calcium release during cardiac excitation-contraction coupling. *J Mol Cell Cardiol*. 2016;92:82-92.
309. Song Z, Liu MB, Qu Z. Transverse tubular network structures in the genesis of intracellular calcium alternans and triggered activity in cardiac cells. *J Mol Cell Cardiol*. 2018;114:288-99.

## References

310. Thul R, Coombes S, Bootman MD. Persistence of pro-arrhythmic spatio-temporal calcium patterns in atrial myocytes: a computational study of ping waves. *Front Physiol.* 2012;3:279.
311. Filardo G, Damiano RJ, Jr., Ailawadi G, Thourani VH, Pollock BD, Sass DM, et al. Epidemiology of new-onset atrial fibrillation following coronary artery bypass graft surgery. *Heart.* 2018;104(12):985-92.
312. Ahlsson A, Fengsrud E, Bodin L, Englund A. Postoperative atrial fibrillation in patients undergoing aortocoronary bypass surgery carries an eightfold risk of future atrial fibrillation and a doubled cardiovascular mortality. *Eur J Cardiothorac Surg.* 2010;37(6):1353-9.
313. Melduni RM, Schaff HV, Bailey KR, Cha SS, Ammash NM, Seward JB, et al. Implications of new-onset atrial fibrillation after cardiac surgery on long-term prognosis: a community-based study. *Am Heart J.* 2015;170(4):659-68.
314. Dobrev D, Aguilar M, Heijman J, Guichard JB, Nattel S. Postoperative atrial fibrillation: mechanisms, manifestations and management. *Nat Rev Cardiol.* 2019;16(7):417-36.
315. Ha AC, Mazer CD, Verma S, Yanagawa B, Verma A. Management of postoperative atrial fibrillation after cardiac surgery. *Curr Opin Cardiol.* 2016;31(2):183-90.
316. Swartz MF, Fink GW, Lutz CJ, Taffet SM, Berenfeld O, Vikstrom KL, et al. Left versus right atrial difference in dominant frequency, K<sup>+</sup> channel transcripts, and fibrosis in patients developing atrial fibrillation after cardiac surgery. *Heart Rhythm.* 2009;6(10):1415-22.
317. Swartz MF, Fink GW, Sarwar MF, Hicks GL, Yu Y, Hu R, et al. Elevated pre-operative serum peptides for collagen I and III synthesis result in post-surgical atrial fibrillation. *J Am Coll Cardiol.* 2012;60(18):1799-806.
318. Goette A, Juenemann G, Peters B, Klein HU, Roessner A, Huth C, et al. Determinants and consequences of atrial fibrosis in patients undergoing open heart surgery. *Cardiovasc Res.* 2002;54(2):390-6.
319. Workman AJ, Pau D, Redpath CJ, Marshall GE, Russell JA, Kane KA, et al. Post-operative atrial fibrillation is influenced by beta-blocker therapy but not by pre-operative atrial cellular electrophysiology. *J Cardiovasc Electrophysiol.* 2006;17(11):1230-8.
320. Ucar HI, Tok M, Atalar E, Dogan OF, Oc M, Farsak B, et al. Predictive significance of plasma levels of interleukin-6 and high-sensitivity C-reactive protein in atrial fibrillation after coronary artery bypass surgery. *Heart Surg Forum.* 2007;10(2):E131-5.
321. Maesen B, Nijs J, Maessen J, Alessie M, Schotten U. Post-operative atrial fibrillation: a maze of mechanisms. *Europace.* 2012;14(2):159-74.
322. Kaireviciute D, Blann AD, Balakrishnan B, Lane DA, Patel JV, Uzdavinyas G, et al. Characterisation and validity of inflammatory biomarkers in the prediction of post-operative atrial fibrillation in coronary artery disease patients. *Thromb Haemost.* 2010;104(1):122-7.
323. Pretorius M, Donahue BS, Yu C, Greelish JP, Roden DM, Brown NJ. Plasminogen activator inhibitor-1 as a predictor of postoperative atrial fibrillation after cardiopulmonary bypass. *Circulation.* 2007;116(11 Suppl):I1-7.
324. Jacob KA, Nathoe HM, Dieleman JM, van Osch D, Kluin J, van Dijk D. Inflammation in new-onset atrial fibrillation after cardiac surgery: a systematic review. *Eur J Clin Invest.* 2014;44(4):402-28.

325. Willeford A, Suetomi T, Nickle A, Hoffman HM, Miyamoto S, Heller Brown J. CaMKII $\delta$ -mediated inflammatory gene expression and inflammasome activation in cardiomyocytes initiate inflammation and induce fibrosis. *JCI Insight*. 2018;3(12).
326. Suetomi T, Willeford A, Brand CS, Cho Y, Ross RS, Miyamoto S, et al. Inflammation and NLRP3 Inflammasome Activation Initiated in Response to Pressure Overload by Ca<sup>2+</sup>/Calmodulin-Dependent Protein Kinase II  $\delta$  Signaling in Cardiomyocytes Are Essential for Adverse Cardiac Remodeling. *Circulation*. 2018;138(22):2530-44.
327. Heijman J, Muna AP, Veleva T, Molina CE, Sutanto H, Tekook MA, et al. Atrial Myocyte NLRP3/CaMKII Nexus Forms a Substrate for Post-Operative Atrial Fibrillation. *Circ Res*. 2020.
328. Duncan DJ, Yang Z, Hopkins PM, Steele DS, Harrison SM. TNF- $\alpha$  and IL-1 $\beta$  increase Ca<sup>2+</sup> leak from the sarcoplasmic reticulum and susceptibility to arrhythmia in rat ventricular myocytes. *Cell Calcium*. 2010;47(4):378-86.
329. Shannon TR, Ginsburg KS, Bers DM. Quantitative assessment of the SR Ca<sup>2+</sup> leak-load relationship. *Circ Res*. 2002;91(7):594-600.
330. Sugishita K, Kinugawa K, Shimizu T, Harada K, Matsui H, Takahashi T, et al. Cellular basis for the acute inhibitory effects of IL-6 and TNF- $\alpha$  on excitation-contraction coupling. *J Mol Cell Cardiol*. 1999;31(8):1457-67.
331. Lee SH, Chen YC, Chen YJ, Chang SL, Tai CT, Wongcharoen W, et al. Tumor necrosis factor- $\alpha$  alters calcium handling and increases arrhythmogenesis of pulmonary vein cardiomyocytes. *Life Sci*. 2007;80(19):1806-15.
332. Kao YH, Chen YC, Cheng CC, Lee TI, Chen YJ, Chen SA. Tumor necrosis factor- $\alpha$  decreases sarcoplasmic reticulum Ca<sup>2+</sup>-ATPase expressions via the promoter methylation in cardiomyocytes. *Crit Care Med*. 2010;38(1):217-22.
333. Hobai IA, Morse JC, Siwik DA, Colucci WS. Lipopolysaccharide and cytokines inhibit rat cardiomyocyte contractility in vitro. *J Surg Res*. 2015;193(2):888-901.
334. McTiernan CF, Lemster BH, Frye C, Brooks S, Combes A, Feldman AM. Interleukin-1  $\beta$  inhibits phospholamban gene expression in cultured cardiomyocytes. *Circ Res*. 1997;81(4):493-503.
335. Sutanto H, Lyon A, Lumens J, Schotten U, Dobrev D, Heijman J. Cardiomyocyte calcium handling in health and disease: Insights from in vitro and in silico studies. *Prog Biophys Mol Biol*. 2020.
336. Bartos DC, Morotti S, Ginsburg KS, Grandi E, Bers DM. Quantitative analysis of the Ca<sup>2+</sup>-dependent regulation of delayed rectifier K<sup>+</sup> current I<sub>Ks</sub> in rabbit ventricular myocytes. *J Physiol*. 2017;595(7):2253-68.
337. Kanaporis G, Blatter LA. Calcium-activated chloride current determines action potential morphology during calcium alternans in atrial myocytes. *J Physiol*. 2016;594(3):699-714.
338. Chang PC, Chen PS. SK channels and ventricular arrhythmias in heart failure. *Trends Cardiovasc Med*. 2015;25(6):508-14.
339. Paulino C, Kalienkova V, Lam AKM, Neldner Y, Dutzler R. Activation mechanism of the calcium-activated chloride channel TMEM16A revealed by cryo-EM. *Nature*. 2017;552(7685):421-5.
340. Grandi E, Pandit SV, Voigt N, Workman AJ, Dobrev D, Jalife J, et al. Human atrial action potential and Ca<sup>2+</sup> model: sinus rhythm and chronic atrial fibrillation. *Circ Res*. 2011;109(9):1055-66.

## References

341. Grandi E. Unpublished. 2020.
342. Schmidt C, Wiedmann F, Voigt N, Zhou XB, Heijman J, Lang S, et al. Upregulation of  $K_{2P3.1}$   $K^+$  current causes action potential shortening in patients with chronic atrial fibrillation. *Circulation*. 2015;132(2):82-92.
343. Grandi E, Dobrev D, Heijman J. Computational modeling: What does it tell us about atrial fibrillation therapy? *Int J Cardiol*. 2019;287:155-61.
344. Clerx M, Collins P, de Lange E, Volders PG. Myokit: A simple interface to cardiac cellular electrophysiology. *Prog Biophys Mol Biol*. 2016;120(1-3):100-14.
345. Liu MB, Ko CY, Song Z, Garfinkel A, Weiss JN, Qu Z. A dynamical threshold for cardiac delayed afterdepolarization-mediated triggered activity. *Biophys J*. 2016;111(11):2523-33.
346. Sutanto H, Cluitmans MJM, Dobrev D, Volders PGA, Bebarova M, Heijman J. Acute effects of alcohol on cardiac electrophysiology and arrhythmogenesis: Insights from multiscale in silico analyses. *J Mol Cell Cardiol*. 2020;146:69-83.
347. Pandit SV, Jalife J. Rotors and the dynamics of cardiac fibrillation. *Circ Res*. 2013;112(5):849-62.
348. Yin D, Hsieh YC, Tsai WC, Wu AZ, Jiang Z, Chan YH, et al. Role of Apamin-Sensitive Calcium-Activated Small-Conductance Potassium Currents on the Mechanisms of Ventricular Fibrillation in Pacing-Induced Failing Rabbit Hearts. *Circ Arrhythm Electrophysiol*. 2017;10(2):e004434.
349. Nerbonne JM, Kass RS. Molecular physiology of cardiac repolarization. *Physiol Rev*. 2005;85(4):1205-53.
350. Duan D. Phenomics of cardiac chloride channels: the systematic study of chloride channel function in the heart. *J Physiol*. 2009;587(Pt 10):2163-77.
351. Zygmunt AC, Gibbons WR. Properties of the calcium-activated chloride current in heart. *J Gen Physiol*. 1992;99(3):391-414.
352. Sorota S. Insights into the structure, distribution and function of the cardiac chloride channels. *Cardiovasc Res*. 1999;42(2):361-76.
353. Li N, Wang T, Wang W, Cutler MJ, Wang Q, Voigt N, et al. Inhibition of CaMKII phosphorylation of RyR2 prevents induction of atrial fibrillation in FKBP12.6 knockout mice. *Circ Res*. 2012;110(3):465-70.
354. Takanari H, Bourgonje VJ, Fontes MS, Raaijmakers AJ, Driessen H, Jansen JA, et al. Calmodulin/CaMKII inhibition improves intercellular communication and impulse propagation in the heart and is antiarrhythmic under conditions when fibrosis is absent. *Cardiovasc Res*. 2016;111(4):410-21.
355. Workman AJ. Cardiac adrenergic control and atrial fibrillation. *Naunyn Schmiedebergs Arch Pharmacol*. 2010;381(3):235-49.
356. Nassal D, Gratz D, Hund TJ. Challenges and Opportunities for Therapeutic Targeting of Calmodulin Kinase II in Heart. *Front Pharmacol*. 2020;11:35.
357. Jost N, Virag L, Comtois P, Ordog B, Szuts V, Seprenyi G, et al. Ionic mechanisms limiting cardiac repolarization reserve in humans compared to dogs. *J Physiol*. 2013;591(17):4189-206.
358. Bell S, Daskalopoulou M, Rapsomaniki E, George J, Britton A, Bobak M, et al. Association between clinically recorded alcohol consumption and initial presentation of 12 cardiovascular diseases: population based cohort study using linked health records. *BMJ*. 2017;356:j909.
359. Kanny D, Naimi TS, Liu Y, Lu H, Brewer RD. Annual total binge drinks consumed by U.S. adults, 2015. *Am J Prev Med*. 2018;54(4):486-96.

360. Busto Miramontes A, Moure-Rodriguez L, Diaz-Geada A, Rodriguez-Holguin S, Corral M, Cadaveira F, et al. Heavy drinking and non-medical use of prescription drugs among university students: A 9-year follow-up. *Int J Environ Res Public Health*. 2019;16(16):2939.
361. Tonelo D, Providencia R, Goncalves L. Holiday heart syndrome revisited after 34 years. *Arq Bras Cardiol*. 2013;101(2):183-9.
362. Brunner S, Herbel R, Drobesch C, Peters A, Massberg S, Kaab S, et al. Alcohol consumption, sinus tachycardia, and cardiac arrhythmias at the Munich Oktoberfest: results from the Munich Beer Related Electrocardiogram Workup Study (MunichBREW). *Eur Heart J*. 2017;38(27):2100-6.
363. Voskoboinik A, Kalman JM, De Silva A, Nicholls T, Costello B, Nanayakkara S, et al. Alcohol abstinence in drinkers with atrial fibrillation. *N Engl J Med*. 2020;382(1):20-8.
364. Voskoboinik A, Prabhu S, Ling LH, Kalman JM, Kistler PM. Alcohol and atrial fibrillation: a sobering review. *J Am Coll Cardiol*. 2016;68(23):2567-76.
365. Bebarova M, Matejovic P, Pasek M, Ohlidalova D, Jansova D, Simurdova M, et al. Effect of ethanol on action potential and ionic membrane currents in rat ventricular myocytes. *Acta Physiol (Oxf)*. 2010;200(4):301-14.
366. Bebarova M, Matejovic P, Pasek M, Simurdova M, Simurda J. Dual effect of ethanol on inward rectifier potassium current  $I_{K1}$  in rat ventricular myocytes. *J Physiol Pharmacol*. 2014;65(4):497-509.
367. Bebarova M, Matejovic P, Pasek M, Horakova Z, Hosek J, Simurdova M, et al. Effect of ethanol at clinically relevant concentrations on atrial inward rectifier potassium current sensitive to acetylcholine. *Naunyn Schmiedebergs Arch Pharmacol*. 2016;389(10):1049-58.
368. Hu H, Zhou J, Sun Q, Yu XJ, Zhang HL, Ma X, et al. Effects of ethanol on action potential of rat myocardium and human  $K_v1.5$  channel. *Sheng Li Xue Bao*. 2011;63(3):219-24.
369. Himmel HM. Suitability of commonly used excipients for electrophysiological in-vitro safety pharmacology assessment of effects on hERG potassium current and on rabbit Purkinje fiber action potential. *J Pharmacol Toxicol Methods*. 2007;56(2):145-58.
370. Muströph J, Wagemann O, Lebek S, Tarnowski D, Ackermann J, Drzymalski M, et al. SR  $Ca^{2+}$ -leak and disordered excitation-contraction coupling as the basis for arrhythmogenic and negative inotropic effects of acute ethanol exposure. *J Mol Cell Cardiol*. 2018;116:81-90.
371. Muströph J, Lebek S, Maier LS, Neef S. Mechanisms of cardiac ethanol toxicity and novel treatment options. *Pharmacol Ther*. 2019;197:1-10.
372. Piano MR. Alcohol's effects on the cardiovascular system. *Alcohol Res*. 2017;38(2):219-41.
373. Courtemanche M, Ramirez RJ, Nattel S. Ionic mechanisms underlying human atrial action potential properties: insights from a mathematical model. *Am J Physiol*. 1998;275(1):H301-21.
374. Passini E, Mincholé A, Coppini R, Cerbai E, Rodríguez B, Severi S, et al. Mechanisms of pro-arrhythmic abnormalities in ventricular repolarisation and anti-arrhythmic therapies in human hypertrophic cardiomyopathy. *J Mol Cell Cardiol*. 2016;96:72-81.

## References

375. Hegyi B, Bossuyt J, Griffiths LG, Shimkunus R, Coulibaly Z, Jian Z, et al. Complex electrophysiological remodeling in postinfarction ischemic heart failure. *Proc Natl Acad Sci U S A*. 2018;115(13):E3036-E44.
376. Clayton RH. Dispersion of recovery and vulnerability to re-entry in a model of human atrial tissue with simulated diffuse and focal patterns of fibrosis. *Front Physiol*. 2018;9:1052.
377. Abd-Elmoniem KZ, Tomas MS, Sasano T, Soleimanifard S, Vonken EJ, Youssef A, et al. Assessment of distribution and evolution of mechanical dyssynchrony in a porcine model of myocardial infarction by cardiovascular magnetic resonance. *J Cardiovasc Magn Reson*. 2012;14:1.
378. Ng FS, Kalindjian JM, Cooper SA, Chowdhury RA, Patel PM, Dupont E, et al. Enhancement of gap junction function during acute myocardial infarction modifies healing and reduces late ventricular arrhythmia susceptibility. *JACC Clin Electrophysiol*. 2016;2(5):574-82.
379. Sobie EA. Parameter sensitivity analysis in electrophysiological models using multivariable regression. *Biophys J*. 2009;96(4):1264-74.
380. Ellinwood N, Dobrev D, Morotti S, Grandi E. In Silico Assessment of Efficacy and Safety of  $I_{Kur}$  Inhibitors in Chronic Atrial Fibrillation: Role of Kinetics and State-Dependence of Drug Binding. *Front Pharmacol*. 2017;8:799.
381. Sanchez C, Bueno-Orovio A, Wettwer E, Loose S, Simon J, Ravens U, et al. Inter-subject variability in human atrial action potential in sinus rhythm versus chronic atrial fibrillation. *PLoS One*. 2014;9(8):e105897.
382. Britton OJ, Abi-Gerges N, Page G, Ghetti A, Miller PE, Rodriguez B. Quantitative Comparison of Effects of Dofetilide, Sotalol, Quinidine, and Verapamil between Human Ex vivo Trabeculae and In silico Ventricular Models Incorporating Inter-Individual Action Potential Variability. *Front Physiol*. 2017;8:597.
383. Dasgupta A. Alcohol a double-edged sword: Health benefits with moderate consumption but a health hazard with excess alcohol intake. In: Dasgupta A, editor. *Alcohol, Drugs, Genes and the Clinical Laboratory*: Academic Press; 2017. p. 1-21.
384. Gould L, Reddy CV, Becker W, Oh KC, Kim SG. Electrophysiologic properties of alcohol in man. *J Electrocardiol*. 1978;11(3):219-26.
385. Zhang H, Ruan H, Rahmutula D, Wilson E, Marcus GM, Vedantham V, et al. Effect of acute and chronic ethanol on atrial fibrillation vulnerability in rats. *Heart Rhythm*. 2020;17(4):654-60.
386. Akar FG, Nass RD, Hahn S, Cingolani E, Shah M, Hesketh GG, et al. Dynamic changes in conduction velocity and gap junction properties during development of pacing-induced heart failure. *Am J Physiol Heart Circ Physiol*. 2007;293(2):H1223-30.
387. Coronel R, Wilders R, Verkerk AO, Wiegerinck RF, Benoist D, Bernus O. Electrophysiological changes in heart failure and their implications for arrhythmogenesis. *Biochim Biophys Acta*. 2013;1832(12):2432-41.
388. Nguyen TP, Qu Z, Weiss JN. Cardiac fibrosis and arrhythmogenesis: the road to repair is paved with perils. *J Mol Cell Cardiol*. 2014;70:83-91.
389. Fernandez-Sola J. The effects of ethanol on the heart: alcoholic cardiomyopathy. *Nutrients*. 2020;12(2):e572.
390. Disertori M, Mase M, Ravelli F. Myocardial fibrosis predicts ventricular tachyarrhythmias. *Trends Cardiovasc Med*. 2017;27(5):363-72.

391. Sachetto R, Alonso S, Dos Santos RW. Killing many birds with two stones: hypoxia and fibrosis can generate ectopic beats in a human ventricular model. *Front Physiol.* 2018;9:764.
392. Klein G, Gardiwal A, Schaefer A, Panning B, Breitmeier D. Effect of ethanol on cardiac single sodium channel gating. *Forensic Sci Int.* 2007;171(2-3):131-5.
393. Simurda J, Simurdova M, Bebarova M. Inward rectifying potassium currents resolved into components: modeling of complex drug actions. *Pflugers Arch.* 2018;470(2):315-25.
394. Sutanto H, Lyon A, Lumens J, Schotten U, Dobrev D, Heijman J. Cardiomyocyte calcium handling in health and disease: Insights from in vitro and in silico studies. *Prog Biophys Mol Biol.* 2020;pii: S0079-6107(20)30016-X.
395. Gardner JD, Mouton AJ. Alcohol effects on cardiac function. *Compr Physiol.* 2015;5(2):791-802.
396. Gemes K, Malmo V, Laugsand LE, Loennechen JP, Ellekjaer H, Laszlo KD, et al. Does moderate drinking increase the risk of atrial fibrillation? The Norwegian HUNT (Nord-Trondelag Health) Study. *J Am Heart Assoc.* 2017;6(10):e007094.
397. Pandit SV, Berenfeld O, Anumonwo JM, Zaritski RM, Kneller J, Nattel S, et al. Ionic determinants of functional reentry in a 2-D model of human atrial cells during simulated chronic atrial fibrillation. *Biophys J.* 2005;88(6):3806-21.
398. Schram G, Pourrier M, Melnyk P, Nattel S. Differential distribution of cardiac ion channel expression as a basis for regional specialization in electrical function. *Circ Res.* 2002;90(9):939-50.
399. Djousse L, Gaziano JM. Alcohol consumption and heart failure: a systematic review. *Curr Atheroscler Rep.* 2008;10(2):117-20.
400. Lopez-Perez A, Sebastian R, Izquierdo M, Ruiz R, Bishop M, Ferrero JM. Personalized cardiac computational models: from clinical data to simulation of infarct-related ventricular tachycardia. *Front Physiol.* 2019;10:580.
401. Balbao CE, de Paola AA, Felon G. Effects of alcohol on atrial fibrillation: myths and truths. *Ther Adv Cardiovasc Dis.* 2009;3(1):53-63.
402. Yang B, Li C, Sun J, Wang X, Liu X, Yang C, et al. Inhibition of potassium currents is involved in antiarrhythmic effect of moderate ethanol on atrial fibrillation. *Toxicol Appl Pharmacol.* 2017;322:89-96.
403. Picones A, Keung E, Timpe LC. Unitary conductance variation in Kir2.1 and in cardiac inward rectifier potassium channels. *Biophys J.* 2001;81(4):2035-49.
404. Benjamin EJ, Virani SS, Callaway CW, Chamberlain AM, Chang AR, Cheng S, et al. Heart Disease and Stroke Statistics-2018 Update: A Report From the American Heart Association. *Circulation.* 2018;137(12):e67-e492.
405. Burashnikov A, Antzelevitch C. New developments in atrial antiarrhythmic drug therapy. *Nat Rev Cardiol.* 2010;7(3):139-48.
406. Dan GA, Dobrev D. Antiarrhythmic drugs for atrial fibrillation: Imminent impulses are emerging. *Int J Cardiol Heart Vasc.* 2018;21:11-5.
407. Lafuente-Lafuente C, Valembois L, Bergmann JF, Belmin J. Antiarrhythmics for maintaining sinus rhythm after cardioversion of atrial fibrillation. *Cochrane Database Syst Rev.* 2015(3):CD005049.
408. Dan GA, Martinez-Rubio A, Agewall S, Boriani G, Borggrefe M, Gaita F, et al. Antiarrhythmic drugs-clinical use and clinical decision making: a consensus document from the European Heart Rhythm Association (EHRA) and European Society of Cardiology (ESC) Working Group on Cardiovascular Pharmacology,

## References

- endorsed by the Heart Rhythm Society (HRS), Asia-Pacific Heart Rhythm Society (APHRS) and International Society of Cardiovascular Pharmacotherapy (ISCP). *Europace*. 2018;20(5):731-2an.
409. Lei M, Wu L, Terrar DA, Huang CL. Modernized Classification of Cardiac Antiarrhythmic Drugs. *Circulation*. 2018;138(17):1879-96.
  410. Antzelevitch C. Ionic, molecular, and cellular bases of QT-interval prolongation and torsade de pointes. *Europace*. 2007;9 Suppl 4:iv4-15.
  411. Heijman J, Guichard JB, Dobrev D, Nattel S. Translational Challenges in Atrial Fibrillation. *Circ Res*. 2018;122(5):752-73.
  412. Weirich J, Antoni H. Rate-dependence of antiarrhythmic and proarrhythmic properties of class I and class III antiarrhythmic drugs. *Basic Res Cardiol*. 1998;93 Suppl 1:125-32.
  413. Barandi L, Virag L, Jost N, Horvath Z, Koncz I, Papp R, et al. Reverse rate-dependent changes are determined by baseline action potential duration in mammalian and human ventricular preparations. *Basic Res Cardiol*. 2010;105(3):315-23.
  414. Dobrev D, Nattel S. New antiarrhythmic drugs for treatment of atrial fibrillation. *Lancet*. 2010;375(9721):1212-23.
  415. Arts T, Delhaas T, Bovendeerd P, Verbeek X, Prinzen FW. Adaptation to mechanical load determines shape and properties of heart and circulation: the CircAdapt model. *Am J Physiol Heart Circ Physiol*. 2005;288(4):H1943-54.
  416. van Oosterom A, Oostendorp TF. ECGSIM: an interactive tool for studying the genesis of QRST waveforms. *Heart*. 2004;90(2):165-8.
  417. Puglisi JL, Bers DM. LabHEART: an interactive computer model of rabbit ventricular myocyte ion channels and Ca transport. *Am J Physiol Cell Physiol*. 2001;281(6):C2049-60.
  418. da Silva RR, Bissaco MA, Goroso DG. MioLab, a rat cardiac contractile force simulator: Applications to teaching cardiac cell physiology and biophysics. *Comput Methods Programs Biomed*. 2015;122(3):480-90.
  419. de Boer TP, van der Werf S, Hennekam B, Nickerson DP, Garry A, Gerbrands M, et al. eSolv, a CellML-based simulation front-end for online teaching. *Adv Physiol Educ*. 2017;41(3):425-7.
  420. Onal B, Gratz D, Hund T. LongQt: A cardiac electrophysiology simulation platform. *MethodsX*. 2016;3:589-99.
  421. Passini E, Britton OJ, Lu HR, Rohrbacher J, Hermans AN, Gallacher DJ, et al. Human In Silico Drug Trials Demonstrate Higher Accuracy than Animal Models in Predicting Clinical Pro-Arrhythmic Cardiotoxicity. *Front Physiol*. 2017;8:668.
  422. Bondarenko VE, Szigeti GP, Bett GC, Kim SJ, Rasmusson RL. Computer model of action potential of mouse ventricular myocytes. *Am J Physiol Heart Circ Physiol*. 2004;287(3):H1378-403.
  423. Luo CH, Rudy Y. A model of the ventricular cardiac action potential. Depolarization, repolarization, and their interaction. *Circ Res*. 1991;68(6):1501-26.
  424. Faber GM, Rudy Y. Action potential and contractility changes in  $[Na^+]_i$  overloaded cardiac myocytes: a simulation study. *Biophys J*. 2000;78(5):2392-404.
  425. Mahajan A, Shiferaw Y, Sato D, Baher A, Olcese R, Xie LH, et al. A rabbit ventricular action potential model replicating cardiac dynamics at rapid heart rates. *Biophys J*. 2008;94(2):392-410.

426. Decker KF, Heijman J, Silva JR, Hund TJ, Rudy Y. Properties and ionic mechanisms of action potential adaptation, restitution, and accommodation in canine epicardium. *Am J Physiol Heart Circ Physiol*. 2009;296(4):H1017-26.
427. Courtemanche M, Ramirez RJ, Nattel S. Ionic mechanisms underlying human atrial action potential properties: insights from a mathematical model. *Am J Physiol*. 1998;275(1 Pt 2):H301-21.
428. Schmidt C, Wiedmann F, Voigt N, Zhou XB, Heijman J, Lang S, et al. Upregulation of K(2P)3.1 K<sup>+</sup> Current Causes Action Potential Shortening in Patients With Chronic Atrial Fibrillation. *Circulation*. 2015;132(2):82-92.
429. Stewart P, Aslanidi OV, Noble D, Noble PJ, Boyett MR, Zhang H. Mathematical models of the electrical action potential of Purkinje fibre cells. *Philos Trans A Math Phys Eng Sci*. 2009;367(1896):2225-55.
430. Sampson KJ, Iyer V, Marks AR, Kass RS. A computational model of Purkinje fibre single cell electrophysiology: implications for the long QT syndrome. *J Physiol*. 2010;588(Pt 14):2643-55.
431. Moreno JD, Zhu ZI, Yang PC, Bankston JR, Jeng MT, Kang C, et al. A computational model to predict the effects of class I anti-arrhythmic drugs on ventricular rhythms. *Sci Transl Med*. 2011;3(98):98ra83.
432. Hondeghem LM, Katzung BG. Antiarrhythmic agents: the modulated receptor mechanism of action of sodium and calcium channel-blocking drugs. *Annu Rev Pharmacol Toxicol*. 1984;24:387-423.
433. Balsler JR. The cardiac sodium channel: gating function and molecular pharmacology. *J Mol Cell Cardiol*. 2001;33(4):599-613.
434. Fedida D, Orth PM, Chen JY, Lin S, Plouvier B, Jung G, et al. The mechanism of atrial antiarrhythmic action of RSD1235. *J Cardiovasc Electrophysiol*. 2005;16(11):1227-38.
435. Bebarova M, Matejovic P, Pasek M, Simurdova M, Simurda J. Effect of ajmaline on action potential and ionic currents in rat ventricular myocytes. *Gen Physiol Biophys*. 2005;24(3):311-25.
436. Fischer F, Vonderlin N, Zitron E, Seyler C, Scherer D, Becker R, et al. Inhibition of cardiac Kv1.5 and Kv4.3 potassium channels by the class Ia anti-arrhythmic ajmaline: mode of action. *Naunyn Schmiedebergs Arch Pharmacol*. 2013;386(11):991-9.
437. Mirams GR, Cui Y, Sher A, Fink M, Cooper J, Heath BM, et al. Simulation of multiple ion channel block provides improved early prediction of compounds' clinical torsadogenic risk. *Cardiovasc Res*. 2011;91(1):53-61.
438. Feng J, Wang Z, Li GR, Nattel S. Effects of class III antiarrhythmic drugs on transient outward and ultra-rapid delayed rectifier currents in human atrial myocytes. *J Pharmacol Exp Ther*. 1997;281(1):384-92.
439. Yue L, Feng JL, Wang Z, Nattel S. Effects of ambasilide, quinidine, flecainide and verapamil on ultra-rapid delayed rectifier potassium currents in canine atrial myocytes. *Cardiovasc Res*. 2000;46(1):151-61.
440. Koidl B, Flaschberger P, Schaffer P, Pelzmann B, Bernhart E, Machler H, et al. Effects of the class III antiarrhythmic drug ambasilide on outward currents in human atrial myocytes. *Naunyn Schmiedebergs Arch Pharmacol*. 1996;353(2):226-32.

## References

441. Walker BD, Singleton CB, Tie H, Bursill JA, Wyse KR, Valenzuela SM, et al. Comparative effects of azimilide and ambasilide on the human ether-a-go-go-related gene (HERG) potassium channel. *Cardiovasc Res*. 2000;48(1):44-58.
442. Kamiya K, Nishiyama A, Yasui K, Hojo M, Sanguinetti MC, Kodama I. Short- and long-term effects of amiodarone on the two components of cardiac delayed rectifier K<sup>+</sup> current. *Circulation*. 2001;103(9):1317-24.
443. Kiehn J, Thomas D, Karle CA, Schols W, Kubler W. Inhibitory effects of the class III antiarrhythmic drug amiodarone on cloned HERG potassium channels. *Naunyn Schmiedebergs Arch Pharmacol*. 1999;359(3):212-9.
444. Crumb WJ, Jr., Vicente J, Johannesen L, Strauss DG. An evaluation of 30 clinical drugs against the comprehensive in vitro proarrhythmia assay (CiPA) proposed ion channel panel. *J Pharmacol Toxicol Methods*. 2016;81:251-62.
445. Kramer J, Obejero-Paz CA, Myatt G, Kuryshev YA, Bruening-Wright A, Verducci JS, et al. MICE models: superior to the HERG model in predicting Torsade de Pointes. *Sci Rep*. 2013;3:2100.
446. Lalevee N, Nargeot J, Barrere-Lemaire S, Gautier P, Richard S. Effects of amiodarone and dronedarone on voltage-dependent sodium current in human cardiomyocytes. *J Cardiovasc Electrophysiol*. 2003;14(8):885-90.
447. Suzuki T, Morishima M, Kato S, Ueda N, Honjo H, Kamiya K. Atrial selectivity in Na<sup>+</sup> channel blockade by acute amiodarone. *Cardiovasc Res*. 2013;98(1):136-44.
448. Watanabe Y, Hara Y, Tamagawa M, Nakaya H. Inhibitory effect of amiodarone on the muscarinic acetylcholine receptor-operated potassium current in guinea pig atrial cells. *J Pharmacol Exp Ther*. 1996;279(2):617-24.
449. De Bruin ML, Pettersson M, Meyboom RH, Hoes AW, Leufkens HG. Anti-HERG activity and the risk of drug-induced arrhythmias and sudden death. *Eur Heart J*. 2005;26(6):590-7.
450. River C. ChanTest Cardiac Channel Panel & SaVety™ Assessment [Available from: <https://www.criver.com/products-services/safety-assessment/safety-pharmacology/vitro-assays/chantest-cardiac-channel-panel-savetytm-assessment?region=3696>].
451. Obejero-Paz CA, Bruening-Wright A, Kramer J, Hawryluk P, Tatalovic M, Dittrich HC, et al. Quantitative Profiling of the Effects of Vanoxerine on Human Cardiac Ion Channels and its Application to Cardiac Risk. *Sci Rep*. 2015;5:17623.
452. Matsuoka S, Nawada T, Hisatome I, Miyamoto J, Hasegawa J, Kotake H, et al. Comparison of Ca<sup>2+</sup> channel inhibitory effects of cibenzoline with verapamil on guinea-pig heart. *Gen Pharmacol*. 1991;22(1):87-91.
453. Sato T, Wu B, Kiyosue T, Arita M. Effects of cibenzoline, a new class Ia antiarrhythmic drug, on various membrane ionic currents and action potentials of guinea-pig ventricular cells. *Naunyn Schmiedebergs Arch Pharmacol*. 1994;350(2):167-73.
454. Zhang S, Zhou Z, Gong Q, Makielski JC, January CT. Mechanism of block and identification of the verapamil binding domain to HERG potassium channels. *Circ Res*. 1999;84(9):989-98.
455. Hanada E, Ohtani H, Hirota M, Uemura N, Nakaya H, Kotaki H, et al. Inhibitory effect of erythromycin on potassium currents in rat ventricular myocytes in comparison with disopyramide. *J Pharm Pharmacol*. 2003;55(7):995-1002.

456. Paul AA, Witchel HJ, Hancox JC. Inhibition of HERG potassium channel current by the class 1a antiarrhythmic agent disopyramide. *Biochem Biophys Res Commun.* 2001;280(5):1243-50.
457. Luo C, Wang K, Zhang H. Modelling the effects of quinidine, disopyramide, and E-4031 on short QT syndrome variant 3 in the human ventricles. *Physiol Meas.* 2017;38(10):1859-73.
458. Weerapura M, Nattel S, Chartier D, Caballero R, Hebert TE. A comparison of currents carried by HERG, with and without coexpression of MiRP1, and the native rapid delayed rectifier current. Is MiRP1 the missing link? *J Physiol.* 2002;540(Pt 1):15-27.
459. Himmel HM, Bussek A, Hoffmann M, Beckmann R, Lohmann H, Schmidt M, et al. Field and action potential recordings in heart slices: correlation with established in vitro and in vivo models. *Br J Pharmacol.* 2012;166(1):276-96.
460. Yang T, Roden DM. Extracellular potassium modulation of drug block of  $I_{Kr}$ . Implications for torsade de pointes and reverse use-dependence. *Circulation.* 1996;93(3):407-11.
461. Yang T, Wathen MS, Felipe A, Tamkun MM, Snyders DJ, Roden DM.  $K^+$  currents and  $K^+$  channel mRNA in cultured atrial cardiac myocytes (AT-1 cells). *Circ Res.* 1994;75(5):870-8.
462. Potet F, Lorinc AN, Chaigne S, Hopkins CR, Venkataraman R, Stepanovic SZ, et al. Identification and characterization of a compound that protects cardiac tissue from human Ether-a-go-go-related gene (hERG)-related drug-induced arrhythmias. *J Biol Chem.* 2012;287(47):39613-25.
463. Gautier P, Guillemare E, Marion A, Bertrand JP, Tourneur Y, Nisato D. Electrophysiologic characterization of dronedarone in guinea pig ventricular cells. *J Cardiovasc Pharmacol.* 2003;41(2):191-202.
464. Varro A, Takacs J, Nemeth M, Hala O, Virag L, Iost N, et al. Electrophysiological effects of dronedarone (SR 33589), a noniodinated amiodarone derivative in the canine heart: comparison with amiodarone. *Br J Pharmacol.* 2001;133(5):625-34.
465. Krafte DS, Davison K, Dugrenier N, Estep K, Josef K, Barchi RL, et al. Pharmacological modulation of human cardiac  $Na^+$  channels. *Eur J Pharmacol.* 1994;266(3):245-54.
466. Paul AA, Witchel HJ, Hancox JC. Inhibition of the current of heterologously expressed HERG potassium channels by flecainide and comparison with quinidine, propafenone and lignocaine. *Br J Pharmacol.* 2002;136(5):717-29.
467. Wang Z, Fermini B, Nattel S. Effects of flecainide, quinidine, and 4-aminopyridine on transient outward and ultrarapid delayed rectifier currents in human atrial myocytes. *J Pharmacol Exp Ther.* 1995;272(1):184-96.
468. Heath BM, Cui Y, Worton S, Lawton B, Ward G, Ballini E, et al. Translation of flecainide- and mexiletine-induced cardiac sodium channel inhibition and ventricular conduction slowing from nonclinical models to clinical. *J Pharmacol Toxicol Methods.* 2011;63(3):258-68.
469. Eldstrom J, Wang Z, Xu H, Pourrier M, Ezrin A, Gibson K, et al. The molecular basis of high-affinity binding of the antiarrhythmic compound vernakalant (RSD1235) to  $Kv1.5$  channels. *Mol Pharmacol.* 2007;72(6):1522-34.

## References

470. Perry M, de Groot MJ, Helliwell R, Leishman D, Tristani-Firouzi M, Sanguinetti MC, et al. Structural determinants of HERG channel block by clofilium and ibutilide. *Mol Pharmacol.* 2004;66(2):240-9.
471. Song W. Human nav1.5 f1486 deletion associated with long-qt syndrome leads to deficiency in inactivation and reduces lidocaine sensitivity: Indiana University; 2011.
472. Wang GK, Russell G, Wang SY. Persistent human cardiac Na<sup>+</sup> currents in stably transfected mammalian cells: Robust expression and distinct open-channel selectivity among Class 1 antiarrhythmics. *Channels (Austin).* 2013;7(4):263-74.
473. Abramochkin DV, Kuzmin VS, Rosenshtraukh LV. A New Class III Antiarrhythmic Drug Niferidil Prolongs Action Potentials in Guinea Pig Atrial Myocardium via Inhibition of Rapid Delayed Rectifier. *Cardiovasc Drugs Ther.* 2017;31(5-6):525-33.
474. Abramochkin DV, Kuzmin VS, Rosenshtraukh LV. Effects of new class III antiarrhythmic drug niferidil on electrical activity in murine ventricular myocardium and their ionic mechanisms. *Naunyn Schmiedebergs Arch Pharmacol.* 2015;388(10):1105-12.
475. Ehlerl FJ, Itoga E, Roeske WR, Yamamura HI. The interaction of [3H]nitrendipine with receptors for calcium antagonists in the cerebral cortex and heart of rats. *Biochem Biophys Res Commun.* 1982;104(3):937-43.
476. Dzimiri N, Almotrefi AA. Comparative effects of procainamide, tocainide and lorcaïnide on Na<sup>+</sup>-K<sup>+</sup>-ATPase in guinea pig heart preparations. *Gen Pharmacol.* 1991;22(2):403-6.
477. Harmer AR, Valentin JP, Pollard CE. On the relationship between block of the cardiac Na<sup>+</sup> channel and drug-induced prolongation of the QRS complex. *Br J Pharmacol.* 2011;164(2):260-73.
478. Cahill SA, Gross GJ. Propafenone and its metabolites preferentially inhibit I<sub>Kr</sub> in rabbit ventricular myocytes. *J Pharmacol Exp Ther.* 2004;308(1):59-65.
479. Gross GJ, Castle NA. Propafenone inhibition of human atrial myocyte repolarizing currents. *J Mol Cell Cardiol.* 1998;30(4):783-93.
480. Po SS, Wang DW, Yang IC, Johnson JP, Jr., Nie L, Bennett PB. Modulation of HERG potassium channels by extracellular magnesium and quinidine. *J Cardiovasc Pharmacol.* 1999;33(2):181-5.
481. Harris K, Aylott M, Cui Y, Louttit JB, McMahon NC, Sridhar A. Comparison of electrophysiological data from human-induced pluripotent stem cell-derived cardiomyocytes to functional preclinical safety assays. *Toxicol Sci.* 2013;134(2):412-26.
482. Antzelevitch C, Belardinelli L, Wu L, Fraser H, Zygmunt AC, Burashnikov A, et al. Electrophysiologic properties and antiarrhythmic actions of a novel antianginal agent. *J Cardiovasc Pharmacol Ther.* 2004;9 Suppl 1:S65-83.
483. Undrovinas AI, Belardinelli L, Undrovinas NA, Sabbah HN. Ranolazine improves abnormal repolarization and contraction in left ventricular myocytes of dogs with heart failure by inhibiting late sodium current. *J Cardiovasc Electrophysiol.* 2006;17 Suppl 1:S169-S77.
484. Fredj S, Sampson KJ, Liu H, Kass RS. Molecular basis of ranolazine block of LQT-3 mutant sodium channels: evidence for site of action. *Br J Pharmacol.* 2006;148(1):16-24.

485. Rajamani S, El-Bizri N, Shryock JC, Makielski JC, Belardinelli L. Use-dependent block of cardiac late Na<sup>+</sup> current by ranolazine. *Heart Rhythm*. 2009;6(11):1625-31.
486. Zygmunt AC, Nesterenko VV, Rajamani S, Hu D, Barajas-Martinez H, Belardinelli L, et al. Mechanisms of atrial-selective block of Na<sup>+</sup> channels by ranolazine: I. Experimental analysis of the use-dependent block. *Am J Physiol Heart Circ Physiol*. 2011;301(4):H1606-14.
487. Wu L, Rajamani S, Li H, January CT, Shryock JC, Belardinelli L. Reduction of repolarization reserve unmasks the proarrhythmic role of endogenous late Na<sup>+</sup> current in the heart. *Am J Physiol Heart Circ Physiol*. 2009;297(3):H1048-57.
488. Jia S, Lian J, Guo D, Xue X, Patel C, Yang L, et al. Modulation of the late sodium current by ATX-II and ranolazine affects the reverse use-dependence and proarrhythmic liability of I<sub>Kr</sub> blockade. *Br J Pharmacol*. 2011;164(2):308-16.
489. Soliman D, Wang L, Hamming KS, Yang W, Fatehi M, Carter CC, et al. Late sodium current inhibition alone with ranolazine is sufficient to reduce ischemia- and cardiac glycoside-induced calcium overload and contractile dysfunction mediated by reverse-mode sodium/calcium exchange. *J Pharmacol Exp Ther*. 2012;343(2):325-32.
490. Verrier RL, Kumar K, Nieminen T, Belardinelli L. Mechanisms of ranolazine's dual protection against atrial and ventricular fibrillation. *Europace*. 2013;15(3):317-24.
491. Wettwer E, Christ T, Endig S, Rozmaritsa N, Matschke K, Lynch JJ, et al. The new antiarrhythmic drug vernakalant: ex vivo study of human atrial tissue from sinus rhythm and chronic atrial fibrillation. *Cardiovasc Res*. 2013;98(1):145-54.
492. Savelieva I, Graydon R, Camm AJ. Pharmacological cardioversion of atrial fibrillation with vernakalant: evidence in support of the ESC Guidelines. *Europace*. 2014;16(2):162-73.
493. Enomoto K, Imoto M, Nagashima R, Kaneko T, Maruyama T, Kaji Y, et al. Effects of ajmaline on non-sodium ionic currents in guinea pig ventricular myocytes. *Jpn Heart J*. 1995;36(4):465-76.
494. Takanaka C, Sarma JS, Singh BN. Electrophysiologic effects of ambasilide (LU 47110), a novel class III antiarrhythmic agent, on the properties of isolated rabbit and canine cardiac muscle. *J Cardiovasc Pharmacol*. 1992;19(2):290-8.
495. Hara Y, Nakaya H. SD-3212, a new class I and IV antiarrhythmic drug: a potent inhibitor of the muscarinic acetylcholine-receptor-operated potassium current in guinea-pig atrial cells. *Br J Pharmacol*. 1995;116(6):2750-6.
496. Kato R, Singh BN. Effects of bepridil on the electrophysiologic properties of isolated canine and rabbit myocardial fibers. *Am Heart J*. 1986;111(2):271-9.
497. Anno T, Furuta T, Itho M, Kodama I, Toyama J, Yamada K. Effects of bepridil on the electrophysiological properties of guinea-pig ventricular muscles. *Br J Pharmacol*. 1984;81(4):589-97.
498. Lathrop DA, Murphy AM, Humphreys T, Schwartz A. Effects of bepridil on force development and transmembrane electrical activity of adult canine Purkinje strands: comparison with nisoldipine and lidocaine. *Eur J Pharmacol*. 1985;118(3):283-92.
499. Satoh H, Ishii M, Hashimoto K. Effect of cibenzoline, a class I antiarrhythmic drug, on action potential in canine ventricular muscle. *Jpn J Pharmacol*. 1987;44(2):113-9.

## References

500. Lacroix D, Delfaut P, Adamantidis M, Cardinal R, Klug D, Kacet S, et al. Differential effects of quinidine, flecainide, and cibenzoline on anisotropic conduction in the isolated porcine heart. *J Cardiovasc Electrophysiol.* 1998;9(1):55-69.
501. Mirro MJ, Watanabe AM, Bailey JC. Electrophysiological effects of disopyramide and quinidine on guinea pig atria and canine cardiac purkinje fibers. Dependence on underlying cholinergic tone. *Circ Res.* 1980;46(5):660-8.
502. Kus T, Sasyniuk BI. Electrophysiological actions of disopyramide phosphate on canine ventricular muscle and purkinje fibers. *Circ Res.* 1975;37(6):844-54.
503. Mirro MJ, Watanabe AM, Bailey JC. Electrophysiological effects of the optical isomers of disopyramide and quinidine in the dog. Dependence on stereochemistry. *Circ Res.* 1981;48(6 Pt 1):867-74.
504. Nakajima H, Hoshiyama M, Yamashita K, Kiyomoto A. Effect of diltiazem on electrical and mechanical activity of isolated cardiac ventricular muscle of guinea pig. *Jpn J Pharmacol.* 1975;25(4):383-92.
505. Lathrop DA, Valle-Aguilera JR, Millard RW, Gaum WE, Hannon DW, Francis PD, et al. Comparative electrophysiologic and coronary hemodynamic effects of diltiazem, nisoldipine and verapamil on myocardial tissue. *Am J Cardiol.* 1982;49(3):613-20.
506. Moro S, Ferreiro M, Celestino D, Medei E, Elizari MV, Sicouri S. In vitro effects of acute amiodarone and dronedarone on epicardial, endocardial, and M cells of the canine ventricle. *J Cardiovasc Pharmacol Ther.* 2007;12(4):314-21.
507. Varro A, Balati B, Iost N, Takacs J, Virag L, Lathrop DA, et al. The role of the delayed rectifier component  $I_{Ks}$  in dog ventricular muscle and Purkinje fibre repolarization. *J Physiol.* 2000;523 Pt 1:67-81.
508. Yue L, Feng J, Li GR, Nattel S. Transient outward and delayed rectifier currents in canine atrium: properties and role of isolation methods. *Am J Physiol.* 1996;270(6 Pt 2):H2157-68.
509. Ikeda N, Singh BN, Davis LD, Hauswirth O. Effects of flecainide on the electrophysiologic properties of isolated canine and rabbit myocardial fibers. *J Am Coll Cardiol.* 1985;5(2 Pt 1):303-10.
510. Lee KS, Tsai TD, Lee EW. Membrane activity of class III antiarrhythmic compounds; a comparison between ibutilide, d-sotalol, E-4031, sematilide and dofetilide. *Eur J Pharmacol.* 1993;234(1):43-53.
511. Lee KS, Lee EW. Ionic mechanism of ibutilide in human atrium: evidence for a drug-induced  $Na^+$  current through a nifedipine inhibited inward channel. *J Pharmacol Exp Ther.* 1998;286(1):9-22.
512. Bigger JT, Jr., Mandel WJ. Effect of lidocaine on the electrophysiological properties of ventricular muscle and purkinje fibers. *J Clin Invest.* 1970;49(1):63-77.
513. Spinelli W, Rosen MR. Frequency-dependent actions of phenytoin in adult and young canine Purkinje fibers. *J Pharmacol Exp Ther.* 1986;238(3):794-801.
514. Lee RJ, Liem LB, Cohen TJ, Franz MR. Relation between repolarization and refractoriness in the human ventricle: cycle length dependence and effect of procainamide. *J Am Coll Cardiol.* 1992;19(3):614-8.
515. Rosen MR, Gelband H, Hoffman BF. Canine electrocardiographic and cardiac electrophysiologic changes induced by procainamide. *Circulation.* 1972;46(3):528-36.

516. Thompson KA, Iansmith DH, Siddoway LA, Woosley RL, Roden DM. Potent electrophysiologic effects of the major metabolites of propafenone in canine Purkinje fibers. *J Pharmacol Exp Ther.* 1988;244(3):950-5.
517. Zaza A, Malfatto G, Schwartz PJ. Diverse electrophysiologic effects of propafenone and flecainide in canine Purkinje fibers: implications for antiarrhythmic drug classification. *J Pharmacol Exp Ther.* 1994;269(1):336-43.
518. Malfatto G, Zaza A, Forster M, Sadowick B, Danilo P, Jr., Rosen MR. Electrophysiologic, inotropic and antiarrhythmic effects of propafenone, 5-hydroxypropafenone and N-depropylpropafenone. *J Pharmacol Exp Ther.* 1988;246(2):419-26.
519. Burashnikov A, Belardinelli L, Antzelevitch C. Atrial-selective sodium channel block strategy to suppress atrial fibrillation: ranolazine versus propafenone. *J Pharmacol Exp Ther.* 2012;340(1):161-8.
520. Wang ZG, Pelletier LC, Talajic M, Nattel S. Effects of flecainide and quinidine on human atrial action potentials. Role of rate-dependence and comparison with guinea pig, rabbit, and dog tissues. *Circulation.* 1990;82(1):274-83.
521. Merot J, Charpentier F, Poirier JM, Coutris G, Weissenburger J. Effects of chronic treatment by amiodarone on transmural heterogeneity of canine ventricular repolarization in vivo: interactions with acute sotalol. *Cardiovasc Res.* 1999;44(2):303-14.
522. Kato R, Ikeda N, Yabek SM, Kannan R, Singh BN. Electrophysiologic effects of the levo- and dextrorotatory isomers of sotalol in isolated cardiac muscle and their in vivo pharmacokinetics. *J Am Coll Cardiol.* 1986;7(1):116-25.
523. Burashnikov A, Pourrier M, Gibson JK, Lynch JJ, Antzelevitch C. Rate-dependent effects of vernakalant in the isolated non-remodeled canine left atria are primarily due to block of the sodium channel: comparison with ranolazine and dl-sotalol. *Circ Arrhythm Electrophysiol.* 2012;5(2):400-8.
524. Frommeyer G, Milberg P, Clauss C, Schmidt M, Ramtin S, Kaese S, et al. Electrophysiological profile of vernakalant in an experimental whole-heart model: the absence of proarrhythmia despite significant effect on myocardial repolarization. *Europace.* 2014;16(8):1240-8.
525. Heijman J, Algalarrondo V, Voigt N, Melka J, Wehrens XH, Dobrev D, et al. The value of basic research insights into atrial fibrillation mechanisms as a guide to therapeutic innovation: a critical analysis. *Cardiovasc Res.* 2016;109(4):467-79.
526. Anno T, Hondeghem LM. Interactions of flecainide with guinea pig cardiac sodium channels. Importance of activation unblocking to the voltage dependence of recovery. *Circ Res.* 1990;66(3):789-803.
527. Ramos E, O'Leary M E. State-dependent trapping of flecainide in the cardiac sodium channel. *J Physiol.* 2004;560(Pt 1):37-49.
528. Peralta AO, John RM, Gaasch WH, Taggart PI, Martin DT, Venditti FJ. The class III antiarrhythmic effect of sotalol exerts a reverse use-dependent positive inotropic effect in the intact canine heart. *J Am Coll Cardiol.* 2000;36(4):1404-10.
529. Rocchetti M, Besana A, Gurrola GB, Possani LD, Zaza A. Rate dependency of delayed rectifier currents during the guinea-pig ventricular action potential. *J Physiol.* 2001;534(Pt 3):721-32.
530. Jurkiewicz NK, Sanguinetti MC. Rate-dependent prolongation of cardiac action potentials by a methanesulfonanilide class III antiarrhythmic agent. Specific

## References

- block of rapidly activating delayed rectifier K<sup>+</sup> current by dofetilide. *Circ Res*. 1993;72(1):75-83.
531. Banyasz T, Horvath B, Virag L, Barandi L, Szentandrassy N, Harmati G, et al. Reverse rate dependency is an intrinsic property of canine cardiac preparations. *Cardiovasc Res*. 2009;84(2):237-44.
532. Kirchhof P, Benussi S, Kotecha D, Ahlsson A, Atar D, Casadei B, et al. 2016 ESC Guidelines for the management of atrial fibrillation developed in collaboration with EACTS. *Europace*. 2016;18(11):1609-78.
533. January CT, Wann LS, Alpert JS, Calkins H, Cigarroa JE, Cleveland JC, Jr., et al. 2014 AHA/ACC/HRS guideline for the management of patients with atrial fibrillation: executive summary: a report of the American College of Cardiology/American Heart Association Task Force on practice guidelines and the Heart Rhythm Society. *Circulation*. 2014;130(23):2071-104.
534. Chang TY, Liao JN, Chao TF, Vicera JJ, Lin CY, Tuan TC, et al. Oral anticoagulant use for stroke prevention in atrial fibrillation patients with difficult scenarios. *Int J Cardiol Heart Vasc*. 2018;20:56-62.
535. Heist EK, Ruskin JN. Drug-induced arrhythmia. *Circulation*. 2010;122(14):1426-35.
536. Elshrif MM, Shi P, Cherry EM. Representing variability and transmural differences in a model of human heart failure. *IEEE J Biomed Health Inform*. 2015;19(4):1308-20.
537. Sasaki N, Watanabe I, Kogawa R, Sonoda K, Takahashi K, Okumura Y, et al. Effects of intravenous amiodarone and ibutilide on action potential duration and atrial conduction kinetics in patients with persistent atrial fibrillation. *Int Heart J*. 2014;55(3):244-8.
538. Shinagawa K, Shiroshita-Takeshita A, Schram G, Nattel S. Effects of antiarrhythmic drugs on fibrillation in the remodeled atrium: insights into the mechanism of the superior efficacy of amiodarone. *Circulation*. 2003;107(10):1440-6.
539. Walker MJ. Antiarrhythmic drug research. *Br J Pharmacol*. 2006;147 Suppl 1:S222-31.
540. Goette A, Hindricks G, Dagues N, Deharo J-C, Dobrev D, Hatala R, et al. EHRA White Paper: knowledge gaps in arrhythmia management—status 2019. 2019.
541. Moreno JD, Clancy CE. Using computational modeling to predict arrhythmogenesis and antiarrhythmic therapy. *Drug Discov Today Dis Models*. 2009;6(3):71-84.
542. Chiamvimonvat N, Chen-Izu Y, Clancy CE, Deschenes I, Dobrev D, Heijman J, et al. Potassium currents in the heart: functional roles in repolarization, arrhythmia and therapeutics. *J Physiol*. 2017;595(7):2229-52.
543. Grunnet M, Bentzen BH, Sorensen US, Diness JG. Cardiac ion channels and mechanisms for protection against atrial fibrillation. *Rev Physiol Biochem Pharmacol*. 2012;162:1-58.
544. Christophe B, Crumb WJ, Jr. Impact of disease state on arrhythmic event detection by action potential modelling in cardiac safety pharmacology. *J Pharmacol Toxicol Methods*. 2018;96:15-26.
545. Morrison TM, Pathmanathan P, Adwan M, Margerrison E. Advancing Regulatory Science With Computational Modeling for Medical Devices at the FDA's Office of Science and Engineering Laboratories. *Front Med (Lausanne)*. 2018;5:241.

546. Boyle PM, Hakim JB, Zahid S, Franceschi WH, Murphy MJ, Prakosa A, et al. The Fibrotic Substrate in Persistent Atrial Fibrillation Patients: Comparison Between Predictions From Computational Modeling and Measurements From Focal Impulse and Rotor Mapping. *Front Physiol.* 2018;9:1151.
547. Vandenberg JI, Varghese A, Lu Y, Bursill JA, Mahaut-Smith MP, Huang CL. Temperature dependence of human ether-a-go-go-related gene K<sup>+</sup> currents. *Am J Physiol Cell Physiol.* 2006;291(1):C165-75.
548. Li Z, Dutta S, Sheng J, Tran PN, Wu W, Colatsky T. A temperature-dependent in silico model of the human ether-a-go-go-related (hERG) gene channel. *J Pharmacol Toxicol Methods.* 2016;81:233-9.
549. Lin C, Cvetanovic I, Ke X, Ranade V, Somberg J. A mechanism for the potential proarrhythmic effect of acidosis, bradycardia, and hypokalemia on the blockade of human ether-a-go-go-related gene (HERG) channels. *Am J Ther.* 2005;12(4):328-36.
550. Li Z, Dutta S, Sheng J, Tran PN, Wu W, Chang K, et al. Improving the In Silico Assessment of Proarrhythmia Risk by Combining hERG (Human Ether-a-go-go-Related Gene) Channel-Drug Binding Kinetics and Multichannel Pharmacology. *Circ Arrhythm Electrophysiol.* 2017;10(2):e004628.
551. Ellinwood N, Dobrev D, Morotti S, Grandi E. Revealing kinetics and state-dependent binding properties of I<sub>Kur</sub>-targeting drugs that maximize atrial fibrillation selectivity. *Chaos.* 2017;27(9):093918.
552. Roubille F, Tardif JC. New therapeutic targets in cardiology: heart failure and arrhythmia: HCN channels. *Circulation.* 2013;127(19):1986-96.
553. Watanabe H, Murakami M, Ohba T, Takahashi Y, Ito H. TRP channel and cardiovascular disease. *Pharmacol Ther.* 2008;118(3):337-51.
554. Glasscock E, Voigt N, McCauley MD, Sun Q, Li N, Chiang DY, et al. Expression and function of Kv1.1 potassium channels in human atria from patients with atrial fibrillation. *Basic Res Cardiol.* 2015;110(5):505.
555. Ravens U. Atrial-selective K<sup>+</sup> channel blockers: potential antiarrhythmic drugs in atrial fibrillation? *Can J Physiol Pharmacol.* 2017;95(11):1313-8.
556. Hashimoto N, Yamashita T, Tsuruzoe N. Characterization of in vivo and in vitro electrophysiological and antiarrhythmic effects of a novel I<sub>KACH</sub> blocker, NIP-151: a comparison with an I<sub>Kr</sub>-blocker dofetilide. *Journal of cardiovascular pharmacology.* 2008;51(2):162-9.
557. Ehrlich JR, Nattel S. Atrial-selective pharmacological therapy for atrial fibrillation: hype or hope? *Current opinion in cardiology.* 2009;24(1):50-5.
558. Linz D, Elliott AD, Hohl M, Malik V, Schotten U, Dobrev D, et al. Role of autonomic nervous system in atrial fibrillation. *Int J Cardiol.* 2018.
559. Guasch E, Benito B, Qi X, Cifelli C, Naud P, Shi Y, et al. Atrial fibrillation promotion by endurance exercise: demonstration and mechanistic exploration in an animal model. *J Am Coll Cardiol.* 2013;62(1):68-77.
560. Wenzel DG, Kleoppel JW. Arrhythmias induced by changing the medium of cultured rat heart muscle cells: A model for assessment of antiarrhythmic agents. *Journal of Pharmacological Methods.* 1978;1(3):269-76.
561. Members of the Sicilian G. New approaches to antiarrhythmic therapy: emerging therapeutic applications of the cell biology of cardiac arrhythmias(1). *Cardiovasc Res.* 2001;52(3):345-60.

## References

562. Molina CE, Heijman J, Dobrev D. Differences in Left Versus Right Ventricular Electrophysiological Properties in Cardiac Dysfunction and Arrhythmogenesis. *Arrhythm Electrophysiol Rev.* 2016;5(1):14-9.
563. Woo SK, Kang WK, Kwon KI. Pharmacokinetic and pharmacodynamic modeling of the antiplatelet and cardiovascular effects of cilostazol in healthy humans. *Clin Pharmacol Ther.* 2002;71(4):246-52.
564. Tylutki Z, Polak S. A four-compartment PBPK heart model accounting for cardiac metabolism - model development and application. *Sci Rep.* 2017;7:39494.
565. Nicola M, Alsafi Z, Sohrabi C, Kerwan A, Al-Jabir A, Iosifidis C, et al. The socio-economic implications of the coronavirus pandemic (COVID-19): A review. *Int J Surg.* 2020;78:185-93.
566. Wang Y, Zhang D, Du G, Du R, Zhao J, Jin Y, et al. Remdesivir in adults with severe COVID-19: a randomised, double-blind, placebo-controlled, multicentre trial. *Lancet.* 2020;395(10236):1569-78.
567. Caly L, Druce JD, Catton MG, Jans DA, Wagstaff KM. The FDA-approved drug ivermectin inhibits the replication of SARS-CoV-2 in vitro. *Antiviral Res.* 2020;178:104787.
568. Lu CC, Chen MY, Lee WS, Chang YL. Potential therapeutic agents against COVID-19: What we know so far. *J Chin Med Assoc.* 2020;83(6):534-6.
569. Gao J, Tian Z, Yang X. Breakthrough: Chloroquine phosphate has shown apparent efficacy in treatment of COVID-19 associated pneumonia in clinical studies. *Biosci Trends.* 2020;14(1):72-3.
570. Colson P, Rolain JM, Lagier JC, Brouqui P, Raoult D. Chloroquine and hydroxychloroquine as available weapons to fight COVID-19. *Int J Antimicrob Agents.* 2020;55(4):105932.
571. Huang M, Tang T, Pang P, Li M, Ma R, Lu J, et al. Treating COVID-19 with Chloroquine. *J Mol Cell Biol.* 2020;12(4):322-5.
572. Arshad S, Kilgore P, Chaudhry ZS, Jacobsen G, Wang DD, Huitsing K, et al. Treatment with hydroxychloroquine, azithromycin, and combination in patients hospitalized with COVID-19. *Int J Infect Dis.* 2020;97:396-403.
573. Mehra MR, Desai SS, Ruschitzka F, Patel AN. RETRACTED: Hydroxychloroquine or chloroquine with or without a macrolide for treatment of COVID-19: a multinational registry analysis. *Lancet.* 2020.
574. Molina JM, Delaugerre C, Le Goff J, Mela-Lima B, Ponscarne D, Goldwirt L, et al. No evidence of rapid antiviral clearance or clinical benefit with the combination of hydroxychloroquine and azithromycin in patients with severe COVID-19 infection. *Med Mal Infect.* 2020;50(4):384.
575. Borba MGS, Val FFA, Sampaio VS, Alexandre MAA, Melo GC, Brito M, et al. Effect of High vs Low Doses of Chloroquine Diphosphate as Adjunctive Therapy for Patients Hospitalized With Severe Acute Respiratory Syndrome Coronavirus 2 (SARS-CoV-2) Infection: A Randomized Clinical Trial. *JAMA Netw Open.* 2020;3(4):e208857.
576. Atkinson JG. Problems with the analysis in "Treatment with Hydroxychloroquine, Azithromycin, and Combination in Patients Hospitalized with COVID-19". *Int J Infect Dis.* 2020;99:37.
577. Varisco TJ, Johnson ML, Thornton D. Comment on Arshad et al: Treatment with Hydroxychloroquine, Azithromycin, and Combination in Patients Hospitalized with COVID-19. *Int J Infect Dis.* 2020.

578. Uzelac I, Irvanian S, Ashikaga H, Bhatia NK, Herndon C, Kaboudian A, et al. Fatal arrhythmias: Another reason why doctors remain cautious about chloroquine/hydroxychloroquine for treating COVID-19. *Heart Rhythm*. 2020.
579. Singh AK, Singh A, Shaikh A, Singh R, Misra A. Chloroquine and hydroxychloroquine in the treatment of COVID-19 with or without diabetes: A systematic search and a narrative review with a special reference to India and other developing countries. *Diabetes Metab Syndr*. 2020;14(3):241-6.
580. Roden DM, Harrington RA, Poppas A, Russo AM. Considerations for Drug Interactions on QTc in Exploratory COVID-19 Treatment. *Circulation*. 2020;141(24):e906-e7.
581. Fossa AA, Wisialowski T, Duncan JN, Deng S, Dunne M. Azithromycin/chloroquine combination does not increase cardiac instability despite an increase in monophasic action potential duration in the anesthetized guinea pig. *Am J Trop Med Hyg*. 2007;77(5):929-38.
582. van den Broek MPH, Mohlmann JE, Abeln BGS, Liebrechts M, van Dijk VF, van de Garde EMW. Chloroquine-induced QTc prolongation in COVID-19 patients. *Neth Heart J*. 2020.
583. Saleh M, Gabriels J, Chang D, Soo Kim B, Mansoor A, Mahmood E, et al. Effect of Chloroquine, Hydroxychloroquine, and Azithromycin on the Corrected QT Interval in Patients With SARS-CoV-2 Infection. *Circ Arrhythm Electrophysiol*. 2020;13(6):e008662.
584. Chorin E, Wadhvani L, Magnani S, Dai M, Shulman E, Nadeau-Routhier C, et al. QT interval prolongation and torsade de pointes in patients with COVID-19 treated with hydroxychloroquine/azithromycin. *Heart Rhythm*. 2020;17(9):1425-33.
585. Jankelson L, Karam G, Becker ML, Chinitz LA, Tsai MC. QT prolongation, torsades de pointes, and sudden death with short courses of chloroquine or hydroxychloroquine as used in COVID-19: A systematic review. *Heart Rhythm*. 2020;17(9):1472-9.
586. Bhatla A, Mayer MM, Adusumalli S, Hyman MC, Oh E, Tierney A, et al. COVID-19 and Cardiac Arrhythmias. *Heart Rhythm*. 2020.
587. Lazzerini PE, Boutjdir M, Capecchi PL. COVID-19, Arrhythmic Risk and Inflammation: Mind the Gap! *Circulation*. 2020.
588. Murphy KR, Baggett B, Cooper LL, Lu Y, J OU, Sedivy JM, et al. Enhancing Autophagy Diminishes Aberrant Ca<sup>2+</sup> Homeostasis and Arrhythmogenesis in Aging Rabbit Hearts. *Front Physiol*. 2019;10:1277.
589. Adameova A, Shah AK, Dhalla NS. Role of Oxidative Stress in the Genesis of Ventricular Arrhythmias. *Int J Mol Sci*. 2020;21(12).
590. Wang Q, Quick AP, Cao S, Reynolds J, Chiang DY, Beavers D, et al. Oxidized CaMKII (Ca<sup>2+</sup>/Calmodulin-Dependent Protein Kinase II) Is Essential for Ventricular Arrhythmia in a Mouse Model of Duchenne Muscular Dystrophy. *Circ Arrhythm Electrophysiol*. 2018;11(4):e005682.
591. Swaminathan PD, Purohit A, Hund TJ, Anderson ME. Calmodulin-dependent protein kinase II: linking heart failure and arrhythmias. *Circ Res*. 2012;110(12):1661-77.
592. Monnerat G, Alarcon ML, Vasconcellos LR, Hochman-Mendez C, Brasil G, Bassani RA, et al. Macrophage-dependent IL-1beta production induces cardiac arrhythmias in diabetic mice. *Nat Commun*. 2016;7:13344.

## References

593. Shah A. Novel Coronavirus-Induced NLRP3 Inflammasome Activation: A Potential Drug Target in the Treatment of COVID-19. *Front Immunol.* 2020;11:1021.
594. Nishiga M, Wang DW, Han Y, Lewis DB, Wu JC. COVID-19 and cardiovascular disease: from basic mechanisms to clinical perspectives. *Nat Rev Cardiol.* 2020;17(9):543-58.
595. Li Z, Mirams GR, Yoshinaga T, Ridder BJ, Han X, Chen JE, et al. General Principles for the Validation of Proarrhythmia Risk Prediction Models: An Extension of the CiPA In Silico Strategy. *Clin Pharmacol Ther.* 2020;107(1):102-11.
596. Ridder BJ, Leishman DJ, Bridgland-Taylor M, Samieegohar M, Han X, Wu WW, et al. A systematic strategy for estimating hERG block potency and its implications in a new cardiac safety paradigm. *Toxicol Appl Pharmacol.* 2020;394:114961.
597. Qu Y, Vargas H, Rodriguez B, Zhou X, Passini E, Liu Y, et al. Pro-arrhythmic risk assessment with a population model of human ventricular myocyte action potentials. *J Pharmacol Toxicol Methods.* 2019;99:106595.
598. O'Hara T, Rudy Y. Arrhythmia formation in subclinical ("silent") long QT syndrome requires multiple insults: quantitative mechanistic study using the KCNQ1 mutation Q357R as example. *Heart Rhythm.* 2012;9(2):275-82.
599. Gong JQX, Susilo ME, Sher A, Musante CJ, Sobie EA. Quantitative analysis of variability in an integrated model of human ventricular electrophysiology and beta-adrenergic signaling. *J Mol Cell Cardiol.* 2020;143:96-106.
600. Wang M, Cao R, Zhang L, Yang X, Liu J, Xu M, et al. Remdesivir and chloroquine effectively inhibit the recently emerged novel coronavirus (2019-nCoV) in vitro. *Cell Res.* 2020;30(3):269-71.
601. Gielen V, Johnston SL, Edwards MR. Azithromycin induces anti-viral responses in bronchial epithelial cells. *Eur Respir J.* 2010;36(3):646-54.
602. Anyukhovskiy EP, Sosunov EA, Rosen MR. Regional differences in electrophysiological properties of epicardium, midmyocardium, and endocardium. In vitro and in vivo correlations. *Circulation.* 1996;94(8):1981-8.
603. Sutanto H, Laudy L, Clerx M, Dobrev D, Crijns H, Heijman J. Maastricht antiarrhythmic drug evaluator (MANTA): A computational tool for better understanding of antiarrhythmic drugs. *Pharmacol Res.* 2019;148:104444.
604. O'Hara T, Rudy Y. Quantitative comparison of cardiac ventricular myocyte electrophysiology and response to drugs in human and nonhuman species. *Am J Physiol Heart Circ Physiol.* 2012;302(5):H1023-30.
605. Weiss JN, Garfinkel A, Karagueuzian HS, Chen PS, Qu Z. Early afterdepolarizations and cardiac arrhythmias. *Heart Rhythm.* 2010;7(12):1891-9.
606. Mercurio NJ, Yen CF, Shim DJ, Maher TR, McCoy CM, Zimetbaum PJ, et al. Risk of QT Interval Prolongation Associated With Use of Hydroxychloroquine With or Without Concomitant Azithromycin Among Hospitalized Patients Testing Positive for Coronavirus Disease 2019 (COVID-19). *JAMA Cardiol.* 2020.
607. Don Michael TA, Ai-wazzadeh S. The effects of acute chloroquine poisoning with special reference to the heart. *Am Heart J.* 1970;79(6):831-42.
608. Jaeger A, Raguin O, Liegeon MN. Acute poisoning by class I anti-arrhythmia agents and by chloroquine. *Rev Prat.* 1997;47(7):748-53.
609. Buckley NA, Smith AJ, Dosen P, O'Connell DL. Effects of catecholamines and diazepam in chloroquine poisoning in barbiturate anaesthetised rats. *Hum Exp Toxicol.* 1996;15(11):909-14.

610. Sofola OA. The effects of chloroquine on the electrocardiogram and heart rate in anaesthetized dogs. *Clin Physiol*. 1983;3(1):75-82.
611. Johnson DM, Heijman J, Bode EF, Greensmith DJ, van der Linde H, Abi-Gerges N, et al. Diastolic spontaneous calcium release from the sarcoplasmic reticulum increases beat-to-beat variability of repolarization in canine ventricular myocytes after beta-adrenergic stimulation. *Circ Res*. 2013;112(2):246-56.
612. Bartos DC, Giudicessi JR, Tester DJ, Ackerman MJ, Ohno S, Horie M, et al. A KCNQ1 mutation contributes to the concealed type 1 long QT phenotype by limiting the Kv7.1 channel conformational changes associated with protein kinase A phosphorylation. *Heart Rhythm*. 2014;11(3):459-68.
613. Heijman J, Spatjens RL, Seyen SR, Lentink V, Kuijpers HJ, Boulet IR, et al. Dominant-negative control of cAMP-dependent  $I_{Ks}$  upregulation in human long-QT syndrome type 1. *Circ Res*. 2012;110(2):211-9.
614. Boczek NJ, Miller EM, Ye D, Nesterenko VV, Tester DJ, Antzelevitch C, et al. Novel Timothy syndrome mutation leading to increase in CACNA1C window current. *Heart Rhythm*. 2015;12(1):211-9.
615. Scheuer J. Catecholamines in cardiac hypertrophy. *Am J Cardiol*. 1999;83(12A):70H-4H.
616. Dang S, Zhang ZY, Li KL, Zheng J, Qian LL, Liu XY, et al. Blockade of beta-adrenergic signaling suppresses inflammasome and alleviates cardiac fibrosis. *Ann Transl Med*. 2020;8(4):127.
617. Sutanto H, Heijman J. Beta-adrenergic receptor stimulation modulates the cellular proarrhythmic effects of chloroquine and azithromycin. *Frontiers in Physiology*. 2020;11:587709.
618. van Gorp PRR, Trines SA, Pijnappels DA, de Vries AAF. Multicellular In vitro Models of Cardiac Arrhythmias: Focus on Atrial Fibrillation. *Front Cardiovasc Med*. 2020;7:43.
619. Libbus I, Wan X, Rosenbaum DS. Electrotonic load triggers remodeling of repolarizing current  $I_{to}$  in ventricle. *Am J Physiol Heart Circ Physiol*. 2004;286(5):H1901-9.
620. Salama G, Hwang SM. Simultaneous optical mapping of intracellular free calcium and action potentials from Langendorff perfused hearts. *Curr Protoc Cytom*. 2009;Chapter 12:Unit 12 7.
621. Jaimes R, 3rd, McCullough D, Siegel B, Swift L, Hiebert J, McLnerney D, et al. Lights, camera, path splitter: a new approach for truly simultaneous dual optical mapping of the heart with a single camera. *BMC Biomed Eng*. 2019;1.
622. Lee P, Calvo CJ, Alfonso-Almazan JM, Quintanilla JG, Chorro FJ, Yan P, et al. Low-Cost Optical Mapping Systems for Panoramic Imaging of Complex Arrhythmias and Drug-Action in Translational Heart Models. *Sci Rep*. 2017;7:43217.
623. Jones JS, Small DM, Nishimura N. In Vivo Calcium Imaging of Cardiomyocytes in the Beating Mouse Heart With Multiphoton Microscopy. *Front Physiol*. 2018;9:969.
624. Lee P, Taghavi F, Yan P, Ewart P, Ashley EA, Loew LM, et al. In situ optical mapping of voltage and calcium in the heart. *PLoS One*. 2012;7(8):e42562.
625. Kim J, Park S, Lee C, Kim JY, Kim C. Organic Nanostructures for Photoacoustic Imaging. *Chemnanomat*. 2016;2(3):156-66.

## References

626. Clauss S, Bleyer C, Schuttler D, Tomsits P, Renner S, Klymiuk N, et al. Animal models of arrhythmia: classic electrophysiology to genetically modified large animals. *Nat Rev Cardiol.* 2019;16(8):457-75.
627. Whittaker DG, Clerx M, Lei CL, Christini DJ, Mirams GR. Calibration of ionic and cellular cardiac electrophysiology models. *Wiley Interdiscip Rev Syst Biol Med.* 2020;12(4):e1482.
628. Ahrens-Nicklas RC, Christini DJ. Anthropomorphizing the mouse cardiac action potential via a novel dynamic clamp method. *Biophys J.* 2009;97(10):2684-92.
629. Mackiewicz U, Lewartowski B. Temperature dependent contribution of  $Ca^{2+}$  transporters to relaxation in cardiac myocytes: important role of sarcolemmal  $Ca^{2+}$ -ATPase. *J Physiol Pharmacol.* 2006;57(1):3-15.
630. Fu Y, Zhang GQ, Hao XM, Wu CH, Chai Z, Wang SQ. Temperature dependence and thermodynamic properties of  $Ca^{2+}$  sparks in rat cardiomyocytes. *Biophys J.* 2005;89(4):2533-41.
631. Muszkiewicz A, Britton OJ, Gemmell P, Passini E, Sanchez C, Zhou X, et al. Variability in cardiac electrophysiology: Using experimentally-calibrated populations of models to move beyond the single virtual physiological human paradigm. *Prog Biophys Mol Biol.* 2016;120(1-3):115-27.
632. Gourdie RG. The Cardiac Gap Junction has Discrete Functions in Electrotonic and Ephaptic Coupling. *Anat Rec.* 2019;302(1):93-100.
633. Mayourian J, Sobie EA, Costa KD. An Introduction to Computational Modeling of Cardiac Electrophysiology and Arrhythmogenicity. *Methods Mol Biol.* 2018;1816:17-35.
634. Lopez-Perez A, Sebastian R, Ferrero JM. Three-dimensional cardiac computational modelling: methods, features and applications. *Biomed Eng Online.* 2015;14:35.
635. Galappaththige SK, Pathmanathan P, Bishop MJ, Gray RA. Effect of Heart Structure on Ventricular Fibrillation in the Rabbit: A Simulation Study. *Front Physiol.* 2019;10:564.
636. Boyle PM, Zghaib T, Zahid S, Ali RL, Deng D, Franceschi WH, et al. Computationally guided personalized targeted ablation of persistent atrial fibrillation. *Nat Biomed Eng.* 2019;3(11):870-9.
637. Prakosa A, Arevalo HJ, Deng D, Boyle PM, Nikolov PP, Ashikaga H, et al. Personalized virtual-heart technology for guiding the ablation of infarct-related ventricular tachycardia. *Nat Biomed Eng.* 2018;2(10):732-40.
638. Virani SS, Alonso A, Benjamin EJ, Bittencourt MS, Callaway CW, Carson AP, et al. Heart Disease and Stroke Statistics-2020 Update: A Report From the American Heart Association. *Circulation.* 2020;141(9):e139-e596.
639. Camm AJ, Savelieva I, Potpara T, Hindriks G, Pison L, Blomstrom-Lundqvist C. The changing circumstance of atrial fibrillation - progress towards precision medicine. *J Intern Med.* 2016;279(5):412-27.
640. Sutanto H, Heijman J. The Role of Calcium in the Human Heart: With Great Power Comes Great Responsibility. *Frontiers for Young Minds.* 2019;7(65).
641. Voigt N, Heijman J, Trausch A, Mintert-Jancke E, Pott L, Ravens U, et al. Impaired  $Na^{+}$ -dependent regulation of acetylcholine-activated inward-rectifier  $K^{+}$  current modulates action potential rate dependence in patients with chronic atrial fibrillation. *J Mol Cell Cardiol.* 2013;61:142-52.



